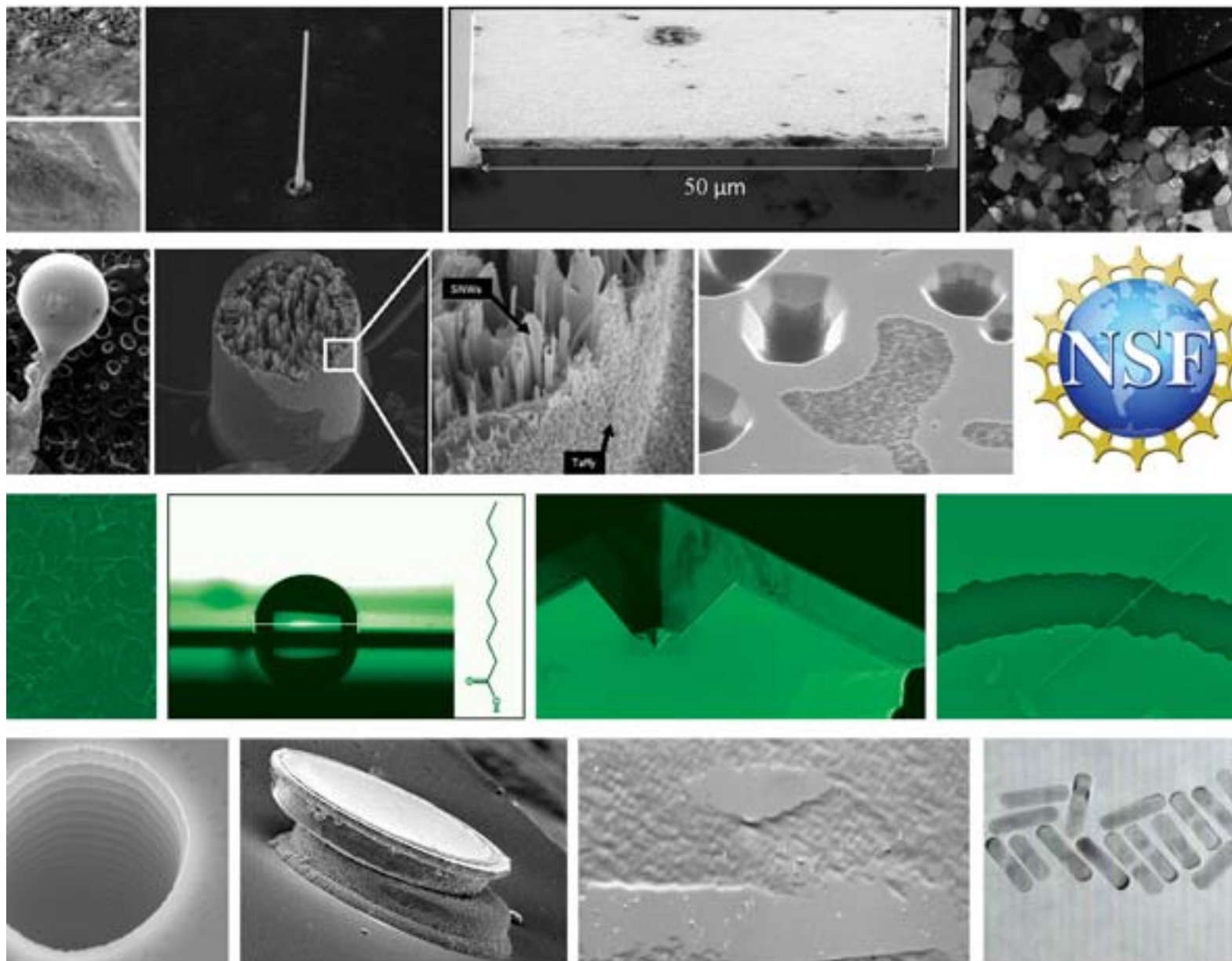


2010 nnin reu research accomplishments



**The National Nanotechnology
Infrastructure Network Research
Experience for Undergraduates Program**

2010 NNIN REU Research Accomplishments

Table of Contents

2010 NNIN REU Reports by Research Focus, pages i-ix

The National Nanotechnology Infrastructure Network Sites, page x

Welcome, Prof. Sandip Tiwari, NNIN Director, page xi

2010 NNIN REU Interns and Coordinators, pages xii-xiii

2010 NNIN Interns, by Site:

Arizona State, page xiv

Cornell, page xiv

Georgia Tech, page xv

Harvard, page xv

Howard, page xvi

Penn State, page xvi

Stanford, page xvii

UCSB, page xvii

University of Colorado, page xviii

University of Michigan, page xviii

University of Minnesota, page xix

University of Texas, page xix

University of Washington, page xx

Washington University, page xix

NNIN iREG Program, page xxi

NNIN iREU Program, page xxi



Biological Applications, pages 2-39

Characterization of dsDNA Binding Protein SlyA for Nanostructure Assembly, page 2

Kathleen Bennett, Biology, Harvey Mudd College

Measurement and Analysis of Blood Platelet Activation within a Microfluidic Device, page 4

Steven Chase, Biomedical Engr. and Biochemistry and Molecular Biology, Rose-Hulman Institute of Technology

Cytotoxicity of Copper Oxide Nanoparticles and Associated Ions on

Human Epithelial Lung Cells (A549), page 6

Sarah Connolly, Microbiology and Cell Science, University of Florida

Characterization of Biomolecular Interactions at the Silicon Photonics Interface, page 8

Lauren Cummings, Chemical Engineering, Oregon State University



Immunomagnetic Detection of Circulating Tumor Cells using a Microfluidic Chip:**Cell Recognition and Analysis, page 10**

Fraser Downing, Mechanical Engineering,
University of Colorado at Boulder

Surface Analysis of DNA Microarrays, page 12

Megan Dunn, Chemical Engineering, University of Arkansas

Electrochemical and Adhesion Properties of PEDOT:PSS**as a Coating for Gold Electrodes for Applications in Metal-Molecule-Metal Junctions, page 14**

Vivian Feig, Chemical Engineering, Columbia University

Portable Diagnostic System for the Purification and Detection of Biomolecules, page 16

Emily Hoffman, Biomedical Engineering,
Case Western Reserve University

Light Dependent Microbial Responses to Cu-doped TiO₂ Nanoparticles, page 18

Kristen Jones, Chemistry, Carthage College

Effect of Deposition Characteristics on Electrochemically Prepared PEDOT Films, page 20

Adam Kozak, Biomedical Engineering, University of Rochester

Nanotherapy for Advanced Cancer Disease, page 22

Christopher Lowe, Chemical Engineering, University of Massachusetts Amherst, page 22

Patterning Neurons with Microcontact**Printing on Silicon Oxide Substrates, page 24**

Margaret Merritt, Biomedical Engineering, Brown University

High Resolution Surface Plasmon Resonance**Microscopy Based Microarray, page 26**

Evan Mirts, Biology and Physics, Truman State University

Synthetic Antiferromagnetic Particles**for Biosensing, page 28**

Kelsey Morse, Chemistry, Beloit College

Plasmonic Nanoparticle Dimer Sensors, page 30

Heidi Nelson, Chemical Engineering, University of Minnesota

Porous Microbeads as Three-Dimensional Scaffolds**for Tissue Engineering, page 32**

Jennifer Wang, Biomedical Engineering, Duke University

**Encapsulation of Single Cells in a Droplet-Based Microfluidic Device, page 34**

Yingxia Wang, Chemical Engineering,
Massachusetts Institute of Technology

Cell Viability and Morphology on Carbon Nanotube Microstructures, page 36

Masaki Watanabe, Applied Chemistry, Nagoya University

Designing Nano-Engineered Substrates to Probe Cell Organization, Motion and Traction Forces, page 38

Erin Watson, Bioengineering, Rice University



Chemistry, pages 40-53

Design of Organic Conductors Comprised of Fullerene and Lanthanum Triple-Decker Porphyrin Complexes, page 40
Mark Borysiak, Chemical and Biomolecular Engr., The Ohio State University

Initial Stages of Tantalum Nitride Atomic Layer Deposition, page 42
John Davis, Department of Chemistry, Carleton College

Synthesis and Characterization of Oxide-Embedded and Surface-Passivated Silicon Nanocrystals, page 44
Hiromasa Fujii, Electrical Engineering, University of Tokyo

Characterization of Dynamics of Solvents Encapsulated in Nano-Scale Volumes, by Selective Enhancement of NMR Signal via Dynamic Nuclear Polarization, page 46
Audrey Hammack, Chemistry, The University of Texas at Tyler

Multimodal Optical and MRI Studies with Multifunctional Spinel Nanoparticles, page 48
Chantalle Le, Chemistry, University of California Los Angeles

Surface Treatments to Control the Wettability of Photonic Crystal Bio-Sensors, page 50
Philip Ponce de Leon, Physics and Mechanical Engineering, New York University, The Stevens Institute of Technology

All-Copper Pillar Interconnects, page 52
Barrett Worley, Chemistry, Samford University



Electronics, pages 54-81

Development of Advanced Carbon Electrodes for use in Microfluidic Vanadium Redox Fuel Cells, page 54
Richard Anger, Mechanical Engineering, SUNY Stony Brook

Ferroelectric Thin Films for Reconfigurable RF Electronics in Next Generation Wireless Communications, page 56
Scott Bakkila, Physics and Computer Science, Lawrence Technological University

Laminated Anodes and Electron Transport Layers in Organic Inverted Bulk Heterojunction Solar Cells, page 58
Lia Bersin, Chemical Engineering, Columbia University

Nanowire Photovoltaics in Photoelectrochemistry and Plasmonic Ring Structures, page 60
Clara Chow, Biomedical Engineering, University of Wisconsin – Madison



Optimization of Ohmic Contacts to III-N Semiconductor Material, page 62*Austin Conner, Electrical Engineering, Vanderbilt University***Heterogeneous Integration of p- and n-type Nanowires****for Complementary Nanowire Circuits, page 64***Zachary Henderson, Electrical Engineering, University of Massachusetts Amherst***Fabrication of Magneto Resistance-Based Magnetic****Quantum-Dot Cellular Automata, page 66***Angeline Klemm, Physics/Engineering, University of Wisconsin-La Crosse***Semiconductor Nanocrystal Inks****for Printed Photovoltaics, page 68***Gabriel Palomino, Chemical Engr., Texas Tech University***Graphene Contacts to****Pentacene Thin-Film Transistors, page 70***Christopher Phare, Physics and Mathematics, Vanderbilt University***Graphene Nanoribbons as Transistors****in Nanoelectronic Devices, page 72***Michelle Pillers, Chemistry, Southern Methodist University***Thermally Enhanced Dynamic Core Migration****with Phase Change Materials, page 74***Amber Pizzo, Mechanical Engineering, Binghamton University***Fabrication and Characterization of****Indium Arsenide Nanowire Transistors, page 76***Devanand Sukhdeo, Electrical Engineering, Columbia University***Heterogeneous Integration of p- and n- type Nanowires****for Complementary Nanowire Circuits, page 78***Takeshi Uchinoumi, Chemical Systems and Engr., Kyushu Univ.***Fabrication of a Gallium Nitride****Nano-Field Effect Transistor, page 80***Amber C. Wingfield, Optical Engineering and Mathematics, Norfolk State University***Materials, pages 82-113****Heterojunction Growth of $\text{Si}_{1-x}\text{Ge}_x$ and C_3N_4** **Nanowires on Silicon, page 82***Siatta Adams, Chemistry, Mercer University***Nanoparticle-Enhanced Tunnel Junctions****for High-Efficiency Multi-Junction Solar Cells, page 84***Gavin P. Campbell, Materials Science and Engineering, UIUC***Investigation of the Effects of Base Additives in****Molecular Glass Photoresist Films, page 86***Sylvia Carroll, E.E. and Biology, University of Texas at El Paso***Contact Resistance of****Graphene-Based Devices by TLM, page 88***Arolyn Conwill, Physics, Pomona College (undergraduate), Massachusetts Institute of Technology (graduate)***Aluminum Induced Crystallization of Silicon****on Quartz for Silicon Wire Array Solar Cells, page 90***Natalie M. Dawley, Physics, University of Virginia*

Fabrication of Dendritic Electrodes for Electroactive Polymer Actuators, page 92

Nathaniel Hogrebe, Chemical Engr., University of Dayton

Grain Boundary Effects on Charge Transport In ZnO:Al Transparent Conducting Films, page 94

Ruby Lee, Bioengineering, Stanford University

Adhesion of Capillary Underfill Epoxies for Flip Chip Packaging, page 96

Gillian Lui, Environmental Studies and Conservation Biology, Middlebury College

Temperature Dependent Growth Properties of Epitaxial Graphene on Carbon-Face Silicon Carbide, page 98

Benjamin D. Mahala, Chemistry, University of Missouri Science and Technology

Composite Cathodes for Intermediate Temperature Solid Oxide Fuel Cells, page 100

Isaac Markus, Chemical Engineering, The Cooper Union for the Advancement of Science and Art

Tuning Graphene Conductivity Using Solid Binding Peptides, page 102

Nkemdilim Oghedo, Chemical Engineering, Yale University

Characterization of SiAlON for Hydrogen Diffusion Barrier Application in Nonvolatile Memory Devices, page 104

Axel Palmstrom, Chemical Engineering, University of California, Santa Barbara

Silicon Phononic Crystals for High Efficiency Thermoelectrics, page 106

Christopher Romanczuk, Chemical and Biomolecular Engineering, Rice University

Characterization of Materials with Epitaxially Embedded Nanoinclusions for Thermoelectric Applications, page 108

Joseph S.T. Smalley, Engineering Science and Mechanics, The Pennsylvania State University

Low Stress Oxides for use in Microfabricated Ion Traps for Quantum Computation, page 110

Margeaux Wallace, Materials Science and Engineering, Cornell University

Solution Synthesis and Aerosol Deposition of Cu₂ZnSnS₄ Nanoparticles, page 112

Denys Zhuo, Material Science and Engineering, MIT





Mechanical Devices, pages 114-129

Real Time Blood Coagulation Sensor, page 114

Jennie Appel, Electrical Engineering, Auburn University

Locomotion of Catalytic Nanomotors, page 116

Jesse Ault, Mechanical Engineering, Purdue University

Fabrication of a Three Terminal

Nanomechanical Graphene Switch, page 118

Lauren Cantley, Physics, Grinnell College

Mechanics of 1-25 nm Thin Films, page 120

Zachary J. Connell, Mechanical Engineering, University of Nebraska

Top-Down Fabrication of Patterned, Vertically Aligned Silicon Nanowires, page 122

Sibu Kuruvilla, Materials Science and Engineering, University of Illinois at Urbana-Champaign

Ion Distribution in Ionomer and High

Temperature Ionic Liquid Actuators, page 124

Stephen Twigg, Electrical Engineering, Villanova University

Micropore Immunosensors

for Fast Disease Diagnostics, page 126

Clare Wardwell, Biological Sciences, University of Delaware

Improving Quality Factor of Drum Resonators via Gas Confinement, page 128

Diana Wu, Chemical Engineering and Biology, Massachusetts Institute of Technology



Optics and Opto-Electronics, pages 130-155

Growth of Graphene Nanostructures on Silicon Wafers, page 130

Brian Benton, Physics, Univ. of Minnesota-Twin Cities

Fabrication of Silver MicroWire

Polarization Filters, page 132

Diana Bolser, Physics, University of Missouri-Columbia

Automation of Sample-Positioning and Data-Collection

for Pulsed-Laser-Melting Experiments, page 134

Edy Cardona, Physics, University of California, Berkeley

Fabrication of High Speed Nanoscale Metal-Semiconductor-Metal Photodetector, page 136

Kevin Chen, Electrical Engineering, Arizona State University

Characterization of Ag-Si Composite for Infrared Photodetectors, page 138

Marie DesHarnais, Civil Engineering, University of Minnesota-Twin Cities



Fabrication of Photonic Crystals**for High Temperature Applications, page 140**

Joseph DeWilde, Chemical Engineering, Oregon State University

Transfer of Electron Beam-Patterned Photonic**Nanobeam Cavities to Flexible Substrates, page 142**

D. Johann Djanal-Mann, Electrical Engr., University of Florida

3D Super-Resolution Using a Phase Mask**Fabricated via Grey-Level Lithography, page 144**

Callie Fiedler, Physics, University of San Diego

Fabrication and Characterizations of Plasmonic**Nanostructures for Organic Photovoltaics, page 146**

Michael Hoerner, Engineering Physics,

Rose Hulman Institute of Technology

Close-Packed Monolayer of Silica Nanoparticles**for use as Etch Mask in LED Active Region, page 148**

Christina Jones, Engineering Physics,

University of Colorado at Boulder

Molecular Specific Biosensing Based on Engineered**Quasi-3D Plasmonic Nanostructures, page 150**

Roger Jordan, Biomedical Engineering, Texas A&M University

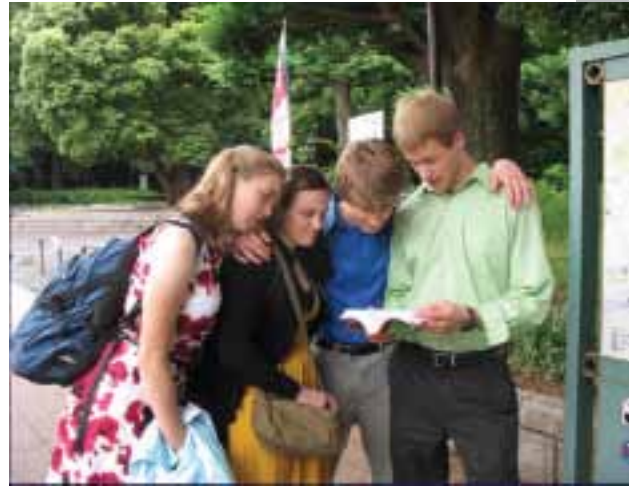
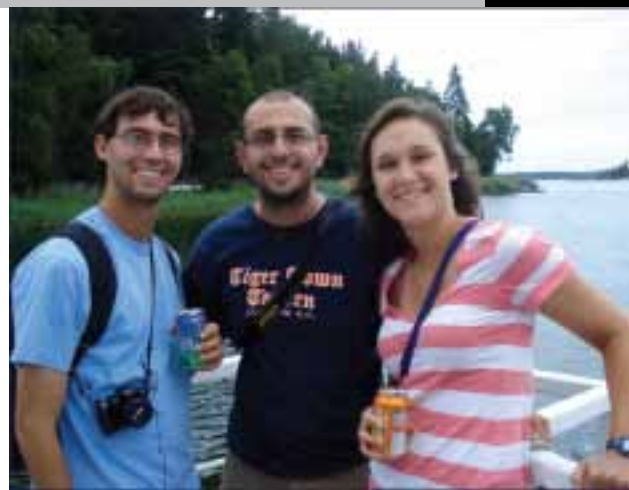
Lifetime of Charge Carriers in Single Si Nanowire, page 152

Jhim Handrex Meza, Electrical Engineering,

University of California, Los Angeles

Quantum Well Intermixing on a Hybrid Silicon or Silicon**Dioxide Bonded AlGaAs/GaAs/InGaAs Platform, page 154**

Mohsin Pasha, Electrical Engineering, University of Texas at Austin

**Physics and Nanostructure Physics,**
pages 156-163**Unipolar Resistive Switching in****100 nm² Pt-NiO-Ni-Pt Cells, page 156**

Matthew T. Hershberger, Physics, Bethel College, Kansas

Tunneling Electron Microscopy Investigation**Strategy for InAs Nanowires, page 158**

Jacob Alexander Sadie, Electrical Engr., UC Berkeley

Domain Wall Track in a Praseodymium Strontium**Manganite Oxide Nanobridge, page 160**

Meng Shi, Physics, Case Western Reserve University

Transport Properties of InAs Nanowires for Applications**in Quantum Information Processing, page 162**

Hamsa Sridhar, Physics and Mathematics, Harvard College

Process and Characterization, pages 164-201**Characterization of Mercury and****Copper Capped DMBP Monolayers, page 164**Narahi J. Alvarez, Chemical Engineering Department,
University of Puerto Rico-Mayaguez Campus



Process Development for Writing Sub-100 nm Linewidths using a Scanning Electron Microscope, page 166

Hilton H. Augustine III, Electrical Engineering,
Harvard University

The Role of Polyvinylpyrrolidone in the Toxicity Evaluation of Silver Nanocubes, page 168

Mark Brunson, Mechanical Engineering,
San Francisco State University

Characterization of Ruthenium Electrodes for Implantable Neurostimulation Applications, page 170

Christine Burdett, Chemical Engineering, NCSU

Characterization of Iron Oxide Integration within Phospholipid Encapsulated Colloids, page 172

Jack Chen, Biomedical Engineering, Duke University

Material Characterization of Advanced III-V Semiconductors for Nanophotonic Integration, page 174

Brian T. Chung, Engineering Physics,
University of Michigan

Fabrication of Locally-Gated Bilayer Graphene Field Effect Transistors, page 176

Corey E. Clapp, Chemistry,
Amherst College, Amherst

Graphene Growth on Palladium (111), page 178

Scott Isaacson, Chemical Engineering,
University of Minnesota

DNA Electrophoresis

in Microfabricated Post Arrays, page 180

Jason Lee, Chemical Engr., University of Massachusetts-Amherst

Process for Detaching Suspended Graphene Structures from Silicon Carbide, page 182

Charles Mackin, Electrical Engineering,
University of Arizona

Sub-20 Nanometer Electron Beam Induced Deposited Gold

Plasmonic Nanostructures, page 184

Claire McLellan, Physics, Wake Forest University

Fabrication of Graphene Structures Using an Atomic Force Microscope, page 186

Christopher O'Connell, Mechanical Engineering,
University of Rhode Island





Fabrication of Gold Nanoparticles Using E-beam Lithography:

Effect of Development Conditions on Shape and Resolution, page 188

Fiona O'Connell, Materials Engineering, Loyola University Maryland

C₁₀ and C₁₂ BTBT Single Crystalline Organic Field Effect Transistor, page 190

Si Hui Athena Pan, Physics, Brandeis University

Transferring Chemical Vapor Deposition Grown Graphene, page 192

Phi Pham, Physics, University of Colorado Boulder

High Spatial Resolution Kelvin Probe Force Microscopy with Shielded Probes, page 194

Kevin J. Satzinger, Physics and Mathematics, Truman State University

Characterization of High Aspect Ratio Silver Micromachining for RF Inductors, page 196

Natalie Swider, Material Science and Engineering, University of Illinois Champaign-Urbana

Template Stripping for High Throughput Fabrication of Nanohole Arrays, page 198

Benjamin Treml, Engineering Physics, University of Wisconsin-Madison

Sputtered TiW/W Emitter Contact Stack Design in Terahertz Bipolar Transistors, page 200

Jeremy Wachter, Physics and Electrical Engineering, Rose-Hulman Institute of Technology

Societal and Ethical Issues (SEI) of Nanotechnology, pages 202-205

Public Service Posters for the Societal and Ethical Issues (SEI) of Nanotechnology, page 202

Chloe Lake, Communication and Psychology, University at Buffalo

Index, pages 207-212

This book was designed and formatted by Melanie-Claire Mallison, NNIN REU Program Assistant. The book was printed using soy-based ink and 10% post consumer paper. We encourage you to reduce, reuse, and recycle. This publication is available online at <http://www.nnin.org/>

The photographs on pages i-ix were taken by Nicole Holdorph (University of Minnesota-Twin Cities), NNIN site staff and iREU interns. The photographs on pages xi-xxi were taken by Nicole Holdorph.

COVER IMAGES LEGEND:

Manali Alvarez, page 184	Kathleen Bennett, page 2	Brian Bostian, page 138	Mark Knutson, page 188	Steven Chone, page 4	Clara Chew, page 60	Brian Cheng, page 174	Zachary Connell, page 120
Natalie Dawley, page 98	Joseph Gerwilde, page 143	D. Jekan Djouani-Korn, page 142	Megan Dunn, page 12	Nathaniel Hugreys, page 92	Siba Karuvella, page 122	Christina Jeesen, page 148	
Charles Mackin, page 160	Isaac Markos, page 166	Roseekit Matsumoto, page 96	Christie O'Connell, page 188	Gabriel Palomino, page 69	Philip Parizo de Leon, page 59	Kevin Gotzinger, page 154	Amber Wingfield, page 80
Mariusz Strikhar, page 182	Jeremy Wachter, page 200		Jennifer Wang, page 52	Clara Wardwell, page 628	Kayroll Worley, page 92	Collin Fields, page 144	Christopher Lewis, page 33

The National Nanotechnology Infrastructure Network

<http://www.nnin.org/>

**is comprised of the following fourteen sites, and is supported by
The National Science Foundation, the NNIN sites,
our corporate sponsors and research users.**

ASU NanoFab, Arizona State University
*Ira A. Fulton School of Engineering • PO Box 876206
Tempe, AZ 85287-6206
(480) 965-3808 • <http://www.fulton.asu.edu/nanofab/>*

**Cornell NanoScale Science & Technology Facility,
Cornell University**
*250 Duffield Hall • Ithaca, NY 14853-2700
(607) 255-2329 • <http://www.cnf.cornell.edu>*

**Nanotechnology Research Center,
Georgia Institute of Technology**
*791 Atlantic Dr NW • Atlanta, GA 30332-0269
(404) 385-4307 • <http://www.mirc.gatech.edu>*

Center for Nanoscale Systems, Harvard University
*11 Oxford Street, LISE 306 • Cambridge, MA 02138-2901
(617) 384-7411 • <http://www.cns.fas.harvard.edu>*

**Howard Nanoscale Science & Engineering Facility,
Howard University**
*Downing Hall Room 1124 • 2300 Sixth St NW
Washington, DC 20059-1015
(202) 806-6618 • <http://www.msrce.howard.edu>*

**Penn State Nanofabrication Laboratory,
The Pennsylvania State University**
*188 Materials Research Institute • 230 Innovation Blvd
University Park, PA 16802-6300
(814) 865-7443 • <http://www.mri.psu.edu/facilities/nnin/>*

**Stanford Nanofabrication Facility,
Stanford University**
*P.G. Allen Bldg, Rm 303x • 420 Via Palou
Stanford, CA 94305-4070
(650) 725-3607 • <http://snf.stanford.edu>*

**Colorado Nanofabrication Laboratory,
University of Colorado at Boulder**
*ECEE Campus Box 425 • Boulder, CO 80309-0425
(303) 492-2809 • <http://cnl.colorado.edu>*

Nanotech, University of California, Santa Barbara
*ECE Dept • Engineering Science Bldg 1109E
Santa Barbara, CA 93106-9560
(805) 893-5999 • <http://www.nanotech.ucsb.edu>*

**Lurie Nanofabrication Facility,
The University of Michigan, Ann Arbor**
*1301 Beal Ave 1241 EECS • Ann Arbor, MI 48109-2122
(734) 763-0231 • <http://www.lnf.umich.edu>*

**Nanofabrication Center,
University of Minnesota-Twin Cities**
*200 Union St SE • 1-165 Keller Hall
Minneapolis, MN 55455-0171
(612) 625-3069 • <http://www.nfc.umn.edu>*

**Microelectronics Research Center,
The University of Texas at Austin**
*J.J. Pickle Research Campus • 10100 Burnet Rd, Bldg 160
Austin, TX 78758-4445
(512) 471-4493 • <http://www.mrc.utexas.edu>*

**Center for Nanotechnology,
University of Washington**
*Box 352140 • Fluke Hall Rm 215
Seattle, WA 98195-1700
(206) 616-9320 • <http://www.nano.washington.edu>*

**Nano Research Facility,
Washington University in St. Louis**
*Earth & Planetary Sciences Bldg Rm 189
Campus Box 1169, One Brookings Dr
St. Louis, MO 63130-4899
(314) 935-6060 • <http://www.nano.wustl.edu>*

2010 NNIN REU Corporate Sponsors

Agilent Technologies
Analog Devices
Applied Materials
Cambridge Nanotech
Canon
Daihen Corporation
Ericsson
IBM Corporation
Infineon
Intel Corporation
Invensense

National Semiconductor Corporation

NEC Corporation
NXP Semiconductors
Olympus Corporation
Panasonic
Qualcomm

Renesas Technology Corporation

Robert Bosch Corp.
STMicroelectronics
Texas Instruments, Incorporated
Toshiba



The 2010 NNIN REU Interns at the convocation, held at the University of Minnesota in August. Photograph by Nicole Holdorph.

Welcome to the 2010 NNIN REU Research Accomplishments

This annual publication reflects the hard work of our undergraduate and graduate researchers. Also very important to this accomplishment is the dedication of the program's principal investigators, mentors, coordinators and site staff.

Given just ten weeks to take on the challenge of completing comprehensive experimental research can be a very compelling and defining experience for the student. Our program tests the many skills of learning and applying the learning, and helps provide factual input to determine the course of life at a very critical stage when one is coming into one's own. Research is a pursuit into the unknown and for many of the students this is the first time when the answer, or even the existence of an answer, is not yet known.

During the summer of 2010; 80 students participated in our Research Experience for Undergraduates (REU) Program, 18 students from the 2009 NNIN REU Program participated in our International Research Experience for Undergraduates (iREU) Program, and five graduate students from Japan participated in our International Research Experience for Graduates (iREG) Program.

We work diligently to ensure that all three of these programs result in very substantial experiences by focusing on

advanced research and knowledge, seeking strong mentors and staff support, exposing our interns to a professional research environment, and having high expectations built into the research projects and the convocation.

In addition, at each site, the exposure to a wider variety of research conducted by peers and other users across diverse disciplines of science and engineering within the unifying facilities, also provides significant complementary experience.

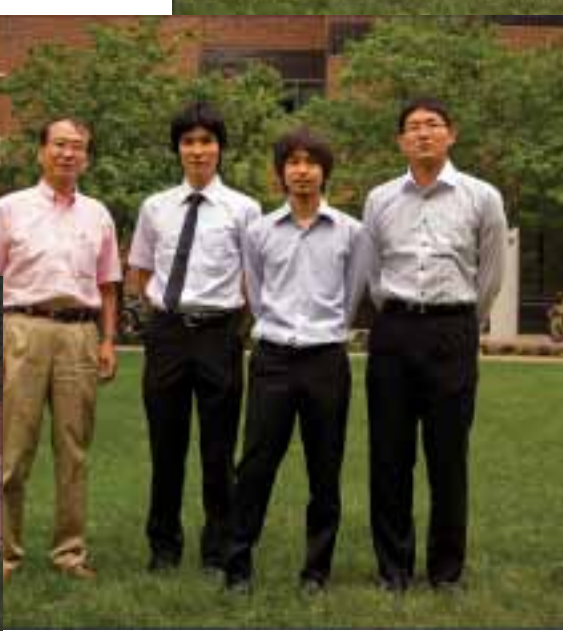
My thanks to the staff, the graduate student mentors and the faculty for their participation and involvement. Particular thanks are due to Melanie-Claire Mallison and Lynn Rathbun at Cornell, and Nancy Healy at Georgia Institute of Technology for their contributions in organizing the logistics of these programs, and many thanks to Becky von Dissen and Jim Marti for organizing the network-wide convocation at the University of Minnesota-Twin Cities.

I wish all our program participants the best wishes for future technical careers; NNIN hopes you will build on this summer's experience and looks forward to hearing from you on your future successes!

Prof. Sandip Tiwari • Director, NNIN • st222@cornell.edu



**The NNIN site coordinators thank
you all for a fabulous summer!**





**Stay
In
Touch!**





**The 2010 NNIN REU Interns
at Arizona State University**

Ault, Jesse page 116
Wardwell, Clare page 126
Mirts, Evan page 26
Appel, Jennie page 114
Lowe, Christopher page 22



**The 2010 NNIN REU Interns
at Cornell University**

O'Connell, Christopher page 186
Lake, Chloe page 202
Anger, Richard page 54
Hoffman, Emily page 16
Mackin, Charles page 182
Conner, Austin page 62
Wu, Diana page 128
Davis, John page 42
Carroll, Sylvia page 86
Phare, Christopher page 70





**2010 NNIN REU Interns at the
Georgia Institute of Technology**

Wallace, Margeaux **page 110**

Chase, Steven **page 4**

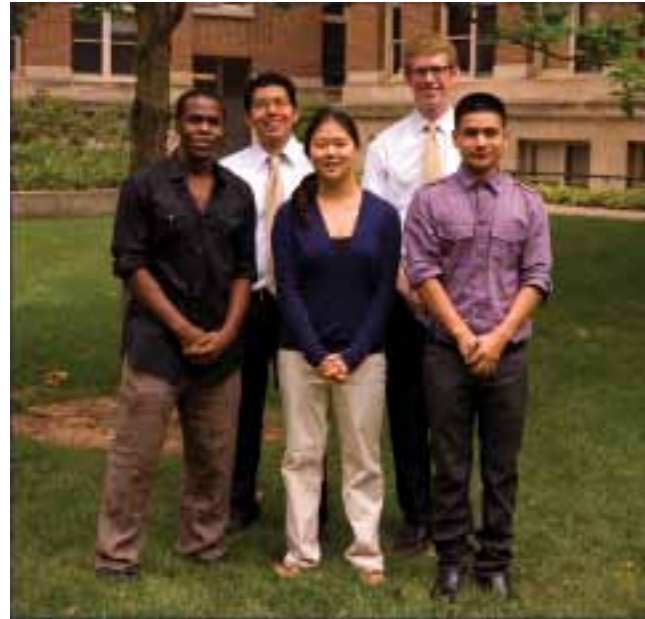
O'Connell, Fiona **page 188**

Mahala, Benjamin D. **page 98**

Pizzo, Amber **page 4**

Worley, Barrett **page 52**

Tsukamoto, Takashiro **na**



**The 2010 NNIN REU Interns
at Harvard University**

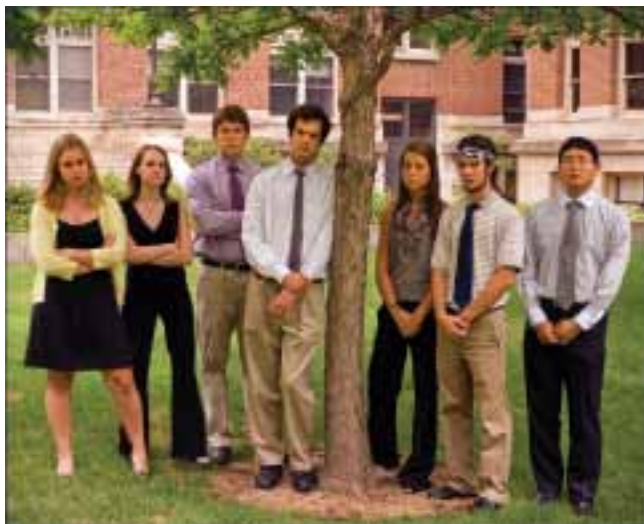
Djanal-Mann, D. Johann **page 142**

Cardona, Edy **page 134**

Lee, Ruby **page 94**

Satzinger, Kevin J. **page 194**

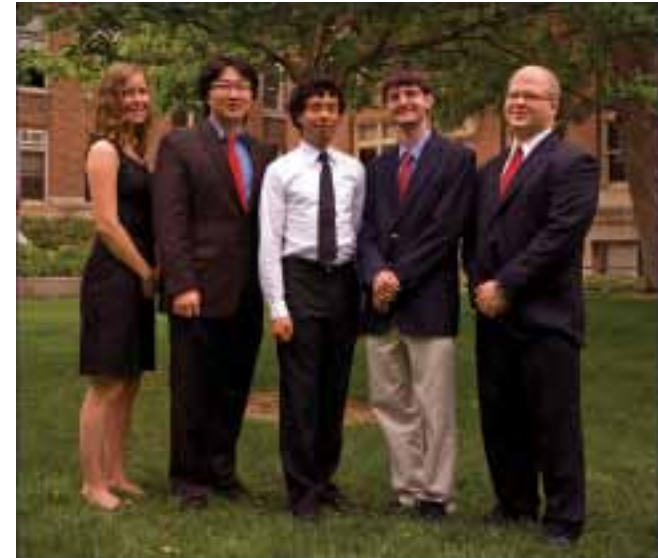
Meza, Jhim Handrex **page 152**





**The 2010 NNIN REU Interns
at Howard University**

DesHarnais, Marie page 138
Adams, Siatta..... page 82
Augustine, III, Hilton H...... page 166
Wingfield, Amber C. page 80
Alvarez, Narahi J...... page 164



**2010 NNIN REU Interns at the
Pennsylvania State University**

Dawley, Natalie M. page 90
Shi, Meng. page 160
Clapp, Corey E. page 176
Twigg, Stephen..... page 124
Connell, Zachary J...... page 120

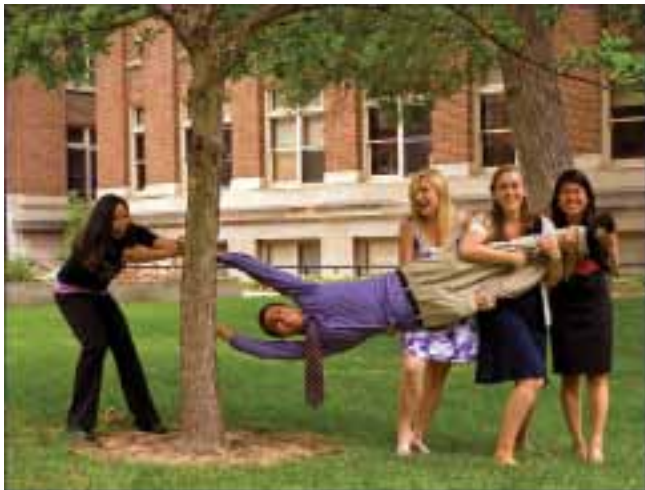




The 2010 NNIN REU Interns at Stanford University



The 2010 NNIN REU Interns at the University of California, Santa Barbara





The 2010 NNIN REU Interns at the University of Colorado, Boulder

Tayson-Frederick, Mallory na

Krueger, Kendra na

Cantley, Lauren **page 118**

Fiedler, Callie **page 144**

Chen, Kevin **page 136**

Benton, Brian **page 130**

Hoerner, Michael **page 146**



The 2010 NNIN REU Interns at the University of Michigan, Ann Arbor

Kuruvilla, Sibu	page 122
Watanabe, Masaki.	page 36
Romanczuk, Christopher	page 106
Jones, Christina.	page 148
Henderson, Zachary	page 64
Swider, Natalie	page 196
Bakkila, Scott	page 56





**The 2010 NNIN REU Interns
at the University of
Minnesota-Twin Cities**

Lee, Jason page 180
Treml, Benjamin page 98
Wang, Yingxia page 34
Klemm, Angeline page 66
DeWilde, Joseph page 140



**The 2010 NNIN REU Interns at
The University of Texas
at Austin**

Palomino, Gabriel page 68
Pham, Phi page 192
Bersin, Lia page 58
Campbell, Gavin P. page 84
Downing, Fraser page 10
Fujii, Hiromasa page 44





**The 2010 NNIN REU Interns at
the University of Washington**

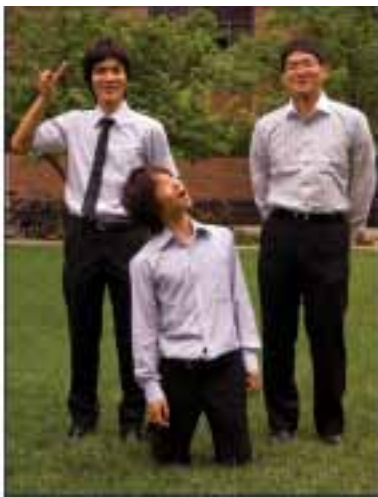
Dunn, Megan **page 12**
Nelson, Heidi **page 30**
Jordan, Roger **page 150**
Bennett, Kathleen **page 2**
Cummings, Lauren **page 8**
Oghedo, Nkemdilim **page 102**



**The 2010 NNIN REU Interns at
Washington University
in St. Louis**

Brunson, Mark **page 168**
Jones, Kristen **page 18**
Le, Chantalle **page 48**
Bolser, Diana **page 132**
Wang, Jennifer **page 32**
Chen, Jack **page 172**





The 2010 NNIN iREG Students

Fujii, Hiromasa page 44

Watanabe, Masaki page 36

Tsukamoto, Takashiro na

Not Pictured:

Kazutoshi, Kubo na

Uchinoumi, Takeshi page 78



The 2010 NNIN International REU Interns

Kozak, Adam page 20

Hershberger, Matthew T. page 156

Connolly, Sarah page 6

Isaacson, Scott page 178

McLellan, Claire page 184

Markus, Isaac page 100

Sukhdeo, Devanand page 76

Sridhar, Hamsa page 162

Hogrebe, Nathaniel page 92

Feig, Vivian page 14

Not Pictured:

Borysiak, Mark page 40

Burdett, Christine page 170

Conwill, Arolyn page 88

Merritt, Margaret page 24

Palmstrom, Axel page 104

Pan, Si Hui Athena page 190

Sadie, Jacob Alexander page 158

Zhuo, Denys page 112

***The National Nanotechnology
Infrastructure Network Research
Experience for Undergraduates Program***

Research Accomplishments

2010

Characterization of dsDNA Binding Protein SlyA for Nanostructure Assembly

Kathleen Bennett
Biology, Harvey Mudd College

NNIN REU Site: Center for Nanotechnology, University of Washington, Seattle, WA
 NNIN REU Principal Investigator(s): Beth Traxler, Microbiology, University of Washington
 NNIN REU Mentor(s): Ruth Hall Sedlak, Microbiology, University of Washington
 Contact: kbennett@hmc.edu, btraxler@u.washington.edu, rah7@u.washington.edu

Abstract and Introduction:

This project explored the suitability of the *Salmonella typhimurium* deoxyribonucleic acid (DNA)-binding protein SlyA (17kDa) for use in the self-assembly of nanoscale inorganics on a DNA scaffold. Self-assembly techniques are attractive because they manufacture structures from the bottom-up. DNA is a potential scaffold for nanostructures because it is stable at room temperature and self-assembles via base pairing.

Previous experimentation with engineered derivatives of the DNA-binding protein TraI (192kDa) demonstrated its ability to spontaneously assemble gold nanoparticles (AuNPs) on DNA [1]. Utility of this TraI derivative is limited by its large size, non-specific affinity for various metals, and multiple DNA-binding domains.

SlyA is a smaller protein, so it may exhibit less nonspecific metal binding than TraI, and its single DNA binding domain allows for increased control during assembly. Additionally, its protein family (MarR) is well characterized and its crystal structure is known (Figure 1) [2].

SlyA was purified to high concentrations via a 10x Histidine-tag. Subsequent efforts focused on cleaving the His-tag from

purified His-SlyA via Factor Xa protease, since the His-tag would likely exhibit background binding to a multitude of materials.

Localized surface plasmon resonance (LSPR) spectrometry characterized His-SlyA binding to 15 nm AuNPs. His-SlyA exhibited high binding overall and caused aggregates at 0.25 μ M and higher. Cloning gold binding peptide (GBP1-7x or AuBP2) sequences into the SlyA gene efforts are ongoing [3,4].

Methods:

His-SlyA Purification. *Escherichia coli* (*E. coli*) cultures were induced to over express His-SlyA and then lysed. The resulting supernatant was mixed with NiNTA resin, which bound to the His-tag, and then loaded into a column. After 100 mM imidazole washes eliminated untagged proteins, 500 mM imidazole washes eluted His-SlyA from the resin.

Factor Xa Cleavage. 0.2 U/ μ l Factor Xa protease was incubated with His-SlyA for 4.5 hours at room temperature to cleave the His-tag. Factor Xa resin removed the protease; NiNTA resin removed cleaved-His-tags and His-SlyA.

Gold-Binding Characterization. His-SlyA was diluted in solutions of 0.01 μ M to 1 μ M and mixed with 15 nm AuNPs. A LSPR spectrometer was used to obtain absorbance vs. wavelength. The peak absorbance wavelength of plain AuNPs was also obtained and subtracted from the peak absorbance wavelength of each dilution to obtain peak wavelength shift vs. His-SlyA concentration.

Insertion of GBP1-7x and AuBP2. The GBP1-7x sequence (MHGKTQATSGTIQS), AuBP2 sequence (WALRRSIRRQSY), and the pet16B plasmid containing the SlyA gene were digested with NdeI [5,6]. Each digested peptide sequence was ligated with varying concentrations of digested pet16B. The region of the plasmid containing the NdeI site was observed through gel electrophoresis to determine if the insert annealed with the plasmid.

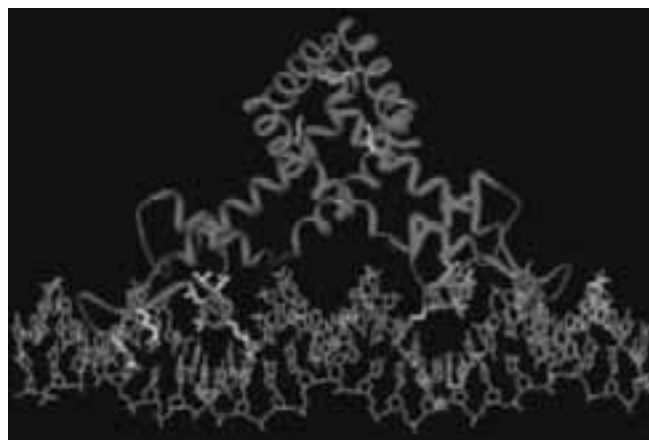


Figure 1: SlyA in complex with DNA [2].

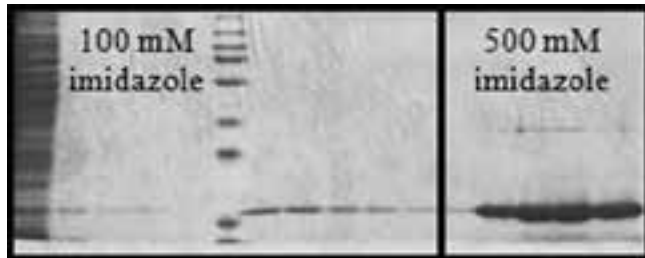


Figure 2: Purification gel of His-SlyA.

Results and Discussion:

His-SlyA purification was effective, repeatable, and high-yield. The imidazole washes successfully eliminated untagged proteins and separated the His-tag from the resin, resulting in $0.66 \text{ mg}/\mu\text{l}$ His-SlyA (Figure 2). Thus, purification via His-tag is a good and reliable method that should work for SlyA variants.

Both the His-SlyA cleavage and subsequent removal of Factor Xa protease were effective. $0.2 \text{ U}/\mu\text{l}$ Factor Xa protease incubation for 4.5 hours cleaved most of the His-SlyA, and Factor Xa resin completely removed the protease (Figure 3). However, SlyA bound to the NiNTA resin during post-cleavage purification, even when imidazole was added to decrease that non-specific binding (Figure 3).

His-SlyA binds gold with high affinity, which is not surprising as histidine is a known gold-binder [7]. A visible color change due to gold aggregation was observed with $0.25 \mu\text{M}$ to $1 \mu\text{M}$ protein, indicating that the $0.01 \mu\text{M}$ to $0.25 \mu\text{M}$ range should be further investigated when examining SlyA.

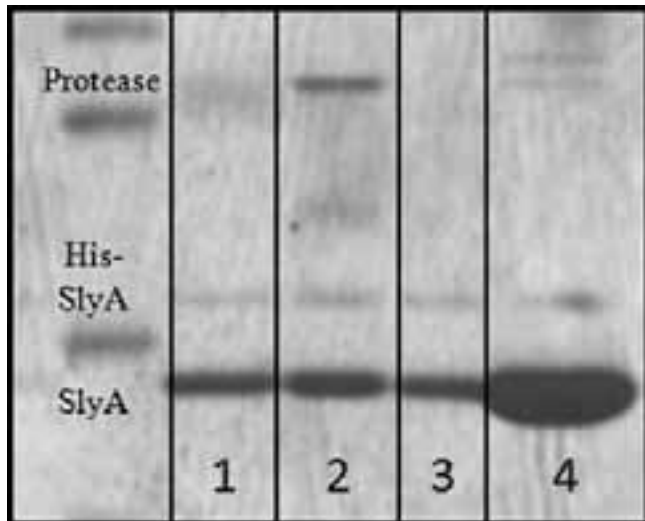


Figure 3: Factor Xa cleavage gel of His-SlyA.
Left to right: post-cleavage, protease resin, post-protease resin.

Conclusions:

Although SlyA has potential for assembling AuNPs on a DNA scaffold, it should have low background binding to gold to validate its use. Significant progress was made in the initial steps to discover SlyA's gold binding. It was determined that a 10x His-tag is a good way to purify SlyA and that the His-tag strongly affects background binding to gold, so it is necessary to cleave the tag and isolate SlyA post-cleavage.

Future work includes troubleshooting the post-cleavage purification process to isolate SlyA, and using LSPR spectrometry to determine SlyA's innate affinity for gold. Additionally, SlyA gold-binding variants SlyA::GBP1-7x and SlyA::AuBP2 will be engineered, their gold affinities examined to determine which is most effective, and their DNA affinities measured to ensure addition of a gold binding motif does not eliminate SlyA's original DNA-binding function.

Acknowledgements:

I would like to thank my mentor, Ruth Hall Sedlak, and Principal Investigator, Beth Traxler, for their guidance, suggestions, and support. I would also like to thank the rest of Traxler Lab. Funding was provided by the National Nanotechnology Infrastructure Network Research Experience for Undergraduates (NNIN REU) Program and the National Science Foundation.

References:

- [1] Hall, Ruth A., Marketa Hnilova, Eliora Gachelet, Laralynne Przybyla, David Dranow, Tamir Gonen, Mehmet Sarikaya, Candan Tamerler, and Beth Traxler. "An Engineered DNA-binding Protein Self-assembles Metallic Nanostructures." *Chembiochem*, in press.
- [2] Brzovic, P.S., I. Le Trong, W.W. Navarre, F.C. Fang, R.E. Stenkamp, and S. J. Libby. "Crystal structure of transcription regulator protein slyA from *Salmonella typhimurium* in complex with salicylate ligands." *PDB*, 3DEU.
- [3] Sarikaya, M., C. Tamerler, A.K. Jen, K. Schulten, F. Baneyx. "Molecular biomimetics: nanotechnology through biology." *Nature Materials* 2.9 (2003): 577-585.
- [4] Traxler, B. and Gachelet, E. "Sets of Transposon-Generated Sequence-Tagged Mutants for Structure-Function Analysis and Engineering." *Methods in Enzymology* 421 (2007): 83-90.
- [5] Brown, S. "Metal-recognition by repeating polypeptides." *Nature Biotechnology* 15.3 (1997): 268-272.
- [6] Hnilova, M., E.E. Oren, U.O.S. Seker, B.R. Wilson, S. Collino, J.S. Evans, C. Tamerler, M. Sarikaya. "Effect of Molecular Conformations on the Adsorption Behavior of Gold-Binding Peptides." *Langmuir* 24.21 (2008): 12440-12445.
- [7] Kogot, J.M., H.J. England, G.F. Strouse, and T.M. Logan. "Single peptide assembly onto a 1.5 nm Au surface via a histidine tag." *J. Am. Soc.* 130.48 (2008): 16156-7.

Measurement and Analysis of Blood Platelet Activation within a Microfluidic Device

Steven Chase

**Biomedical Engineering and Biochemistry and Molecular Biology,
Rose-Hulman Institute of Technology**

NNIN REU Site: Nanotechnology Research Center, Georgia Institute of Technology, Atlanta, GA

NNIN REU Principal Investigator(s): Dr. Craig Forest, Ph.D., Mechanical Engineering, Georgia Institute of Technology

NNIN REU Mentor(s): Melissa Li, Biomedical Engineering, Georgia Institute of Technology

Contact: chasesc@rose-hulman.edu, cforest@gatech.edu, melissa_li@gatech.edu

Abstract:

Cardiovascular disease (CVD) is the leading cause of death in the United States. In CVD, slow accumulation of fat and plaque within blood vessels forms a local constriction, known as a stenosis, whose flow conditions make it prone to clot formation and subsequent occlusion resulting in heart attack or stroke. We have developed an *in vitro* microfluidic device to model arterial flow conditions in stenosis clot formation. Heparinized porcine blood was flowed through the device at shear rates of 500 s^{-1} , $4,000\text{ s}^{-1}$, and $10,000\text{ s}^{-1}$, conditions representing normal to pathological patient conditions. *In vitro* clot formation was monitored using simultaneous readings of mass flow and light transmission. Additionally, scanning electron microscopy (SEM) was utilized to visualize the activation-related morphological changes in individual platelets and platelet aggregates within our device. Our device allows for high throughput, simultaneous evaluation of clotting behavior over a large range of shear rates, while SEM provides a visual confirmation of platelet behavior.

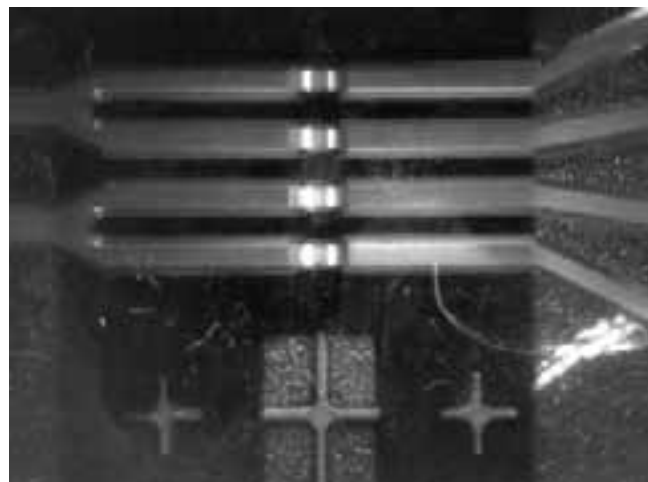


Figure 1: A finished device with applied printed aperture allows for easy alignment and limits channel-channel communication.

Materials and Methods:

Device Manufacture. Microfluidic devices were molded using polydimethylsiloxane (PDMS) on a milled master mold. PDMS was degassed and set at 70°C for 1.5 hours. Devices were bonded to glass slides using corona treatment. After bonding, a printed black aperture was aligned with the device on the back side, to prevent channel-channel communication. A finished device is shown in Figure 1. Devices were filled with collagen and allowed to sit overnight.

Blood Preparation. Porcine blood was obtained each morning of experiments from a local slaughterhouse and heparinized with 3.5 mL heparin per 1000 mL of blood. All experiments were conducted within six hours of slaughter. Blood was filtered through $125\text{ }\mu\text{m}$ polypropylene mesh before trials to remove large aggregates.

Flow Testing. Device, input lines, and output lines were primed with 43.4% glycerol, with a viscosity matched to blood. Blood was flowed through device at shear rates of 500 s^{-1} , $4,000\text{ s}^{-1}$, and $10,000\text{ s}^{-1}$. The shear rate was varied by the changing length and diameter of the output lines. Clot formation was monitored using simultaneous mass flow and light transmission measurements. Devices were visualized under light microscope after trial to confirm clot formation.

Scanning Electron Microscopy (SEM). Devices were removed from their glass slide, and the channels were gently washed with distilled water. Clots were fixed using 10% buffered formalin overnight and dehydrated using increasing concentrations of ethanol from 50% to 100% for 15 minutes at each concentration. SEM was performed using a Hitachi S3700 Variable pressure SEM running at 30 Pa and 15kV.

Results and Discussion:

Flow Testing. Light transmittance through thrombus has been previously confirmed using light microscopy (data not shown) [1]. Optical transmission and mass flow rates recorded for a single representative trial are shown in Figure 2. Both mass flow and light transmission were plotted

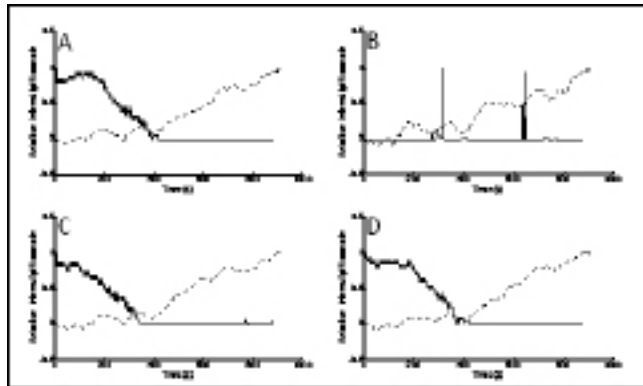


Figure 2: Representative relative mass flow (solid line) and light transmission (dotted line) results. Shear rates are $10,000\text{ s}^{-1}$ (A, D), $4,000\text{ s}^{-1}$ (B), and 500 s^{-1} (C).

relative to their respective maximums. An increase in optical transmittance correlated with occluded mass flow at 409 and 416 seconds for $10,000\text{ s}^{-1}$ and 336 seconds for $4,000\text{ s}^{-1}$, for this trial. The mass flow and light transmission showed an intersection point. This point will be used to determine when flow has been occluded using only the light transmission data, the ultimate goal of this study. Preliminary data suggests that this point is approximately 0.1 relative. Data (not shown) also suggests that $4,000\text{ s}^{-1}$ clots more quickly than $10,000\text{ s}^{-1}$, and the time to occlusion increases as the time from slaughter increases. Further study is needed to better characterize the effective range of shear rates for our device and the relationship between time to occlusion and time since slaughter.

Scanning Electron Microscopy. SEM images show increased platelet and decreased fibrin composition as the shear rate increases in platelet aggregates. This agrees with previous results [2]. Figure 3 shows representative micrographs of thrombus run at $10,000\text{ s}^{-1}$, $4,000\text{ s}^{-1}$, and 500 s^{-1} . The high shear rate shows a composition of mostly activated (irregularly shaped) platelets, the low shear rates shows a composition of unactivated (spherical) and fibrin, and the middle shear rate shows components of both. The location within the thrombus also affects composition. Regions where flow eddies form have low shear rates and allow fibrin deposition [3]. Figure 3, D and E, show a transition zone between platelet deposition and fibrin deposition. Fibrin deposition is also preferred in the corners where flow is slowed (Figure 2, F). Further histological studies should be performed to confirm results seen here.

Conclusions:

We have created a device that is capable of high throughput, low volume clotting assays of blood at up to four different conditions simultaneously. This device has application as a clinical tool to monitor blood clotting in individuals with unusual clotting response or as a high throughput research tool for cardiovascular applications. Further studies will be performed to study the effectiveness of this device to test pharmaceuticals and biomaterials.

Acknowledgements:

I would like to thank the National Science Foundation, National Nanotechnology Infrastructure Network Research Experience for Undergraduates (NNIN REU) Program, and the Nanotechnology Research Center at Georgia Tech. I would also like to thank the Precision Biosystems Laboratory, especially Melissa Li and Dr. Craig Forest, for their guidance through-out this project.

References:

- [1] Li, M., A. Sodemann, et al. (2009). "High throughput formation and measurement of occlusive thrombosis in porcine blood."
- [2] Ku, D. N. and C. J. Flannery (2007). "Development of a flow-through system to create occluding thrombus." *Biorheology* 44: 273-284.
- [3] Nesbitt, W. S., E. Westein, et al. (2009). "A shear gradient-dependent platelet aggregation mechanism drives thrombus formation." *Nature Medicine* 15(6): 665-673.

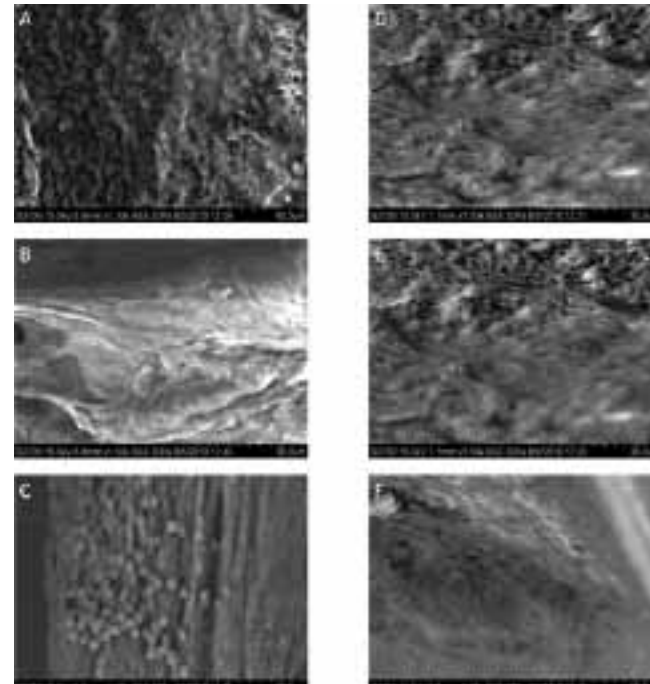


Figure 3: Representative SEMs of thrombus at different shear rates, $10,000\text{ s}^{-1}$ (A), $4,000\text{ s}^{-1}$ (B), 500 s^{-1} (C), and different regions of a $10,000\text{ s}^{-1}$ clot, downstream (D, E), and upstream corner (F). Flow is toward the top of the page in all cases.

Cytotoxicity of Copper Oxide Nanoparticles and Associated Ions on Human Epithelial Lung Cells (A549)

Sarah Connolly

Microbiology and Cell Science, University of Florida

NNIN iREU Site: National Institute for Materials Science, Tsukuba, Ibaraki, Japan

NNIN iREU Principal Investigator(s): Dr. Nobutaka Hanagata, Graduate School of Life Science, Hokkaido University

NNIN iREU Mentor(s): Fei Zhuang, Graduate School of Life Science, Hokkaido University

Contact: sarahsconnolly@gmail.com, hanagata.nobutaka@nims.go.jp, zhuangfei@nims.go.jp

NNIN iREU Program

Abstract:

The rapidly advancing field of nanotechnology offers many practical applications in consumer goods. As this area of science continues to grow and its uses become more widespread human contact with nanoparticles increases in likelihood, whether it is in consumption or production. This study focuses on determining the mechanism of toxicity caused by copper oxide (CuO) nanoparticles (NP) and the ions released from them on the A549 line of human epithelial lung cells. This is an *in vitro* representation of metal oxide nanoparticles being inhaled and accumulating in the lungs. Toxicity was assayed via deoxyribonucleic acid (DNA) microarray to determine up-regulated and down-regulated genes followed by gene ontology to classify those genes into categories such as cellular component and biological process. A mechanism of cytotoxicity was then proposed.

Experimental Procedure:

Treatment medium for cells was prepared by ultrasonicating a stock solution of CuO nanoparticles [1] and preparing a 25 $\mu\text{g}/\text{ml}$ solution of nanoparticles in normal cell culture medium. Ion medium was prepared by shaking the 25 $\mu\text{g}/\text{ml}$ metal oxide medium for four days at medium speed, followed by centrifugation at 22,000 $\times g$ for five minutes at 4°C to remove the nanoparticles from solution. Inductively coupled plasma (ICP) was then used to measure ion concentration in medium.

For DNA microarray assay cells were plated at 5,000 cells/ cm^2 and incubated for 72 hours until cells reached about 90% confluence. After incubation time elapsed cells were treated with 25 $\mu\text{g}/\text{ml}$ CuO-NP or Cu^{2+} medium and incubated for 24 hrs. Following incubation RNA was extracted, amplified, purified, and dyed using the Amino Allyl MessageAmp™ II aRNA Amplification Kit: RNA Amplification for Array Analysis by Ambion. Microarray samples were then hybridized, washed, and scanned. Data was filtered to remove duplicate genes, and then compared with a second set; reproducible genes were calculated by averaging genes from both sets when the absolute value of the difference in fold change was less than one. Significant up and down regulation was determined to be genes with a fold change greater than absolute value 1. These affected genes were organized using gene ontology and the mechanism in Figure 1 was proposed.

Cell cycle arrest was tested by plating cells at 5,000 cells/ cm^2 and incubating them for 48 hours after which they were exposed to 25 $\mu\text{g}/\text{ml}$ CuO nanoparticle medium for 24 hours.

Cells were washed twice with PBS, removed from culture dish, counted, and re-plated in a new culture dish at 5,000 cells/ cm^2 in normal cell culture medium and incubated for 72 hours. The wash procedure was then repeated and these second generation cells were counted. They were again re-plated at 5,000 cells/ cm^2 , incubated for 72 hours in normal cell culture medium, and counted for the third generation.

Results and Conclusions:

A count of viable cells using Cell Counting Kit-8 (CCK-8) after exposure to nanoparticles or associated ions yielded the results in Figure 2. About 40% of cells died when exposed to Cu^{2+} and about 80% died when exposed to CuO-NP. Therefore we can conclude that about 50% of CuO toxicity is attributable to effects of the Cu^{2+} ion.

The up-regulation of metallothionein expression in cells exposed to both Cu^{2+} and CuO nanoparticles indicates the generation of reactive oxygen species (ROS). In cells exposed to CuO nanoparticles heat shock proteins were also up-regulated indicating a more intense environmental stress causing proteins to unfold. ROS have been known to cause damage to DNA, which in turn up-regulates the GADD45G/B genes which can inhibit PCNA, CDC2, and CCNB1 genes that control cell cycle. The GADD45G/B genes can also interact with MTK1 and active the JNK p38 pathway leading to the formation of dimeric transcription factor AP-1 suggesting that CuO nanoparticles affect the expression of genes regulated by AP-1 transcription factor

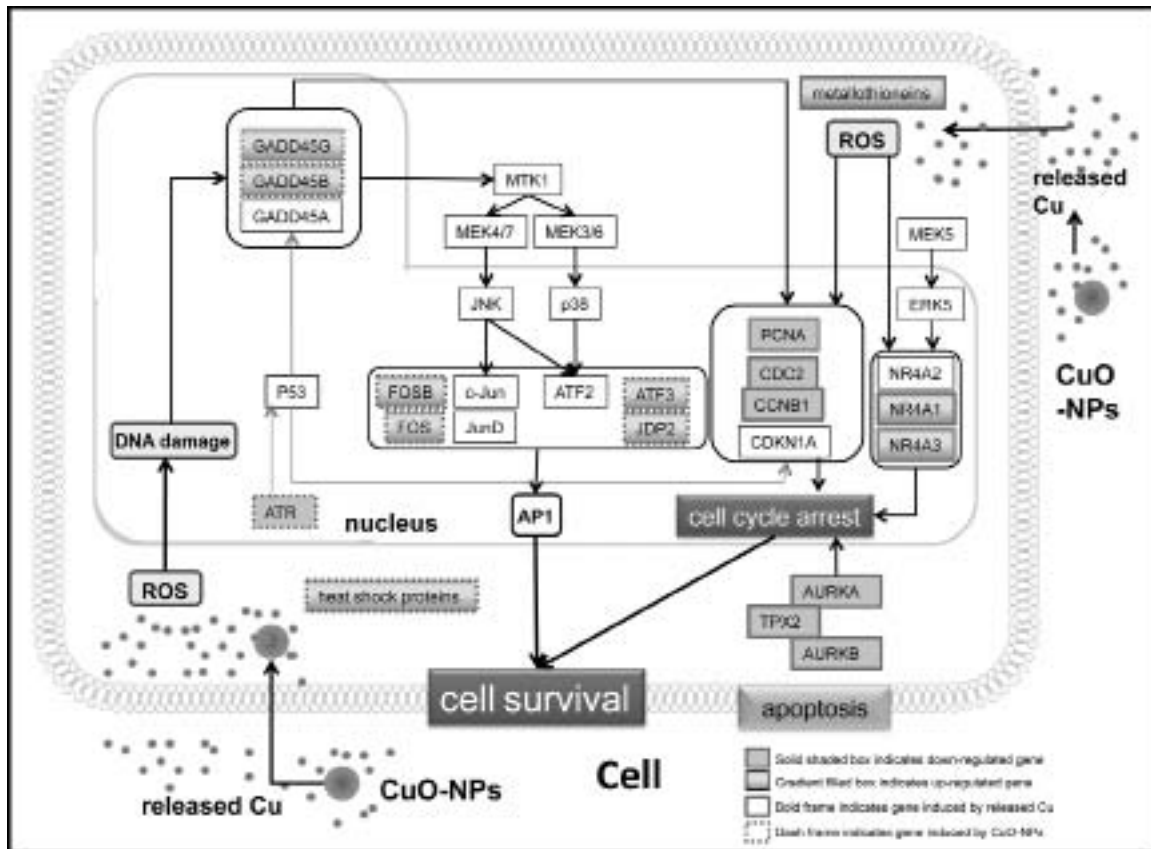


Figure 1: The proposed mechanism of cytotoxicity for CuO nanoparticles and Cu²⁺ ions.

[2]. AP-1 has been known to play roles in cell survival as well as apoptosis [3, 4] so more experiments are needed to confirm its role in this context. A future experiment would include inhibiting the JNK p38 pathway. If more cells are viable after this assay it can be determined that the pathway leads to apoptosis; the reverse is true if fewer cells are viable.

The down regulation of cell cycle regulating genes PCNA, CDC2, and CCNB1 indicate an arrest in cell cycle and the down regulation of AURKA/B and TPX2 indicate an arrest in cell division. Cell division experiments confirm that second generation cells whose parent generation was treated with CuO nanoparticles did not experience apoptosis, but did encounter an arrest in cell cycle and division. In the third generation recovery was evident as the cells resumed division.

Our hypothesis is that cell cycle arrest is a means by which cells can buy extra time to repair damaged DNA before dividing, ultimately resulting in cell survival instead of apoptosis.

Acknowledgements:

I would like to thank Dr. Hanagata, Fei Zhuang, and the Biomaterials Control Group for kindly sharing their lab with me and patiently mentoring me. Also, I would like to thank Emi Odaka and the Graduate Student Office at NIMS for

hosting our stay in Japan. Finally, I would like to thank the NNIN iREU Program for this opportunity and the National Science Foundation for funding.

References:

- [1] Xu M, Fujita D, Kajiwara S, Minowa T, Li X, Hanagata N. Contribution of Physicochemical Characteristics of Nano-oxides to Cytotoxicity. *Biomaterials* (In Press).
- [2] Takekawa M, Saito H: A family of stress-inducible GADD45-like proteins mediate activation of the stress-responsive MTK1/MEKK4/MAPKKK. *Cell* 1998, 95:521-30.
- [3] Shaulian E, Karin M. AP-1 as a regulator of cell life and death. *Nature Cell Biology* 2002 4: E131-E136.
- [4] Shaulian E, Karin M. AP-1 in cell proliferation and survival. *Oncogene* 2001 20: 2390-2400.

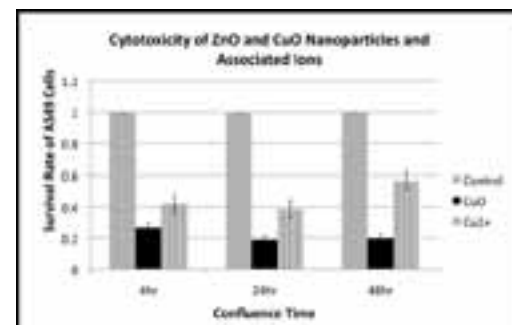


Figure 2: Cu²⁺ is responsible for about half of the toxicity of CuO nanoparticles.

Characterization of Biomolecular Interactions at the Silicon Photonics Interface

Lauren Cummings
Chemical Engineering, Oregon State University

NNIN REU Site: Center for Nanotechnology, University of Washington, Seattle, WA

NNIN REU Principal Investigator(s): Dr. Daniel Ratner, Bioengineering, University of Washington

NNIN REU Mentor(s): Jeff Chamberlain, Bioengineering, University of Washington

Contact: cumminla@onid.orst.edu, dratner@u.washington.edu, jeffwc@u.washington.edu

Introduction:

Through recent advancements in optics and semiconductor fabrication, silicon photonics has lent itself to the development of a versatile class of real-time, label-free biosensors. One of the most promising biosensing platforms to emerge from this field is the silicon photonic ring resonator array. The array used in these studies consisted of 32 microrings, each of which had been fabricated onto a silicon-on-insulator chip using complementary metal oxide semiconductor (CMOS) processing [1]. Light from a tunable laser was coupled into each ring cavity via an adjacent waveguide, and a photodetector was used to measure the resonant spectra of each microring [2]. Biomolecular samples were then introduced to the array using syringe pumps and on-chip microfluidics [1]. When biomolecules bind at or near a ring cavity functionalized with its complimentary ligand, they induce a shift in the ring's refractive index, and thus, a shift in its resonant wavelength [2]. Using data acquisition software, these shifts can be measured in real-time—allowing us to both detect and quantify biomolecular binding.

A fundamental challenge to this technology is our limited understanding of how surface chemistries influence biomolecular interactions at the biosensor interface. As a simple validation model for the platform, we investigated the binding of the protein, Concanavalin A (ConA), to mannose-functionalized ring resonators. To examine how chemical modification affects biomolecular binding, we implemented two different methods to immobilize the mannose ligand onto the silicon surface. We then used atomic force microscopy (AFM) to characterize silicon substrates modified for biomolecular detection and to investigate the binding of biomolecules to the biosensor surface. Real-time binding experiments offered further insight into how immobilization methods influenced the performance of the biosensing platform.

Experimental Procedure:

Surface Functionalization. The ring resonator chips were first cleaned in a piranha solution (1:1 sulfuric acid: hydrogen

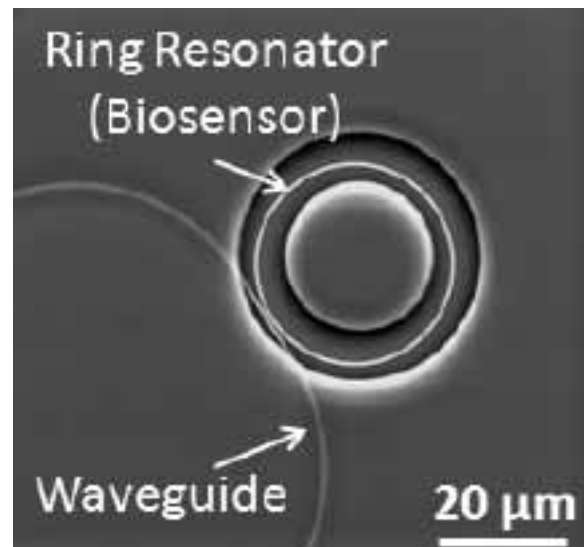


Figure 1: SEM micrograph of a ring resonator.

peroxide), then dried under a stream of nitrogen. Mannose was then immobilized either covalently using silanization chemistry, or non-covalently via physical adsorption of a bovine serum albumin (BSA)-mannose conjugate. Covalent immobilization of mannose began with the activation of the silicon oxide surface by immersing the silicon chips in a 1% (v/v) epoxy-silane in toluene solution for six hours. The chips were then incubated in 0.2 mM D-mannose-(OEG)₂-SH for 12 hours. To prevent non-specific binding to the biosensing surface, functionalized substrates were blocked with 1 μ M BSA for one hour. Functionalized chips were then allowed to equilibrate in HEPES buffer for at least eight hours. On separate silicon chips, mannose was instead non-covalently immobilized onto the surface by immersing cleaned substrates in a 0.5 mg/mL solution of BSA-mannose for 90 minutes at 37°C. The surface was then thoroughly rinsed in deionized (DI) water and dried under a nitrogen stream.

Protein Adhesion. For the purpose of AFM characterization, both the covalently and non-covalently functionalized

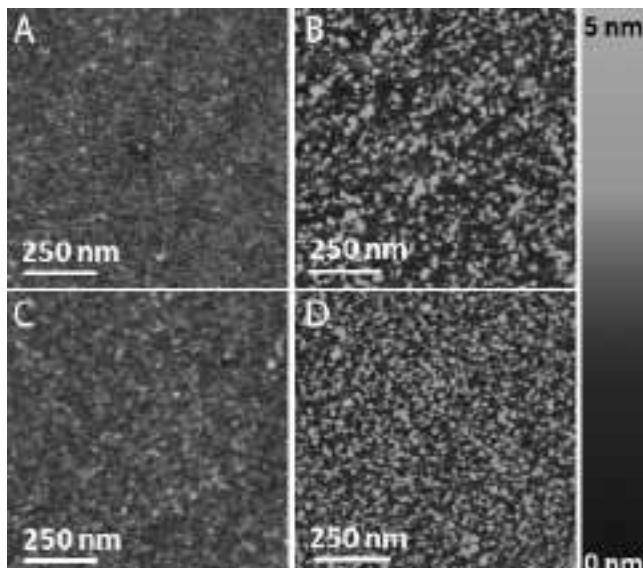


Figure 2: AFMs of silicon modified with BSA-mannose (A) and ConA (B), and covalently-immobilized mannose (C) and ConA (D).

substrates were incubated in a $1 \mu\text{M}$ solution of ConA for 30 minutes at room temperature. Chips were then rinsed under de-ionized (DI) water and blown with nitrogen. Alternatively, some covalently and non-covalently functionalized ring resonator chips were used to monitor protein binding in real-time. Different concentrations of ConA were flowed directly over ring resonator chips, and binding was quantified by measuring shifts in the resonant wavelengths of each mirroring.

Characterization. AFM images were acquired in tapping mode using a Dimension 3100 Atomic Force Microscope. A FESP tip was used to obtain topographic maps of the silicon surface after each stage of surface modification (i.e., cleaning, mannose immobilization, ConA binding). Nanscope software was used to measure surface roughness by averaging three $250 \times 250 \text{ nm}$ areas from each image.

Results and Conclusions:

Preliminary AFM characterization indicates that the methods used to immobilize mannose influenced the adhesion of protein to the biosensor surface. AFM scans showed a homogeneous distribution of ConA on surfaces modified with covalently-bound mannose (see Figure 2d). Conversely, surfaces modified with physically adsorbed BSA-Mannose showed aggregation and uneven distribution of ConA (see Figure 2b), with some images (not shown) displaying little or no protein binding. After ConA binding, covalently-functionalized surfaces were found to have a surface roughness of $0.69 \pm 0.04 \text{ nm}$, whereas non-covalently functionalized

surfaces were found to have an average roughness of $0.97 \pm 0.11 \text{ nm}$. As uniform biomolecular adhesion is critical for a reliable and reproducible biosensing device, the lower surface roughness suggests that covalent immobilization is optimal for the detection and adhesion of ConA.

ConA binding was also detected in real-time using ring resonators that were functionalized by means of either silane chemistry or physical adsorption (see Figures 3 and 4). Results were characteristic of specific binding and demonstrate the ring resonator's ability to detect carbohydrate-mediated protein adhesion. Binding profiles showed larger response curves for ring resonators functionalized with covalently immobilized mannose, suggesting that the covalent immobilization of mannose enhanced protein-surface interactions.

These results demonstrate the ring resonator platform's potential as a versatile bioanalytical tool. By further optimizing the surface chemistries used for detecting ConA and other more clinically-relevant biomolecules, this novel biosensing technology will be poised to renovate conventional paradigms for disease diagnostics.

Acknowledgments:

I would like to thank my mentor, Jeff Chamberlain, and my PI, Dan Ratner, for giving me the opportunity to work with them this summer. Also, many thanks are due to the University of Washington's Nanotechnology User Facility and Staff. Lastly, I would like to acknowledge the National Science Foundation and the National Nanotechnology Infrastructure Network REU Program for their funding of my research.

References:

- [1] Bailey, R.C. et al.; "A Robust Silicon Photonic Platform for Multiparamter Biological Analysis." Proc. SPIE, 7220 (2009).
- [2] Iqbal, M. et al.; "Label-Free Biosensor Arrays Based on Silicon Ring Resonators and High-Speed Optical Scanning Instrumentation;" IEEE, 16, 654-661 (2010).

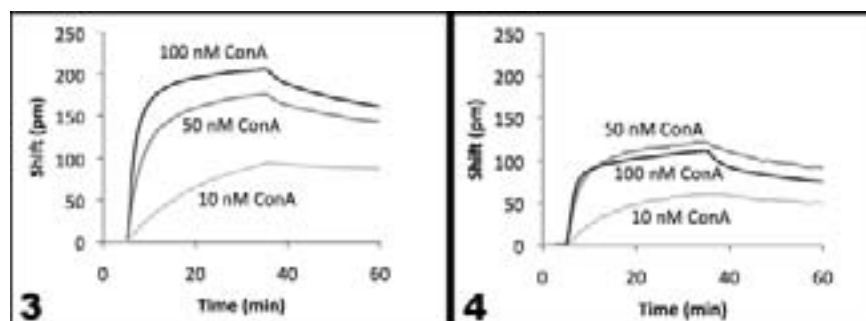


Figure 3, above left: Binding profiles showing the detection of ConA by rings modified with covalently-immobilized mannose.

Figure 4, above right: Binding profiles showing the detection of ConA by rings modified with BSA-Mannose.

Immunomagnetic Detection of Circulating Tumor Cells using a Microfluidic Chip: Cell Recognition and Analysis

Fraser Downing
Mechanical Engineering, University of Colorado at Boulder

NNIN REU Site: Microelectronics Research Center, The University of Texas, Austin, TX

NNIN REU Principal Investigator(s): Professor John X.J. Zhang, Ph.D., Biomedical Engineering, Stanford University

NNIN REU Mentor(s): Dr. Kazunori Hoshino, Department of Biomedical Engineering, University of Tokyo, Japan;

Yu-Yen Huang, Ph.D. Graduate Student, Department of Biomedical Engineering, University of Texas at Austin

Contact: fraser.downing@colorado.edu, john.zhang@engr.utexas.edu, hoshino@mail.utexas.edu, n9692416@gmail.com

Abstract:

Early recognition of cancer within a patient has proven to be a key component in successful treatment and survival. Given a blood sample containing circulating tumor cells (CTCs), these cells can be marked with ion oxide nanoparticles using a specific functionalization process. By running this prepared sample through a system that includes a microfluidic chip and a magnet, the labeled CTCs can be captured for analysis. Using three different dyes and exposure types, identification of a CTC is based on physical characteristics and appearances as they are observed under each exposure condition. Although CTCs possess a unique physical appearance in terms of fluorescence, size and shape, correct identification can be a challenging task. After working with several persons trained in cell identification, a tool was developed in MATLAB to facilitate the identification of CTCs based on the measurements and calculations for key characteristics as taken from the experiment images. By using explicit definitions for identification, a large volume of images can be analyzed quickly and efficiently while also ensuring judgment of each cell is based on the same criteria.

Introduction:

As new and innovative ways to fight cancer continue to develop, although an absolute cure has not yet been discovered, vast improvements have been made to where the disease has become treatable if the correct steps are made. Early recognition of cancer within the body can play a significant role in a patient's survival. One specific technique currently under investigation involves the positive selection of circulating tumor cells (CTCs) with an ion oxide nanoparticle.

Experimental Procedure:

By executing this process of marking using antigens such as cytokeratin, cancer cells within a sample were now bound with magnetic particles. The sample was then drawn through a microfluidic channel consisting of a polydimethylsiloxane (PDMS) mold sealed off by a glass capture slide (see Figure 1). The set up also possessed a permanent magnet aligned in parallel to the glass capture slide along the channel. Due to the magnetic field that was created, marked cells traveling through the channel became suspended on the glass capture slide. Upon trial completion, the captured cells were bonded permanently to the capture slide and the PDMS mold could be removed after a mild heat treatment. Once the slide had been isolated, a post-analysis process could begin, which was critical to determining the level of success achieved during the experiment.

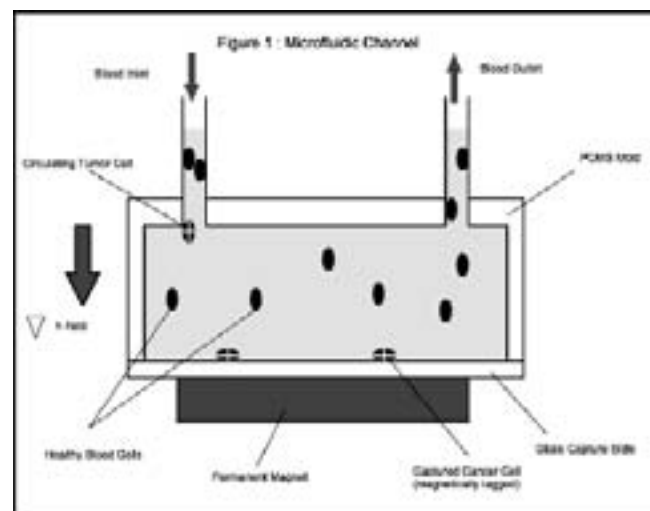


Figure 1: Microfluidic channel.

To begin this process, the slide was stained using three different substances. Cytokeratin (CK), an enzyme called CD45, and a stain referred to as DAPI were used as dyes due to a desired characteristic for binding. Each dye has unique fluorescent characteristics when exposed to different light conditions under a microscope. CTCs would appear bright green in CK, dim and red in CD45, and bright blue

in DAPI. Each exposure condition for a possible cell was photographed, as the images would be used to draw a conclusion on cell type.

Due to the ambiguity of parameter guidelines, identification could be a tedious and challenging task. Depending on the type of sample that was being utilized, there could be anywhere from 60 to 80 cells in need of investigation. Foreign particles, as well as wrongly tagged cells, were likely to exist, as a perfect experiment is impossible to achieve. Different dye concentrations caused variable brightness from slide to slide. Between these factors and the fact that the conclusion depended on a set of implicit definitions interpreted by the observer, a large possibility for misidentification existed.

In order to solve this issue, the implementation of an original program written in MATLAB to quantify the identification characteristics and express an opinion on cell type was explored. The defining properties obtained from the images could be used together to make a decision based on tangible quantities rather than user interpretations. In

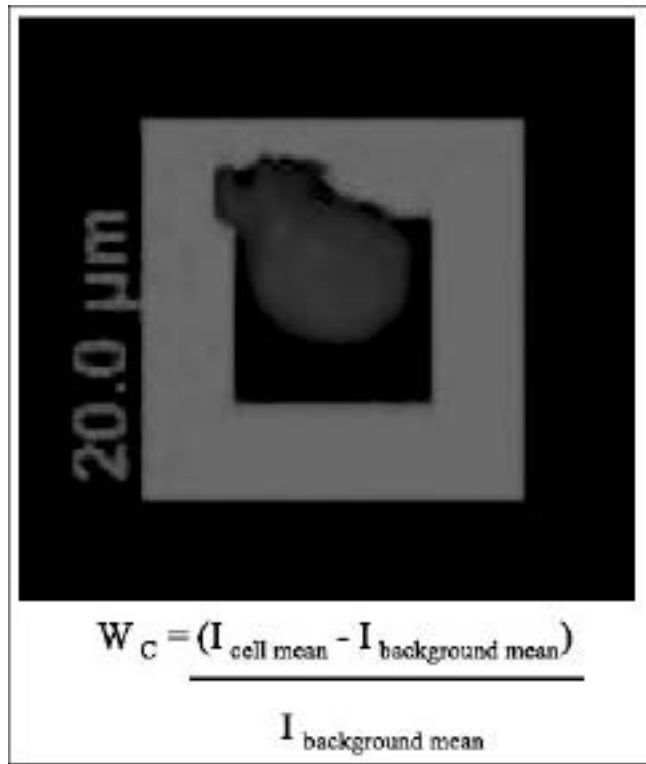


Figure 2: Weber contrast determination.

order to perform analysis, the location of the cell within the images needed to be obtained. This was done by the user adjusting a light-intensity threshold value or by manually selecting a region of interest if many visible bodies existed. Coordinate locations were obtained by finding the positions of the pixels within the selected regions. Once the locations were known, the Weber contrast ratio was taken in order to quantify color-specific light intensity.

As shown in Figure 2, the ratio took the mean value of the pixels for each color in the cellular region and an immediate background region, omitting any regions of high intensity. The Weber value was used as it normalized the light intensity measurements, eliminating the problem of variable brightness.

Results and Conclusions:

By implementing the previous steps into a graphical user interface, a user could easily explore the data for each cell. After running several image sets through analysis, a consistent result for the defining characteristics was determined. By saving these values to a database organized by cell type, normal distributions for the characteristic values could be generated and used to gage cell type. The program also showed results consistent with the database for real patient samples as well as for different cancer types.

Future Work:

The explicit definitions used to define cancer cells show good promise, but much more research and testing needs to be carried out in order to ensure consistency. Although uniform results were shown between cancer types, little is known about the reactions of other cancer types. However, if the consistency in results hold true, this program normalizes judgment while vastly increasing confidence in concluding cell type. This would be vital in a real-world setting, as a correct identification could mean a patient's survival.

Acknowledgements:

Thank you to the Zhang research group at the University of Texas at Austin as well as the NNIN REU Program for hosting me this summer.

References:

- [1] Lara-Velasco, O.; "Immunomagnetic Cell Separation: Further Applications of the Quadrupole Magnetic Cell Sorter"; Ohio State University, 2003.

Surface Analysis of DNA Microarrays

Megan Dunn

Chemical Engineering, University of Arkansas

NNIN REU Site: Center for Nanotechnology, University of Washington, Seattle, WA

NNIN REU Principal Investigator(s): Dr. David G. Castner, Department of Bioengineering and Department of Chemical Engineering, University of Washington

NNIN REU Mentor(s): Matthew Ryder, Department of Bioengineering, University of Washington

Contact: mdunn@uark.edu, castner@nb.engr:washington.edu, mryder@u.washington.edu

Abstract and Background:

Surface-bound deoxyribonucleic acid (DNA)-based arrays have shown the potential to be powerful tools to diagnosis and analyze several different diseases.

However, for microarrays to meet theoretical expectations for detection sensitivity and the potential for single base mutation detection, the current technologies need to be optimized. The purpose of this study was to analyze model DNA arrays in order to determine potential optimization area in the current methods. Surface analysis techniques such as surface plasmon resonance (SPR) and x-ray photo electron spectroscopy (XPS) were used to analyze the arrays. In addition, fluorescent imaging was used to evaluate individual spot uniformity within an array on a commercial substrate.

Methods:

Gold covered SPR slides were modified with maleimide-ethylene glycol disulfide (MEG) self-assembled monolayers (SAMs). The maleimide group specifically binds with thiol terminated single stranded DNA (HS-ssDNA). Monolayers were made using the previously reported method [1]. The MEG SAM coated slides were manually spotted with 40-mer-ssDNA. The spotted DNA had a 15 μ M concentration in buffer (1.5 M sodium chloride and 0.015 M sodium citrate in water) and was treated with a reducing agent, 0.2 mM tris(2-carboxyethyl)phosphine. The slides were incubated at \sim 70% humidity for 1.5 hr before repeated rinsing in both buffer and water. The slides were blocked with 6-mercaptop-1-hexanol (MCH) to inhibit the target DNA from binding to unreacted maleimide groups.

XPS provided an elemental analysis of what was on the top \sim 8 nm of the surface. XPS was performed on a MEG-SAM modified slide before and after the immobilization of DNA onto the slide.

XPS Line	MEG SAM DATA			Previously Published Values (1)		DNA-Covered Spot	
	BE - Ayo	Atomic %	% STDV	Atomic %	% STDV	Atomic %	% STDV
Au 4f	84	19	0.3	17.4	1.4	15.1	0.4
O 1s	533	19.4	0.6	15.1	1.6	20.6	0.9
N 1s	400	3.2	0.3	2.8	0.7	3.1	0.4
C 1s	296	57.3	0.7	63.8	0.4	60.1	0.9
S 2p	162	1.1	0.3	0.9	0.1	1.1	0.3
P 2p	na	na	na	na	na	na	na

Figure 1: XPS comparison of MEG-SAM atomic composition and DNA immobilized slide.

A Plexera imaging SPR was used to compare hybridization efficiencies for three different spot sizes on the model DNA array surface. The Plexera imaging SPR works by shining monochromatic light through a prism at multiple angles to the slides. The light excites a plasmon wave at specific angles dependent on the interactions on the slide and solution [2]. When target DNA is flowed through the SPR flow-cell, there is a change in index of refraction caused by interactions on the slide. These results can be used to determine real time kinetic information of the spotted DNA. The SPR experiment was set up to run buffer, non-complementary DNA and then complementary DNA across the slide.

Fluorescence imaging was used to characterize individual spots on a set of commercial slides that were printed using an automated printer. The images were obtained by using a confocal laser scanning microscope with a 543 nm laser and a 610 nm filter.

Results and Discussions:

The XPS analysis of the MEG-SAM slide coating was compared to previously published XPS data [1] for the monolayer as seen in Figure 1. The atomic composition of the tested MEG-SAM slide was similar to previously published results, suggesting that the protocol used for the MEG-SAM slide coating worked. XPS was also used to determine if there was DNA immobilized onto the slide after spotting. If there was DNA immobilized onto the slide, it would be evident by the presence of phosphorous

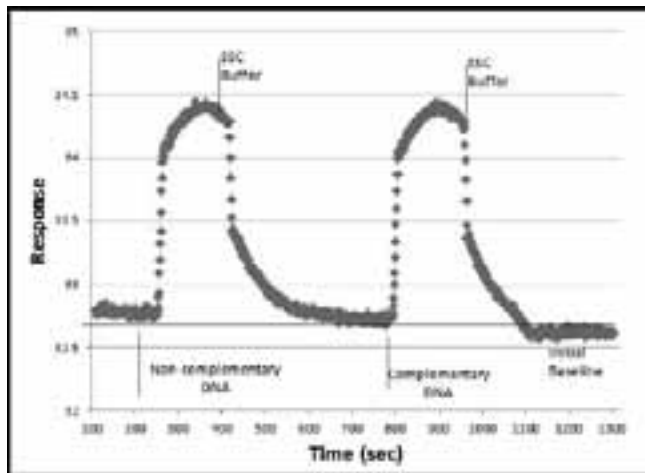


Figure 2: SPR analysis of hybridization.

in the atomic composition (from the DNA backbone) as well as attenuation of the gold signal and an increase in the nitrogen signal. As shown in Figure 1, phosphorous was not detected by XPS of the DNA immobilized slide. However, the Au signal was slightly attenuated and the nitrogen signal increased slightly indicating that there might be a very small addition of DNA to the surface.

The SPR results (Figure 2) show the spotted slide response to non-complementary DNA and complementary DNA. If hybridization occurred, it would be expected that after the addition of the complementary DNA the response would be higher than the baseline after the addition of the buffer. These SPR results indicated no detectable hybridization occurred. This result, in combination with the XPS data, indicated that there was little DNA bound to the surface after the spotting step. However, these results did indicate the DNA did not non-specifically bind, suggesting that the MCH blocking step was successful.

Fluorescence results of the commercial DNA array suggested that there may have been an issue with sample storage of this particular commercial substrate, correlating to a problem with spot reproducibility.

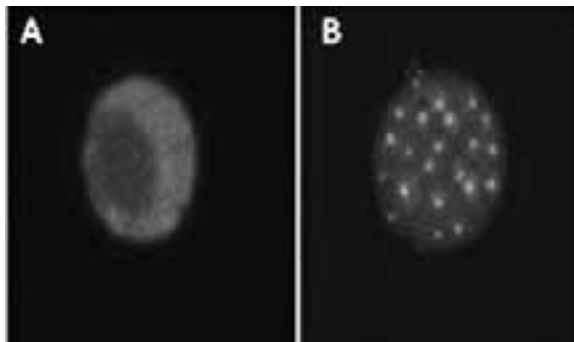


Figure 3: Comparison of two fluorescence images; a) image of general spot uniformity (left), b) image showing segregated spot taken months after hybridization (right).

Figure 3 compares two fluorescence images taken at different time-points. As can be seen with the image from the aged slide, there seems to be segregation within the individual spot.

Conclusions:

This study illustrates the importance of surface analysis in better understanding DNA microarrays and the usefulness of these methods for detecting previously unknown problems. Knowing these problems exist is the first step in being able to fix them and ultimately leading to a better microarray.

Future Work:

Further investigations must be done in order to optimize the surface chemistry used for the MEG-SAM DNA immobilization. This will be done by analyzing each step in the process to determine which step is working improperly. Once the surface chemistry is optimized, these slides can be used in model hybridization experiments characterized by SPR. Also, more fluorescence data needs to be obtained and compared to other supplementary methods in order to determine the cause of the segregation on the slide.

Acknowledgements:

I would like to thank NESAC/Bio lab group, The NanoTech User Facility at the University of Washington, the National Nanotechnology Infrastructure Network Research Experience for Undergraduates (NNIN REU) Program, the National Science Foundation, and NIH grants EB-002027 and EB-001473 from the National Institute of Biomedical Imaging and Bioengineering.

References:

- [1] Lee, C., Nguyen, P., Grainger, D., Gamble, L., and Castner, D. (2007). Analytical Chemistry, 79(12), 4390-4400.
- [2] Homola, J., Yee, S., Gauglitz, G. (1999). Sensors and Actuators B, 59, 3-15.

Electrochemical and Adhesion Properties of PEDOT:PSS as a Coating for Gold Electrodes for Applications in Metal-Molecule-Metal Junctions

Vivian Feig

Chemical Engineering, Columbia University

NNIN iREU Site: Institut Für Bio- Und Nanosysteme (IBN), Forschungszentrum Jülich, Germany

NNIN iREU Principal Investigator(s): Dr. Dirk Mayer, Institute for Bio and Nanoelectronics (IBN-2), Forschungszentrum Jülich

NNIN iREU Mentor(s): Nils Sanetra, Institute for Bio and Nanoelectronics (IBN-2)

Contact: vivianfeig@gmail.com, dirk.mayer@fz-juelich.de, n.sanetra@fz-juelich.de

NNIN iREU Program

Introduction:

Crossbar junctions with gold top and bottom electrodes are a promising type of metal-molecule-metal junction for the purpose of electrically addressing defined small biomolecules. However, the surface roughness of gold poses a number of challenges for working at the single molecular scale, such as piercing the molecule and causing shorts in the device. To solve this problem, we investigated the application of a conducting polymer, poly(3,4-ethylenedioxythiophene)/poly(4-styrenesulfonic acid) (PEDOT:PSS), as a way to coat and smoothen the electrode surface.

For our application, it is further important to examine the adhesion of PEDOT:PSS to molecules that we hope to incorporate into our molecular electronics devices. This paper examines the electrochemical properties of PEDOT:PSS and its interaction with cytochrome *c* as well as certain self-assembled monolayers (SAMs).

Experimental Procedure:

Three different solutions of PEDOT:PSS were tested, each differing by amount of dopant: Clevius P and Clevius FE solutions provided by Sony, and a Clevius P solution made at the Forschungszentrum Jülich (Clevius P (FZJ)). PEDOT:PSS solutions were applied to silicon and gold substrates by spin coating. Substrates were prepared by cleaning in O₂ plasma at 140 W and 0.7 mbar for three minutes. The plasma additionally served to hydrophilize the substrate surface, which was important for PEDOT:PSS adhesion. Samples were spin-coated first at 1000 rpm for eight seconds, then for one minute at a variable rate. Afterwards, they were baked for two minutes at 150°C. Film thicknesses, at various spin rates, were measured using scanning electron microscopy, and were found to generally decrease with increasing spin rate until converging at around 4000-5000 rpm, with Clevius P (FZJ) and Clevius FE reaching a minimum thickness of about 50 nm, and Clevius P reaching a thickness of about 30 nm.

To examine electrochemical properties of PEDOT:PSS, 50 nm layers of each solution were spin-coated onto gold (Au) substrates and cyclic voltammetry (CV) measurements were

performed with an Autolab potentiostat. A three electrode setup was used with phosphate buffer solution (PBS, pH = 7) as the electrolyte. To test the interaction of PEDOT:PSS with octadecanethiol and 11-MUA SAMs, monolayers were assembled by immersing the substrate in solution for 20 minutes and 24 hours, respectively, then rinsing with ethanol and drying in a nitrogen stream. To test cytochrome *c* adhesion, 20 μM of cytochrome *c* in PBS was used as the electrolytic solution. CV analysis was performed directly using the GPES software.

Results and Analysis:

The CV of plain Au was dominated by capacitive current with a capacitance of 20 μF. By comparison, CVs of 50 nm PEDOT:PSS on Au also showed predominantly capacitive current, but of a larger magnitude. Clevius FE had a capacitance of 22.6 μF, Clevius P 22 μF, and Clevius P (FZJ) 30.2 μF, suggesting that the PEDOT:PSS layers are conductive. Further, the capacitive current also increased with PEDOT:PSS thickness: for a 140 nm layer of Clevius P (FZJ), the capacitance was 95.4 μF, significantly higher than for the 50 nm layer.

Next, the interaction of PEDOT:PSS with an octadecanethiol SAM was tested. On plain Au, octadecanethiol self-assembles effectively and forms a dielectric layer that decreases the capacitive current. We found that octadecanethiol is similarly capable of self-assembling to form a monolayer on top of PEDOT:PSS layers and has a similar effect on capacitance. For instance, the capacitance of SAM on Clevius P was 14 μF, as opposed to 22 μF for pure Clevius P.

Additionally, cyclic voltammograms of PEDOT:PSS coated on top of an SAM were measured. Since PEDOT:PSS requires a hydrophilic surface for successful coating, 11-mercaptopoundecanoic acid (11-MUA), which has carboxylic acid end groups, was used to form the SAM. The capacitive current for Au/11-MUA/PEDOT:PSS actually increased compared to Au/PEDOT:PSS. This is surprising, as 11-MUA should form an insulating layer.

One explanation may be that PEDOT:PSS adheres better to the SAM than to gold, resulting in a thicker layer when spin coated at the same speed. This can be checked in the future by comparing PEDOT:PSS film thicknesses when spun at the same speed on 11-MUA and on gold.

Finally, the interaction of PEDOT:PSS with cytochrome *c*, a heme protein involved in the electron transport chain within mitochondria and in cell apoptosis, was investigated. CVs of PEDOT:PSS films taken in 20 μ M cytochrome *c* and PBS solution showed clear redox peaks attributable to the protein. Integrating the current under the peaks and then dividing it by the potential sweep rate yields the total number of charges, which was roughly constant for different sweep rates.

Since the total number of charges per area stays about constant, it can be concluded that the cytochrome *c* was able to adsorb onto the PEDOT:PSS surface and form a relatively homogeneous surface, and that the redox behavior in the CVs was indicative of a surface-bound reaction and not diffusion from the bulk solution. Fluctuations in the total charge calculations were minimal and due perhaps to surface roughness. Additionally, the charge density at the surface was reasonable given the surface area of our samples, 8×10^{13} nm². For Clevius P (FZJ), considering that cytochrome *c* undergoes one electron transfer per oxidation/reduction [1], for an average total charge of 1.25×10^{-5} C, our results indicated a transfer rate of one electron per nm² area. Cytochrome *c* has a diameter of roughly 3-3.4 nm, so we would expect a transfer rate of one electron per at least 9.4-10.7 nm² area. Our large result may be due to some molecules being absorbed by the PEDOT:PSS film [2].

Conclusion and Future Work:

Our results show that PEDOT:PSS is a promising coating for gold electrodes in fabricating molecular crossbar junctions, since it can be spin-coated onto electrodes at small thicknesses and is capable of adhesion to SAMs and cytochrome *c*. To continue this research, future work may involve electrical tests once a top electrode has been placed on top of gold/PEDOT:PSS bottom electrode. Overall, PEDOT:PSS appears to be an effective coating for creating functional metal-molecule-metal junctions.

Acknowledgements:

Thank you to the National Nanotechnology Infrastructure Network International Research Experience for Undergraduates (NNIN iREU) Program and the National Science Foundation for this wonderful opportunity. Also thank you to Dr. Dirk Mayer and Nils Sanetra for their gracious help and supervision. Finally, thanks to everyone at IBN-2 for creating an intellectually stimulating and supportive work environment.

References:

- [1] Bernard, S., N. Leygue, H. Korri-Youssoufi, and S. Lecomte. "Kinetics of the electron-transfer reaction of Cytochrome *c* (552) adsorbed on biomimetic electrode studied by time-resolved surface-enhanced Raman spectroscopy and electrochemistry". *Eur. Biophys. J.* 36(8): 1039-48 (2007).
- [2] Guo, L., D. Pietkiewicz, E. V. Pavlov, S. M. Grigoriev, J. J. Kasielowicz, L. M. Dejean, S. J. Korsmeyer, B. Antonsson, and K. W. Kinnall. "Effects of cytochrome *c* on the mitochondrial apoptosis-induced channel MAC". *Am. J. Physiol. Cell Physiol.* 286:C1109-C1117 (2004).

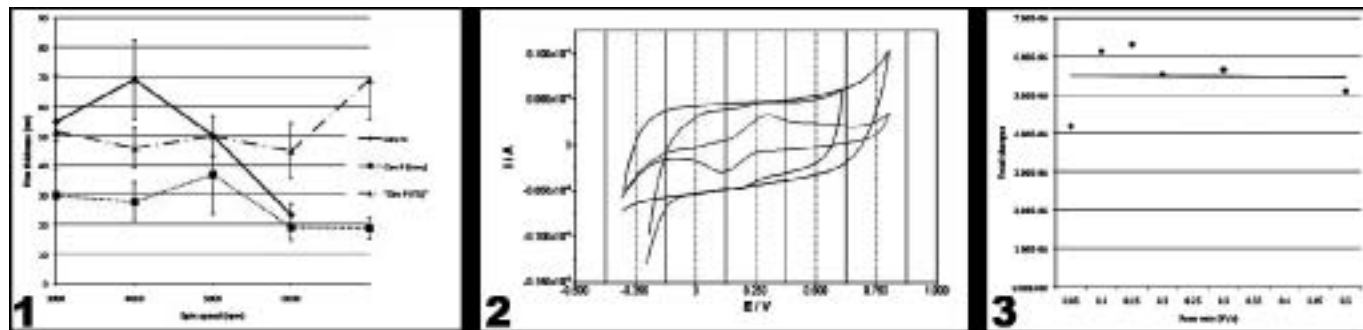


Figure 1: Thicknesses of Clevius solutions spin-coated at different rates.

Figure 2: CVs of plain gold chip; Clevius P (FZJ) on gold; and octadecanethiol SAM on Clevius P (FZJ) on gold.

Figure 3: Total charges under cathodic peaks for Clevius P (Sony) films in cytochrome *c* at different spin rates.

Portable Diagnostic System for the Purification and Detection of Biomolecules



Emily Hoffman

Biomedical Engineering, Case Western Reserve University

NNIN REU Site: Cornell NanoScale Science and Technology Facility, Cornell University, Ithaca, NY

NNIN REU Principal Investigator(s): Dr. Harold Craighead, Applied and Engineering Physics, Cornell University

NNIN REU Mentor(s): Dr. Madhukar Varshney, Applied and Engineering Physics, Cornell University

Contact: eh423@cornell.edu, hgc1@cornell.edu, mv265@cornell.edu

Abstract:

A microfluidic based integrated system was designed for the purification and detection of target ribonucleic acid (RNA) from crude samples. The significant features of this system include low-cost, rapid, flexibility in design, and suitability for multiplexing. Glass beads conjugated with streptavidin were used to purify target RNA from crude plant extract using biotinylated probes.

Introduction:

Polymerase chain reaction (PCR) is used in diagnostic systems for detecting RNA targets, but the amplification method is complex, laborious, expensive, and time-consuming [1]. As an alternative method, biobarcodes amplification techniques have been found to be extremely sensitive and also offered multiplex detection capabilities [1,2]. Combining this technique with a glass bead (GB)-based purification method, an integrated microfluidic system was designed.

Our device allowed for both purification and detection in one stand-alone system. For purification, streptavidin conjugated GB and target-specific biotinylated probes were used to purify target RNA, followed by a biobarcodes method for the detection. The target RNA was hybridized with the probes on the surface of the GB. Following hybridization, RNA probe functionalized gold nanoparticles with biobarcodes

were flowed through the channel. After washing away the unbonded probes and dehybridizing the biobarcodes on the nanoparticle, the biobarcodes were used to detect the presence of the target RNA. Because the nanoparticle carried a large number of biobarcodes per RNA binding event, there was substantial amplification. This process is shown in Figure 1.

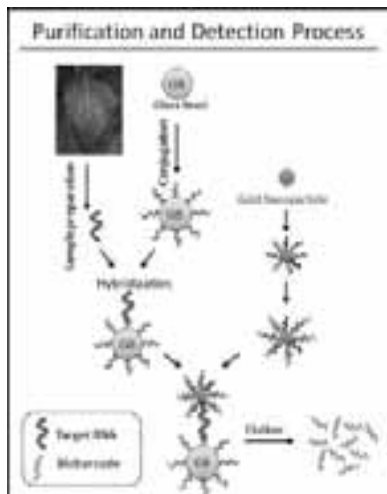


Figure 1: RNA purification and detection.

Objectives:

- To determine the functionalization chemistry to maximize the purification of high amounts of RNA from the samples.
- To optimize the elution of RNA from a crude sample.
- To design and fabricate microfluidic channels.
- To successfully use the GB inside the microfluidic channels to elute the target RNA.

Methods:

Glass Bead Functionalization. Two sizes of beads were used, 100 μm and 300 μm . Various chemistries were used to conjugate streptavidin on the surface of GB, including gluteraldehyde (GA), bis[sulfosuccinimidyl] substrate (BS3), and hydrazine.

Optimization of Separation of RNA. As a model, we selected cucumber mosaic virus (CMV). The plants were inoculated, and the symptomatic leaves were picked for the extraction and detection of virus. The extract was incubated at room temperature for one hour with various batches of GB. The excess extract was washed, the beads were heated to 95°C for 10 minutes, and the target RNA was eluted from the beads. The eluted target RNA was quantified using reverse-transcriptase and real-time PCR, and the batches were compared.

Device Design. Channels were fabricated with molded polydimethylsiloxane (PDMS) bonded to a glass slide. Tubing provided the inlet and outlet of the channel while a nylon membrane with 20 μm pore size covers the outlet tube to trap the GB. A syringe pump controlled volume and flow rate in the channels. The channel configuration is shown in Figure 2 and the syringe pump set-up is shown in Figure 3.

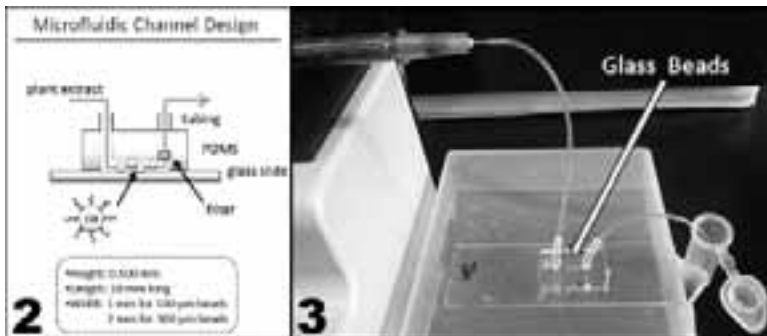


Figure 2: Microfluidic channel configuration and materials.

Figure 3: Syringe pump and microfluidic channel with plant extract.

RNA Separation in Channels. The GB, previously prepared outside of the channel, were enclosed in the microfluidic channel while the plant extract was flowed through. This was followed by a washing buffer to remove unbound RNA. The microfluidic channel was placed in 95°C water for 10 minutes to elute the RNA, and PCR was used to quantify the results. Blocking agents bovine serum albumin (BSA), PolyA, chromosomal salmon sperm RNA (CSS), and synthetic block (SB) were injected into the channels to prevent nonspecific binding.

Results and Discussion:

Since magnetic beads and commercial GB are known to be successful, our GB are compared to these PCR C_t values. The C_t values are shown in Figure 4. Our beads show a similar PCR C_t value as the commercial, showing that RNA bound to all of our beads successfully.

For our channel design, 300 μm beads were selected to be used for the 2 mm channel, and 100 μm beads were selected for the 1 mm channels. These sizes of GB fit best in the channels to allow for a constant flow of fluid.

Inside the channels, the GB did not produce consistent results due to nonspecific binding. This is shown in Figure 4, as without beads, an infected plant sample will still have a low C_t value. The higher cycle number for the healthy sample showed that this process could distinguish healthy from infected plant samples once nonspecific binding was minimized.

Blocking agents were investigated to reduce nonspecific binding. The BSA is a proteinaceous blocker and was possibly denatured when it contacted guanidine isothiocyanate (GUSCN), used in the plant extract lysis buffer. PolyA and CSS were first added to the channels as these blockers are of a similar conformation as CMV RNA. SB was added as well as it is non-proteinaceous and will not deform with GUSCN. These blockers allowed the GB to only bind specifically to the targeted CMV RNA.

Conclusion:

Glass beads are suited for use in microfluidic channels with proper surface chemistry, but a blocking agent is needed to prevent nonspecific binding. To further advance this design, biobarcodes and gold nanoparticles need to be optimized for success in microfluidic channels. This integrated stand-alone system is ideal for purification and detection of RNA from crude plant samples.

Acknowledgements:

I would like to thank Dr. Harold Craighead, Dr. Keith Perry, and Dr. Madhukar Varshney. I would like to thank the Cornell NanoScale Science and Technology Facility, the coordinators Melanie-Claire Mallison and Rob Ilic, and the National Nanotechnology Infrastructure Network Research Experience for Undergraduates Program. I would like to thank the United States Department of Agriculture and the National Science Foundation for funding.

References:

- [1] Nam, J-M, C Thaton, and C Mirkin; "Nanoparticle-Based Bio-Bar Codes for Ultrasensitive Detection of Proteins"; *Science*, 301, 1884-1886 (2003).
- [2] Nam, J-M, S Stoeva, and C Mirkin; "Bio-Bar-Code-Based DNA Detection with PCR-like Sensitivity"; *J. Am. Chem. Soc.*, 126, 5932-5933 (2004).

MAGNETIC BEADS: infected plant sample			
Batch	Size	PCR C_t Value	
magnetic	1 μm	13.28 \pm 0.16	
GLASS BEADS: optimization outside of channels with infected plant samples			
Batch	Size	Treatment / Functionalization	PCR C_t Value
1	300 μm	Pirana / GA	15.60 \pm 0.16
2	300 μm	Pirana / Hydrazine, (1)	15.24 \pm 0.03
3	300 μm	Pirana / Hydrazine, (2)	13.96 \pm 0.11
4	100 μm	Sodium Hydroxide / GA	15.78 \pm 0.00
5	100 μm	Sodium Hydroxide / BSA	16.13 \pm 0.03
6	100 μm	Commercial	13.27 \pm 0.17
GLASS BEADS: inside of channels			
Batch	Plant Sample	Blockers	PCR C_t Value
1	Infected	BSA	14.93 \pm 0.01
1	Healthy	BSA	20.89 \pm 0.22
None	Infected	BSA	11.27 \pm 0.03

Figure 4: Summary of PCR tests run.
The value indicates the cycle when the RNA was detectable.

Light Dependent Microbial Responses to Cu-doped TiO_2 Nanoparticles

Kristen Jones
Chemistry, Carthage College

NNIN REU Site: Nano Research Facility, Washington University in St. Louis, St. Louis, MO

NNIN REU Principal Investigator(s): Dr. Yijie Tang, Energy Environmental and Chemical Engr, Washington University in St. Louis

NNIN REU Mentor(s): Bing Wu, Energy Environmental and Chemical Engineering, Washington University in St. Louis

Contact: kjones4@carthage.edu, yijie.tang@seas.wustl.edu, wub@seas.wustl.edu

Abstract:

Shewanella oneidensis MR-1 is an environmental bacterium that can reduce metals and survive in both anaerobic and aerobic conditions. *Mycobacterium smegmatis* is a pathogenic bacterium, but a non-virulent species. Titanium dioxide (TiO_2)-based nanoparticles, commonly used as catalysts, have photocatalytic properties that allow the nanoparticles to absorb ultraviolet (UV) light. The results showed that neither the TiO_2 nor the copper (Cu)-doped TiO_2 nanoparticles reduced the viability of *S. oneidensis* MR-1 under dark or fluorescent light conditions because the bacterium has evolved the strong capability to reduce metal ions and oxidative stresses. *S. oneidensis* MR-1 is highly sensitive to ultraviolet (UV) light, but the presence of TiO_2 nanoparticles or Cu-doped TiO_2 nanoparticles dramatically increased the cell viability. *M. smegmatis* showed a dramatic decrease in viability at a higher doping amount of Cu-doped TiO_2 nanoparticles. The UV light absorbing properties and aggregation of the nanoparticles may contribute to our findings.

Introduction:

Titanium dioxide (TiO_2) is a semiconductor with photocatalytic properties. TiO_2 nanoparticles can produce free radicals and exert strong oxidizing capabilities [1]. Doping the TiO_2 with transition metals enhances the photocatalytic properties of the nanoparticles [2]. The process of doping the semiconductor reduces the band gap energy, thus performing photoactivity even in the visible range of the spectrum [2]. Metal doped TiO_2 nanoparticles in the anatase crystalline form is a strong bactericidal agent when exposed to near-UV light or visible light [3]. This is due to the fact that metal doped TiO_2 nanoparticles produce hydroxyl radicals which oxidize the complex proteins in the cell inhibiting the enzymatic function thus leading to cell death [3].

Methods:

S. oneidensis MR-1 was grown in a minimal MR-1 medium at 30°C at a shaking speed of 200 rpm. When the growth of *S. oneidensis* MR-1 approached the stationary phase ($\text{OD}_{600} \sim 1.0$), cells were diluted with 5 mL minimal MR-1 medium in the absence of carbon source in a glass bottle to an optical density at 600 nm ~ 0.1 ($\sim 10^8 \text{ CFU/ml}$). *M. smegmatis* was grown in a Sauton liquid medium at 37°C at a shaking speed of 200 rpm. When the growth of the *M. smegmatis* approached the stationary phase ($\text{OD}_{600} \sim 1.0$), cells were diluted with 5 mL of the carbon-free medium in a glass bottle to an optical density at 600 nm ~ 0.1 ($\sim 10^8 \text{ CFU/ml}$).

After determining the correct volume of bacteria to obtain the OD of 0.1, nanoparticle stock solution was added after sonication for one minute to prevent aggregation.

After the bacterial cells had been exposed to dark, or to fluorescent light or to UV light for a period of time, 100 μl of the sample was taken and then diluted in a series, before being spread onto the agar plates. The total number of viable cells was estimated based on a colony-forming unit (CFU) after one day's incubation at 30°C for *S. oneidensis* MR-1 and at 37°C for *M. smegmatis*.

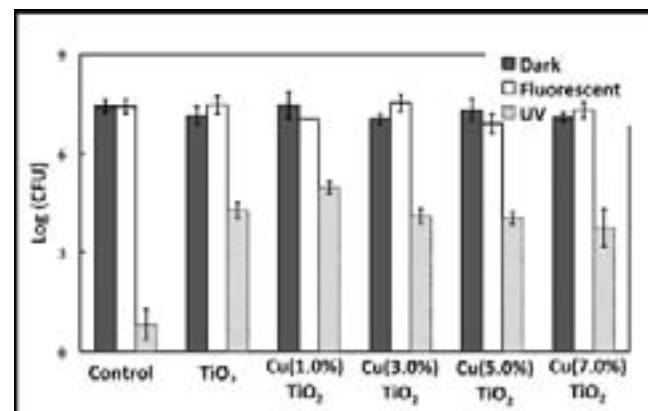


Figure 1: Responses of *S. oneidensis* MR-1 to Cu-doped TiO_2 NPs.

Results and Conclusions:

Figure 1 showed that neither the TiO_2 nor the Cu-doped TiO_2 nanoparticles reduced the viability of *S. oneidensis* MR-1 under dark or fluorescent light conditions because the bacterium has evolved the strong capability to reduce metal ions and oxidative stresses. *S. oneidensis* MR-1 is highly sensitive to ultraviolet (UV) light, but the presence of TiO_2 nanoparticles or Cu-doped TiO_2 nanoparticles dramatically increased the cell viability. The 1% Cu-doped TiO_2 nanoparticles had the greatest increase in cell survival by nearly 196-fold. The aggregation of the nanoparticles shielded the bacteria from the UV light. In addition, the characteristics of nanoparticles, such as absorbing the light within a specific wavelength and tuning the reflection light density, could lead to control their effectiveness for protection of *S. oneidensis* MR-1 against UV stresses.

Figure 2 showed that nanoparticles decreased the viability of the *M. smegmatis* bacteria under dark or fluorescent light conditions. The *M. smegmatis* could tolerate the stresses of UV light, but after the nanoparticles were added into the cell culture, the survival cell amount decreased. Hydroxyl radicals were released from the TiO_2 nanoparticles when exposed to UV light; the *M. smegmatis* cannot tolerate these radicals, which was associated with a decrease in *M. smegmatis* survival. Figures 3 and 4 show the interaction of *S. oneidensis* MR-1 and *M. smegmatis* with Cu-doped TiO_2 nanoparticles. We found that the surface structure of stressed cells became twisted and rougher with regular wrinkles, although without significantly morphological changes.

Acknowledgments:

I would like to thank the NNIN Research Experience for Undergraduates Program for the opportunity to participate in this program. I am also grateful to the National Science Foundation for funding the research project. I want to thank my Principal Investigator, Dr. Yinjie Tang, and my Mentor, Bing Wu, for all of their guidance throughout the research project. I would like to thank Yogesh Goyal, for working on the project with me. Thanks to Kate Nelson, Brent Riggs, and Kristy Wendt for providing training on all of the instruments I used for my research project. Finally I would like to thank God for giving me such a fantastic opportunity to participate in this amazing program, and my family for supporting me and encouraging me to follow my dreams.

References:

- [1] Hu, Xiaoke, Sean Cook, Peng Wang, Huey-min Hwang. "In vitro evaluation of cytotoxicity of engineered metal oxide nanoparticles," *Science of the Total Environment*, 407, 3070-3072, (2009).
- [2] Colón, G., M. Maicu, M.C. Hidalgo, J.A Navío. "Cu-doped TiO_2 systems with improved photocatalytic activity." *Applied Catalysis B: Environmental*. 67. 41-51, (2006).
- [3] Hamal, Dambar B., Johanna A. Haggstrom, George L. Marchin, Myles A. Ikenberry, Keith Hohn, Kenneth J. Klabunde. "A Multifunctional Biocide/Sporocide and Photocatalyst Based on Titanium Dioxide (TiO_2) Codoped with Silver, Carbon, and Sulfur." *Langmuir*. 26 (4). 2805-2810, (2010).

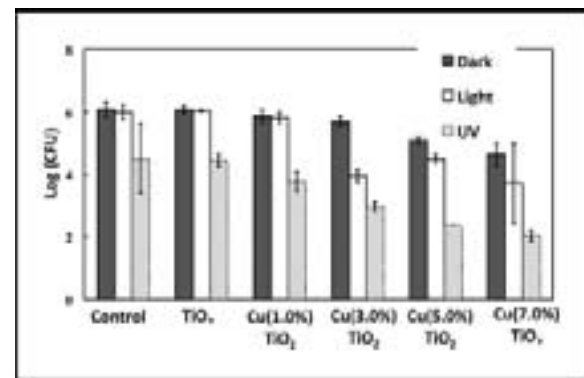


Figure 2: Responses of *M. smegmatis* bacterium to Cu-doped TiO_2 NPs.

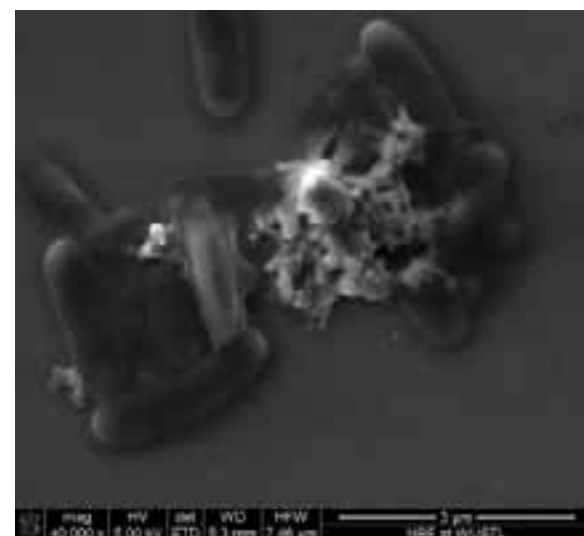


Figure 3: SEM image of *S. oneidensis* MR-1 with Cu (1.0%) TiO_2 after UV exposure.

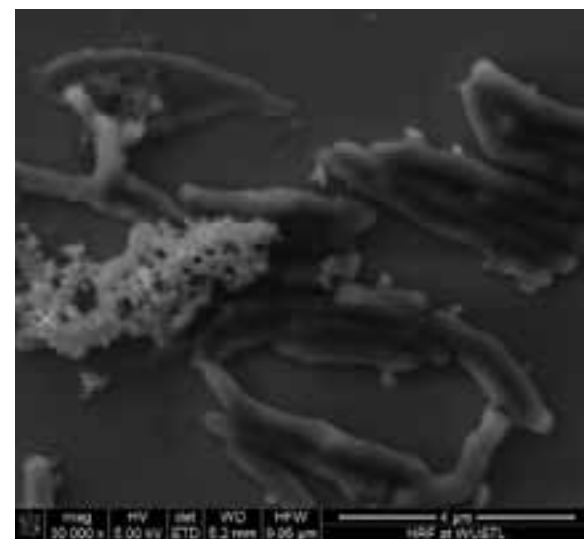


Figure 4: SEM image of *M. smegmatis* with Cu (3.0%) TiO_2 after UV exposure.

Effect of Deposition Characteristics on Electrochemically Prepared PEDOT Films

Adam Kozak

Biomedical Engineering, University of Rochester

NNIN iREU Site: Interuniversity Microelectronics Center (IMEC), Leuven, Belgium

NNIN iREU Principal Investigator(s): Dr. Hercules Neves, IMEC, Leuven, Belgium

NNIN iREU Mentor(s): Filip Vanherberge, IMEC, Leuven, Belgium

Contact: akozak2@gmail.com, herc@imec.be, vanlerbe@imec.be

NNIN iREU Program

Abstract:

Electrodes coated with poly(3,4-ethylenedioxytiophene), or PEDOT, are characterized by low impedance and high charge delivery capacity. However, papers in the literature present a broad spectrum of parameters for electrochemically depositing PEDOT. Presented here is a systematic evaluation of PEDOT deposition variables, with the goal of guiding the fabrication of a low-impedance, structurally stable electrode. The variables investigated were deposition charge, deposition time, PEDOT dopant, galvanostatic/potentiostatic deposition, pulsed deposition, temperature, substrate, and surface preparation.

Introduction:

The interface between neural tissue and implantable micro-electrodes is of critical importance for neural stimulation and recording. The desire to record the activity of individual neurons *in vivo* has lead to the fabrication of microelectrodes, whose reduced geometrical area increases electrode impedance, decreases sensitivity, and decreases signal-to-noise ratio. A potential solution is to coat the electrodes with PEDOT, a conductive and biocompatible polymer film that has been shown to reduce electrode impedance [1]. However, no systematic survey of the polymer's deposition parameters has been reported in the literature, despite evidence that these variables significantly affect electrode performance and stability.

Methods:

All depositions were conducted in a three electrode cell. The working electrode was the substrate to be coated with PEDOT, the counter electrode was platinum or stainless steel, and the voltages were taken with respect to an silver/silver chloride reference electrode. The working electrode was taped to expose a 1 cm² surface area, and the deposition was controlled with an Ivium Technologies CompactStat [2].

Electrochemical impedance spectroscopy was performed in 0.9% sodium chloride to measure electrode impedance at 71 frequencies logarithmically spaced between 0.1 Hz and 1 MHz. Scanning electron microscopy (SEM) was used to observe surface roughness and estimate film thickness. A tape test was conducted to qualitatively measure film stability.

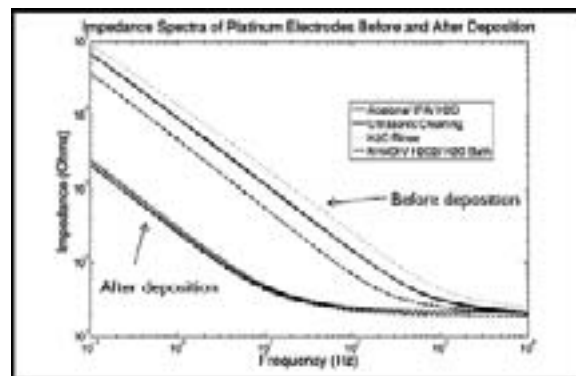


Figure 1: Electrochemical impedance spectra before and after cleaning procedures.

Results:

Four different methods of preparing the electrode surface were tested: a water wash, an acetone/isopropanol/water wash, ultrasonic cleaning in acetone, and a bath of ammonium hydroxide, hydrogen peroxide and water. Although the cleaning method was not observed to affect the electrodes' electrical properties (see Figure 1), it did affect their stability. Only the electrodes prepared with the ammonium hydroxide/hydrogen peroxide/water bath consistently passed the tape test, displaying superior adhesion.

Two PEDOT dopants were tested in the course of this experiment: chlorine and polystyrene sulfonate. PEDOT doped with polystyrene sulfonate was observed to yield films of lower impedance and superior stability compared to PEDOT doped with chlorine. The concentration of the

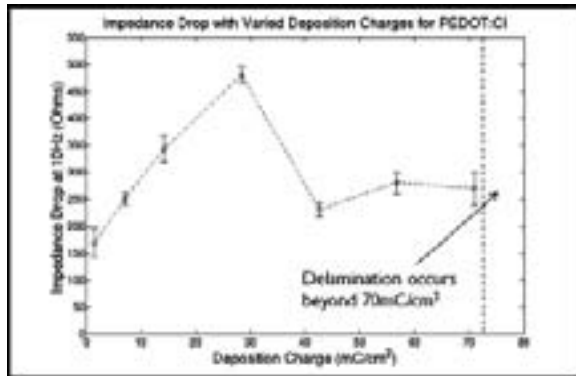


Figure 2: Impedance drop measured before and after PEDOT dep. Error bars represent standard error ($n = 3$).

dopant in the electrochemical cell also affected electrode performance; higher concentrations yielded superior films until saturation.

Deposition charge was observed to significantly affect electrode impedance. Figure 2 shows the reduction in electrode impedance as a function of deposition charge, with a clear optimum appearing at 30 mC/cm^2 .

Longer deposition times were found to be superior to shorter deposition times when depositing at a fixed deposition charge, as seen in Figure 3. Very long depositions, however, necessitated an insufficiently low current density to drive the PEDOT polymerization reaction.

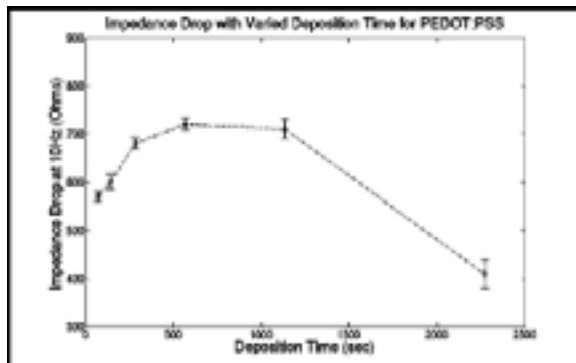


Figure 3: For a fixed deposition charge, the deposition time can be optimized for a low-impedance film.

There was no statistically significant difference observed between galvanostatic, potentiostatic, and pulsed deposition methods. For pulsed depositions, a range of pulse times and duty cycles were tested.

All three methods exhibited similar optimization windows. On one side of the window, low current densities or low potentials were insufficient to drive PEDOT's polymerization reaction. At high current densities or high potentials, oxidation occurred on the electrode surface and formed an insulating oxide layer. It was between these two extremes that ideal deposition parameters were located.

The temperature at which the deposition was performed was found to have little effect on electrode performance. At temperatures above 60°C , however, the adhesion of the polymerized film was poor and films consistently failed the tape test.

The substrate on which the PEDOT film was deposited was observed to affect the qualities of the final electrode. Of the four substrates tested (platinum, gold, indium tin oxide, and silver), indium tin oxide displayed the greatest reduction in impedance. Films deposited on silver consistently failed the tape test.

Discussion:

Of the results presented, one stands in contrast with the literature. It has been reported that potentiostatic depositions yield non-uniform films and inferior electrical characteristics on microelectrode arrays [3]. We report no morphological difference between galvanostatic and potentiostatic depositions, but because our electrodes are significantly larger than microelectrode arrays, further investigation is necessary.

Additional tests remain to be conducted to evaluate electrode performance. Cyclic voltammetry will measure electrical stability and charge delivery capacity, and a scratch test will yield a quantitative measure of film stability.

Conclusions:

Presented is a systematic evaluation of PEDOT deposition parameters. The parameters that were observed to significantly affect electrodes' electrical characteristics or stability were deposition charge, deposition time, polymer dopant, substrate, and the method for preparing the electrode surface. The parameters that would not be suitable for optimization were observed to be deposition type (galvanostatic/potentiostatic/pulsed) and temperature.

Acknowledgments:

I would like to thank my advisor, Hercules Neves, as well as my mentor, Filip Vanherberge, for their guidance in this work. I would also like to thank the staff at the Interuniversity Microelectronics Centre, the National Nanotechnology Infrastructure Network International Research Experience for Undergraduates Program and the National Science Foundation for funding.

References:

- [1] Cogan, S; "Neural Stimulation and Recording Electrodes;" Annual Reviews Biomedical Engineering, 10, 275-309 (2008).
- [2] Ivium Technologies. Retrieved from <http://www.ivium.nl/>.
- [3] Martin, D; "Electrochemical Deposition and Characterization of Poly(3,4-Ethylenedioxythiophene) on Neural Microelectrode Arrays;" Sensors and Actuators B, 89, 92-102 (2003).

Nanotherapeutics for Advanced Cancer Disease

Christopher Lowe

Chemical Engineering, University of Massachusetts Amherst

NNIN REU Site: ASU NanoFab, Arizona State University, Tempe, AZ

NNIN REU Principal Investigator(s): Dr. Kaushal Rege, Chemical Engineering, Arizona State University

NNIN REU Mentor(s): James Ramos, Bioengineering, Arizona State University

Contact: cjlowe@student.umass.edu, krege@asu.edu, jimr975@gmail.com

Introduction:

Plasmonic nanoparticles are gaining increased attention for use in biological systems due to their versatile, tunable optical properties [1]. In particular, gold nanorods (GNR) can be tuned to specifically absorb light in the near infrared region, at wavelengths which do not harm living tissues. The absorbed infrared energy is then dissipated as heat from the nanorods to their surroundings. Sufficient heating within living tissues can induce hyperthermic cell death and damage due to hyperthermic temperatures ($> 43^{\circ}\text{C}$) [2]. Delivery of these nanoparticles to cancerous cells at concentrations that will be responsive to treatment from an infrared laser is key. This project demonstrates that GNR coated with branched cationic polymers synthesized in our laboratory can be employed to deliver plasmid deoxyribonucleic acid (DNA) to PC3 prostate cancer cells, leading to transgene expression. Ongoing work explores the use of GNR for simultaneously administering laser-induced hyperthermia and delivering therapeutic genes to cancer cells.

Methods:

Hexadecyltrimethylammonium bromide capped GNR were synthesized via seed growth method as described by El-Sayed, et al. [3].

Cationic polymers investigated were synthesized as described previously by the Rege group [4] by reacting

equimolar amounts of the desired diglycidyl ethers and poly(amines) shown in Figure 1.

Polyelectrolyte layers were added to the CTAB capped GNR via electrostatic interactions to form polyelectrolyte gold nanorods (PE-GNRs). As-synthesized CTAB-GNRs were centrifuged at 6000 rcf for 10 minutes to remove excess water. 100 μL of 10 mg/mL poly(styrene

sulfonate) (PSS) (anionic) was added to the collected rods under sonication. The solution was sonicated for 30 minutes to allow a layer of PSS to form on the surface of the GNR and then centrifuged as before. 300 μL of nanopure water and 200 μL of desired cationic polymer were added in the same manner as PSS. Collected cationic polymer coated rods were resuspended in serum free media and their optical density adjusted to 0.25 a.u.

PE-GNR cytotoxicity studies were carried out by introducing different concentrations of as described PE-GNRs to PC3 human prostate cancer cells which were seeded at 50,000 cells per well and allowed to incubate overnight. The final well volume was always brought to 500 μL and treatment occurred over six hrs. After six hrs, 20 μL of MTT reagent was added to each well and allowed to incubate for two hrs. At the two hr mark, 100 μL of detergent was added to each well. After an additional two hours and endpoint absorbance reading was taken at 570 nm in a Bio-Tek Synergy 2 plate reader. Cell viability was recorded as percentages of live and dead controls.

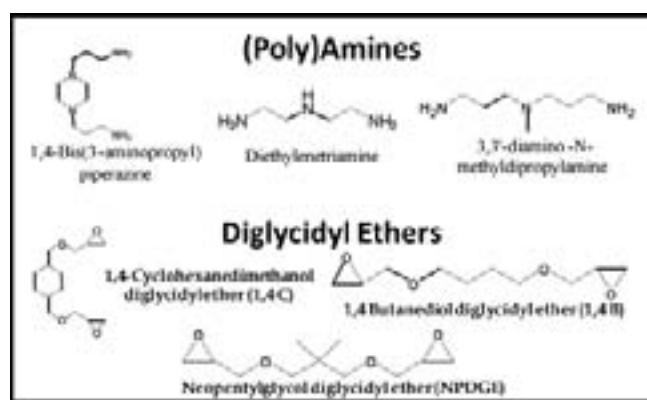


Figure 1: Diglycidyl ethers and poly(amines) used to synthesize novel cationic polymers (reproduced from reference 4).

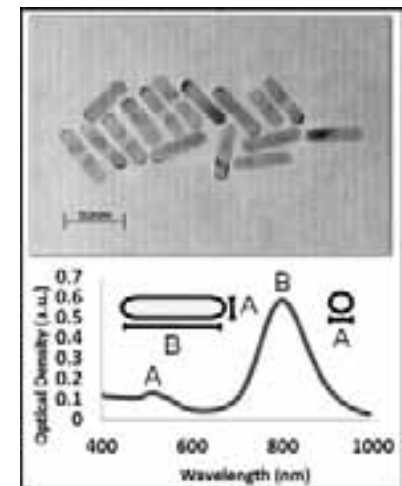


Figure 2: (a) TEM of as-synthesized GNRs, and (b) Typical absorbance spectra of as synthesized GNRs.

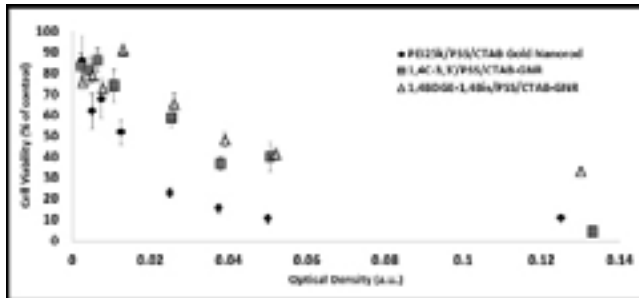


Figure 3: Cytotoxicity data of PE-GNRs made from investigated polymers.

25 μ L of as-described PE-GNRs were placed into wells in 96 well plates. Addition of the plasmid DNA layer was accomplished by adding the desired mass of plasmid DNA to each well. After ensuring that the solution was well dispersed, the plasmid DNA layer was allowed to form via electrostatic interaction at room temperature for 30 minutes.

Transfection studies were carried out as described previously by the Rege group [4].

Results and Discussion:

Figure 3 illustrates the results of the PE-GNR cytotoxicity studies for two of the polymers used, 1,4C-3,3' and 1,4BDGE-1,4C as compared to poly(ethyl imine) (PEI), which is regarded as the current standard in polymeric gene delivery. The figure illustrates that at the lowest concentrations of PE-GNRs the investigated polymers showed cytotoxicity that was similar to that of PEI. As concentrations increased however; it is clear that both of the investigated polymers are less cytotoxic than PEI.

Successful delivery of PE-GNRs to PC3 cells was quantified through transfection study. In order for the plasmid DNA

to be expressed by the cell, the assumption made was that the entire PE-GNR complex had to be taken up by the cell. Figure 4 illustrates the results of transfection studies with all four investigated polymers. Results are reported as relative to PEI. Greater luminescence indicates higher expression of the luciferase protein in cells following delivery of the plasmid DNA. Investigated polymers 1,4C-1,4Bis and 1,4C 3,3' show a clear advantage over PEI, while the 1,4BDGE-1,4Bis protein approaches the efficacy of PEI at most loadings.

Conclusions and Future Work:

These studies have illustrated that delivery of GNRs to PC3 cancer cells can be achieved at high levels as compared to PEI by utilizing certain novel cationic polymers investigated. Investigated polymers are less cytotoxic and more effective in transfection as compared to PEI. Future work includes additional trials to reduce error and inconsistencies between trials. Investigating transfection at higher treatment concentrations may yield even further increases in expression of desired protein as compared to PEI based on cytotoxicity data. Zeta potential studies are required to determine if accumulated negative charge as a result of higher amounts of DNA is having a detrimental effect on cellular uptake.

Acknowledgements:

I would like to thank James Ramos, Dr. Kaushal Rege, and the Rege Group for their guidance and support. I'd also like to acknowledge the National Science Foundation and the National Institute of Health for their support of the Rege Group and the National Science Foundation, the National Nanotechnology Infrastructure Network and the Center for Solid State Electronics Research at Arizona State University for their support of the NNIN REU program.

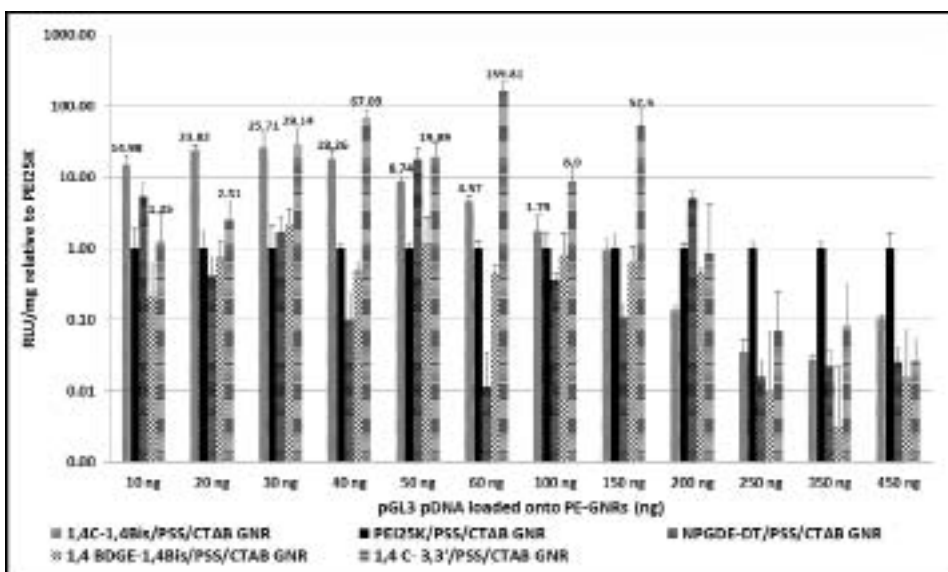


Figure 4: Transfection efficacy of investigated polymers as compared to PEI.

References:

- [1] Perez-Juste, J. et al. Coordination Chemistry Reviews 249 1870–1901 (2005).
- [2] Lepock, JR., Cellular Effects of Hyperthermia: Relevance to the Minimum Dose for Thermal Damage. Int J Hyperthermia 19 (3) 252-66 (2003).
- [3] Nikoobakht, B.; El-Sayed, M. A., Preparation and Growth Mechanism of Gold Nanorods (NRs) Using Seed-Mediated Growth Method. Chem. Mater. 15 (10) 1957-1962 (2003).
- [4] Baura, S. et al. Parallel Synthesis and Screening of Polymers for Nonviral Gene Delivery. Molecular Pharmaceutics. 6 (1) 86-97 (2009).

Patterning Neurons with Microcontact Printing on Silicon Oxide Substrates

Margaret Merritt
Biomedical Engineering, Brown University

NNIN iREU Site: Institut Für Bio- Und Nanosysteme (IBN), Forschungszentrum, Jülich, Germany

NNIN iREU Principal Investigator and Mentor: Dr. Simone Meffert, Institute for Bio- and Nanosystems (IBN-2),

Forschungszentrum Jülich GmbH

Contact: mhhmerritt@gmail.com, s.meffert@fz-juelich.de

NNIN iREU Program

Abstract:

Signal transduction and processing between groups of neurons is yet to be fully understood. Guiding cell growth to create defined *in vitro* neural networks with specific synaptic connectivities will allow for the analysis of signal transduction and processing. Therefore, the present study aimed to use microcontact printing to pattern neurons *in vitro*. Microgradient protein patterns on silicon oxide substrates were created using laminin and poly-L-lysine. Primary rat embryonic cortical neurons were subsequently seeded onto these patterns. Neuron morphology and growth were analyzed using fluorescence and scanning electron microscopy. Although several scanning electron microscopy (SEM) pictures appeared quite promising, much remains to be investigated before a comprehensive understanding of the behavior of neural networks can be gained.

Introduction:

The process by which neural connections form is of particular interest. It is not entirely known how and why connections between specific neurons occur. Therefore, it is necessary to study neural networks on a small scale. Neural guidance through protein patterning techniques, such as microcontact printing, can be used to create neural networks to analyze network formation, individual neuron growth, and signal transduction and processing [1].

Microcontact printing is a process that was established for the purpose of creating micro-sized patterns on substrates. It is becoming more and more widely used because it is a simple, customizable process. A hydrophobic polymer, such as polyolefin elastomer (POE), is used as the “stamp” and a hydrophilic protein, like poly-L-lysine (PLL), acts as the “ink.” The stamp contains a micropattern that has been created by hot embossing. By first soaking the “stamp” in “ink” and then pressing it onto the substrate, the protein pattern is transferred. The choice of protein should be cell specific; for example, laminin is used to promote neural cell adhesion and guidance. Ideally, cells will only attach to regions where protein is present.

Experimental Procedure:

Microcontact printing with POP stamps, which were produced through a hot embossing process from a Teflon® master, was performed on silicon oxide substrates. Silicon oxide was used in order to enhance contrast for imaging. A protein solution of fluorescein isothiocyanate labeled poly-L-lysine (FITC-PLL, 10 μ g/mL) and laminin (5 μ g/mL)

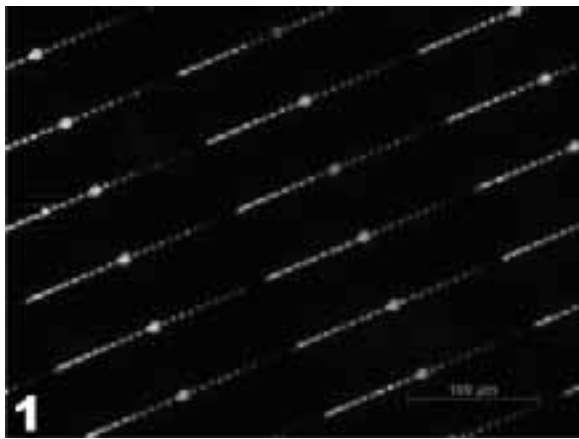
diluted in Hank’s balanced salt solution (HBSS) was mixed on ice. The POP stamp was immersed in this solution for 20 minutes, dried with nitrogen gas, and then pressed onto a silicon oxide substrate that had been pre-hydrophilized by flame. After two minutes, the stamp was removed, thereby transferring the protein pattern to the substrate. Patterns were inspected with a fluorescence microscope to ensure good, usable quality. Primary rat embryonic cortical neurons were seeded at 16,000 cells/cm² onto these patterned substrates and grown for three days. At three days, cells were fixed with 5% glutaraldehyde in 20 mM HEPES and dehydrated in increasing concentrations of ethanol for SEM observation.

Results and Conclusions:

Microcontact printing of microgradient patterns onto silicon oxide was successfully achieved, as shown in Figure 1. Ideally, a neuron’s soma should attach to the circular node, which has a 10 μ m diameter, and its neurites should extend only along the gradient pattern and not in any other direction.

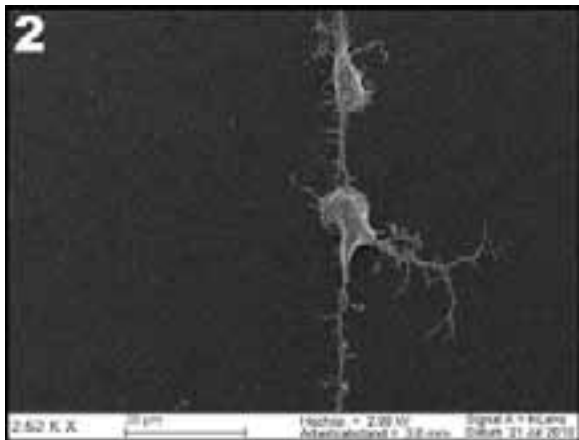
However, it was difficult to induce this type of neuronal growth under the given conditions. Many of the SEM images that were taken reveal numerous neurons growing in many directions and not on the pattern. Fortunately, a few images, such as those shown in Figures 2 and 3, adequately displayed neurons growing along the pattern.

The SEM image in Figure 2 is not ideal because neurite branching occurs in several directions and both soma are not



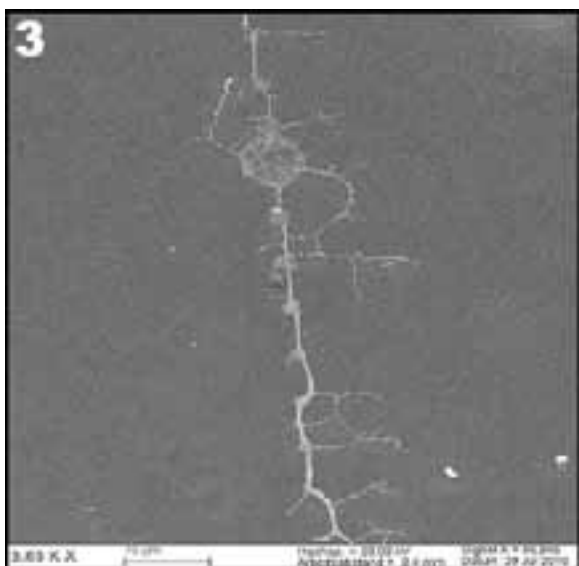
1

Figure 1: Fluorescence image of a microgradient pattern produced by microcontact printing of FITC-PLL (10 μ g/mL) and laminin (5 μ g/mL) on silicon oxide (20X objective).



2

Figure 2: SEM image of two neurons growing on microgradient patterns.



3

Figure 3: SEM image of a neuron growing in alignment with the microgradient pattern.

localized on the nodes. Figure 3 shows excellent neurite attachment and growth along the pattern.

It will be necessary to improve the stamping process to obtain better neuron alignment with the microgradient patterns. Several factors could have contributed to the fact that the majority of the neurons did not grow in alignment with the pattern. For example, smudging the stamp during the microcontact printing process may have caused the cell adhesive proteins to spread across the surface, which would promote neuron growth in every place where laminin or poly-L-lysine was present.

Future Work:

Enhancing the microcontact printing process will result in better SEM images that show alignment of the neurons to the pattern and more confined neural growth. These images can then be used to more comprehensively analyze how neurons grow and how networks develop in response to a gradient protein pattern. Future work, which has been preliminary investigated, includes using cell-repulsive materials, such as agarose, to pattern neurons to create neural networks. The early stages of this project were carried out in conjunction with the present study, but a lot remains to be explored. This idea could lead to exciting applications in the field of bioelectrical and neuroengineering.

Acknowledgements:

Thank you to the National Nanotechnology Infrastructure Network International Research Experience for Undergraduates Program and the National Science Foundation for funding this incredible opportunity. Special thanks to Dr. Simone Meffert, Dr. Andreas Offenhäusser, members of IBN-2, and my friends and family for their guidance and support.

References:

[1] Offenhäusser, A et al. "Microcontact printing of proteins for neuronal cell guidance." *Soft Matter*, 3, 1-9 (2007).

High Resolution Surface Plasmon Resonance Microscopy Based Microarray

Evan Mirts
Biology and Physics, Truman State University

NNIN REU Site: ASU NanoFab, Arizona State University, Tempe, AZ

NNIN REU Principal Investigator(s): Prof. Nongjian Tao, Center for Bioelectronics and Biosensors, The Biodesign Institute at ASU

NNIN REU Mentor(s): Christopher MacGriff, Center for Bioelectronics and Biosensors, The Biodesign Institute at ASU

Contact: enm6216@truman.edu, ntao1@asu.edu, christopher.macgriff@asu.edu

Introduction:

Surface plasmon resonance (SPR) has become a powerful tool in recent years for the real-time, label free characterization of molecular binding kinetics. SPR-based biosensors detect changes in the refractive index of a liquid medium near a metallic sensor surface as an analyte interacts with a layer of fixed ligands [1]. These sensors use flow cells that require minimum sample volumes ranging from 20 to hundreds of microliters and are typically capable of measuring $< 1 \text{ s}^{-1}$ dissociation rates [2,3].

Our goal was to design a lower volume, high resolution flow cell for use in a novel SPR-based microscopy platform which pairs the capabilities of a powerful optical microscope with an SPR biosensor.

Methods:

Microfluidic flow cells of several geometries were modeled in COMSOL to achieve the desired fluid flow dynamics and were fabricated with a recipe modified from established procedures [4,5]. Flow rates and pressures were modeled using MATLAB.

Flow Cell Fabrication. Several flow cell geometries and channel dimensions were fabricated. Four port channels ranged from $500 \times 200 \mu\text{m}$ to $500 \times 700 \mu\text{m}$. Similar dimensions were used for 3-port geometries. Complete flow cells consisted of a polydimethylsiloxane (PDMS) channel on a gold patterned glass chip and achieved rapid sample-buffer transitions by switching between two waste channels (Figures 1, 2).

Channel molds were fabricated by spin-coating SU-8 2015 (28 μm thickness) onto piranha cleaned silicon wafers. The SU-8 molds were coated *in vacuo* with (tridecafluoro-1,1,2,2-tetrahydrooctyl) trichlorosilane to facilitate multiple PDMS coatings. Liquid PDMS was poured over the molds, cured for one hour at 80°C, and finished channels were then peeled away from the SU-8 molds.

Gold (Au) patterned chips were fashioned by evaporating Au (45 nm) onto a chromium (Cr) adhesion layer (1.6 nm) on BK7 glass microscope cover slips. Five 150 μm

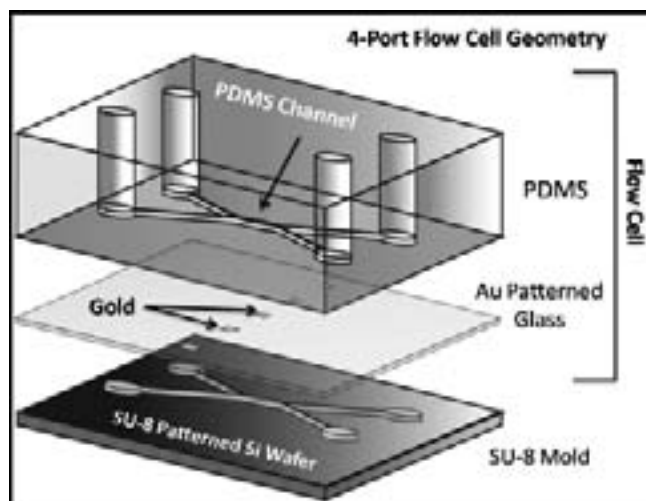


Figure 1: Flow cell assembly.

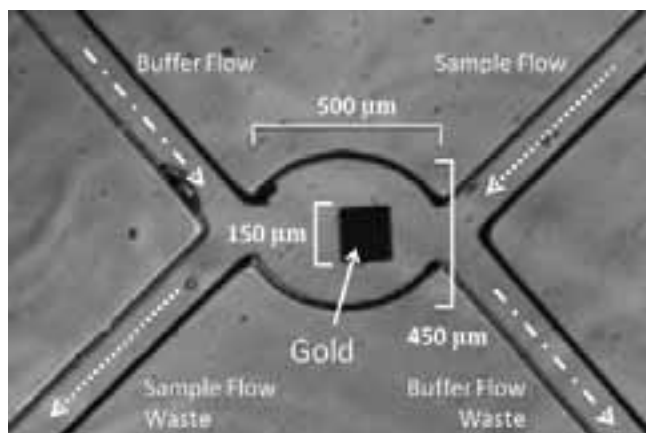


Figure 2: Four port flow cell photographed through our SPR microscopy platform.

Au squares were patterned onto each chip through simple photolithography. One PDMS channel and glass chip were simultaneously treated with oxygen plasma for one minute immediately prior to bonding them together.

Platform:

Our novel measurement platform combined a SPR biosensor with a powerful optical microscope. The SPR components were in modified Kretschmann configuration, replacing the prism with a 60x APON TIRFM (UIS2) oil immersion objective. A Pike CCD camera recorded data through an Olympus IX81 optical microscope. Surface plasmons were excited by a 680 nm super LED. For testing, raw data was converted to image files with a MATLAB program and analyzed with ImageJ software. A WPI SP101I model syringe pump maintained a well controlled buffer and sample flow, and a VICI Cheminert multiport actuator and Rheodyne 6-port rear injection valve facilitated waste channel switching and sample delivery, respectively. A 0.004 inch inner diameter 1 μ L sample loop ensured identical sample injections.

Results:

Flow cells were tested with 1 μ L injections of 1x Dulbecco's phosphate buffered saline solution and 0.1%, 0.5%, and 1.0% ethanol solutions to characterize and increase the temporal resolution and sensitivity of the platform. Figure 3 depicts two 1.0% ethanol injections at different levels of sensitivity in arbitrary units, smoothed with a five point running average. We achieved a 60% increase in mean intensity for these injections and a significant reduction in short term noise over initial trials, yielding a signal to noise ratio $> 200:1$. The measurable temporal resolution was also increased from 300 ms to 50 ms, suggesting probable event measurements on the order of 20 s⁻¹.

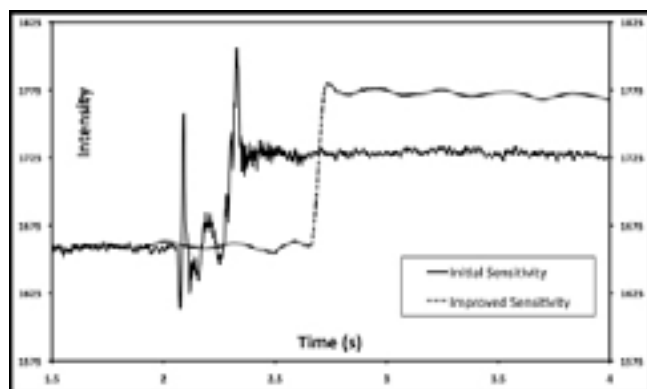


Figure 3: Sensorgram of two 1.0% ethanol injections at initial and improved sensitivities.

Discussion:

Simple tests of the new flow cells have affirmed that the platform operates well with sample volumes of 1 μ L; though, it is our belief that volumes as low as 10-100 nL would yield measurable results. At present, our low volume cells collect data with sample volumes twenty times lower than the minimum requirements for top of the line commercial SPR biosensors. Additionally, we regularly obtained temporal resolutions > 2 s⁻¹; double the resolution of some commercial systems. The angular resolution of our system (~ 1 mDeg), however, is still well below desired sensitivity, and for tested ethanol concentrations lower than 1.0%, the sensitivity was too low to justify transitions more rapid than 300 ms. Maximum possible resolution for the system ultimately depends on its mechanical limitations. The 1000 fps maximum frame rate camera can conceivably achieve temporal resolutions on the order of 10-100 s⁻¹, but at our current limit of sensitivity we observed long-term, high amplitude background oscillations which, due to flow rate dependence, we determined resulted from the syringe pump. Moreover, the time and pressure restrictions of the waste channel actuator limit our switching speed. However, with a custom actuator valve head that reduces the no-flow time between internal openings we expect a marked reduction in transition time from 300 ms to 1-10 ms while maintaining a high signal to noise ratio.

Acknowledgements:

Thanks to my principal investigator, Professor N.J. Tao, and my mentor, Christopher MacGriff, for their guidance and insight, as well as the other members of the Center for Bioelectronics and Biosensors. For funding and support, thanks to the National Nanotechnology Infrastructure Network REU, the National Science Foundation, the Ira A. Fulton School of Engineering Center for Solid State Electronics Research, and The Biodesign Institute at Arizona State University.

References:

- [1] Handbook of Surface Plasmon Resonance. Richard B M Schasfoort and Anna J Tudos, ed. RSC Publishing, Cambridge, UK, 2008. pp. 1-78,173-218.
- [2] Myszka, David G. Analysis of small-molecule interactions using Biacore S51 technology. Center for Biomolecular Interaction Analysis, University of Utah. Analytical Biochemistry. Volume 329, 2004. pp. 316-323.
- [3] Sample volumes and dissociation rates obtained from company representatives and instrument data sheets: Biosensing Instruments, EcoChemie/Autolab, GE Healthcare/Biacore, and Nomadics/Texas Instruments.
- [4] SU-8 Photoresist Processing Standard Operating Procedure. School of Engineering, Tufts University, 2007.
- [5] SU-8 Information Page. Department of Electrical and Computer Engineering, Brigham Young University, 2009.

Synthetic Antiferromagnetic Particles for Biosensing

Kelsey Morse
Chemistry, Beloit College

NNIN REU Site: Stanford Nanofabrication Facility, Stanford University, Stanford, CA

NNIN REU Principal Investigator(s): Professor Shan X. Wang, Materials Science and Engineering, Stanford University

NNIN REU Mentor(s): Mingliang Zhang and Dr. Robert Wilson, Materials Science and Engineering, Stanford University

Contact: morsek@beloit.edu, sxwang@stanford.edu, zmlrobin@gmail.com, bobmse@stanford.edu

Abstract:

Magnetic nanoparticles can be highly useful in many biological applications. The magnetic moments of these particles need to be large to provide large magnetic signal or to facilitate magnetic manipulation of biomolecules. In traditionally synthesized superparamagnetic nanoparticles, increasing the size of the particle increases the magnetic moment. Larger particles, however, do not always revert to a non-magnetic state when not in the presence of a magnetic field, making them non-ideal for work in biological systems. Synthetic antiferromagnetic particles, however, do not have this restriction due to their structure. In this study, particles were synthesized using a nanoimprint method followed by layered deposition of metals. The nanoimprint process was improved by using a spin-coated polymer layer as the release layer rather than a metal (which requires deposition), thus saving fabrication time. The magnetism of the particles was measured using alternating gradient magnetometry. Once the process for synthesizing the synthetic antiferromagnetic particles had been optimized, they could be functionalized for many different biological processes such as protein sorting or cancer signaling.

Introduction:

In order to achieve high magnetic moments without remanence caused by superparamagnetic particles at sizes above the superparamagnetic limit, synthetic antiferromagnetic particles were designed [1]. Their structure was that of a titanium cap followed by a layer of ferromagnetic iron. At such small sizes, the layer had an aligned total moment. The following titanium layer acted as a spacer and was followed by another ferromagnetic iron layer. Due to the small sizes of the layers, as the iron was deposited the layers' total magnetic moment aligned opposite to the previous iron layer. This created the synthetic antiferromagnetic condition of the particles and was what gave it zero remanence outside of a magnetic field.

Experimental Procedure:

A nanoimprint technique was used on a tri-resist coated standard silicon wafer followed by layered metallic deposition to produce the synthetic antiferromagnetic particles.

First durimide, as a final release layer, was spin-coated onto the wafer at 3000 rpm for 60 seconds. The wafer was then baked at 300°C for 10 minutes and allowed to cool. A second layer of polymethylglutarimide was spin-coated at 6000 rpm for 30s and then baked at 200°C for five minutes. After cooling, a final layer of polymethylmethacrylate (PMMA) was spin-coated onto the wafer at 6000 rpm for 30 seconds and then baked at 140°C for five minutes.

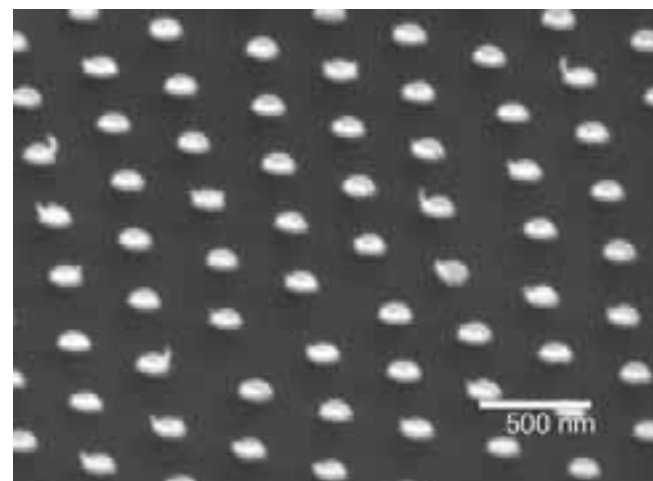


Figure 1: Scanning electron microscope image of synthetic antiferromagnetic particles before final release.

Once cooled, the wafer underwent nanoimprint with a nanopillar stamp at 180°C under 40 bar for 60 seconds. After removing the stamp, the wafer underwent oxygen plasma etching to remove 20 nm of PMMA. Deposition wells were etched into the PMMA layer with chemical development for 20 seconds. The reaction was then quenched with distilled water, and the wafer rinsed a second time.

Evaporation of the metallic layers was done in the order of 5 nm of titanium followed by 10 nm of iron, followed by 3 nm of titanium, followed by 10 nm of iron, and capped with 5 nm of titanium.

Particles were then released into solution by selectively lifting off the individual resist layers. Once in solution they were centrifuged repeatedly to change the solvent to distilled water.

Results and Conclusions:

Images of the particles were obtained before release from the durimide polymer layer via scanning electron microscope (SEM). As seen in Figure 1, the particles were evenly distributed on the silicon wafer. This indicated the reliability of the stamp used during nanoimprint. The fact that the particles were found on the wafer indicated that each layer could be independently removed, so the lift off process was successful. Figure 2 shows an alternating gradient magnetometry graph of the total moment of a small portion of the particles before final release. The graph shows a small amount of remanence at zero external applied field. This indicated that the particles were of a non-ideal shape and suggested an issue with the metallic deposition.

In conclusion, the process works but needs to be further optimized to increase output of ideal particles.

Future Work:

Future studies of the particles will center on functionalization. After they are released into solution they can be functionalized with a silica shell. This shell can then be further functionalized with different proteins for various applications. It is important that each particle is covered in its own shell and not aggregated into a large particle with multiple cores. As seen in Figure 3, it is difficult to be certain that each magnetic particle has a distinct silica shell. Tuning of the functionalization parameters is necessary to reduce aggregation of the particles into bulk material.

Acknowledgments:

I would like to thank Mike Deal for coordinating this program, Professor Wang for allowing me to work with his group, the Stanford Nanofabrication Facility for use of their facilities, the National Nanotechnology Infrastructure Network REU for facilitating this program, and the National Science Foundation for their funding.

References:

[1] Hu, W; "High-Moment Antiferromagnetic Nanoparticles with Tunable Magnetic Properties"; Advanced Materials, 20, 1479-1483, 2008.

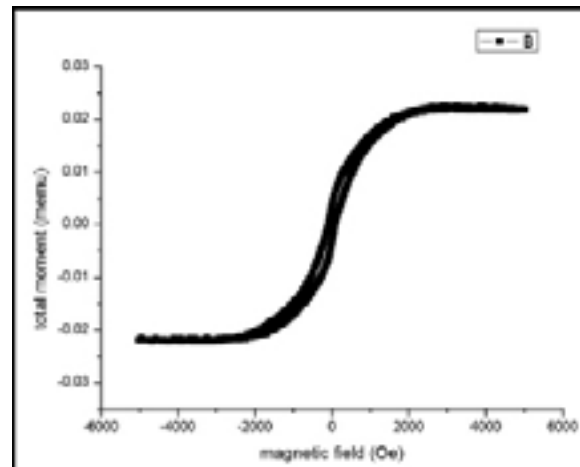


Figure 2: Alternating gradient magnetometry graph of the total moment of particles vs. applied magnetic field.

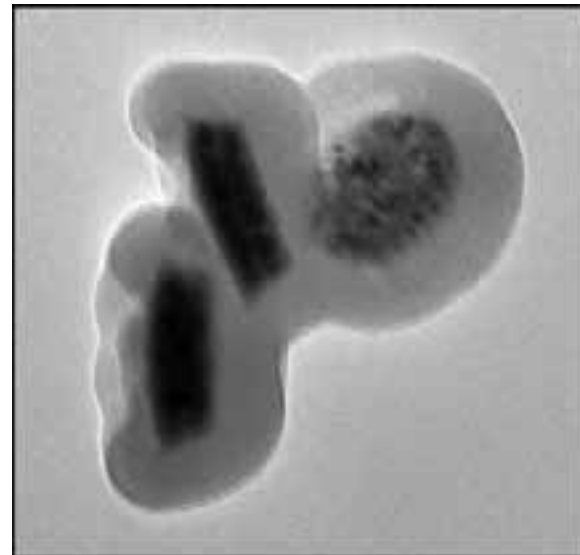


Figure 3: TEM image of synthetic antiferromagnetic particles after functionalization with silica shell.

Plasmonic Nanoparticle Dimer Sensors

Heidi Nelson

Chemical Engineering, University of Minnesota

NNIN REU Site: Center for Nanotechnology, University of Washington, Seattle, WA

NNIN REU Principal Investigator(s): Professor David S. Ginger, Chemistry, University of Washington

NNIN REU Mentor(s): Dr. Jennifer I.L. Chen, Chemistry, University of Washington

Contact: nels5798@umn.edu, ginger@chem.washington.edu, jilchen@u.washington.edu

Abstract:

We explored actuable nanoparticle dimers as sensors for small molecules, employing the distance dependence of the hybridized plasmon resonance. By linking the nanoparticles with oligonucleotides that can undergo geometric changes, we detected the analyte via its intercalation into the deoxyribonucleic acid (DNA) linker. The resulting spectral blue shift in the dimer plasmon resonance confirmed that this sensing modality can detect small molecules via their interactions with DNA.

Introduction:

In metal nanoparticles, free electrons in the material move in a collective oscillation known as a surface plasmon. When two nanoparticles are close together, their plasmons interact to form two hybridized modes of different energy. The strength of this coupling depends on the distance between the particles [1]. We considered the lower-energy dimer plasmon mode, which displays a red shift as the particles move together and the coupling strengthens, and a blue shift as the particles move apart and the coupling weakens.

We applied this relationship for sensors by assembling nanoparticle dimers with linkers that extend geometrically in the presence of the target molecule. For example, linking gold nanoparticles with hairpin DNA allowed us to sensitively and selectively detect oligonucleotides based on the blue shift in the plasmon resonance wavelength [2].

These dimer sensors represent a potential improvement over single-particle plasmonic sensors, which rely on refractive index changes and are susceptible to interfering species.

We demonstrated this sensing modality for small molecules using daunorubicin, an anticancer drug that intercalates into right-handed-DNA, binding specifically to the CGA base sequence. Upon intercalation, daunorubicin distorts the structure of DNA, unwinding the helix by 8° and lengthening the DNA by 0.34 nm per molecule intercalated [3].

We hypothesized that the intercalation of daunorubicin into DNA-linked gold nanoparticle dimers would produce a blue shift in plasmon resonance. By varying the number of CGA base repeats in the DNA linker, we confirmed that this spectral response is specific for sequences containing these repeats and dependent on the number of repeats. We also showed that the spectral response is selective for daunorubicin vs. its enantiomer.

Experimental

Procedure:

We attached 100 nm gold nanoparticles (GNP) to a silanized glass substrate, then functionalized them with single-stranded DNA (Figure 1a).

We coupled these to 60 nm GNP that had been functionalized in solution with the complementary DNA strand (Figure 1b).

We identified dimers based on color changes seen in darkfield optical images, in which single nanoparticles appear green while dimers appear yellow or brown. We collected darkfield scattering spectra for these individual dimers in buffer, as well as one hour and 24 hours after the addition of daunorubicin (1 μ M; Figure 1c). The peak positions were determined using a Lorentzian fit in a selected interval around the peak.

We used DNA sequences containing 6, 10, and 15 CGA repeats (denoted as CGA6, CGA10, and CGA15 respectively), as well as a random control sequence.

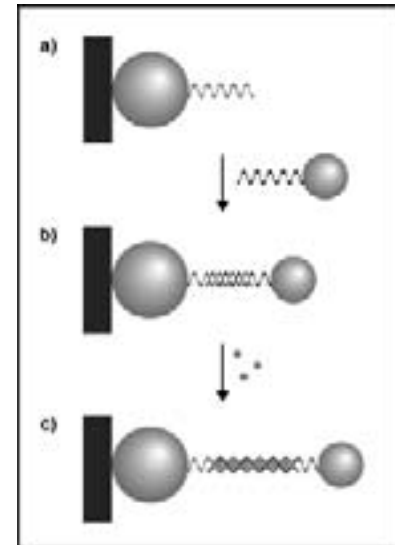


Figure 1: Schematic showing dimer formation and drug intercalation.

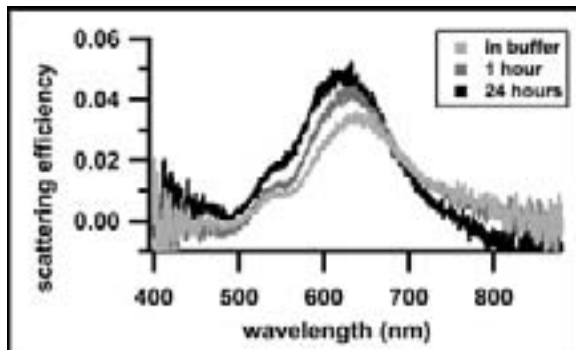


Figure 2: Spectra collected for a CGA15 dimer.

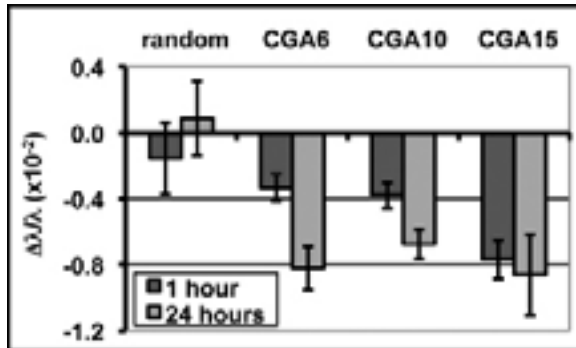


Figure 3: Average fractional shifts for different DNA sequences.

DNA sequence	Calculated change in interparticle distance (nm)	Number of intercalation sites (theoretical)	Number of molecules intercalated (experimental)
CGA6	1.22	6	3.6
CGA10	1.85	10	5.4
CGA15	3.27	15	7.9

Table 1: Theoretical vs. experimental number of molecules intercalated.

Results:

Figure 2 shows scattering spectra for a dimer linked with CGA15 in buffer and after incubation with daunorubicin for one hour and 24 hours. The average fractional shifts (defined as $\Delta\lambda/\lambda$) for dimers using different DNA sequences are shown in Figure 3. The CGA15 sequence displayed the largest blue shift after one hour (average $\Delta\lambda/\lambda = -0.0077 \pm 0.0012$). The CGA10 sequence displayed an intermediate shift (-0.0038 ± 0.0008). Finally, the CGA6 sequence displayed the smallest shift (-0.0033 ± 0.0008). The cause of the large shift for these sequences after 24 hours is still under investigation. Dimers using a random DNA sequence did not display a significant shift in either direction after one hour or 24 hours.

We extrapolated the average change in particle separation distance for each type of dimer after one hour, using a calibration curve that relates the dimer peak position to the particle separation distance [4]. We then estimated the average number of molecules intercalated into each dimer, based on crystal structure data which suggests that each daunorubicin molecule lengthens DNA by 0.34 nm. We found that the experimental number of daunorubicin molecules intercalated scales linearly with the theoretical number of intercalation sites (Table 1).

Additionally, we tested the chiral selectivity of the dimers by monitoring their response to daunorubicin vs. its enantiomer WP900, which does not intercalate into right-handed DNA. Introducing WP900 to CGA15 dimers did not produce a significant shift, in contrast to the large blue shift induced by daunorubicin.

Conclusions:

We conclude that monitoring the plasmon resonance of gold nanoparticle dimers is a viable method for the detection of daunorubicin. A significant blue shift is displayed when daunorubicin is added to dimers whose DNA linkers contain CGA repeats, with the magnitude of the shift dependent on the number of repeats. In addition, this response is selective for daunorubicin over its enantiomer, WP900.

Future Work:

The next steps in our specific project are to determine the detection limit of this dimer sensor and evaluate its performance in complex media.

Acknowledgements:

I would like to thank Professor David Ginger, Dr. Jennifer Chen, and all other members of the Ginger Research Group. I am also grateful to the National Nanotechnology Infrastructure Network Research Experience for Undergraduates Program and the National Science Foundation, and to Ethan Allen, the University of Washington NNIN REU site coordinator. This work is supported by the Air Force Office of Scientific Research and the NSF MRSEC Program (DMR 0520567/MMI 0709131).

References:

- [1] Norlander P, et al. "Plasmon Hybridization in Nanoparticle Dimers." 2004. *Nano Lett.* 4(5): 899-903.
- [2] Chen JIL, Chen Y, Ginger DS. "Plasmonic Nanoparticle Dimers for Optical Sensing in Complex Media." 2010. *J. Am. Chem. Soc.* 132(28): 9600-9601.
- [3] Fritzsche H, et al. "Studies on Interaction of Anthracycline Antibiotics and Deoxyribonucleic Acid." 1982. *Biochem.* 21: 3940-3946.
- [4] Reinhard, BM, et al. "Calibration of Molecular Rulers Based on Plasmon Coupling between Gold Nanoparticles." 2005. *Nano Lett.* 5(11): 2246-2252.

Porous Microbeads as Three-Dimensional Scaffolds for Tissue Engineering

Jennifer Wang
Biomedical Engineering, Duke University

NNIN REU Site: Nano Research Facility, Washington University in St. Louis, St. Louis, MO

NNIN REU Principal Investigator(s): Professor Younan Xia, Biomedical Engineering, Washington University in St. Louis

NNIN REU Mentor(s): Dr. Sung-Wook Choi, Yu Zhang, and A. Lake Wooten, Biomedical Engineering, WUSTL

Contact: jmw73@duke.edu, xia@biomed.wustl.edu, chois@seas.wustl.edu, yz12@cec.wustl.edu, alw2@cec.wustl.edu

Abstract:

The goal of this project included fabricating uniform porous poly(lactic-co-glycolic) acid (PLGA) microbeads using a fluidic device, seeding fibroblasts into these beads, and culturing these cell-loaded beads in a mold of a desired shape. The fibroblasts attached and proliferated in porous beads with average pore diameters of $30\ \mu\text{m}$. These fibroblast-loaded beads connected to neighboring beads by a network of cells and extracellular matrices (ECM) to form the beginnings of a tissue construct inside the mold. These preliminary results have promising implications, such as the possibility of creating shape-specific tissues to better fit injury sites.

Introduction:

Tissue engineering seeks to create replacements for tissues and organs, in an effort to maintain, improve, or regain biological functions [1]. Three dimensional porous scaffolds are commonly used to enhance cell attachment, facilitate nutrient and oxygen transport, and create a suitable microenvironment for proper cell activities [2]. Recently, microbeads with interconnecting inner and outer pores have been studied as a viable carrier scaffold for better implants. Since scaffolds need to be biocompatible, biodegradable, and mechanically strong, porous microbeads are a viable choice to fulfill these basic requirements [3]. However, the difficulty lies in making microbeads with large enough pores for cells to penetrate and grow inside.

Porous microbeads promote cell migration and allow for nutrient and waste transport through the pores, protect cells growing inside, and are small enough to be used for many purposes, including cell and drug delivery, direct injection to injury sites, and as scaffolds to culture cells *in vitro* for improved implants [3].

Our group has recently reported the fabrication of uniform PLGA porous microbeads by introducing a phase-separated emulsion into a simple fluidic device [3]. This project was carried out to produce uniform PLGA porous beads with controllable pore sizes, and examine if mouse fibroblasts could successfully grow within these beads packed inside a specified mold.

Experimental Procedure:

To fabricate porous microbeads, we used a simple fluidic device consisting of a bent needle inserted into polyvinyl chloride (PVC) tubing with an attached glass capillary tube. A homogenized mixture of a 2% polyvinyl alcohol

(PVA) and 15% gelatin solution in water and a 2% PLGA solution in dichloromethane (DCM) was filled into a syringe attached to the bent needle as the discontinuous phase. Another syringe filled with 2% PVA was used as the continuous phase, attaching to the PVC tube.

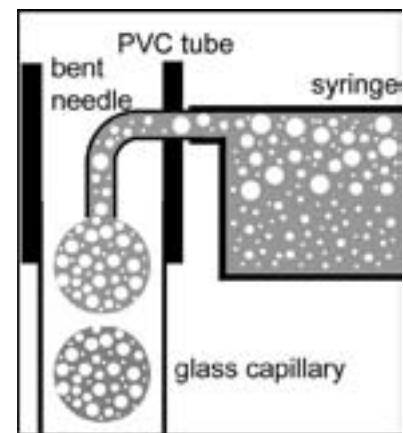


Figure 1: Fluidic device to fabricate porous microbeads [3].

Figure 1 shows a schematic of the bead fabrication process. The steady flow of 2% PVA aqueous solution from the syringe into the PVC tubing knocked off the beads leaving the tip of the needle. The pores in these microbeads were filled with gelatin particles from the emulsion. These beads were collected in a beaker filled with 0.2% ice-cold PVA aqueous solution, where the gelatin inside the beads hardened upon gelling. The beads were kept stirring overnight to evaporate DCM and solidify PLGA. By heating the beads, the gelatin dissolved, leaving only the PLGA beads with interconnected pores.

NIH/3T3 mouse fibroblasts were seeded into porous beads using a spinner flask for 24 hours. Various molds were fabricated using agar in the shape of small circular wells. A 15 mL centrifuge tube was also used as a mold. After placing

the cell-loaded beads in the molds to pack into a pellet form, the pellets were kept in culture for approximately 5-7 days before staining.

Scanning electron microscope (SEM) images confirmed the outer pore sizes of the beads and their size distribution. Both SEM and confocal microscope images were used to characterize cell attachment and proliferation within the beads, as well as the cell and ECM networks connecting neighboring beads together.

Results and Conclusions:

We successfully fabricated uniform PLGA porous microbeads with an average diameter of $300\text{ }\mu\text{m}$ and average pore sizes of $30\text{ }\mu\text{m}$ using a fluidic device (Figure 2).

From confocal micrographs of cytosol staining (Figure 3, where white dots indicate cells) and SEM images (Figure 4) of the cell-loaded porous beads, it is evident that the mouse fibroblasts attached to the porous beads and penetrated into the inner space to proliferate. The beads connected with each other by a network of cells and secreted ECM. These interconnected beads with cells agglomerated together, forming the beginnings of a construct inside the mold. These findings support the application of porous microbeads as scaffolds of specific shapes to promote, influence, and support cell growth, and as a support system to facilitate the healing and recovery process after an injury.

Future Work:

The success rate of porous bead fabrication must be improved by further optimizing and standardizing our methods. With enough porous beads, tissues could be grown on a larger scale, making transplants with these procedures more feasible. Eventually, studies will be done with animal models to better understand the *in vivo* effects of these porous beads. Our findings must also be substantiated with long-term cell cultures using human cells, as the use of a patient's own cells will eliminate possible complications associated with transplantation.

Acknowledgements:

I would like to thank the National Science Foundation, the National Nanotechnology Infrastructure Network Research Experience for Undergraduates, the Nano Research Facility at Washington University in St. Louis, my PI Prof. Younan Xia, my mentors Dr. Sung-Wook Choi, Yu Zhang, and A. Lake Wooten, and member of the Xia lab, Yi-Chun Yeh.

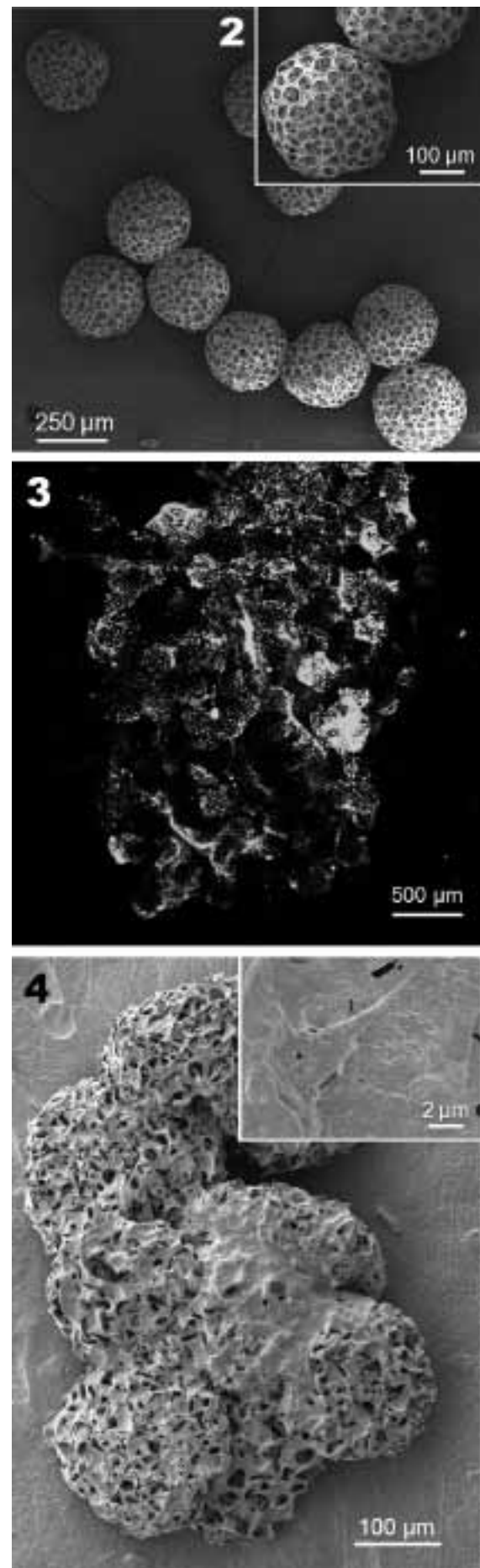
References:

- [1] Langer, R. and Vacanti, J.P. "Tissue engineering"; *Science*, 260, 920-926 (2003).
- [2] Wei, G. and Ma, P. "Nanostructured Biomaterials for Regeneration"; *Advanced Functional Materials*, 18, 3568-3582 (2008).
- [3] Choi, S.-W., Yeh, Y.-C., Zhang, Y., Sung, H.-W. and Xia, Y. "Uniform Beads with Controllable Pore Sizes for Biomedical Apps"; *Small*, 6, 1492-1498 (2010).

Figure 2: SEM images of uniform porous microbeads. Inset: magnified view.

Figure 3: Confocal micrograph of a cell-bead construct at day six in culture.

Figure 4: SEM images of a cell-bead construct. Inset: magnified view.



Encapsulation of Single Cells in a Droplet-Based Microfluidic Device

Yingxia Wang

Chemical Engineering, Massachusetts Institute of Technology

NNIN REU Site: Nanofabrication Center, University of Minnesota-Twin Cities, Minneapolis, MN

NNIN REU Principal Investigator(s): Dr. Christy Haynes, Chemistry, University of Minnesota-Twin Cities

NNIN REU Mentor(s): Donghyuk Kim, Chemistry, University of Minnesota-Twin Cities

Contact: insia@mit.edu, chaynes@umn.edu, kimx1660@umn.edu

Abstract:

Microfluidic devices have great potential in cell analysis due to their small scale, high-throughput operation, and adaptability to a variety of analytical methods. The applications of microfluidics include droplet-based microfluidic devices, which would allow for more robust single-cell measurements than conventional electrochemical detection in Petri dishes, thus better revealing cellular functions and dynamics. For this idea to be beneficial, high-throughput encapsulation of single cells in a droplet-based microfluidic device is necessary. Cells must be individually encapsulated and stored in droplets of media dispersed in a continuous carrier phase. In this project, standard soft-lithography techniques were used for polydimethylsiloxane (PDMS)-based chip fabrication. Tris buffer and perfluorinated polymer solution were utilized as the media and carrier phase, respectively. Lastly, polystyrene beads were used to simulate cells. The devices should have a high percentage of one-cell droplets to be useful for single cell measurements. Ultimately, electrodes will be integrated into this device to produce an ideal tool for electrochemical measurements of immune cell exocytosis.

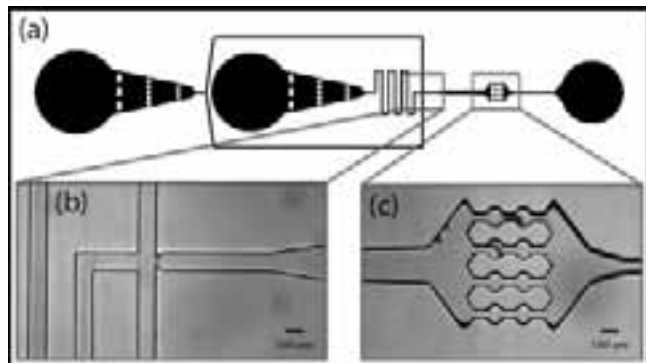


Figure 1: (a) Device design. From left to right: oil inlet and filter, aqueous inlet and filter, aqueous channel, constriction, storage array, outlet. (b) Image of fabricated channel constriction. (c) Image of fabricated storage array, where droplets will be eventually be stored for measurements.

Introduction:

Exocytosis is the critical cellular process by which cells secrete chemical messengers to each other; measuring exocytosis on-a-chip was the ultimate goal of this project. One current method of measuring cell exocytosis is carbon-fiber microelectrode amperometry (CFMA), which measures the excretes of a stimulated cell using electrochemistry. Although this method provides excellent temporal and

spatial resolution, its disadvantages include inefficiency and difficulty of electrode fabrication, thus resulting in a low-throughput method.

To overcome the disadvantages of CFMA, a droplet-based microfluidic device was designed to provide a high-throughput method of measuring single cell exocytosis (Figure 1a). In this device, an aqueous cell suspension flowed between an oil carrier phase. When these fluids came to a constriction in the design, droplets of single cells in aqueous media formed.

This approach is advantageous because the droplets are identical, thus allowing for statistically reliable measurements. It also avoids the low level-of-detection issues present in CFMA due to diffusion of excretes. For this design, a high percentage of droplets containing single cells is desired.

Experimental:

Fabrication. Standard soft-lithography with negative photoresist (SU-8) was employed to fabricate the microfluidic devices. Photoresist was spun onto a wafer at 100 μm thickness, following instructions provided by MicroChem. The photoresist was exposed to UV light through a photomask with the desired device designs. After developing the wafer, PDMS was poured over the wafer and cured overnight.

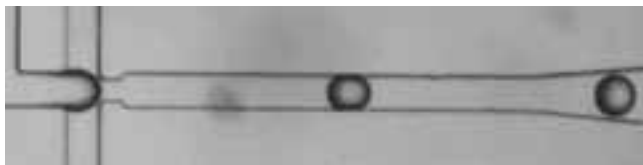


Figure 2: Formation of water droplets in carrier phase.

Two methods of bonding between PDMS and glass substrate were tested. The reversible process, performed by soaking PDMS in HCl and binding to glass over heat, was not strong enough for the fluid pressures exerted on the device. The irreversible process, using silicon-oxide bonds between the PDMS and glass, proved to be reliable for this experiment.

Holes were punched at the inlet and outlet of each device, allowing Teflon® tubes to connect the device to syringe pumps. Each device was also coated with an Aquapel solution, making the channels highly hydrophobic, thus forming smaller aqueous droplets in the carrier phase.

Operation. To test the droplet formation of the devices without cells, MilliQ water (aqueous phase) was flowed between a perfluorinated polymer solution (carrier phase). Rapid formation of water droplets was observed (Figure 2). Droplet size could be decreased by increasing carrier phase flow-rate or decreasing aqueous phase flow-rate.

To test encapsulation, 10 μm polystyrene beads were used to simulate cells. The beads were suspended in Tris buffer at a concentration of 1.8×10^6 beads/mL. This suspension was flowed between a perfluorinated polymer solution.

Results and Discussion:

At a bead concentration of 1.8×10^6 beads/mL, oil/carrier flow-rate of 300 $\mu\text{L}/\text{hr}$, and aqueous flow-rate of 100 $\mu\text{L}/\text{hr}$, the observed percentage of droplets containing a single cell was 31.4% (Figure 3).

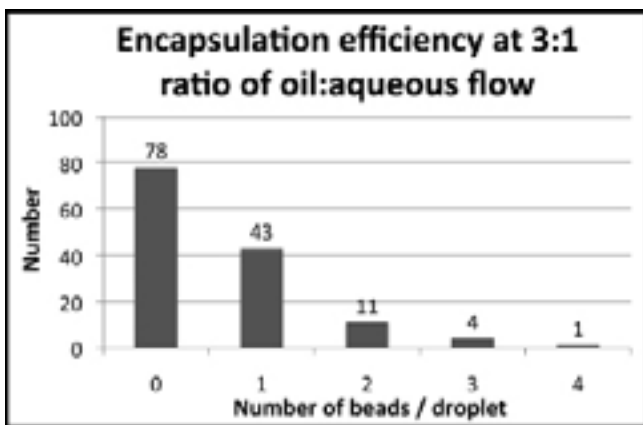


Figure 3: Encapsulation efficiency results at carrier flow-rate of 300 $\mu\text{L}/\text{hr}$ and aqueous flow-rate of 100 $\mu\text{L}/\text{hr}$.

Although encapsulation of single beads was seen (Figure 4), many problems were encountered during operation. First, stray PDMS pieces occasionally collected inside the channels and flowed to the channel constriction. This caused beads to also collect at the constriction, thereby restricting regular flow. PDMS parts were sonicated before bonding to glass, which diminished but did not solve the problem. Next, beads aggregated in the channels and settled in the Teflon tubing, preventing regular formation of single-bead droplets. Different pH of Tris buffer were tested to minimize aggregation and settling. Testing showed that pH 7 buffer worked best, but did not eliminate the problem. Finally, the bead concentration used was not ideal for forming single-bead droplets. A curved aqueous channel can be tested to focus the location of beads in the channel.

Future Work:

The percentage of droplets containing single beads can be improved upon. After a maximum efficiency is achieved, the encapsulation efficiency of cells (e.g. mast cells) will be tested in place of polystyrene beads. Ultimately, microelectrodes will be integrated into this device to produce an ideal tool for electrochemical measurements of immune cell exocytosis.

Acknowledgements:

I would like to extend a special thanks to my mentor Donghyuk Kim, Professor Christy Haynes, and the entire Haynes Lab for a wonderful research experience in Minnesota. This project was made possible with thanks to the National Nanotechnology Infrastructure Network Research Experience for Undergraduates Program, the National Science Foundation, University of Minnesota Nanofabrication Center, and Becky von Dissen.

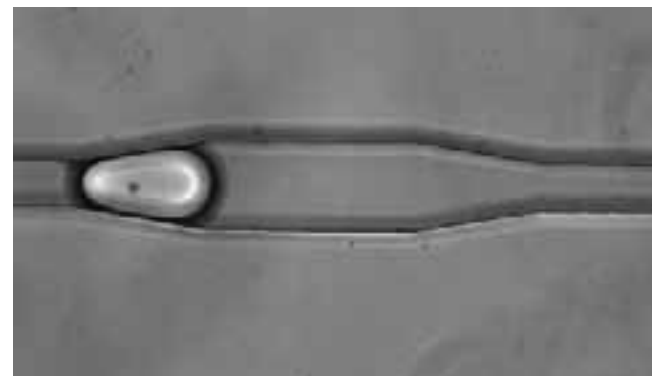


Figure 4: Aqueous droplet containing a single bead.

Cell Viability and Morphology on Carbon Nanotube Microstructures

NNIN Grad Program

Masaki Watanabe
Applied Chemistry, Nagoya University

NNIN Graduate Research Site: Lurie Nanofabrication Facility, University of Michigan, Ann Arbor, MI

NNIN Graduate Research Principal Investigator(s): Prof. Anastasios John Hart, Mechanical Engineering, University of Michigan

NNIN Graduate Research Mentor(s): Davor Copic and Megan J. Roberts, Mechanical Engineering, University of Michigan

Contact: watanabe.masaki@b mbox.nagoya-u.ac.jp, ajohnh@umich.edu, copicd@umich.edu, megjro@umich.edu

Abstract:

Carbon nanotubes (CNTs) are useful in a variety of applications including electronic, mechanical, energy, and biomedical due to their outstanding properties. The objectives of this study were to investigate the structural interaction between CNTs microstructures and cells as well as CNTs-biomolecule composites and cells. This study fills a gap in studies of cell behavior on the multi-scale geometries of CNTs forests. Vertically aligned CNTs were grown by chemical vapor deposition (CVD) and then, made in to three-dimensional (3D) shapes by capillary forming. After fabrication of the substrates, fibronectin was deposited on the CNTs microstructures and mouse fibroblast (3T3) cells were seeded and cultured for several days. Cells attached more readily to the CNTs-fibronectin composite than non-composited CNTs. Also, cell morphology was changed on CNTs micro-pillars compared to unprocessed substrates. In addition, cells were capable of growth on CNTs-fibronectin micropillars.

Introduction:

Carbon nanotubes (CNTs) are cylindrical macromolecules of carbon, and have unique mechanical, electrical, and thermal properties. Due to their outstanding properties, there are a variety of applications of CNTs such as electronics, mechanical, energy, and biomedical applications. In particular, CNTs could be used for studies of cell mechanotransduction, as scaffolds for tissue engineering, for regulation of stem cell differentiation, and for intracellular tracking and labeling. Recently, the fabrication of complex CNTs microstructures was achieved from vertically aligned CNTs and made into 3D shapes using liquid vapor condensation [1].

The objectives of this program were to investigate the structural interaction between CNTs micro-pillars structures and cells, CNTs-biomolecule composite and cells, because there are few studies of cell behavior on the multi-scale geometries of CNTs forests. This study focused on cell adhesion, morphology and viability on the substrate with CNTs and CNTs-fibronectin composite.

Experimental Procedure:

First, a catalyst film of 1/10 nm Fe/Al₂O₃ was deposited by e-beam evaporation on thermally-oxidized silicon wafers. The catalyst was patterned by photolithography using SPR 220 photoresist before catalyst deposition and lifted-off by ultrasonic agitation in acetone. Next, CNTs were grown by chemical vapor deposition (CVD) in a tube furnace with flows of 100/400/100 sccm H₂/He/C₂H₄ at 775°C.

After growth, the substrate was put to an aluminum mesh plate and reverse over a beaker, which was containing boiling acetone. The substrate was exposed to the acetone vapor and then the substrate was removed from the beaker to allow the acetone to completely evaporate. After densification of CNTs, the substrates were sterilized by UV exposure for 10 min. Next, the substrates were soaked to fibronectin solution (25 µg/mL) for 24 hours. Then, mouse fibroblast (3T3) cells (5,000 cells/cm²) were seeded to the substrates and cultured in Dulbecco's modified Eagle's medium (DMEM), supplemented with 10% bovine serum, 1% L-glutamine, 100 U/mL penicillin/streptomycin at 37°C with 5% CO₂ for 24 hours or three days. After cultured, cells were washed with phosphate buffered saline (PBS) and fixed with 4% paraformaldehyde in PBS for 30 min and then, washed with PBS again.

For scanning electron microscope (SEM) observation, the cells were dehydrate in ethanol solutions of 10% to 100% in 10% increments for 30 min, and twice of hexamethyldisilazane (HMDS) for five min. After drying, the substrates were sputtered with a thin film of gold (4-5 nm) and imaged by SEM.

Results:

After one day culture on the CNTs-fibronectin microstructures, various cell morphologies were observed including densely packed, aligned along CNTs, bridged between two pillars, widely extended and round, and so on.



Figure 1: (a) Aligned cell to CNTs direction on CNTs microstructure (scale bar = 50 μ m). (b) Perpendicular attached cell on CNTs microstructure (scale bar = 50 μ m).

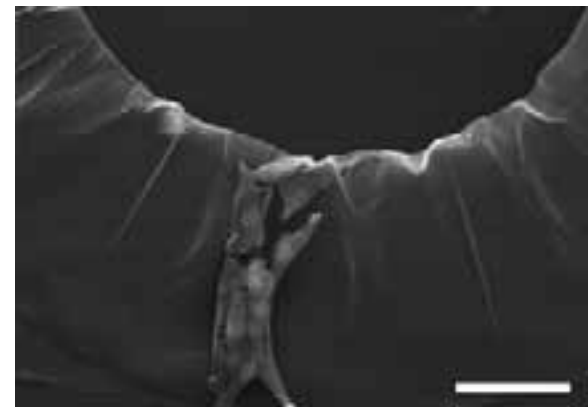


Figure 2: Multiplied cells on CNTs microstructure (scale bar = 50 μ m).

As a result of more detailed observation by SEM, some of cells on the CNTs-fibronectin microstructures were aligned along CNTs direction, and some were perpendicularly attached (Figure 1). In addition, cells were capable of growth on CNTs-fibronectin microstructure and maintained their direction of alignment even after three days culture (Figure 2). In contrast, cells were not attached to CNTs microstructure without fibronectin coating. Finally, cell morphologies were sorted into five different types (parallel, perpendicular, bottom of substrate, bridged, attached to the top) and cell number were counted.

In the region with CNTs micropillars, which spacing and diameter were about 35 μ m and 90 μ m respectively, there were more than the twice number of cells on the fibronectin coated substrate than non-coated substrate. Moreover, about 70% cells were perpendicularly attached to CNTs pillars in fibronectin coated substrate (Figure 3). In contrast, most of cells were attached to the bottom of substrate in non-coated substrate.

In addition, in the region with twisted CNT micropillars with spacing and diameter of about 75 μ m and 30 μ m, respectively, the cell number was about same and more than 60% of cells attached to the bottom of substrate on both fibronectin coated substrate and non-coated substrate (Figure 4).

Conclusions and Future Work:

Cells attached readily to CNTs-fibronectin microstructures and their morphology was altered on CNTs-fibronectin microstructures. Cells were capable of growth on CNTs-fibronectin microstructures. The morphology of cells depends on the spacing and size of CNTs-fibronectin microstructures. More detailed observations such as orientation of focal adhesion and distribution of cytoskeleton are needed to understand cell attachment on CNTs-fibronectin microstructures.

Acknowledgments:

I would like to thank Professor John Hart, Davor Copic, and Megan J. Roberts and the Mechanosynthesis group,

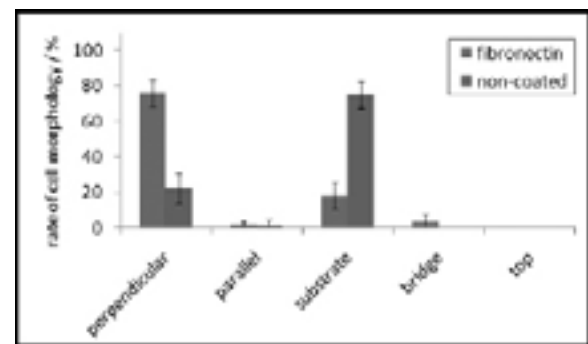


Figure 3: Evaluation of cell morphology in the region with CNTs microstructures (spacing: 35 μ m, diameter: 90 μ m).

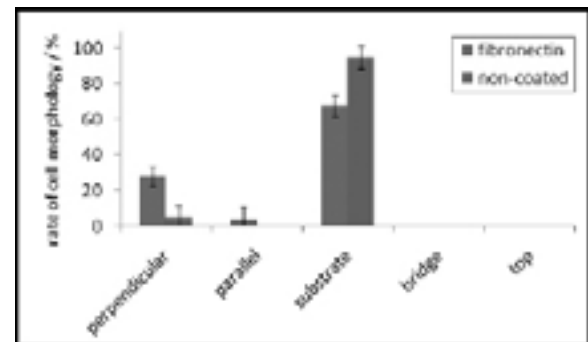


Figure 4: Evaluation of cell morphology in the region with CNTs microstructures (spacing: 75 μ m, diameter: 30 μ m).

and Professor Jianping Fu and Jennifer Mann for guiding me throughout this program. Also, I would like to thank Pilar Herrera-Fierro for taking SEM images and the site coordinators: Sandrine Martin, Brandon Lucas, and Trasa Burkhardt, and the staff at Lurie Nanofabrication Facility for their help. Finally, I would like to acknowledge the National Science Foundation, and the National Nanotechnology Infrastructure Network Research Experience for Graduates Program, and the National Institute for Materials Science.

References:

[1] M. De Volder, S. Tawfick, S.J. Park, D. Copic, Z. Zhao, W. Lu, A.J. Hart. Diverse 3D microarchitectures made by capillary forming of carbon nanotubes. *Advanced Materials* (in press), (2010).

Designing Nano-Engineered Substrates to Probe Cell Organization, Motion and Traction Forces

Erin Watson

Bioengineering, Rice University

NNIN REU Site: Nanotech, University of California, Santa Barbara, CA

NNIN REU Principal Investigator(s): Dr. Megan T. Valentine, Mechanical Engineering, University of California, Santa Barbara

NNIN REU Mentor(s): Ryan Meschevski, Mechanical Engineering, University of California, Santa Barbara

Contact: enw1@rice.edu, valentine@engineering.ucsb.edu, rmesche2@gmail.com

Abstract:

The mechanical forces involved in interactions between cancer cells and their environment are poorly understood and may present new diagnostic and treatment opportunities. The present study aimed to develop a technique to measure the traction forces cancerous cells exert on their environment. We developed deformable gels with specific and adjustable stiffnesses. The cell traction forces were quantified by the gel deformation. This study has led to the successful creation of gels and the development of a technique to characterize the gel elastic spring constant, and a method for measuring cell response to different mechanical environments. Preliminary results show the gels have an elastic response, characterized by a reasonably consistent spring constant. Additionally, results demonstrate a correlation between the bone cancer cell attachment and substrate stiffness.

Introduction:

Mechanical forces play an essential role in a variety of cell processes and are often altered in diseased tissue [1]. Cancerous tissues are often diagnosed by their abnormal stiffness, indicating cancer cells may have abnormal mechanical properties on a cellular level. This study aimed to create a technique to increase the understanding of cancer cell mechanics by measuring the forces that cells exert on their substrates, and studying the effects of different mechanical environments on cells. This device will measure cancer cell traction forces during mitosis, which is important for cancer proliferation, and during cell locomotion, which is necessary for metastasis [2].

The technique used a deformable polyacrylamide gel with embedded fluorescent beads. Gel deformation was related to the applied force, and was detected by bead displacement (Figure 1). Specifically, this study focused on measuring the mechanical properties of the gel and characterizing the cancer cells' responses to different gel stiffnesses.

Experimental Procedure:

The polyacrylamide gel solutions were made using a previously described procedure [3]. Ten microliters of the gel solution were sandwiched between a hydrophobic glass slide and a silanized cover glass. After the gel polymerized, the glass slide was removed and the gel was ready for use.

For gel stiffness characterization, a 230 pascal modulus gel was made according to standard protocols [3]. Acryloyl-X conjugated biotinylated bovine serum albumin was added to the gel solution to promote attachment of streptavidin-conjugated magnetic beads to the gel surface. The magnetic beads were added to the polymerized gels and magnetic forces ranging from 0.0 to 60 piconewtons were applied to the beads. The bead displacement was calculated from the diffraction patterns of the beads, observed via microscopy.

U2OS (bone cancer cells), H460 (lung cancer cells) and HeLa (cervical cancer cells) were plated onto tissue culture treated plastic, and the fraction of cells attached was measured at multiple times. Cell morphologies were analyzed after twenty hours of incubation. Next, gels with 230 pascal, 2.8 kilopascal and 16.3 kilopascal moduli were made. Acryloyl-X conjugated fibronectin was added to the gel solution at 10% volume fraction to promote cell attachment. After gel polymerization, an ultraviolet germicidal lamp was employed to sterilize the gels. U2OS cells were plated onto the gels, tissue culture treated plastic, and untreated coverglasses. After twenty hours, cell morphology was analyzed.

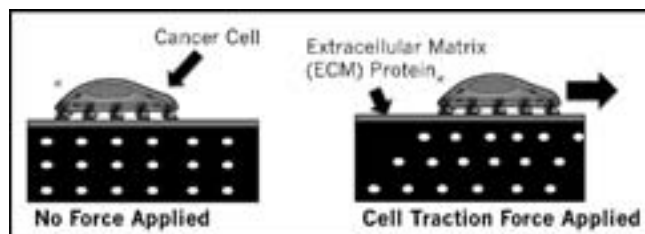


Figure 1: Schematic of substrate for cell traction force microscopy.

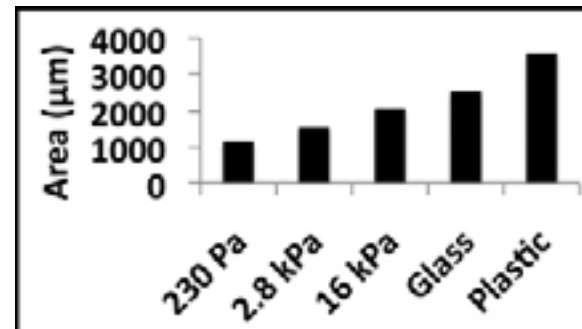
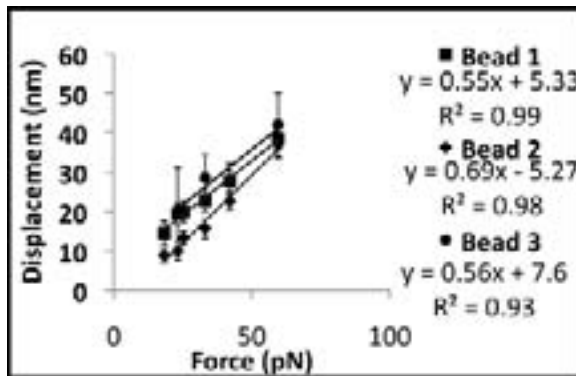


Figure 4: Correlation between mean U2OS cell area and substrate stiffness.

Results and Conclusions:

The data from the magnetic bead displacement tests were used to characterize the gel moduli. A linear regression was used to fit a plot of mean magnetic bead displacement versus force (Figure 2). Preliminary results show a linear relationship between force and displacement, signifying an elastic response from the gel. The spring constant of the gel was given by the inverse of the slope and was calculated to be 1.68 ± 0.20 piconewton/nanometer.

Assuming constant bead contact area for each trial, this result indicates that gel modulus was fairly consistent and uniform from gel to gel (13% variation). It is critical that the gel moduli are consistent and predictable, to ensure the accuracy of the cell traction force measurements.

As cells attach, they begin to spread and become more irregularly shaped. We used the mean area and roundness ($4 \cdot \text{area}/(\pi \cdot \text{major_axis}^2)$) of the cells to quantify the degree of attachment to gels. We chose to use U2OS cells to plate onto gels because results showed that U2OS cells had the greatest area and the lowest roundness of the three cell types, which would allow us to see a greater range of results.

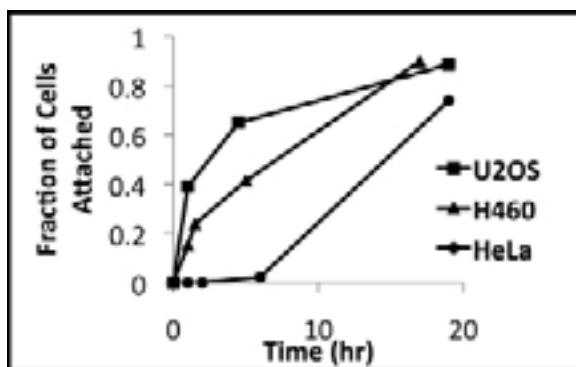


Figure 3: Results of cell attachment assay for three cell types.

Additionally, the U2OS cells had the highest rate of cell attachment (Figure 3). In tests of the effects of substrate stiffness on U2OS cells, we saw a strong positive correlation between gel stiffness and cell area (Figure 3). There was no obvious correlation between substrate stiffness and cell roundness (Figure 4).

Future Work:

Next steps include continuing gel modulus characterization by measuring the gel deformation field using the displacement of embedded beads. Additionally, future work includes determining the cell response to various mechanical environments using H460, HeLa, and other cancer cell lines. Cell traction force measurements have recently begun. These measurements will focus on the effects of substrate stiffness on mitosis and cell motility, and potentially increasing the understanding of the role of cell mechanics in cancer growth and metastasis.

Acknowledgements:

Thank you to the National Nanotechnology Infrastructure Network Research Experience for Undergraduates Program and National Science Foundation for funding my research. Special thanks to Dr. d T. Valentine, Ryan Meschewski, Jun Lin, Angela Berenstein, other Valentine lab members, and our collaborators.

References:

- [1] Lautenschläger et al. The regulatory role of cell mechanics for migration of differentiating myeloid cells. PNAS (2009) 106(37):15696-701.
- [2] Silletti et al. Tumor Cell Motility and Metastasis: Autocrine Motility Factor as an Example of Ecto/Exoenzyme Cytokines. Pathology and Oncology Research (1997) 3(3), 230-254.
- [3] Aratyn-Schaus et al. Preparation of compliant matrices for modulating and quantifying cellular contraction. Publication pending.

Design of Organic Conductors Comprised of Fullerene and Lanthanum Triple-Decker Porphyrin Complexes

Mark Borysiak

Chemical and Biomolecular Engineering, The Ohio State University

NNIN iREU Site: National Institute for Materials Science (NIMS), Tsukuba, Ibaraki, Japan

NNIN iREU Principal Investigator(s): Dr. Masayuki Takeuchi, Organic Nanomaterials Center, NIMS, Japan

NNIN iREU Mentor(s): Michael Frank, Organic Nanomaterials Center, NIMS, Japan

Contact: borysiak.1@osu.edu, takeuchi.masayuki@nims.go.jp, frank.michael@nims.go.jp

NNIN iREU Program

Abstract:

Over the past few years, the use of organic semiconductors in field effect transistors (OFETs) as an alternative to more traditional inorganic semiconductors has received increasing attention. This is a result of low cost production of OFETs due to solution processability, as well as other factors such as the incorporation of functionality by design [1]. Single crystal organic field effect transistors (SCOFETs) are of particular interest because they allow for the study of intrinsic charge transport properties of the organic semiconductor, and they also have shown relatively high mobility's compared to thin film OFETs due to the absence of grain boundaries [1]. The research that was conducted focused on the synthesis, purification, and characterization of a novel lanthanum triple-decker (LaTD; three porphyrinato complexes encompassing two lanthanum metal ions) complex for potential creation of a single crystal organic semiconductor. The LaTD will be used as an alternative to a cerium double decker (CeDD; two porphyrinato complexes encompassing a cerium metal ion) molecule in an already existing CeDD-fullerene C_{60} organic co-crystal (Figure 1). The CeDD- C_{60} co-crystal has shown impressive properties including anisotropic conducting behavior and a very high mobility ($\sim 10 \text{ cm}^2 \text{ V}^{-1} \text{ s}^{-1}$). The LaTD substitution in this co-crystal is hoped to improve the electronic transport properties of the crystal through increased spacing of the charge-carrying fullerene molecules. In addition, the novel LaTD molecule is an intriguing compound due to its tetraarylporphyrinato, homoleptic structure.

Introduction:

There have been numerous double and triple-decker structures synthesized in the past. These structures consist of a metal ion(s) (M) sandwiched between porphyrin (P) or phthalocyanine (Pc) tetrapyrrole ligands, or a combination of the two. This results in a coordination compound in which the metal ion has a cationic charge of +3, +4, or +5 with the tetrapyrrole ligands in the -2 anionic state, forming structures of the nature $M(P)_2$, $M_2(P)_3$, or their Pc equivalents (or heteroleptic combinations) [2]. The LaTD molecule that was synthesized is of the $M_2(P)_3$ form, with the porphyrin containing four 4-methoxy phenyl substituents. The large steric compression caused by these phenyl substituents has prevented the isolation of homoleptic, tetraarylporphyrin triple-deckers in the past [2]. As a result, the LaTD molecule that was synthesized is a novel compound, most likely stabilized by the very large ionic radius of lanthanum (1.16 pm), as compared to other double or triple-decker forming metal ions.

The synthesis of the LaTD molecule begins by metal insertion, yielding a monoporphyrinate of octacoordinate chemistry, stabilized by ligands (Figure 2a) [2]. A raise-by-one-story reaction of this metal mono(porphyrinate) with another

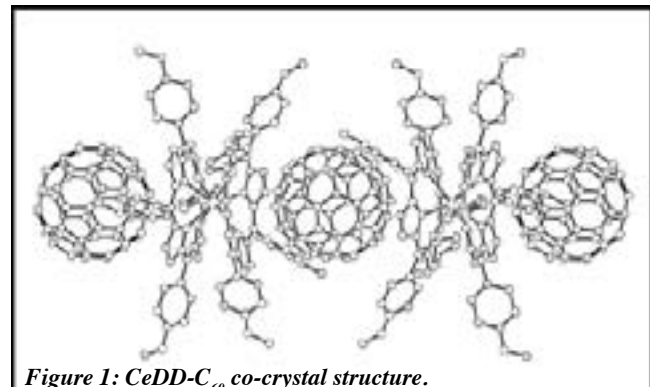


Figure 1: CeDD- C_{60} co-crystal structure.

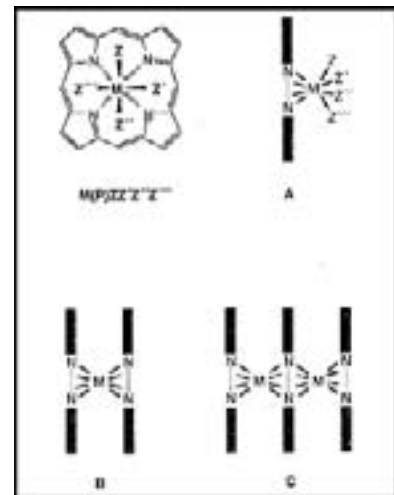


Figure 2: Triple-decker mechanism
(Image Source: [2] Buchler and Ng).

porphyrinate results in a double-decker structure (Figure 2b) [2]. Another raise-by-one-story reaction with the double-decker structure and a third porphyrinate results in the triple-decker structure (Figure 2c).

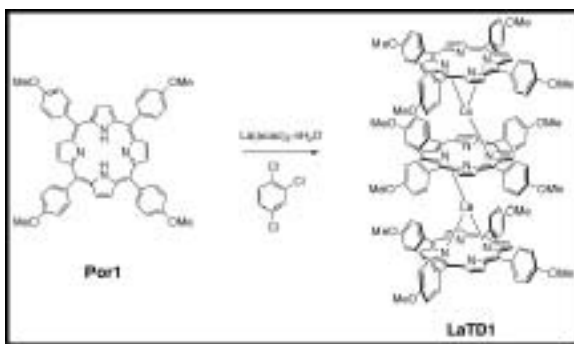


Figure 3: LaTD synthesis.

Experimental Procedure:

Synthesis of dilanthanum(III)tris[5,10,15,20-tetrakis-(4-methoxyphenyl) porphyrinate], LaTD (Figure 3). 3.74 g (8.56 mmol) of tris(acetylacetonato) lanthanum(III) n-hydrate, La(acac)₃·nH₂O, 99.9% (purchased from Wako Chemicals) and 710 mg (0.966 mmol) of 5,10,15,20-tetrakis(4-methoxyphenyl)-21H,23H-porphyrin (prepared from 4-methoxybenzaldehyde and pyrrole in propionic acid) in 96 mL of 1,2,4-trichlorobenzene (purchased from Kanto Chemical) was refluxed at 260–280°C for 36 hours under argon atmosphere. The solution started out purple and changed to a dark brown/black color as the reaction progressed. After 36 h, the TCB was removed via vacuum at a bath temperature of 100°C. The resulting solid was vacuum filtered, washed with hexane in which it is insoluble, and collected with chloroform. Using silica gel chromatography on the sample, a dark brown fraction was eluted following a purple, fluorescent fraction. The dark brown fraction was further purified via size exclusion chromatography (SEC) with chloroform. The sample was recrystallized using either methanol or ethanol, purified via recycling GPC, and re-precipitated using a toluene-hexane mixture (1:1). The final sample was taken to dryness in vacuum. The resulting LaTD solid (36.49 mg, 4.6%) was characterized using MALDI-TOF mass spectroscopy, ¹H NMR spectroscopy, GPC, thin layer chromatography and elemental analysis.

Results and Discussion:

The synthesis of the LaTD was confirmed through MALDI-TOF mass spectrometry (Figure 4). The molecular weight (2475 amu) is clearly shown after purification of the sample, demonstrating the clear presence of LaTD. The reaction was found to have a greater yield with increased temperature and time of reaction, although the increase in temperature is also believed to

introduce bi-products that were difficult to remove. After the trial of many purification techniques, it was determined that re-precipitation using toluene and hexane was the most efficient and effective method for final purification of the sample. The sample was characterized via ¹H NMR spectroscopy, GPC, and elemental analysis, showing high purity, allowing the LaTD to be used in the creation of co-crystals with C₆₀. At the time of writing, the results of these crystals are unknown.

Conclusion and Future Work:

A novel LaTD molecule was successfully synthesized, purified, and characterized. The substitution of this molecule in place of CeDD in a CeDD-C₆₀ co-crystal is anticipated to improve an already impressive electron mobility of ~ 10 cm² V⁻¹ s⁻¹ for use as a single crystal organic semiconductor. Future work on this project will depend heavily on the results of the co-crystal formation, but consists of improving reaction yield, further characterization, and modifications to the LaTD/crystal structure.

Acknowledgements:

I would like to thank the National Science Foundation, National Nanotechnology Infrastructure Network Research Experience for Undergraduates program, and the National Institute Materials Science of Japan for the funding and opportunity to participate in this great program. In addition, I would like to thank my PI, Dr. Masayuki Takeuchi for the opportunity to work with his outstanding group and my mentor Mike Frank for his assistance throughout my project.

References:

- [1] Reese, C. and Bao, Z. "Organic single-crystal field-effect transistors." *Materials Today*. March 2007.
- [2] Buchler J. and Ng D. "Metal Tetrapyrrole Double and Triple-Deckers with Special Emphasis on Porphyrin Systems." *Inorganic, Organometallic, and Coordination Chemistry*.

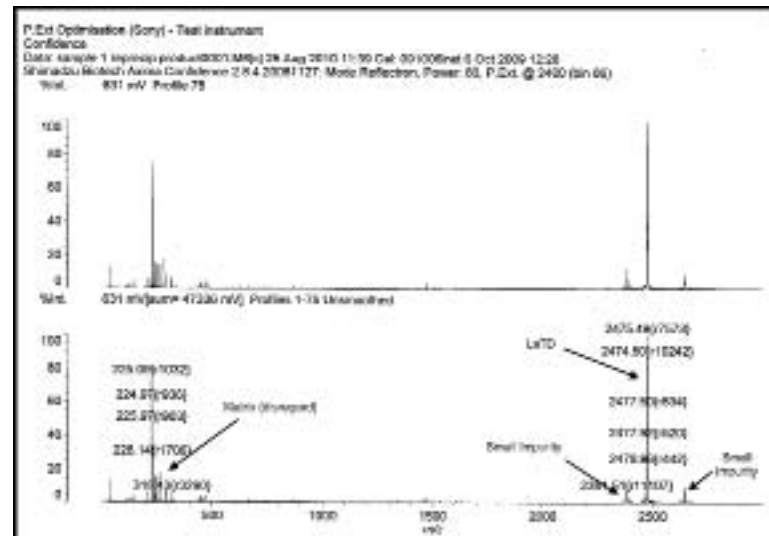


Figure 4: MALDI-TOF mass spectrum of sample (LaTD MW = 2475 amu).

Initial Stages of Tantalum Nitride Atomic Layer Deposition

John Davis

Department of Chemistry, Carleton College

NNIN REU Site: Cornell NanoScale Science and Technology Facility, Cornell University, Ithaca, NY

NNIN REU Principal Investigator(s): Professor James R. Engstrom, Department of Chemical Engineering, Cornell University

NNIN REU Mentor(s): Kevin Hughes, Department of Chemical Engineering, Cornell University

Contact: davisj@carleton.edu, jre7@cornell.edu, kjh47@cornell.edu

Abstract:

Since the semiconductor industry has moved to porous low- κ dielectrics, thin-film barrier layers to prevent copper diffusion have become increasingly important. In this project, the initial stages of thin-film growth of tantalum nitride deposited via atomic layer deposition were characterized on both low- κ dielectrics and copper, and growth-promoting surface treatments were developed. An ultrathin coating of an interfacial organic layer, polyethyleneimine, increased the growth of tantalum nitride on porous low- κ by reducing diffusion of the precursors and increasing the number of active sites on the surface. Tantalum nitride growth on untreated copper, in contrast, exhibited a long incubation period; while pre-treatments of the surface were found to decrease the incubation time.

Introduction:

As feature sizes in integrated circuits approach the nanometer scale, there is an increasing need for highly conformal, precisely-controlled thin film deposition. Atomic layer deposition (ALD) has emerged as an ideal method to deposit a variety of materials used in modern semiconductor devices. Its conformal growth arises out of its layer-by-layer process—precursors are alternately injected and purged from a low-pressure system, which builds up a film, layer by layer. Though it is very useful, many materials remain difficult to deposit via ALD because chemical interactions at the thin film-substrate interface govern the initial stages of nucleation and growth in this deposition process. This project investigated ALD of tantalum nitride (TaN), one of the most attractive materials for diffusion barriers between copper interconnects and the dielectrics that surround them. Growth on both copper and porous low- κ dielectrics was studied, and interfacial organic layers were identified to promote growth in the early stages of ALD. Growth rates and film uniformity were studied using x-ray photoelectron spectroscopy and spectroscopic ellipsometry, while atomic force microscopy was used to characterize the nucleation of the TaN films.

Experimental Procedures:

Atomic layer deposition was carried out at 250°C on an Oxford FlexAL machine using pentakis(dimethylamino)tantalum and ammonia precursors. Industry-supplied porous low- κ

and copper wafers were used for all experiments. The polyethyleneimine capping layer was deposited on the porous low- κ wafers with a 15-minute soak in a 0.1% by weight solution of polyethyleneimine in water. Ellipsometry revealed that the thickness of the capping layer was on the order of 3 Å. This solution was prepared using polyethyleneimine purchased from commercial suppliers with no further purification.

Results:

Deposition on Porous Low- κ . Angle-resolved x-ray photoelectron spectroscopy and atomic force microscopy (AFM) were used to examine the initial stages of growth of TaN on porous low- κ . As illustrated by angle-resolved

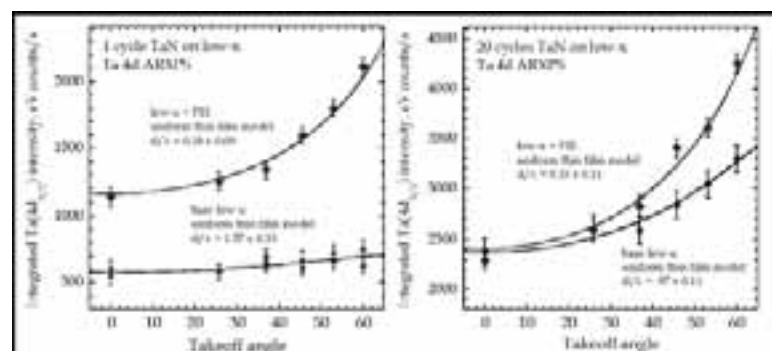


Figure 1: Angle-resolved x-ray photoelectron spectroscopy of the tantalum signal in untreated and porous low- κ treated with an interfacial organic layer at one cycle (left) and 20 cycles (right) of ALD.

x-ray photoelectron spectroscopy results in Figure 1, deposition on untreated porous low- κ resulted in poor growth and TaN diffusion into the dielectric. This diffusion was virtually eliminated by the use of the interfacial organic layer, polyethyleneimine. While the TaN film uniformity on untreated porous low- κ improved by 20 cycles, the low- κ treated with the interfacial organic layer still exhibited superior performance.

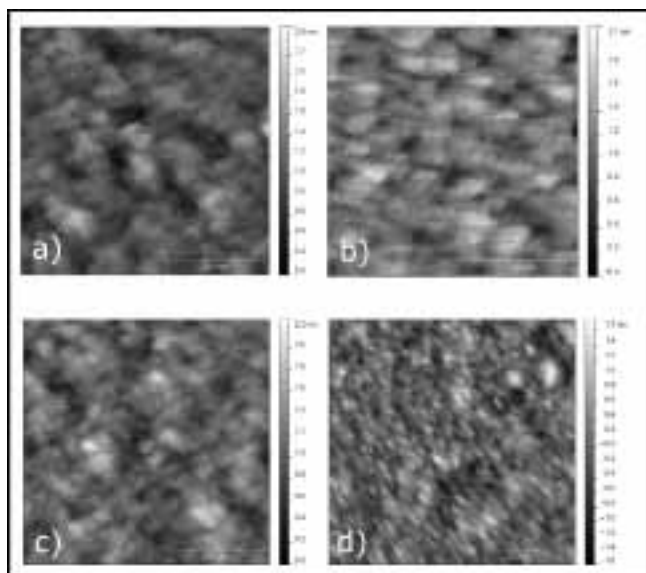


Figure 2: AFM images of; a) untreated porous low- κ before deposition, b) polyethyleneimine-treated porous low- κ before deposition, c) untreated porous low- κ after 20 cycles of TaN deposition, and d) polyethyleneimine-treated porous low- κ after 20 cycles of TaN deposition.

Improvements in growth and nucleation on the polyethyleneimine-treated porous low- κ were confirmed by comparing AFM images of the treated and untreated wafers after a number of cycles. As shown in Figure 2, the treated and untreated porous low- κ are virtually indistinguishable before deposition (2a and 2b), but after 20 cycles of TaN ALD, the TaN film on the treated porous low- κ (2d) shows a developing grain structure, while the untreated porous low- κ still has the cloud-like morphology of the pre-deposition substrates. Unfortunately, since ellipsometry on porous low- κ yielded unreliable results, we were unable to characterize the growth rate per cycle.

Deposition on Copper. As shown by the previous results with the polyethyleneimine-treated porous low- κ , even the first few angstroms (\AA) of the surface can heavily influence growth. As such, we hypothesized that the native oxide layer might play a significant role in the deposition of TaN on copper.

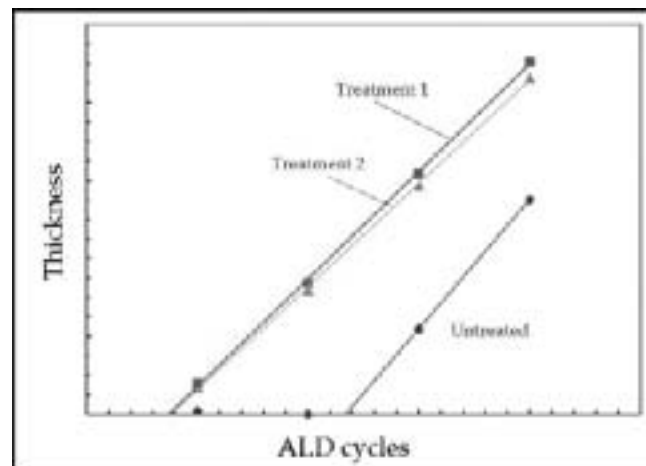


Figure 3: Growth rates and incubation time of untreated, and pretreated copper samples.

To study the possible effects of the state of the starting surface, we measured deposition on untreated copper, and copper exposed to one of two treatments. Figure 3 illustrates the growth rate and incubation time for the three different sets of conditions. As can be seen in the figure, both pretreatments significantly reduce the length of the incubation period. Furthermore, since they have statistically identical effects on the deposition, we propose that the decrease in incubation time was indeed achieved by chemically modifying the state of the starting surface.

Conclusions:

The initial stages of TaN growth by ALD were studied on porous low- κ dielectrics and copper. A polyethyleneimine interfacial organic layer on porous low- κ reduced tantalum diffusion into the dielectric and facilitated uniform growth on the surface. These results were confirmed by angle-resolved x-ray photoelectron spectroscopy and atomic force microscopy. On copper, ellipsometry was used to determine the growth rate and incubation time on untreated surfaces, and surfaces exposed to treatments intended to modify the starting surface. These treatments both significantly reduced the incubation time.

Acknowledgements:

The author would like to acknowledge the National Science Foundation, the National Nanotechnology Infrastructure Network Research Experience for Undergraduates (NNIN REU) Program, the Cornell NanoScale Science and Technology Facility, Professor James R. Engstrom, Kevin Hughes, Wenyu Zhang, and Melanie-Claire Mallison.

Synthesis and Characterization of Oxide-Embedded and Surface-Passivated Silicon Nanocrystals

NNIN Grad Program

Hiromasa Fujii
Electrical Engineering, University of Tokyo

NNIN REU Graduate Research Site: Microelectronics Research Center, The University of Texas, Austin, TX

NNIN Graduate Research Principal Investigator(s): Brian A. Korgel, Chemical Engineering, University of Texas at Austin

NNIN Graduate Research Mentor(s): Dr. Colin Hessel, Chemical Engineering, University of Texas at Austin

Contact: fujii@hotaka.t.u-tokyo.ac.jp, korgel@che.utexas.edu, hessel@che.utexas.edu

Introduction:

Silicon nanocrystals (SiNCs) emit light, a nanoscale phenomenon that is being explored for new biomedical and optoelectronic applications. Quantum confinement effects govern the light emission properties for silicon, and various colors of light can be obtained by changing the crystal size [1]. However, the size at which quantum confinement effects subside to bulk electronic properties is still unclear. Here, our goal was to elucidate the size at which quantum confinement effects vanish in Si nanocrystals by measuring the photoluminescence properties of SiNCs with diameters greater than the Bohr exciton radius (5 nm), the size at which quantum confinement effects are proposed to emerge.

Experimental Procedures:

Bulk oxide-embedded SiNCs were synthesized using hydrogen silsesquioxane (HSQ) as a precursor. Solvent (methyl isobutyl ketone) was evaporated from HSQ stock solution to obtain solid white HSQ, which was subsequently processed at 1100-1400°C for one hour in a 7% H₂ / 93% N₂ atmosphere. All samples were heated at 18°C / min in a furnace. The products were ground with a mortar and a pestle and then characterized by x-ray diffraction (XRD) and photoluminescence (PL).

Thin film oxide-embedded SiNCs were also fabricated in order to compare the PL intensities. HSQ stock solution was spin-coated on quartz substrates and readily heated in the furnace under the same processing condition as mentioned above. Photoluminescence was measured for these thin film samples.

SiNCs were etched from the oxide matrix and passivated with dodecene by thermal hydrosilylation to produce hydrophobic colloidal nanocrystals. First, the ground oxide-embedded composites were shaken with 3 mm glass beads for 10 hours to reduce their grain size. The shaken particles were etched with hydrofluoric acid (HF) for 3.5 hours to remove oxide matrix surrounding the SiNCs. These nanocrystals were washed and extracted by centrifugation with ethanol and chloroform and their surfaces were subsequently passivated with dodecene by thermal

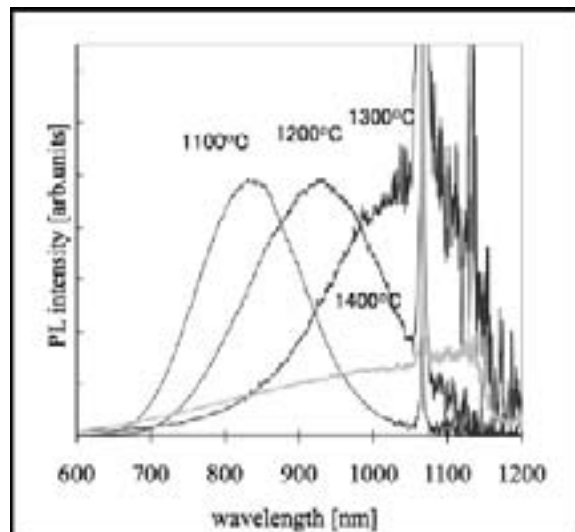


Figure 1: PL of bulk HSQ processed at 1100-1400°C.

hydrolylation. Finally, SiNCs were washed and extracted by centrifugation with ethanol and methanol, and readily dispersed in chloroform. The products were observed by a transmission electron microscope (TEM) and characterized by PL and photoluminescence excitation (PLE).

Results and Conclusions:

Figure 1 is the PL results of oxide-embedded composites processed at various temperatures. The PL emission red-shifted from 850 nm to approximately 1100 nm as processing temperature was increased from 1100°C to 1300°C. The PL intensity dropped significantly for HSQ processed at 1400°C and an accurate peak wavelength could not be obtained due to spectral range limitations. XRD studies on HSQ processed at these temperatures show the SiNCs from HSQ processed at 1300 and 1400°C are 7.5 and 13.4 nm, respectively [2]. Luminescence from these samples demonstrates that SiNCs emit light at sizes much larger than is predicted by traditional quantum confinement theory. This also shows light emission at bulk silicon bandgap (1.1 eV, 1100 nm).

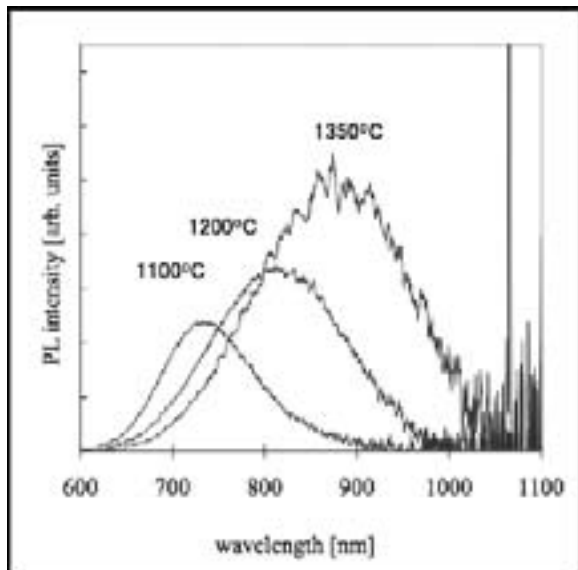


Figure 2: PL of thin film HSQ processed at 1100-1350°C.

Figure 2 shows the PL emission of thin film HSQ samples red shifts and increases in intensity with higher process temperatures. The former trend can be explained by typical quantum confinement effects, but the latter trend is opposite to our prediction. It is because we believe that quantum confinement effects diminish in larger nanocrystals. We think that these unexpected results were due to nonuniformity of the films. We note that only few luminescent spots could be obtained from some film samples, and that the PL intensities were different depending on the spots. Therefore, preparation of uniform samples and more accurate investigation are needed. The PL emission intensity from freestanding SiNCs was very strong, and easily observed under a hand held UV light (lambda = 366 nm). Figure 3 shows the PL red-shifts with higher process temperatures. An unknown peak in the PL spectrum from the 1300°C sample seems to be coming from oxide residue. The PLE results indicate that peak excitation wavelengths were similar (Figure 4). In order to determine optical property of surface-passivated SiNCs,

further measurements including absorption spectroscopy are needed.

In conclusion, various sizes of SiNCs were synthesized and characterized in bulk, thin film, and freestanding morphologies. Luminescence from SiNCs larger than Bohr exciton radius (5 nm) was observed, a phenomenon that is the most interesting result in this study. Emission red shifts with larger nanocrystals were observed from all the three morphologies, indicating quantum confinement effects govern optical property of SiNCs.

Future Works:

- XRD measurement using the exact same bulk samples which were used for PL spectroscopy.
- Fabrication of and uniform thin-film samples in order to visualize the diminishing quantum confinement effects with increasing the crystal size.
- Process at higher temperature (1500-1700°C) to obtain larger SiNCs.
- Longer process at the critical temperature which gives the crystal size with weakened luminescence.
- Time resolved and low temperature PL.

Acknowledgements:

National Nanotechnology Infrastructure Network Research Experience for Graduates Program and the National Science Foundation are acknowledged for supporting and funding this research. Prof. Brian Korgel, Korgel group, Jean Toll and Allison Cargile are appreciated for their supports. Junwei Wei is thanked for assistance with thin-film study. Matt Panthani is thanked for taking a TEM image of a silicon nanocrystal.

References:

[1] Zhizhong Yuan, et al., Proceedings of the IEEE, Vol. 97, No. 7, pp. 1250-1268, 2009. [2] Colin M. Hessel, et al., J. Phys. Chem. C, Vol. 111, Vo. 19, pp. 6956-6961, 2007.

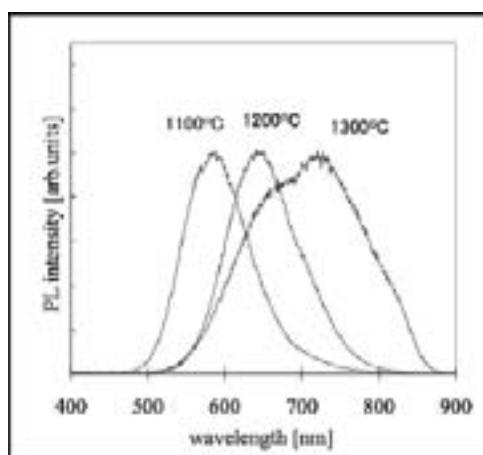


Figure 3: PL of surface-passivated SiNCs processed at 1100-1300°C.

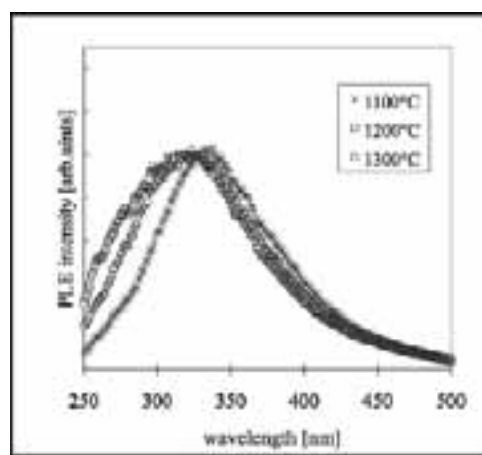


Figure 4: PLE of surface-passivated SiNCs processed at 1100-1300°C.

Characterization of Dynamics of Solvents Encapsulated in Nano-Scale Volumes, by Selective Enhancement of NMR Signal via Dynamic Nuclear Polarization

Audrey Hammack

Chemistry, The University of Texas at Tyler

NNIN REU Site: Nanotech, University of California, Santa Barbara, CA

NNIN REU Principal Investigator(s): Professor Song-I Han, Chemistry and Biochemistry, University of California, Santa Barbara

NNIN REU Mentor(s): John Franck, Department of Chemistry and Biochemistry, University of California, Santa Barbara

Contact: ahammack@patriots.uttyler.edu, songi@chem.ucsb.edu, johnfranck@gmail.com

Abstract:

Lipid vesicles have been spotlighted for their potential applications, but few methods characterize the behavior of encapsulated solvents, either in terms of exchange or in terms of local dynamics inside the vesicle [1]. Our work sought to characterize the dynamics of solvent encapsulated in nano-scale vesicles, which were dispersed in a dilute solution. We achieved dynamic nuclear polarization (DNP), which selectively enhanced the signal from the encapsulated solvent. As the level of enhancement depends on the timescale of solvent dynamics, this gives information on the timescale of intra-vesicular water dynamics.

Introduction:

Since their development, lipid vesicles have been regarded as novel nano-scale containers, and are used as models of cellular compartments [2]. Despite the developments in liposome applications, existing methods have difficulty in characterizing the dynamics of the encapsulated solvent or the rates of exchange across the lipid membrane, since they cannot distinguish the intra-vesicular solvent from the extra-vesicular solvent. Nuclear magnetic resonance (NMR) spectroscopy has high specificity that can elucidate chemical structure and produce images of soft tissues (i.e., magnetic resonance imaging); however, NMR relies on the premise that different chemicals have distinct signatures. In the case of vesicles, the encapsulated solvent and the bulk solvent are the same chemical, and thus, resonate at the same frequency; traditional spectroscopy cannot distinguish these two components.

DNP can selectively enhance an NMR signal, even against a large background signal. DNP arises from cross-relaxation, during which electron spins transfer their polarization to nuclear spins, via dipolar interactions, as a result of excitation by microwave radiation. This polarization transfer results in enhanced signal. Furthermore, it only occurs over short distances, 3-5Å; so when a vesicle encapsulates the spin label, only the NMR signal of protons within the vesicles will be enhanced.

Enhancement of the NMR signal (and polarization) is related to solvent dynamics by the following equation

$$E = 1 - pfs \frac{|\gamma_e|}{\gamma_s} \quad (1)$$

γ_e and γ_s , are the gyromagnetic ratios of the electron and proton, respectively; the leakage factor, f , can be calculated from T_1 and $T_{1,0}$, the signal decay time for spin-labeled and non spin-labeled solutions, respectively; and, when extrapolated to infinite power, s is 1. This equation thus isolates the coupling factor, p , which depends only on the timescales of solvent dynamics, as given by the translational correlation time, τ [3]. With proper modeling and data analysis, a value for τ can be extracted from p [4].

Methods:

The vesicles were prepared by depositing 75 mg of a 4:1 mixture of 1,2-dipalmitoyl-*sn*-glycero-3-phosphocholine (DPPC) and 1,2-dimyristoyl-*sn*-glycero-[phospho-*rac*-(1-glycerol)] (DPPG) in a test tube. To this, a solution of 250 μ L of 140 mM CAT₁, dissolved in Hepes-buffered saline, was added. The mixture was warmed above 42°C, the transition temperature of the lipids, vortexed, and extruded through a polycarbonate filter with 400 nm pores. For some samples, 0.35M ascorbic acid was reacted with the unencapsulated radical, in a 5:1 molar ratio.

Results and Conclusions:

The EPR spectra in Figure 1 demonstrate encapsulation of the spin label CAT₁ inside the vesicles. For vesicles containing intra- and extra-vesicular CAT₁, the spectrum has a very broad lineshape, indicating a very high concentration. When the extra-vesicular CAT₁ was partially removed, the spectrum had a broad component, but also included narrow peaks, corresponding to the lowered extra-vesicular CAT₁

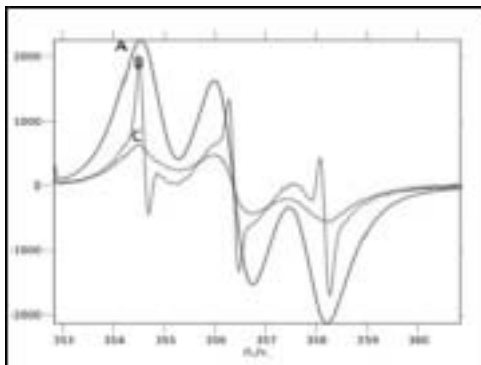


Figure 1: X-band EPR of samples of vesicles, with 140 mM intra- and extra-vesicular CAT₁ (A), partially removed extra-vesicular CAT₁ (B), and no extra-vesicular CAT₁ (C).

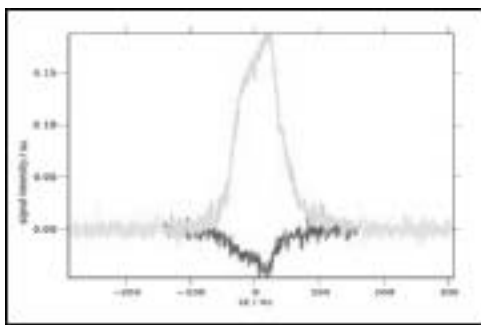


Figure 2: NMR spectra of 400 nm vesicles, containing 140 mM CAT₁, before and after, DNP enhancement.

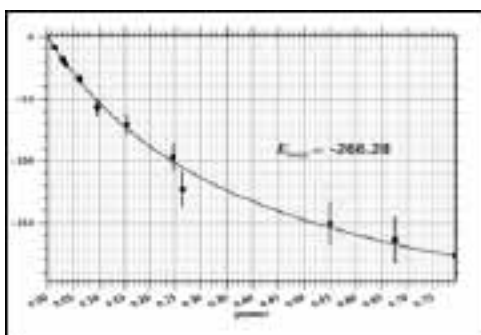


Figure 3: Measurement of DNP enhancement of signal from 140 mM CAT₁.

concentration. Finally, when reaction with ascorbic acid removed all extra-vesicular CAT₁, only the broad components remained, indicating that CAT₁ remained encapsulated.

The T₁ time of the NMR signal can determine the residence time of water in the two environments. Therefore, we measured the T₁ time for a 140 mM spin label solution, before and after treatment with ascorbic acid, as 23.7 ms and 2.3 s, respectively. For a sample of vesicles containing 140 mM CAT₁ and treated with ascorbic acid, T₁ was found to be 1.13 s, a weighted average between the two cases which indicates rapid exchange of water across the membrane.

Figure 2 shows an unenhanced spectrum, and a spectrum that had been substantially enhanced by DNP. Since it had been demonstrated that CAT₁ was encapsulated, it can be concluded that DNP exclusively enhanced the NMR signal of water inside the vesicle.

Finally, signal enhancement, from a solution of 140 mM CAT₁, was acquired as a function of microwave power, as shown in Figure 3. Extrapolating to infinite power yields, E_{max} = -266.28, and by means of Equation 1, $\rho = 0.40$, yielded a τ for this sample of 12.6 ps.

Future Work:

Future work includes measurement of ρ for a sample of vesicles that encapsulate CAT₁, thus selectively determining τ for water diffusion dynamics inside the vesicles. Additionally, it has been shown that it is possible to slow water exchange across the membrane and resolve the two simultaneous T₁ time constants for intra-vesicular CAT₁ solution and extra-vesicular pure water [5]. This would allow determination of rates of exchange and permeation across the membrane.

Acknowledgements:

I would like to thank my mentor John Franck, my principal investigator, Song-I Han, the Han lab, the National Nanotechnology Infrastructure Network Research Experience for Undergraduates (NNIN REU) Program and the National Science Foundation support and funding.

References:

- [1] P. Walde, S. Ichikawa Biomolecular Engineering. 18,4 (2001) 143-77.
- [2] K. L. Chan, P. R. C. Gascoyne, F. F. Becker and R. Pethig. Biochimica et Biophysica Acta (BBA) - Lipids and Lipid Metabolism, 1349, 2 (1997) 182-196.
- [3] K.H. Hausser and D. Stehlik, D. Adv. Magn. Reson., 3, (1968), 71-139.
- [4] Armstrong, B and Han, S. J. Am. Chem. Soc. 131, 2009, 4641-4647.
- [5] G. Bacic, M.R. Niesman, H.F. Bennett, R.L. Magin, H.M. Swartz, Mag. Reson. Med., 6 (1988), 445-458.

Multimodal Optical and MRI Studies with Multifunctional Spinel Nanoparticles

Chantalle Le
Chemistry, University of California Los Angeles

NNIN REU Site: Nano Research Facility, Washington University in St. Louis, St. Louis, MO

NNIN REU Principal Investigator(s): Professor Samuel Achilefu, Ph.D., Radiology, Washington University in St. Louis

NNIN REU Mentor(s): Rui Tang, Ph.D., Radiology, Washington University in St. Louis

Contact: lechantal000@ucla.edu, achilefus@mir:wustl.edu, tangr@mir:wustl.edu

Abstract:

Magnetic resonance imaging (MRI) and optical imaging are commonly used medical imaging techniques for the visualization of the internal structures of the body and molecular events in tissues. Together, the exceptionally high spatial resolution provided by MRI complements the high detection sensitivity of optical methods. Thus, a multimodal imaging approach that combines both reporting strategies would allow accurate localization of signal source and assessment of molecular processes in tissue by MRI and optical methods, respectively. To attain this goal, we are developing a tissue-specific multimodal nanoprobe with a superparamagnetic spinel metal ferrite core and fluorescent dye.

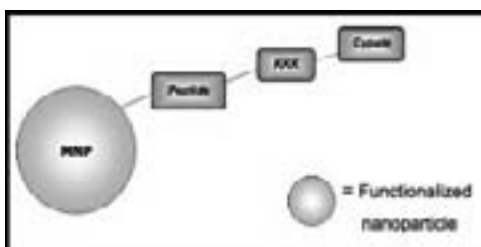


Figure 1: Schematic of synthetic pathway.

Introduction:

MRI contrast can be enhanced with positive or negative contrast agents resulting in brighter (T1-weighted) or darker (T2-weighted) images, respectively. Spinel ferrite magnetic nanoparticles (MNPs) are proven negative contrast agents [1]. The normal spinel structure, AFe_2O_4 , creates a non-compensated magnetic moment and offers the greatest possible magnetic susceptibility due to the higher number of Fe sites compared to metal cation, A [2].

Tissue specificity directly resulted from our chosen peptide sequence. The cleavable linker, lys-lys-lys (KKK), was activated by the enzyme, cathepsin B (Figure 1). Cathepsin B plays a significant role in the detection of inflammatory breast cancer (IBC) [3]. IBC is an especially aggressive, locally advanced breast cancer, and is therefore usually diagnosed at a late stage. However, an enzyme specific nanoprobe such as ours would enable early disease detection and subsequently more accurate diagnosis.

Optical imaging easily detects fluorophores. To take advantage of this high sensitivity, our design included the near infrared fluorescent dye, cypate. The novelty of our experimental nanoprobe was based upon its action of self-quenching. While the dye remained conjugated to the nanoparticle surface, its fluorescent activity was quenched. However, once the specific enzyme, cathepsin B, cleaved the conjugated cypate dye from the MNP, the probe regained its fluorescence.

This special property can be powerfully used to our advantage to supplement enhanced MRI images with clearer molecular visualization. In addition, this particular nanoprobe can act as a cathepsin B indicator for IBC diagnosis.

Methods:

Surface Coating. It has been reported that coating the MNP surface is integral to biocompatibility and increased circulation lifetime in the body [4]. For our research, we used meso-2,3-dimercaptosuccinic acid (DMSA) as the hydrophilic surfactant for aqueous solubility. Coating had the added advantage of providing the necessary functional group for amine peptide conjugation, $-\text{COOH}$. To prepare DMSA coated spinel MNPs, various paths were taken. The experiment was conducted at several pH levels ranging from 3-10 and in an assortment of solvents. DMSA was pre-dissolved, then added to the MNP mixture. The reaction mixture was then sonicated for 2-3 hours under argon to minimize disulfide cross-linking. The nanoparticles were washed with methanol and water.

	<i>T₁</i> (ms)	<i>T₂</i> (ms)
Water	3460	400
Fe₃O₄	2137.03 Δ= -1322.9	1750.03 Δ= +1350.73
NiFe₂O₄	759.81 Δ= -2700.2	13.40 Δ= -386.6

Table 1: MR contrast of spinel ferrite nanoparticles.

Peptide Dye Conjugation. The peptides used in this study possess an amine functional group at the N-terminus. The conjugation of the peptide amine (-NH₂) and surface functionalized carboxyl groups (-COOH) creates a strong amide bond. The soluble MNP solution was isolated and a ratio of MNP:peptide conjugate was established. The reaction mixture was left overnight in a 4°C refrigerator and away from the light to forestall photobleaching. Spinel ferrite nanoparticles possess enhanced magnetic properties and have already been reported as effective negative contrast agents for improved MRI sensitivity. Negative contrast agents are typified by lower T₁ and T₂ values. As such, spinel structures show greater magnetization than current ferrite (Fe₃O₄) contrast agents (Table 1).

Surface Coating. The MNPs were successfully coated and functionalized. FT-IR (Table 2) shows evidence for the necessary carboxylic acid group. Functionalized MNPs experience significant shifts in C = O stretches and C—O stretches as compared to free DMSA. Presence of doublet peaks around 2553.89 nm and 2556.27 nm on the coated MNP suggest free unconjugated thiol groups. From previous knowledge, the surface of gold nanoparticles have shown to have a very strong interaction with thiols [5]. However, if spinel MNPs displayed the same bonding interaction as gold nanoparticles, we would have expected both thiols of DMSA to conjugate to the particle surface in a *cis* configuration, leaving only the two -COOH functionalities free (Table 2). Coating was accomplished in two ways: one using a double ligand exchange method, the other being directly in DI water. Double ligand exchange offered gentler reaction conditions and required fewer washes.

Substance	Peak Locations (Wavelength)			
	-CH	-SH	C=O	C—O
DMSA		2561.68	1687.24	1310.68
		2537.19		1179.03
Coated	2923.30	2553.89	1698.25	1379.98
MNP		2556.27		1157.31

Table 2: FT-IR data.

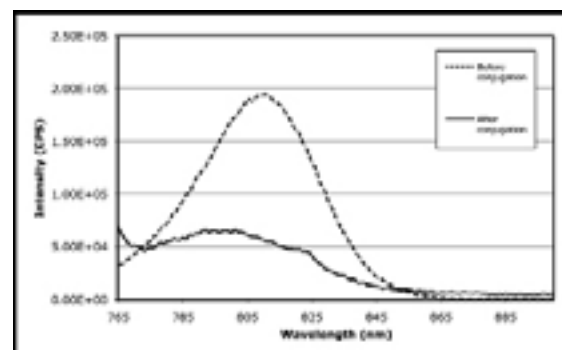


Figure 2: Fluorescence data before and after conjugation.

Peptide Dye Conjugation. The extent of successful peptide conjugation was measured by fluorescence and UV-vis. By UV-vis, we found the excitation wavelength for fluorescence to be 780 nm. Normal fluorescence for unconjugated peptide dye amounted to about 2×10^5 counts per second (CPS), while conjugated peptide dye had a lower intensity at 5×10^4 CPS—a 4-fold decrease (Figure 2). Although we expected a complete loss of fluorescent signal, the observed intensity decrease hints to a partial quenching. This can be a result of incomplete surface coating, which thereby provided an insufficient number of available -COOH functional groups for amide bond formation.

Conclusion:

Molecular imaging techniques are pivotal for the *in vivo* assessment of biological processes in a wide spectrum of diagnostic roles. However, since every technique carries inherent advantages and disadvantages, it is necessary to formulate imaging strategies that will capitalize on the increasingly sophisticated capabilities of molecular imaging.

In a two-step process, a nanoprobe was created that harnesses the individual strengths of MRI and optical imaging, while simultaneously compensating for their weaknesses.

Acknowledgments:

I thank my principal investigator, Samuel Achilefu, my mentor, Rui Tang, and the Optical Radiology Lab members for their invaluable support. I am also grateful to the NNIN REU Program for giving the opportunity to participate in the 2010 summer program.

References:

- [1] Lee, J.H., et al. Nature Medicine. 2007. Vol. 13. 95.
- [2] Barcena, C. et al. Chem. Commun. 2008. 2224.
- [3] Decock, J., et al. International Journal of Biological Markers. 2008. Vol. 23. Iss. 3. 161-168.
- [4] Thorek, D. L.J., et al. Annals of Biomedical Engineering. 2006. Vol. 34. Iss.1. 23.
- [5] Daniel, M.C. et al. Chem. Rev. 2004. Vol. 104. 293-346.

Surface Treatments to Control the Wettability of Photonic Crystal Bio-Sensors

Philip Ponce de Leon

**Physics and Mechanical Engineering, New York University,
The Stevens Institute of Technology**

NNIN REU Site: Stanford Nanofabrication Facility, Stanford University, Stanford, CA

NNIN REU Principal Investigator(s): Professor James S. Harris, Electrical Engineering, Stanford University

NNIN REU Mentor(s): Pascale El Kallassi and Meredith M. Lee, Electrical Engineering, Stanford University

Contact: ppd212@nyu.edu, harris@snowboard.stanford.edu, elkallas@stanford.edu, mmlee@stanford.edu

Abstract:

Photonic crystals offer a promising means of biosensing, because they can confine light to a small volume where its interaction with matter is strong. As a result, the binding of relatively few bio-molecules to receptors on the photonic crystal can potentially change the optical properties of the sensor. The binding events can be detected by monitoring resonant peak shifts in the transmission spectrum through the crystal. A crucial challenge in the sensing process is treatment of the photonic crystal surface to ensure binding of analytes delivered in fluids. We investigated surface treatments for gallium phosphide and silicon nitride in hopes of establishing reliable processes to control surface wettability. Using contact angle goniometry, we monitored the relative hydrophobicity or hydrophilicity of each treated surface. We assessed the thickness and structure of any layers with a spectroscopic ellipsometer and an atomic force microscope (AFM). A fairly large range of wettability was achieved on our treated surfaces, as well as possible protein immobilization. With greater surface control, one can optimize sensor fabrication steps and more effectively deliver bio-molecules.

Introduction:

The photonic crystal is a lattice of cavities nano-patterned and etched in a dielectric layer. We investigated gallium phosphide (GaP) and silicon nitride (SiN), because their optical properties are suitable for operation of a sensor at visible wavelengths where light interacts strongly with biospecimens. We monitored the wettability of our sensing surface, because it was an easily observed property offering valuable insight into a material's preferred type of binding.

Hydrophobicity indicates that a surface tends to interact with non-polar functional groups via dispersion, while hydrophilicity indicates polar interaction. By controlling the nature of a surface's interaction with water, we can control its directional binding preference with biomolecules.

There are many ways to alter a surface's wettability; we examined chemical etching techniques, vapor/plasma deposition, and the formation of self-assembled monolayers out of solution. We tested monolayer-forming chemicals that had been tried on similar substrates such as GaAs [1,2].

Experimental Procedure:

We cleaned our GaP samples by soaking them in methanol for 10 min and, then, etching them with 25W oxygen plasma at 300 mTorr and a flow rate of 20 sccm for five minutes. We cleaned SiN by soaking it in hydrofluoric acid for three minutes. These cleaning techniques are standard [2,3], and we verified their adequacy with contact angle measurements over several days after cleaning.

Treatment was performed by soaking a sample in a given solution for a set amount of time. Decanoic acid and mercaptoundecanoic acid were dissolved in methanol, while octadecanethiol was dissolved in anhydrous ethanol. We used treatment times in the range from 20s to 18h and concentrations between 1 and 120 mM. Some samples were pre-treated by soaking in 27% hydrochloric acid for 5 min to remove oxide. Some solutions included 35% ammonium hydroxide at 3% volume of the total solution to inhibit oxide growth. After removal, samples underwent various intensities of rinsing and drying.

Vapor deposition of hexamethyldisilazane (HMDS) was performed in an oven at 150°C. Plasma deposition of the CF₃ ion was performed at 100W, 650 mTorr, and a flow rate of 100 sccm for two minutes.

After surface modification, 100 μ M concentrations of bovine serum albumin (BSA) in phosphate buffered solution were pipetted onto a small area of a sample and allowed to sit for 10 min. The samples were then rinsed with deionized water for 30s and analyzed with an AFM.

Results and Conclusions:

We observed contact angles of approximately 90° and 70° on GaP treated with decanoic and mercaptoundecanoic acid, respectively (Figures 1 and 2). Samples treated with octadecanethiol remained hydrophilic. These results suggest we were observing binding between the GaP oxide and the

carboxyl group, not the thiol group.

Layer thicknesses of approximately 0.75 nm on our decanoic acid samples suggested we had a monolayer angled roughly 60-70° from normal incidence. We discovered that this thickness did not vary significantly with variation in treatment time or concentration, except that precipitation occurred in higher concentration trials (Figure 3). By monitoring the layer thicknesses and contact angles, we found that longer treatment times resulted in layers more robust against rinsing damage. The best resistance to rinsing resulted from an 18h treatment at 40°C in 1 mM solution containing ammonium hydroxide. We suspect this treatment enabled the formation of the most densely packed monolayer. However, steric hindrance among the carboxyl groups placed an upper limit on packing density, thus leaving all of our monolayers susceptible to degradation by polar solvents, given enough rinsing.

CF₃ ion deposition yielded a contact angle of about 104° on both substrates. HMDS-coated GaP had a contact angle of about 65°, while HMDS on SiN yielded about 45°. This suggests a different orientation of the HMDS molecule on our two substrates.

The initial results of protein binding were promising. AFM images of SiN, both clean and coated with HMDS, show surface structures approximately 5 nm in height (Figure 4). A BSA molecule is 2-7 nm long depending on the angle of binding.

Further studies varying the parameters of protein exposure are necessary to confirm the presence and strength of BSA binding. Our results suggest HMDS-coated and bare SiN are suitable candidates for liquid delivery of biospecimens, while decanoic and mercaptoundecanoic acid are, perhaps, better suited for air delivery. Future surface treatments should be attempted in oxygen-free environments to potentially enable covalent binding between thiol groups and pure GaP.

Acknowledgements:

Thank you for funding: Center for Integrated Systems, National Nanotechnology Infrastructure Network Research Experience for Undergraduates (NNIN REU) Program, National Science Foundation. Much thanks to Mike Deal, Coach, Meredith, and Pascale.

References:

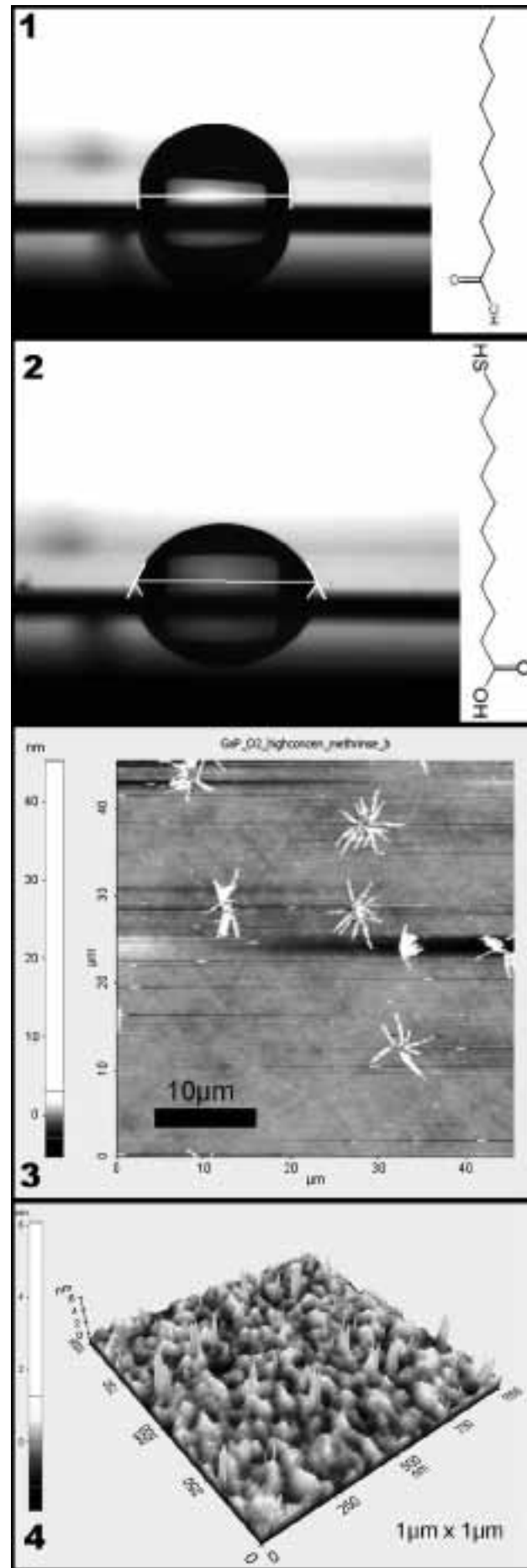
- [1] Adlkofer, K.; Tanaka, M. *Langmuir* 2001, 17, 4267.
- [2] Martz, J.; Zuppiroli, L. *Langmuir* 2004, 20, 26, 11428-11432.
- [3] Arafat, A.; Schroen, K. *J. Am. Chem. Soc.* 2004, 126, 8600-8601.

Figure 1: Decanoic acid coated gallium phosphide – 90°.

Figure 2: Mercaptoundecanoic acid coated GaP – 70°.

Figure 3: Precipitation occurs for solutions over 10 mM.

Figure 4: Possible binding of BSA molecules.



All-Copper Pillar Interconnects

Barrett Worley
Chemistry, Samford University

NNIN REU Site: Nanotechnology Research Center, Georgia Institute of Technology, Atlanta, GA

NNIN REU Principal Investigator(s): Dr. Paul A. Kohl, Chemical and Biomolecular Engineering, Georgia Institute of Technology

NNIN REU Mentor(s): Dr. Hyo-Chol Koo, Chemical and Biomolecular Engineering, Georgia Institute of Technology

Contact: bcworley@samford.edu, paul.kohl@chbe.gatech.edu, hyochol.koo@chbe.gatech.edu

Abstract:

As modern electronics decrease in size, one of the major problems which arises is the signal delay between the transistor and substrate through the current tin-based solder sphere connections. The focus of this project is to replace solder spheres with all-copper pillar interconnects. The pillars are to be grown from a copper (Cu) seed area on each chip or wafer via Cu electroplating, and then bonded together via electroless Cu plating, as seen in Figure 1.

Further stabilization of the bond results from polymer collars and optimization of the Cu electroplating and Cu electroless plating conditions. Various electroplating bath conditions were tested to form flat-ended Cu pillars. Similarly, various electroless plating bath conditions were tested to achieve the greatest all-Cu bond strength. These experiments took place on both processed wafers and on actual microchips.

Experimental Procedure:

In order to experimentally electroplate Cu pillars, we processed 4" silicon (Si) wafers to resemble the Cu lines of microchips where electrical connections to the substrate are made. We grew a $1\text{ }\mu\text{m}$ silicon dioxide (SiO_2) layer on each wafer, and then sputtered chrome (Cr), Cu, and titanium (Ti) layers in respective thicknesses of 30, 300, and 20 nm. The Cr layer ensured adhesion of the Cu layer to the wafer, while the Ti layer protected the Cu from oxidation when the second SiO_2 layer was grown, 1.5 μm thick. The purpose of this SiO_2 layer was to insulate the unexposed Cu from the electrolytic plating solutions.

Next, SC 1813 photoresist was spun and baked onto the wafer. We then exposed the photoresist to 365 nm wavelength light under a patterned mask, developed it, and cleaned away residual photoresist with reactive ion etching to expose the SiO_2 layer in a pattern. Buffered oxide etchant was used to wet etch through the SiO_2 and Ti layers to fully expose the Cu seed area. After stripping off this

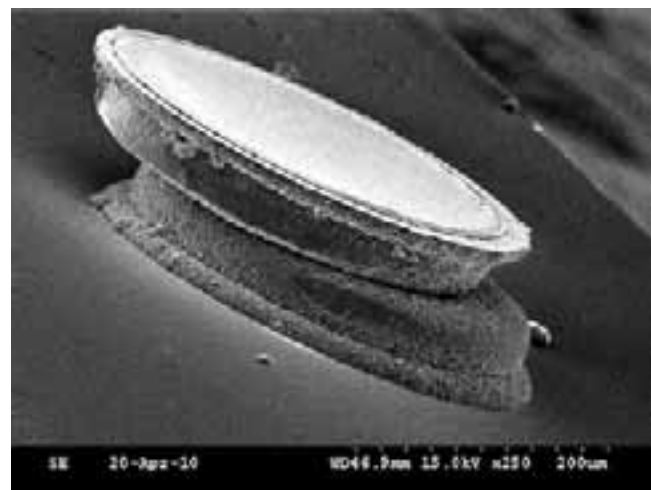


Figure 1: Side view of electroless-bonded copper pillars.

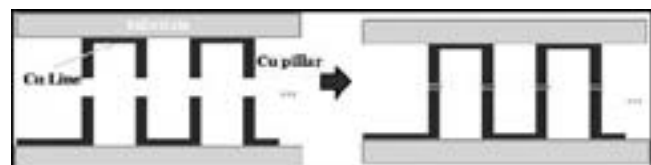


Figure 2: Schematic of "daisy-chain" structure.

photoresist, we spun and baked on an Aquatrel™ polymer layer. As with the photoresist, we then exposed, developed, and cleaned this layer to form our polymer collars for each pillar hole. For future electrical characterization and bond yield measurement experimentation, we used an alternative patterned mask, which resulted in the formation of a "daisy-chain" pillar structure, seen in Figure 2.

We used Cu electroplating to grow Cu pillars with heights of 50 μm and diameters of 150 μm . Electroplating is a process where in-solution cations of a desired material are reduced onto the surface of another conductive material. The electrical current supplied to our Cu metal anode oxidizes the Cu atoms, the ions of which are reduced at the cathode, a processed wafer, to plate Cu metal onto the surface (Figure 3).

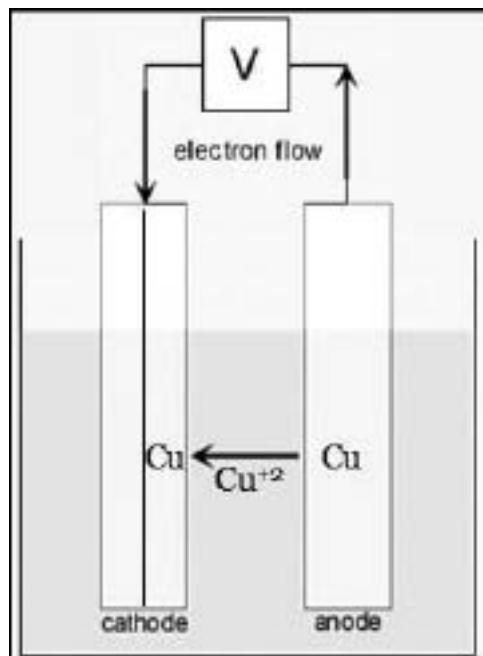


Figure 3: Electroplating system schematic.

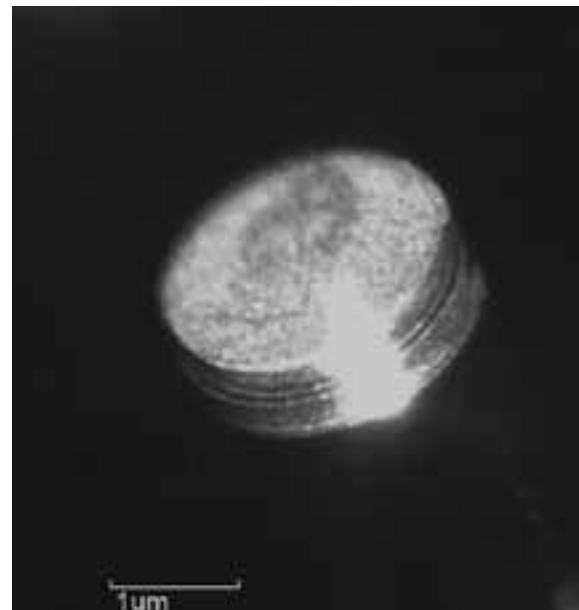


Figure 4: A flat-ended copper pillar.

Electroplating on the processed wafers resulted in the precise growing of Cu pillars from the Cu seed areas of the wafer. The electroplating bath was an acidic solution of copper sulfate (CuSO_4), sulfuric acid (H_2SO_4), the surfactant polyethylene glycol (PEG, MW: 4000 g/mol), and sodium chloride (NaCl) dissolved in deionized water. This research focused partly on studying the pillar surfaces in order to optimize the electroplating bath solution, and the results of this will be discussed later.

We also sought to design an optimal electroless plating bath in which to bond the Cu pillars. While electroless plating serves the same purpose as electroplating, it uses the following chemical reaction: $\text{Cu}^{+2} + 2 \text{HCHO} + 4 \text{OH}^- \rightarrow \text{Cu} + 2\text{HCOO}^- + 2\text{H}_2\text{O} + \text{H}_2$, instead of external electrical power, to drive the Cu redox reaction. Our bath consisted of 3.6 grams (g) Cu sulfate, 9.6 g EDTA, 9.87 g KOH, approximately 20 mg potassium ferrocyanide, 0.2 mL of HCl, 1.79 g of paraformaldehyde, and other experimental additives dissolved in 200 mL of DI water. With heating and stirring, Cu^{+2} ions were complexed to EDTA in solution before they were reduced at the electroplated Cu pillar surface. Simultaneously, formaldehyde (HCHO) molecules were oxidized to formic acid.

Results and Conclusions:

Our best electroplating results came from a bath designed for a high current density maximum and low conductivity, with the corrosion inhibitor benzotriazole (BTA) as the optimizing additive. To achieve these conditions, we used 30 g of CuSO_4 and 24 mL H_2SO_4 in 300 mL of deionized water. This bath composition, which also included 0.18 g of PEG, 0.03 g NaCl, 0.6 mL SPS, and 0.03 g of BTA, resulted

in the even electroplating of flat-ended Cu pillars (Figure 4).

Flat-ended pillars are an improvement over the concave-ended pillars grown previously, because they reduce the possibility of voids becoming trapped in the subsequent electroless bond. These voids, which result from a long solution transfer length over the concave top of the pillar, weaken both the physical structure and electrical conductivity of the electroless bonds pillars.

In optimizing the electroless plating bath, we found that the additives 2,2'-dipyridyl and PEG in the respective concentrations of 20 mg/L and 7.5 mg/L produced the most uniform and crystalline electroless plated Cu structure in comparison to other electroless plating experiments. Thus, these additives will help reduce trapping of voids resultant from evolved hydrogen gas bubbles and improve the strength and conductivity of electroless bonds.

Future Work:

In the future, we would like to continue optimizing the electroless bath conditions and develop dome-ended pillars. We would also like to refine the “daisy chain” structure with an adhesion promoter between the polymer and SiO_2 layer, and begin electrical characterization and bond yield testing.

Acknowledgements:

I would like to thank Dr. Paul Kohl, Dr. Hyo-Chol Koo, Dr. Rajarshi Saha, the National Nanotechnology Infrastructure Network Research Experience for Undergraduates Program, and the National Science Foundation, without whom this summer would not have been possible.

Development of Advanced Carbon Electrodes for use in Microfluidic Vanadium Redox Fuel Cells

Richard Anger

Mechanical Engineering, State University of New York at Stony Brook

NNIN REU Site: Cornell NanoScale Science and Technology Facility, Cornell University, Ithaca, NY

NNIN REU Principal Investigator(s): David Erickson, Sibley School of Mechanical and Aerospace Engineering, Cornell University

NNIN REU Mentor(s): Sean Moore, Sibley School of Mechanical and Aerospace Engineering, Cornell University

Contact: anger.richard@gmail.com, de54@cornell.edu, sdm85@cornell.edu

Abstract:

We report on the current progress to develop advanced carbon electrodes with improved performance in microfluidic vanadium redox cells. In vanadium cells, carbon electrodes are typically used as a conductor and catalyst. Carbon fiber paper electrodes have had a silver nanolayer applied to function as an integrated current collector. This resulted in a 34.2% decrease in sheet resistance in the material, in turn increasing the cell performance; however the voltage generated by the cell caused electrostripping of the deposited silver. In addition, graphite electrodes were microfabricated using pyrolyzed micropatterned polyamide-imide films. The microfabricated graphite electrodes are designed to have a smaller pore size than the carbon paper electrodes, allowing for shorter diffusional distances, reducing mass transport losses. These advancements should decrease ohmic losses and increase the performance of the microfluidic fuel cell.

Introduction:

The advancement of fuel cell technology is amongst the most pursued topics in the effort to develop alternative energy generation methods. Microfluidic fuel cells are a relatively new development which take advantage of the characteristics of laminar flow to control the interaction between the fuel and oxidant entering the cell. Because the fuel and oxidant are able to flow concurrently and separately in a single microfluidic channel, it is possible for the cell to function without the need of a physical barrier such as a proton exchange membrane.

Microfluidic vanadium redox fuel cells commonly use carbon paper as an electrode and as a catalyst for the reaction. Carbon paper electrodes, which are made from sheets of interlaced carbon fibers, are not without a few drawbacks. The carbon paper electrodes have a relatively high resistivity when compared to that of metallic electrodes. This results in ohmic losses in the cell. Further, the carbon paper sheets have a larger pore size than desired, resulting in greater mass transport losses, and fuel cross over due to large diffusion distance with the catalyst.

The application of a silver (Ag) nanolayer acting as an integrated current collector could aid in increasing the conductivity

of the carbon paper, and reducing the ohmic losses of the electrode. Additionally, it is possible to use micromolding and carbonization techniques to microfabricate a new graphite electrode tailored with small pore sizes for use in the cell.

Experiment:

Our microfluidic cell consisted of a series of interconnected square manifold pieces, with ports designed to allow the flow of the fluid in and out through the corners (see Figure 1). The fuel entered the cell through one port, then flowed over and through one of the carbon electrodes. Through a lower port, oxidant flowed into the cell and through a separate carbon electrode. The two flows met in a gap between the two electrodes, and exited through the waste port. The manifold pieces were fabricated using 3D printing (Bjet Connex 500).

The carbon paper electrodes were made with Torray carbon paper (Torray, Inc.) The silver current collector was deposited using electron-beam evaporation (CVC SC4500 e-gun evaporator). In a side experiment attempting to maximize the carbon surface area on the Ag-coated electrode, we fabricated an electrode that

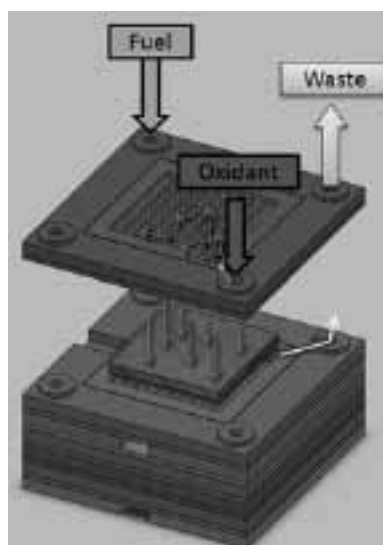


Figure 1: Flow characteristics through microfluidic fuel cell manifolds.

had a micropatterned Ag current collector. We generated a comb-shaped Ag pattern using photolithography (with Microchem Microspray™ photoresist) and etching (Transene TFA etchant, diluted 1:9).

The microfabricated graphite electrodes were manufactured using micromolded polyamide-imide films (see Figure 2).

First a peg-array (10 μm and 20 μm diameter, 50 μm height) micromold was manufactured using photolithography and DRIE (Unaxis 770 Deep Si Etcher). A polymer solution (Torlon polyamide-imide, NMP, acetone) was spincoated on to the micromold. The mold was then introduced to a humid environment, resulting in a vapor-induced phase separation. The film was immersed in water and then released from the mold. Finally the films were carbonized by heating to 800°C in a nitrogen environment. This resulted in a highly porous glossy carbon electrode.

Results:

The sheet resistance of the Ag-coated carbon paper was measured using 4-terminal resistance mapping (CDE ResMap™). A 34.2% decrease in sheet resistance was measured. Performance tests were then performed for the carbon paper electrode and the Ag-plated carbon electrode (see Figures 3 and 4). The Ag-plated carbon electrode had a maximum current density 13 times higher than the carbon paper alone with a 6 ml/hr flow rate.

Discussion and Conclusions:

There has been some inconsistency with the measurements of the cell performance, particularly with the uncoated

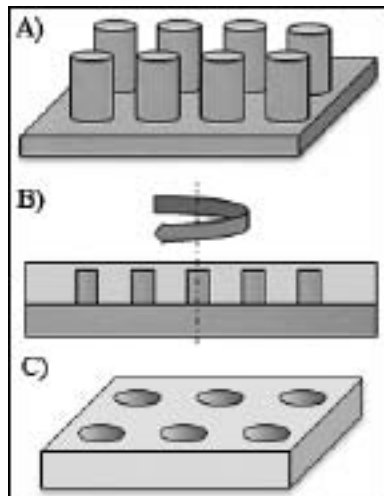


Figure 2: A) Micromold, B) Spinning of polymer, C) Polymer film.

carbon-paper electrode performance. This may be due to trapped air bubbles in the cell assembly, which resulted in dramatically reduced surface area on the carbon electrode. Future work will be focused on improving the cell assembly and design to achieve proper flow of fuel and oxidant.

While the Ag did result in higher performance, the potential caused by the cell, caused electrostripping of the silver layer, rendering it as an unsuitable metal for use as a current collector. We suspect gold will be a much more suitable candidate, and should serve as an effective current collector.

Future Work:

Our next step is to test the microfabricated graphite electrode, and compare it to standard carbon paper electrode performance. We are working on methods to reduce the air bubble presence in the cell. We intend on repeating all Ag-coated electrode fabrication, patterning, and performance testing using an evaporated gold current collector. Finally, we intend on gold-coating the microfabricated graphite electrode and measuring performance.

Acknowledgements:

I would like to thank David Erickson, Sean Moore, and everyone in the Erickson lab. I would also like to thank the NSF, the NNIN, and the CNF, for creating and supporting the REU. Finally, I would like to thank Rob Illic and Melanie-Claire Mallison for coordinating and helping make the program happen.

References:

- [1] Kjeang, E., et al. "High-performance microfluidic vanadium redox fuel cell." *Electrochimica Acta* 52.15 (2007): 4942-46. Web. 8 Aug 2010.
- [2] Kjeang, E., N. Djilali, and D. Sinton. "Microfluidic fuel cells: A review." *Journal of Power Sources* 186. (2009): 353-69. Web. 8 Aug 2010.
- [3] Vogelaar, L. "Phase separation micro molding." University of Twente (2005): 1-126. Web. 8 Aug 2010.
- [4] Cowie, J.M.G., and S. Palsule. "Miscibility in molecular composites of polyamide-imide/polyetherimide." *Polymer Bulletin* 33.2 (1994): 241-47. Web. 8 Aug 2010.
- [5] Ohnishi, et al. T. Ohnishi, I. Murase, T. Noguchi and M. Hirooka, Preparation of graphite film by pyrolysis of polymers, *Synth. Metals* 18 (1987), p. 497.

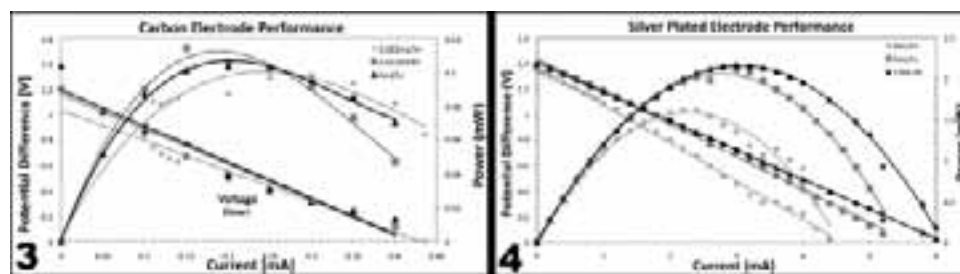


Figure 3: Performance of uncoated carbon paper electrode.

Figure 4: Performance of silver coated carbon paper electrode.

Ferroelectric Thin Films for Reconfigurable RF Electronics in Next Generation Wireless Communications

Scott Bakkila

Physics and Computer Science, Lawrence Technological University

NNIN REU Site: Lurie Nanofabrication Facility, University of Michigan, Ann Arbor, MI

NNIN REU Principal Investigator(s): Jamie Phillips, Electrical Engineering and Computer Science, University of Michigan

NNIN REU Mentor(s): Weiming Wang, Electrical Engineering and Computer Science, University of Michigan

Contact: sbakkila@ltu.edu, jphilli@umich.edu, umwwm@umich.edu

Abstract:

Ferroelectric materials exhibit field-dependent permittivity effects that are useful in making voltage-dependent capacitors (varactors) that can be applied to electronically tunable radio frequency (RF) circuits, tunable filter circuits, and other wireless communication devices. The purpose of these experiments was to maximize the tunability of ferroelectric thin-film capacitors by varying material process parameters. The materials used in these experiments were barium strontium titanate (BST) and barium titanate (BTO), which were deposited by pulsed laser deposition. The thin film deposition parameters under study were deposition and annealing temperature, oxygen partial pressure, laser energy, material thickness and material/deposition type. BST has shown lower current leakage allowing a higher applied electric field, while BTO has shown a greater degree of dielectric tunability. Efforts to minimize the leakage in BTO while maintaining its tunability included depositing a thin layer of BST on either side of a BTO deposition and depositing a thin amorphous “dead” layer of BTO at lower temperatures prior to a higher temperature deposition. Initial direct current (DC) testing yielded positive results with various deposition parameters, which were reproduced in the fabrication of capacitors with planar waveguide contacts for high frequency testing.

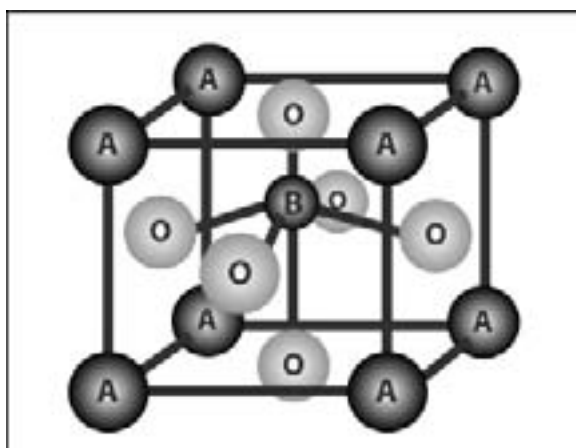


Figure 1: Generalized form of the perovskite structure.

Introduction:

Tunable capacitors (varactors) are desirable for use in frequency-agile microwave devices. Ferroelectric materials can be employed to create varactors, as the permittivity of such materials varies with an applied electric field. This phenomenon arises due to the perovskite crystalline structure these materials assume. In this arrangement, the material takes the generalized form of ABO_3 (Figure 1)

where A and B represent varying metallic atoms, such as barium and titanium (BTO).

The purpose of these experiments was to study the influence of pulsed laser deposition conditions, annealing conditions, and material structures to create tunable capacitors with low current leakage and high tunability.

Experimental Procedure:

Our experiments focused on the study of the dielectric properties of barium strontium titanate (BST) and barium titanate (BTO) thin films deposited via pulsed laser deposition. The variables studied during these experiments included the oxygen partial pressure during deposition, the deposition and annealing temperatures, laser power, and the material type/configuration.

First, substrates of platinum/silicon dioxide/silicon were loaded onto a heater stage using silver paint and placed in a vacuum chamber. The target material to be deposited was placed opposite the substrate at a distance of seven centimeters. The chamber was then closed and pumped down to approximately 2×10^{-6} Torr. Once the chamber reached the target pressure, the substrate was heated to between 600°C and 700°C for a ten-minute thermal cleaning process. Oxygen was then introduced into the chamber at a

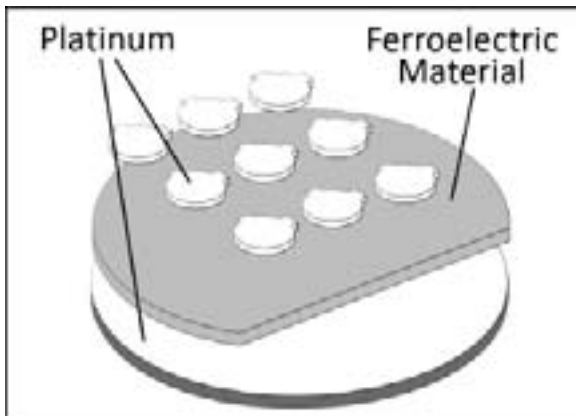


Figure 2: Completed array of simple capacitors after device fabrication.

predetermined pressure. Initial experiments were done using a pressure of 100 milliTorr (mTorr) and later experiments were performed at 200 mTorr. A pulsed KrF excimer laser (248 nm) struck the target material (either BTO or BST) which created an ionized plume of material that deposited onto the substrate. When the deposited film reached the desired thickness, it was annealed for 1h at the deposition temperature and an oxygen partial pressure of 100 Torr.

Capacitor structures, based on the thin films, were fabricated using the platinum (Pt) on the substrate as the bottom electrode, and using standard photolithography, metallization, and liftoff procedures to deposit top Pt electrodes. Through another photolithography step, a small strip of the sample was exposed and developed, and then placed in a 20:1 hydrofluoric acid solution to etch the exposed area down to the base Pt. This allowed access to the bottom contact in all parallel plate capacitor devices (Figure 2).

Once the sample was processed, it was electrically tested using a Keithley 4200 Semiconductor Characterization System to determine current-voltage and capacitance-voltage characteristics.

Results and Conclusions:

Experiments with BST yielded lower current leakage than BTO, allowing a higher applied electric field, while BTO showed a greater degree of dielectric tunability. Efforts to minimize the leakage in BTO while maintaining its tunability included depositing a thin layer of BST on either side of a BTO deposition, and depositing a thin amorphous layer of BTO at lower temperatures prior to a higher temperature deposition.

These techniques drastically decreased the tunability of the material, but greatly decreased the current leakage. Thinner amorphous layers may provide a more desirable result with a more optimal tradeoff between leakage current and dielectric properties.

Higher temperature depositions increased the dielectric tunability of the deposited material but also increased the current leakage. Experiments combining higher temperature depositions with thinner low-temperature amorphous layers are underway. A partial oxygen pressure of 200 milliTorr significantly reduced the particulates that were prevalent at 100 milliTorr depositions. This decreased the deposition rate significantly, but resulted in a cleaner sample with fewer defects.

The best results obtained were from BTO deposited with a laser fluence of 250 milliJoules, an oxygen partial pressure of 200 mTorr, and a deposition and annealing temperature of 600°C. The greatest measured tunability range of the resulting devices, defined as the maximum permittivity divided by the minimum permittivity measured, was 7.4 (Figure 3) with a peak permittivity value of 1250 (Figure 4).

Future Work:

Devices will be tested at microwave frequencies to get an accurate representation of the material's response in communications devices. Planar waveguide devices have been fabricated using successful deposition parameters and are currently being tested. Results of those tests will dictate whether a variance in deposition parameters is necessary in future fabrication of microwave devices. Additionally, other materials such as lead zirconate titanate (PZT) will be tested, as will a rapid thermal annealing process.

Acknowledgements:

National Science Foundation; National Nanotechnology Infrastructure Network Research Experience for Undergraduates Program; Jamie Phillips; Weiming Wang; Victor Lee; Jinyoung Hwang; Adrian Bayraktaroglu; Melanie-Claire Mallison; Sandrine Martin; Brandon Lucas.

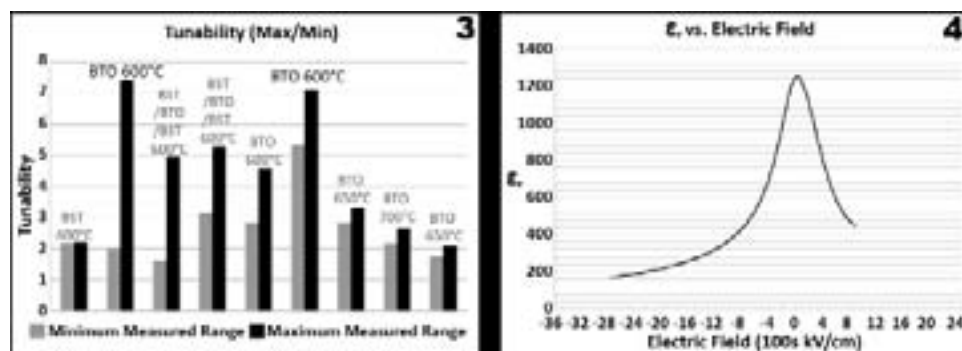


Figure 3: Tunability range of fabricated capacitors.

Figure 4: Relative permittivity versus electric field graph of best result.

Laminated Anodes and Electron Transport Layers in Organic Inverted Bulk Heterojunction Solar Cells

Lia Bersin
Chemical Engineering, Columbia University

NNIN REU Site: Microelectronics Research Center, The University of Texas, Austin, TX

NNIN REU Principal Investigator(s): Dr. Ananth Dodabalapur, Electrical Engineering, The University of Texas at Austin

NNIN REU Mentor(s): Davianne Duarte, Electrical Engineering, The University of Texas at Austin

Contact: lmb2169@columbia.edu, ananth.dodabalapur@engr.utexas.edu, davianned@gmail.com

Abstract and Introduction:

Organic photovoltaic cells (OPV) are promising for the future of the solar energy industry due to their solution processability, which can result in lightweight, low cost, flexible solar cells. Traditionally, OPV cells are bottom illuminated because of the availability of transparent anodes and substrates, but some integrated device applications require the use of a top illuminated structure. Laminating the anode to the top of the device is one way to fabricate inverted OPV cells.

The most efficient OPV cells are based upon a bulk heterojunction (BHJ) structure, which is a phase-separated layer of electron-donating and electron-accepting materials. BHJs have an increased exciton dissociation efficiency as opposed to bilayers.

This project involved the fabrication and characterization of laminated anodes utilizing indium tin oxide (ITO), poly(3,4-ethylenedioxythiophene):poly(styrenesulfonate) (PEDOT:PSS), and PEDOT:PSS with ethylene glycol (EG) in various configurations. The effectiveness of zinc tin oxide (ZTO), an n-type semiconductor, as a potential electron transport layer is also investigated due to its solution processability, high electron mobility, and favorable energy band alignment with PCBM.

Lamination of the Anode:

Lamination can protect the OPV cell from oxygen and moisture present in the atmosphere, which would result in the degradation of the semiconductor layer. To achieve a successful lamination, the anode must form a low resistance electrical contact with the hole transporting layer. Several structures were fabricated with PEDOT:PSS as a hole transporting layer, and ITO top and bottom electrodes prior to lamination. A two layer configuration was fabricated by spin-casting PEDOT:PSS on both the top and bottom ITO electrodes at 4000 rpm for 60 seconds. Substrates were then annealed at 120°C for 20 minutes before lamination. A single layer configuration was fabricated by spin-casting PEDOT:PSS on only the bottom ITO electrode, using the same process parameters. The conductivity of PEDOT:PSS

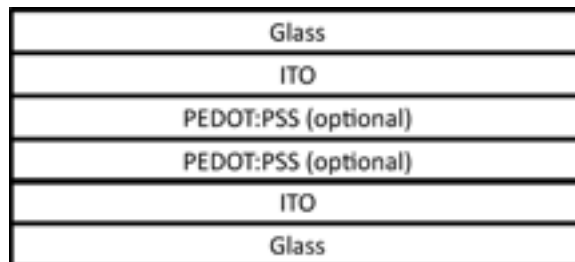


Figure 1: Cross sectional structure of laminated devices.

has been found to increase with the addition of EG, so a solution of PEDOT:PSS with EG was also tested [1]. The total electrical resistance per unit area of the electrical contacts was measured for each sample by laminating the electrodes with an overlap on each edge, to allow access to the device with the alligator clips. The structure of the laminated anodes is shown in Figure 1.

The PEDOT:PSS alone exhibited a resistance per area of 541 and 29,400 Ω/cm^2 for the two layer and one layer configurations, respectively. The PEDOT:PSS/EG solution resulted in a resistance per area of 6.82 and 5.99 Ω/cm^2 for the two layer and one layer configurations, respectively. A complete set of results is shown in Table 1.

Device	Bottom	Top	R/Area (Ω/cm^2)
1	PEDOT:PSS	PEDOT:PSS	541
2	PEDOT:PSS w/ EG	PEDOT:PSS w/ EG	6.82
3	PEDOT:PSS		29,400
4	PEDOT:PSS w/ EG		5.99
control			5.07

Table 1: Laminated device structures and corresponding resistance per area.

Based on these results, laminating an ITO anode is a possible way to fabricate OPV devices. Mixing PEDOT:PSS/EG made a low resistance electrical contact in either a one or two layer configuration as compared to using only PEDOT:PSS.

Effectiveness of Zinc Tin Oxide:

ZTO's favorable energy band alignment with PCBM could increase the open circuit voltage of these solar cells, which could lead to a higher power conversion efficiency. A series of devices was fabricated by spin-casting the solution on ZTO on patterned ITO and gold:palladium (Au:Pd) cathodes at 1000 rpm for 30 seconds. The substrates were then annealed for one hour at 500°C. A 1:1 solution of P3HT:PCBM in chloroform was spun-cast on top of the ZTO at 1200 rpm for 60 seconds and annealed at 140°C for 15 minutes. This was followed by a layer PEDOT:PSS. Patterned ITO on a glass substrate was then laminated to the PEDOT:PSS to form the top anode. A control device, without ZTO, was also fabricated on patterned aluminum (Al) cathodes. Silver conductive paint was used to access the downward facing anode to allow electrical access to both contacts from the top of the device so that the I-V characteristics could be measured. The structure of these top illuminated OPV cells is shown in Figure 2.

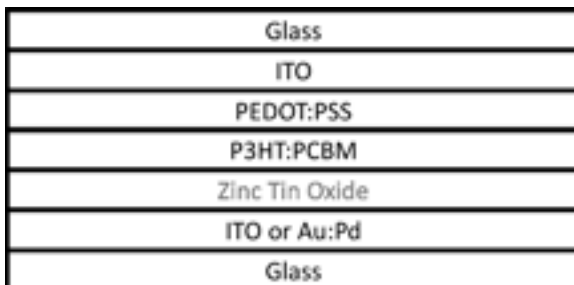


Figure 2: Organic solar device structure fabricated with ZTO electron transport layer on ITO and Au/Pd cathodes.

The current voltage characteristics of the three different solar cells are shown in Figure 3. The device with an ITO/ZTO cathode and the control device (Al cathode) showed an open circuit voltage (V_{oc}) of 0.27 V and 0.31 V respectively. The device with the Au:Pd/ZTO cathode showed no photovoltaic activity with a V_{oc} of 0 V. The slightly lower V_{oc} of the ITO/ZTO device as compared to the Al control shows that ZTO

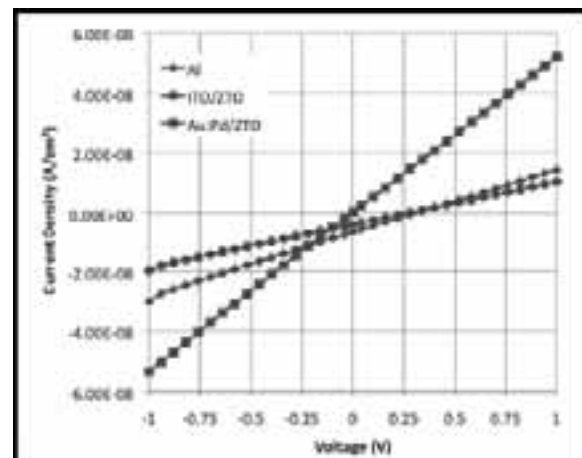


Figure 3: Current density vs. voltage plots for various device structures. The Al and ITO/ZTO show power generation in the 4th quadrant.

does not increase the open circuit voltage even though it may function as an effective electron transport layer.

Conclusion:

Characterization of the anode and the new materials for an electron transport layer are important aspects to understand in OPV devices, in order to achieve high efficiencies. Lamination of a top anode has been shown to produce a low resistance electrical contact using a solution of PEDOT:PSS/EG solution. ZTO did not increase the open circuit voltage of these OPV cells but it still may be an effective electron transport layer.

Acknowledgements:

I would like to thank the Dodabalapur Research Group, especially Christopher Lombardo, Eric Danielson, and Chen-Guan Lee for fabrication assistance and help with data analysis. I would also like to thank the facilities staff at the Microelectronics Research Center. This work has been funded by the National Science Foundation and the National Nanotechnology Infrastructure Network Research Experience for Undergraduates (NNIN REU) Program.

References:

[1] J.Ouyang, C. Chu, F. Chung, Q. Xu, Y. Yang, *Adv. Func. Mat.*, 15 203, 2005.

Nanowire Photovoltaics in Photoelectrochemistry and Plasmonic Ring Structures

Clara Chow

Biomedical Engineering, University of Wisconsin – Madison

NNIN REU Site: Stanford Nanofabrication Facility, Stanford University, Stanford, CA

NNIN REU Principal Investigator(s): Prof. H.-S. Philip Wong, Electrical Engineering, Stanford University

NNIN REU Mentor(s): Jason Parker and Xinyu Bao, Electrical Engineering, Stanford University

Contact: chow5@wisc.edu, hspwong@stanford.edu, jaypark@stanford.edu, xinyubao@stanford.edu

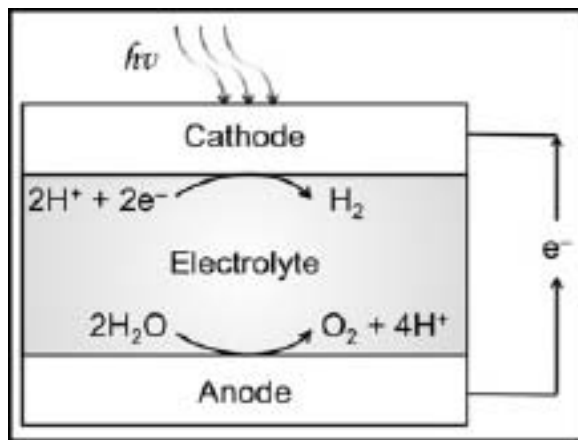


Figure 1: Schematic of a photoelectrochemical cell.

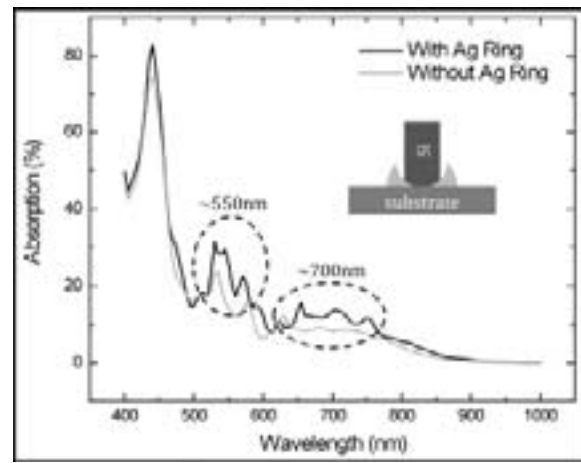


Figure 2: Simulation results of 90 nm diameter nanowires in 200 nm outer diameter silver rings.

Introduction:

Advances in solar technology using nanowires include improved photoelectrochemical cells and photovoltaics with integrated plasmonic structures. The high aspect ratio of nanowires can improve efficiency in the solar cell because they provide increased surface area and increased extraction of photogenerated charge carriers.

In the application of photoelectrochemical cells, light energy is used to split water by combining solar photovoltaics and water electrolysis into one device. As shown in Figure 1, light energy absorbed by the semiconducting electrode excites electrons to drive two half-reactions, ultimately producing hydrogen. Photoelectrochemical cells based on III-V semiconductors have higher efficiencies than devices separately producing electricity and splitting water [1]. III-V materials are ideal because their bandgap can be tailored for both efficient light absorption and water splitting. This study employs the use of gallium phosphide (GaP) nanowires as the semiconducting cathode in a photoelectrochemical cell.

In plasmonics, plasmons are light waves at a metal-dielectric interface bound to oscillating charges. Their properties have led to research in subwavelength optics, microscopy, biophotonics, and light enhancement [2]. Resonating plasmons within metallic nanoring structures can enhance electric

fields at geometry-dependent wavelengths. To harness the energy from plasmons, nanowires were incorporated into silver rings because simulations show increased visible light absorption in such a structure (Figure 2). This study implemented and optimized the fabrication of nanowires in silver (Ag) rings for future use in solar applications.

Methods:

Nanowires were grown on silicon substrates by chemical vapor deposition using the vapor-liquid-solid mechanism with gold (Au) colloid catalysts.

Photoelectrochemistry. In this study, GaP was chosen as the III-V material because of its 2.26 eV band gap, sufficient to drive the 1.23 eV electrolysis of water. Trimethylgallium and tertbutylphosphine were source gases of gallium and phosphorus in metal-organic chemical vapor deposition. The wires were grown at 460°C, 76 torr, and with a V/III ratio of 30:1. After growth, the nanowires were assessed with a 3-electrode photoelectrochemical compression cell using 0.1 M H₂SO₄ electrolyte. Approximately 0.5 cm² of the sample was exposed to the electrolyte.

Plasmonic Ring Structures. The process to fabricate germanium (Ge) nanowires in Ag rings began with a deposition of 200 nm Au colloids on silicon. A 5 nm coating of aluminum oxide using atomic layer deposition was applied for electrical isolation. Ag was sputtered and subsequently plasma-etched to form Ag rings around the Au colloids. Then, the Au was wet-etched to the desired diameter. Finally, nanowires were grown via chemical vapor deposition with germane source gas. This study optimized the Au wet etch and nanowire growth. The Au etch used consisted of 17% sodium iodide, 2% iodine, and 81% water.

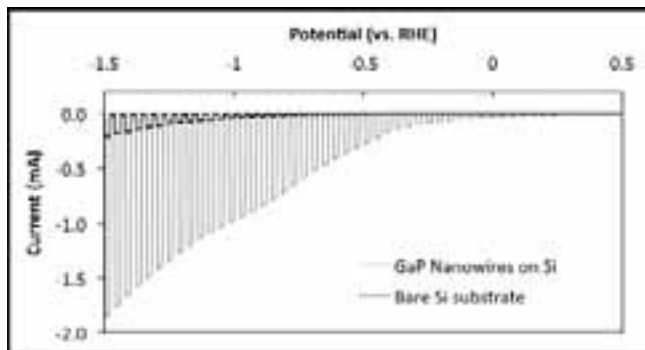


Figure 3: Photocurrent generated with changing potential. Light chopping occurred every one second.

Results and Discussion:

GaP nanowires in photoelectrochemical cells showed improved performance over bare silicon control samples and Ge nanowires in silver rings were successfully fabricated.

Photoelectrochemistry. In the GaP nanowire cells, photocurrent was measured with a potentiostat and the nanowire cells were compared to a control, bare silicon substrates. As shown in Figure 3, the nanowires generated up to 3 mA more photocurrent than bare silicon substrates under light illumination. Moreover, gas bubbles were observed at the interface, indicating the production of hydrogen. Photocurrent generated by the GaP nanowires on silicon was measured over one hour and the current remained stable, although scanning electron microscope (SEM) images indicate some roughness on the wires after testing.

Plasmonic Ring Structures. In the nanowire-in-a-ring structure, the Au colloids were etched smaller for proper nanowire growth to occur. The optimal Au wet etch process consisted of two steps: one longer etch of low concentration Au etch and one shorter etch of high concentration Au etch. Typical etch times and concentrations for one sample were 15 seconds in 1.25% Au etch followed by one second 100% Au etch. The lower concentration etch decreased the volume of Au colloids to desirable size while the higher concentration etch removed any unwanted Au surrounding the silver rings.

Nanowire growth times were also explored and the nanowires grew successfully with a longer nucleation step,

in comparison to nanowires grown without rings. Nucleation occurred at 370°C and growth occurred at 310°C. With this recipe, up to 50% of rings with Au colloids grew a wire. A successful germanium nanowire grown in a silver ring is shown in Figure 4.

Conclusions:

In photoelectrochemical cells, water splitting by III-V nanowires is a promising approach to produce hydrogen for energy. Gallium phosphide nanowires can generate photocurrent and split water. Future work will increase density of nanowires, further tune the band gap with the addition of indium, and explore alternative non-photoactive substrates such as indium tin oxide, fluorine tin oxide, or Au. The plasmonic ring structures studied provide experimental insight into the field of plasmonics and germanium nanowires were successfully grown in silver rings.

Future work includes; further fabrication optimization to increase yield, reflectance measurements, and fabrication of a solar cell with integrated rings. Ultimately, nanowires are versatile for a number of applications. For the advance of solar technology, the use of nanowires can decrease cost, improve light absorption, and increase cell efficiency.

Acknowledgements:

I would like to thank my PI Philip Wong, my mentors Jason Parker and Xinyu Bao, director Mike Deal, staff at the Stanford Nanofabrication Facility, Stanford's Center for Integrated Systems, the National Nanotechnology Infrastructure Network (NNIN) Research Experience for Undergraduates, and the National Science Foundation.

References:

- [1] M. Grätzel; "Photoelectrochemical Cells"; Nature, Vol. 414, p. 338-344 (2001).
- [2] W. L. Barnes, A. Dereux and T. W. Ebbesen; "Surface Plasmon Subwavelength Optics"; Nature, Vol. 424, p. 824-830 (2003).

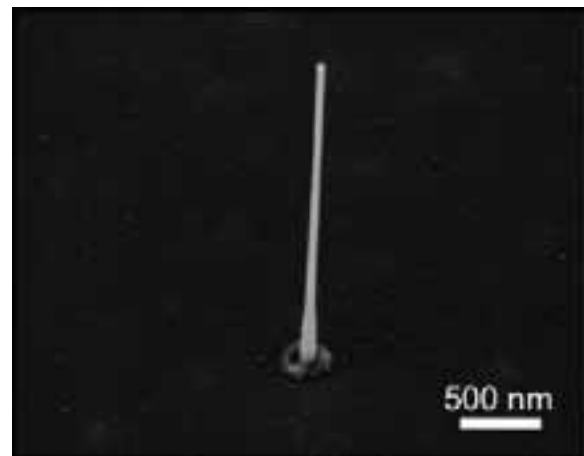


Figure 4: 45° SEM of Ge nanowire in Ag ring.

Optimization of Ohmic Contacts to III-N Semiconductor Material

Austin Conner

Electrical Engineering, Vanderbilt University

NNIN REU Site: Cornell NanoScale Science and Technology Facility, Cornell University, Ithaca, NY

NNIN REU Principal Investigator(s): Prof. Lester Eastman, Electrical Engineering, Cornell University

NNIN REU Mentor(s): Dr. Quentin Diduck and Jonathan Felbinger, Electrical Engineering, Cornell University;

Kristopher Matthews, Materials Science, Cornell University

Contact: austin.d.conner@vanderbilt.edu, lfe2@cornell.edu, qed2@cornell.edu, jgf27@cornell.edu

Abstract:

High electron mobility transistors (HEMTs) are a class of material which yield higher power and higher frequency devices than on traditional silicon [1]. In the aluminum gallium nitride (AlGaN) and indium aluminum nitride (InAlN) devices studied, electric current flowed through a thin conductive plane 10-20 nm below the surface of the material; this property made the problem of contacting this plane from outside the device a nontrivial one. Traditional approaches rely on depositing and then annealing stacks of metal to make ohmic contacts. In this process, metal diffused into the material, and donor sites were created by the out-diffusion of nitrogen, both increasing conductivity in the barrier layer. Novel metal stacks were studied at a range of thicknesses and anneal conditions. In addition, because in this process edge acuity can be negatively affected, an alternate approach was tried in which the material was etched in discrete places below the conductive plane prior to metal deposition to create nanoporations. We demonstrate that ohmic contacts can be achieved as deposited using this technique.

Introduction and Material:

The material studied consists of AlGaN- and AlInN-GaN grown by molecular beam epitaxy on substrates of silicon (Si) and silicon carbide (SiC), respectively. This materials geometry resulted in a potential well forming at the interface of the top epilayer and the GaN in which free electrons from the lattice tend to congregate. This two dimensional electron gas (2DEG) was highly conductive and formed without any doping of the material. The absence of impeding ions allowed the electrons in the 2DEG to have a very high mobility. The quality of metal contacts to this material was a function of the metals used and their thicknesses, as well as the annealing conditions. In particular, metal solid solubility and reaction rates with the material, as well as conductance and band structure of the resulting alloys and states were all considerations for choosing optimal metal contacts.

Methodology:

To measure contact resistance for the various metal stacks tested, transfer length measurement (TLM) structures were fabricated. First the material was etched below the 2DEG to create electrically isolated mesas 200 μm in width. Nanoperforations, if applicable, were created using electron beam lithography. Since this process was expensive to run, only 50 μm of the contact width and 2.5 μm of length was perforated, and the perforations were roughly 40 nm in diameter with 200 nm spacing from center to center (Figure 1). Small perforations were used so that a large total surface

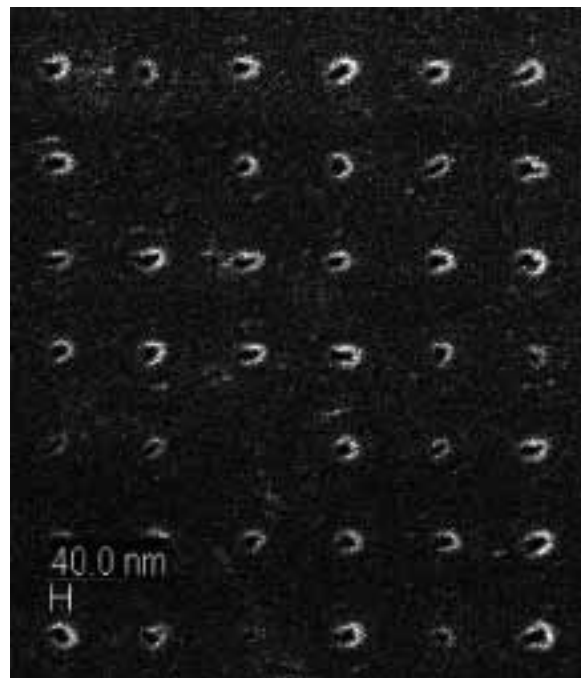


Figure 1: Scanning electron micrograph of nanoporations before metal deposition.

contact area was achieved, as several small holes closely spaced provide more contact area with the 2DEG than larger holes further apart. An oxygen plasma descum and buffered oxide etch were both performed to effect a clean surface immediately prior to metal evaporation. Then, on each of the mesas, metal was evaporated in nine rectangles spanning the mesa width and 50 μm in length, spaced so that between adjacent rectangles, there were 5, 10, 15, 20, 25, 30, 35, and 40 μm gaps. The resistance of adjacent contacts was measured by the four-point-probe technique. We used these values to work out R_c [ohm-mm], the contact resistance.

Traditional Approach Results:

Six novel metal stacks were tested. V-Al-Si-Cu (15 nm, 60 nm, 40 nm, 50 nm), Ti-Cu-Mo-Au (12.5 nm, 60 nm, 45 nm, 55 nm), V-Ti-Au (12.5 nm, 15 nm, 50 nm), and V-Al-V-Au (10 nm, 40 nm, 40 nm, 50 nm) resulted in non-conductive alloys. V-Ti-Al-Mo-Au (10 nm, 12.5 nm, 75 nm, 45 nm, 55 nm), and Ti-Al-Ti-Al-Mo-Au (7.5 nm, 45 nm, 7.5 nm, 45 nm, 45 nm, 55 nm) were ohmic, but did not surpass previously achieved results in the literature.

In addition, stacks of Ta-Ti-Al-Mo-Au (X, 12.5 nm, 60 nm, 40 nm, 50 nm) where X is 7.5 nm, 10 nm, 12.5 nm, 15 nm, 17.5 nm, were tested at a constant annealing condition of 700°C for 60s and 800°C for 20s (Figure 2).

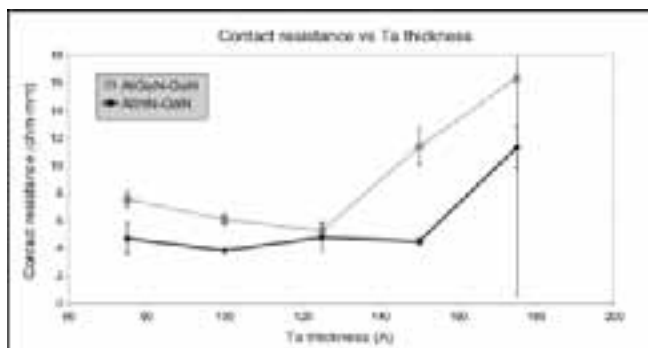


Figure 2: Contact resistance of Ta-Ti-Al-Mo-Au, as a function of Ta thickness.

These values were an order of magnitude worse than what was previously been achieved with this metal stack, which suggests an issue with either the material or the surface preparation for these experiments.

Nevertheless, it is interesting to note that the AlInN performed better than the AlGaN in these tests, whereas traditionally AlInN has been more difficult to contact than AlGaN. Further tests on different epilayers are needed.

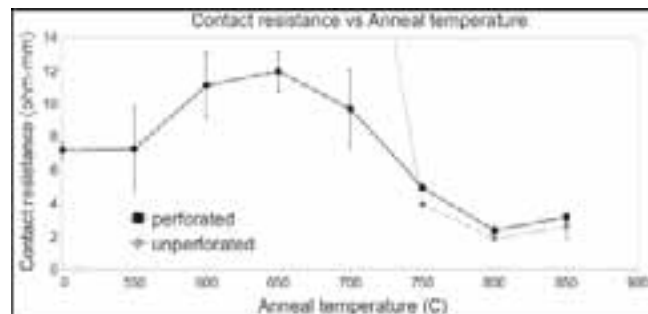


Figure 3: Contact resistance of nanoperforations as a function of anneal temperature.

Nanoperforation Results:

Three stacks were tested on the perforated material and its unperforated equivalent: Ti-Al-Mo-Au (15 nm, 90 nm, 45 nm, 55 nm), Sc-Au (10 nm, 55 nm), and Ti-Au (15 nm, 40 nm). Neither the Ti-Au nor the Sc-Au formed ohmic contacts at any anneal temperature, but the Ti-Al-Mo-Au was ohmic as deposited and at every annealing temperature tested (Figure 3). The perforated contact seemed to degrade at low anneal temperatures, but then approached the performance of the unperforated contact at high anneal temperatures. Even though the perforated contact was not optimal as deposited, this was a rough first effort, and only a fraction of the contact area was patterned.

In the future, we will test alternate methods for creating the nanoperforations, such as polymer self-assembly, which allows for cheaper fabrication over a larger area.

Acknowledgments:

Special thanks to Prof. Lester Eastman and his research group, especially Quentin Diduck, Jonathan Felbinger, and Kristopher Matthews; the National Nanotechnology Infrastructure Network Research Experience for Undergraduates (NNIN REU) Program; The National Science Foundation (NSF); the Cornell NanoScale Science and Technology Facility (CNF); the CNF staff, especially Melanie-Claire Mallison and Rob Illic.

References:

[1] Quay, R. (2008). Gallium nitride electronics. Berlin: Springer.

Heterogeneous Integration of p- and n-type Nanowires for Complementary Nanowire Circuits

Zachary Henderson
Electrical Engineering, University of Massachusetts Amherst

NNIN REU Site: Lurie Nanofabrication Facility, University of Michigan, Ann Arbor, MI

NNIN REU Principal Investigator(s): Wei Lu, Electrical and Computer Science, University of Michigan, Ann Arbor

NNIN REU Mentor(s): Wayne Fung and Seok-Youl Choi, Electrical and Computer Science, University of Michigan, Ann Arbor

Contact: zhenders@student.umass.edu, wluee@umich.edu, fungw@umich.edu, seokyc@umich.edu

Abstract:

Nanowires have shown promising results for use in creating future electronic devices that go beyond the end of metal-oxide semiconductor field effect transistor (MOSFET) scaling and for the use in three dimensional (3D) complementary circuits. Our efforts here focused on the optimization of the nanowire contact printing method, a critical step for fabricating nanowire field-effect transistors (NW FETs) at large scale. NW FETs have been studied extensively by Professor Lu's research group at the University of Michigan [1]. The parameters of the contact printing optimized here were the applied pressure of the nanowires on the substrate, the lubricant applied to the nanowires, the distance traveled by the substrates and the average speed of the transfer process. We also demonstrated and studied simple NW FETs based on these optimization efforts, which showed comparable performance to previously constructed devices. Using this optimized method, a simple integration process could be used to combine two types of NW FETs, one SnO₂ n-type and the other Ge/Si core/shell p-type, for possible 3D complementary nanowire circuit applications. 3D circuits can offer a larger integration density, faster operation speed and lower overall power consumption than current MOSFET technologies [2].

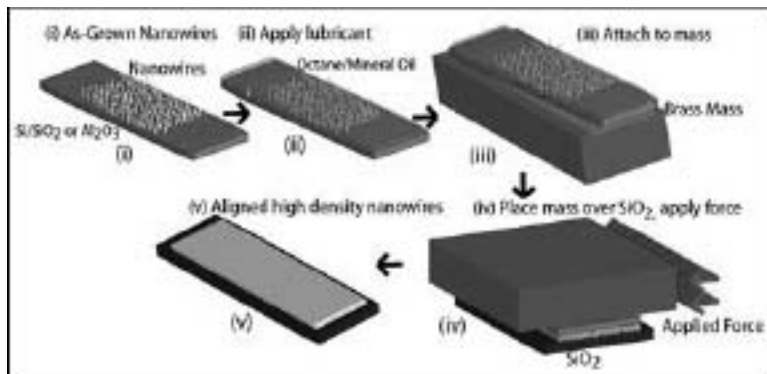


Figure 1: Diagram of contact transfer method.

Experimental Procedure:

The nanowire contact printing transfer method works by using two competing forces, the van der Waal's force of attraction and the application of an external mechanical shear force to cause the nanowires to be deposited on a device substrate. The details of the contact transfer process are described in Figure 1.

We began the transfer process by taking a growth substrate of as-grown nanowires and applying a layer of lubricant with a specific ratio of octane and mineral oil. Secondly, a brass mass, whose total mass was determined by the desired applied downward pressure, was attached to the

growth substrate. Thirdly the mass, with the growth substrate firmly attached was placed in direct contact with the device substrate, which caused the nanowires to loosely adhere to the device substrate by the van der Waal's forces of attraction. Thirdly, a micrometer applied an external shear force onto the brass mass, which caused the growth substrate to slide over the device substrate. The opposing competition of the van der Waal's force and applied shear force resulted in the breakage of the nanowires at about midway of the nanowires' total length.

The broken nanowires were then aligned on the device substrate in the direction of the external shear force. The lubricant layer was then gently

rinsed off with acetone and isopropanol, and left to air dry.

The resulting nanowire layer was then ready to be used in the fabrication of a nanowire transistor. In order to quickly analyze and characterize the Ge/Si core/shell nanowires, a simple back gated transistor was fabricated using standard photolithography procedures and nickel contact deposition. Nickel was chosen as the contact for these nanowires so that the p-type Ge/Si core/shell nanowire created an ohmic metal-semiconductor interface. The SnO₂ device was fabricated using a top gate approach with gold contact deposition in order to simulate the actual device used for fabricating a 3D complementary circuit.

Parameter	Low Effect	High Effect	Explanation
Distance upon which shear force is applied	Low surface area of transferred nanowires with overall high density	Larger surface area of transferred nanowires but transferred density decreases with increasing distance	Nanowires are initially transferred during the beginning of the sliding process, leaving less nanowires on the growth substrate to at further distances
Applied Downward Pressure	Longer, less aligned nanowires with a lower nanowire transfer density	shorter, more aligned nanowires with a higher overall nanowire density	Increased pressure causes stronger nanowire adhesion to the receiving substrate which causes the nanowires to break more easily
Composition of Lubricant	Less viscous lubricant causes a higher transfer density with shorter, less aligned nanowires	More viscous lubricant causes a lower transfer density with longer, more aligned nanowires	More viscous lubricant causes the nanowires to be suspended within the lubricant layer and not strongly adhered to the SiO_2 causing the lower transfer density and the longer, aligned nanowires
Lubricant Removal	Less of a rinse in acetone and isopropanol down not remove the applied lubricant layer	Higher amounts of rinsing in acetone and isopropanol causes the transferred nanowires to become unaligned and less dense	Increased forces applied by the higher quantities of the lubricant removal causes the nanowires to detach from the SiO_2 substrate while the lower quantities do not remove the lubricant fully

Table 1: Observations of modified contact transfer parameters.

Nanowire Diameter	Applied Pressure	Applied Lubricant	Distance Moved	Speed Traveled
20 nm	5 psi (SnO_2) 10 psi (Ge/Si)	1 drop of 2:1 v/v octane/mineral oil	3 mm	.5 mm / min

Table 2: Optimal nanowire transfer parameters.

Results and Discussions:

The observations of the distance, force, lubricant composition and lubricant removal are shown in Table 1 with the optimal nanowire transfer conditions shown in Table 2. These conditions provided high density aligned nanowires that were of good length for fabricating NW FETs.

An SEM image that displays the good alignment, density and length of the optimized SnO_2 transferred nanowires is shown in Figure 2 (i).

The nanowire field effect transistors fabricated from the optimal transferred nanowires showed comparable performance to recently fabricated nanowire transistor devices [1]. The back-gated Ge/Si core/shell device carried a fair amount of current and displayed a gate response even though the gate dielectric was thick at 600 nm. The device did not display linear IV behavior as was expected, which could have been due to Schottky effects at the Ni-nanowire contacts as seen in Figure 2 (iv). The top-gated SnO_2 device demonstrated a strong gate response, as expected, but appeared to not reach saturation as the device current continually increased with the source-drain voltage which is seen in Figure 2 (iii).

Future Work:

In order to combine the n-type SnO_2 nanowire field-effect transistor and the p-type Ge/Si nanowire field-effect transistor, we first must be able to get increased performance from the

devices separately. This can be accomplished by optimizing the fabrication process and ensuring that the properties of the as-grown nanowires are unaffected by the transfer process. After finishing fabricating the separate NW FETs, the two can be combined by placing a separate SiO_2 isolation layer over the SnO_2 device, and fabricating the Ge/Si device on the SiO_2 isolation layer. After this process is completed, we can test to see if the SnO_2 device performance or geometry is affected by the isolation layer or the fabrication of the second layer Ge/Si device.

Acknowledgments:

I would like to acknowledge Dr. Wei Lu, Seok-You Choi and Wayne Fung for their help and guidance throughout this project. I also would like to recognize my fellow REU interns, along with Brandon Lucas, Sandrine Martin, and the staff of Lurie Nanofabrication Center at the University of Michigan for their support. Finally I would like to thank the NNN REU Program and the National Science Foundation for their generous funding and support.

References:

- [1] E.N. Dattoli, Q. Wan, W. Guo, Y. Chen, X. Pan, and W. Lu, "Fully Transparent Thin-Film Transistor Devices Based on SnO_2 Nanowires," *Nano Letters*, vol. 7, 2007, pp. 2463-2469.
- [2] S. Nam, X. Jiang, Q. Xiong, D. Ham, and C.M. Lieber, "Vertically integrated, three-dimensional nanowire complementary metal-oxide-semiconductor circuits," *Proceedings of the National Academy of Sciences*, vol. 106, Dec. 2009, pp. 21035-21038.

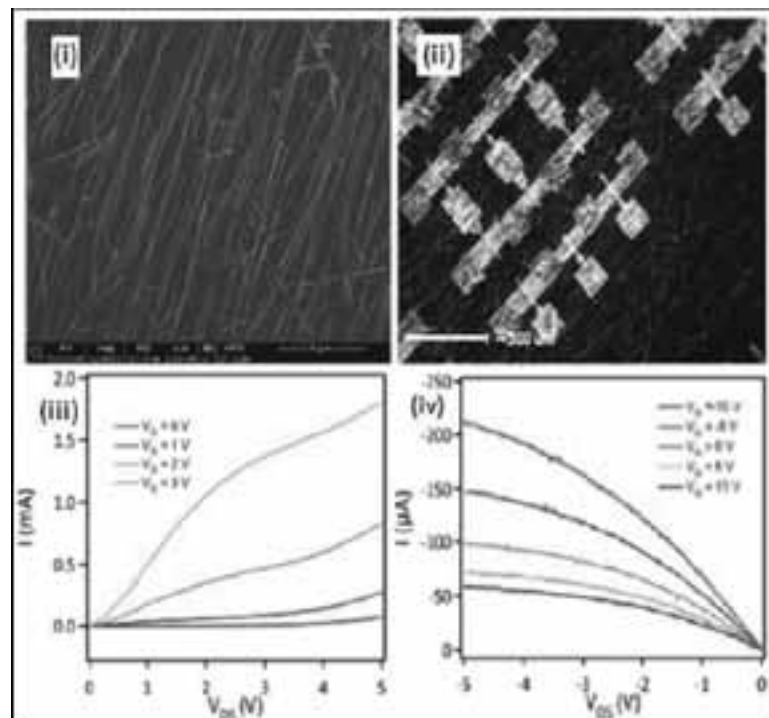


Figure 2: (i) Optimal transferred SnO_2 , (ii) SnO_2 device nanowires, (iii) IV curve of n-type device, and (iv) IV curve of p-type device.

Fabrication of Magneto Resistance-Based Magnetic Quantum-Dot Cellular Automata

Angeline Klemm

Physics/Engineering, University of Wisconsin-La Crosse

NNIN REU Site: Nanofabrication Center, University of Minnesota-Twin Cities, Minneapolis, MN

NNIN REU Principal Investigator(s): Professor Jian-Ping Wang, Electrical and Computer Engr, University of Minnesota-Twin Cities

NNIN REU Mentor(s): Andrew Lyle, Electrical and Computer Engineering, University of Minnesota-Twin Cities

Contact: klemm.ange@uwlax.edu, jpwang@umn.edu, lylex031@umn.edu

Abstract and Introduction:

Modern day electronics, which are based on complementary metal-oxide semiconductor (CMOS) technologies, are reaching limitations. As CMOS technologies are scaled, power dissipation increases beyond reasonable levels for applications. This is causing an increase in the demand for alternative or hybrid technologies. One promising approach is magnetic quantum-dot cellular automata (MQCA), which is nonvolatile and lower power. MQCA have the capability to perform all primitive Boolean functions including majority gate which is a universal logic that is inefficiently realized in CMOS technologies. Limited experimental demonstrations with single magnetic layers showed these basic logic functions; however, they could only be read with magnetic force microscopes and are not in a usable form for integration with technology [1,2].

Our goal was to fabricate MQCA devices with magnetic tunnel junctions (MTJs) [3] which will allow us to utilize magneto resistance to electrically read, measure real time operation, speed, and reliability for the first time. MTJs consist of two ferromagnetic layers separated by a nonmagnetic spacer layer. Electrons can tunnel through the barrier when a current is applied across the top and bottom electrodes. The magnetic direction of the bottom ferromagnetic layer only lies in one direction and is called the fixed layer. The magnetic direction of the top ferromagnetic layer can be switched between parallel and antiparallel to the fixed layer and is called the free layer. When the free layer is parallel to the fixed layer, electrons can pass freely through the barrier, and the resistance is low. However, when the free layer magnetization is antiparallel to the fixed layer, electrons cannot pass easily through the barrier, and the resistance is high.

MQCA are nanomagnets that become magnetically coupled due to dipole-dipole interactions when in close proximity (~ 30 nm). The magnetic moment of each elliptical nanomagnet has two stable ground states. If the nanomagnets are aligned with their long edges together, they will couple antiferromagnetically; if the nanomagnets are aligned with their short edges together, they will couple ferromagnetically [2]. Logic can be performed by applying

a magnetic field to input magnets to switch their state. This causes a chain reaction in which the states of the remaining magnets switch in a domino-like fashion dependant on the state of the adjacent magnets.

There are several key challenges to fabricate MTJ-based MQCA. First, $100\text{ nm} \times 200\text{ nm}$ features need to be resolved with 30 nm of spacing or less. Second, ion milling needs to transfer the patterned features to the MTJ while maintain the pattern's integrity. Finally, top electrodes near the elements must be 80 nm wide and spaced next to each other within 80 nm so that adjacent elements can be contacted.

Furthermore, the top electrodes need to be aligned within 50 nm so that only one MTJ element is contacted by each electrode.

Experimental Procedure:

We began the fabrication process with a silicon wafer. A magnetic tunnel junction stack and capping layer was deposited on the wafer. Photolithography techniques were used to pattern the bottom electrodes, and ion milling to etch and expose the bottom electrodes. Electron beam (e-beam) lithography was used, with positive resist, to pattern the MQCA elliptical features. Titanium was deposited using e-beam evaporation followed by liftoff. Ion milling was used to define the MQCA pillars in the MTJ film. Figure 1 a) and b) show an optimized majority gate before and after

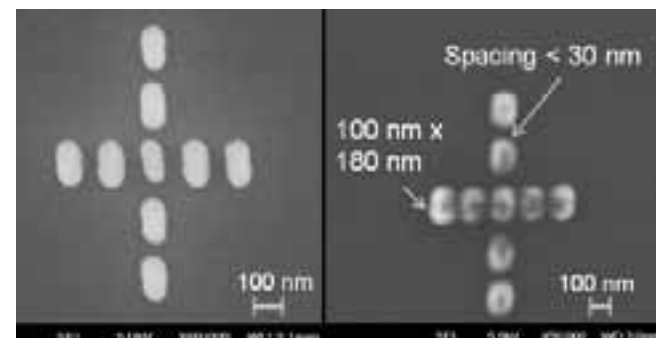


Figure 1: a) Majority gate before milling,
b) Majority gate after milling.

ion milling, respectively. The dose for e-beam lithography was finely tuned to account for the proximity effect and non-ideal pattern transfer from the ion milling.

Silicon dioxide was deposited over the wafer to isolate the bottom and top electrodes. Photoresist and reactive ion etching were used to planarize and expose the top of the MTJ pillars. Photolithography and reactive ion etching were used to form contact vias to the bottom electrodes. Finally, e-beam lithography and photolithography were used to form the top contacts. E-beam lithography was used near the MTJ elements where the 80 nm wide electrodes with 80 nm spacing and 50 nm alignment was required. E-beam evaporation was used to deposit the top contact followed by liftoff. Then photolithography, e-beam evaporation, and liftoff was used to pattern the large contact pads.

Results and Conclusions:

We fabricated MQCA devices using magnetic tunnel junctions to allow direct reading of individual elements. After several trial patternings, we achieved 100 nm \times 200 nm MQCA elements with 30 nm or less spacing and 80 nm wide contact electrodes with 80 nm spacing as shown in Figure 2. The contact electrodes were repeatedly aligned within 50 nm using a manual alignment procedure we developed. The electrical measurement shown in Figure 3 indicates contact was achieved from the bottom and top contacts. Figure 4 shows that a magnetic signal was successfully measured signifying that the contact is indeed through the MTJ element. Future work will include improving magneto resistance measurements, which will allow us to measure real time operation, speed, and reliability of the devices.

Acknowledgments:

I would like to thank the National Nanotechnology Infrastructure Network Research Experience for Undergraduates Program and the National Science Foundation for making this research opportunity possible. I would also like to thank Professor Jian-Ping Wang, Andrew Lyle, and Professor Wang's group for their guidance and support, Kevin Roberts, and the University of Minnesota's Nanofabrication Center for the use of their facilities.

References:

- [1] Orlov, et al, "Majority logic gate for magnetic quantum-dot cellular automata," *Science*, 311, 205-208 (2006).
- [2] Orlov, et al, "Magnetic quantum-dot cellular automata: recent developments and prospects," *Journal of Nanoelectronics and Optoelectronics*, 3, 1-14 (2008).
- [3] S. Parkin, et al., "Magnetically engineered spintronic sensors and memory," *Proc. IEEE*, 91, 661-680 (2003).

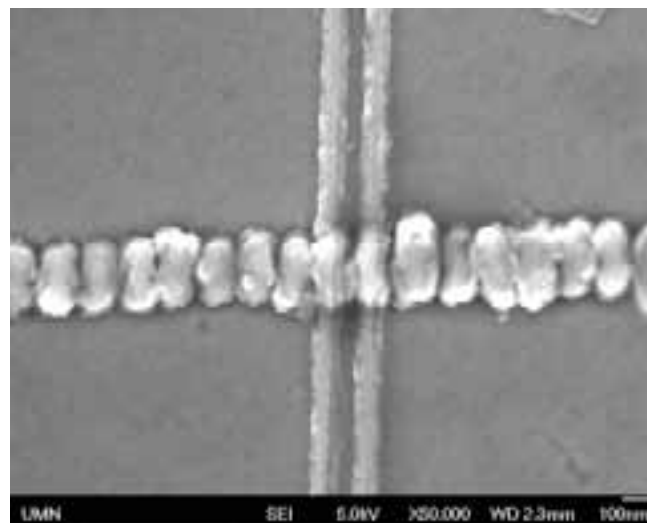


Figure 2: Alignment between MQCA features and contact electrodes.

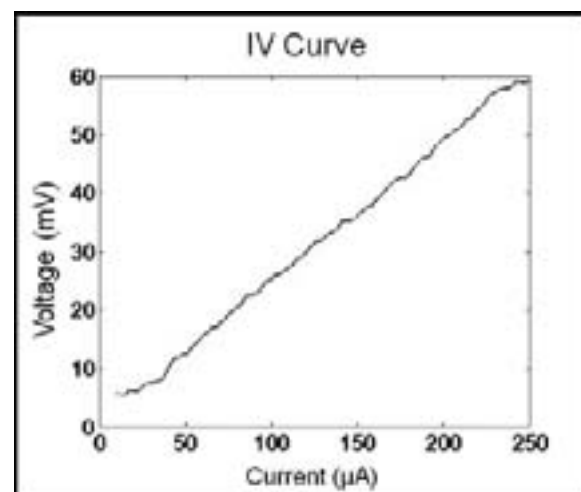


Figure 3: Resistance for MQCA device.

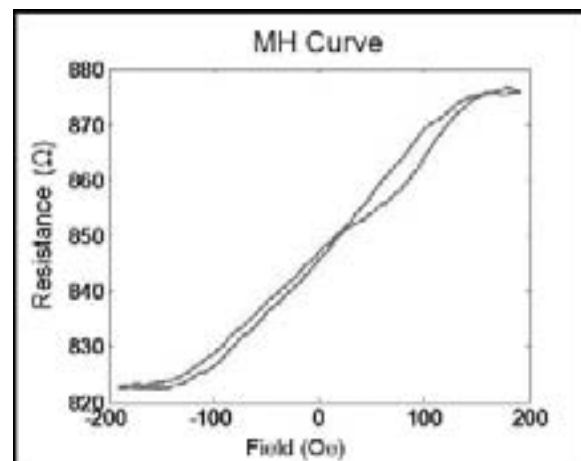


Figure 4: Magnetic signal for MQCA device.

Semiconductor Nanocrystal Inks for Printed Photovoltaics

Gabriel Palomino
Chemical Engineering, Texas Tech University

NNIN REU Site: Microelectronics Research Center, The University of Texas, Austin, TX

NNIN REU Principal Investigator(s): Professor Brian Korgel, Chemical Engineering, The University of Texas, Austin, TX

NNIN REU Mentor(s): Vahid Akhavan, Chemical Engineering, The University of Texas, Austin, TX

Contact: gabriel.palomino@ttu.edu, korgel@che.utexas.edu, vahid@che.utexas.edu

Abstract:

Copper indium gallium diselenide (CIGS) is an effective light-absorbing material for photovoltaic devices (PVs). Commercially fabricated CIGS films are vapor-deposited. A different approach to CIGS film deposition that is potentially much cheaper is to formulate nanocrystal-based inks that can be coated onto the substrate under ambient conditions, thus alleviating the need for vacuum or high temperature processing. Such an approach could greatly reduce the processing complexity and cost of CIGS deposition. Recently, we demonstrated 3.1% power conversion efficiency under AM 1.5 illumination from spray-deposited CIGS nanocrystal-based PVs. The nanocrystal films in those devices were deposited manually from a spray gun; thus, leading to variations in film thickness and uniformity across the entire substrate that gave significant differences in device performance. To better control the uniformity and thickness of the nanocrystal films, we have developed an automated deposition process that is described here. The focus of this research project was to understand how the deposition parameters, including tip-sample distance, ink formulation, raster rate and flow rate influenced the morphology and thickness of the films.

Introduction:

The changeover from the manual spray deposition to the automated process required an identification of how the deposition parameters impacted the film morphology and thickness. The key parameters were the tip-to-substrate distance, spray pressure, dispersion concentration, flow rate, and spray gun angle to the substrate. The dimensionless parameters involved in the spray process, including the Reynolds (Re), Weber (We), and Ohnesorge (Oh) numbers were calculated and correlated with the film morphology.

The Reynolds number characterizes the flow regime of the carrier gas and solvent in stream. It was found that laminar flow was desired in which the droplets are carried in the stream. The Weber number provides insight about how stable the suspension droplet was in the carrier gas.

Under conditions of high We (i.e., $We > 10$) the stream would disintegrate, leading to poor deposition morphology. Therefore, $We < 1$ were found to provide uniform micro-droplets that settled on the substrate and quickly dried, leaving the most uniform film. The Ohnesorge number of the process revealed how individual droplets impacted the substrate.

Figure 1 shows scanning electron microscopy (SEM) images of a nanocrystal layer that was manually spray-deposited, compared to a layer deposited using the automated spray process. The optimal deposition conditions for a uniform 200-300 nm thick film were a nanocrystal dispersion concentration of 20 mg/ml in toluene, a 10.2 cm distance from the nozzle to the substrate, and a gauge pressure between $3.45 \times 10^5 - 3.79 \times 10^5$ Pa (50~55 Psi). The most uniform films were obtained by spraying several coats with a 180 degree rotation of the substrate between each one coat.

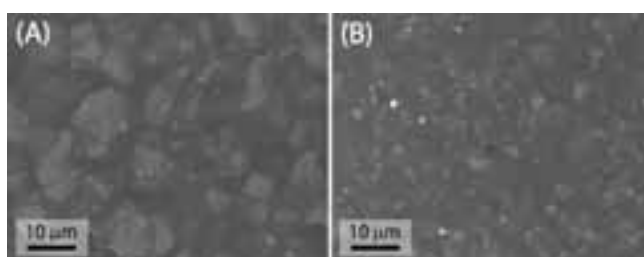


Figure 1: SEM image of (A) manually sprayed and (B) auto-sprayed CIGS nanoparticles on Au back contact.

Controlling Deposition Morphology:

The nanocrystal layer morphology and thickness of manually-deposited films could be reproduced using the automated spray deposition process. Devices fabricated with nanocrystal layers deposited with the automated spray process were also found to have similar power conversion efficiencies as those made with manually deposited films.

Over the course of understanding how to control the nanocrystal film morphology, it became apparent that there could be an opportunity to control and exploit the roughness of the films to obtain higher device efficiency. In some cases, the deposition gave corrugated films with raised features that could perhaps be utilized to improve the interfacial contact area between junctions in the device. Therefore, an effort was made to very precisely understand the role of the spray deposition parameters on the film morphology.

The separation between the spray head and the substrate was found to be the most influential parameter on the film morphology. A series of depositions were carried out by varying the tip-to-sample distance. When the separation was less than 2.5 cm, the nanocrystal film exhibited a “mud-slide” consistency, indicating that the spray had not disintegrated into individual droplets.

Separations of 2.5-4.5 cm led to stripe like features. Under these conditions, the stream had become unstable, but had not reached a stage with well-defined droplets. For separations between 5.1 and 8.2 cm, the spray was in the droplet regime, and at distances greater than 8.2 cm, there was evidence of solvent, as the particles appeared to reach the substrate as dried aggregates.

Figure 2 illustrates the regimes in the stream and the transitions between each stage. Such changes are well understood in terms of the dimensionless numbers that govern the deposition.

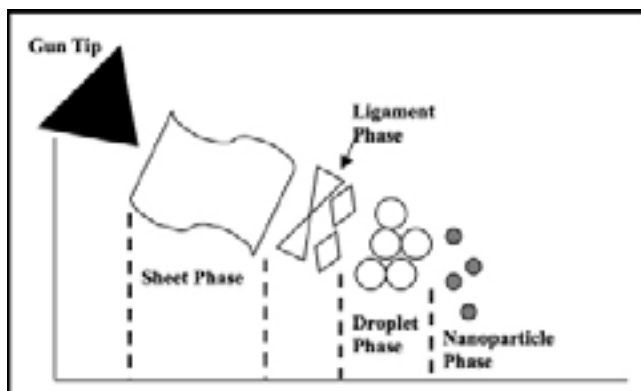


Figure 2: The regimes in the stream and the transitions between each stage.

Results:

The transition from turbulent to laminar flow occurs at $Re = 1$. At large Reynolds numbers greater than 100, the nanocrystal film had a “mudslide”-looking morphology. The film morphology became much more uniform as the Re decreased. The critical value of We of 0.01 was found to be necessary for droplet formation and deposition from the spray. Higher values of We resulted in sheet-like deposition that had the “mudslide” appearance, similar to the films obtained at high Re . Low values of We produced scattered clusters of nanoparticles on the substrate, which gave rough non-uniform films. When operated at low values of Oh , droplets bounced off the substrate and did not absorb.

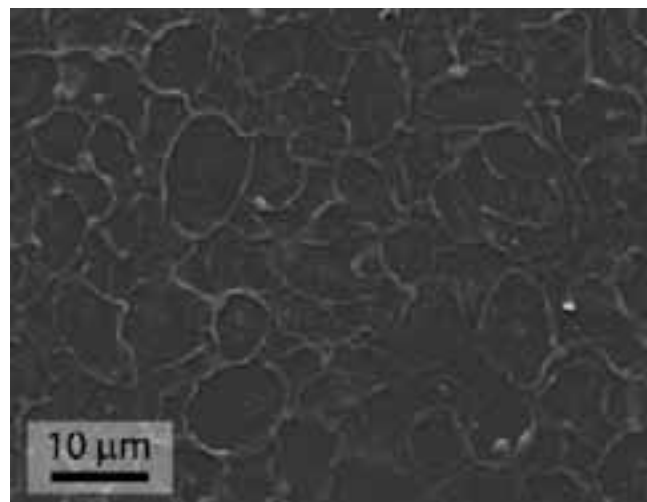


Figure 3: SEM image of structured film enabled through automatic spray deposition.

At high Oh , each droplet impinged onto the substrate and left a circular splash effect. The solvent then dried from this droplet to leave a characteristic “coffee-ring” effect, as shown in Figure 3.

A critical value of $Oh = 0.05$ is believed to be the point where a single droplet absorbs evenly on the substrate without any distortion.

Future Work:

It may be possible to improve device performance by increasing the interfacial contact area at the p-n junction in a device without increasing the average nanocrystal film thickness by depositing featured—not planar—films of nanocrystals. Although many rather exotic methods are being explored to create such heterojunctions, like nanopillar arrays for example, the spray deposition process may have the ability to create textured surfaces in a single deposition step, which could potentially improve device efficiency compared to devices made with uniform, flat nanocrystal films. The appropriate deposition conditions were identified in the automated spray process to deposit such structured films across large-area substrates, as shown in Figure 3. This may now facilitate studies of how featured electrodes might impact device efficiency.

References:

- [1] Dombroski and Johns, Chem. Eng. Sc., 18, 203, 1963
- [2] M. G. Panthani, V. Akhavan, B. Goodfellow, J. P. Schmidtke, L. Dunn, A. Dodabalapur, P. F. Barbara and B. A. Korgel, J. Am. Chem. Soc., 2008, 130, 16770-16777.
- [3] V. A. Akhavan, B. W. Goodfellow, M. G. Panthani, D. K. Reid, D. J. Hellebusch, T. Adachi and B. A. Korgel, Energy Environ. Sci., 2010, DOI:10.1039/c0ee00098a.
- [4] V. A. Akhavan, M. G. Panthani, B. W. Goodfellow, D. K. Reid and B. A. Korgel, Optics Express, 2010, 18(103), A411-A420.

Graphene Contacts to Pentacene Thin-Film Transistors

Christopher Phare

Physics and Mathematics, Vanderbilt University

NNIN REU Site: Cornell NanoScale Science and Technology Facility, Cornell University, Ithaca, NY

NNIN REU Principal Investigator(s): Dr. Jiwoong Park, Chemistry and Chemical Biology, Cornell University

NNIN REU Mentor(s): Adam Wei Tsen, Applied and Engineering Physics, Cornell University

Contact: chris.phare@vanderbilt.edu, jp275@cornell.edu, ww86@cornell.edu

Introduction:

Organic thin-film transistors (OTFTs) have attracted significant interest in recent years as their performance approaches that of traditional amorphous and polycrystalline silicon electronics. OTFTs are especially promising for large-area, flexible, and low-cost circuits, such as organic light-emitting diode displays and RFID tags. Despite recent improvements, however, traditional gold (Au)-contact OTFTs still suffer from somewhat poor performance, in part because of their large contact resistance.

We propose single-layer graphene as a novel contact material for pentacene-based OTFTs. Graphene's 2D hexagonal lattice and pentacene's linked benzene ring structure are remarkably similar, motivating a belief in improved electrical contact. Additionally, atomically thin and flat graphene allows uninterrupted contact to the pentacene active region, facilitating improved performance. Despite this potential, graphene remains almost entirely unexplored in this application.

Methods I:

We began with a 285 nm thermal oxide on a highly doped silicon wafer, on which we deposited a 495 nm copper (Cu) film with a 5 nm nickel adhesion layer. We then grew

graphene on the Cu film via CVD in a low-pressure methane and hydrogen atmosphere at 1000°C, as has been described elsewhere [1]. This created a uniform, low-defect single layer of graphene, as confirmed by Raman spectroscopy (Figure 1) [2]. Graphene was patterned with standard contact lithography and an oxygen plasma reactive ion etch. A dilute ferric chloride / hydrochloric acid solution removed exposed Cu and under-etched graphene, leaving a ~10 μm lip of graphene resting directly on the gate oxide. After drying in a vacuum oven to adhere the graphene to the oxide surface, remaining photoresist was vigorously stripped in acetone.

As a standard of comparison for the graphene devices, we also fabricated identical gold electrodes (45 nm gold with a 5 nm chromium adhesion layer) via evaporation and lift off on a wafer with the same thermal oxide.

Because pentacene is incompatible with standard lithographic processes, we first patterned windows in a second layer of photoresist and then thermally evaporated 50 nm of pentacene in a dry nitrogen glovebox, leaving the photoresist as a permanent part of the device (Figure 2). An HMDS vapor treatment was applied just prior to pentacene deposition to improve growth behavior and the quality of the final film. The highly doped silicon wafer serves as a back-gate electrode. Finished devices were stored in a glove box and analyzed under vacuum to avoid atmospheric degradation of the pentacene layer.

Results and Discussion I:

Electrical measurements for these devices were less than ideal. Graphene devices showed mobility several orders

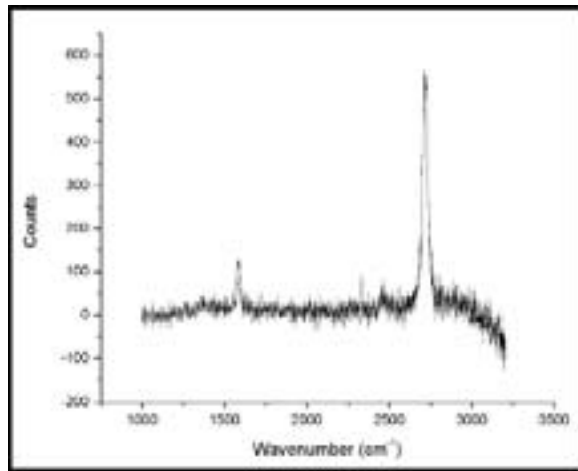


Figure 1: Graphene Raman spectrum.

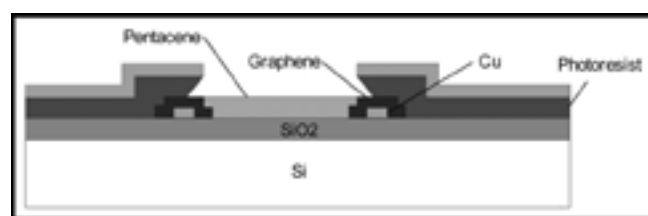


Figure 2: Device cross-section.

of magnitude lower than published gold devices, and had a negative contact resistance when analyzed by standard methods [3]. Scanning electron and atomic force microscopy (SEM and AFM) revealed an uneven and ridged graphene edge, and we hypothesized that iron compounds from the copper etch built up at the edge and affected behavior of the pentacene layer. Additionally, iron is a known dopant for pentacene; contamination at the contacts and dopant-induced channel-length shortening perhaps explain deviation in behavior from the standard contact resistance model.

Methods II:

To circumvent this problem, we fabricated identical devices using a graphene transfer process. Here, we grew graphene on a copper foil, spun on a thin layer of PMMA (2% in anisole), and etched away the copper foil entirely, leaving the PMMA-coated graphene floating in the etch solution. We then transferred well-rinsed graphene onto an oxide-coated wafer, removed the PMMA in acetone, and continued fabrication as before.

Results and Discussion II:

The electrical performance of these transferred graphene devices was approximately one hundred times better than under-etched transistors, with mobility and contact resistance comparable to published gold-contact transistors. Significantly, mobility did not substantially decrease with shorter channel length, unlike most published OTFT designs.

To examine the physical causes of this performance, we deposited only 5 nm of pentacene, equivalent to approximately 2.5 monolayers, on both graphene and gold devices. We then examined the deposition with an SEM (Figure 3). While overall nucleation was similar on both devices, pentacene grains grew across the edge of the graphene / silicon dioxide interface, while nucleation predominantly stopped at the edge of the gold electrodes. We believe this was primarily caused by the difference in thickness between the two materials (approximately 1 nm for graphene versus 50 nm for gold). Pentacene films only conduct in an approximately 3 nm thick active layer [4]; the thin graphene not only contacted this layer more directly, but also did not disrupt it with a large height step at the electrode edge (Figure 4).

The full depositions of pentacene on Au electrodes, however, were not as successful. The Au-based devices did not conduct significant current regardless of applied gate voltage. Electrically probing various parts of the device pointed to a problem at the gold/pentacene interface.

This bad contact could have perhaps been caused by trace organic contamination of the gold from photoresist residue or other factors. It is possible that the graphene contacts were less sensitive to similar contamination because of the purely organic interface. Simply cleaning the gold surface was difficult because of gold's tendency to sputter off in a reactive ion etch and the need to preserve the permanent layer of photoresist.

Going forward, we hope to further investigate the Au surface chemistry and various cleaning methods to fabricate working gold electrodes and complete the device comparison.

Acknowledgements:

We gratefully acknowledge support from the National Science Foundation, the National Nanotechnology Infrastructure Network Research Experience for Undergraduates (NNIN REU) Program, and the Cornell NanoScale Science and Technology Facility. I especially thank Dr. Jiwoong Park, Adam Wei Tsen, and other members of the Park group; Rob Ilic and Melanie-Claire Mallison, CNF REU Program Coordinators; and CNF Staff.

References:

- [1] Levendorf, M. P., et al; "Transfer-free Batch Fabrication of Single Layer Graphene Transistors"; *Nano Lett.* 2009, 9, 4479-4483.
- [2] Ferrari, A.C., et al; "Raman Spectrum of Graphene and Graphene Layers"; *Phys. Rev. Lett.* 2006, 97, 187401.
- [3] Necliudov, P. A., et al; "Contact Resistance Extraction in Pentacene Thin Film Transistors"; *Solid-State Electronics* 2003, 47, 259-262.
- [4] Noda, M., et al; "Two Causes of Source/Drain Series Resistance in Bottom-Contact Pentacene Thin-Film Transistors"; *Mat. Res. Soc. Symp. Proc.* 2004, 814, I4.4.1.

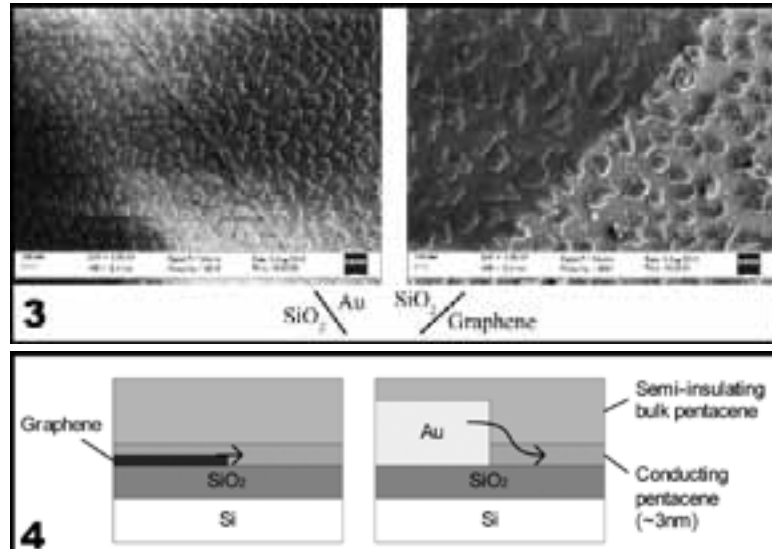


Figure 3: Partial deposition SEM.

Figure 4: Pentacene active layer cross-section.

Graphene Nanoribbons as Transistors in Nanoelectronic Devices

Michelle Pillers

Chemistry, Southern Methodist University

NNIN REU Site: Stanford Nanofabrication Facility, Stanford University, Stanford, CA

NNIN REU Principal Investigator(s): Professor Hongjie Dai, Department of Chemistry, Stanford University

NNIN REU Mentor(s): Liying Jiao, Department of Chemistry, Stanford University

Contact: mpillers@smu.edu, hdai1@stanford.edu, lyjiao@stanford.edu

Abstract:

Graphene nanoribbons (GNRs) have recently been considered to be possible alternatives to silicon semiconductors in electronic devices. Graphene, a single layer of the carbon lattice structure graphite, has a high conductivity and electron mobility. When single sheets of graphene form narrow strips, they are considered GNRs. The properties of GNRs are being studied extensively because GNRs less than 10 nm wide have a band-gap suitable for making field-effect transistors (FETs).

In this project, the effects of the GNR dimensions on their electrical properties were analyzed. To make sure GNRs are suitable for use in nanoelectronic devices, the relationships between width and conductance as well as height and conductance must be understood. Our results indicated that, even at the nanometer scale, there is a positive relationship between both width and conductance and height and conductance.

Introduction:

As technology has advanced, the scientific community has strived to make electronics smaller and more efficient. These advances in technology and shrinking of electronic devices were largely due to the implementation of silicon semiconductors. However, there is a limit to how small one can design devices using silicon semiconductors, and that limit is being approached; the scientific community has begun to search for a suitable replacement. One option could be narrow graphene nanoribbons (GNRs). The high conductivity and ability to control the band-gap of GNRs by controlling their width makes GNRs an interesting option. For their successful implementation and the development of nanoelectronic devices using GNRs, their electrical properties must be studied and understood.

There are several different ways to produce GNRs. The process used for this project was that of “unzipping” multiwalled carbon nanotubes (MWNTs); the GNRs that are produced are high-quality, narrow, and have smooth edges.

The procedure for “unzipping” MWNTs has two steps: gas-phase oxidation and sonication. During gas-phase oxidation, the nanotubes were calcinated and small defects on the walls were etched away, producing a small hole. The nanotubes were then dispersed in a 1,2-dichloroethane (DCE) organic solution of poly(*m*-phenylenevinylene-co-2,5-dioxy-*p*-phenylenevinylene) (PmPV) by sonication, during which the carbon-carbon bonds were broken around the small hole and the nanotubes “unzipped” [1].

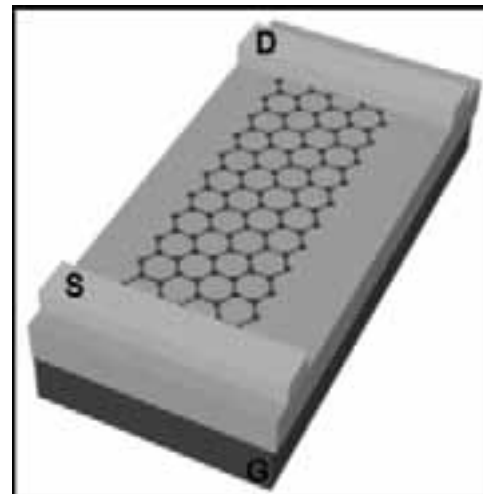


Figure 1: FET with source (S) and drain (D) Pd contacts, Si back gate (G), and SiO_2 dielectric.

The GNRs produced were suitable for making FETs. As seen in Figure 1, these FETs had source and drain palladium (Pd) contacts connected to the GNR, a Si back gate, and a 300 nm SiO_2 dielectric [2]. Flow of current from the source to the drain was regulated by an electric field, produced by a voltage at the gate. The current produced by various gate voltages could be measured and the electrical properties of the individual GNR understood.

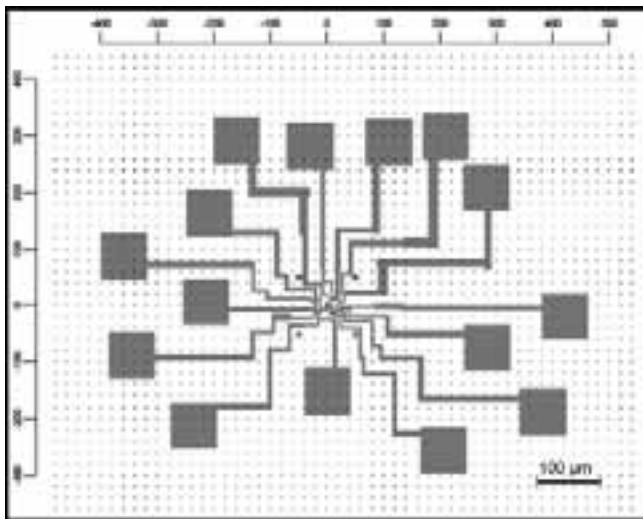


Figure 2: Final nanoelectronic device design.

Experimental Procedure:

Standard electron-beam-lithography (EBL) was used to expose markers onto a Si/SiO₂ wafer. The wafer was cut into small chips and a solution of “unzipped” GNRs was spin-coated onto the chips. Suitable GNRs were located on a chip using atomic force microscope (AFM); their widths and heights were also measured with AFM. The nanoribbons had to be straight, fully unzipped, and longer than one micron to allow for application of electrodes. Once several GNRs were located on a chip, the device was designed. Three to four 1 μ m wide electrodes were placed across and perpendicular to the nanoribbon. As can be seen in Figure 2, the electrodes extended in a parallel and perpendicular sequence to an 80 μ m wide contact.

Device fabrication consisted of four steps. First, EBL exposed the device pattern on the Si/SiO₂ chip. Second, Pd was deposited to coat the pattern and form Ohmic contacts with the GNRs. Excess Pd was lifted off of everything other than the device pattern. The final step was thermal annealing, which ensured that the Pd was in proper contact with the GNRs.

Testing of the device was achieved with a micro-probe station in vacuum at room temperature. The applied gate voltage was varied from -40 V to 40 V. If the electrodes were connected by a GNR, a current would flow through the device and a current (I_{sd}) vs. voltage (V_g) graph would be obtained. From this information, the electrical properties of each GNR could be studied.

Results and Conclusions:

Two relationships were studied during this experiment. The first was width vs. conductance. In Figure 3, it can be seen that there is a positive relationship between the width of GNRs of similar heights and the conductance. This information, compiled from GNRs of similar heights, shows that as width increases, conductance increases. Additionally, in Figure 4, there is a positive relationship of GNRs of similar widths and conductance. It is apparent that as height increases, conductance increases. Even at these small dimensions, these relationships hold.

With these values and the understanding of these relationships, the conductance of a GNR can be controlled when the dimensions of the GNR are controlled, producing specialized GNRs with specific properties that may be used in nanoelectronic devices.

Summary:

In this experiment, the electrical properties of GNRs were studied. These properties included the effect of width and height on conductance. Through the use of GNRs produced by “unzipping” MWNTs, simple FETs were fabricated. The procedure was a four step process of locating GNRs, designing devices, fabricating the devices, and testing the devices with micro-probe station.

The results indicate a positive relationship between both width and conductance and height and conductance of GNRs. Understanding these relationships is key to controlling the dimensions of GNRs and producing specialized GNRs for possible use in nanoelectronic devices.

Acknowledgements:

NSF, NNIN REU, SNF, Professor Hongjie Dai (Principal Investigator), Liying Jiao (Mentor), Mike Deal (Program Coordinator).

References:

- [1] L. Jiao. “Facile synthesis of high-quality GNRs.” *Nature Nanotechnology*, 2010.
- [2] L. Jiao. “Narrow GNRs from carbon nanotubes.” *Nature*, 2009.

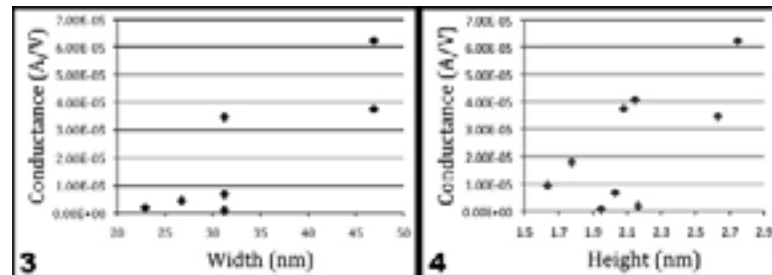


Figure 3: Width vs. Conductance graph of GNRs with similar heights.

Figure 4: Height vs. Conductance graph of GNRs with similar widths.

Thermally Enhanced Dynamic Core Migration with Phase Change Materials

Amber Pizzo
Mechanical Engineering, Binghamton University

NNIN REU Site: Nanotechnology Research Center, Georgia Institute of Technology, Atlanta, GA

NNIN REU Principal Investigator(s): Dr. Andrei Fedorov, Department of Mechanical Engineering, Georgia Institute of Technology

NNIN REU Mentor(s): Craig Green, Department of Mechanical Engineering, Georgia Institute of Technology

Contact: apizzo1@binghamton.edu, andrei.fedorov@me.gatech.edu, cgreen8@gatech.edu

Abstract:

Due to the presence of hotspots in microprocessors, localized cooling solutions have become a significant area of research. This study's aim was to fabricate a chip containing heaters of varying size, to simulate these hotspots. Resistance temperature devices (RTDs) were fabricated around these heaters to measure the temperature of the hotspots and the heat spread through the substrate. The chip will be used to characterize the ability of various phase change materials (PCMs) to mitigate the effect of transient hotspots. Fabrication included electron beam deposition, plasma enhanced chemical vapor deposition (PECVD), and reactive ion etching (RIE). Material deposition consisted of titanium (Ti), as a layer of adhesion, and platinum (Pt), as the sensing material. The devices were calibrated to determine the relationship between temperature and the electrical resistivity of the heaters and RTDs.

Introduction:

Hotspots are areas of high heat flux and high temperature. Certain areas of a chip consume more power by performing more processes, and therefore these hotspots form [1]. After reaching the threshold temperatures, the chips must be allowed to cool to avoid damage from the hotspots. A localized cooling solution would lengthen the amount of time the device could be used, and make the device more efficient.

A chip containing eight heaters of varying size was fabricated to imitate these areas. Surrounding these heaters are several RTDs to measure the heat spread through the substrate of the chip.

Method:

A layer of negative resist, NR9-1500PY, was spun on a Pyrex® wafer in order to deposit metal in the pattern of the mask on the wafer. Pyrex wafers were employed as the substrate due to the fact that they have a low thermal conductivity, and therefore minimize heat spread. The resist was exposed and developed. Then Ti and Pt were deposited using e-beam deposition. Ti was deposited as an adhesion layer, and Pt as the sensing material. Pt is an extremely accurate material for use in RTDs. The resist was then removed, leaving only the first layer of the devices. Next, a layer of negative resist, NR9-8000, was spun on the wafer. It was then exposed and developed. Ti was again deposited for adhesion purposes, followed by copper (Cu) and then gold (Au), using e-beam deposition. Cu was utilized as a high conductivity material for the leads of the device, and Au was needed in order to wire bond the device for testing. The resist was removed, leaving the final layer of the devices.

To characterize this device, the resistance of the RTDs and the heaters must be measured and compared to one another. In addition, the electrical resistivity of the devices versus temperature must be calibrated.

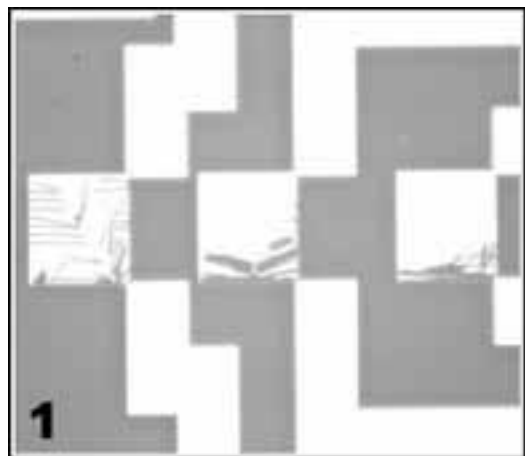
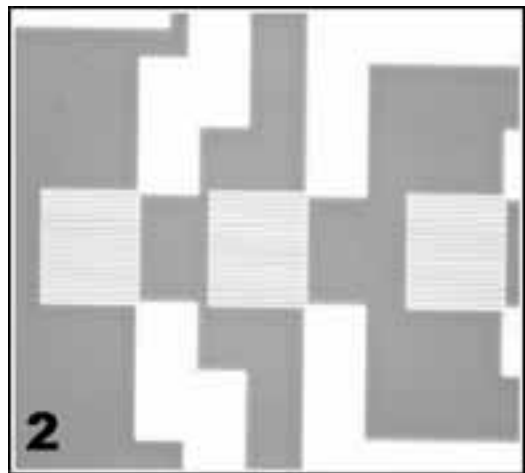


Figure 1, above: Devices are damaged due to improper adhesion. Figure 2, below: Devices are intact due to proper adhesion.



Results and Discussion:

One major fabrication difficulty was obtaining correct resist adhesion to the wafer. Normally, the resist used is heated on a hotplate. However, since Pyrex has a low conductivity, a temperature gradient would be produced between the bottom and the top of the wafer. To avoid this, the wafer was soft baked in an oven to achieve uniform heating. The bake time was recalculated to account for this alternate form of heating.

It was seen that many of the devices appear damaged after development, as seen in Figure 1. These devices were found consistently in the center of the wafer. At first, the wafer was placed on a dish in the oven to bake. The dish caused the devices to heat unevenly in the center of the wafer, causing the resist to bake improperly, and thus detach from the substrate. Instead, the wafer was placed on several dishes so only the edges of the wafer, where no devices were present, would be in contact with the dishes. This method produced fully developed devices over the entire wafer, as shown in Figure 2.

An oxide layer was deposited to protect the leads of the device. A small area of the leads was etched using RIE to expose the metal for testing. However, it appeared the etching was extremely uneven. Certain leads appeared to have oxide present, while other areas showed signs of metal being etched. Therefore, it was decided to test future devices before the oxide layer was deposited.

After calibrating the resistance of the devices versus temperature, it could be seen that the resistance of the heater wires was much lower than the average resistance of the RTD's, as seen in Figure 3. This was due to the fact that the cross-sectional area of the heater was much greater than that of the RTD.

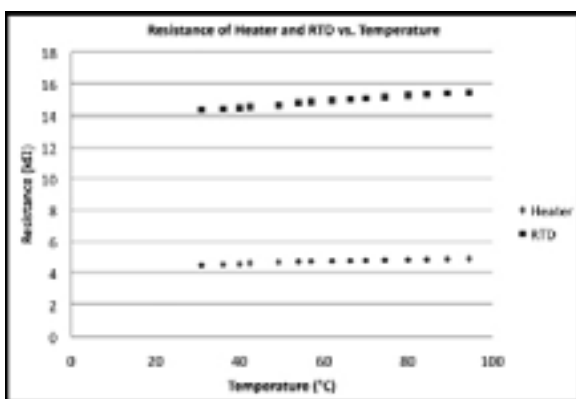


Figure 3: Resistance of heater wires is much lower than the resistance of the RTDs.

The relationship between resistance and area can be seen in Equation 1, where R is resistance, ρ is resistivity, l is length, and A is the cross-sectional area:

$$R = \rho \frac{l}{A} \quad (1)$$

Conclusion:

The oxide etch process needs to be researched further in order to provide uniform etching over the wafer. Continued testing of this heater device will allow possible cooling solutions to be tested utilizing an accurate hotspot simulation.

Future Work:

One cooling solution that is being researched currently is the use of phase change materials (PCMs). A phase change material is a material with a melting temperature at or around the working temperature of the device that it will be implemented in. Thus, when the device reaches its working temperature, the PCM will melt, absorbing thermal energy and cooling the device. A chip utilizing PCMs will be fabricated and tested, using the heaters as hotspot simulations.

Acknowledgements:

I would like to thank the National Science Foundation (NSF) and National Nanotechnology Infrastructure Network Research Experience for Undergraduates (NNIN REU) Program for funding my summer research. I would like to thank Dr. Andrei Fedorov and Craig Green for their generosity and guidance, as well as Dr. Nancy Healy, Katie Hutchison, and Joyce Palmer.

References:

- [1] Link, G., Vijaykrishnan, N.; "Hotspot Prevention Through Runtime Reconfiguration in Network-On-Chip" (2005)

Fabrication and Characterization of Indium Arsenide Nanowire Transistors

Devanand Sukhdeo
Electrical Engineering, Columbia University

NNIN iREU Site: Institut Für Bio- Und Nanosysteme (IBN), Forschungszentrum, Jülich, Germany

NNIN iREU Principal Investigator and Mentor: Dr. Mihail Lepsa, III-V Semiconductor Technology, Forschungszentrum Jülich

Contact: dsukhdeo@stanford.edu, m.lepsa@fz-juelich.de

NNIN iREU Program

Abstract and Introduction:

III-V compound semiconductors such as indium arsenide (InAs) have long been known to have favorable electronic properties such as high electron mobilities. For this project, top-gated transistors were fabricated from InAs nanowires using a lanthanum lutetium oxide (LaLuO_3) high- κ dielectric in a horizontal geometry. The InAs nanowires were all grown by molecular beam epitaxy (MBE), and some nanowires were n-doped with silicon, using beam flux values corresponding to doping calibration of layers.

These transistors were then characterized by I-V measurements using a DC probe station. The gate influence was clearly visible in these I-V measurements, and cutoff was observed at sufficiently negative biases. Additionally, attempts were made to perform C-V measurements. However, these attempts proved unsuccessful due to parasitic contributions from the contact pads and the substrate.

Experimental Procedure:

First, a silicon (Si) substrate with an oxide layer was pre-patterned with alignment marks using photolithography. Previously-grown nanowires with different intentional dopings were then transferred onto predefined regions of the substrate such that each region contained wires of a known single doping. The wires were transferred by physically contacting them with cleanroom paper and then contacting a region of the target substrate. Because this leaves the nanowires in a random arrangement, a scanning electron microscope (SEM) was used to locate suitable nanowires on the substrate in relation to the alignment marks.

From there, electron beam lithography with a poly(methyl methacrylate) (PMMA) resist was used to pattern source/drain contacts on the nanowires. A brief argon sputtering was used to etch away the native oxide from the nanowires, and the gold (Au) contacts were then deposited with a titanium (Ti) adhesion layer. 50 nm of LaLuO_3 , a high- κ gate dielectric, was then deposited over the entire sample using pulsed laser deposition. Ti-Au gate contacts were then patterned using e-beam lithography and metal deposition. An SEM of a typical device is shown in Figure 1.

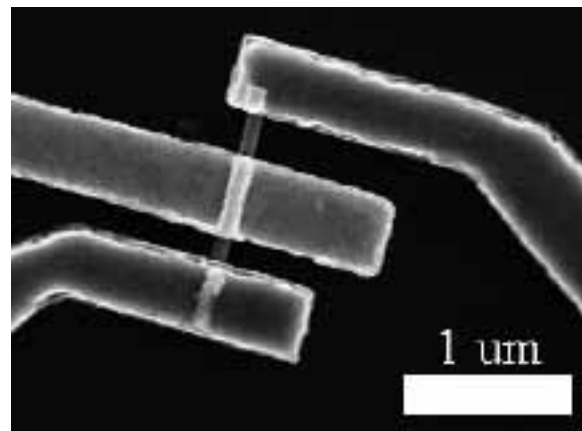


Figure 1: SEM of a typical top-gated InAs nanowire transistor.

Various I-V measurements were then performed on all of these devices using a DC probe station. Attempts were also made to perform C-V measurements on the gates using an impedance analyzer.

Results and Conclusions:

Direct current (DC) measurements showed that approximately 60% of the devices fabricated were non-functional. However, for all the devices that were functional, the gate influence was clearly visible, with higher drain currents at higher gate voltages for any given source-drain voltage, a behavior indicative of n-channel devices. The drain current response of a typical device during a gate voltage sweep is shown in Figure 2. The drain current response of another typical device during a source-drain voltage sweep is shown in Figure 3. All devices showed a threshold voltage of approximately -4V, as illustrated in Figure 3.

The nanowires' resistances were measured to be generally between 15 k Ω and 1500 k Ω for both undoped and n-doped nanowires. Given an average nanowire diameter of approximately 100 nm and device lengths of about 1000 nm, we can calculate the resistivity of the wires to be between approximately 0.01 Ω cm and 1 Ω cm.

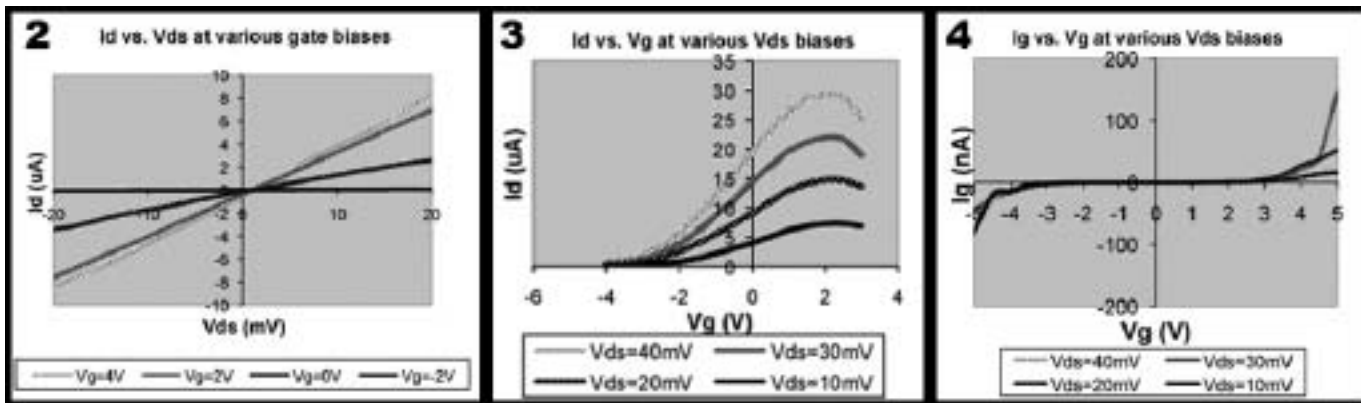


Figure 2: I_d - V_{ds} response of a top-gated nanowire transistor at various gate biases. The nanowire was undoped.

Figure 3: I_d - V_g response of a top-gated nanowire transistor at various source-drain biases. The drop in I_d at higher gate voltages is likely a result of the gate voltage being swept from high to low in this instance. The nanowire was undoped.

Figure 4: Gate leakage current as a function of V_g at various source-drain biases. The nanowire was n-doped with a Si beam flux corresponding to $1 \times 10^{17} \text{ cm}^{-3}$ in layers.

The peak gate transconductance was computed at several source-drain biases. At a 40 mV source-drain bias, the peak gate transconductance was about $4 \mu\text{A}/\text{V}$, accurate to within a factor of two. However, the accuracy of the doping process has not yet been experimentally confirmed, and the contact resistance has not yet been de-embedded. Thus, no mobility values can yet be confidently reported.

We also measured the gate leakage current, which varied substantially from one device to another. In most cases the leakage current would remain under 100 nA for gate biases between -4V and +4V, as illustrated in Figure 4, however the variation between individual devices was quite substantial.

Attempts to measure the C-V response of the devices' gates were unsuccessful; even with an open compensation parasitics from the contact pads and the substrate were overwhelming. While the expected capacitance response was on the order of femtofarads or attofarads based on previously reported values [1], the parasitic capacitance was on the order of picofarads. Moreover, the parasitic capacitance was not constant due to depletion of the underlying silicon substrate, further complicating any possibility of de-embedding.

Future Work:

Further investigation is necessary to extract parameters such as mobilities. However, the exact doping levels of the nanowires in relation to the dopant beam flux remains an open question. This will be resolved by analysis of both this

data and forthcoming measurements. The contact resistance must also be de-embedded. From there, further studies may be done to see how relevant factors, such as a nanowire's doping, length and width, affect device performance.

Additionally, high-frequency measurements would provide valuable insight about such devices' suitability for high-performance electronics. As for C-V measurements, an alternate setup such as a capacitance bridge may overcome the parasitics. Another option is to rebuild these devices on a completely insulating substrate.

Acknowledgements:

I would like to thank my principal investigator, Dr. Mihail Lepsa of Forschungszentrum Jülich, for his guidance and assistance throughout this project. I also wish to acknowledge the assistance of Jürgen Schubert, Stefan Trelenkamp, Karl Weis, Thomas Grap, Stephan Wirths, Christian Blömers and Torsten Rieger, all of whom are affiliated with Forschungszentrum Jülich.

I would also like to thank the National Science Foundation and the National Nanotechnology Infrastructure Network International Research Experience for Undergraduates (NNIN iREU) Program for funding this project.

References:

[1] Alexandra Ford et.al., "Diameter-Dependent Electron Mobility of InAs Nanowires", Nano Letters 2009, 9 (1), 360-365.

Heterogeneous Integration of p- and n- type Nanowires for Complementary Nanowire Circuits

NNIN Grad Program

Takeshi Uchinoumi
Chemical Systems and Engineering, Kyushu University

NNIN REU Site: Lurie Nanofabrication Facility, University of Michigan, Ann Arbor, MI

NNIN Graduate Research Principal Investigator(s): Wei Lu, Electrical Engineering, University of Michigan

NNIN Graduate Research Mentor(s): Wayne Fung, Seok-Youl Choi, Electrical Engineering, University of Michigan

Contact: Takeshi.Uchinoumi@mail.cstm.kyushu-u.ac.jp, wlu@umich.edu, fungw@umich.edu, seokyc@umich.edu

Abstract:

Semiconductor nanowires are of considerable interest as an advanced building block for the next generation nanodevices because of their promising and fascinating properties. For successful implementation in wide variety of applications, however, the ability to tightly define the diameter of the semiconductor nanowires is becoming indispensable because their fundamental properties are strongly dependent on the radial dimension. Therefore, there have been increasing demands for the development of new efficient methods that precisely control the nanowire geometries for more practical applications. We report growth of diameter-controlled tin oxide (SnO_2) nanowires by vapor-liquid-solid (VLS) process via boiled aluminum oxide/silicon ($\text{Al}_2\text{O}_3/\text{Si}$) substrate for develop of a heterogeneous integration technique to build complementary circuits based positive and negative type nanowires.

Introduction:

SnO_2 nanowires were chosen in our studies due to the low growth cost, high optical transmittance. Particularly, single-crystalline SnO_2 nanowires may be grown using a simple vapor transport synthesis method that allows for the growth of large quantities of nanowires at a low cost. We have developed a reliable *in situ* doping process that has been shown to dramatically affect the nanowires' electrical properties in a controlled fashion. In previous work, we focused on lightly tantalum (Ta)-doped SnO_2 nanowires that serve as the channel material in nanowire field-effect transistor and transparent thin-film transistor devices [1]. The Ta-doped SnO_2 nanowires were synthesized on Si substrates by a catalyst-mediated VLS process in which the Ta and Sn source materials were provided by a vapor transport method. In this work, we grew diameter-controlled SnO_2 nanowires by VLS process via boiled $\text{Al}_2\text{O}_3/\text{Si}$ substrate.

Experimental Procedure:

The first step was to create a substrate. First, a Al_2O_3 film was deposited on bare Si surfaces by evaporator (80 nm). The $\text{Al}_2\text{O}_3/\text{Si}$ was boiled in deionization water at 95°C (by thermometer) in Pyrex® beaker on a hot plate around 300°C. The boiled $\text{Al}_2\text{O}_3/\text{Si}$ was cleaned up by oxygen plasma cleaning for 30 seconds at 150 W. Poly-lysine solution was coated on the $\text{Al}_2\text{O}_3/\text{Si}$ for five minutes and rinsed with deionization water. Poly-l lysine functionalization of the $\text{Al}_2\text{O}_3/\text{Si}$ surface was utilized in order to promote gold (Au) nanoparticle adhesion. 20 nm Au nanoparticle colloid

solution procured was coated on the surface for five minutes and rinsed with deionization water. The boiled $\text{Al}_2\text{O}_3/\text{Si}$ with 20 nm Au nanoparticle was used as the growth substrate.

The second step was to grow SnO_2 nanowires via VLS process. First, Argon gas flowed, acting as the carrier gas of 0.55 SCFH, which was made to flow through a tube using metered flows and at atmospheric pressure. The growth process proceeded as follows. The source material, consisting of a mixture of Sn and Ta powder and the boiled $\text{Al}_2\text{O}_3/\text{Si}$ growth substrate, was loaded into a separate quartz tube that had a diameter of 1.0 cm and a length of 10.1 cm. The ratio of mixture of Sn and Ta was 500/1 and the amount of mixture was 0.5 g. The distance between the source and the growth substrate was 3 cm. The temperature ramp rates were fixed at 20°C/min, the tube furnace was allowed to heat up to 900°C and was held there at 900°C. Once the furnace temperature reached 900°C, the furnace was opened and the quartz boat was pushed into the center of the furnace using a stainless steel rod while the furnace was still at the process temperature. After heating at 900°C for 15 min, the quartz boat was unloaded from the furnace.

Results and Conclusion:

Following growth, SEM imaging of the growth substrate showed diameter-controlled VLS SnO_2 nanowire growth (Figure 1). The images show ~ 30 nm diameter SnO_2 nanowires growing from 20 nm Au nanoparticles.

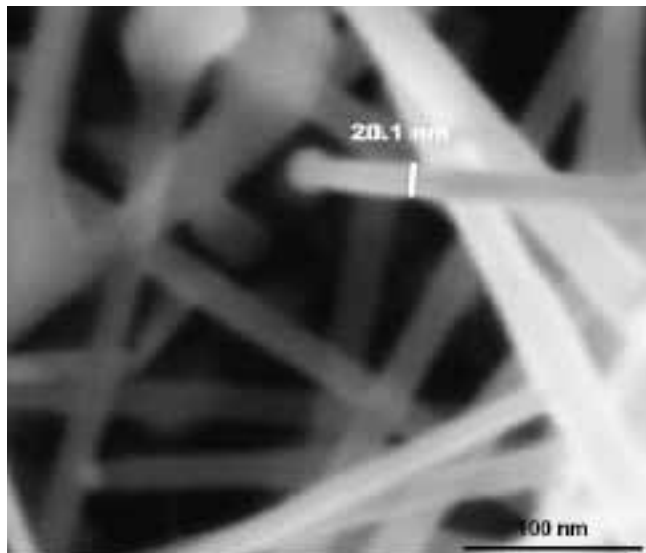


Figure 1: SEM image of SnO_2 nanowires.

It can be clearly seen that there is a catalyst at the tip of the nanowires. In addition, a spherical Au nanoparticle was observed at the end of each as grown nanowire, which is a common characteristic of the nanoparticle nucleated VLS nanowire growth process. This was due to pores of boiled Al_2O_3 that can fix nanoparticles.

We demonstrated the effect of pores of boiled Al_2O_3 by heating 20 nm Au nanoparticles on Si substrate, 20 nm Au nanoparticles on boiled Al_2O_3 /Si substrate in the same condition, except for a source. SEM imaging after heating 20 nm Au nanoparticles on a Si substrate showed the agglomeration of 20 nm Au particles (Figure 2), whereas SEM imaging after heating 20 nm Au nanoparticles on a boiled Al_2O_3 /Si substrate showed no agglomeration of 20 nm Au particles (Figure 3). This result indicates that pores of boiled Al_2O_3 can prevent agglomeration of Au particles.

In conclusion, we reported a simple and effective method for fabrication of semiconductor nano-

wires. The boiled Al_2O_3 /Si substrate enables control of the agglomeration of nanoparticle catalysts, and thereby, the diameter of semiconductor nanowires can be manipulated depending on the catalyst size in the VLS growth process.

Future Works:

Diameter-dependent electrical properties of the controlled SnO_2 nanowires will be explicitly embodied by the application to nanowire field effect transistors. The ability to control a well-defined radial dimension of the semiconductor nanowires could facilitate implementation of integration of nanowires for complementary nanowire circuit.

Acknowledgements:

I would like to thank my mentors Wayne Fung, Seok-You Choi for training and teaching me during this project as well as my advisor Professor Wei Lu for helping me to understand the background knowledge of the project. I would say thank you to Brandon Lucas and Sandrine Martin for making my stay at the University of Michigan so comfortable, and the staff of the Lurie Nanofabrication Facility for their assistance and coordination of the program. Finally, thank you to the National Nanotechnology Infrastructure Network Research Experience for Graduates Program and the National Institute for Materials Science for this opportunity.

References:

[1] Wei Lu et al., *Nano Lett.*, 2007, 7, 2463-2469.

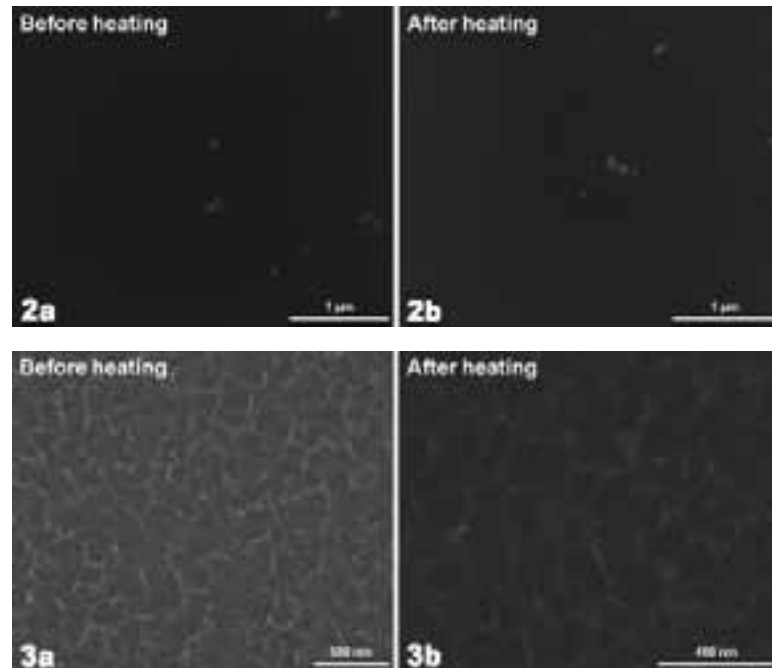


Figure 2, top: SEM images of Au particles on Si substrate.

Figure 3, bottom: SEM images of Au particles on boiled Al_2O_3 /Si substrate.

Fabrication of a Gallium Nitride Nano-Field Effect Transistor

Amber C. Wingfield

Optical Engineering and Mathematics, Norfolk State University

NNIN REU Site: Howard Nanoscale Science and Engineering Facility, Howard University, Washington, DC

NNIN REU Principal Investigator(s): Dr. Gary Harris, Electrical Engineering, Howard University

NNIN REU Mentor(s): Dr. William Rose, Electrical Engineering, Howard University

Contact: a.c.wingfield@spartans.nsu.edu, gharris@msrce.howard.edu, wbulrose@gmail.com

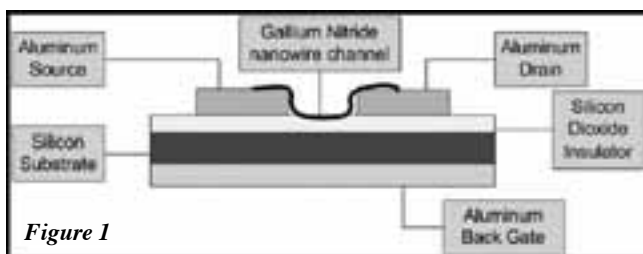
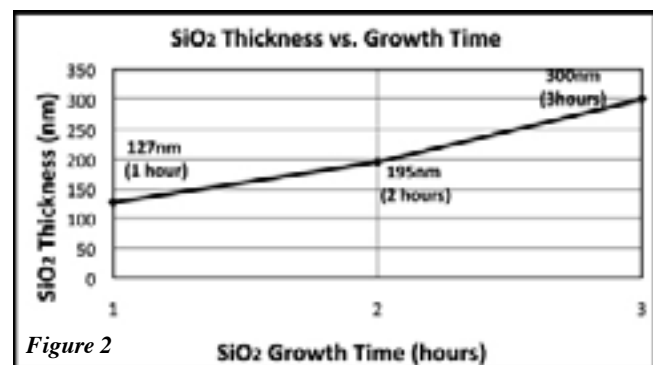


Figure 1



Abstract and Introduction:

The complimentary metal oxide field effect transistor (CMOSFET) continues to be an impacting device within the semiconductor industry. Known for its amplification and switch like capabilities, the MOSFET has great significance in logic circuits, which is central to the operation of computing systems. Components forming the MOSFET include a source, drain, channel, and gate (Figure 1). Miniaturizing such technology to the “nanolevel” has been of great interest to the semiconductor industry. Since the beginning of the twenty-first century, and even before, there has been a push in the semiconductor industry towards the miniaturization of devices. This miniaturization would lead to the compacting of more devices on a single chip, decreased chip size, increased speed and decrease overall component and finished product size. However using the prediction of Moore’s law with the present technology, by the year 2020, the steadfast approach to miniaturization will reach its limitations.

Nanotechnology, which some view as the new era in technology, presents us with the possibility to surmount this barrier. Hence, the focus of this research was to demonstrate the use of gallium nitride (GaN) nanowires to fabricate a CMOSFET using the nanowire as the conducting channel.

Methodology:

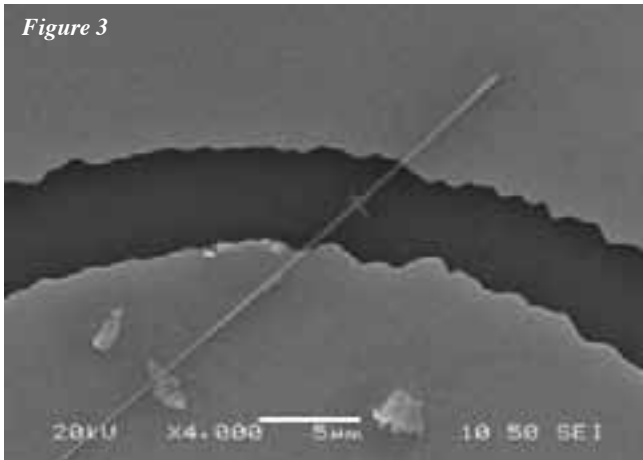
Fabrication of the nanoFET was initiated with a low resistive, highly doped silicon (Si) wafer, which was cut into one inch² pieces. These Si wafers were then thermally oxidized in a quartz furnace at 1100°C to form a layer of

silicon dioxide (SiO₂), which will be used as the gate dielectric. The thickness of the grown SiO₂ layer was measured by ellipsometry. For this project, SiO₂ layers of thickness between 275-300 nm were used (Figure 2).

To form the gate contact, a 150 nm thick aluminum (Al) ohmic contact layer was deposited onto the backside of the Si wafer by electron beam evaporation. Prior to evaporation the backside of the wafer was cleaned with hydrogen peroxide to remove any extraneous oxide from the surface. To protect the layer during subsequent fabrication processes, a layer of photoresist was spun onto the surface and baked for 30 mins. Employing photolithography, the source and drain electrodes for the nanoFET were defined atop the SiO₂ layer. We then evaporated 150 nm of Al, or gold (Au), over this surface. A liftoff process was then used to form the source drain contacts. The mask used in this work was specifically designed to maximize the probability of getting nanowires across the source and drain.

The GaN nanowires used were grown in house and measured roughly 50 nm in diameter and 10-100 μ m in length. The GaN nanowires were suspended in toluene to aid in their dispersion across the wafer when applied. Using a syringe, the solution was dropped onto the wafer surface where many source-drain contacts were. The solvent was allowed to evaporate, and the sample was then examined under an optical microscope and a scanning electron microscope to confirm nanowire placement on the source-drain contacts (Figure 3).

Figure 3



Results:

With many source-drain contacts on each wafer, only a few nanowires landed across the source and drain. Of those which did, electrical contact was not made when tested with an I-V curve tracer. After applying a large voltage across the contacts, some devices began to conduct current, which served to burn-in the metal-nanowire interface, which may have been contaminated by metal and/or nanowire oxides or toluene residue. This is the main reason why Au was substituted for Al.

Figure 4 is the I-V curve of a working device. Application of low voltages is typically indicative of a nanowire channel. The graph resembles a back to back diode, and is applicable for this device.

Along with applying voltage to the source and drain, a voltage was also applied to the backgate to modulate the channel current. However after a number of attempts with different nanoFETs, modulation was not achieved. This was most likely due to the nanowire floating above the oxide surface instead of resting on the oxide, and the thickness of the oxide.

Conclusion:

Oxidation rates for SiO_2 were determined and gate oxides were successfully grown. I-V measurements confirmed the existence of a source-drain channel in the nanowire. Although we were unable to modulate the nanowire channel

in our devices, we were able to fabricate GaN nanoFETs using conventional fabrication processes. Although the method of depositing nanowires by dropping them in solution needs improving, nanowire were deposited this way. Perhaps a different solvent would help. To insure nanowires-oxide contact in the future, the source and drain spacing could be widened to allow the nanowires to hang down and the thickness of the source-drain contacts could be made thinner.

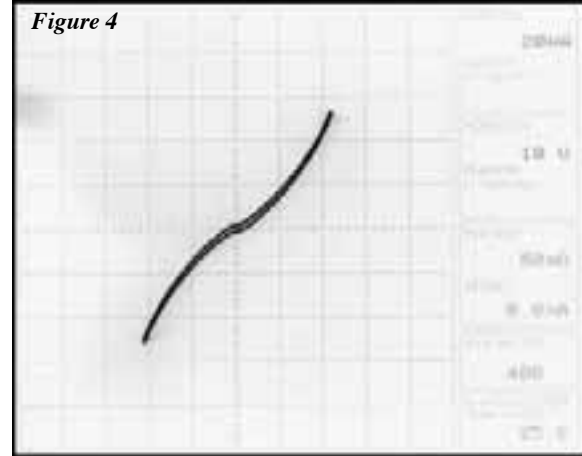
Acknowledgements:

Being a part of this research experience has been like no other. Thus, I would like to thank Dr. Gary Harris, Dr. William Rose, and Mr. James Griffin for all their help, support, and advice. I would also like to spread gratitude to the National Science Foundation (National Nanotechnology Infrastructure Network Research Experience for Undergraduates (NNIN REU) Program. A last, but certainly not least, thanks goes to the entire HNF staff for all their support.

References:

- [1] Ayres, V. M. "Investigations of Heavy Ion Radioation of Gallium Nitride Nanowires and Nanocircuits." Diamond and Related Materials (2006). Science Direct. Web. 7Feb2006. <<http://www.sciencedirect.com>>.
- [2] Zhou, Z. (James). Photolithography and Mask Creation at MiRC. Georgia Institute of Technology. 30 Sept. 2003. Web. 22 June 2010.

Figure 4



Heterojunction Growth of $\text{Si}_{1-x}\text{Ge}_x$ and C_3N_4 Nanowires on Silicon

Siatta Adams
Chemistry, Mercer University

NNIN REU Site: Howard Nanoscale Science and Engineering Facility, Howard University, Washington, DC

NNIN REU Principal Investigator(s): Dr. Gary Harris, Electrical Engineering, Howard University

NNIN REU Mentor(s): Mr. Crawford Taylor, Electrical Engineering, Howard University

Contact: osiatta@gmail.com, gharris@msrce.howard.edu, crawford@msrce.howard.edu

Abstract:

Silicon germanium ($\text{Si}_{1-x}\text{Ge}_x$) and carbon nitride (C_3N_4) nanowires (NWs) constitute promising building blocks for future electronic and medical applications respectively. SiGe's energy bandgap and thermal conductivity makes it very attractive for use in mobile communication applications. On a nearly strain free material, the energy-band discontinuity of SiGe allows for enhanced speed and performance, allowing for smaller and more defect free transistors. Carbon nitride has promising biological applications for the treatment of breast cancer. Carbon nitride nanowires conjugated to Herceptin can selectively target breast cancer cells.

Silicon germanium and carbon nitride nanowires were grown using chemical vapor deposition (CVD). Wires were grown on silicon substrates of $<111>$ and $<100>$ orientation with metal catalysts (5 nm and 20 nm gold nanoparticles (Au NPs), and 1 nm and 3 nm thick nickel (Ni), aluminum (Al) and platinum (Pt) films). High purity silane (SiH_4) and germane (GeH_4) were used for the synthesis of SiGe NWs. Carbon nitride nanowires were grown using high purity propane (C_3H_8) and ammonia (NH_3) gas. The synthesized nanowires were then studied by energy dispersive spectroscopy (EDS), Raman and Auger spectroscopy. The SiGe NWs were 100-300 nm in diameter with an average length of greater than 200 μm .

Introduction:

Nanowires will play a key role in future electronic and optoelectronic devices [1] due to their relatively easy and low-cost synthetic preparation by CVD [2]. Researchers are interested in silicon-germanium and carbon nitride because of their abilities to produce high performance devices. Group IV NWs (Si, Ge, and SiGe) are ideal for complementary metal oxide semiconductor (CMOS) processes [3]. Nitrogen's presence within the carbon nanostructures can enhance the mechanical, conducting, field emission, and energy storage properties of materials making for more efficient electronic devices. This has been the driving force behind C_3N_4 NWs. This work studied the effects of SiH_4 and C_3H_8 concentration on the synthesis of silicon-germanium and carbon nitride NWs respectively by CVD.

Experimental:

SiGe and C_3N_4 NWs were synthesized using a cold-walled reduced pressure CVD reactor. NWs were grown on an Si wafer of $<111>$ and $<100>$ orientation with gold (Au), nickel (Ni), aluminum (Al), and platinum (Pt) metal catalysts.

Si wafers were first washed with acetone, followed by isopropyl alcohol to remove any surface contaminants and then dried using nitrogen (N) gas. Three nanometers of Ni

and 1 nm of Al were deposited on the surface by electron-beam evaporation to serve as metal catalysts for SiGe and C_3N_4 , respectively. Poly-l-lysine (0.1 v/w) was used as an adhesive to apply Au NPs to the Si wafer.

The samples were dipped in poly-l-lysine for two minutes, then rinsed with deionized (DI) water, and dried with nitrogen before being washed with a 10% isopropyl solution. After washing, the samples were dipped into either a 5 nm or a 20 nm Au NP solution (7×10^{11} particles/ml) for two minutes. The samples were then rinsed with DI water and dried in an oven for 30 minutes. Finally, any remaining organic traces were removed by a 200W oxygen plasma step for two minutes. The Pt catalyst was deposited by sputtering at a current of 2 mA and a voltage of 8kV for five minutes. After deposition of the metal catalysts, substrates were then placed in a horizontal quartz tube in a cold-wall CVD reactor. The chamber was pumped down to 10 mtorr and purged with H_2 for 10 minutes.

Growth parameters for SiGe and C_3N_4 were determined from the previous work of Givian, et al. [1] and Sakamoto, et al. [4], respectively. Table 1 lists the growth parameters of both SiGe and C_3N_4 . Energy dispersion spectroscopy (EDS) was used to analyze the NWs composition.

Results and Conclusions:

Figure 1(a) shows a scanning electron microscopy (SEM) image of the SiGe NWs, and Figure 1(b) shows the spectral analysis of the NWs. The highest atomic percentage of germanium was 3.83 in all SiGe NWs grown.

The diameter of SiGe NWs was between 100-300 nm. Optimal NW growth was achieved with Au NPs at a temperature of 700°C with gas flow ratio of 15/10 standard cubic centimeters per minute (sccm) for SiGe. No growth was observed with Al and Ni catalysts. Pt produced micro-sized NWs, with gas flow ratios of 100/5 sccm for SiGe at 700°C. Shorter wires were observed when the concentration of silane was increased. Silane concentration on the synthesis of SiGe NW showed that higher concentrations of germane affected the length of the wires. Silane concentration also affects the amount of germane present in NWs. NWs with high Ge content were observed when germane concentrations exceeded that of silane.

Figure 2 shows an SEM image of carbon nitride rods. Rods grew at 950°C with the gas flow rates of 10 and 20 sccm for propane and 200 sccm for ammonia. Large growth clusters were seen on <111> and <100> wafers coated with the Ni catalyst. Au, Al and Pt catalysts had no rod growth. Results for carbon nitride rods were inconclusive due to the difficulty in obtaining elemental nitrogen within the reactor.

Acknowledgements:

I would like to thank Dr. Gary Harris, Crawford Taylor, James Griffin, Karina Moore, Mallory Lambert and all other faculties at the Howard Nanoscale Facility. I would also like to extend my gratitude to both the NNIN REU Program and the NSF for funding this research project.

References:

- [1] Givan, U., and Patolsky, F. "Pressure Modulated Alloy-Composition in $\text{Si}_{1-x}\text{Ge}_x$ Nanowires"; *Nano Letters* Vol. 9 No. 5, 1775-1779.
- [2] X.-J. Huang, S.-W. Ryu, H.-S. Im, and Y.-K. Choi. Wet Chemical Needlelike Assemblies of Single-Walled Carbon Nanotubes on a Silicon Surface. *Lagmuir* 2007, 23, 991-994.
- [3] X. Lu, H. Wang, S. Zhang, D. Cui, and Q. Wang. "Synthesis, Characterization and Electrocatalytic Properties of C₃N₄ NTs for Methanol Electrooxidation"; *Solid State Science* 11 (2009), 428-432.
- [4] Sakamoto, Y., and Takaya, M. "Growth of carbon nitride using microwave plasma CVD"; *Thin Solid Films* 475 (2005) 1981-201.

C ₃ H ₈ flow rates (SCCM)	7, 10, 20, 30, 40, 50
NH ₃ (SCCM)	100
Pressure	200 torr
Growth temperature	950-1100°C
SiH ₄ flow rates (SCCM)	5, 15, 100
GeH ₄ (SCCM)	10
Pressure	200 torr
Growth temperature	700-900 °C

Table 1: Growth parameters of C₃N₄ and SiGe.

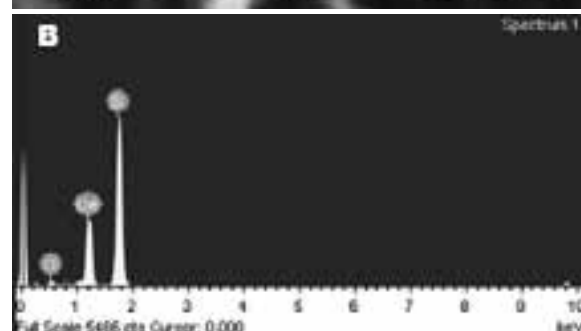


Figure 1: A (top), SEM of SiGe NWs on 20 nm gold nanoparticulates <100> orientation. B (bottom), EDS spectrum of SiGe NWs.

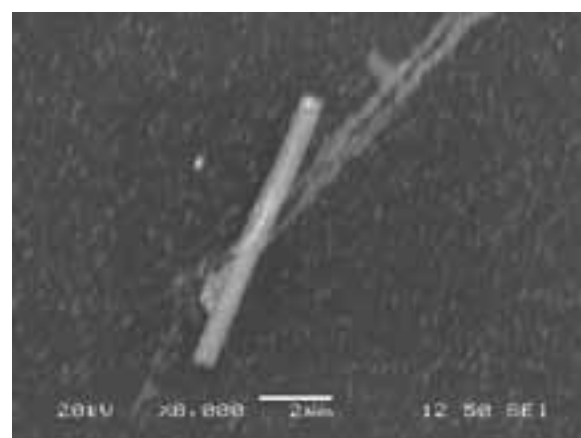


Figure 2: Carbon nitride rods in Ni <100> catalyst.

Nanoparticle-Enhanced Tunnel Junctions for High-Efficiency Multi-Junction Solar Cells

Gavin P. Campbell

Materials Science and Engineering, University of Illinois at Urbana-Champaign

NNIN REU Site: Microelectronics Research Center, The University of Texas, Austin, TX

NNIN REU Principal Investigator(s): Seth R. Bank, Electrical Engineering, University of Texas at Austin

NNIN REU Mentor(s): Adam C. Crook, Electrical Engineering, University of Texas at Austin

Contact: campbel2@uillinois.edu, sbank@ece.utexas.edu, acrook@mail.utexas.edu

Abstract:

Multi-junction solar cells employ tunnel junctions to interconnect the serially-connected p/n junctions. Erbium arsenide nanoparticle (ErAs NP)-enhanced tunnel junctions, grown on gallium arsenide, have Schottky-like tunneling barriers that show substantial improvements in tunneling current density, when compared to conventional p/n junctions. Future multi-junction solar cells incorporate dilute-nitrides to achieve technologically significant band-gaps, which require thermal annealing to remove point defects from the gallium indium nitride arsenide (GaInNAs) lattice. Preliminary data indicates that post growth thermal annealing can enhance the tunneling currents of nanoparticle-enhanced tunnel junctions; however, thermal annealing has not been carefully studied. We are performing the first careful study of thermal annealing, consisting of an *in situ* and *ex situ* study. Results of the study suggest erbium arsenide tunnel junctions improve with thermal annealing.

Introduction:

A single p/n junction extracts one band-gap of energy per photon. Multi-junction solar cells use multiple junctions to divide the solar spectrum and increase efficiency. Tunnel junctions are used to serially interconnect p/n junctions. Current multi-junction solar cell design incorporates an overdriven germanium (Ge) junction. Adding a 1.0 electron volt material junction bifurcates the Ge junction without a substantial loss in junction performance. Dilute-nitrides are a potential candidate for the new junction material. As seen in Figure 1, GaInNAs can achieve the technologically significant 1.0 electron volt band-gap while maintaining the same lattice parameter as gallium arsenide (GaAs). However, GaInNAs requires a post-growth thermal anneal to reduce point defects.

Conventional tunnel junctions are formed from a heavily doped p/n junction. However, there is a doping limit due to material properties. Erbium arsenide (ErAs) nanoparticles deposited at the p/n junction form back-to-back Schottky contacts and leads to a significant improvement in tunneling current density. As shown in Figure 2, incorporating ErAs nanoparticles at the p/n junction effectively splits the tunneling barrier, reducing height and width. In order to function in a multi-junction solar cell, erbium arsenide nanoparticles must be robust to thermal annealing associated with dilute-nitrides. We are performing the first in-depth thermal annealing study of erbium arsenide nanoparticle-enhanced tunnel junctions.

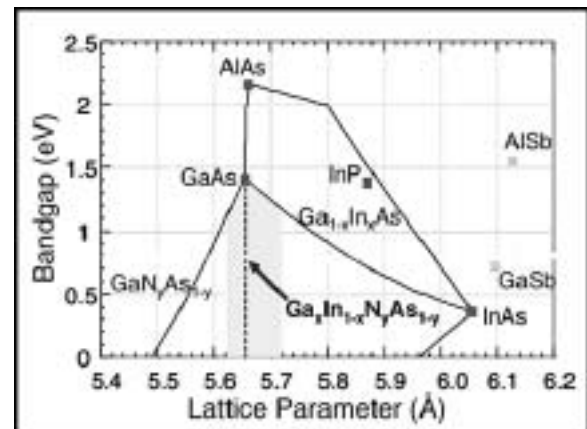


Figure 1: Band-gap versus lattice parameter for various semiconductors. GaInNAs varies with composition.

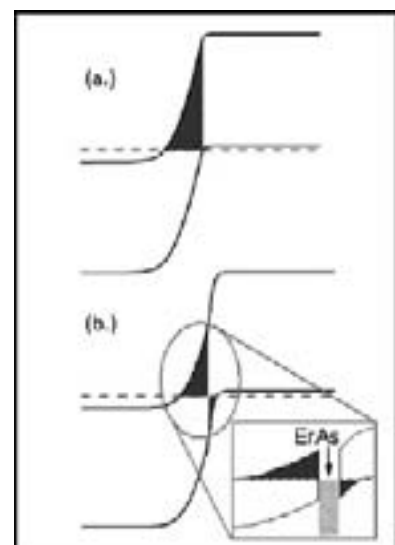


Figure 2: Band diagram of; (a) a conventional heavily doped p/n tunnel junction, and (b) an ErAs NP-enhanced tunnel junction. The shaded triangular regions represent the tunneling barriers.

Experimental Procedure:

We performed an *in situ* and an *ex situ* annealing study to mimic the conditions of multi-junction solar cell growth and the post-growth anneal required for dilute-nitrides. Heavily n-doped GaAs, ErAs NPs, followed by heavily p-doped GaAs were deposited on an n-doped GaAs substrate using molecular beam epitaxy. The *in situ* anneal occurred at 600°C under an arsenic flux. The *ex situ* anneal was performed in a rapid thermal annealer at varying temperatures for one minute under a nitrogen flux. For top contact lithography, we employed an image reversal photoresist, AZ 5214E-IR.

Immediately prior to both metallizations, the samples were treated with a hydrochloric acid to remove the native oxide. E-beam evaporation was employed for metallization; the top p-type contact consisted of 100 angstroms (Å) of titanium followed by 1000 Å of gold (Au). Lift-off took approximately 30 minutes in an agitated acetone bath. Bottom contact metallization consisted of 100 Å Au, 100 Å Ge, 100 Å nickel (Ni), and 1000 Å Au. The bottom contact metallization requires thermal treatment to improve contact quality. P-type and n-type doping calibration wafers were measured using the transmission line method to verify contact performance. Both the n-type and p-type contact showed acceptable performance after a 400°C anneal for one minute. After metallization, an inductively coupled plasma etch was used to etch through and isolate the tunnel junctions to improve measurement accuracy.

Measurements were taken using a four-point probe station to reduce parasitic resistance present in the probes. Two low resistance probes pushed current, while two high resistance probes measured the voltage difference. Current to voltage measurements were taken on circles of known radius. Tunnel junction resistance dominates for small mesa diameters. Therefore, a 35 nm diameter mesa was measured to extract the current density.

As shown in Figure 3, the *ex situ* annealed samples showed a substantial improvement in tunnel junction quality. The *in situ* annealing study, shown in Figure 4, also yielded an improvement in tunnel junction performance.

Results and Conclusions:

We have demonstrated erbium arsenide nanoparticle-enhanced tunnel junctions do not degrade, and in fact improve for both the *in situ* and *ex situ* anneal. The *ex situ* anneal demonstrates ErAs tunnel junctions are compatible with growth conditions of multi-junction solar cells. Whereas the *in situ* demonstrates the tunnel junctions are compatible with the post growth thermal anneal required for dilute-nitrides. The resulting tunnel junction resistance is acceptable for use in high-efficiency multi-junction solar cells. A publication will be prepared once a more complete thermal study and other ancillary experiments are performed.

Eventually, we would like to create a multi-junction solar cell incorporating both ErAs nanoparticle-enhanced tunnel junctions and dilute-nitrides.

Acknowledgements:

Thank you to Dr. Seth Bank, Adam Crook, LASE group, and the staff at Microelectronics Research Center at the University of Texas at Austin for assisting this research. This work was supported by the National Science Foundation and the National Nanotechnology Infrastructure Network Research Experience for Undergraduates Program.

References:

- [1] H. Nair, A. Crook, S. Bank; "Enhanced conductivity of tunnel junctions employing semimetallic NPs through variation in growth temperature and deposition"; *Appl. Phys. Lett.*, 96, 222104 (2010).
- [2] S. Bank; "Growth of 1.5 μ m GaInNAsSb Vertical Cavity Surface Emitting Lasers by Molecular Beam Epitaxy"; [dissertation], (2006).

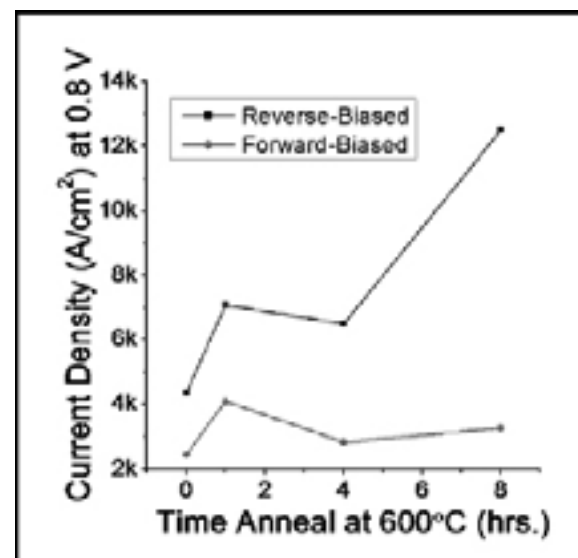


Figure 3: *In situ* anneal data at 0.8 volts.

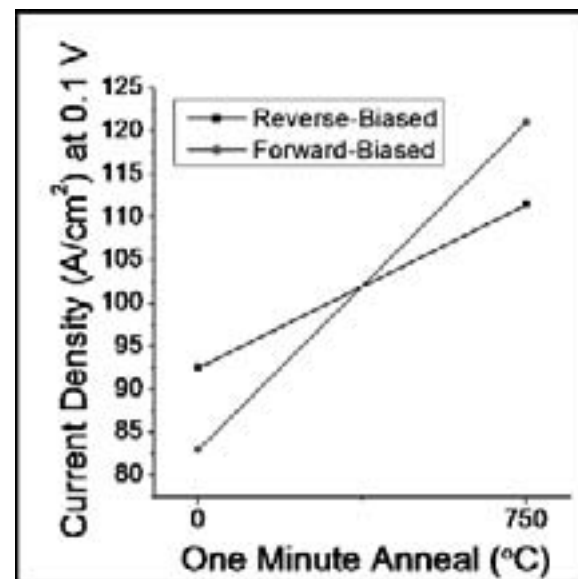


Figure 4: *Ex situ* anneal data at 0.1 volts.

Investigation of the Effects of Base Additives in Molecular Glass Photoresist Films

Sylvia Carroll

Electrical Engineering and Biology, University of Texas at El Paso

NNIN REU Site: Cornell NanoScale Science and Technology Facility, Cornell University, Ithaca, NY

NNIN REU Principal Investigator(s): Prof. Christopher K. Ober, Materials Science and Engineering, Cornell University

NNIN REU Mentor(s): Marie Krysak, Chemistry, Cornell University

Contact: scarroll@miners.utep.edu, cko3@cornell.edu, mek97@cornell.edu

Abstract:

Advances in the semiconductor industry are spurred by the need for higher resolution. To accomplish this, molecular glasses are used as photoresists in this project; they are potentially capable of higher resolution than traditional polymeric resists. Acid diffusion in the post exposure bake step leads to blur and widening of lines. This undesirable effect is counteracted by introducing a small concentration of base in the resist mixture. This project examines new base molecules with larger cores as opposed to commonly used base additives.

Introduction:

Molecular glasses possess several desirable qualities such as smaller molecule size and disordered arrangement, but enough cohesion to not be liquid [1]. A good resist has structural features that promote steric hindrance, such as a bulky, asymmetrical configuration. These properties also increase the glass transition temperature (T_g) [2]. The desired T_g is $> 80^\circ\text{C}$ because if it is too low, resist reflow will occur, and this decreases feature sharpness. Figure 1 shows the molecules that were studied.

These molecular glasses belong to the category of chemically amplified resists. They require a photoacid generator (PAG): a molecule added to the resist mixture which releases strong acid after exposure and post-exposure bake. In addition, some of the resist's free hydroxyl groups are protected with *tert*-butoxycarbonyl (*t*-BOC). Deprotection occurs when the *t*-BOC group is in the presence of acid, increasing solubility in the developer.

Some acid diffusion is desirable, as that is what creates the

pattern in the exposed area of the wafer, where the PAG is activated by UV and post-exposure bake. However, too much acid diffusion in the unexposed area will adversely affect resolution [3]. Some acid will migrate into the unexposed area. Hence the focus of this project: introducing base additives to counteract acid diffusion in the unexposed area. Base additives are not expected to affect the exposed area of the wafer, as there is so much more acid in that area. However, in the unexposed area the base will have more of an effect on a small amount of stray acid.

Experimental Procedure:

The resist mixture consisted of 57 mg resist, 5% photoacid generator with respect to resist, and 0.3% base additive with respect to resist. This was solvated with ethyl lactate to make a 5% solution. Wafers were spun for one minute at 2000 rpm with an acceleration of 1000 rpm/sec, followed by baking at 115°C for one minute. Exposure arrays were done using the Autostep AS200 365-nm stepper as well as the ASML PAS 5500 deep-UV stepper. Post-exposure bake was 80°C for one minute, then wafers were developed using dilutions of 0.26 N tetramethylammonium hydroxide. The amount of time and the strength of dilution were varied.

Contrast curves were constructed using the ABM contact aligner with a 254 nm mirror. The sensitivity was the exposure dose required to clear 50% of the resist, while the dose to clear was the exposure dose required to clear all the resist [1].

Etch rate studies were performed in order to further characterize the behavior of resist/base systems. Three etch gases were tested: trifluoromethane (CHF_3), tetrafluoromethane (CF_4), and sulfur hexafluoride (SF_6). Figure 4 shows the etch conditions, as well as the etch results.

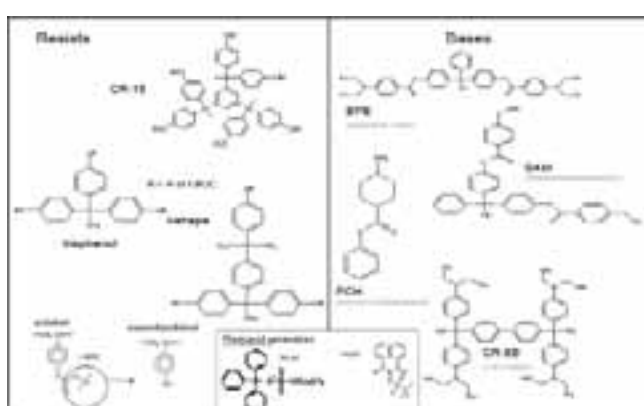


Figure 1: Resists, bases, and photoacid generators.

Results and Discussion:

Exposure arrays were done on the AutoStep i-Line stepper for combinations of the resists and bases shown in Figure 1, as well as control wafers of resist without base. Neither trisphenol resist nor BPB base produced any image and were eliminated from consideration. The remaining combinations were redone on the ASML deep-UV stepper, and we found that the consistently best-performing base was the BAM base, which gave the smallest lines as well as the best quality.

Figure 3 shows 254 nm contrast curves for all resist/base systems. It is found that in general, base additives are seen to increase sensitivity. The etch rate studies, shown in Figure 4, show that BAM base increases etch resistance in all etch gases. In addition, an Ohnishi number and ring parameter were calculated for each resist/base system; a small Ohnishi number or large ring parameter should correspond to a low etch rate, i.e., high etch resistance [4]. The measured data were found to deviate from the predictions, however this can be accounted for by the fact that the models were originally developed for polymers and hence are inadequate for molecular glasses.

Future Work:

Since BAM base has consistently shown to be the best-performing base, further studies on it are warranted, such as testing it on higher-resolution equipment. In addition, it would be useful to expand the study to even more base additives for comparison purposes, such as aminosulfonate onium salts.

Acknowledgements:

The author wishes to thank the NSF, the NNIN REU Program, and the CNF. Special thanks go to Prof. C.K. Ober and Marie Krysak, as well as Rob Ilic and Melanie-Claire Mallison (CNF REU Program Coordinators), and the CNF staff, especially G.J. Bordonaro (helped with ASML) and D.A. Westly (helped with SEM).

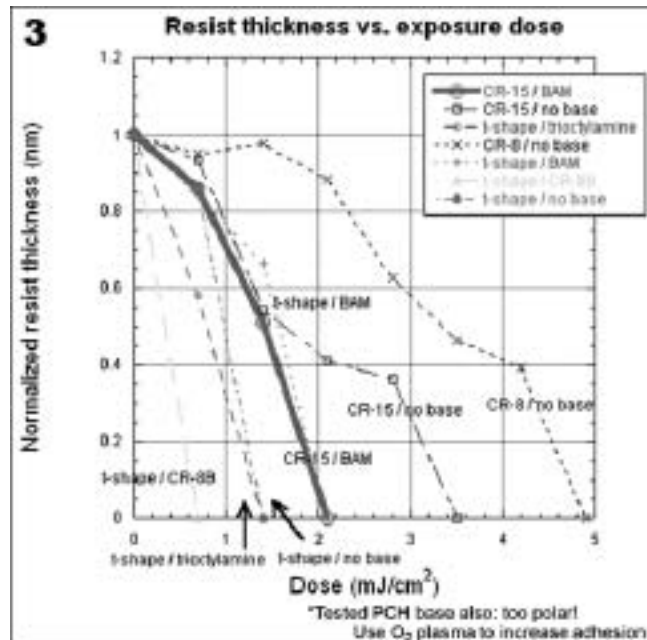
References:

- [1] Ito, H. Chemical amplification resists for microlithography. *Adv Polym Sci*, 172, 37-245. (2005).
- [2] De Silva, A., Lee, J.K., Andre, X., Felix, N.M., Cao, H.B., Deng, H., and Ober, C.K. Study of the Structure-Properties Relationship of Phenolic Molecular Glass Resists for Next Generation Photolithography. *Chem Mater*, 20 (4), 1606-1613. (2008).
- [3] Pawloski, A.R., and Nealey, P.F. The Multifunctional Role of Base Quenchers in Chemically Amplified Photoresists. *Chem Mater*, 14 (10), 4192-4201. (2002).
- [4] Gogolides, E., Argitis, P., Couladourous, E.A., Vidali, V.P., Vasilopoulou, M., Cordoyannis, G., Diakoumakos, C.D., and Tserepi, A. Photoresist etch resistance enhancement using novel polycarbocyclic derivatives as additives. *J Vac Sci Technol B*, 21(1), 141-147. (2003).

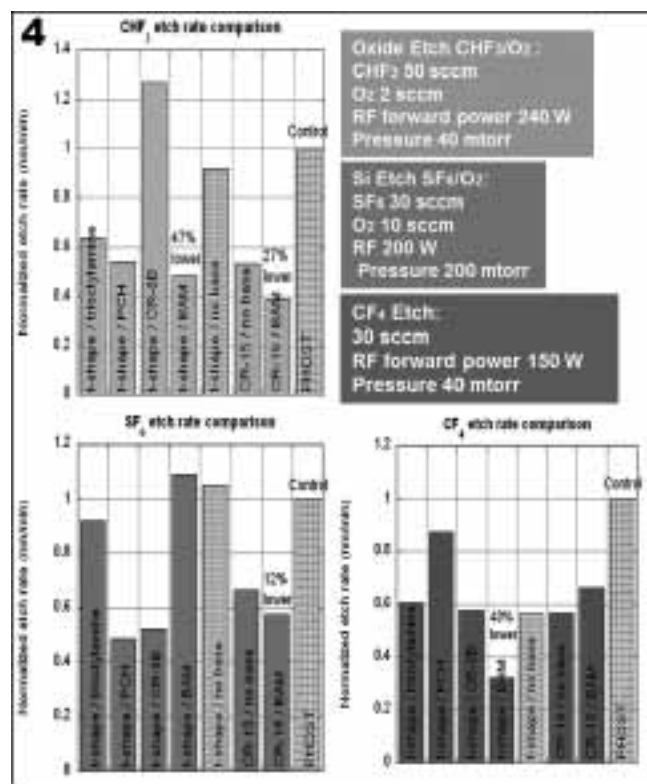
Figure 2, top: Representative ASML lines with t-shape resist and BAM base.

Figure 3, middle: 254-nm contrast curves.

Figure 4, bottom: Etch rate studies.



*Tested PCH base also: too polar!
Use O₂ plasma to increase adhesion



Contact Resistance of Graphene-Based Devices by TLM

Arolyn Conwill

Physics, Pomona College (undergraduate)

Massachusetts Institute of Technology (graduate)

NNIN iREU Site: National Institute for Materials Science, Tsukuba, Ibaraki, Japan

NNIN iREU Principal Investigator(s): Dr. Yasuo Koide, National Institute of Materials Science, Tsukuba, Japan

NNIN iREU Mentor(s): Dr. Eiichiro Watanabe and Dr. Daiju Tsuya, National Institute of Materials Science, Tsukuba, Japan

*Contact: amc02006@mymail.pomona.edu, koide.yasuo@nims.go.jp,
watanabe.eiichiro@nims.go.jp, tsuya.daiju@nims.go.jp*

NNIN iREU Program

Introduction:

Graphene is a 2D allotrope of carbon atoms arranged in a planar, hexagonal lattice. It features useful electronic properties [1] including bipolarity, high purity, high mobility, and high critical current density. Bipolarity refers to its ability to transport charge using either electrons or holes; the carrier type can be controlled by applying a gate voltage which shifts the Fermi energy. Graphene's high purity, mobility, and critical current density reflect its reliability and accessibility, its responsiveness to electric fields, and its resistance to breakdown. Hence graphene is considered a promising material for future electronic devices.

Crucial to the realization of feasible graphene devices are metal-graphene connections with low contact resistance. Contact resistance is the portion of total resistance attributed to the metal lead or its connection to the graphene, as opposed to the graphene itself. Initial studies [2] have informed us that contact resistance is a significant portion of total resistance. Prior work is inconclusive, some reporting that contact resistance is gate-independent [2], but others reporting both gate independent and dependent contributions [3].

We were interested in the relation of contact resistance to carrier type and to sheet resistance. We tested basic graphene transistors which consisted of metal contacts connected to

each side of a rectangular graphene strip separated from the gate by a substrate. Figure 1 is a top view optical image of a sample with many devices where the black leads make contact with the darker gray graphene strips of varying length. Here, we examined titanium/gold (Ti/Au) contacts as a starting point because they are most common.

Experimental Procedure:

Fabrication. We deposited graphene, originating from Kish graphite, by exfoliation onto an silicon/silicon dioxide (Si/SiO₂) substrate. We used the electron beam lithography system to expose the graphene etch pattern into poly(methyl methacrylate) (PMMA) resist atop an hexamethyldisilazane (HMDS) adhesion layer. Reactive ion etching (RIE) with oxygen plasma removed the excess graphene such that only rectangular strips remained. We dissolved the protective resist layer with n-methyl-2-pyrrolidone (NMP) at 80°C.

Next, we fabricated metal contacts in two stages. First, we placed metal leads, separated by half and whole micron intervals, along the graphene strips. We used e-beam lithography to transfer the lead pattern to a PMMA bilayer (PMMA atop MMA/MAA EL12), e-beam evaporation to deposit Ti/Au, and lift-off in NMP to produce the leads. Second, we extended the metal leads with metal pads that were large enough to be accessed by macroscopic electrical probes. We used the laser lithography system to pattern a PMGI SF9 and TSMR8800 photoresist bilayer, the sputtering system to deposit metal, and NMP for lift-off. Finally, the devices were annealed at 300°C for 5 min in Ar.

Characterization. The transfer length measurement (TLM) method regards total resistance, R_T , as having two terms, according to Equation 1.

$$R_T = \frac{R_S}{W_{ch}} d + 2R_C$$

Equation 1: Total resistance as a function of lead separation.

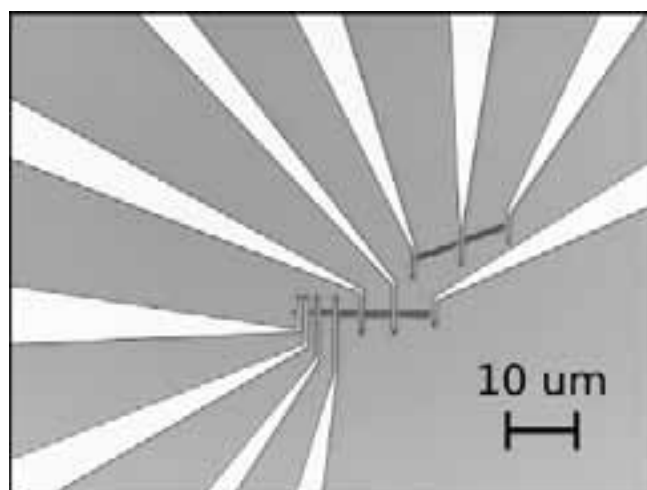


Figure 1: Graphene device with leads.

The first term is directly proportional to d , the separation between leads, and accounts for the contribution to resistance from the graphene sheet (R_s is sheet resistance and W_{ch} is channel width). The remaining term is twice the contact resistance, R_c , representing the resistance from the two contacts per device. We report measurements for both contact resistance, R_c , and transfer length, L_t . Transfer length is the distance the current flows through the graphene below the contact and is another indicator of contact quality. L_t is approximately equal to half the horizontal intercept and R_c to half the vertical intercept of an R_c versus d line. The contact resistivity, ρ_c , is equal to the sheet resistance multiplied by the transfer length squared.

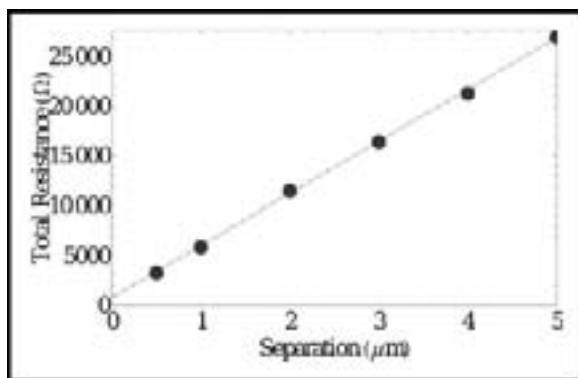


Figure 2: Total resistance versus lead separation.

Upon completing the fabrication of a device, we first verified that the contacts were ohmic, that is, that the drain current was directly proportional to the drain voltage. Then, we varied the gate voltage (thus changing the carrier type) and measured the total resistance. This measurement yielded a peak-shaped curve where the maximum resistance occurred at the Dirac point, the point at which carrier type changes. For each lead separation, we recorded resistance at the Dirac point and at ± 10 volts to either side. We fit a line to a graph of total resistance versus lead separation (see Figure 2), from which we extracted contact resistance and transfer length following Equation 1.

Results and Conclusions:

The TLM analysis suggests that contact resistance is independent of carrier type. In addition, we find that both contact resistance and specific contact resistivity are independent of sheet resistance (the two-dimensional

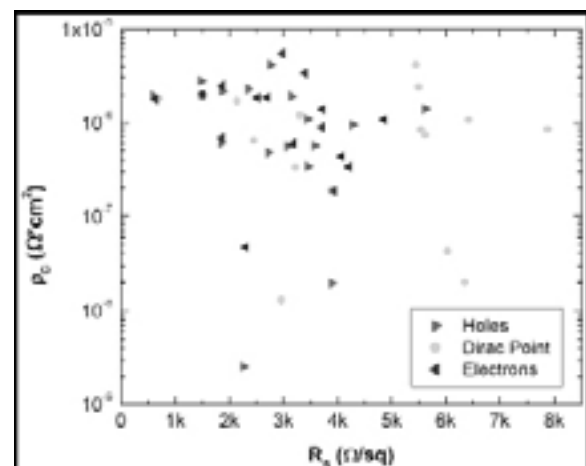


Figure 3: Contact resistivity versus sheet resistance.

analogy to resistivity). Figure 3 plots contact resistivity, ρ_c , versus sheet resistance where green squares indicate data taken at the Dirac point and triangles indicate data taken for holes and electrons. The majority of our devices feature ρ_c values on the order of $10^{-6} \Omega \cdot \text{cm}^2$ or less, which is one order of magnitude lower than previously reported values for ρ_c in graphene devices [2].

Future work will involve testing a variety of types of metals as contacts in order to determine the dependence of contact resistance on variables such as metal work function. This property is of particular interest because [4] has already demonstrated that, in the case of carbon nanotubes, contact resistance is dependent on the metal's work function.

Acknowledgments:

I would like to acknowledge the National Nanotechnology Infrastructure Network Research International Experience for Undergraduates (NNIN iREU) Program and the National Science Foundation (NSF) for funding. I would also like to thank the National Institute for Materials Science (NIMS) in Tsukuba, Japan, for hosting me, especially Dr. Yasuo Koide (group leader) as well as Dr. Eiichiro Watanabe and Dr. Daiju Tsuya (mentors).

References:

- [1] K. S. Novoselov et al., *Science* 306, 666 (2004).
- [2] A. Venugopal et al., *Applied Physics Letters* 96, 013512 (2010).
- [3] S. Russo et al., *Physica E* 42, 677 (2010).
- [4] Y. Noshio et al., *Nanotechnology* 17, 3412 (2006).

Aluminum Induced Crystallization of Silicon on Quartz for Silicon Wire Array Solar Cells

Natalie M. Dawley
Physics, University of Virginia

NNIN REU Site: Penn State Nanofabrication Laboratory, The Pennsylvania State University, State College, PA

NNIN REU Principal Investigator(s): Prof. Joan M. Redwing, Materials Science and Engineering, Pennsylvania State University

NNIN REU Mentor(s): Dr. Chito E. Kendrick, Department of Materials Science and Engineering, Pennsylvania State University

Contact: nmd8d@virginia.edu, jmr31@psu.edu, cuk11@psu.edu

Abstract:

Radial junction silicon (Si) wire array solar cells are being developed as an inexpensive and potentially more efficient alternative to planar crystalline Si solar cells. Currently, Si wires are grown on bulk Si substrates, an expensive commodity. Aluminum-induced crystallization of Si on quartz was studied as a low cost substitute for bulk Si wafers for wire array growth. Samples were prepared with a quartz / 100 nm aluminum (Al) / 100 nm amorphous Si layer structure and were annealed in nitrogen at 550°C to facilitate Al/Si layer transfer and Si crystallization. Crystallized Si regions up to 50 μm in size were obtained. X-ray diffraction (XRD) and Raman spectrometry analysis confirmed the formation of polycrystalline Si islands. Samples with successful Al/Si layer exchange were then tested as a substrate for Si nanowire growth.

Introduction:

Aluminum-induced crystallization (AIC) of silicon was studied as a low cost alternative to fabricate a thin (100-500 nm) silicon <111> layer on quartz. The <111> orientation is required for the growth of vertically oriented silicon wires, which are preferred for the solar cell fabrication [1].

The AIC process consists of depositing layers of aluminum (Al) and amorphous silicon (α -Si) which are then annealed below the eutectic temperature of silicon, 577°C. During the annealing process, the Si diffuses into the Al layer, at a high enough concentration nucleates and grows, forming a bottom layer of crystalline Si with an Al surface layer [2].

Experiment:

To create the crystalline Si layer, via Al-induced crystallization, 100 nm layers of Al and amorphous silicon (α -Si) were deposited on a quartz substrate using chemical vapor deposition (Semicore electron-gun evaporator). Two types of α -Si were examined, pure and hydrogenated (Applied Materials (AMAT) P-5000 PECVD Cluster tool). The surface of the aluminum layer was oxidized by controlled exposure to air before Si deposition; air exposure has been reported to promote Si <111> during the AIC process [3]. Two samples were investigated for Si wire growth, as tabulated in Table 1.

Name	Al	Air Exposure	α -Si	α -Si tool
Sample 1	100 nm	3 days	105 nm	Semicore
Sample 2	100 nm	1 day	140 nm	AMAT cluster tool

Samples were annealed in a tube furnace at 550°C for a set amount of time, under nitrogen gas flow. The Al was then removed using a commercial etching solution (Type A, Transene Co.) so that only the crystallized Si layer remained. The annealed and etched samples were then characterized. The crystallization process and surface morphology were examined using a scanning electron microscope (SEM) and optical microscope. The quality of the crystallized Si and its orientation were studied with x-ray diffraction (PANalytical X'Pert Pro MPD) and Raman spectroscopy (Renishaw micro-Raman Spectrometer).

A developed wire growth technique was then used on annealed and etched samples that included seeding the substrates with gold and annealing in a furnace with 35 sccm of SiCl_4 in 65 sccm of H_2 at 1050°C for 1.5 min [4].

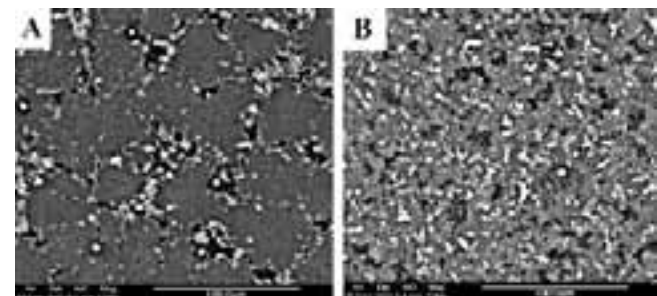


Figure 1: SEM images of A) Sample 1, and B) Sample 2, annealed for 42 hours.

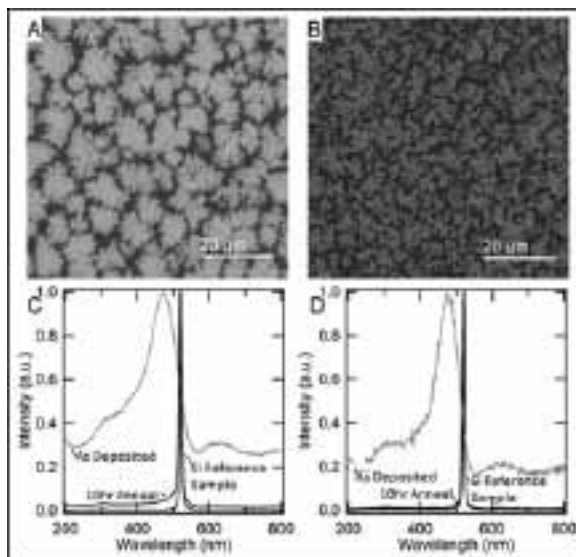


Figure 2: Optical microscopy and Raman Spectroscopy of 10hr annealed Sample 1 a) and c) and Sample 2 b) and d).

Characterization and Results:

Figure 1a shows the top surface of the Semicore crystallized Si, with relatively flat, 'blotchy' nucleation islands. The hydrogenate α -Si was found to produce nucleation with porous dendritic growth and a rough textured surface as shown in Figure 1b. To examine the quality of the crystallized Si, Raman spectroscopy was done, shown in Figure 2c and d.

Both samples showed a transition from α -Si to poly-Si after the annealing process. The Raman data showed the crystallinity of the poly-Si of both samples was of high quality as it closely matched the crystallinity of commercial polycrystalline Si wafers.

To confirm the orientation of the crystallized Si, each sample was examined with x-ray diffraction, shown in

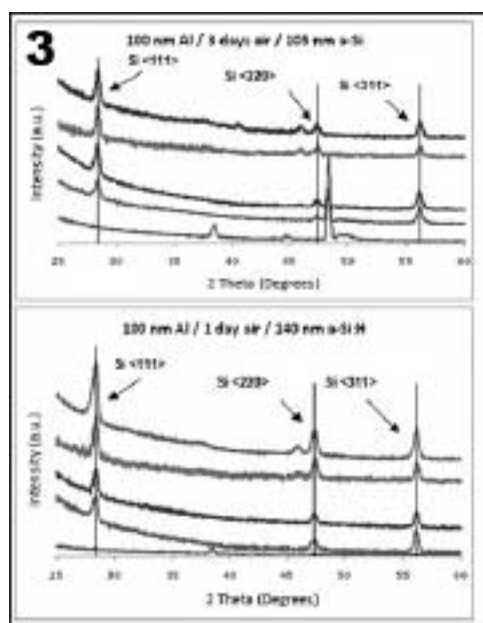


Figure 3: X-ray diffraction spectra of Samples 1 and 2 with increasing annealing times. The bottom spectrum is the as-deposited Al/ α -Si. Following that is the 4hr, 10hr, 24hr, and 42hr anneal.

Figure 3. The x-ray diffraction patterns confirmed that the Si was polycrystalline and exhibited some <111> orientation needed for vertical wire growth.

Wire Growth:

Samples were used as the base for patterned Si wire growth. Wire growth was achieved on Al-induced crystallization samples as seen in Figure 4. Wires grew in randomly oriented directions with some kinks due to the polycrystalline nature of the Si confirmed with x-ray diffraction.

Conclusion:

Al-induced crystallization was found to effectively crystallize α -Si as a low cost process. From scanning electron microscopy, it was found that the layer exchange process was still not complete after 40 hours of annealing. The annealed Si islands were found to be polysilicon from Raman measurements and x-ray diffraction. Samples were successfully used as a base for Si wire growth. Further optimization is needed of the Al-induced crystallization process.

Acknowledgments:

Special thanks to Dongjin Won, the Redwing group, and the Materials Research Institute staff at Penn State University. This project was funded by the National Science Foundation through the National Nanotechnology Infrastructure Network Research Experience for Undergraduates (NNIN REU) Program. Additional support was provided by the Department of Energy through grant DE-FG36-08GO18010.

References:

- [1] R. S. Wagner and W. C. Ellis, *Appl. Phys. Lett.* 4, No. 89 (1964).
- [2] O. Nast and S. R. Wenham, *J. Appl. Phys.*, Vol. 88, No. 1, (2000).
- [3] M. Kurosawa, N. Kawabata, T. Sadoh, and M. Miyao, *Appl. Phys. Lett.* 95, No. 132103 (2009).
- [4] J. Maoio III, B. Kayes, M. Filler, M. Putnam, M. Kelzenberg, H. Atwater, and N. Lewis. *J. Am. Chem. Soc.* 9 Vol. 129, No. 41, (2007).

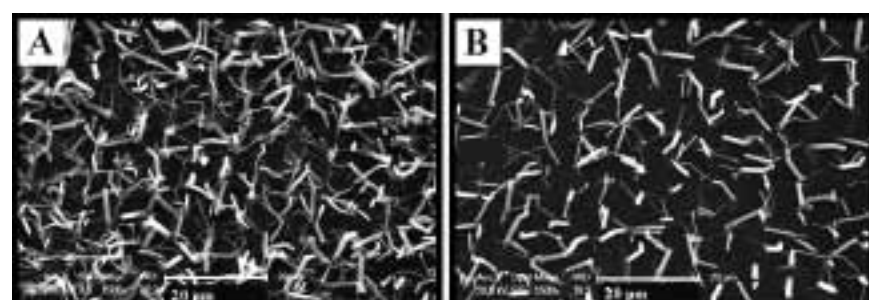


Figure 4: SEM images of Si wires grown on samples annealed for 24hrs. Image a) is Sample 1 and b) Sample 2.

Fabrication of Dendritic Electrodes for Electroactive Polymer Actuators

Nathaniel Hogrebe
Chemical Engineering, University of Dayton

NNIN iREU Site: Interuniversity Microelectronics Center (IMEC), Leuven, Belgium

NNIN iREU Principal Investigator(s): Dr. Hercules Neves, IMEC, Leuven, Belgium

NNIN iREU Mentor(s): Dr. Michael De Volder, IMEC, Leuven, Belgium

Contact: nathaniel.hogrebe@gmail.com, herc@imec.be, devol@imec.be

NNIN iREU Program

Abstract:

Dendritic microchannels were successfully created by the chemical dissolution of calcium sulfate dihydrate with water. In a second step, the negative shape of the channels was replicated by polydimethylsiloxane (PDMS) or a eutectic bismuth tin alloy. A proof of concept was delivered, although procedural difficulties prevented optimum results from being obtained. The low-melting metal offered the most promising results, and future work will attempt to improve on these methods to obtain tree-like electrodes with sub-micron branches.

Introduction:

Polymeric hydrogels can be tailored to respond physically to an applied voltage. An induced electric field causes them to either uptake or expel water, resulting in a physical expansion or contraction of the gel's overall shape [1]. Because of their controllable shape and biocompatibility, these gels can function as actuators in biochemical systems. One problem in implementing hydrogels, however, lies in the fact that their mechanical properties can become compromised if rigid electrodes are used to apply the electrical field. As the gel changes size, the non-uniform electric field and the localized stress around fixed electrodes either constrains the expansion of the hydrogel or causes the electrodes or gel to tear.

In order to solve this problem, a network of electrodes that moves with the expansion and contraction of the gel must be developed. As previously shown in literature, the chemical dissolution of plaster with water can be used to create fractal patterns [2]. These structures can then be molded to create positive casts of flexible, tree-like electrodes.

Experimental Procedure:

Calcium sulfate dihydrate ($\text{CaSO}_4 \cdot 2\text{H}_2\text{O}$), commonly referred to as gypsum, was first heated to over 150°C to dehydrate the crystalline structure to ordinary Plaster of Paris ($\text{CaSO}_4 \cdot 0.5\text{H}_2\text{O}$). Water was then mixed with the plaster in a 5:4 ratio by weight. The mixture was poured onto a 100 mm diameter metal plate with premade arrays of

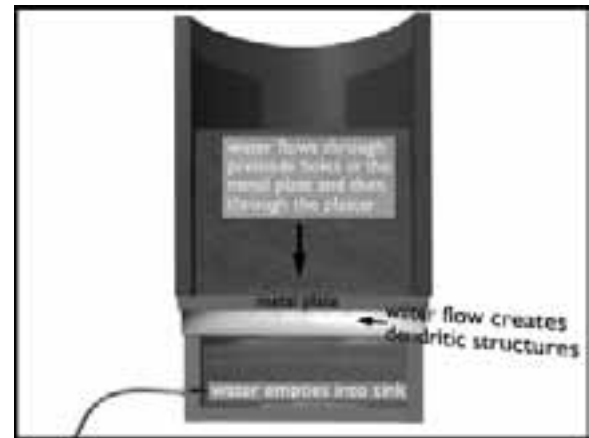


Figure 1: Setup for fabricating fractal patterns in plaster.



Figure 2: Dendritic structures created in plaster.

1 mm and 400 μm holes. After the plaster hardened, water was forced through the holes into the plaster via a reservoir on top of the plate. The size of the resulting fractal channels varied according to both the hole size of the metal plate and the pressure at which the water was injected. This water pressure was controlled by simply varying the height of the reservoir. Once the dendritic structures had formed, the plaster was removed from the plate. It was then baked again at over 150°C to dehydrate the crystalline structure back to $\text{CaSO}_4 \cdot 0.5\text{H}_2\text{O}$. This allowed for easy removal of the plaster from the molding material by placing it in water.

Two molding materials were used to create positive casts from the negative plaster molds. PDMS was poured into the channels, and the results of curing it under vacuum and at atmospheric pressure were compared. In the second method of casting, a eutectic bismuth tin alloy was melted and cast into the channels under pressure. Once the molding materials had hardened, the dehydrated plaster was placed in water to remove it from the dendritic structures.

Results and Conclusions:

Fractal structures were successfully fabricated within the plaster. The combination of a diffusion-limited chemical reaction between the water and plaster and the flow of the water through the porous media resulted in these branching structures [3]. The amount of branching was controlled by altering the force at which the water was pushed through the plaster. Higher pressures and longer flow times resulted in larger channels. In addition, structures created through the larger holes of the metal plate resulted in bigger structures.

Several problems were encountered when attempting to cast these structures due to the inherent porosity of the plaster. When casted under vacuum conditions, the low viscosity 184 PDMS entered not only the fabricated channels, but also the small pores within the plaster, making it impossible to separate the two materials. The high viscosity 186 PDMS, on the other hand, was unable to enter all the smaller channels. When the 184 PDMS was casted under atmospheric conditions, the tree-like structures could be removed manually from the plaster. When viewed under the scanning electron microscope (SEM), however, it could be seen that the plaster was still sticking to the PDMS, making the branches thicker and the fractal pattern less pronounced.

In order to solve these issues, a eutectic bismuth tin alloy was melted and cast into the channels under pressure. The molten metal was able to penetrate the larger channels and create free-standing structures that possessed high strength and yet flexibility due to the ductile characteristics of the material.

As a result of the crude nature of the injection setup, however, proper molding of the smaller channels was not achieved. Nevertheless, some of these initial experiments created free-standing micron-scale structures as well as branching formations, hereby providing a proof of concept for the proposed fabrication process.

Future Work:

A more advanced setup for the insertion of the molten metal into the plaster channels will be constructed in order to increase the injection pressure, resulting in a greater number of small branches. The goal of this future setup is to create tree-like electrodes with branch dimensions below $5\text{ }\mu\text{m}$ and implement them within electroactive hydrogels.

Acknowledgements:

This research was made possible by the National Science Foundation and the National Nanotechnology Infrastructure Network International Research Experience for Undergraduates Program. I would also like to extend special thanks to my mentor Dr. Michael De Volder along with Dr. Hercules Neves and everyone at IMEC for their help and support throughout the summer.

References:

- [1] Pons, Jose L. "Emerging Actuator Technologies: A Micromechatronic Approach." Chichester: John Wiley & Sons Ltd, 2005.
- [2] Daccord, Gerard, and Roland Lenormand. "Fractal patterns from chemical dissolution." *Nature* 325 (1987): 41-43.
- [3] Daccord, Gerard. "Chemical dissolution of a porous medium by a reactive fluid." *Physical Letters Review* 58 (1987): 479-482.

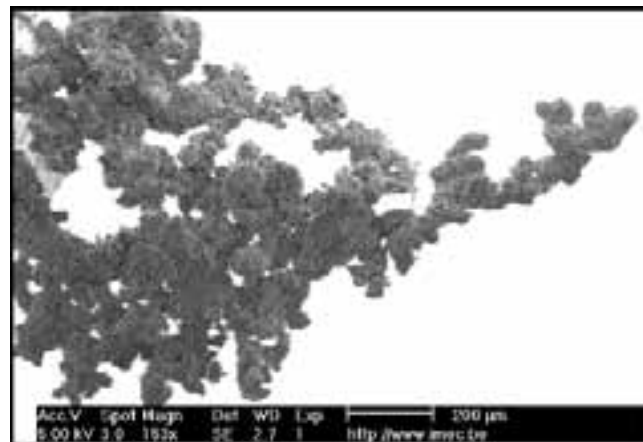


Figure 3: SEM of a PDMS tree casted from the plaster mold.

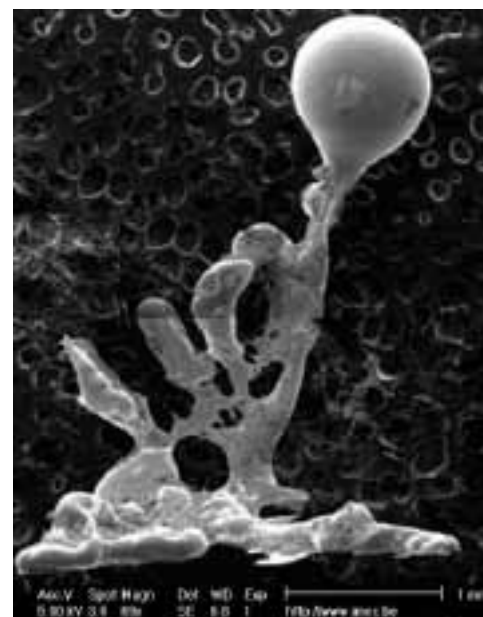


Figure 4: Bismuth tin alloy cast of a dendritic structure.

Grain Boundary Effects on Charge Transport In ZnO:Al Transparent Conducting Films

Ruby Lee

Bioengineering, Stanford University

NNIN REU Site: Center for Nanoscale Systems, Harvard University, Cambridge, MA

NNIN REU Principal Investigator(s): Professor Shriram Ramanathan, Engineering and Applied Sciences, Harvard University

NNIN REU Mentor(s): Dr. Rafael Jaramillo, School of Engineering and Applied Sciences, Harvard University

Contact: rubylee@stanford.edu, shriram@seas.harvard.edu, rjaramil@seas.harvard.edu

Abstract:

The work function of transparent conducting oxides is critical in determining the efficiency of charge transfer in certain solar cells and light emitting diodes. Previous research has indicated that this quantity is not well-described by the known properties of bulk zinc aluminum oxide (ZnO:Al), and may be strongly affected by grain boundaries. We have used Kelvin force microscopy for high resolution measurements of the work function, which is found to vary significantly on and off the grain boundaries. Our results show that work function granularity increases with oxygen content, due to the oxygen species segregated at the grain boundaries. This suggests that the work function can be tuned with post-processing treatments. Both exposure to UV/ozone and annealing in a hydrogen gas atmosphere are found to affect the material work function and the electronic granularity. It remains to be seen whether these treatments can be used to increase the efficiency of optoelectronic devices.

Introduction:

Transparent conducting oxides (TCOs) are materials commonly used in photovoltaics and other optoelectronic devices. Although indium tin oxide ($In_2O_3:Sn$) is currently the most widely used material on, zinc aluminum oxide (ZnO:Al) is becoming an attractive alternative due to improvements in processing techniques and lowered cost [1]. ZnO:Al films are also non-toxic and highly stable after heat cycles [2]. Thus, it is increasingly important to understand the electronic properties of this doped metal oxide on a nanostructure scale.

Kelvin force microscopy (KFM) is a powerful technique that uses an atomic force microscope to measure work function with nanometer resolution. We are interested in the work function, because it affects the performance of devices such as solar cells and light-emitting diodes. We have demonstrated through KFM measurements that work function varies significantly on and off grain boundaries of ZnO:Al. We have also shown that post-processing treatments affecting the distribution of oxygen species at the grain boundaries can further modify the work function level and granularity of the material.

Methods:

Film Growth. ZnO:Al thin films were grown on soda lime glass by RF magnetron sputtering from a Zn:Al 1.2 wt.% target (99.99%, ACI Alloys, Inc.). The RF power, substrate heater temperature, Ar gas flow rate, and total process pressure were held constant at 100 W, 100°C, 40 sccm, and 2.5 mTorr, respectively, and all film thicknesses were nearly 350 nm. The maximum temperature attained at the substrate surface during growth is estimated to be 160°C. The three films measured differ only in oxygen content, controlled by O_2 process pressure which varied between 0.32 mTorr (oxygen-deficient), 0.36 mTorr (optimal), and 0.41 mTorr (oxygen-rich).

Kelvin Force Microscopy. In Kelvin force microscopy, a conductive tip scans across the sample surface, and an external bias is applied to null the electrostatic force between the tip and the sample. The magnitude of the bias is equal to the contact potential difference (CPD), which can then be used to calculate the work function of the sample. KFM was performed with MikroMasch DPE and DPER probes, and an Asylum Research MFP-3D atomic force microscope.

Post-Processing Treatments. The three ZnO:Al films of varying oxygen content were exposed to ultraviolet radiation and ozone under 500 Torr O_2 for one hour and two hours. The films were also annealed inside a Lindberg furnace at 400°C under Forming gas (95% He, 5% H_2) flowing at 300 sccm for one hour and two hours.

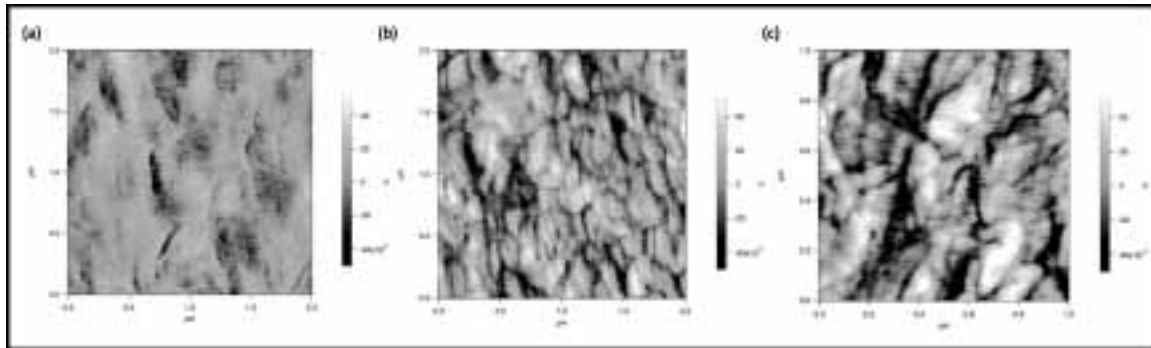


Figure 1: KFM measurements of (a) oxygen-poor, (b) optimal, and (c) oxygen-rich ZnO:Al films.
Data has been flattened in order to emphasize electronic granularity.

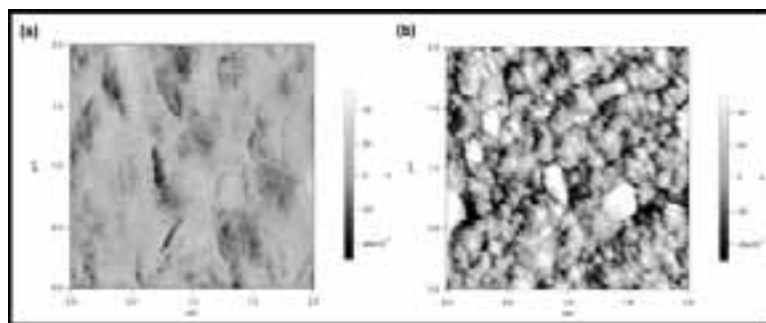


Figure 2: KFM measurements of oxygen-poor ZnO:Al film
(a) as-grown, and (b) after exposure to UV/ozone for 2h.

Results and Discussion:

As shown in Figure 1, the work function of ZnO:Al films varied significantly on and off grain boundaries. Both average work function levels and electronic granularity increased with oxygen content. We propose that this is due to the chemisorbed oxygen species at the grain boundaries, which form surface dipoles that increase work function. This implies that the work function can be further tuned with post-processing treatments that affect oxygen content at the grain boundaries. In Figure 2, work function granularity increased after exposure to UV/ozone for 2h.

Conclusion:

Our study has presented a novel use of KFM to measure work function across grain boundaries. With this technique, we have shown an increase in both work function level and electronic granularity due to oxygen content in ZnO:Al films. We have also demonstrated that post-processing treatments can be used to further tune the work function. We hope that these results will impact further investigation of the material properties of ZnO:Al as a transparent conducting oxide for electronic devices.

Acknowledgements:

I would like to thank Dr. Rafael Jaramillo and Dr. Shriram Ramanathan for their mentorship this summer, as well as Dr. Jiangdong Deng for his support on the atomic force microscope. I would also like to thank Dr. Kathryn Hollar, Dr. John Free, and Ms. Melanie-Claire Mallison for coordinating the Harvard and NNIN Research Experience for Undergraduates Programs. Finally, I would like to thank both the National Nanotechnology Infrastructure Network and the National Science Foundation for their generous funding.

References:

- [1] E. Fortunato, D. Ginley, H. Hosono, and D. Paine, MRS Bull. 32, 242 (2007).
- [2] M.L. Addonizio, A. Antonaia, G. Cantele, and C. Privato, Thin Solid Films 349, 393 (1999).

Adhesion of Capillary Underfill Epoxies for Flip Chip Packaging

Gillian Lui

Environmental Studies and Conservation Biology, Middlebury College

NNIN REU Site: Stanford Nanofabrication Facility, Stanford University, Stanford, CA

NNIN REU Principal Investigator(s): Professor Reinhold Dauskardt, Materials Science and Engineering, Stanford University

NNIN REU Mentor(s): Dr. Taek-Soo Kim, Materials Science and Engineering, Stanford University

Contact: gului@middlebury.edu, dauskardt@stanford.edu, tskim1@stanford.edu

Abstract:

Flip chip packaging is a popular means of compactly connecting silicon (Si) devices to their external circuitry. However, environmental factors can compromise the adhesive strength of capillary underfill epoxies used to seal and support the region between the devices and their substrates in such assemblies. In this study, methods of alleviating bisphenol-F (BPF) underfill epoxy delamination from Si through the addition of ductility-increasing flexibilizers and integration of organic-inorganic zirconium (Zr) hybrid layer sol-gels were explored. Double cantilever beam fracture mechanics tests used to quantify adhesive strength revealed that flexibilizers improve epoxy adhesion. Furthermore, through optimization of the hybrid layer preparation procedure, it was shown that while both stirring the sol-gel during aging and increasing the sol-gel cure time enhanced sol-gel adhesion, shorter sol-gel aging time most drastically improved upon the adhesion of hybrid layer-epoxy structures to silicon. These results, which identify flexibilizers and sol-gels as BPF adhesion promoters, will benefit the development of more reliable, high-performance microelectronics.

Introduction:

In flip chip packaging, Si devices are connected to their external circuitry with solder balls for space efficiency and reduced thermal resistance [1]. Underfill resins such as BPF-type epoxies can be deposited between the device and substrate to protect the device, enhance mechanical connectivity, and alleviate stresses from device-substrate thermal expansion mismatch [1]. However, standard processing and operating conditions of flip chip assemblies can introduce heat and moisture to the system, which accelerate epoxy delamination.

The addition of ductility-increasing flexibilizer functional groups to the epoxy matrix was investigated as one means of enhancing epoxy adhesion. Also explored were Zr sol-gels; graded hybrid films whose organic epoxy groups and inorganic Zr oxides covalently bind to organic epoxy surfaces and inorganic metal oxides on substrate surfaces, respectively (Figure 1). To determine BPF plus flexibilizer and hybrid layer (HL) effectiveness in improving upon BPF adhesion, their fracture energies, or the amount of energy per unit area required to propagate a crack through a material, were calculated using double cantilever beam fracture mechanics testing. The sol-gel preparation procedure was also optimized for coupling with BPF.

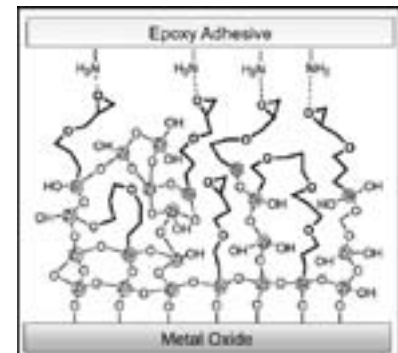


Figure 1: Network composition of the zirconium hybrid layer [2].

Experimental Procedure:

Double Cantilever Beam Specimen Fabrication and Testing (Figure 2). Pairs of rectangular Si substrates were sputtered with gold pre-cracks and bonded together with a 50 μm thick epoxy layer, either BPF or BPF with flexibilizers. Specimens were then cured at 165°C for two hours and sliced with a wafer saw into four identical beams. After loading tabs were attached, specimens were subjected to tensile testing, from which applied load and subsequent beam displacement values were obtained. Fracture energy of the epoxies sandwiched between the Si beams was then calculated from these values.

Sol-Gel Sample Preparation. Ether 3-glycidoxypropyl-trimethoxysilane (GPTMS) was homogeneously mixed with deionized water, while tetra n-propoxylzirconium (TPOZ) (70% in 1-propanol) and glacial acetic acid (GAA) were hand-swirled separately until cool to the touch. After the GPTMS/water was added to the TPOZ/GAA for a final 0.77:1 Zr/Si molar ratio and 3.75% volume GPTMS+TPOZ, the solution was aged at room temperature. Solutions were prepared with and without magnetic stirring during aging, as well as with variable aging times.

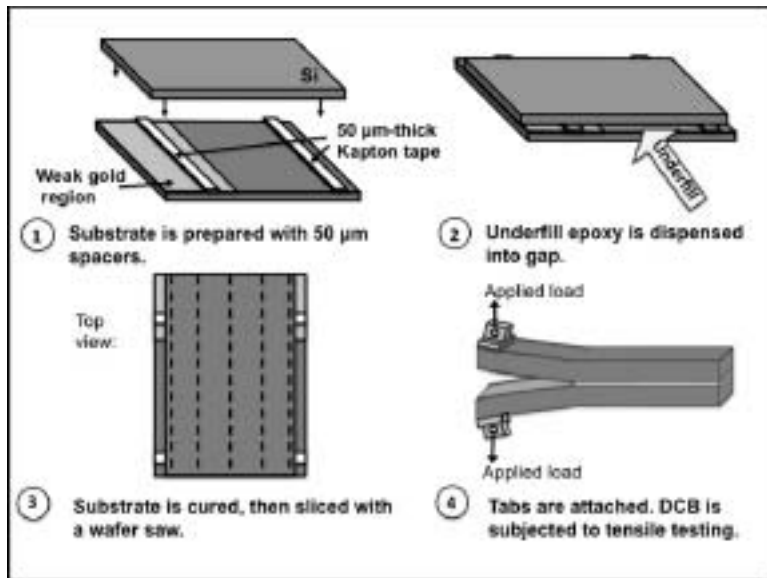


Figure 2: Double cantilever beam specimen fabrication and testing.

UV-ozone cleaned rectangular Si substrates were dip-coated into the sol-gel at 10 mm/sec and immediately withdrawn at 0.2 mm/sec. HL-coated pieces were then cured at 120°C for variable times and used to fabricate double cantilever beams with BPF underfill for tensile testing.

Results and Discussion:

Ductility-increasing flexibilizers increased BPF fracture energy (Figure 3a).

Stirring the HL during aging, and longer HL curing times, increased the HL fracture energy (Figure 3b), due to the sol-gel achieving a more condensed state with more network cross-linking.

Shorter sol-gel aging time drastically improved upon the fracture energy of BPF with HL (Figure 3c). The observed mixed-mode cohesive failure path within the BPF under shorter aging conditions explains this phenomenon, as more energy is required to plastically deform BPF than to delaminate BPF from substrates. Shorter HL aging time is thought to correlate with a shorter solution condensation time, thus leaving a fresher and higher-quality material for thin-film deposition onto Si substrates.

Summary and Future Work:

Both flexibilizers and Zr HLs improve BPF adhesion to Si. An optimized HL preparation procedure for coupling with BPF includes stirring while aging, longer curing times, and shorter aging times. Future work involves continued optimization of the Zr HL preparation process, such as optimizing cure temperature and determining the respective upper and lower limits on curing and aging times. Further characterization of the HL's physical and chemical properties is also necessary to more thoroughly understand its mechanism of fracture energy enhancement. Finally,

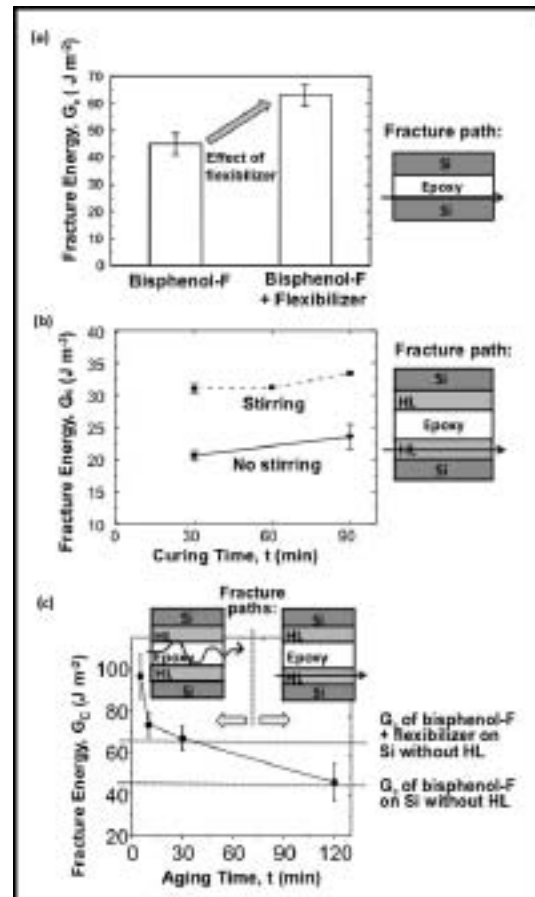


Figure 3: a) The effect of flexibilizers on BPF fracture energy. The effects of varying b) stirring presence and cure time, and c) aging time on HL fracture energy.

fracture mechanics testing of the HL under high humidity levels and temperatures will determine whether HL fracture energy enhancements can be sustained in harsher environmental conditions.

Acknowledgments:

I would like to thank Stanford's Center for Integrated Systems, the NNIN REU Program and the National Science Foundation for providing the facilities and funding for this project, as well as Professor Reinhold Dauskardt for his guidance and the opportunity to work in his lab, Taek-Soo Kim for mentoring me throughout this project and the Dauskardt research group for their support. My sincerest gratitude to the Stanford Nanofabrication Facility (SNF) staff—especially Mike Deal and Maureen Baran—and the SNF REUs.

References:

- 1] Wang, L.C. "Adhesion of polymer/inorganic interfaces: Effects of filler addition, environment and chemistry." Ph.D. dissertation, Stanford University (2003).
- 2] Oliver, M.S., Blohowiak, K.Y. and Dauskardt, R.H. "Molecular structure and fracture properties of ZrOX/Epoxy silane hybrid films." Journal of Sol-Gel Science and Technology, 55, 360-368 (2010).

Temperature Dependent Growth Properties of Epitaxial Graphene on Carbon-Face Silicon Carbide

Benjamin D. Mahala

Chemistry, University of Missouri Science and Technology

NNIN REU Site: Nanotechnology Research Center, Georgia Institute of Technology, Atlanta, GA

NNIN REU Principal Investigator(s): Raghunath Murali, Nanotechnology Research Center, Georgia Institute of Technology

NNIN REU Mentor(s): Sarah Bryan, Electrical and Computer Engineering, Georgia Institute of Technology

Contact: bdm972@mst.edu, raghu@gatech.edu, sebryan@gatech.edu

Abstract:

The use of silicon-based transistors has been a staple in computer technology for decades, but due to fundamental material and device limitations, progress in chip speed and computing power has begun to slow. Graphene-based transistors have the potential to break through these limitations and put us back on the path of increased performance gains with scaling. As a first step towards implementing graphene technology, it is necessary to have high-quality graphene sheets from which a chip with billions of devices can be fabricated. In this work, graphene was grown by silicon sublimation from semi-insulating silicon carbide (SiC) using a high temperature vacuum furnace. Both substrate preparation and growth processes were experimented with; variables included temperature, gaseous environment, and soak time. After growth, samples were characterized in a number of ways to determine sample quality, including Raman spectroscopy, atomic force microscopy, and van der Pauw electrical measurements. A relationship between growth temperature, graphene morphology, and sheet resistance was extracted.

Introduction:

Graphene has many important properties that make it exceptional for use in electronics, including high charge carrier mobility [1] and thermal conductivity [2]. However, obtaining significant quantities of graphene for industrial use has proven difficult. Graphene can be grown epitaxially on the surface of SiC simply by heating the substrate to a high temperature. Graphene can be grown on either of the species-terminating faces, silicon-face or carbon-face, of SiC, both of which show significant differences in graphene morphology and electrical properties. The atomic force microscopy images (Figures 1 and 2) reveal how the surface morphology differs between graphene grown on the silicon-face and the carbon-face. The silicon-face graphene grows along straight terraces, while the carbon-face graphene nucleates at certain points, grows outward, and ultimately forms domains which meet in a ridge or pucker. Carbon-face graphene is rotationally stacked, which allows for individual monolayers in a thick, stacked film to behave as electrically isolated graphene monolayers [3].

Experimental Procedure:

The temperature dependence of epitaxial graphene growth was tested by cleaning 4 × 4 mm pieces of SiC with acetone, methanol, and isopropanol for five minutes each in an ultrasonic bath. The samples were then dried with a nitrogen gun and immediately loaded into the vacuum furnace.

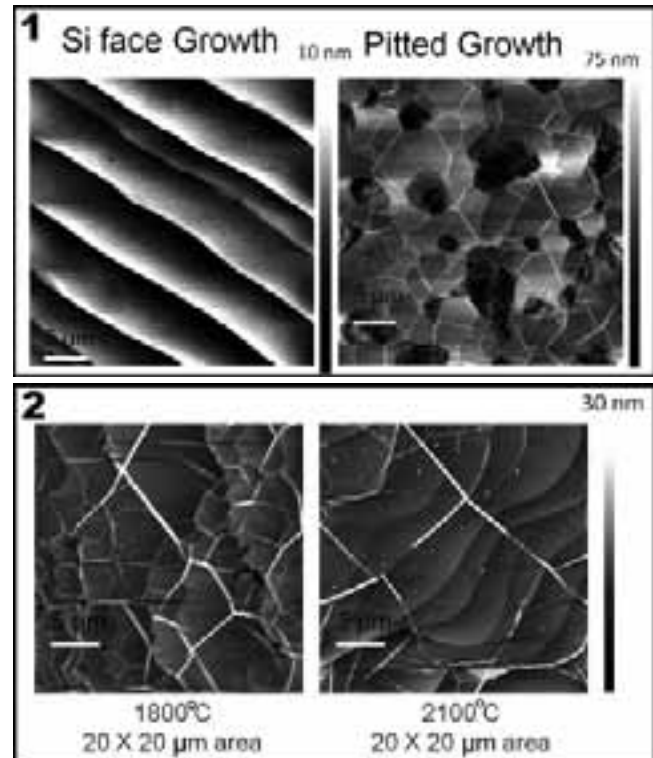


Figure 1, top: On the right is an image of silicon-face graphene. On the left is an image of pitted carbon-face graphene.

Figure 2, bottom: The right image is carbon face graphene grown at 1800°C, on the left is carbon-face graphene at 2100°C.

The samples were hydrogen-etched in the furnace to remove chemical mechanical polishing damage by flowing 3000 standard cubic centimeters per minute (sccm) of argon (Ar) and 1000 sccm of H₂ at 1400°C. The cleaned samples were then graphitized without exposure to air by heating the system to 1400°-2100° C for 10 minutes at a pressure of ~ 10⁻⁵ Torr.

The samples were characterized with atomic force microscopy imaging, Raman spectroscopy, and van der Pauw electrical testing.

Results and Conclusions:

Graphene layers grown at higher temperatures show different electrical, spectroscopic, and morphological properties in comparison to graphene layers grown at lower temperatures. As shown in Figure 2, the graphene layers exhibit increased domain sizes at higher temperatures. However, as shown to the right in Figure 1, higher temperatures also lead to increased pitting in the graphene layers and SiC substrate which make device fabrication challenging. The Raman spectra obtained from grown graphene samples (Figure 3) exhibits two main peaks of interest, the D peak and the 2D peak.

The 2D peak is correlated to the thickness of the graphene layer and increases as the temperature increases. The D peak is correlated to defects in the graphene and is surprisingly not present in any of the Raman spectra, suggesting that the graphene grown in these experiments is high quality even in the presence of unwanted pits on the surface. The electrical measurements imply that as the growth temperature increases, the sheet resistance of the graphene layer decreases exponentially, thereby leading to exceptional conductivity at higher growth temperatures.

Acknowledgements:

I would like to thank my principal investigator, Raghunath Murali, and my mentor, Sarah Bryan, along with the staff at the Nanoelectronics Research Center and my site coordinators, Katie Hutchison, Nancy Healy, and Joyce Palmer. I am also grateful to the National Nanotechnology Infrastructure Network Research Experience for Undergraduates (NNIN REU) for supporting this program and the National Science Foundation for funding.

References:

- [1] Bolotin, K. I.; Sikes, K. J.; Jiang, Z.; Klima, M.; Fudenberg, G.; Hone, J.; Kim, P.; Stormer, H. L., Ultrahigh electron mobility in suspended graphene. *Solid State Commun* 2008, 146 (9-10), 351-355.
- [2] Balandin, A. A.; Ghosh, S.; Bao, W. Z.; Calizo, I.; Teweldebrhan, D.; Miao, F.; Lau, C. N., Superior thermal conductivity of single-layer graphene. *Nano Lett* 2008, 8 (3), 902-907.
- [3] Hass, J.; Varchon, F.; Millan-Otoya, J. E.; Sprinkle, M.; Sharma, N.; De Heer, W. A.; Berger, C.; First, P. N.; Magaud, L.; Conrad, E. H., Why multilayer graphene on 4H-SiC(000) behaves like a single sheet of graphene. *Phys Rev Lett* 2008, 100 (12), 125504.

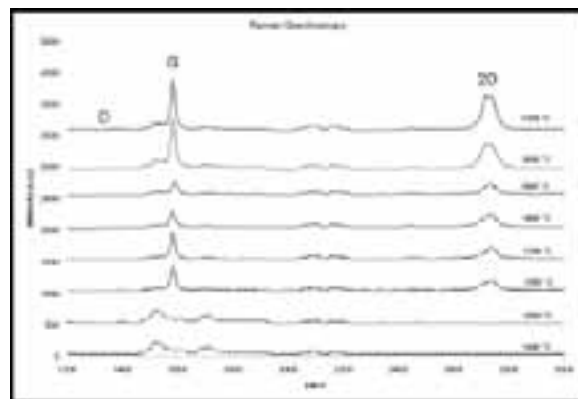


Figure 3, top: The Raman spectroscopy of carbon-face graphene grown at temps ranging from 1400°C to 2100°C.

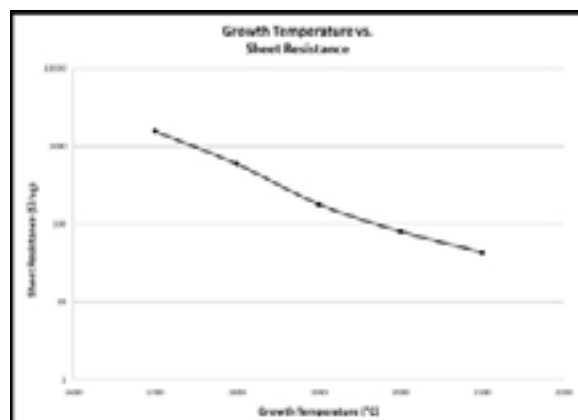


Figure 4: The sheet resistance of carbon-face graphene decreases as growth temperature increases, leading to improved resistivity at higher temperatures.

Composite Cathodes for Intermediate Temperature Solid Oxide Fuel Cells

Isaac Markus

Chemical Engineering, The Cooper Union for the Advancement of Science and Art

NNIN iREU Site: National Institute for Materials Science (NIMS), Tsukuba, Ibaraki, Japan

NNIN iREU Principal Investigator(s): Dr. Enrico Traversa, NIMS, MANA Nano-Green Field, Tsukuba, Ibaraki, Japan

NNIN iREU Mentor(s): Dr. Emiliana Fabbri, NIMS, MANA Nano-Green Field, Tsukuba, Ibaraki, Japan

Contact: markus@cooper.edu, traversa.enrico@nims.go.jp, fabbri.emiliana@nims.go.jp

NNIN iREU Program

Introduction:

Solid oxide fuel cells (SOFCs) are electrochemical devices capable of achieving high thermodynamic efficiency with low environmental impact. Conventional SOFCs operate above 800°C, limiting their applications, requiring special construction materials and large start-up energy inputs. These limitations have led to the exploration of SOFCs that operate at intermediate temperatures (IT, 400-700°C).

These efforts have been focused on using protonic conductors as the electrolyte material. Protonic conductors have the advantage of lower activation energies compared to oxygen-ion conductors, as well as the formation of water vapor on the cathode side which prevents fuel dilution [1]. However, the use of proton conductors as electrolytes has been limited by the unavailability of compatible and optimal materials for the cathode. This project focused on exploring the chemical and electrical properties of different compositions of $\text{BaZr}_{1-x-y}\text{Pr}_x\text{YyO}_{3-\delta}$ (BZPYxy), for its implementation as a composite cathode for IT-SOFCs.

Experimental:

BZPYxy ($x = 10-40$, $y = 20$) was synthesized through the combustion method. Metal nitrates were dissolved in water by stoichiometric ratio. Citric acid was added in a 2:1 ratio to the metal nitrates, and 5 mL of nitric acid was added; pH was adjusted to 3, using ammonium solution. Solution was heated until all water was removed and solution was combusted.

The resulting powder was calcined at 1100°C for six hours. X-ray diffraction (XRD) analysis was used to confirm that samples were single phase. Powder was mixed with 5% poly(vinyl butynal)1000. Dense pellets were obtained by uniaxially pressing

powders at 200 MPa and sintering at 1600°C for 10 hrs.

Conductivity measurements were performed by electrochemical impedance spectroscopy (EIS) analysis in the range of 50 mHz to 500 kHz between 350-750°C. BZPY pellets were painted with silver, placed in a current collector with gold wires in a ceramic screw-and-bolt assembly. Gold wires were connected to an alumina reactor, which was placed in a tube furnace. Different oxygen partial pressures were obtained by mixing air with argon gas. Wet atmosphere conditions were obtained by flowing gas through water at ambient temperature. The conductivity values for each measurement were obtained by analyzing the IES spectra at the transition between medium and high frequencies.

Composite cathodes inks were prepared by mixing PBCO with respective BZPY powder along with α -terpineol and ethyl cellulose. Symmetric cells were prepared by paint brushing the cathode ink on each side of a BZPY2020 pellet and sintering at 1000°C for 3 hrs. Pellets were then analyzed with the same setup as previously described. The area specific resistivity was calculated by looking at the low frequency range for the EIS spectra.

Complete fuel cells were fabricated by co-pressing the anode (BZY+Ni) with a thin layer of BZPY1020 for the electrolyte and sintering at 1400°C for 10 hrs. The cathode was paint-brushed on the electrolyte through a 5 mm mask and sintered at 1000°C for 3 hrs. The cathode was repainted

with Pt ink and dried for 10 min at 1000°C to aid the current collectors. Fuel cells were sealed around the anode using silver paint and silver current collectors were connected to the cathode. Cells were tested at 700°C flowing wet-H₂ at anode side and using ambient air at the cathode.

Composition	Temperature (°C)	Dry Air		Wet Air	
		Transport Ionic	Transport Electronic	Transport Ionic	Transport Electronic
BZPY2020	500	0.14	0.86	0.52	0.48
	600	0.09	0.91	0.33	0.67
	700	0.07	0.93	0.28	0.72
BZPY3020	500	0.04	0.96	0.30	0.70
	600	0.03	0.97	0.20	0.80
	700	0.02	0.98	0.13	0.87
BZPY4020	500	0.19	0.81	0.33	0.67
	600	0.21	0.79	0.26	0.74
	700	0.20	0.80	0.20	0.80

Table 1: Transport number results for different temperatures, atmospheres and compositions.

Results and Discussions:

XRD results proved that the four BZPY compositions were obtained in single phase. Figures 1 shows an Arrhenius plot of conductivity vs. temperature measured in wet air. All the BZPY composition had similar conductivities throughout the temperature range examined.

Table 1 displays the different transport numbers for the compositions obtained by varying the oxygen partial pressure and modeling the results using the “defect model” [2]. Under dry conditions the electronic contribution to the conductivity dominates, while in wet atmosphere there is a closer ratio between the ionic and electronic contributions.

The results also indicate that with increasing Pr content the electronic contribution increases. This suggests that BZPY4020 is a better candidate for the composite cathode, since the electrodes need to have high electron mobility for higher current density to be achieved.

Figure 2 summarizes the ASR results for BZPY1020 and BZPY4020, with the latter having lower resistance overall. Figure 3 shows a scanning electron microscope (SEM) picture of the symmetrical cell at the cathode and electrolyte interface. The image suggests that lower ASR values can be obtained by reducing the cathode thickness to 20 μm and by optimizing the sintering temperature to increase cathode porosity and adhesion to electrolyte.

The performance of the composite BZPY4020+PBCO cathode was tested in an anode supported dual chamber fuel cell. The maximum open circuit voltage (OCV) for the cell was 0.91V; however, due to poor manufacturing, the maximum power density was only 1.26 mW/cm².

Conclusions:

Single phase powders for BZPY_{xy} were synthesized and stable pellets were pressed from them. The conductivity of the different compositions were tested and found to not differ largely under wet atmosphere. The electronic conductivity contribution to the overall conductivity was found to increase with Pr content. The symmetrical cell results showed BZPY4020 had overall lower resistance with a minimum ASR value of 0.45 Ωcm^2 . The fuel test did not yield successful power density measurements with problems in cell sealing and cathode attachment limiting performance to only 1.26 mW/cm². However, an OCV of 0.91V was obtained establishing a proof of concept model.

Acknowledgements:

This work was supported by the NSF, NNIN iREU and NIMS. This work was carried out with the assistance, support and contribution of Emiliana Fabbri, Lei Bi and Dr. Enrico Traversa.

References:

- [1] Brett D, Atkinson A, Brandon N, Skinner S. *Chem. Soc. Rev.* 2008, 37, 1568.
- [2] Fabbri E, Oh T, Licoccia S, Traversa E, Wachsman E. *Electrochemical Society* 2009, 156, 1, B38.
- [3] Fabbri E, Licoccia S, Traversa E, Wachsman E. *Fuel Cells* 2009, 2, 128.

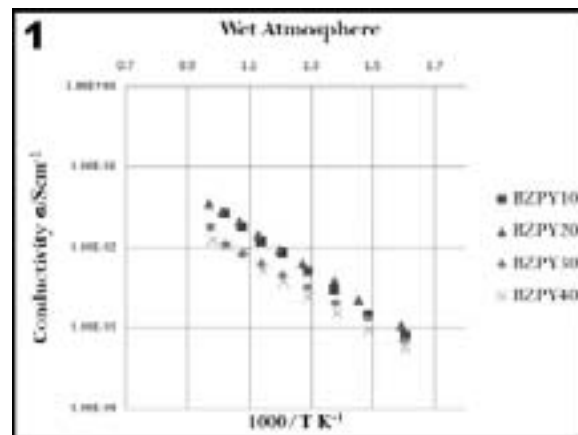


Figure 1: Conductivities for all four BZPY compositions examined under wet air.

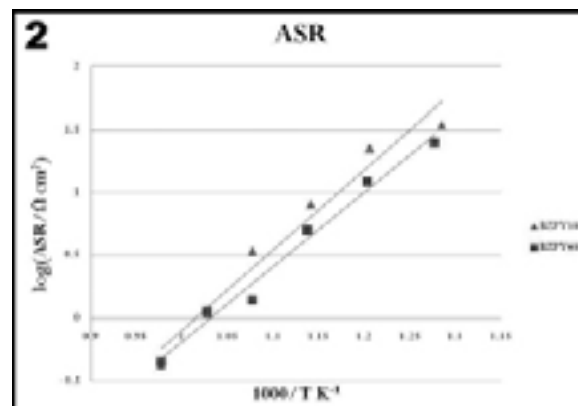


Figure 2: ASR results for BZPY1020 and BZPY4020.

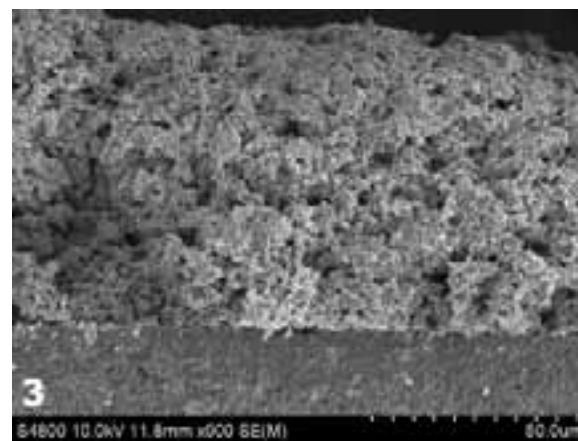


Figure 3: SEM of the cathode (top) and electrolyte (bottom) interface.

Tuning Graphene Conductivity Using Solid Binding Peptides

Nkemdilim Oghedo
Chemical Engineering, Yale University

NNIN REU Site: Center for Nanotechnology, University of Washington, Seattle, WA

NNIN REU Principal Investigator(s): Mehmet Sarikaya, Genetically Engineered MSE Center, University of Washington

NNIN REU Mentor(s): Dr. Yuhei Hayamizu, Genetically Engineered MSE Center, University of Washington

Contact: nkemdilim.oghedo@yale.edu, sarikaya@u.washington.edu, hayamizu@u.washington.edu

Abstract and Introduction:

Single-layer graphene has emerged as a significant material for post-silicon nano-electronics. Due to its two-dimensional structure, all carbon atoms are exposed to the atmosphere, rendering graphene highly sensitive. Thus, localized surface disturbances can modify its electronic structure and conductivity [1].

Genetically engineered peptides for inorganics are small biomolecules found to selectively bind to inorganic solids such as gold, silica and graphite [2]. This research focused on two forms of graphite binding peptides (GrBP5): the original Wild-Type (WT) peptide (-2 charge) and a mutant peptide (+2 charge). The mutant peptide was designed by replacing two negatively charged amino acids on a WT peptide sequence with two positively charged ones. This project investigated the doping capabilities these peptides have on single-layer graphene with respect to their sequence changes. We also examined the degree of doping as it relates to peptide solution concentrations and incubation times.

Raman spectroscopy unobtrusively provides information on the chemical composition and electronic properties of a sample. Analysis of the characteristic G ($\sim 1580 \text{ cm}^{-1}$) and 2D ($\sim 2690 \text{ cm}^{-1}$) peaks of graphene spectra reveals the number of graphene layers in a sample [3]. One can also use Raman to monitor changes in graphene's electronic structure by observing shifts in the G and 2D bands. These shifts correlate to alterations in charge carrier density and conductivity. Theory predicts that both p- and n- doping on graphene correspond to an increase in G band energy and decrease in G band width [4]. Observation of these changes indicates the occurrence of molecular doping on graphene.

Environmental Procedures:

Graphene was made using the micro-mechanical exfoliation technique and deposited onto a silicon substrate (silicon layer topped by a 300 nm thermally oxidized layer). Raman measurements were performed with a 514 nm laser, 1 μm in diameter, for 30 seconds at 40% laser exposure (Renishaw Raman Microscope). These parameters obtained the most information without overheating the sample. 2D and G peaks were analyzed with the "Start Fit" operation on the Wire 2.0

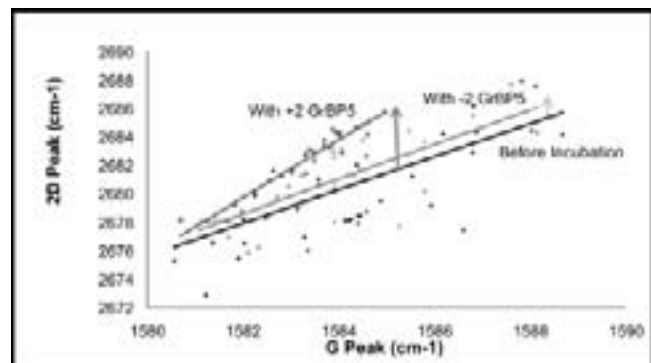


Figure 1: G versus 2D-peak positions before and after peptide incubations (1 μM , 24 hours).

software from Renishaw. Peak position, width and height were recorded. Samples were incubated under a humidity controlled hood, and then rinsed twice with deionized water. Previously probed locations were found and probed again under the same laser parameters. Peak information was re-recorded.

Results:

Changes in both the G and 2D bands after incubation were examined. From Figure 1, it is clear that both peptides caused an increase in the G and 2D peak positions, with +2 GrBP5 peak positions increasing more significantly. Figure 2

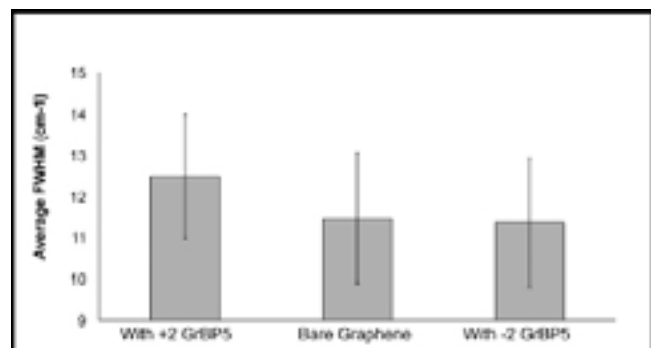


Figure 2: Average full-widths-at-half-maximum (FWHM) of G-peaks before and after peptide incubation (1 μM , 24 hours).

shows that +2 GrBP5 causes a widening of the G band while -2 GrBP5 causes a slight narrowing. This inconsistency can be explained by theory, which predicts very minor changes in G band width for ± 50 meV shifts in Fermi Energy [4]. Our peptides caused energy shifts in this range, and therefore did not affect noticeable changes in G band width.

Internal strain, induced by the micro-mechanical exfoliation procedure, also contributed to this discrepancy. Peak positions higher and lower than average correspond to regions of compression and tension, respectively. This strain caused a widening of the G band, which opposed the narrowing of the G band caused by peptide doping [5]. This conflict further explains the inconsistent changes of the G band width.

From these results, we concluded that +2 and -2 GrBP5 are able to dope graphene, with mutant +2 GrBP5 doping more significantly.

Discussion:

Samples incubated with a $1 \mu\text{M}$ peptide solution concentration for 24 hours provided the clearest results. Other incubation parameters included $1 \mu\text{M}$ solution for one hour and $0.1 \mu\text{M}$ solution for 24 hours. $0.1 \mu\text{M}$ concentrations were too low to significantly influence doping. Twenty-four hour incubations proved more informative than one hour incubations due to the fact that longer incubation times gave peptides more time to bind, assemble and align on graphene. A more crystalline peptide alignment resulted in more uniform interactions between the peptides and graphene, leading to more consistent and significant doping effects.

Figures 3 and 4 show that compressed graphene regions exhibit opposite peak shifts than regions with little to no strain. This may result from a change in peptide-graphene interactions due to the distorted graphene lattice with significant compression. This suggests an interesting relationship between internal strain and doping capabilities to be studied further.

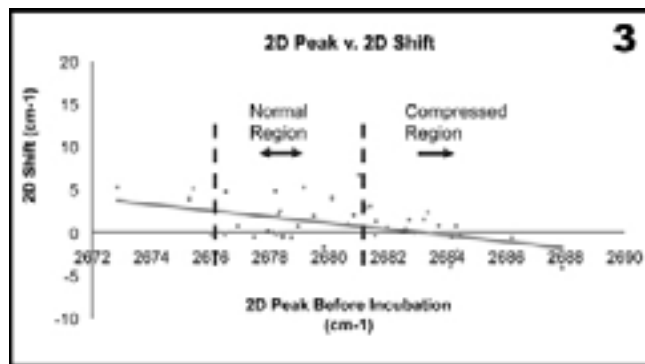


Figure 3: Initial 2D-peak versus 2D-peak shift for both peptides ($1 \mu\text{M}$, 24 hours).

Conclusion:

Results show that -2 GrBP5 and oppositely charged mutant, +2 GrBP5, successfully dope charges onto single-layer graphene. These peptides cause positive shifts in G and 2D Raman peaks and changes in the G Band width, which, in accordance with theory, result from molecular doping. In addition, internal strain may affect molecular doping and/or peptide binding behavior.

Acknowledgements:

I would like to thank the National Science Foundation, National Nanotechnology Infrastructure Network Research Experience for Undergraduates (NNIN REU) Program, the University of Washington Materials Research Science and Engineering Centers (MRSEC) and the Genetically Engineered Materials Science and Engineering Center (GEMSEC). The research was carried out at the NNIN and GEMSEC facilities, a part of the MRSEC-Materials Research Facilities Network. I would like to thank my mentor, Dr. Yuhei Hayamizu, and my faculty supervisor, Prof. Mehmet Sarikaya.

References:

- [1] Dong, X., et. al.; "Doping Single-Layer Graphene with Aromatic Molecules"; *Small*, 5, 1422-1426 (2009).
- [2] Tamerler, et. al., M.; "Molecular Biomimetics: GEPI-Based Biological Routes to Technology"; *PeptideScience*, 94, 78-94 (2009).
- [3] Ferrari, A.C., et. al.; "Raman Spectrum of Graphene and Graphene Layers"; *PRL*, 187401 (2006).
- [4] Yan, J., Zhang, Y., Kim, P., Pinczuk.; "Electric Field Effect Tuning of Electron-Phonon Coupling in Graphene"; *PRL*, 98, 166802 (2007).
- [5] Otakar, F., et. al.; "Compression Behavior of Single-Layer Graphenes". *ACS Nano*, 4, 3131-3138, (2010).

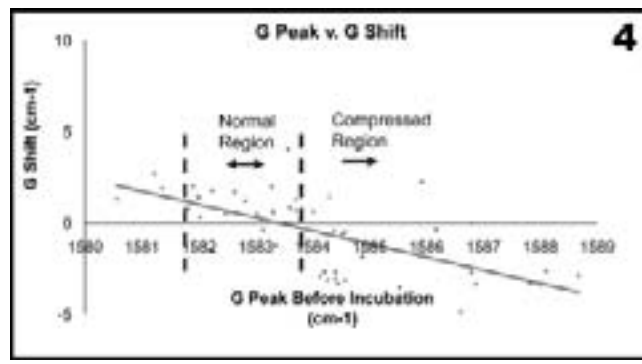


Figure 4: Initial G-peak versus G-peak shift for both peptides ($1 \mu\text{M}$, 24 hours).

Characterization of SiAlON for Hydrogen Diffusion Barrier Application in Nonvolatile Memory Devices

Axel Palmstrom

Chemical Engineering, University of California Santa Barbara

NNIN iREU Site: National Institute for Materials Science (NIMS), Tsukuba, Ibaraki, Japan

NNIN iREU Principal Investigator(s): Dr. Toyohiro Chikyow, Advanced Electronic Materials Center, NIMS, Tsukuba, Ibaraki, Japan

NNIN iREU Mentor(s): Dr. Nam Nguyen, Advanced Electronic Materials Center, NIMS, Tsukuba, Ibaraki, Japan

Contact: apalmstrom@umail.ucsb.com, chikyo.toyohiro@nims.go.jp, nguyen.nam@nims.go.jp

NNIN iREU Program

Abstract:

In this study, silicon aluminum oxynitride alloys (SiAlON), were investigated as a candidate material for a hydrogen diffusion barrier in non-volatile memory (NVM) devices. SiAlON/SiO₂/Si samples were fabricated using combinatorial pulsed laser deposition and the electrical properties throughout the full composition spectrum of SiAlON ranging from pure Si₃N₄ to pure Al₂O₃ (x = 0-1) were determined. The capacitance-voltage and current-voltage measurements of the SiAlON films indicate good dielectric performance, making the electronic properties of SiAlON sufficient to warrant the investigation of its use as a hydrogen diffusion barrier in NVM devices.

Introduction:

Non-volatile memory (NVM) has a metal/oxide/nitride/oxide/semiconductor (MONOS) structure and it retains data by trapping charges at the lower nitride-oxide interface.

Hydrogen diffusion is believed to limit the device performance and reliability [1]. If a hydrogen diffusion barrier were incorporated in the MONOS structure, there would be an anticipated improvement in the device endurance and retention.

In a successful diffusion barrier, a high capacitance and low leakage current are desired to reduce the electron leakage from the nitride/oxide trap layer, increasing the maximum retention time of the device and the film should not trap charges, which would result in eventual device failure. Therefore, it is important to investigate the SiAlON electronic properties as well as its properties as a hydrogen diffusion barrier in order to determine its potential to improve the performance of NVM devices.

This report emphasizes the electronic properties of SiAlON.

Experimental Procedure:

SiAlON Deposition. Thin films of SiAlON were deposited on thermally oxidized SiO₂ substrates. The SiO₂ was prepared in an oxidation furnace at 800°C under an oxygen flow of 400 mL/min for five minutes and annealed for another five minutes without an additional oxygen flow. In order to deposit a single SiAlON layer with a variation in composition ranging from Si₃N₄ to Al₂O₃ (x = 0-1), a combinatorial technique was applied to a pulsed laser deposition process [2]. The procedure included moving a mask with a 7 × 7 mm square cutout across the substrate

as material was deposited. This resulted in thin wedges, of approximately 2.5 nm at its thickest, deposited on the substrate with each pass.

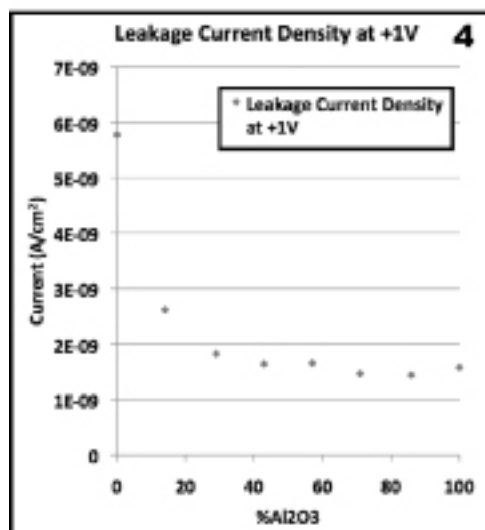
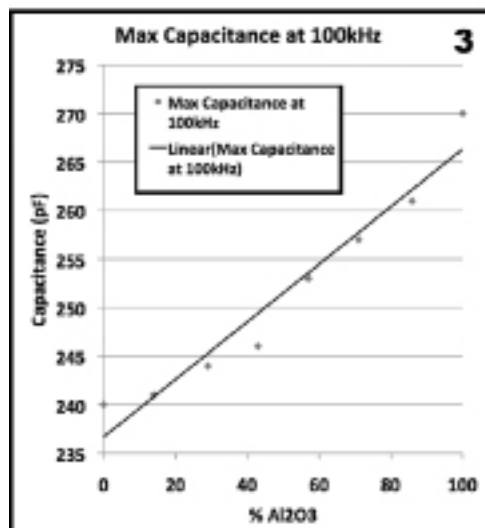
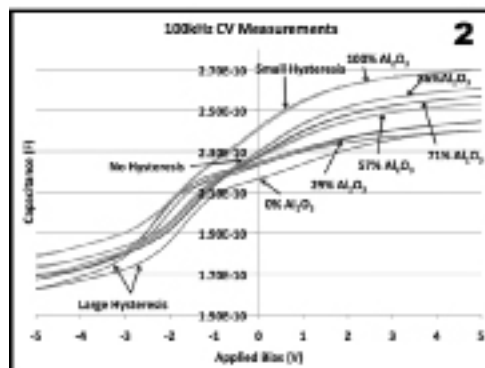
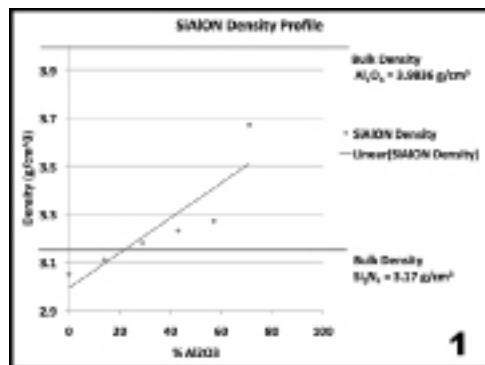
During deposition, the mask started in a central position and moved 7 mm in one direction as a layer of Al₂O₃ was deposited. The mask then moved back to the central position and moved in the other direction 7 mm as a layer of Si₃N₄ was deposited. A total of four layers of Al₂O₃ and four layers of Si₃N₄ were deposited in an alternating fashion on the substrate at a substrate temperature of 300°C, oxygen pressure of 1 × 10⁻⁵ torr, and KrF (248 nm) laser energy of 90 mJ per pulse at 5 Hz to obtain a 10 nm thick composition spread of Si₃N₄/Al₂O₃.

The thickness, roughness, and density of the film were characterized by x-ray reflectivity (XRR) and the electrical performance of the film was characterized with capacitance-voltage (C-V) and current-voltage (I-V) measurements.

Results:

X-ray reflectivity [3] scans were taken every 1 mm on the SiAlON/SiO₂/Si sample using a 0.1 mm beam size. The x-ray reflectivity results indicated that the average SiO₂ and SiAlON layer thicknesses were 6.4 nm and 10.6 nm with an average deviation of 0.15 nm and 0.05 nm, respectively. The average layer roughness was measured to be 0.78 nm in the SiO₂ film and 0.46 nm in the SiAlON film. Figure 1 shows the measured density of SiAlON, which exhibits a linear relationship with the Al₂O₃ fraction, x.

The C-V [4] data showed large hysteresis in the pure Si₃N₄ film (which is typical for Si₃N₄), no hysteresis for Al₂O₃



compositions between 70% and 85%, and a slight hysteresis in the pure Al_2O_3 film (Figure 2). The presence of a hysteresis in C-V measurements suggested trapping of charge at the film/ SiO_2 interface or in the SiAlON film itself. At +5V and 100 kHz, the maximum capacitance increased linearly from 240 pF to 270 pF as the Al_2O_3 concentration increased from 0.0% to 100% (Figure 3). These results illustrated that the SiAlON film did not trap charge and that its capacitance was within a tolerable range for hydrogen diffusion barrier application.

The current-voltage measurements [4] (Figure 4) exhibited significantly higher leakage current in the sample at +1V with low Al_2O_3 concentration, but were low and nearly constant for all measurements taken at Al_2O_3 concentrations from 29% to 100%.

The low leakage current density ($\sim 10^{-9} \text{ A/cm}^2$) shows that the SiAlON can be used not only for a hydrogen diffusion barrier but also as a top block oxide layer to reduce the leakage current to the gate contact.

Conclusions:

A binary composition spread of Si_3N_4 and Al_2O_3 was successfully fabricated using the combinatorial pulsed laser deposition technique. Based on the C-V and I-V characterization, the electronic properties indicate that the SiAlON with a composition between 70% and 85% Al_2O_3 has the best potential to be used as a hydrogen diffusion barrier in non-volatile memory devices. Future research should be done to determine the effect of annealing in hydrogen on the SiAlON film, and diffusion rate experiments should be performed at various SiAlON compositions on single composition samples.

Acknowledgements:

I would like to thank Dr. Nam Nguyen and Dr. Toyohiro Chikyow for all of their advice and assistance throughout the project. I would also like to thank the National Nanotechnology Infrastructure Network International Research Experience for Undergraduates (NNIN iREU) Program and the National Science Foundation for this research opportunity.

This project was supported by the National Nanotechnology Infrastructure Network, the National Science Foundation, and the National Institute for Materials Science.

References:

- [1] Liu et al. IEEE, IRPS10, 417-423 [2010].
- [2] Pulsed Laser Deposition of Thin Films: Applications-Let Growth of Functional Materials, by R. Eason, John Wiley and Sons. Inc. [2007].
- [3] L. G. Parratt, Surface Studies of Solids by Total Reflection of X-Rays, Phys. Rev., 95, 359-369 [1954].
- [4] Sze, S. M. Physics of Semiconductor Devices, by S. M. Sze 2nd edn (Wiley-Interscience, New York, 1981).

Figure 1: Density profile of SiAlON film vs. Al_2O_3 composition.

Figure 2: C-V measurements of SiAlON film with 100 kHz at varying Al_2O_3 compositions.

Figure 3: Maximum capacitance at 5V vs. Al_2O_3 fraction in SiAlON films.

Figure 4: Leakage current density vs. Al_2O_3 composition.

Silicon Phononic Crystals for High Efficiency Thermoelectrics

Christopher Romanczuk

Chemical and Biomolecular Engineering, Rice University

NNIN REU Site: Lurie Nanofabrication Facility, University of Michigan, Ann Arbor, MI

NNIN REU Principal Investigator(s): Akram Boukai, Materials Science and Engineering, University of Michigan;

Anish Tuteja, Materials Science and Engineering, University of Michigan

NNIN REU Mentor(s): Xianhe Wei, Materials Science and Engineering, University of Michigan

Contact: cdr1@rice.edu, boukai@umich.edu, atuteja@umich.edu, xianhew@umich.edu

Abstract:

Thermoelectric materials can generate an electric current in response to an applied temperature gradient (Seebeck effect), or cause cooling in response to an applied current (Peltier effect). For thermoelectrics to be useful in application, higher efficiencies must be attained. This project focused on developing phononic crystals with a feature size of roughly 20 nanometers, utilizing a phononic band gap to decrease thermal conductivity, in order to achieve never before attained thermoelectric efficiencies.

Introduction:

Thermoelectrics devices can use a temperature gradient to produce an electric current. The effectiveness of these devices is often measured by the dimensionless figure of merit, ZT, as described by this equation:

$$ZT = \frac{S^2 \sigma}{\kappa} T$$

For thermoelectric devices to become commercially viable, ZT needs to be three times larger, ($ZT > 3$) than is currently available in the best thermoelectric materials. To accomplish this, the electrical (σ) and thermal (κ) conductivities must be varied independently, which is challenging since they are interdependent in bulk materials. The proposed method for decreasing thermal conductivity without impacting electrical conductivity was the use of nanostructured phononic crystals. Phononic crystals are materials that are created with periodic variations, which allow for the presence of a phononic band gap. A phononic band gap is a region of frequencies in which phonons are impeded or stopped from moving through the crystal, which decreases lateral heat transfer. A phononic band gap in the terahertz (THz) range will decrease thermal conductivity without affecting electrical conductivity. To accomplish this effect, periodic holes 10-50 nm in size needed to be created—much smaller than holes in previous phononic crystals [1]. Block copolymers could create an array with this feature size due to phase separation. The two polymers polystyrene and poly(methyl methacrylate) or PS/PMMA that were investigated, separate into periodic rods, 20 nm in diameter [2]. This template, with a wet etch process, should allow for the small feature diameters and high aspect ratios required for phononic crystals with hole depths in the micron range.

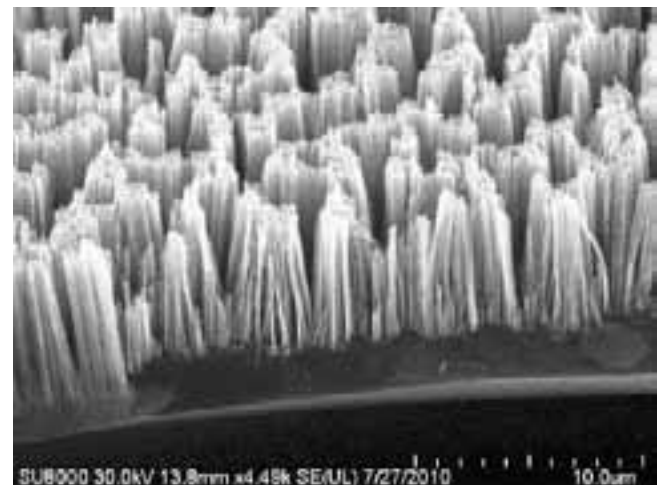


Figure 1: SEM of a 15 minute undirected HF etch on silicon.

Methods and Results:

A wet etch technique was explored using a solution of silver nitrate (AgNO_3 , 1.87g), 48% hydrofluoric acid (HF, 100 mL) and distilled water (451 mL). Ag nanoparticles formed out of solution from the AgNO_3 onto the surface of the silicon (Si) substrate. The Ag oxidized the Si surface forming SiO_2 , which was readily etched by the HF. This process was repeated, allowing for the high aspect ratios necessary. When not directed, this solution provided randomly etched Si nanowires (Figure 1). The targeted pattern was achieved on a thin film of Si, but to create phononic crystals, the wet etch process had to be used (Figure 2). While the polymer could provide the pattern of small diameter holes required, the polystyrene (PS) could not withstand the etching process long enough to obtain the high aspect ratios.

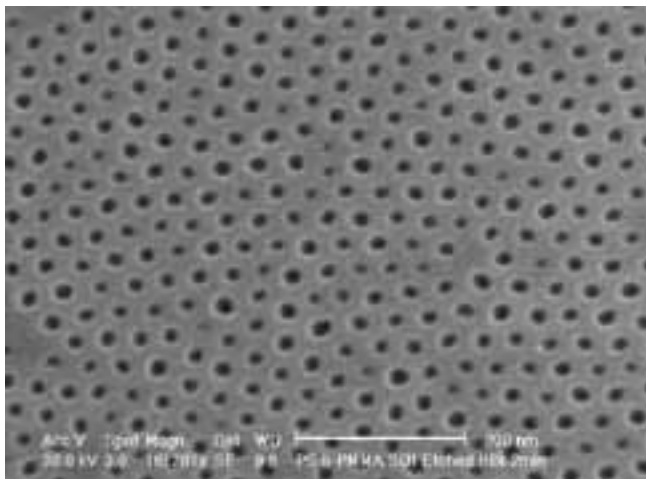


Figure 2: Ideal pattern for crystal, shown on a thin film using reactive ion etching.

Metals were examined based on the ability to evaporate onto the block copolymer easily. The first step was to make a pattern with larger features for testing. Photolithography was used to create an array with 3-8.5 μm features. Chromium (Cr), titanium and nickel were evaporated at a thickness of 50 nm to examine durability during the etching process. Cr was the most promising metal tested; lasting 15 minutes with no etching present where the Cr was shielding the Si (Figure 3). Optical microscopy was used to view the integrity of the overall array with scanning electron microscopy (SEM) performed to determine if there was any etching under the Cr mask. The next step was to use the block copolymer as the template for the Cr.

The PS/PMMA copolymer was developed by a member of the Boukai/Tuteja lab. The PMMA was removed, yielding the desired polystyrene array of hexagonally close-packed holes. The Enerjet evaporator was used to evaporate varying thicknesses of Cr (7-15 nm) over the PS-coated Si. The PS was then lifted off by first soaking in benzene for 24 hours, and then using a syringe to spray benzene for 20 minutes at a sharp angle from the edges of the sample.

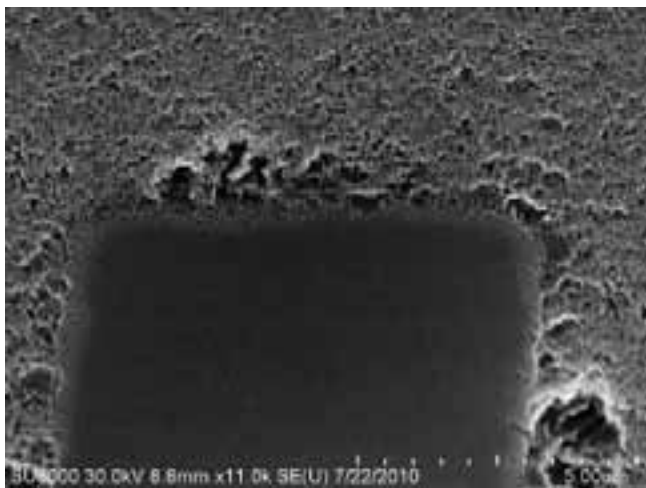


Figure 3: SEM of successful shielding of Si by Cr after HF etch.

These samples were then etched with the HF technique for various times, and images were obtained using SEM. The images showed the PS had not completely peeled off in the removal process—most likely due to the Cr forming a layer shielding the PS from the benzene. The 10 minute etch cracked the pattern, and where Si was visible, the Cr was left in the desired pattern of 20 nm sized features (Figure 4).

Conclusions and Future Work:

Cr completely shielded the Si underneath for 15 minutes, making it the most effective mask tested. The hydrofluoric acid and Ag nitrate solution proved to be capable of the high aspect ratios needed, while the polystyrene template was shown to provide features of the necessary size.

The polystyrene removal and thickness of deposited Cr need to be optimized before phononic crystals can be etched. A PDMS copolymer is also being examined as a possible replacement for the PS/PMMA. Once a crystal is assembled, a device will be required to test the thermoelectric capabilities. A testing device is being developed which will allow for ZT values to be calculated for the sample materials.

Acknowledgements:

I would like to thank my principal investigators Dr. Akram Boukai and Dr. Anish Tuteja. I would also like to thank my mentor Jonathan Wei as well as Jae Young Kwon, and everyone else in the Boukai/Tuteja labs. Lastly I would like to acknowledge the National Nanotechnology Infrastructure Network Research Experience for Undergraduates (NNIN REU) Program, the Lurie Nanofabrication Facility and the National Science Foundation.

References:

- [1] Gorishnyy et al, Physical Review Letters, 2005, 94, 11, 115501.
- [2] Jung and Ross, Small, 2009, 5, 14, 1654-1659.

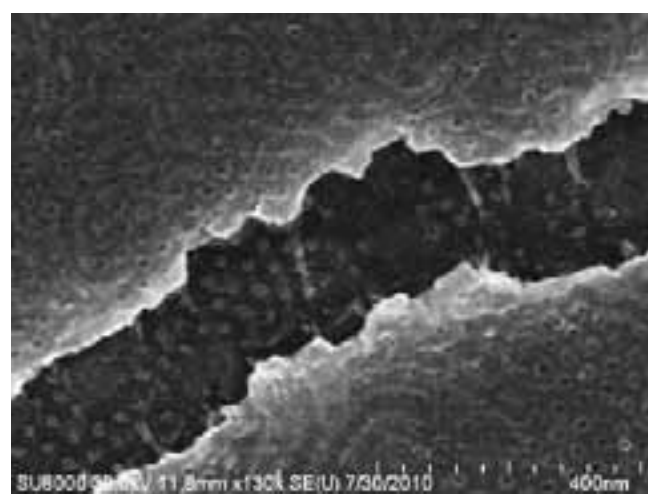


Figure 4: SEM image of 10 minute etched sample.

Characterization of Materials with Epitaxially Embedded Nanoinclusions for Thermoelectric Applications

Joseph S.T. Smalley

Engineering Science and Mechanics, The Pennsylvania State University

NNIN REU Site: Nanotech, University of California, Santa Barbara, CA

NNIN REU Principal Investigator(s): Dr. John Bowers, Electrical and Computer Engineering, University California, Santa Barbara

NNIN REU Mentor(s): Ashok Ramu, Electrical and Computer Engineering, University California, Santa Barbara

Contact: jss357@psu.edu, bowers@ece.ucsb.edu, ashok.ramu@gmail.com

Abstract:

The engineering of thermoelectric materials for better electrical and thermal transport properties is an essential part of increasing the efficiency of thermoelectric modules and generators. In this work, we report on the implementation of the third harmonic (3ω) method for measuring the thermal conductivity of thin films. At the time of this writing, proof-of-concept tests for measuring thermal conductivity of silicon dioxide (SiO_2) thin films on Si and aluminum oxide (Al_2O_3) substrates were successfully completed. Additionally, the effect of doping III-V semiconductor compounds with rare-earth semimetal nanoparticles is reported through comparison of simulation results to published experimental data.

Background:

More than half of all energy generated and imported into the United States is wasted [1]. The vast majority of this wasted energy takes the form of heat. Recovering this waste heat for the improvement of power system efficiencies has become a major research problem in the field of thermoelectric materials [2-4].

Recent studies have demonstrated the benefits of tailoring thermoelectric materials on the nanoscale [4-6]. Comparisons of these materials are made via a dimensionless figure of merit, ZT, which includes the following parameters related by Equation 1: Seebeck coefficient (S), electrical conductivity (σ), thermal conductivity (κ), and absolute heat source temperature (T).

$$ZT = \frac{S^2 \sigma}{\kappa} T$$

Equation 1

To become commercially useful, ZT values of 1.5-2.0 are desired [4].

Experimental Methods:

All measurements and simulations in this report assume room temperature and pressure.

Thermal conductivity was measured according to the 3ω method [7, 8]. This method was originally proposed by Cahill, et al., for thick samples, and was later modified for measurement on thin-films. The experimental apparatus is outlined in Figure 1. The potentiometer was tuned such

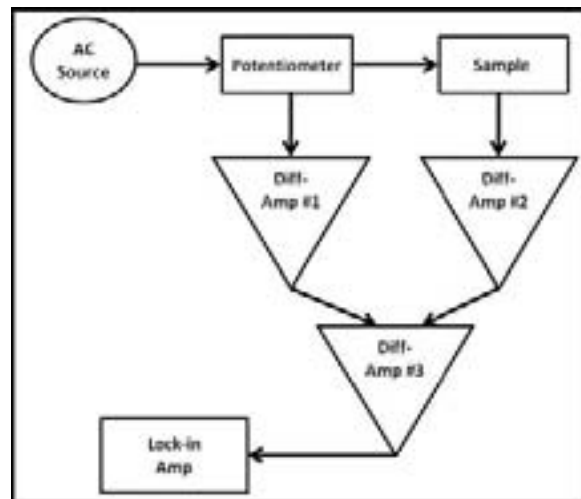


Figure 1: Functional block diagram of 3ω apparatus.

that the output of diff-amp #3 approached zero, eliminating the 1ω signal from the source. Only the sample contributed a substantial 3ω voltage, which was read by the lock-in amp. This 3ω voltage was proportional to the thermal conductivity.

To improve the ratio of the third harmonic with respect to the first, a signal conditioning circuit was built, the design of which was closely based on available circuits in the literature.

The Seebeck coefficient of materials was determined by measuring the voltage across a sample, upon which was

applied a varying temperature gradient. Thermocouples and voltmeters were used to capture the Seebeck coefficient, which is defined as the ratio of open circuit voltage to the temperature gradient. A MatLab[®] routine was used to automate the temperature sweep and data collection.

Carrier concentration, n , was determined via the Hall effect, and electrical conductivity, σ , was determined via the van der Pauw method. Hall carrier mobility, μ , was found through the relationship $\sigma = nq\mu$, where q is the elementary charge.

MatLab[®] code created by A.T. Ramu [9] for calculating Seebeck coefficient of III-V compounds was calibrated via comparing simulation results of silicon-doped gallium arsenide, as a function of carrier concentration, with measurement results. The ultimate purpose of the simulation work was to characterize the improvement in the Seebeck coefficient of indium gallium aluminum arsenide (InGaAlAs) by doping with erbium arsenide (ErAs) nanoparticles [6], compared to a control sample of InGaAlAs doped with Si.

Results and Conclusion:

To confirm the proper implementation of the 3ω experimental apparatus, a sample from UC Berkeley with known thermal conductivity was measured and the results compared to our measurements. As evident from Figure 2, the measurements agree within 3% of each other.

The results of the simulations are presented in Figure 3. The Seebeck coefficient of 0.6%ErAs:InGaAlAs was found to be from 15% to 35% greater than the control Si:InGaAlAs. The carrier concentration of the simulated Si:InGaAlAs was fixed at $1.9 \times 10^{18} \text{ cm}^{-3}$ since optimum thermoelectric properties of Si:InGaAlAs are found at this concentration.

In conclusion, we have established the 3ω method at UCSB and illustrated the benefits of ErAs doping. Future work of immediate relevance to this report consists of using the 3ω apparatus for measurement of thermal conductivity of the III-V semiconductor compounds doped with rare-earth

nanoparticles and expanding the simulation programs, e.g., enabling alloy scattering for InGaAlAs, adding more exotic material systems.

Acknowledgments:

Foremost, I thank my mentor, A.T. Ramu, who answered my countless number of questions and guided me in my work. Thanks also to P. Burke, B. Curtin, A. Sztein, and H. Lu of UCSB, and Dr. D. Xu, J. Feser and Prof. A. Majumdar of UC Berkeley, for collaborating in this endeavor. This work was made possible by Prof. J. Bowers, principal investigator of this project and director of the Center for Energy Efficient Materials at UCSB, by the National Nanotechnology Infrastructure Network Research Experience for Undergraduates (NNIN REU) Program, and the National Science Foundation. Finally, I thank Angela Berenstein for her coordination of internship logistics.

References:

- [1] Lawrence Livermore National Laboratory, DOE. <https://publicaffairs.llnl.gov/news/energy/energy.html> (2009).
- [2] Rowe, D.M CRC Handbook of Thermoelectrics. CRC Press. Boca Raton, FL: 1995.
- [3] Yang, J. Potential applications of thermoelectric waste heat recovery in the automotive industry. 24th Int'l Conf. on Thermoelectrics. 170-174 (2005).
- [4] Shakouri, A. et al. Nanoengineered materials for thermoelectric energy conversion. Chapter in Thermal Nanosystems and Nanomaterials, Topics in applied physics, 118. S. Volz (ed.) Springer-Verlag. Berlin: 2009.
- [5] Zebarjadi, M. et al. Effect of nanoparticle scattering on thermoelectric power factor. Applied Physics Letters, 94, 202105 (2009).
- [6] Zeng, G. et al. Power generator modules of segmented Bi₂Te₃ and ErAs:(InGaAs)_{1-x}(InAlAs)_x. J. Electronic Materials. Special issue paper, 1786-1792 (2008).
- [7] Cahill, D.G. Thermal conductivity measurement from 30 to 750K: the 3ω method. Rev. Sci. Instrum., 61, 2 (1990).
- [8] Kim, W.C. Thermal transport in nanostructured materials. Doctoral Thesis. University California, Berkeley (2005).
- [9] Ramu, A. et al. Rigorous calculation of the Seebeck coefficient and mobility of thermoelectric materials. J. of App. Physics, 107, 8 (2010).

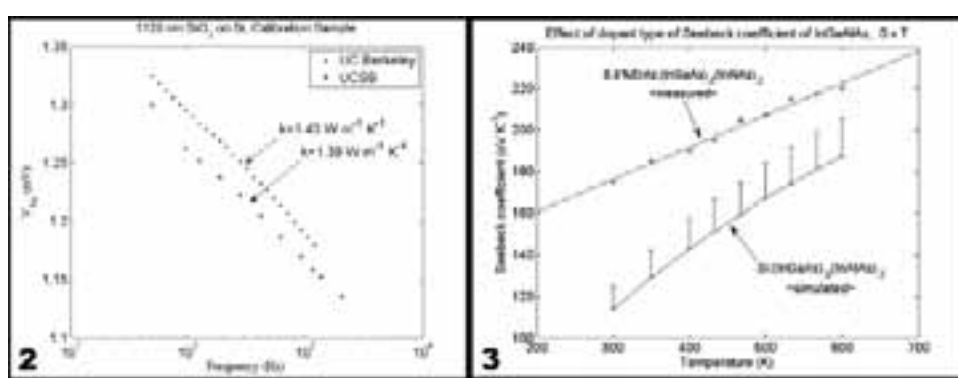


Figure 2: Verification of implementation of 3ω method.

Figure 3: Effect of dopant type on Seebeck coefficient of Si:InGaAlAs. The error in the simulated Seebeck coefficient of Si:InGaAlAs is based on variance from measurements and neglect of alloy scattering.

Low Stress Oxides for use in Microfabricated Ion Traps for Quantum Computation

Margeaux Wallace
Materials Science and Engineering, Cornell University

NNIN REU Site: Nanotechnology Research Center, Georgia Institute of Technology, Atlanta, GA

NNIN REU Principal Investigator(s): Dr. Kenneth R. Brown, School of Chemistry and Biochemistry, Georgia Institute of Technology

NNIN REU Mentor(s): J. True Merrill, School of Chemistry and Biochemistry, Georgia Institute of Technology

Contact: mlw239@cornell.edu, ken.brown@chemistry.gatech.edu, true.merrill@gatech.edu

Abstract and Introduction:

Trapped atomic ions are a leading technology for performing quantum computation [1]. The Brown Lab, in collaboration with the Quantum Information System group at the Georgia Tech Research Institute, is fabricating surface-electrode radio frequency ion traps for trapping and controlling calcium ions. On the trapping device, a set of electrodes produce a time-dependent potential in which an ion with sufficiently low kinetic energy is trapped. To insulate these electrodes, we require thick dielectric films that will survive cooling to 4.2K without substantial deformation to the devices. Internal stresses of these oxides will be further aggravated by the extreme change in temperature when the trap is cooled. Upon cooling, the film and substrate will shrink to different sizes due to different coefficients of thermal expansion. However, they must remain the same length; this creates an uncompensated bending moment. The film will cause the substrate to bend up or down with tensile or compressive stresses, respectively. Reducing the stress in the film minimizes the possibility of the oxide buckling [2].

The focus of this project was to create a recipe for the lowest stress oxide on one specific plasma enhanced chemical vapor deposition (PECVD) tool. Baseline stress measurements of standard recipes were taken and the parameters, pressure, radio frequency (RF) power, gas ratios and gas flow rates, were changed to optimize the stress.

Process Optimization:

Oxides were deposited on <100> silicon wafers at 250°C using PECVD. Variations of pressure, RF power and reactive gas ratios had perceptible effects on the stress of the films. These parameters were varied to find the optimal film deposition recipe for the production of low stress oxides. For every change, stresses were measured using a contact profilometer and an optical stress measurement tool. The gas flow ratios were substantially altered, thus changing the material being deposited. To verify that the film was indeed an oxide, the index of refraction was measured. In addition, since the oxide needs to be a sufficient insulator, the breakdown voltage was measured.

Results:

Figure 1 demonstrates the dependence of stress on the pressure. Increasing the pressure resulted in a decrease in stress; as the pressure was increased to the limit of the machine, the stresses dropped by about 100 MPa. RF power was varied next. Lower RF powers corresponded with lower stresses. However, as demonstrated in Figure 2, as the RF power was lowered below 25 watts, what appears to be a lower limit was observed. The last changed parameter was the ratio of the nitrous oxide (N₂O) to the 2% silane gas mixture. As the ratio of the silane gas was increased, drastic changes in the stresses were observed. It had the largest impact on the stress, turning the film from a compressive stress to a tensile one (Figure 3).

Oxides deposited with varied gas ratios were tested and ellipsometry data revealed index of refractions that were very close to each other, differing by only 2.7%. The highest index of refraction was 1.50 — higher than a typical silicon dioxide (about 1.46), but still within a reasonable range, indicating that the deposited film was an oxide.

The breakdown voltage was measured to be 8.53 MV/cm with a standard deviation of 1.823 MV/cm. The accepted literature values for the breakdown voltage of silicon dioxide falls within this range [3]. The maximum voltage used for the device was 0.35 MV/cm, so this oxide will be more than sufficient for use in the traps.

Discussion:

Possible mechanisms to explain these trends involve the density and amount of silicon in the film.

Films with a higher density exhibit lower values of stress. This is likely related to the organization of the lattice, a concept which is easily demonstrated by looking at a dislocation as seen in Figure 4. The extra half plane of atoms causes the top half to be stressed in compression and the bottom half, tension. While the stresses of the oxides are more complicated than a single dislocation, it is easy to extrapolate and see how the disorganized lattice associated with low density films would give high stresses.

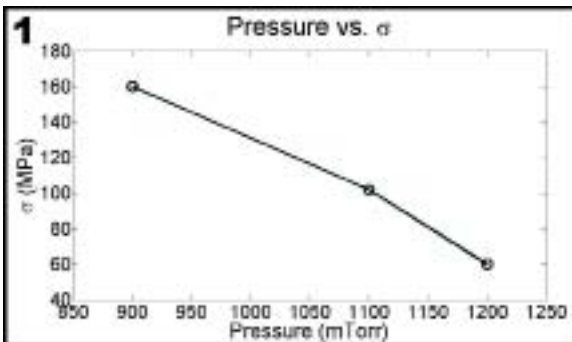


Figure 1: Pressure versus absolute value of compressive stress.

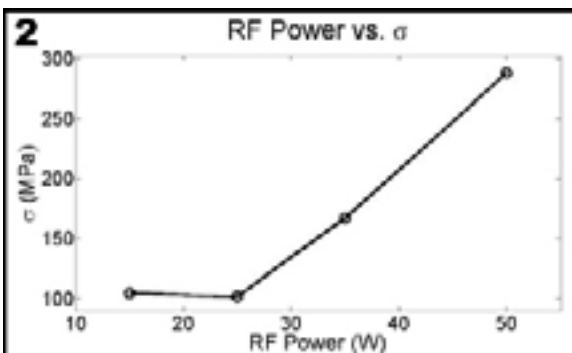


Figure 2: RF power versus absolute value of compressive stress.

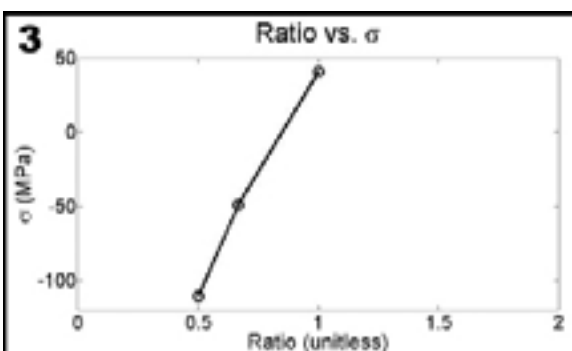


Figure 3: Gas ratio versus stress. The ratio is N_2O to silane.

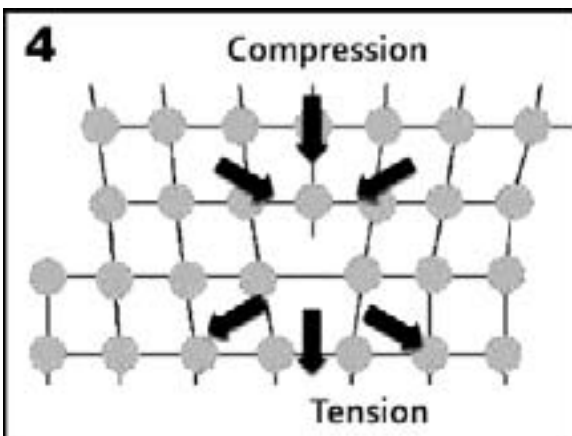


Figure 4: Edge dislocation demonstrating lattice disorganization inducing stresses.

In addition, silicon-rich oxides demonstrate significantly lower stresses than their traditional oxide counterparts. While it is possible the lattice constant may be more similar to silicon, and thus there is less stress due to lattice matching, a more likely source for the lowered values is a change in the thermal expansion coefficient of the film. It is likely the thermal expansion coefficients become more similar the more silicon rich the film. This convergence translates to a reduced bowing of the film.

Conclusion:

Based on the results of these experiments, the films with the lowest stress were found to be those with lower RF powers and gas ratios, for instance 1:1, and the higher pressures.

Acknowledgements:

Thanks to NSF and NNIN for funding my summer at Georgia Tech. I would like to thank Dr. Kenneth R. Brown and my mentor True Merrill for their continuous help throughout the entire process. Also, thank you to Nancy Healy, Katie Hutchison, Joyce Palmer and the National Nanotechnology Infrastructure Network Research Experience for Undergraduates Program.

References:

- [1] S. Seidelin, J. Chiaverini, R. Reichle, J. J. Bollinger, D. Leibfried, J. Britton, J. H. Wesenberg, R. B. Blakestad, R. J. Epstein, D. B. Hume, J. D. Jost, C. Langer, R. Ozeri, N. Shiga and D. J. Wineland. "A microfabricated surface-electrode ion trap for scalable quantum information processing." Phys. Rev. Letter. Vol 96, 253003 (2006).
- [2] M. Ohring, Materials Science of Thin Films: Deposition and Structure (Second Edition), Academic Press, San Diego (2002).
- [3] S.A. Campbell, The Science and Engineering of Microelectronic Fabrication, Oxford University Press, New York (1996).

Solution Synthesis and Aerosol Deposition of $\text{Cu}_2\text{ZnSnS}_4$ Nanoparticles

Denys Zhuo

Material Science and Engineering, Massachusetts Institute of Technology

NNIN iREU Site: National Institute for Materials Science (NIMS), Tsukuba, Ibaraki, Japan

NNIN iREU Principal Investigator(s): Dr. Naoki Ohashi, MANA Principal Investigator and Director of Optronic Materials Center, National Institute of Material Science

NNIN iREU Mentor(s): Dr. Jesse Williams, International Center for Young Scientists, NIMS

Contact: dzhuo@mit.edu, ohashi.naoki@nims.go.jp, williams.jesse@nims.go.jp

NNIN iREU Program

Introduction:

Copper zinc tin sulfide (CZTS) is being studied as an absorber material for thin film solar cells and as an alternative to copper indium gallium selenide (CIGS), which is expensive to produce because it contains the rare element indium. CZTS is an ideal absorber material due to its optimal band gap (1.5 eV), high absorption coefficient ($> 10^4 \text{ cm}^{-1}$), abundant/cheap materials, nontoxicity, and adaptability to various growth techniques [1].

Aerosol deposition (AD) is a type of powder spraying utilizing nanoparticles and is a cheap alternative deposition method to those requiring vacuum. Upon impact with the substrate, the nanoparticles' kinetic energy converts into thermal energy and a rise in temperature at the impact point promotes particle-particle/particle-substrate bonding to produce a dense film. Advantages of AD include high deposition rate, high density resultant films, low process temperature, scalability for mass production, and low cost equipment [2].

From this background, this work aims to synthesize CZTS nanoparticles via solution method appropriate for thin film AD. Advantages of solution synthesis include non-vacuum, single-step processing, utilization of inexpensive equipment/precursors, and scalability for mass production.

Experimental Procedure:

Solution Synthesis. CZTS powder was synthesized by a solution deposition process. Precursor powders, according to reaction $2\text{Cu}(\text{s}) + \text{Zn}(\text{s}) + \text{Sn}(\text{s}) + 4\text{S}(\text{s}) \rightarrow \text{Cu}_2\text{ZnSnS}_4$, were put into a reaction vessel with tetraethylene glycol (TetraEG) as a solvent. The precursors reacted at the solvent boiling temperature (317°C). This process was optimized by varying precursor chemicals, precursor/solution ratio, and reaction time (Table 1). Some samples were prepared using copper, tin, or zinc chloride salts instead of metallic precursors.

Two amounts of solvent (200/100 mL) were examined for effect of solubility and synthesis varied between 19–48 hours to determine sufficient reaction time. In a second variation, nanoparticles were grown onto a copper sheet, also serving as a source of copper for the reaction. Post-synthesis, the nanoparticles were centrifuged to separate from the solvent.

Characterization. Crystalline phases in the synthesized powders were identified by x-ray powder diffraction (XRD). Phase identification was done by referring to literature reporting XRD pattern of CZTS (kesterite-type structure) [3] and ICDD files. Chemical composition of synthesized powder was analyzed by means of energy dispersive x-ray (EDX) analysis. Particle size distribution in the resultant powder was determined by laser scattering.

Results and Conclusions:

X-Ray Diffraction. The crystal structure and XRD patterns for many of the residual phases and CZTS were very similar, so exact phase identification based solely on XRD was difficult. The possibilities were narrowed down to a few probable phases based on the best match between reference ICDD files and experimental peaks (Table 1).

The XRD pattern of sample 100715 corresponded most closely to kesterite and was also most similar to that of kesterite reported in literature (Figure 1). XRD peaks labeled 'Mo' in the reference pattern were from a molybdenum substrate used in the reference, which are absent in our results because we used glass as a substrate. CZTS phase was also produced in synthesis 100726 and 100802, though

Sample	Time [hours]	Cu source	S source	Zn source	Sn source	TEG [mL]	XRD	
							Main Phase	Possible 2nd Phases
100629	19	Cu powder	S powder	Zn powder	Sn powder	200	CuS, Cu ₂ Sy, Sn, Zn	
100706	20	Cu powder	S powder	Zn powder	Sn powder	200	CuS, Zn, Sn	Cu ₂ Sy
100715	24	CuCl	S powder	Zn powder	Sn powder	200	CZTS	Cu ₂ Sy, ZnS, Cu ₃₅ n ₅₄
100726	24	CuCl	S powder	Zn powder	Sn powder	100	ZnS, CZTS	Cu ₂ Sy, ZnS, Cu ₃₅ n ₅₄
100802	48	CuCl	S powder	Zn powder x 2	Sn powder	200	ZnS, CZTS	Cu ₃₅ n ₅₄ , Cu ₂ Sy
100818	24	Cu sheet & CuCl	S powder	Zn powder	Sn powder	200	Cu ₂ Sy, ZnS	
100823	24	Cu sheet	S powder	ZnCl ₂	SnCl ₂	200	ZnS	
100824	24	Cu powder	S powder	ZnCl ₂	SnCl ₂	200	Cu ₃₅ n ₅₄	CZTS, ZnS

Table 1: Summary of conditions for CZTS nanoparticle solution synthesis.

the amount of residual phase was much higher than in 100715. These results indicated a tendency for syntheses with CuCl instead of metallic Cu to form CZTS.

Chemical Composition. Results of EDX analyses (Figure 2) indicate that sample 100715 had the composition closest to ideal CZTS, consistent with results that sample 100715 is almost pure CZTS from XRD. Formation of CZTS was confirmed by XRD in synthesis 100726 and 100802, and consequently, compositions of those samples were also closer to ideal. Thus, it is clearly indicated that usage of CuCl as precursor enhanced formation of CZTS. Comparison of three samples prepared using CuCl also indicated that the amount of solvent is a crucial parameter for successful synthesis of CZTS. Chemical composition of 100726 deviated from the ideal composition, although the precursor composition was the same as that used in 100715.

Grain Size Distribution. Grain size distribution had three maximums. Peak 1 (0.7 nm) corresponded to an unknown source. Peak 2 (100-400 nm) corresponded to grain size, while peak 3 (~5 μ m) corresponded to agglomerated grain size. Looking at synthesis 100715 where almost pure CZTS was obtained, grain size was 200 nm, a little smaller than the ideal size of 500 nm for AD. However, agglomerated size of 100715 was 5.7 μ m which indicates that obtained grains were composed of primary particles.

Summary:

Based on XRD, EDX, and laser scattering, sample 100715 was the most successful synthesis, producing nanoparticles of the kesterite phase of CZTS with near stoichiometric composition and approaching ideal particle size. The combination of CuCl, Zn, Sn, and S powders appears to be the most promising precursors for producing kesterite nanoparticles. Increased synthesis time may enlarge grain size.

Future Work:

We hope to improve phase purity of CZTS by further optimization of precursor composition, solvent/precursor fraction, and particle size distribution by increasing primary grain size and dispersing grains to prevent agglomerations. We would also like to perform photoelectrical characterization to determine valence band structure and Fermi level with XPS, band gap with optical absorption, and concentration of carriers and mobility with Hall measurements.

Acknowledgments:

I would to extend my sincerest gratitude to my PI, Dr. Naoki Ohashi, my mentor, Dr. Jesse William, the NNIN iREU Program, the National Institute for Material Science, and

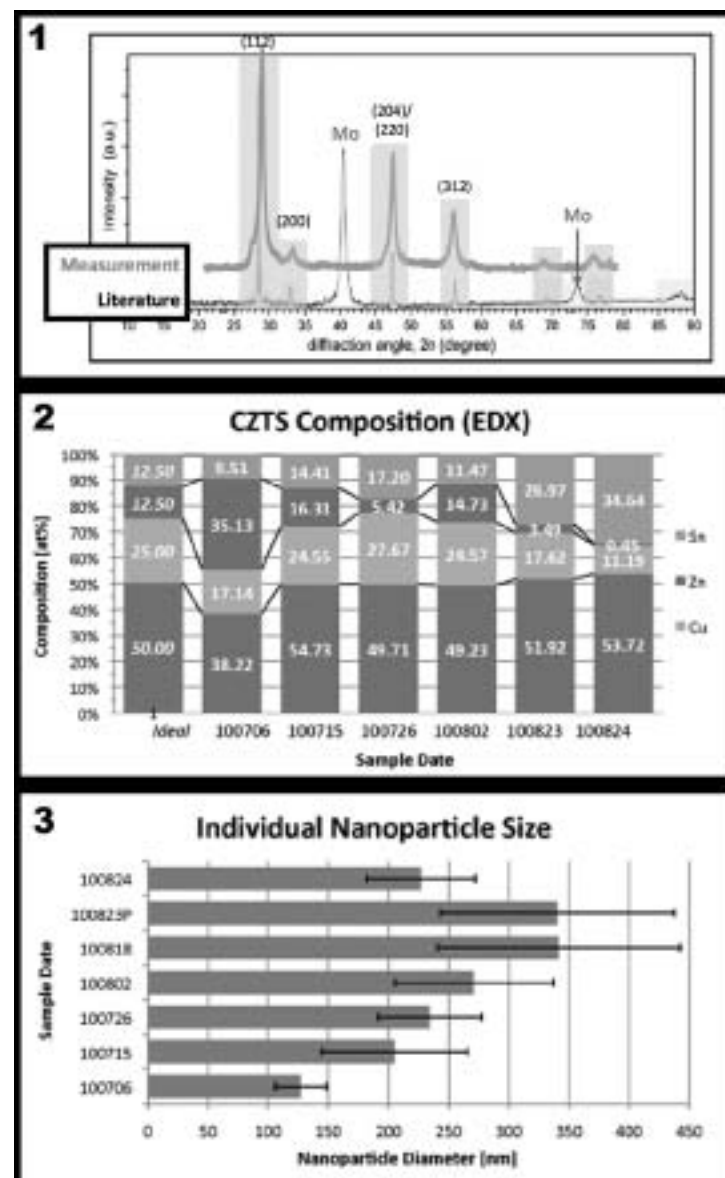


Figure 1: XRD spectra of sample 100715 compared to literature spectra for kesterite phase of CZTS [1].

Figure 2: Composition of syntheses from energy dispersive x-ray (EDX).

Figure 3: Size of primary grains of CZTS.

the National Science Foundation for the opportunity to do research in Japan and for funding.

References:

- [1] Chen, Shiyou, X. G. Gong, Aron Walsh, and Su-Hai Wei. "Defect physics of the kesterite thin-film solar cell absorber Cu_xZnSnS₄." *Applied Physics Letters* 96 (2010): 1-3. Web. 20 July 2010.
- [2] Akedo, Jun. "Room Temperature Impact Consolidation (RTIC) of Fine Ceramic Powder by Aerosol Deposition Method and Applications to Microdevices." *Journal of Thermal Spray Technology* 17.2 (2008): 181-98. Print.
- [3] http://bentgroup.stanford.edu/Research/research_PVmaterials.html

Real Time Blood Coagulation Sensor

Jennie Appel

Electrical Engineering, Auburn University

NNIN REU Site: ASU NanoFab, Arizona State University, Tempe, AZ

NNIN REU Principal Investigator(s): Dr. Junseok Chae, Electrical Engineering, Arizona State University

NNIN REU Mentor(s): Wencheng Xu, Electrical Engineering, Arizona State University

Contact: appeljh@auburn.edu, junseok.chae@asu.edu, wencheng.xu@asu.edu

Introduction:

Non-compressible hemorrhage is the leading cause of potentially survivable deaths from combat injuries in Operation Iraqi Freedom. In trauma injuries, naturally produced coagulation proteins are quickly depleted, which can lead to hemorrhage-related death [1]. The blood coagulation process can be described as an enzymatic cascade, which is activated in two cases: i) immediately after the damage of any blood vessel as the intrinsic system, or ii) if blood contacts with foreign materials as an extrinsic system [2]. There are numerous methods of monitoring the coagulation process such as prothrombin time and activated thromboplastin time. Acoustic resonators such as the quartz crystal microbalance, which resonates in a pure thickness shear mode, shift their resonant frequency with proportion to the square root of the viscosity density product of the coagulating blood sample [3].

We report a method of measuring blood coagulation in real time, using microelectromechanical systems (MEMS)-based small-size, portable, and disposable devices. The devices utilize contour-mode acoustic waves to measure viscosity change in real time. The contour mode MEMS-based film bulk acoustic resonator (C-FBAR) has a suspended ring-shaped piezoelectric layer of aluminum nitride thin film, sandwiched between two metal electrodes. The C-FBAR is excited in its radial directions and has a low motional impedance when coupled with liquids, allowing the device to maintain a high quality factor (Q) in liquids, up to 189. The high Q offers high sensitivity to the viscosity change during the coagulation process.

Experimental Procedure:

To characterize the C-FBAR as a viscosity sensor, we measured the viscosity of several controlled aqueous glycerine solutions using the C-FBAR. These solutions have

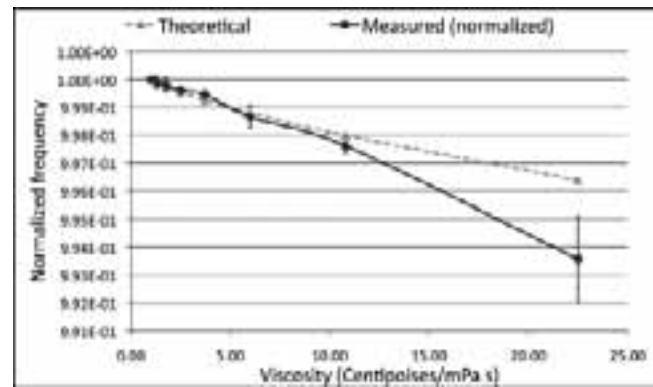


Figure 1: Desired range is 1-10 cP because blood coagulates occurs at 3-5 cP.

been characterized for their viscosity and density at room temperature [4]. As shown in Figure 1, the theoretical and the measured viscosity values are closely correlated in the range from 1 to 10 centipoises (cP). For the blood coagulation experiments, samples of citrated blood were prepared. Citrate prevents blood from coagulation, and calcium ions reverse the anti-coagulation process. The C-FBARs were placed on a probe station and were connected to a network analyzer (Agilent 5071C) to measure the one-port reflection coefficient (S_{11}). The C-FBARs were first characterized in the air and consequently performed blood coagulation monitoring as follows: after the citrated blood samples restored to 20 °C, we added different amounts of CaCO_3 powder to the blood samples, gently agitated, and dispensed a droplet to the C-FBAR surface immediately using a micromanipulator. The micromanipulator allowed very precisely controlled 3-axis movements, so that the minute volumes of liquid could be dispensed onto the delicate suspended resonator safely. The resonant frequency was recorded in real time after the sample droplet was applied via a LabVIEW program.

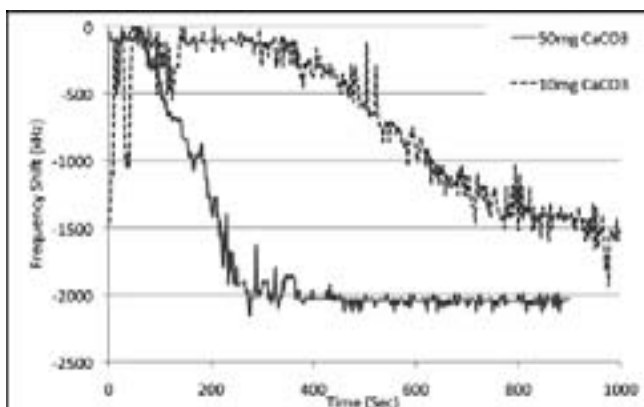


Figure 2: Real time frequency response of C-FBAR.

Results:

Figure 2 shows the real time frequency responses of the C-FBAR monitoring the blood coagulation process.

The addition of Ca^{2+} ions initiated the coagulation process, resulting in negative frequency shifts of the C-FBAR. Two different concentrations of CaCO_3 -added blood samples were tested. The frequency was steady during the initial stage, where the enzymatic cascade occurred and no viscosity changes were observed, resulting in a plateau phase in the frequency response. Consequently, at the end of the coagulation cascade, thrombin as central-protein cleaved fibrinogen to fibrin. The fibrin monomers eventually polymerized into fibers. As a result of the build-up and growth of polymerization clusters, the viscosity of the liquid increased [5], which demonstrated a continuous decrease of the resonant frequency. When the fibrin creation ended, a steady state was reached with no further change of the resonant frequency, indicating a constant viscosity was reached. Higher Ca^{2+} concentrations expedited the

coagulation process.

With 10 mg of CaCO_3 added to 0.5 mL citrated blood, the coagulation cascade completed at approximate six minutes and the creation of fibrin started. The fibrin formation ended and the final plateau phase began at around 14 min.

With 50 mg CaCO_3 in 0.5 mL citrated blood, the coagulation time was about two minutes and the fibrin creation ended before five minutes.

Conclusions:

By measuring resonant frequency shift we demonstrate that the MEMS-based C-FBAR can be used to monitor blood's coagulation in real time. The full coagulation time and the start and end of fibrin creation can be determined by monitoring the frequency shift in real time. The observation suggests that the C-FBAR has the potential to become a small-size, light-weight, low cost tool for medics in the field.

Acknowledgements:

I would like to thank my principal investigator, Dr. Junseok Chae, and my mentor, Wencheng Xu, for all of their help and guidance. My thanks also go to the NNIN REU Program, the National Science Foundation, and the Center for Solid State Electronics Research at Arizona State University for research support and funding.

References:

- [1] JB Holcomb, NR McMullin, L Pearse, et al. "Causes of death in US Special Operations Forces in the global war on terrorism": 2001-2004, Ann Surg, v. 245 n. 6, p. 986-991, 2007.
- [2] Macfarlane, R. G., 1964. Nature. 202, 498-499.
- [3] Kanazawa K. K., Gordon J. G., 1985. Anal. Chim. Acta., 175, 99-105.
- [4] Segur J. B., Oberstar H. E., 1951. Ind. Eng. Chem., 43, 2117-2120.
- [5] Muller L., Sinn S., Drechsel H., Ziegler C., Wendel H-P., Northoff H., Gehring F. K., 2010. Anal. Chem. 82, 658-663.

Locomotion of Catalytic Nanomotors

Jesse Ault

Mechanical Engineering, Purdue University

NNIN REU Site: ASU NanoFab, Arizona State University, Tempe, AZ

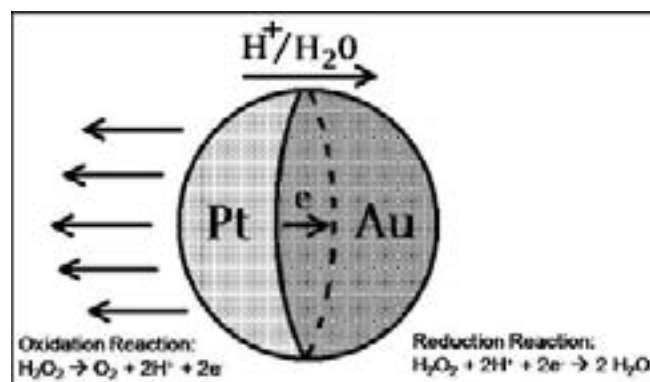
NNIN REU Principal Investigator(s): Dr. Jonathan Posner, Mechanical Engineering and Chemical Engineering, ASU

NNIN REU Mentor(s): Jeffrey Moran, Mechanical Engineering, Arizona State University

Contact: jtault@purdue.edu, jposner@asu.edu, jeffrey.moran@asu.edu

Abstract:

Bimetallic nanomotors propel themselves autonomously in solutions of hydrogen peroxide (H_2O_2). The asymmetric catalytic decomposition of H_2O_2 at the nanomotor surface creates a proton imbalance and self-generated electric field, driving fluid from the anode to the cathode, through a method known as Reaction Induced Charge Auto-Electrophoresis [1]. The nanomotors' velocities have been shown to vary directly with the concentration of H_2O_2 in solution. The effective diffusivity of the nanomotors is controlled by the coupling of the nanomotors' thermal, rotational, and translational diffusivities, as well as their advective velocities. We quantify the effective diffusivities of spherical bimetallic nanomotors by tracking their positions over long times (> 30 minutes) and calculating the root mean square displacement. We find that a motor's effective diffusivity depends on its diameter as well as the local fuel concentration.



Introduction:

The study of nanomotors has recently become one of the great foci in nanotechnology. Bimetallic nanomotors, which are Janus nanoparticles composed of two different metals, have been shown to spontaneously propel themselves when in solutions of hydrogen peroxide (H_2O_2). This phenomenon was first demonstrated by Paxton, et al. [2]. Figure 1 shows the net reaction proposed by Paxton, et al. [3]. Later, Moran, et al. suggested that the nanomotors move by a mechanism called Reaction Induced Charge Auto-Electrophoresis [1]. Consuming the peroxide as fuel, these nanomotors have been used to pick up, transfer, and deposit cargo particles.

During this project, we sought to: 1. Determine the relationships between the nanomotor's velocity, diffusivity, and local H_2O_2 concentration; 2. Quantify the nanomotors' effective diffusivities; and 3. Understand their underlying behavior by decoupling their thermal, rotational, and translational diffusivities from their effective diffusivities.

Self-propelled nanomotors offer the possibility for controlled drug delivery in the body and the mimicry of biological systems on the nanoscale.

Experimental Procedure:

Our nanomotors were created using the multi-stage deposition coating method of Wheat, et al. [4]. As can be seen in Figure 2, 3 μm diameter polystyrene spheres were

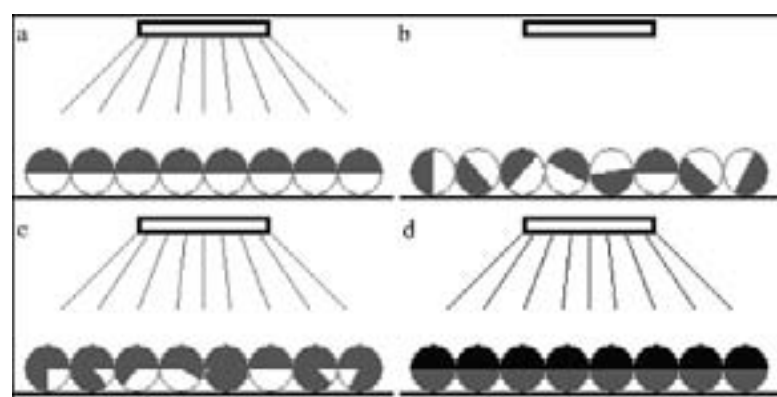


Figure 2: Experimental setup as devised by Wheat, et al. [4].

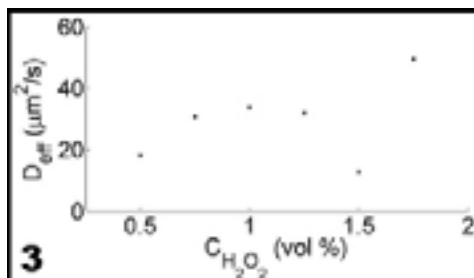


Figure 3: Nanomotor effective diffusivity.

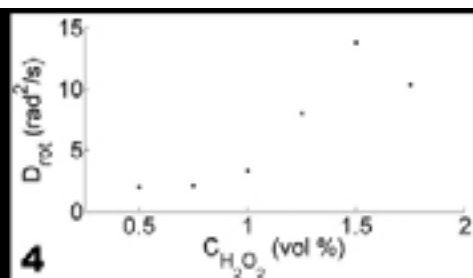


Figure 4: Nanomotor rotational diffusivity.

deposited on a glass substrate and half-coated with gold. The spheres were then resuspended and deposited with random orientations. The new exposed face was then plated with gold. Repeating this process for several cycles, fully coated the spheres in gold. Finally, they were plated with a single coating of platinum. Solutions of these nanomotors were diluted to approximately 10-20 spheres per mL. 30% H_2O_2 was then added to this solution to obtain the desired fuel concentration. 750 mL of this solution were placed in a microfluidic channel, and individual nanomotors were then located using a microscope under 20X magnification.

The motion of the nanomotors was then recorded using image capture software and analyzed using MATLAB. After tracking each nanomotor for long time periods (> 30 minutes), the effective diffusivities of the nanomotors were quantified by calculating the root mean square displacements of the particles. This method was used for a range of 0.25% - 2.00% hydrogen peroxide fuel concentrations.

Results and Conclusions:

Our preliminary data suggested a nearly linear relationship between the nanomotors' velocities and the local peroxide concentrations, a relationship that has been shown by Paxton, et al. [3]. This evidence gave initial confidence in the functionality of the motors. Due to the increase in velocity with peroxide concentration, we expect the effective diffusivity to increase with concentration as well. However, Figure 3 shows that the effective diffusivity increases and then decreases with peroxide concentration. The effective diffusivity decreases at high peroxide concentration because, as Figure 3 shows, the rotational diffusivity tends to increase with increasing peroxide concentration. When a nanomotor's rotational diffusivity is high, the increased rotation tends to prevent the motor from translating an appreciable distance from the motor's origin, despite the increased translational velocity.

These results indicate that the interplay between nanomotor velocity, rotational diffusivity, and effective diffusivity may govern the motion of these bimetallic spheres. In addition, by calculating the Brownian diffusivity for a $3 \mu\text{m}$ sphere in water, and comparing this value to experimental values of effective diffusivity, we have shown that our measured diffusivities are two orders of magnitude higher than

the calculated thermal diffusivity of $0.143 \mu\text{m}^2/\text{s}$. This demonstrates that the diffusivity of the nanomotors is greatly enhanced due to the locomotion.

Future Work:

We have shown that the effective diffusivity of bimetallic spherical motors is limited by their rotational diffusivity. However, we have not established how these two properties relate to each other, and how the velocity affects this relationship. Nor have the reasons for the spheres' increase in rotational diffusivity with peroxide concentration been established.

The experimental methods performed in this study were preliminary, and much additional experimentation will be required to determine the precise relationship between the motor velocity, effective diffusivity and rotational diffusivity. In addition, the more far-reaching long-term goal for this research is to design motors capable of autonomous but predetermined motion. This would allow for the statistically controlled delivery of cargo by the nanomotors through knowledge of the motors' swimming tendencies.

Acknowledgments:

I would like to acknowledge Dr. Jonathan Posner, Jeffrey Moran, and Nathan Marine for their guidance, and the National Nanotechnology Infrastructure Network Research Experience for Undergraduates Program, the National Science Foundation, the Center for Solid State Electronics Research, and Arizona State University for providing funding and facilities for this research.

References:

- [1] Moran, J.L.; Wheat, P.M.; Posner, J.D. "Locomotion of Electrocatalytic Nanomotors due to Reaction Induced Charge Auto-Electrophoresis." *Phys. Rev. E* 81, 065302(R) (2010).
- [2] Paxton, W.F. et al. "Catalytic Nanomotors: Autonomous Movement of Striped Nanorods." *J. Am. Chem. Soc.* 126, 13424-13431 (2004).
- [3] Paxton, W.F.; Mallouk, T.E.; Sen, A. "Motility of Catalytic Nanoparticles Through Self-Generated Forces." *Chem. Eur. J.* 11, 6462-6470 (2005).
- [4] Wheat, P.M.; Marine, N.A.; Moran, J.L.; Posner, J.D. "Rapid Fabrication of Bimetallic Spherical Nanomotors." *Langmuir Letter* DOI: 10.1021/la102218w

Fabrication of a Three Terminal Nanomechanical Graphene Switch

Lauren Cantley
Physics, Grinnell College

NNIN REU Site: Colorado Nanofabrication Laboratory, University of Colorado, Boulder, CO

NNIN REU Principal Investigator(s): Scott Bunch, Mechanical Engineering, University of Colorado, Boulder

NNIN REU Mentor(s): Xinghui Liu, Mechanical Engineering, University of Colorado, Boulder

Contact: cantley@grinnell.edu, jbunch@colorado.edu, exinghui@gmail.com

Abstract and Introduction:

Nanomechanical switches can be used in a variety of applications, such as memory design or computational elements. Due to their temperature and radiation resistance, nanomechanical switches are advantageous over semiconductor switches in some applications, such as extreme environments where computational devices would need to withstand large amounts of radiation or extreme heat.

Graphene, a single atomic sheet of graphite, has superior electrical, mechanical and thermal properties. The high Young's Modulus, extremely low mass, low resistivity and planar surface make suspended graphene ideally suited for the active component of a nanomechanical switch. Thus, the objective of this project was to fabricate and test a graphene based nanomechanical switch.

Device Design and Operation:

The device geometry consisted of a graphene sheet suspended over a silicon/silicon dioxide substrate and in electrical contact with a gold electrode. Voltage applied to the underlying silicon substrate was used to actuate the switch. By applying a voltage, the graphene was brought into physical contact with the underlying silicon step and was in the closed state. By removing the voltage, the graphene was no longer in contact, and returned to the open state, as seen in Figure 1.

The three terminal design can adapt to transistor logic and allows for separate gate and circuit voltages, resulting in a low voltage drop across the graphene during the On State. Additionally, the mechanical nature of the switch allows for a high On/Off ratio.

Fabrication:

The switch was fabricated using standard photolithography (Figure 2). Starting with a bare silicon-on-insulator (SOI) wafer (top silicon [Si] layer 2 μm , SiO_2 0.5 μm) (Step 1), a 65 nm oxide was grown on the top surface through thermal oxidation (Step 2). Gold electrodes were deposited using

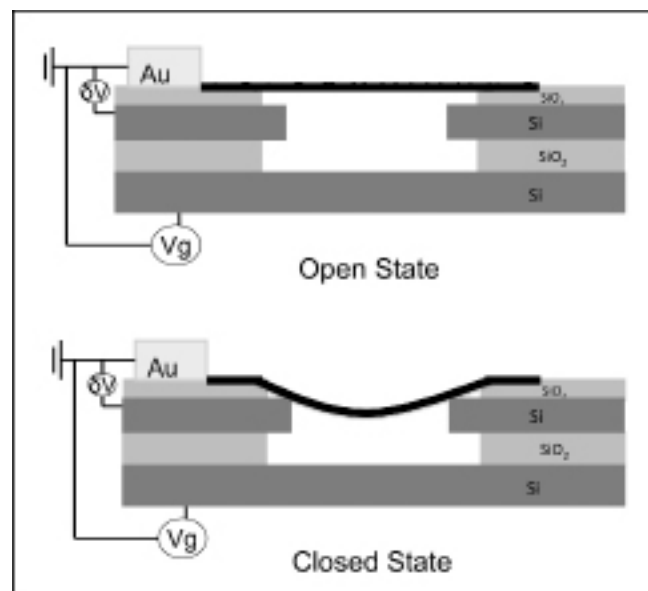


Figure 1: Three terminal switch design.

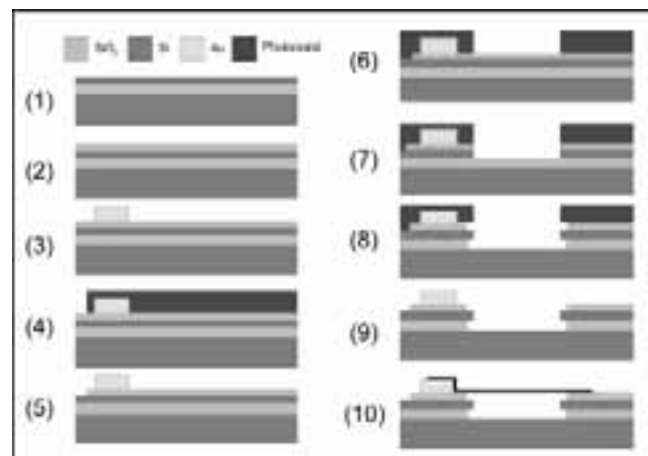


Figure 2: Fabrication process outline.

evaporation and lift-off techniques (Step 3). A pattern was formed with photoresist for probe access windows (Step 4), which were then etched into the top layer of Si by buffered oxide etching (Step 5). The switch cavities were patterned onto the substrate with photoresist (Step 6), and etched into the bottom layer of SiO_2 with reactive ion etching ($\sim 2.5 \mu\text{m}$ depth) (Step 7).

This was followed by buffered oxide etching to remove the excess SiO_2 and form the Si step ($\sim 1 \mu\text{m}$ wide) to which the graphene would make contact (Step 8). Photoresist was then removed (Step 9). Additionally, a trench, surrounding each device, was etched down to the bottom layer of Si in order to electrically isolate the top and bottom layers of Si. This was done in order to prevent electrical shorts between the two layers.

The final geometry of the substrate can be seen in Figure 3.

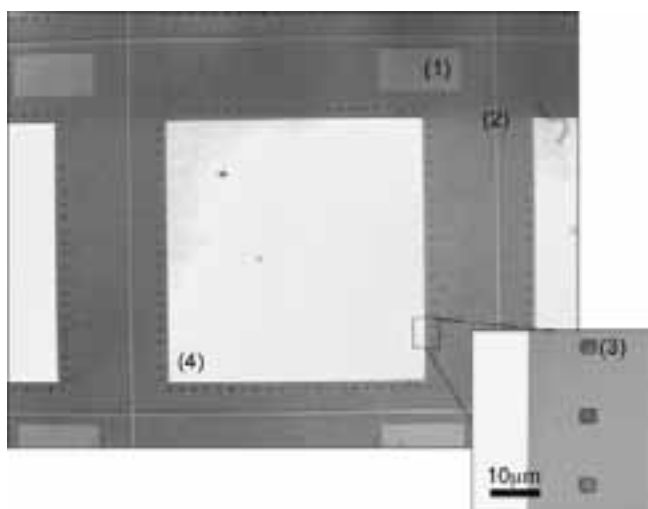


Figure 3: Overhead view of final substrate geometry. Access window to top layer of silicon (1), electrical isolation trench (2), switch cavity (3), gold electrode (4).

The final step in the fabrication process was to suspend a graphene sheet over the cavity by way of mechanical exfoliation (Step 10). Figure 4 shows an overhead view of the final switch with each cavity $5 \mu\text{m}$ in diameter and $\sim 2.5 \mu\text{m}$ deep.

Results and Conclusions:

The graphene nanomechanical switch was successfully fabricated to the desired geometry. Electrical testing using a probe station is currently in progress. By sweeping the voltage and measuring the current associated with the graphene in physical contact with the underlying silicon substrate, one is able to read out the open and closed states of the switch. The distance between the suspended graphene

and the bottom layer of silicon to which the actuation voltage is applied is fairly large, thus requiring a much greater voltage than desired to pull down the graphene sheet into physical contact with the sense electrode. Future designs will incorporate a smaller gap between the graphene and underlying silicon substrate to lower the actuation voltage of the switch.

Future Work:

Future work includes the continuation of electrical testing with the current graphene switches and alterations in the geometry of the substrate to reduce the required actuation voltage. Alterations include reducing the overall depth of the cavity as well as experimenting with the width of the top silicon step.

Acknowledgements:

I would like to thank the National Nanotechnology Infrastructure Network REU Program and the National Science Foundation for their support of this research. I would especially like to thank Dr. Scott Bunch, Xinghui Liu, the rest of the Bunch Lab as well as the entire Colorado Nanofabrication Lab for their professional help and guidance on this project.

References:

- [1] J. S. Bunch et al. "Electromechanical Resonators from Graphene Sheets." *Science*, 315, 490-493. 2007.
- [2] J. S. Bunch et al. "Impermeable Atomic Membranes from Graphene Sheets." *Nano Letters*, 8.8, 2258-2462. 2008.
- [3] A.K. Geim and K. S. Novoselov. "The Rise of Graphene." *Nature*, 6, 183-191. 2007.
- [4] A.K. Geim. "Graphene: Status and Prospects." *Science*, 324, 1530-1534. 2009.

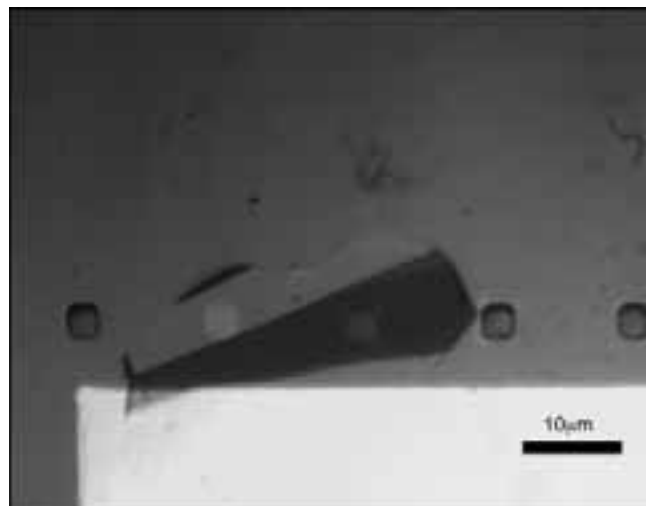


Figure 4: Image of completed switch.

Mechanics of 1-25 nm Thin Films

Zachary J. Connell
Mechanical Engineering, University of Nebraska

NNIN REU Site: Penn State Nanofabrication Laboratory, The Pennsylvania State University, State College, PA
 NNIN REU Principal Investigator(s): Dr. Aman Haque, Mechanical and Nuclear Engineering, Pennsylvania State University
 NNIN REU Mentor(s): Sandeep Kumar, Mechanical and Nuclear Engineering, Pennsylvania State University
 Contact: zjconnell@huskers.unl.edu, mah37@engr.psu.edu, suk191@psu.edu

Abstract:

Nanoscale thin films are used in a wide array of technologies, ranging from computer processing to solar panels. The purpose of this project was to fabricate a device capable of testing mechanical, electrical, and thermal properties of a wide range of free standing thin films within a transmission electron microscope (TEM) environment. Using various photolithography, deposition, and etching techniques, devices were fabricated with free standing platinum thin films. *In situ* TEM experiments on high current-density electromigration in 100 nm platinum thin films were conducted. The specimen began with very small, randomly oriented grains. Current was slowly increased from 100 μ A to 10 mA over the course of three and a half hours. Almost instantaneous grain growth was observed at 10 mA. After passing this current for several minutes, average grain size increased dramatically and dislocation pile-up was observed. Selected area electron diffraction (SAED) patterns show grain rotation to the <111> plane during the grain growth. Using the methods and devices developed in this project, a vast array of experiments on nanoscale thin films can be conducted.

Introduction:

It is important to be able to test the mechanical, electrical, and thermal properties of nanoscale thin films, as they often behave significantly different from their bulk material counterparts. The goal of this project was to create a process for fabricating devices for *in situ* transmission electron microscope (TEM) testing of a wide variety of nanoscale thin films. TEM is able to give qualitative information on mechanics, which, coupled with quantitative data from the device, gives great detail on the behavior of these thin films.

Experimental Procedure:

The device design, shown in Figure 1, incorporated mechanical, electrical, and thermal testing. Area 1 of the figure shows the thermal actuators, which expanded due to Joule heating when current was passed through them, imparting stress on the specimen. Area 2 shows the cooling fins which limited thermal leakage to the specimen. Area 3 shows the microelectrodes which allowed for electrical readings using a four-probe method. Thermal information could also be gathered from these microelectrodes using the 3ω method. Area 4 is the thin film itself, made free-standing by the TEM through-hole.

Evaporation deposition techniques were used to deposit 100 nm platinum on the device side of a silicon-on-insulator wafer. The device was fabricated using device and back side photolithography patterning followed by deep reactive ion

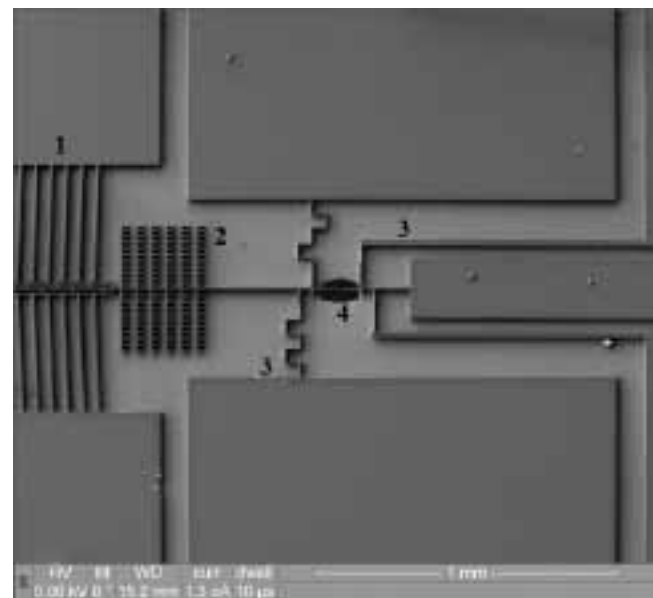


Figure 1: Scanning electron microscope image of device design.

etching on both sides. Finally, the device was released using hydrofluoric vapor etching.

An electromigration experiment was performed on the platinum sample within the TEM. Current was passed through the sample and slowly increased from 100 μ A to 10 mA over three and a half hours.

Results:

Initial TEM, shown in Figure 2, indicated that the film began with a very small average grain size, approximately 5 nm. Initial SAED patterns, seen in the upper right of Figure 2, indicated that the sample had a randomly oriented face centered cubic crystalline structure, similar to that of a powder.

After passing 10 mA current for approximately one minute, the size of the grains increased significantly. SAED indicated that the sample maintained a random crystal structure throughout this growth. The 10 mA current was passed through the sample again and more grain growth was observed. Once the grains reached a certain size, approximately 50-100 nm, dislocation pile-up was seen in TEM imaging, as shown in Figure 3. Most grains ceased to rotate upon reaching this size, indicating that the primary mechanism for accommodating stress had shifted from grain rotation to dislocation motion.

Current was increased to 13 mA, after which the specimen failed. TEM imaging of the remaining areas showed an average grain size of approximately 100 nm, as seen in Figure 4. In some areas of the remaining sample, both the $<111>$ and $<200>$ rings in the SAED pattern vanished completely, while the $<220>$ ring was brightly illuminated, as seen in the upper-right of Figure 4, indicating the grains had almost completely rotated such that the $<111>$ plane was in alignment with the stress direction.

Conclusions:

Significant amounts of grain growth resulted from the high density current passing through the nanoscale platinum thin film, changing the average grain size from ~ 5 nm to ~ 100 nm. The observed grain growth is most likely due to atomic diffusion as a result of electromigration. However, further studies are needed to precisely determine the underlying cause for this grain growth. Specifically, additional studies are needed to isolate the effects of electromigration from any thermal effects due to Joule heating from the electric current that may be contributing to the observed phenomena.

Additionally, the primary mechanism for stress accommodation changed from grain growth and grain rotation to dislocation motion when the grains become large enough to accommodate dislocation pile up. Before this point, the grains rotated to orient the $<111>$ plane in alignment with the stress. In face-centered cubic structures, $<111>$ is the closed-packed family of planes. Therefore, when grains are too small to accommodate dislocation pile-ups, they tend to rotate such that the closed-packed plane is in alignment with the stress.

This experiment demonstrated that our method for creating devices for *in situ* transmission electron microscopy testing of nanoscale thin film mechanics was successful and is viable for future experiments on a vast array of thin films. Devices are currently being fabricated with zinc oxide, aluminum, and poly(3,4-ethylenedioxythiophene) thin films.

Acknowledgments:

I would like to thank my graduate mentor Sandeep Kumar, advisor Dr. Aman Haque, the NNIN Research Experience for Undergraduates Program, and the Penn State Nanofabrication Lab.

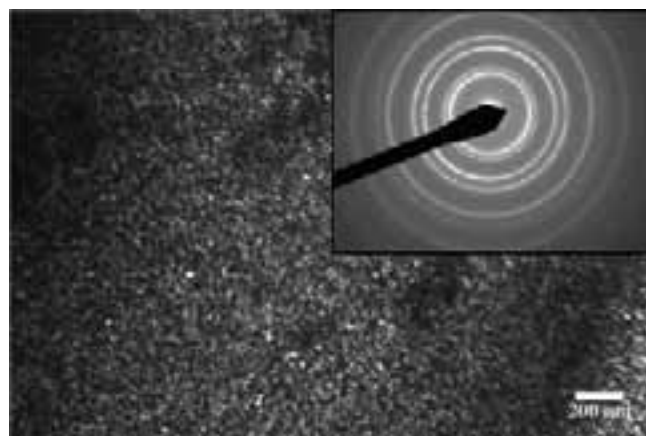


Figure 2: Initial very small grains with random crystalline structure.



Figure 3: Dislocation pile-up observed in larger grains.

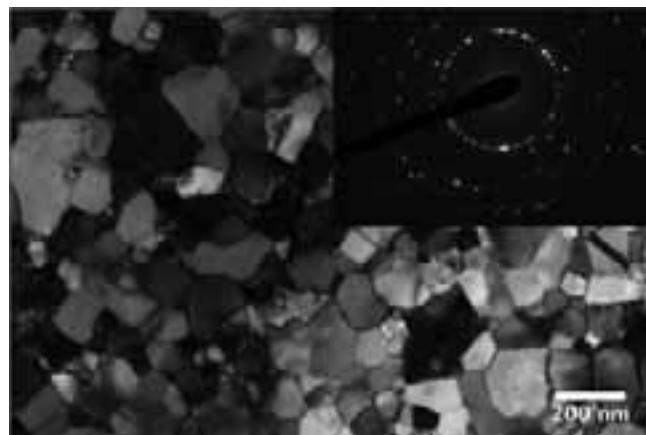


Figure 4: 100 nm grain size with oriented crystalline structure.

Top-Down Fabrication of Patterned, Vertically Aligned Silicon Nanowires

Sibu Kuruvilla

Materials Science and Engineering, University of Illinois at Urbana-Champaign

NNIN REU Site: Lurie Nanofabrication Facility, University of Michigan, Ann Arbor, MI

NNIN REU Principal Investigator(s): Prof. Anastasios John Hart, Mechanical Engineering, University of Michigan at Ann Arbor

NNIN REU Mentor(s): Sameh H. Tawfick, Mechanical Engineering, University of Michigan at Ann Arbor

Contact: skuruvi2@illinois.edu, ajohnh@umich.edu, stawfick@umich.edu

Abstract and Introduction:

Silicon nanowires (SiNWs) have recently attracted significant attention due to their one-dimensional structure [1] and semiconducting properties [2]. With many potential applications in micro- and nano-electro-mechanical systems (M/NEMS) [3], the development of various SiNW conformations is a popular area of current research. Challenges, however, such as controlled fabrication, presently keep this promising technology from reaching mainstream industry.

The aim of this project, therefore, was to develop a method of synthesizing patterned, vertically-aligned SiNWs with highly controlled diameters and lengths using a top-down fabrication method. The ultimate use of this methodology will be to develop various three-dimensional (3D) shapes and curvatures of SiNWs, with the hopes that the manipulation of these structures can offer many applications, especially in M/NEMS devices.

In order to realize the ultimate goal of 3D SiNW microstructures, controlled synthesis must first be accomplished. Recently, there has been success in NW fabrication with relatively controlled dimensions and densities using both bottom-up and top-down methods [4]. In the present work, the latter approach was used, in order to properly pattern the nanowires into desired microstructures.

The process began by photolithographically patterning Si wafers, and then etching them so that Si micropillars remained on the wafers. Then, in order to form SiNWs from the pillars, a metal-assisted chemical etching (MACE) mechanism [5] was employed, during which the wafer was submerged in a solution of hydrofluoric acid (HF) and silver nitrate (AgNO_3), resulting in SiNWs that collectively were shaped in the original patterned structure.

For the current purpose, however, there were restrictions present. During the etching process, the desired mechanism was for etching to occur only at the top of a micropillar, and not at its sides nor at the substrate level. In order to achieve this, an etch mask had to be laid down to coat the sidewalls and the substrate to protect them from the MACE process. Various masks were tested, and the results showed that a Teflon®-like polymer deposited by deep reactive ion etching (DRIE) from C_4F_8 plasma produced an effective mask.

Experimental Methods:

A basic photolithography process combined with DRIE was employed to pattern micropillars on bare Si wafers (Figure 1). After the spin-coating of photoresist (PR, SPR 220-3.0, $3.5\ \mu\text{m}$), the wafers were exposed to ultraviolet light for six seconds in a mask aligner, exposing the areas intended for patterns. After development of the PR for one minute, Si micropillars ($20\text{--}40\ \mu\text{m}$ tall) were formed by DRIE. Then, the etch mask was deposited using only the passivation layer (no etchant) in the DRIE process, flowing C_4F_8 plasma (200 sccm, 0.5–1.5 minutes).

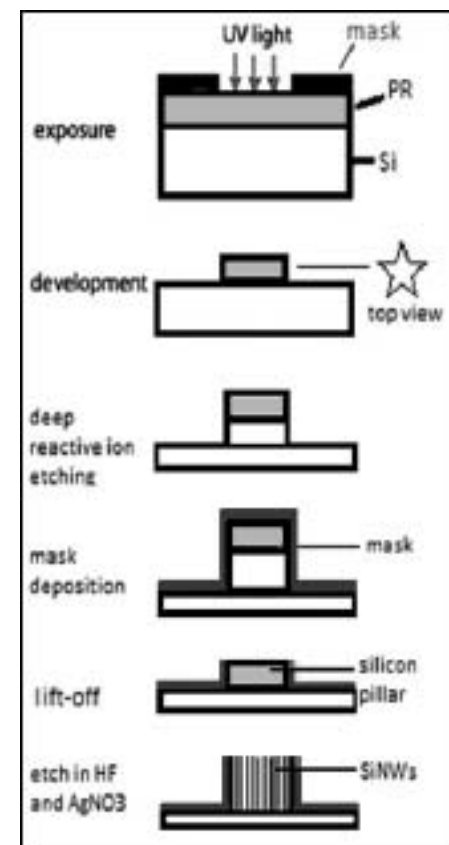


Figure 1: A map of the step by step SiNW fabrication method.

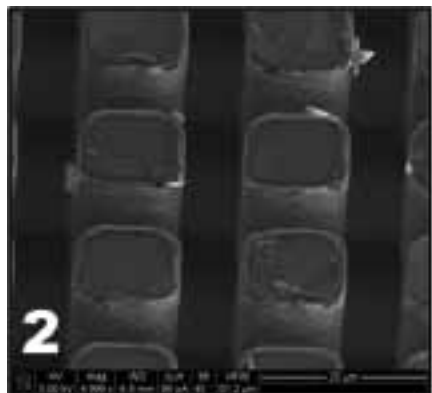


Figure 2: Patterned micropillars of Si coated by Taffy that are now ready for the MACE process.

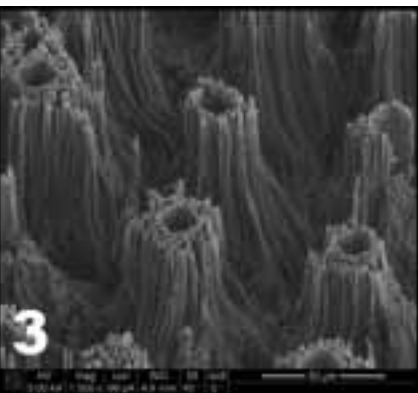


Figure 3: SiNWs that have self-densified into structures during a one hour etch.

Next, after lifting off the mask from the top of the pillars by sonicating in acetone (16 minutes), the samples were ready to etch (Figure 2). The etch bath consisted of 5M HF and 0.04M AgNO₃ at 50°C, and the samples were placed in it for 10 minutes. They were then removed and rinsed with nitric acid. Finally, the samples were imaged using scanning electron microscopy (SEM).

Results and Discussion:

Our first tests set out to investigate the effect of patterning Si substrates on the SiNW fabrication process. After photolithography and DRIE were done to form shaped micropillars, samples were placed in the etch bath for one hour. As we can see in Figure 3, the process was successful. SiNWs were synthesized with aspect ratios of up to 3000, and they, in fact, seemed to self-densify based on the pre-patterning of the substrate. Although it was promising, this behavior did not occur everywhere, however. Certain patterns (like the one shown) formed SiNWs as anticipated, but for others, there was more etching at their sides and at the substrate level than there was at their tops. Therefore, it was evident that the original etch mask—aluminum oxide, Al₂O₃—was insufficient and needed to be replaced.

After testing many materials, one was found to effectively mask the micropillar sides and substrate—a Teflon-like polymer deposited by the DRIE process. Depositions between 0.5-1.5 minutes resulted in thicknesses of the polymer, or “Taffy,” that ranged from 100-500 nanometers. These thicknesses worked well to protect the sidewalls of the pillars, as well as the substrate, while still allowing for etching to occur at the top. In Figure 4, we can see that bundles of SiNWs, about 50-300 nm in diameter, are evident only at the top of a micropillar. This process was therefore very promising

in fabricating vertically aligned SiNWs that assume a pre-patterned shape, and ultimately, 3D structures.

Future Work:

Despite the promising results, there is still optimization to be done. In some areas between patterns, the Taffy did not seem to adhere to the substrate. For this reason, it came off during the etching and exposed the underlying area to the HF/AgNO₃ combination. Further studies should try to understand why this occurs and change the parameters so that uniform masking can occur. Once the minor hurdles are settled, controlled synthesis of patterned, 3D SiNW structures should be realized.

Acknowledgements:

The support from the National Science Foundation (NSF) and the National Nanotechnology Infrastructure Network Research Experience for Undergraduates (NNIN REU) Program, as well as the guidance from Sameh Tawfick, Professor John Hart, and the Mechanosynthesis Group at the University of Michigan has made this work possible.

References:

- [1] Chang, S., et al. “Densely Packed Arrays of Ultra-High-Aspect Ratio Si Nanowires.” *Advanced Functional Materials* (2009): 2495-2500.
- [2] Cui, Y. et al. “Nanowire Nanosensors for Highly Sensitive and Selective Detection of Biological and Chemical Species.” *Science* (2001): 1289-1292.
- [3] Feng, X.L., et al. “Substrate Bending for Reversible Control of Frequency and Quality Factor of Nanostring Resonators.” *Nano Letters* (2007): 1953-1959.
- [4] Hahm, J. and C.M. Lieber. “Direct Ultrasensitive Electrical Detection of DNA and DNA Sequence Variations Using Nanowire Nanosensors.” *Nano Letters* (2004): 51-54.
- [5] Hochbaum, A.I., et al. “Enhanced thermoelectric performance of rough silicon nanowires.” *Nature* (2008): 163-167.

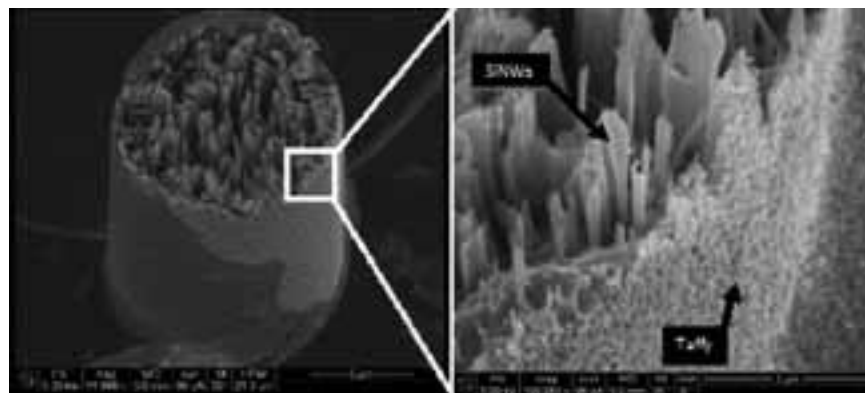


Figure 4: A micropillar that has SiNWs forming at the top, while the sides remain coated by Taffy.

Ion Distribution in Ionomer and High Temperature Ionic Liquid Actuators

Stephen Twigg

Department of Electrical Engineering, Villanova University

NNIN REU Site: Penn State Nanofabrication Laboratory, The Pennsylvania State University, State College, PA

NNIN REU Principal Investigator(s): Dr. Qiming Zhang, Department of Electrical Engineering, Pennsylvania State University

NNIN REU Mentor(s): Yang Liu, Department of Electrical Engineering, Pennsylvania State University

Contact: stephen.twigg@villanova.edu, qxz1@psu.edu, yul165@psu.edu

Abstract:

Proper understanding of the ion transport and concentration distribution in low voltage ionomer-based actuators is crucial for optimizing their performance in medical and optical devices. Actuators were built using Aquivion™ swelled with ionic liquid of 1-butyl-2,3-dimethylimidazolium chloride ($[BMMI^+][Cl^-]$). Electrical impedance, I-V characteristics, and charging current for the actuator were characterized using both room temperature, and a temperature above the 99°C melting point for $[BMMI^+][Cl^-]$ [1]. The direct current (DC) conductivity of the actuator was found to be 30 μ S/cm at 100°C and two orders of magnitude higher, compared to room temperature measurements. The electrochemical window of the device was determined to be 3V. Charge accumulation was measured to be one order of magnitude greater at 100°C compared to room temperature. Bending actuation under 2.5 V was observed at $100 \pm 10^\circ C$, but not at room temperature. A semi-quantitative depth profile of ion concentration was measured by using SIMS imaging. Depth profiling suggests that, in a charged actuator, concentration gradients for $[BMMI^+]$ are thicker compared to corresponding $[Cl^-]$ gradients. The charged actuator also demonstrated unexpected accumulation of $[Cl^-]$ in the cathode and $[BMMI^+]$ in the anode which was due to a clustering effect in ionic liquids.

Introduction and Objective:

Ionomer and ionic liquid actuators show great promise for effectively converting electrical stimulus into mechanical motion. Application of a few volts of bias across the actuator causes ion accumulation near the electrodes. These ion accumulations swell the electrode region causing expansion of the polymer matrix and, due to the larger size of the cation compared to the anion, subsequent bending of the actuator towards the anode [2].

This project analyzed the ion distribution inside a charged actuator. Prior work with these types of actuators generally used ionic liquids with a melting point below room temperature. These ionic liquids were unsuitable for use in this analysis since the ions would quickly discharge or evaporate while inside a room temperature spectroscopy chamber. To avoid this issue, actuators were built using the ionic liquid 1-butyl-2,3-dimethylimidazolium chloride ($[BMMI^+][Cl^-]$) from Aldrich, due to its high melting point of 99°C.

Synthesis:

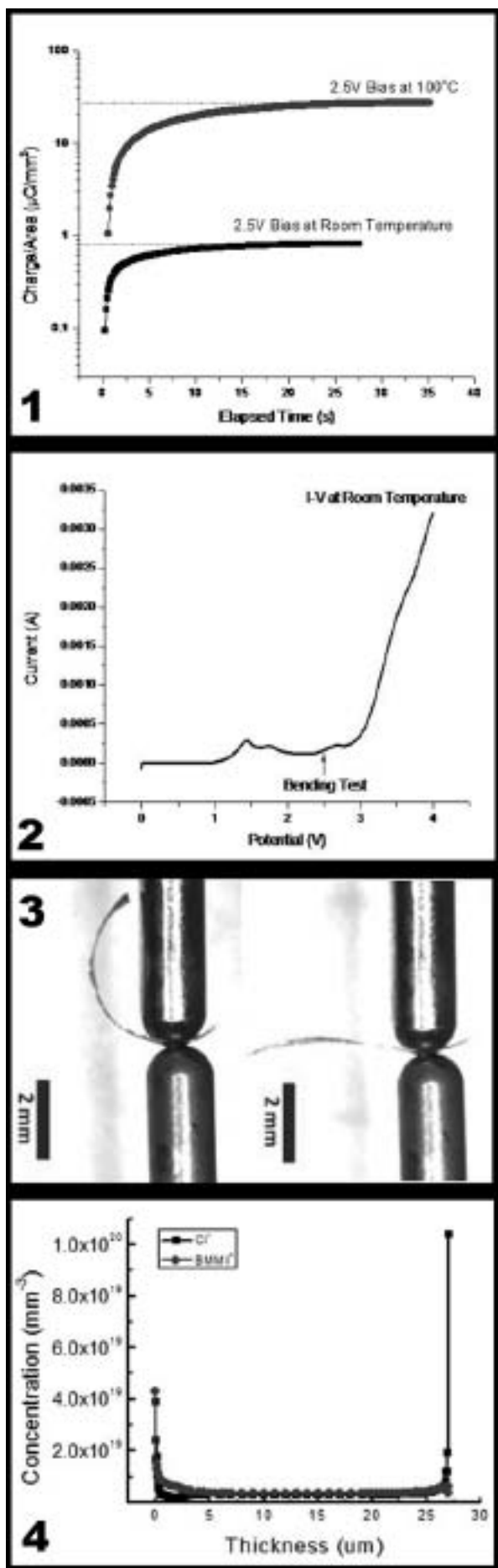
The use of a solvent was necessary to precisely control the uptake of $[BMMI^+][Cl^-]$ into the Aquivion™ polymer purchased from Solvay Solexis. A solution by mass of 66% $[BMMI^+][Cl^-]$ and 34% ethanol was prepared and held at 63°C. A sample of 30 μ m thick Aquivion polymer was immersed into the solution and soaked for 20 minutes,

before solvent removal. Filter paper was used to remove residual solution from the sample surface. The sample was then placed in a vacuum oven held at a temperature of 50°C for two hours to evaporate the ethanol. The final uptake of $[BMMI^+][Cl^-]$ was found to be 45.6%, a level sufficient for observable actuator performance.

Two layers of 50 nm gold were hot-pressed to the prepared Aquivion™ with 3100 N of force at 90°C for approximately 45s. If inspection revealed inadequate binding, the hot pressing procedure was repeated with the same parameters for one minute. Prepared samples were stored in a dry box to minimize water contamination before actuation tests. Actuators tested in this experiment were 1.5 mm by 12 mm.

Results and Conclusions:

Electrical measurements were performed at both room temperature and 100°C to ensure the device deactivated by lowering temperature. Figure 1 demonstrates the charge density increased by over an order of magnitude at the higher temperatures. Other tests also demonstrated a two-order of magnitude increase in the DC conductivity for the device at the higher temperatures. This shows that the higher temperatures yielded a greater free ion concentration and thus more potent electrical activity.



The I-V curve for the device, shown in Figure 2, was used to determine the electrochemical window within which the device may reliably operate. Only the room temperature curve is shown since the curve at 100°C has the same shape except with higher currents. The linear increase in current draw at greater than 3V indicated the presence of reduction-oxidation reactions. To prevent device damage, the maximum operating voltage for these devices was set as 2.5 V. Figure 3 shows the device tip moved 5 mm with applied DC voltage at 100°C.

The results of these electrical tests and presence of bending indicated that, at high temperatures, actuators constructed with $[\text{BMMI}^+][\text{Cl}^-]$ have comparable behavior as similar actuators with room temperature ionic liquids. This allowed for conclusions drawn from analysis to be applied to the actuators in general.

Secondary ion mass spectroscopy (SIMS) with 40 KeV C_{60}^- sputtering was employed to depth profile the actuator. Four 5-7 μm deep craters were created for probing the ion distribution near two electrodes. Figure 4 shows the determined concentrations in the polymer calculated from the SIMS data, and ensuring conservation of charge between the ionic liquid and ionomer. The remarkable increase of $[\text{BMMI}^+]$ in anode and $[\text{Cl}^-]$ in cathode indicated the ions do not fully separate and instead remained strongly attracted to each other, forming clusters. These formations contrasted with qualitative explanations given in literature.

Another notable result was the significantly higher concentration of $[\text{Cl}^-]$ at the anode compared to more widely distributed $[\text{BMMI}^+]$ at the cathode. This indicated the smaller size of $[\text{Cl}^-]$ versus $[\text{BMMI}^+]$ permitted denser accumulation near the actuator surface.

Acknowledgements:

Thank you to Dr. Qiming Zhang, Yang Liu, and all members of the Zhang group, and to REU Site Coordinator Dr. Ronald Redwing and staff for all their guidance throughout the project. Special thanks to Caiyan Lu and Prof. Nick Winograd from PSU chemistry for the use of their SIMS equipment. Thanks to the National Nanotechnology Infrastructure Network Research Experience for Undergraduates Program and National Science Foundation for organizing and funding the project. This material is based upon work supported in part by the U.S. Army Research Office under Grant No. W911NF-07-1-0452 Ionic Liquids in Electro-Active Devices (ILEAD) MURI.

References:

- [1] Merck Chemical. "Ionic Liquid Product Brochure." <http://www.emdchemicals.com/ionic-liquids-brochures/c_qAGb.s1OHEIAAAh2AURLYY3>
- [2] Liu, Y. et al. "Ion Transport and Storage of Ionic Liquids in Ionic Polymer Conductor Network Composites." *Appl. Phys. Lett.* 96, 223503-1,2 (2010).

Figure 1: Charge density increases with temperature.

Figure 2: Electrochemical window limited to 3V.

Figure 3: Before/After photos of bending with 2.5V bias applied at 100°C.

Figure 4: Concentrations from SIMS suggests ion clustering effects.

Micropore Immunosensors for Fast Disease Diagnostics

Clare Wardwell

Biological Sciences, University of Delaware

NNIN REU Site: ASU NanoFab, Arizona State University, Tempe, AZ

NNIN REU Principal Investigator(s): Dr. Michael Goryll, Electrical Engineering, Arizona State University

NNIN REU Mentor(s): Purnavasu Joshi, Electrical Engineering, Arizona State University

Contact: ccw@udel.edu, michael.goryll@asu.edu, pjoshi1@asu.edu

Introduction:

Single molecule biosensors using etched silicon micropores provide an alternative to, and an advantage over, traditional immunoassays. By reducing the sample volume necessary for the assay and supplying an electrical readout of the measurements, the silicon micropore system reduces the cost, time, and chemical reagents involved in current standard immunoassays. These differences, as well as the portable nature of the biosensor, make it ideal for point-of-care diagnostics.

For this project, a microbead-based assay was performed. A constant voltage was applied across a silicon micropore filled with an ionic electrolyte solution. The pore acted as a resistor. The ionic electrolyte solution contained suspended 1 μm diameter silica beads. As a microbead entered and traveled through the pore, it increased the resistance of the pore, therefore causing a reduction in the measured current. This decrease in current, ΔI corresponds to the ratio of the diameter of the bead 'd', to the diameter 'D' and length, 'L' of the pore.

Equations:

$$(1) L = RA/\rho$$

$$(2) \Delta I = I_g(d^3/LD^2)$$

The detection of the translocation of the beads through the pore via resistive pulse measurements is similar to the method used for Coulter Counting. The silica beads and the micropore itself were then biofunctionalized with an antibody specific to the antigen being tested for, in this case, Interleukin-6. In the presence of a sufficient concentration of the antigen, the functionalized beads bound inside of the pore and caused a sustained reduction in the measured current.

Device Fabrication and Characterization:

The silicon micropores were fabricated using a series of photolithography processes and a deep silicon reactive ion etcher. First, a pore with a desired diameter of 100 μm was patterned and etched into the backside of the silicon wafer.

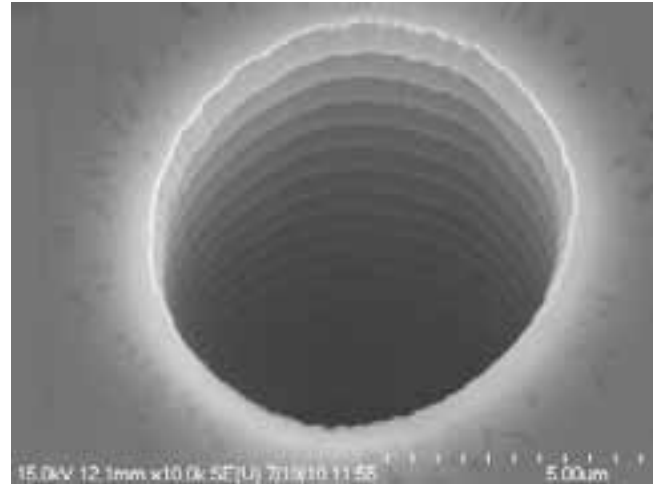


Figure 1: SEM image of frontside (8 μm) pore.

Then, a pore with a desired diameter of 5 μm was aligned, patterned, and etched on the topside of the wafer, in series with the 100 μm pore.

Due to the relationship between the measured reduction in current, bead, diameter, pore length and pore diameter, it was necessary to characterize the micropore, specifically the length and diameter of the topside pore. This was accomplished using the field-emission scanning electron microscope (FESEM) to determine the diameter, which was found to be 8 μm (Figure 1).

This value was then substituted into Equation 2, along with the measured value of electrolyte solution conductivity ρ to determine pore length, which was determined to be 32 μm . Each of these values was also substituted into Equation 1 to predict the change in current that resulted from the passing of a 1 μm bead in the fabricated micropore.

Biofunctionalization and Experimental Procedure:

The silicon micropore and the silica microbeads can be functionalized with a series of different biomolecules,

depending on the identity and specificity of the target biomarker. For this experiment, the pore and beads were functionalized with anti-Interleukin-6 (anti-IL6). This monoclonal antibody specifically binds to Interleukin-6, an antigen linked to rheumatoid arthritis and several cancers.

First, the antibody, anti-IL6, was attached to the beads. To create a lasting binding between the inorganic silica beads and organic antibodies, the beads were coated with amine group. They were incubated overnight with glutaraldehyde, which acted as a linker between the amine group and antibody, then rinsed in TRIS buffer solution, and finally, incubated for two hours with anti-IL6. The micropore was functionalized separately, using the same glutaraldehyde and anti-IL6 incubation protocol as the beads.

The functionalized micropore was sandwiched between two custom-made Teflon® chambers with wells. Bovine serum albumin was left to incubate in the wells and micropore to coat any silicon surface not covered in anti-IL6. Varying concentrations of IL6, from 200 pM to 1 μ M, were added into each well and left to incubate for two hours. The IL6 bound to the anti-IL6 antibodies present in the micropore. The functionalized beads were added into the wells. Ag/AgCl electrodes were dipped in each well and a constant voltage of 400mV was applied, causing the beads to move. As the beads migrated through the pore, the anti-IL6 on their surface interacted with the IL6 present in the micropore. This caused the beads to stick inside the micropore. The current through the pore was measured, and bead sticking and binding events were recorded.

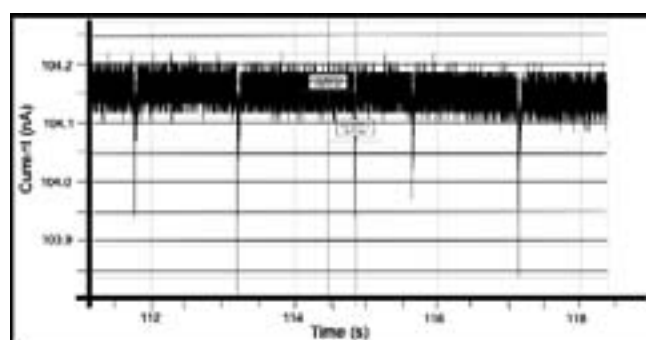


Figure 2: Translocation of amine-coated beads through an unfunctionalized pore.

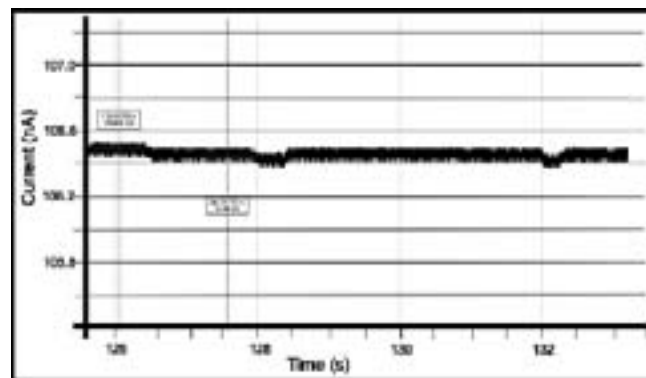


Figure 3: Bead binding and bead sticking events with functionalized beads in functionalized pore with 10 nM IL6.

Results and Conclusions:

In the experiments, we were able to observe the translocation of beads through an unfunctionalized pore (Figure 2). After biofunctionalizing the beads and pore, bead translocation events were still observed in the presence of low concentrations of IL6. Increasingly higher concentrations of IL6 resulted in more frequent and pronounced bead sticking and blocking events (Figure 3).

It was found that very high concentrations of IL6, in the micron range, caused the blocking of the pore in the absence of beads. This was due to the multiple binding sites on the antigen, which caused it to bind to itself and multiple antibodies, creating bridge-like structures and blocking the pore.

Through this series of experiments, it was found that a lower concentration of beads and antigen, and an increase in incubation time with glutaraldehyde and anti-IL6 resulted in greater consistency of data. These experiments showed that the detection of biomarkers, such as Interleukin-6, can be achieved using a silicon micropore and bead-based assay.

Acknowledgements:

I would like to thank my PI, Dr. Michael Goryll, and my mentor, Punarvasu Joshi, for their time and for everything they taught me. Thanks to Dr. Shalini Prasad and Dr. Trevor Thornton. Finally, thank you to the NNIN REU Program, the NSF, and the Center for Solid State Electronics Research at Arizona State University for providing the opportunity and funding for this experience.

References:

- [1] Mathew, T.; Joshi, P.; Prasad, S.; Goryll, M.; Spanias, A.; Thornton, T.J.; "Silicon Based Pore Systems for Emerging Biosensor Applications"; ASME Congress and Exposition, 2, 263-270 (2009).

Improving Quality Factor of Drum Resonators via Gas Confinement

Diana Wu

Chemical Engineering and Biology, Massachusetts Institute of Technology

NNIN REU Site: Cornell NanoScale Science and Technology Facility, Cornell University, Ithaca, NY

NNIN REU Principal Investigator(s): Professor Jeevak Parpia, Physics, Cornell University

NNIN REU Mentor(s): Robert Barton, Physics, Cornell University

Contact: dianawu@mit.edu, jmp9@cornell.edu, rab375@cornell.edu

Abstract:

The frequency of micro- and nano- scale devices is sensitive to stress, force, and mass, which makes the devices useful for applications in chemical and biological sensing. The ability to resolve small changes in frequency is dependent on the quality factor, Q , a measure of how much energy is lost relative to the stored energy of the resonator. Mechanical resonators vibrating in air lose energy to the surrounding gas, which negatively impacts Q and diminishes the sensitivity of these devices.

Drum resonators were fabricated with a self-aligned glass cap to prevent the formation of sound waves and minimize energy loss. At atmosphere, high frequency devices show larger improvements in Q than low frequency devices.

Introduction:

Micro- and nano- mechanical resonators have the potential for many chemical and biological sensor applications because of their ability to resolve small changes in frequency. In order to be useful, the resonators need to perform well when exposed to air. One measure of performance is the quality factor, since a higher quality (Q) factor equates to better sensitivity [1].

Several types of energy loss diminish the Q of mechanical resonators in air: squeeze film damping, sound radiation, and energy transfer in a free molecular flow regime. Squeeze film damping describes the behavior of air between a stationary and moving plate. In the resonators studied, damping occurs in the incompressible regime, where air is trapped between two plates and acts as a spring, and the squeeze number, σ , is greater than 10. In the incompressible regime, dissipation falls as $\sigma^{0.4}$, offering a pathway to improve Q [2, 3].

Sound radiation is another source of energy loss. As the resonators are driven, their movements propagate sound waves, which remove energy from the system. Sound is governed by the equation $c = \lambda f$ where c is the speed of sound, λ is the wavelength and f is frequency. Sound waves can be blocked from forming, however, when $\lambda \ll c/f$.

However, these energy loss models are less accurate when the dimensions of nanomechanical devices are comparable to the mean free path of the gas particles. Damping in this “free molecular flow regime” (fmf) arises because of energy transfer from the resonator to the gas molecules, which

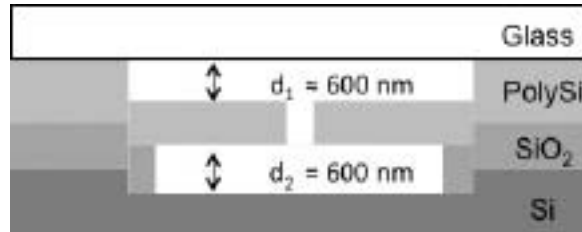
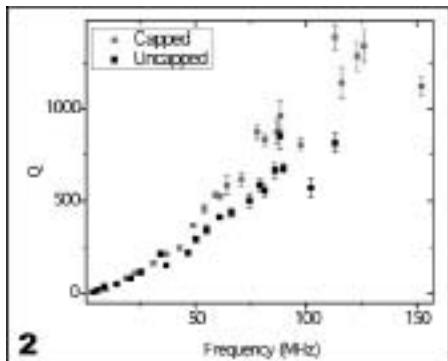
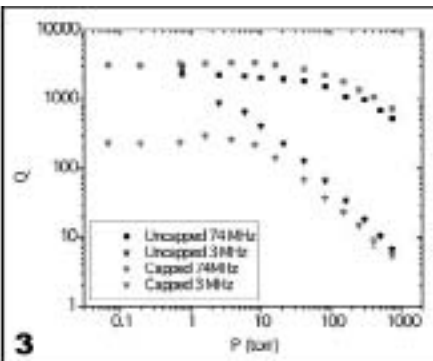
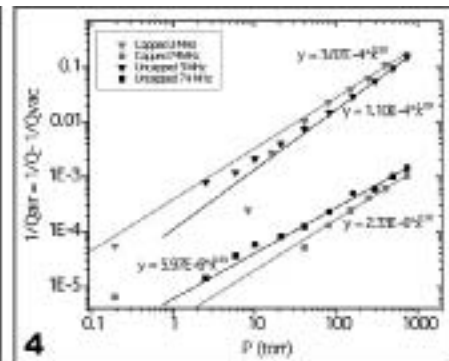


Figure 1: Side view of drum resonator.

occurs more frequently than particle-particle interactions. Fmf is characterized by Q having inverse pressure dependence [4].

Methods:

A self-aligned glass cap procedure was used to fabricate capped drum devices. Channels were etched in silicon using photolithography techniques. Complementary metal oxide semiconductor (CMOS) processes were used to put down silicon oxide and n+ polysilicon. Some of the underlying oxide layer was removed using 49% HF, creating drum resonators within the channels. Poly(methyl methacrylate) (PMMA) was spun on diced borosilicate glass. The glass was clamped on top of the resonator chip with a C clamp and baked at 200°C. A side view of the device can be seen in Figure 1.

Figure 2: 48 μm drum resonators at 1 atm.Figure 3: 48 μm drum resonators at varying pressures.Figure 4: 48 μm drum resonators at varying pressures with intrinsic losses subtracted.

Motion was actuated and detected optically as described in detail by Ilic, et al. [5]. Q was calculated by dividing the resonant frequency by the full width half maximum of observed Lorenzian peaks.

Results and Discussion:

By interrogating multiple modes of a single device, we obtained the frequency dependence of the dissipation and results are displayed in Figure 2. At frequencies below 35 MHz, the Q of the uncapped drums is the same or higher than the capped drums. At frequencies above 35 MHz, capped devices performed better than uncapped devices.

A pressure dependence experiment was performed and results are displayed in Figure 3.

For all frequencies and at low pressure, Q is dominated by intrinsic energy losses due to imperfections in the resonator. As pressure increases, losses due to air impact Q more. We attribute these losses to energy transfer in the fmf regime. At high frequency, we hypothesize that squeeze film terms are diminishing, and therefore Q is better for both capped and uncapped devices. However, the capped devices have less squeeze film damping than uncapped devices because the gas is clamped.

The ratio of $Q_{\text{capped}} : Q_{\text{uncapped}}$ for drums driven at 3 MHz, ranges from 0.07 to 0.81. The same ratio for drums driven at 74 MHz ranges from 1.38 to 1.66. The capped devices see approximately a 50% improvement in quality factor.

Intrinsic resonator energy losses were subtracted from original data and the resulting pressure dependency of damping due to air is shown in Figure 4. Trend-lines show

slopes close to the inverse pressure dependence expected from fmf theory; however, the dramatic improvement when comparing coefficients of the trend-lines for Q is unexpected.

Conclusions:

At higher frequencies, the cap has improved the quality factor by 50%, by decreasing energy loss from squeeze film damping and/or sound radiation. Further work must be done to understand which modes of energy loss are dominating and optimize dimensions and design accordingly.

Acknowledgments:

We acknowledge the NSF, NNIN REU Program and CNF for funding. We also thank Jeevak Parpia, Harold Craighead, Rob Barton, Rob Ilic, Timo Veijola, Melanie-Claire Mallison and CNF staff for their guidance and advice.

References:

- [1] Waggoner, P.S., Craighead, H.G.; "Micro-and nanomechanical sensors for environmental, chemical, and biological detection," Society, pp. 1238-1255 (2007).
- [2] Bao, M., Yang, H., "Squeeze film air damping in MEMS," Sensors and Actuators A: Physical, vol. 136, pp. 3-27 (2007).
- [3] Andrews, M., Harris, I., Turner, G., "A comparison of squeeze-film theory with measurements on a microstructure," Sensors and Actuators A: Physical, vol. 36, pp. 79-87 (1993).
- [4] Verbridge, S.S., Ilic, R., Craighead, H.G., Parpia, J.M., "Size and frequency dependent gas damping of nanomechanical resonators," Applied Physics Letters, vol. 93, p. 013101 (2008).
- [5] Ilic, B., Krylov, S., Aubin, K., Reichenbach, R., Craighead, H.G., "Optical excitation of nanoelectromechanical oscillators," Applied Physics Letters, vol. 86, p. 193114 (2005).

Growth of Graphene Nanostructures on Silicon Wafers

Brian Benton

Physics, University of Minnesota-Twin Cities

NNIN REU Site: Colorado Nanofabrication Laboratory, University of Colorado, Boulder, CO

NNIN REU Principal Investigator(s): Thomas Schibli, Physics, University of Colorado at Boulder

NNIN REU Mentor(s): Chien-Chung Lee, Physics, University of Colorado at Boulder

Contact: bento024@umn.edu, trs@colorado.edu, chienchung.lee@colorado.edu

Abstract and Introduction:

Due to its optical properties, high electrical conductivity, and high mechanical strength, graphene has attracted much interest in a variety of scientific and engineering applications. Our project focused on its use for quantum interference control (QIC) devices.

The QIC effect can be exploited to generate ballistic photocurrents in single layer graphene (SLG) through interference of charge carriers excited by single- and two-photon absorption [1,2]. This can be used as a more effective and robust method for stabilizing femtosecond frequency comb lasers, which have applications in ultrafast physics and precision metrology.

To realize such a device, evaporated copper (Cu) on silicon (Si) wafers was used as a catalyst for the chemical vapor deposition (CVD) growth of SLG. Photolithography techniques were employed to pattern QIC devices on the wafers, and the Cu thin film was subsequently etched and undercut to achieve the suspended graphene bridge necessary for a QIC device. Resistance measurements were taken to characterize and compare various device geometries, with results as low as ~ 7 kOhms. Devices with a wide variety of graphene bridge sizes, ranging from 5-15 μm wide and 0.0-16 μm long, with an appropriate undercut have been achieved. Injected photocurrents have been measured, showing good response to photonic excitation.

Experimental Procedure:

Our device fabrication procedure is diagramed in Figure 1. We used a thermal evaporator to evaporate a 25 nm titanium adhesion layer and a 500 nm Cu layer onto Si wafers with a 100 nm oxide layer on their surface. The wafers were then cleaved and loaded into the CVD reaction tube. The sample was heated to 950-1000°C with a flow of hydrogen and argon gas before carrying out the graphene growth with an additional flow of methane gas for ten minutes. The methane flow was then turned off and the sample rapidly cooled to room temperature before removal. We employed both ambient-pressure and low-pressure (~ 400 mTorr) growths [3,4].

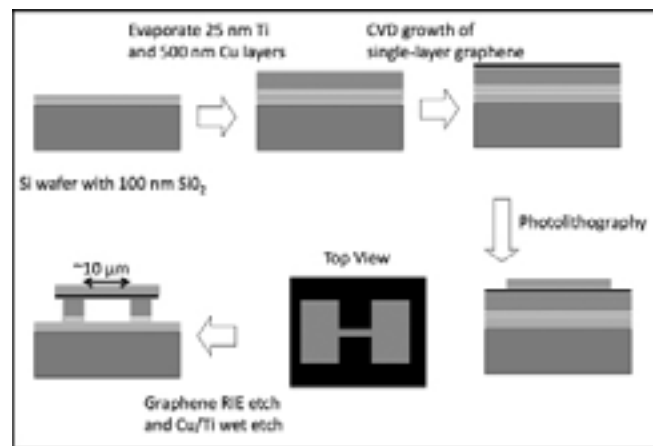


Figure 1: Fabrication process diagram.

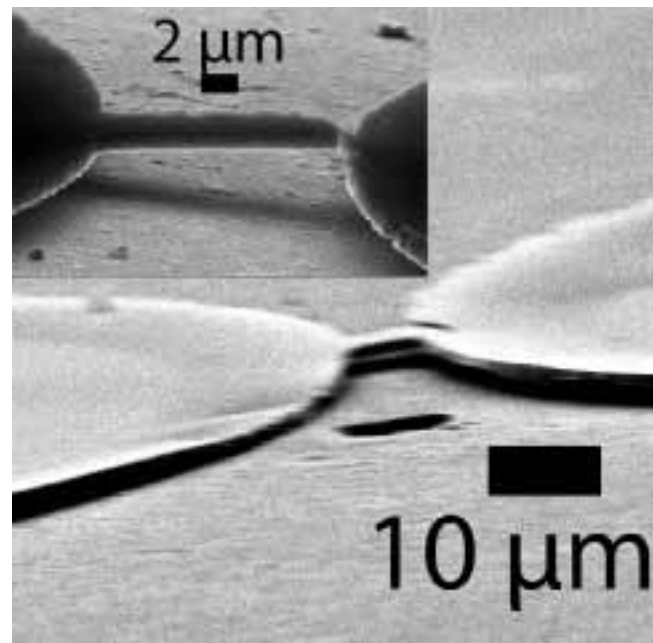


Figure 2: Scanning electron microscope (SEM) images of completed devices. Photoresist was left on the devices; gold was sputtered on for use in the SEM.

The samples were then spin-coated with negative photoresist (NR9-1000P), exposed, and developed. The resulting structures consisted of two pads ($\sim 0.12 \text{ mm}^2$) connected by a narrow bridge $0.0\text{-}16 \mu\text{m}$ long and $5\text{-}15 \mu\text{m}$ wide. The exposed graphene was removed with a 20 second run in the reactive ion etcher (RIE) with oxygen plasma, after which the exposed Cu was removed with a wet-etch in a 0.05 molar ferric chloride solution with precise timing to achieve the appropriate undercut, yielding suspended graphene bridges (see Figure 2). After partial mechanical removal of the photoresist, wires were bonded to the Cu pads with conductive epoxy. Some photoresist was left to help support the graphene bridge.

Results and Conclusions:

Resistance measurements were taken of devices with a wide range of geometries from a variety of different samples (see Figure 3). It can be seen that the low-pressure graphene growth yielded significantly lower sheet resistances, roughly $30 \text{ kOhms}/\square$, than the ambient-pressure growth, with roughly $120\text{-}150 \text{ kOhms}/\square$. These sheet resistances represent an upper limit of the actual graphene sheet resistances, as they were calculated using the pre-etched bridge dimensions. The actual bridges are longer due to undercutting of the pads. Also, contact resistance between the Cu pads and the graphene, as well as small cracks in the graphene bridges, might lead to a further increase of the measured resistances.

To assess the opto-electronic device properties, we measured changes of the electric resistivity of the graphene bridge as a function of illumination (photoresistivity). In this measurement, a pulsed laser centered at 1550 nm with a spot diameter of $\sim 400 \mu\text{m}$ was focused on the device bridge, which was $4 \mu\text{m}$ long and $10 \mu\text{m}$ wide. A variable bias voltage was applied to the pads, and photo-generated current was measured with lock-in technique to eliminate dark current. Figure 4 shows the results of these measurements. The main graph shows two sets of data: photocurrent vs. applied bias voltage, and photocurrent vs. peak intensity. The inset shows photocurrent as a function of position of the beam relative to the graphene bridge. This shows the linear relationship between current and intensity, as well as other photocurrent effects. We were able to show that these effects were due to the graphene structure and not something else on the wafer.

Acknowledgements:

Special thanks to Professor Thomas Schibli and Chien-Chung Lee for their support and guidance throughout the project. Also, thanks to the Colorado Nanofabrication Laboratory staff, including Professor Bart Van Zeghbroeck and Tomoko Borsa, for their efforts and assistance. We would also like to thank Professor Scott Bunch and his research group for their help with the graphene growth process. Funding was provided by the National Nanotechnology Infrastructure Network Research Experience for Under-

graduates (NNIN REU) Program and the National Science Foundation. Research facilities and support were provided by the University of Colorado at Boulder and the Colorado Nanofabrication Laboratory.

References:

- [1] Fortier, T.M. et al.; "Carrier-Envelope Phase Controlled Quantum Interference of Injected Photocurrents in Semiconductors"; *Phys. Rev. Lett.* 84, 147403 (2004).
- [2] Sun, D. et al.; "Coherent Control of Ballistic Photocurrents in Multilayer Epitaxial Graphene Using Quantum Interference"; *Nano Lett.* 10, 1293-1296 (2010).
- [3] Li, X. et al.; "Large-Area Synthesis of High-Quality and Uniform Graphene Films on Copper Foils"; *Science* 324, 1312 (2009).
- [4] Levendorf, M.P. et al.; "Transfer-Free Batch Fabrication of Single Layer Graphene Transistors"; *Nano Let.* 9, 4479-4483 (2009).

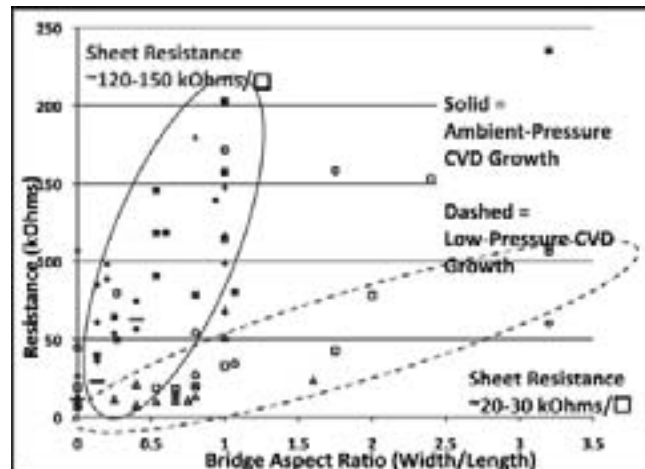


Figure 3: Resistance measurements. Shapes indicate different evaporator and CVD runs. Dashed line / hollow shapes are low-pressure CVD; solid line / solid shapes are ambient-pressure CVD.

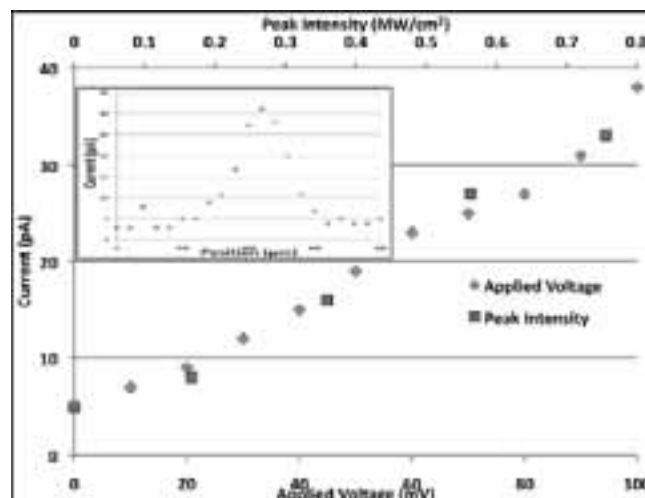


Figure 4: Photocurrent vs. applied voltage at a peak intensity of 0.75 MW/cm^2 , and photocurrent vs. peak intensity at an applied voltage of 98 mV . Inset: Photocurrent vs. position at a peak intensity of 0.75 MW/cm^2 and an applied voltage of 100 mV .

Fabrication of Silver MicroWire Polarization Filters

Diana Bolser

Physics, University of Missouri-Columbia

NNIN REU Site: Nano Research Facility, Washington University in St. Louis, St. Louis, MO

NNIN REU Principal Investigator(s): Professor Viktor Gruev, Engineering and Applied Science, Washington University in St. Louis

NNIN REU Mentor(s): Timothy York and Raphael Njuguna, Engineering and Applied Science, Washington University in St. Louis

Contact: dkbc59@mail.missouri.edu, vgruev@wustl.edu, tey1@cec.wustl.edu, njugunar@seas.wustl.edu

Abstract:

Nanowires make good sensors because their small dimensions enhance their sensitivity. To be useful, wire sensors must be integrated with electronics capable of processing those signals. In this project, we demonstrated a method to fabricate arrays of micron-sized wire-grid optical polarization devices. Using photolithography and other experimental techniques, we developed a reliable procedure for producing silver wires with micron-scale features. This procedure was optimized by altering the dose and bake times so as to achieve the best possible fabrication process. The polarization filters produced in this project are prototypes of much smaller arrays that will eventually be implemented in optical engineering devices.

Introduction:

There are three fundamental properties of light: intensity, wavelength, and polarization. The latter has been overlooked mainly due to its invisibility to the human eye. However, polarization images contain information that is unreported in traditional color and intensity pictures, which makes improving the capabilities of polarization imaging sensors a novel and necessary endeavor. Recently, there has been an increased interest in developing nanostructures for optical applications [1,2]. Much work has already been done to integrate polarization filters into high-resolution imaging devices [3,4].

Propagation of light within a biological medium depends on its optical properties. Scattered radiation contains information about the size and composition of the biological

sample, so by examining the polarization of this radiation, scientists can learn valuable physical information [5].

Polarization-resolved imaging can provide insights into the composition and topography of biological environments, which can be used to detect bacteria and image cancerous tissues. Since the human eye is incapable of perceiving polarization effects without the aid of a polarization-sensitive imaging system, the development of such a system is essential to biologists and medical professionals.

Experimental Procedure:

1. Bake glass slide to ensure substrate is completely dry.
2. Spin-coat with Omnicote™ to promote adhesion. The Omnicote layer helps lift the resist and remove it from the substrate during the development step.
3. Spin-coat the negative resist SU-8-2010 at 500 rpm for five seconds with 100 rpm per second acceleration, then at 3000 rpm for 30 seconds with 300 rpm per second acceleration.
4. Prebake the resist at 95°C for 3 minutes.
5. Expose the slide with a chrome mask for 10 seconds with 12 mW/cm² intensity radiation. The mask used to pattern features contained three different arrays, one with 10 μm wires and 10 μm spaces, another with 10 μm wires and 20 μm spaces, and a third with 20 μm wires and 10 μm spaces.
6. Post-bake the sample at 95°C for 3.5 mins and develop. In a negative resist, the exposed portion of the material cross-linked to become insoluble in the developer solution. The unexposed portion remained soluble

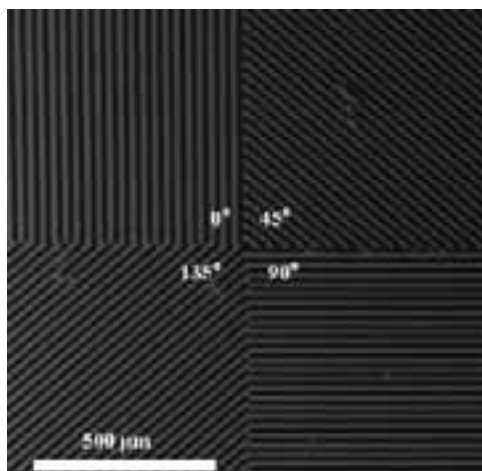


Figure 1: SEM image of 45° offset pixels.

and was consequently removed. The final features on the substrate were those exposed to the ultra-violet light. Silver was deposited on top of a chrome adhesion layer via thermal evaporation. Finally, the sample was submerged in Microchem's Remover PG.

Results and Conclusions:

The pixels were arranged in four different orientations offset by 45° , as shown in Figure 1. During lift-off, the structures were completely removed from the glass slide. To solve this problem, the original experimental procedure was amended to eliminate the Omnicoat layer in favor of a second layer of photoresist. This additional layer was spin-coated on top of the first layer, following a hard bake of one or more hours. The dual layer approach resulted in improved lift-off, with the array remaining intact, as shown in Figure 2. We varied the pre-bake and post-bake times in an effort to achieve reliable line width and spacing. Table 1 lists the different bake times and indicates the optimum combinations for sample preparation.

Additionally, we experimented with varying exposure times. Under-exposing resulted in tapered features with scalloped edges. The best samples were produced using an exposure of 10 seconds. Based on the recipe described in *Experimental Procedure*, the width of the features should be $10\ \mu\text{m}$; however, the true size of the structures was around $8\ \mu\text{m}$. Figure 3 shows the height of the wires determined by atomic force microscopy (AFM).

Future Work:

Future projects include fabrication of nanometer-sized wire arrays for improved optical capabilities, which can be achieved by using electron beam lithography instead of photolithography. Metal nanowires are important components of future imaging technologies, since wire-grid polarizers are easily incorporated within a pixel detector array. Additional fabrication experiments with other materials like gold and aluminum will also be necessary. The ultimate goal of this research is the successful integration of nanowire polarization filters in a high-resolution mega pixel camera.

Acknowledgments:

The guidance of Dr. Viktor Gruev was especially appreciated. Additionally, Kristy Wendt and Brent Riggs of the WUSTL Nano Research Facility provided invaluable advice and assistance. Financial support through National Science Foundation's National Nanotechnology Infrastructure Network Research Experience for Undergraduates (NNIN REU) Program is gratefully acknowledged.

References:

- [1] Zhang, X., Liu, H., Tian, J., Song, Y., Wang, L., Song, J., Zhang, G. Optical polarizers based on gold nanowires fabricated using colloidal gold nanoparticles. *Nanotechnology*, 19, 28, 285202 (2008).
- [2] Schider, G., Krenn, J., Gotschy, W., Lamprecht, B., Ditlbacher, H., Leitner, A., Aussenegg, F. Optical properties of Ag and Au nanowire gratings. *Journal of Applied Physics*, 90, 8, 3825-3830 (2001).
- [3] Gruev, V., Ortu, A., Lazarus, N., Van der Spiegel, J., Engheta, N. Fabrication of a dual-tier thin film micro polarization array. *Optics Express*, 15, 4994-5007 (2007).
- [4] Zhou, Y., Klotzkin, D. Design and parallel fabrication of wire-grid polarization arrays for polarization-resolved imaging at $1.55\ \mu\text{m}$. *App.Optics*, 47, 20, 3555-3560 (2008).
- [5] Demos, S., Radousky, H., Alfano, R. Deep subsurface imaging in tissues using spectral and polarization filtering. *Optical Express*, 7, 23-38 (2000).

Pre Bake (minutes)	Post Bake (minutes)	Most Accurate (■)
3.5	4	X
	4.5	X
	5	■
4	4	X
	4.5	X
	5	■
4.5	4	X
	4.5	■
	5	X

Table 1: Pre-bake and post-bake times. The samples with most accurate feature sizes are indicated with a box.



Figure 2: SEM image of $20\ \mu\text{m}$ wire and $10\ \mu\text{m}$ space pixel.

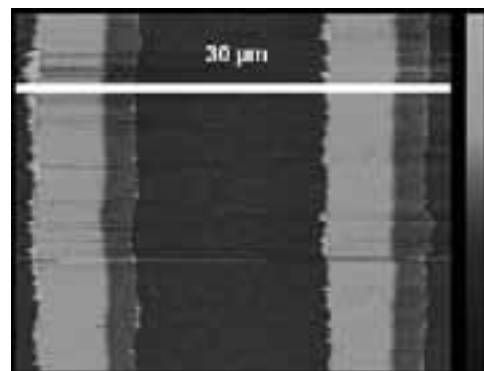


Figure 3: AFM image of wire height.

Automation of Sample-Positioning and Data-Collection for Pulsed-Laser-Melting Experiments

Edy Cardona

Physics, University of California, Berkeley

NNIN REU Site: Center for Nanoscale Systems, Harvard University, Cambridge, MA

NNIN REU Principal Investigator(s): Michael Aziz, Applied Physics, School of Engineering and Applied Sciences, Harvard

NNIN REU Mentor(s): Daniel Recht, Applied Physics, School of Engineering and Applied Sciences, Harvard University

Contact: ecardona@berkeley.edu, maziz@harvard.edu, drecht@fas.harvard.edu

Abstract:

Pulsed laser melting, a powerful technique for producing new alloy materials, is typically time-consuming and labor-intensive. A computer-controlled sample positioning and data collection system was designed and built to improve the efficiency and reproducibility of this process. Three automated stages driven by stepper motors positioned samples with micron-scale precision. Data from high-speed photodiodes tracking laser pulse duration and sample melt duration was captured by a 500 MHz oscilloscope. A high-resolution beam profiling camera recorded the uniformity of every laser pulse. These instruments were integrated by a graphical user interface developed to facilitate user operation of the system. The improvements implemented are expected to speed sample production substantially.

Introduction:

The current experimental setup is depicted in Figure 1. This setup consisted of manual calibration of the samples, storing of collected data into a floppy disk, and formatting data to see results more clearly. However, with the incorporation of new devices and implementation of new programs, a new setup would have a fast and accurate positioning system with immediate data transfer and readily available results. These enhancements were designed and built in a simpler environment for easier development and testing (see Figure 2).

Experimental Setup:

The positioning system consisted of three motorized Velmex slides with four, six, and thirty inch lengths, which were assembled into a stage as shown in Figure 3. The 4" slide was assigned to represent the z-axis, the 6" slide to the y-axis, and the 30" slide to the x-axis. The stage allowed for samples to be mounted onto the y-axis and to be moved in a three-dimensional space. The slides could be moved one at a time with variable speeds up to 3 mm per second along the x and y axis, and 1.5 mm per second along the z axis. The x and y slides had a precision of 5 μ m and the z slide had a precision of 2.5 μ m.

The data collection devices were a Coherent attenuator and high resolution UV camera, and

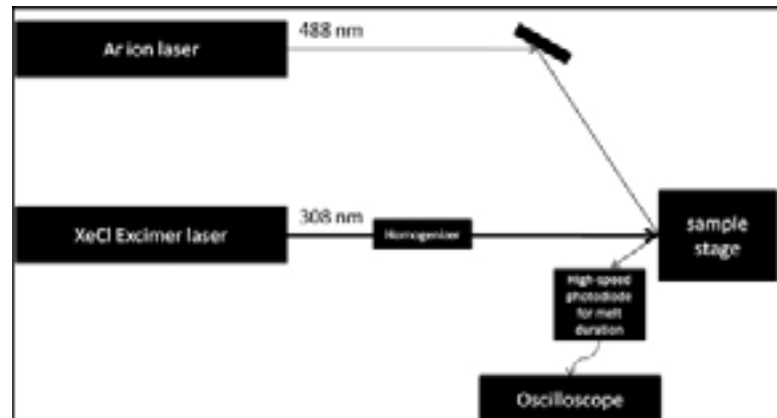


Figure 1: Top view diagram of current pulsed laser melting experimental setup.

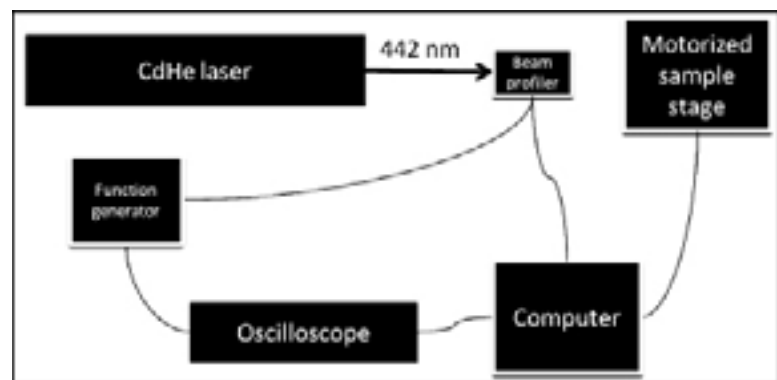


Figure 2: Top view diagram of testing setup for the data collection and sample positioning system.

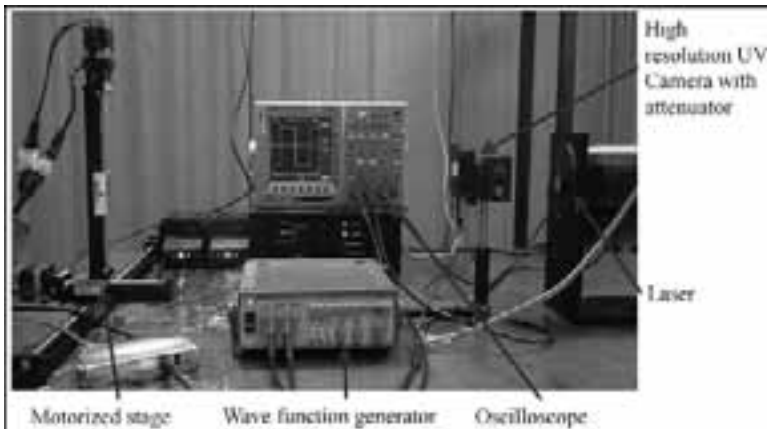


Figure 3: Testing setup for the data collection and sample positioning system.

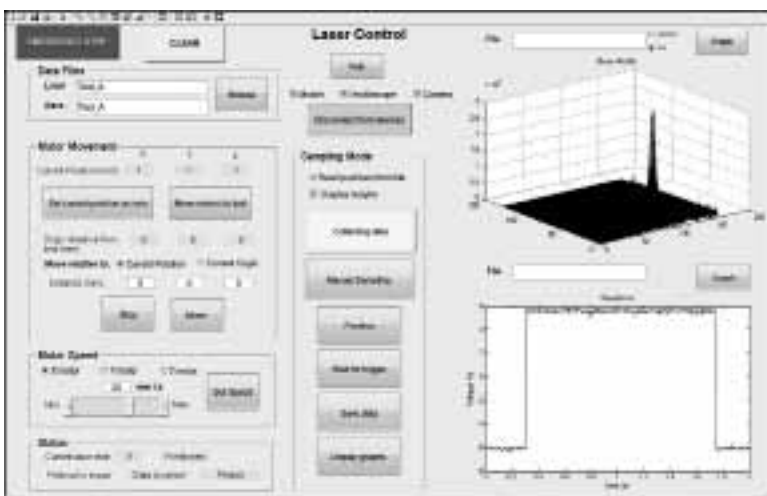


Figure 4: Graphical User Interface in continuous sampling mode.

a Tektronix oscilloscope, Figure 3. The camera captured beam profile data from the laser beam and the oscilloscope recorded trigger signals, which represented the melt and pulse duration data from two high-speed photodiodes.

The probe instruments were an Omnichrome laser and a Tektronix function generator, Figure 3. The laser emitted a constant beam onto the camera and the function generator sent pulsed triggers to the camera and oscilloscope, so that together, the laser and trigger, would simulate a pulsed laser. These trigger signals would alert both the camera and the oscilloscope to start capturing data.

Device Communication:

The slides and the oscilloscope were connected via a RS232 cable to a RS232-to-USB adapter. The adapter was connected to a USB port in a HP touch screen computer. Commands and queries were sent and received to the motor and oscilloscope by establishing a serial communication using Matlab's Instrument Control Toolbox. The camera was linked to the computer via TCP/IP. Basic commands could be sent to the camera, although its own software, BeamView, had to open in order to establish communication.

Interfacing:

A graphical user interface (GUI), Figure 4, was developed in Matlab's graphical user interface design environment. The purpose of the GUI was to create a level of abstraction that allowed the user to focus on the parameters and results of the experiment and overlook the underlying code and data manipulation. The GUI consisted of push and radio buttons, check and input boxes, and display windows that offered the user the ability to control motor movement and speed while monitoring the status of the experiments. The GUI also gave the user several options when conducting an experiment, such as graphing data on the fly, loading files containing experiment settings, and choosing the file location to save the data.

Conclusion and Future Work:

The time it takes to run an experiment is expected to decrease by having the sample move automatically from one position to the next with micron-scale precision in a matter of seconds. This same precision will also increase the reproducibility of the experiment, and subsequently decrease the production cost of the samples.

In addition, with the faster and more direct serial communication established with the oscilloscope, pulse and melt duration data can be obtained and analyzed almost instantly; this translated into having readily available data that allows the user to make more immediate and wiser decisions for subsequent experiments.

Finally, the camera allows the user, for the first time, to analyze the beam quality of each laser pulse. This is critical as measurements of beam diameter, intensity, and hot spots can potentially be used to explain new phenomena and abnormalities in the experiments.

The next step in this project is to incorporate the sample positioning and data collection system into the actual laser melting setup. As experiments are conducted, the code will be adjusted to improve the efficiency of the experiments and to fit the necessities of the users.

Acknowledgements:

I would like to thank: Professor Michael Aziz for giving me the opportunity to work in his laboratory; my mentor, Daniel Recht, for all his patience, guidance, and knowledge imparted during the summer; group members Juan Hernandez-Campos, Brian Huskinson, Charbel Madi, Jason Rugolo for all their help and insight on the development of the project; Ms. Melanie-Claire Mallison and Dr. Kathryn Hollar for their efforts in organizing the program; the NNIN REU Program for their sponsorship; and the NSF for their funding under grant ECCS-0821565.

Fabrication of High Speed Nanoscale Metal-Semiconductor-Metal Photodetector

Kevin Chen
Electrical Engineering, Arizona State University

NNIN REU Site: Colorado Nanofabrication Laboratory, University of Colorado, Boulder, CO

NNIN REU Principal Investigator(s): Prof. Bart Van Zeghbroeck, Electrical Engineering, University of Colorado at Boulder;

Dr. Paul D. Hale and Dr. Dylan F. Williams, National Institute of Standards and Technology

NNIN REU Mentor(s): Zefram Marks, Electrical Engineering, University of Colorado at Boulder

Contact: kqchen@asu.edu, [bart@colorado.edu](mailto bart@colorado.edu), [hale@boulder.nist.gov](mailto hale@boulder.nist.gov), [dylan.williams@nist.gov](mailto dylan.williams@nist.gov), [zefram.marks@colorado.edu](mailto zefram.marks@colorado.edu)

Abstract and Introduction:

Introduced in 1975, metal-semiconductor-metal (MSM) photodetectors consist of two metal electrodes with interdigitated “fingers” deposited onto a semiconducting substrate [1]. Using substrates, such as low temperature grown gallium arsenide, MSM photodetectors with bandwidths over 500 GHz have been successfully fabricated [2], making it a viable source for ultra-fast optical pulse measurements.

To increase speed, we introduced an array of metal nanodot electrodes between the fingers of the photodetector. The dots decreased the capacitance of the device with larger finger spacing while also allowing us to lower the transit distance to meet this lower resistance/capacitance (RC) time constant by acting as artificial recombination centers. We were also able to increase maximum applicable bias voltage before causing dielectric breakdown between the electrodes, which is important as the maximum output voltage is limited by the bias voltage applied.

In addition, we added an epitaxial layer of aluminum gallium arsenide to prevent electron-hole pair generation deep in the substrate, in order to further improve speed [3].

A $10 \times 10 \mu\text{m}$ device, with three rows of dots between the fingers, was chosen as a balance between speed and signal strength (Figure 1). The size of the device was limited by the minimum beam size of the 775 nm excitation laser used to test the device. The addition of more rows of dots would speed up the device, but the loss of signal would be too great.

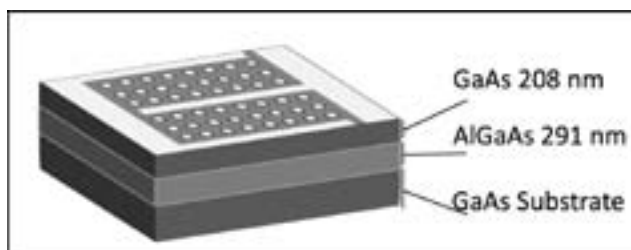


Figure 1: MSM photodetector with nanodots and epitaxial layer.

Experimental Procedure:

To fabricate our device, we started with a cleaning step with acetone and isopropyl alcohol (IPA) followed by a one-minute dip in hydrochloric acid:water (HCl:H₂O) 1:1 solution to remove any arsenic oxide present on the wafer surface, and therefore improve electrical contact. Photolithography was used to fabricate a coplanar waveguide necessary for measurement purposes. 20 nm of titanium was evaporated as an adhesion layer, followed by 100 nm of gold. Lift-off using RR2 resist remover completed the fabrication of the waveguide followed by another cleaning step with acetone and IPA then HCl:H₂O 1:1 to remove any remaining residue.

Due to the small anticipated feature sizes of approximately 350 nm, electron beam lithography (EBL) was necessary to fabricate the actual photodetector.

A bilayer resist of copolymer methyl-methacrylate-co-methacrylic acid (MMA-MAA) and poly(methyl methacrylate) (PMMA) was used to create a good lift-off profile [3]. An alignment structure around the device writing area ensured that the exposed device would be properly aligned.

After development in a methyl isobutyl ketone:IPA 1:3 solution, the use of an IPC Asher followed by an HCl:H₂O 1:1 bath removed any remaining resist in the exposed areas. Seven nm of titanium and 35 nm of gold were evaporated to create the device. Finally lift-off was performed using PG remover to finish the fabrication of the device.

Speed testing of the devices was performed at the National Institute of Standards and Technology (NIST) using an electro-optic sampling setup with a 100 fs laser at 775 nm wavelength. The laser pulse was much shorter than the speed of our device and so the impulse response of our photodetector could be found. The photogenerated current traveled down the transmission line from the device causing a change in voltage between the signal and ground electrodes. This voltage caused the change in polarization of a 1550 nm sampling beam traveling through the substrate between the electrodes, which was measured to determine the impulse response (Figure 2, left).

Results and Conclusions:

A device with line widths of 450 nm, dot diameters of 250 nm and spacing of 200 nm was successfully fabricated and tested (Figure 2, right, inset). The impulse response of the device was found to have a full width at half max of 4.5 ps (Figure 3), which corresponds to a bandwidth of approximately 100 GHz.

A relatively low signal to noise ratio was observed, pointing to a low responsivity in the device, which is most likely explained by the addition of nanodot arrays and the epitaxial layer. All carriers that would have been generated deeper into the substrate are lost due to the epitaxial layer and those that recombine at the dots do not contribute to the output current.

However, the bias voltage applied during testing was only four volts due to fear of causing dielectric breakdown, which was still in the range that may be applied to normal MSM photodetectors. The much higher bias voltage allowed by the larger finger spacing [1] should be able to make up for some of the lost responsivity.

Future Work:

More work must be done on the fabrication of the device to increase speed, such as implementing feature sizes that are more optimized towards faster speeds.

Extensive direct current testing can be done to find the maximum bias voltage that can be applied to maximize the output voltage though many improvements such as the addition of an anti-reflective coating on the surface of the substrate may be used to increase responsivity.

Once the device is optimized, we will be able to package it into a system designed by collaborators at NIST to measure ultra-fast optical pulses at 775 nm wavelength.

Acknowledgements:

Special thanks goes to NNIN REU Program and the NSF for the funding that made this research project possible.

Also, thanks to Prof. Bart Van Zeghbroeck and Zefram Marks for guiding me throughout the project, along with our collaborators at NIST, Dylan Williams and Paul Hale, for conducting high-speed measurement tests.

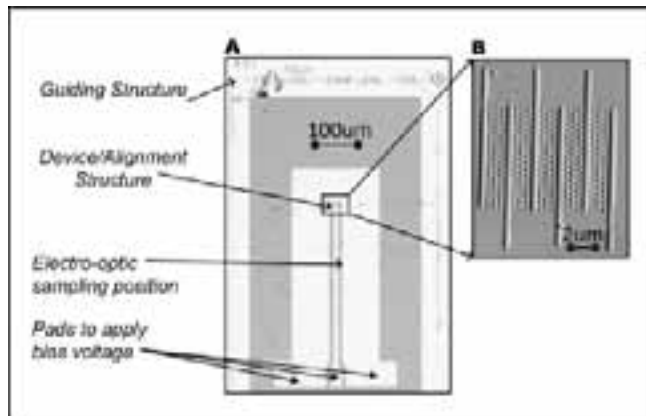


Figure 2: (left) Optical image of fabricated wave guide, (right, inset) Atomic force microscope image of final device.

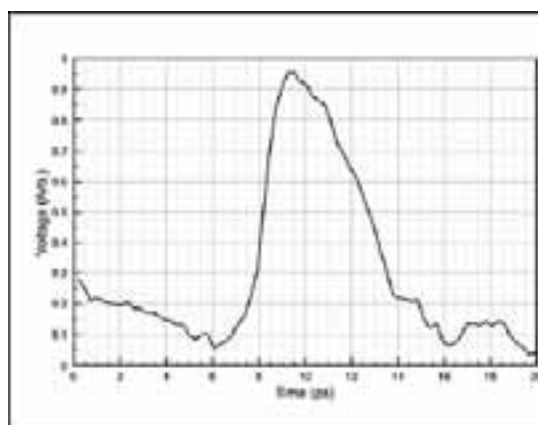


Figure 3: Impulse response of device.

References:

- [1] T.Borsa, D.F. Williams, P.D. Hale, and B.J. Van Zeghbroeck; "Novel Nano-structured Metal-Semiconductor-Metal Photodetector with High Peak Voltage"; Japanese Journal of Applied Physics, 48 (2009) 06FD03.
- [2] S.Y. Chou and M.I. Liu; "Nanoscale Tera-Hertz Metal-Semiconductor-Metal Photodetectors"; IEEE Journal of Quantum Electronics, 28, 2358-2366 (1992).
- [3] A. L. Bogdanov and E. K. Andersson; "Fine Undercut Control in Bilayer PMMA-P(MMA-MAA) Resist System for E-beam Lithography with Submicrometer Resolution"; Proc. SPIE, Vol. 1465, 324 (1991).

Characterization of Ag-Si Composite for Infrared Photodetectors

Marie DesHarnais

Civil Engineering, University of Minnesota-Twin Cities

NNIN REU Site: Howard Nanoscale Science and Engineering Facility, Howard University, Washington, DC

NNIN REU Principal Investigator(s): Dr. Clayton Bates, Electrical and Computer Engineering, Howard University

NNIN REU Mentor(s): Chichang Zhang, Electrical and Computer Engineering, Howard University

Contact: desh0044@umn.edu, bates@msrce.howard.edu, cczhang@msrce.howard.edu

Introduction:

This project sought to characterize the response to infrared radiation of a silver-silicon composite for possible use in photodetectors. The material studied was a thin layer of n-doped silicon embedded with silver particles about 16 nanometers in diameter [1]. When hit with infrared radiation, the silver particles absorbed photons and emitted their excited electrons into the silicon. In order to enter the silicon, those electrons had to overcome a Schottky barrier, a distortion of energy levels at the metal-semiconductor interface. This barrier fell off over distance, allowing quantum tunneling for electrons with lower energy [2]. By applying an electric field to the material, the electrons that escaped into the silicon were collected to measure the response of the material. The use of particles on the nano-scale allowed enhanced efficiency in capturing photons.

In order to make this material more effective, we adjusted our method of fabrication to increase the magnitude of the response and to get responses at longer wavelengths. The longer wavelengths corresponded to lower energy photons which would require quantum tunneling for any response to be measured. This study specifically looked at the effects of oxygen, annealing, and composite layer thickness on the response.

Procedure:

A magnetron sputtering system was used to deposit a silver contact layer onto an insulating n-silicon substrate, which acted as the base, followed by the buffer and composite layers. The final structure is shown in Figure 1. We carefully controlled the pressure, distance, and temperature in our system so that we knew the thickness of our layers based on the length of time during which deposition occurred. The buffer layer came between the silver and composite layer in order to promote the crystallization of the silicon in the composite. The composite layer could either be deposited by co-sputtering a silver and silicon target or by using a composite target. The layered structure created allowed us to apply a voltage across the thickness of the composite which created a strong electric field to collect electrons.

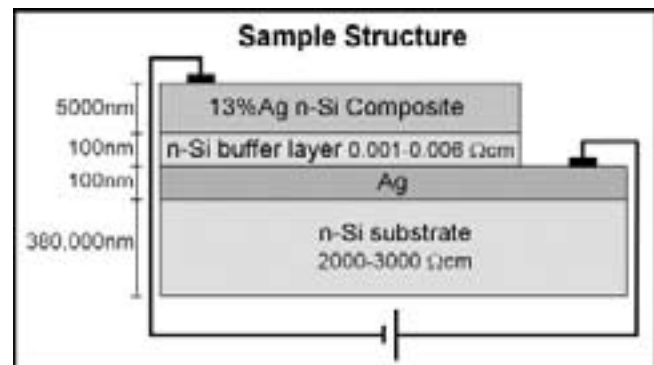


Figure 1: An illustration of the sample's structure with example values for thicknesses, resistivity, and concentration of silver. These values were adjusted for different trials. Diagram is not to scale.

After deposition, smaller samples, generally about 1 cm², were cut from the larger wafers in order to be tested. Some of the samples were annealed with argon at 600°C for several hours. Other samples were oxygenated for 5, 18, and 13 minutes.

In order to characterize the reaction of the material to radiation, we placed samples in a vacuum, temperature controlled chamber and exposed them to black body radiation. This radiation was chopped in order to eliminate sources of noise. We adjusted the direct current running through the sample to get multiple measurements of the signal voltage. We also had a number of filters which we applied to the radiation in order to determine which wavelengths of radiation stimulated a response. This characterization procedure was performed both with the sample at room temperature and at liquid nitrogen temperature.

Results and Conclusions:

Three samples were tested this summer. The first sample, #100, was deposited at 600°C and had a 10% silver

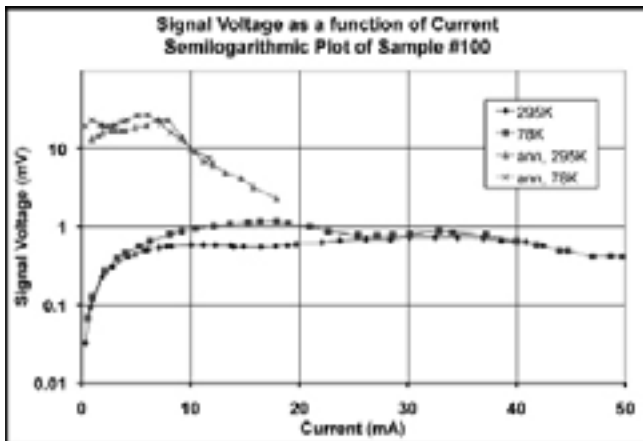


Figure 2: Sample #100 responsivity results before and after being annealed at 600°C for six hours. Each measurement was done at 295K and 78K.

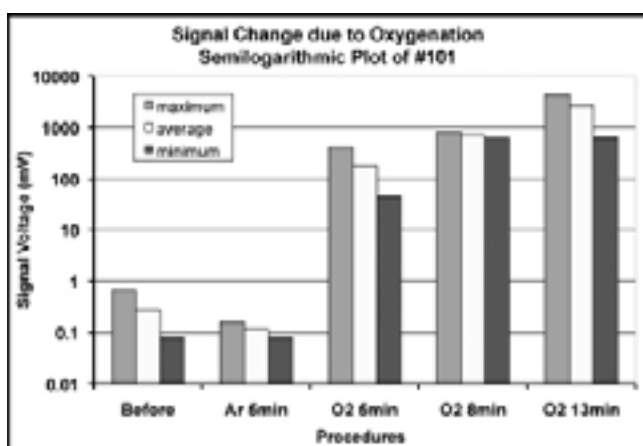


Figure 3: Summary of responsivity data for sample #101. Samples were exposed to the given gas at 500°C for different lengths of time.

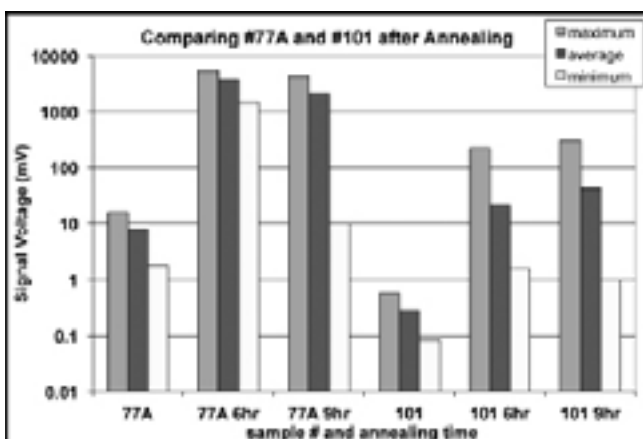


Figure 4: Summary of responsivity data for samples #77A and #101 after being annealed for the given lengths of time at 600°C. The two samples were fabricated identically except that #77A had a 5 μm thick composite layer whereas #101 had a 10 μm thick composite layer.

composite 5 μm thick. The responsivity was measured before and after annealing pieces of the sample at 600°C for six hours. The signal voltage was significantly improved after annealing, as shown in Figure 2.

The second sample, #101, was deposited at 550°C and had a 13% silver composite 10 μm thick. A piece of the sample was exposed to oxygen at 500°C for a short period of time (minutes rather than hours). Figure 3 shows a summary of the responsivity data collected for different exposure times. A significant improvement in the signal voltage was found.

In order to make sure this improvement was a result of the oxygen and not the heat, another piece of the sample was exposed to argon for five minutes at 500°C. The signal voltage was similar to before exposure, showing that the oxygen was having a positive impact.

Sample #101 was made to see if more of the signal could be absorbed and measured using a thicker composite, and so it was made exactly the same as sample #77A except that #77A only had a composite thickness of 5 μm. Pieces of both samples were annealed for six and nine hours at 600°C, and their signal voltages were compared. Summary data for their responsivity are shown in Figure 4.

Every sample tested was also tested using filters. Responses to wavelengths as long as 1.2 μm were observed.

Future Work:

Drs. Zhang and Bates are continuing to work on improving the response at longer wavelengths. They are currently focusing on the effects of oxygen during and after deposition.

Acknowledgements:

I would like to thank Dr. Clayton Bates, my principal investigator, Chichang Zhang, my mentor, and James Griffin, our site coordinator. Also thanks to the people at Howard Nanoscale Science and Engineering Facility for all their help. Additional thanks to the National Nanotechnology Infrastructure Network Research Experience for Undergraduates Program and the National Science Foundation for funding.

References:

- [1] Zhang, C. and Bates, C.W.; "Metal-mediated crystallization in Si-Ag systems"; *Thin Solid Films*, 517, p.5783-5785 (2009).
- [2] Bates, C.W. and Zhang, C.; "Electric field dependence of quantum efficiencies of Ag/n-Si composites in the infrared at room temperature"; *Journal of Applied Physics*, 104, 076101 (2008).

Fabrication of Photonic Crystals for High Temperature Applications

Joseph DeWilde

Chemical Engineering, Oregon State University

NNIN REU Site: Nanofabrication Center, University of Minnesota-Twin Cities, Minneapolis, MN

NNIN REU Principal Investigator(s): Professor Andreas Stein, Department of Chemistry, University of Minnesota-Twin Cities

NNIN REU Mentor(s): David Josephson, Department of Chemistry, University of Minnesota-Twin Cities

Contact: dewildej@onid.orst.edu, a-stein@umn.edu, josep193@umn.edu

Introduction:

Photonic crystals are materials with periodic order on an optical length scale. These materials affect the optical transmission, reflection, and thermal emission of light at specific wavelengths. Within these materials, photons with specific wavelengths cannot propagate in certain directions. Thus, photonic crystals can be used to suppress unwanted thermal emissions (i.e., unwanted heat) or to emit light in a well defined range of wavelengths [1]. For this reason, these materials could be used in more efficient thermophotovoltaic devices.

Theoretical calculations have shown that tungsten photonic crystals with a modified inverse opal structure should be able to alter thermal emission of light [2]. Tungsten photonic crystals were previously fabricated using colloidal crystal templating [3]. Tungsten was used due to its high melting point and refractive index. However, these crystals experienced grain coarsening at temperatures above 1000°C [4]. Three-dimensionally ordered macroporous (3DOM) carbon has been shown to be thermally stable at temperatures up to 2400°C. Thus, the fabrication of tungsten-coated carbon photonic crystals was investigated in hope of fabricating a thermally stable photonic crystal while

maintaining the desired photonic properties of tungsten photonic crystals.

Fabrication and Measurements:

The 3DOM carbon substrate was fabricated by infiltrating a face-centered cubic array of monodisperse poly (methylmethacrylate) (PMMA) spheres, 425 nm in diameter, with a resorcinol formaldehyde polymer resin. The PMMA spheres were then removed and the resin was carbonized by pyrolysis. The pyrolysis was performed under a nitrogen atmosphere with a ramp rate of 5°C/min up to 900°C, with a final dwell time of two hours. A scanning electron microscopy (SEM) image of the resulting carbon substrate can be seen in Figure 1. The structure possesses open windows between the pores with an average diameter of 115 ± 10 nm.

Tungsten was deposited onto the carbon substrate via a chemical vapor deposition technique. 0.2 g of tungsten hexacarbonyl precursor was placed into a flask along with a metal boat containing the carbon substrate. The flask was then treated three times by flushing with nitrogen gas followed by evacuation. The now evacuated flask was then placed into a 400°C sand bath for 20 min. Finally, the flask was cooled to room temperature. The carbon substrates underwent this deposition process three times per sample. Another photonic crystal was similarly manufactured by performing three depositions; each deposition using 0.1 g of tungsten hexacarbonyl precursor.

An SEM image of this crystal is shown in Figure 4, while Figures 2 and 3 show the crystal fabricated with 0.2 g of precursor used per deposition.

Results and Conclusions:

The fabricated photonic crystals possessed sufficient tungsten deposits at depths of about $100 \mu\text{m}$ for a 1 mm thick crystal. This depth corresponds to at least 250 layers of pores. This depth is, in principle, sufficient to exhibit the desired photonic properties.

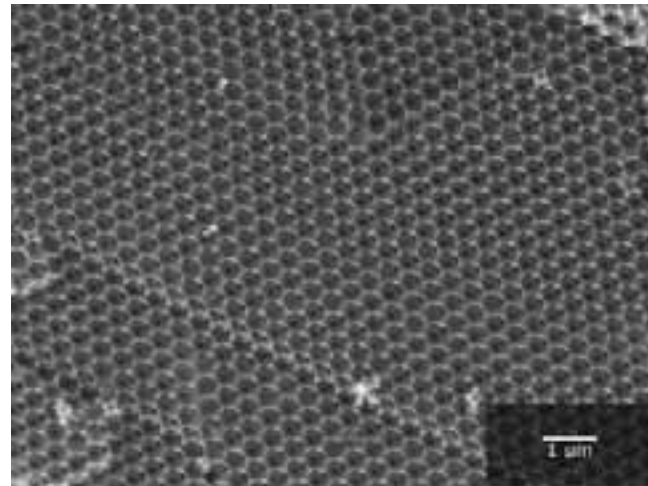


Figure 1: SEM image of a 3DOM carbon substrate. The open windows between the pores have a diameter of 115 ± 10 nm.

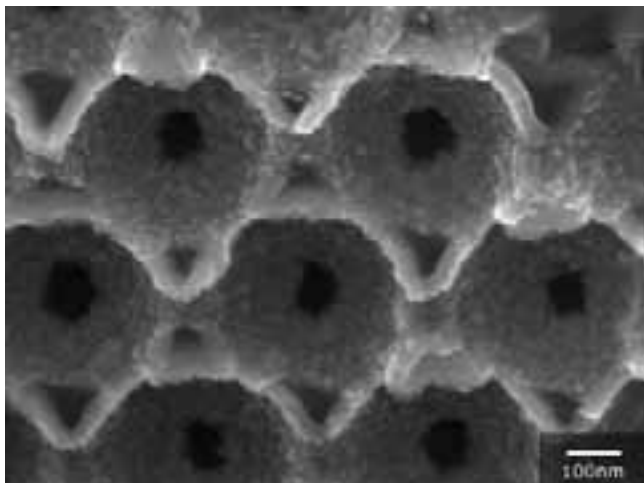


Figure 2: SEM image of tungsten-coated 3DOM carbon pores of the crystal fabricated using 0.2 g of tungsten hexacarbonyl precursor per deposition. The pores in this image have shrunk due to the tungsten deposition, possessing an average diameter 86 ± 9 nm. In addition, the roughness of the deposition and the coarse grains can be seen.

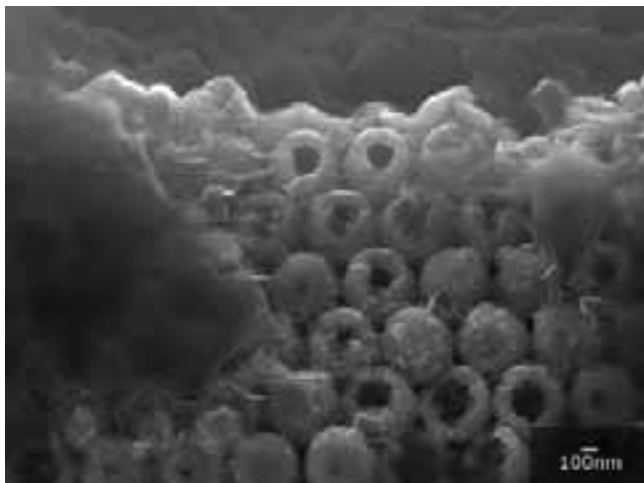
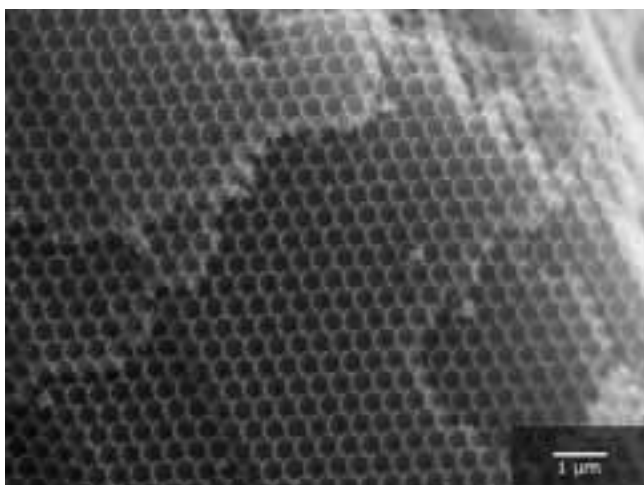


Figure 3: SEM image of tungsten-coated 3DOM carbon pores close to the surface of the crystal fabricated using 0.2 g of tungsten hexacarbonyl precursor per deposition. The pores in this image are blocked by tungsten deposits.



When 0.2 g of precursor were used, the tungsten deposits at some sites close to the surface completely blocked the pores, as shown in Figure 3. By reducing the amount of precursor to 0.1 g, windows between the pores with a diameter of 70 ± 13 nm are formed. This is seen in Figure 4. One can see in Figure 2 that the tungsten deposits constrict the windows between the pores of the photonic crystal.

Before the tungsten was deposited onto the 3DOM carbon substrate, the windows between the pores had a diameter of 115 ± 10 nm. After the tungsten deposition, the windows have been blocked by tungsten and have a reduced window diameter of 86 ± 9 nm. Pore blockages and window constrictions limit the amount of light that can interact with the photonic crystal. Additionally, the tungsten appears to have deposited in coarse grains that can cause light scattering which, in turn, can weaken the photonic properties of the crystal.

Finally, the thickness of the deposited tungsten varied with depth. This inconsistency is undesirable in photonic devices.

With some future improvements, these problems could be minimized, and this synthesis technique could hold promise for the fabrication of thermally stable photonic crystals. Current and future work will focus on increasing the pore size of the photonic crystal as well as providing a more even and disperse distribution of tungsten throughout the crystal.

References:

- [1] Denny et al., Chem. Mater. 2007, 19, 4563-4569.
- [2] Han et al., Phys. Rev. Lett. 2007, 99, 053906/1-4.
- [3] Stein et al., Chem. Mater. 2008, 20, 649-666.
- [4] Denny et al., J. Mater. Chem. 2010, 20, 1538-1545.

Figure 4: SEM image of tungsten-coated 3DOM carbon pores close to the surface of the crystal fabricated using 0.1 g of tungsten hexacarbonyl precursor per deposition. Open windows between the pores with a diameter of 70 ± 13 nm are present.

Transfer of Electron Beam-Patterned Photonic Nanobeam Cavities to Flexible Substrates

D. Johann Djanal-Mann
Electrical Engineering, University of Florida

NNIN REU Site: Center for Nanoscale Systems, Harvard University, Cambridge, MA

NNIN REU Principal Investigator(s): Prof. Marko Lončar, School of Engineering and Applied Sciences, Harvard University

NNIN REU Mentor(s): Ian Burgess, School of Engineering and Applied Sciences, Harvard University

Contact: johmann@ufl.edu, loncar@seas.harvard.edu, ibburges@fas.harvard.edu

Abstract:

The recent demonstrations of high-Q/V photonic-crystal nanobeam cavities in low-index materials allows for their application in a broad array of material systems (polymers, glasses, etc.). An elastomeric platform for high Q/V cavities has a wide range of potential applications in biosensing and microfluidics. We studied the transfer of an e-beam resist, ZEP 520, as well as cavities fabricated in it, onto the silicon elastomer PDMS (Sylgard 184). Films were deposited on various sacrificial substrates. PDMS bonding was facilitated through deposition of a thin silicon dioxide (SiO_2) layer on the ZEP520 film and plasma oxidation of the PDMS surface. Oxide adhesion to the ZEP520 layer was found to be poor, limiting the effectiveness of the transfer process.

Introduction:

The past few years have seen a significant advancement in the field of nanoscale optics. Nanophotonics is now at the forefront of research agendas for applications in communication and information processing systems [1]. This progress was driven by innovations in microfabrication techniques, due to continuous demands for faster, smaller, and cost-efficient computation systems, as well as new insight into fundamental physical laws that govern the behavior of photons on a nanoscale level [1].

Nanobeam cavities are photonic resonators that confine light in one dimension with the use of Bragg mirrors, and in the other two directions by total internal reflection [2]. Wavelength-scale nanobeam cavities can have ultra-high quality (Q) factors, even in materials with a low refractive index ($n \sim 1.5$) [3]. Fabricating nanobeam cavities in low-index materials has many promising applications in photonic devices at visible frequencies, as many materials that are sufficiently lossless in this range have a low refractive index. The incorporation of soft materials (polymers, glasses etc.) into high- Q photonic-crystal cavities also allows the exploitation of the diverse properties of this class of materials into future photonic devices. One such material property is the ability to stretch. Recent advances in mechanics and materials research are leading to means for integrated circuits to be stretched, compressed, and deformed, while still maintaining their electrical properties and functionality. Nanostructured electronic materials integrated with elastomeric substrates offer mechanical properties and other attractive characteristics, such as bendability, light-weight, and rugged construction. This technology has promising applications in many sub-categories, such as robotics and *in vivo* imaging [4].

The broad goal of this research project was to fabricate high-quality, soft material nanophotonic devices on a flexible platform. This study focused on PDMS as a substrate. The nanobeam cavities could either be fabricated directly on a PDMS substrate, or fabricated on a sacrificial substrate and subsequently transferred onto the flexible platform. We chose to focus on the latter option for the following reasons: High- Q nanobeam cavities in low-index materials require, for sufficient index-contrast, an immediate substrate of either air (suspended geometry [2]) or an artificial material with a refractive index close to that of air (e.g. mesoporous silica [5]). We hypothesized that both options would be more compatible with a transfer-based fabrication protocol. Successful transfer would instigate the development of flexible photonic technology, making possible, for example, bio-conformable and stretch-tunable photonic devices.

Experimental Procedure:

Thin-films of e-beam resist, as well as devices fabricated in e-beam resist, were fabricated on sacrificial substrates. After bonding the resist to the PDMS substrate, the original substrate was wet-etched in a carefully chosen solvent. Cavities were made from the high-resolution electron-beam resist ZEP520 (Zeon Corporation). We explored the following sacrificial substrates: PVA, spin-coated on top of a Si wafer, dissolved in water; NaCl rock salt cubes, also dissolved in water as the solvent; and bare Si wafers, with a 30% w/v aqueous potassium hydroxide solution as the etching solution. A thin layer of gold (~ 30 nm) was sputtered onto the NaCl substrates to allow sufficient adhesion of the ZEP520 film. In order to promote adhesion of the ZEP520 layer to an oxidized PDMS surface, we deposited a thin

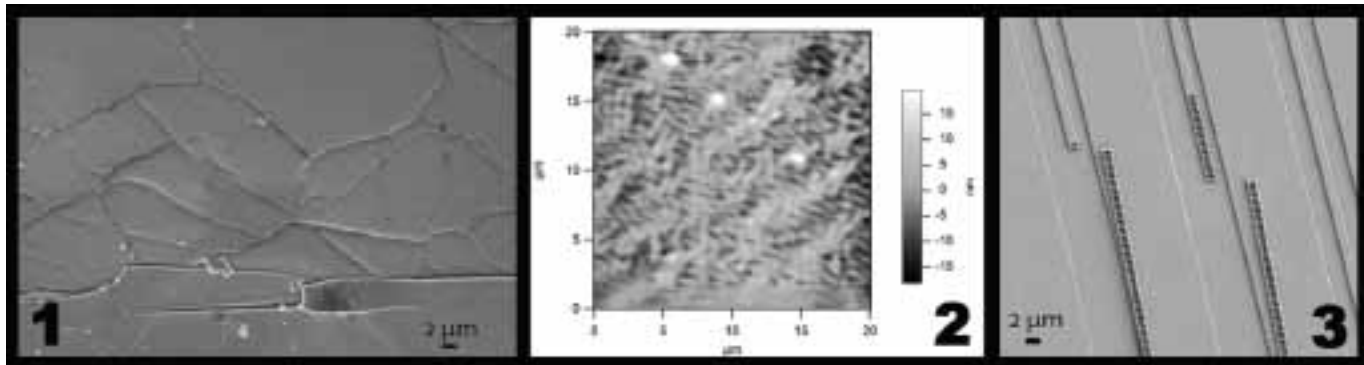


Figure 1: Thin film of ZEP 520 transferred onto PDMS from an NaCl sacrificial substrate.

Figure 2: AFM image of a PDMS slab that was cured from liquid on top of a ZEP layer and manually separated, demonstrating the potential transfer of the ~ 10 nm SiO_2 layer deposited to enhance adhesion.

Figure 3: ZEP520 nanobeams remained on the original Si substrate after the dry-transfer procedure.

(~ 10 nm) layer of SiO_2 on the ZEP520 layer before bonding using a room temp. process developed by Hatton, et al. [6].

In addition, a dry transfer process was also attempted, whereby the removal of the sacrificial substrate took place before the bonding of the devices. For these experiments, a sacrificial layer of sol-gel silica, prepared from a weakly acidic aqueous solution of TMOS, was spin-coated on top of a clean Si wafer. $300\text{ }\mu\text{m}$ long beams containing cavities were fabricated in ZEP520 on top of the sacrificial layer. The sacrificial silica layer was then etched in a buffered oxide etching solution ($\text{HF:NH}_4\text{F:H}_2\text{O}$), releasing the beams, which remained attached to the substrate only at the endpoints. The beams were then bonded to the PDMS substrate as described above, followed by manual separation of the two substrates. Transferred films and devices were characterized by optical microscopy, scanning electron microscopy (SEM) and atomic force microscopy (AFM).

Results and Conclusions:

Figure 1 shows the PDMS substrate after a typical transfer of a bulk thin film of ZEP520 from a NaCl substrate. Cracking and delamination of the film were observed with thin films transferred from all sacrificial substrates listed above, indicative of poor adhesion between the resist and the PDMS. To examine the properties of this adhesion, we cured liquid PDMS on top of a ZEP520 film (on a Si substrate) that had been coated with 10 nm of SiO_2 (as described above). Having found that the two substrates easily separated before etching of the underlying Si, we observed that while the ZEP520 film remained on the Si substrate, there was some faint iridescence on the surface of the PDMS slab. Examining the PDMS surface with AFM, we observed a periodic ridge pattern (see Figure 2), with a vertical amplitude of ~ 30 nm and a period of $\sim 1\text{ }\mu\text{m}$, suggesting that the ~ 10 nm SiO_2 layer had been transferred, detaching from the underlying ZEP substrate. This, combined with the ease at which the PDMS and ZEP520 layers separated implies poor adhesion between ZEP520 and the deposited SiO_2 .

Figure 3 shows a typical result of the dry-transfer process: while cracking of the beams indicates that some force has been applied to the beams during the transfer process, the beams consistently remained on the original substrate, and none were found to have sufficiently bonded to the PDMS substrate.

Based on our results, we believe that our procedure of room temperature deposition of SiO_2 onto the ZEP520 does not sufficiently enhance bonding between ZEP520 and PDMS to allow for successful transfer of devices fabricated in ZEP520 to PDMS substrates.

Future Work:

In the future, we hope to transfer devices fabricated in the silica-based negative electron beam resist HSQ/FOx, as a substitute for ZEP520. While high resolution control of the three-dimensional shape and refractive index of nanobeams is more compatible with ZEP520 structures, we expect HSQ to have an improved adhesion compatibility with PDMS in comparison to ZEP520. As all of the sacrificial layers used here would be incompatible with the HSQ-patterning process, substitutes for the sacrificial layer and various etching techniques are also being explored.

Acknowledgements:

Thanks and appreciation are directed towards the NNIN REU Program, as well as the NSF. I would also like to thank my mentor, Ian Burgess, my principal investigator, Prof. Marko Loncar, and the rest of the Loncar Group, Prof. Joanna Aizenberg and the Aizenberg Group, and the School of Engineering and Applied Sciences at Harvard University.

References:

- [1] Vahala, K.J. *Nature* 424, 839 (2003).
- [2] P. B. Deotare, M. W. McCutcheon, I. W. Frank, M. Khan, and M. Lončar, *Appl. Phys. Lett.*, 94, 121106 (2009).
- [3] Y. Zhang, M. McCutcheon, and M. Lončar, *CLEO/IQEC*, paper CFE3, (2009).
- [4] Rogers, J. A., Someya, T., and Huang, Y. *Science*, 1603-1606, (2010).
- [5] M. Schmidt, G. Boettger, M. Eich, W. Morgenroth, U. Huebner, H.G. Meyer, D. Konjhodzic, H. Bretinger, F. Marlow, *Appl. Phys. Lett.* 85, 16 (2004).
- [6] B. Hatton, V.Kitaev, D.Perovic, G.Ozin, and J.Aizenberg, *JMC*, 6009-03, 2010.

3D Super-Resolution Using a Phase Mask Fabricated via Grey-Level Lithography

Callie Fiedler

Physics, University of San Diego

NNIN REU Site: Colorado Nanofabrication Laboratory, University of Colorado, Boulder, CO

NNIN REU Principal Investigator(s): Rafael Piestun, Electrical Engineering, University of Colorado at Boulder

NNIN REU Mentor(s): Ginni Sharma and Sean Quirin, Electrical Engineering, University of Colorado at Boulder

Contact: callie.fiedler@gmail.com, rafael.piestun@colorado.edu, ginni.sharma@colorado.edu, sean.quirin@colorado.edu

Abstract:

Three dimensional (3D) super-resolution can be achieved in microscopy instruments by means of phase masks that shape the point spread function [1]. Grey level lithography is an attractive procedure for the generation of these phase masks. The photolithographic phase masks (PPM) encode the light emitted from a specimen via a topographical index of refraction variation consisting of a series of phase-singularities [2]. In our case, the mask produces a double helix point-spread function (DH-PSF), which allows for the estimation of the object position throughout the depth of focus of a typical system [3]. The goal of this project was to develop processes to fabricate and characterize PPMs. We manipulated the grey-scale lithography capabilities of a maskless lithography system by priming the photoresist with multiple exposures prior to the final exposure pattern. This procedure allowed us to produce the desired topography expressed by the photoresist after exposure and development (with feature sizes on the order of 10^{-6} m). Upon testing these phase masks in an optical system, we were able to observe the desired DH-PSF. Currently, experiments are being done to translate the fabricated topography of the photoresist into quartz through reactive ion etching.

Introduction:

Implementing phase masks that shape the PSF of an imaging system using a spatial light modulator (SLM) to produce 3D super-resolution is impractical for widespread use in the scientific world. Current high-end SLMs operate in reflective mode so systems are bulky in addition to being expensive. Also, an SLM is only capable of processing polarized light, which means 50% of the light emitted by a specimen is lost before any imaging can be done. Utilizing a PPM that is inherently transparent and isotropic would allow for all light to be imaged and analyzed and would also allow for a more practical, affordable microscopy set-up to produce 3D super-resolution.

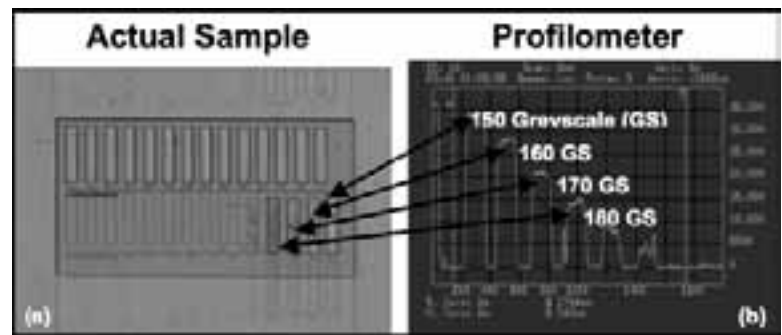


Figure 1: The optical image of the photoresist's topographical surface after exposure to a mask consisting of varying greyscale values; (a) displays the linear correlation to the photoresist's height, and (b) after varying exposure doses via different greyscale values.

Experimental Procedure:

Materials. A microscope slide was used as the substrate upon which we spun a negligible amount of hexamethyldisilazane (HMDS) as an adhesion layer before spinning 3.5 μ m of positive AZ-4210 photoresist.

Calibration. A phase mask requires a linear slope in the exposure and development rate of the photoresist. The experiment used positive photoresist AZ-4210, but further experimentation showed that other resists may improve the quality of the devices. To utilize the greyscale lithography

abilities of the SF-100 Xpress maskless lithography instrument, we first developed a procedure to calibrate the photoresist with the instrument, which had to be done on a daily basis. The greyscale values interpreted by the instrument were correlated to a linear exposure rate, as seen in Figure 1.

AZ-4210 has a linear exposure rate and produces linearly sloped topographical features in the photoresist after exposure, but the slope of these features was far too steep for

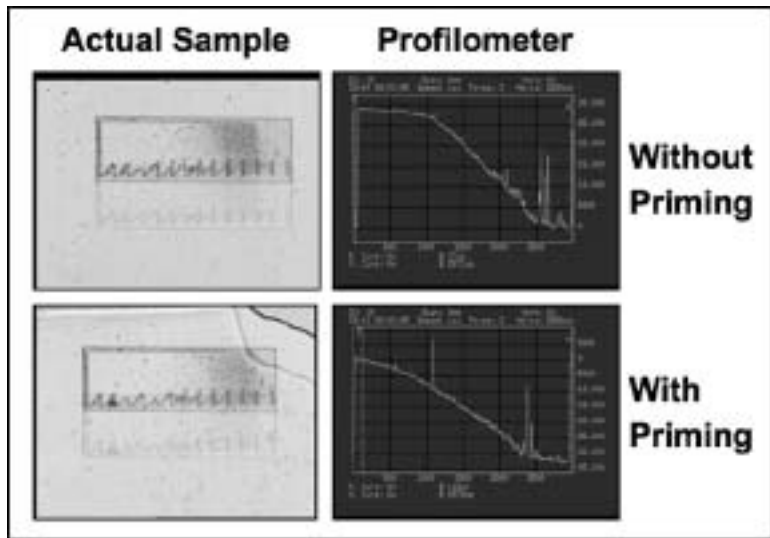


Figure 2: The slope of the photoresist topography in the calibration sample with priming (bottom row) is significantly less steep than that of the sample without priming (top row), which is desired.

the sensitive topography of the PPM. To reduce the slope, a series of pre-exposures to the photoresist were conducted as a method of priming the photoresist for the final image. Priming the area of exposure first, yielded a lower slope in the linear topography of the PPM, as seen in Figure 2.

Fabrication. Using bitmap files created in MatLab for the desired phase mask in the desired range of greyscale values, we primed our substrate and then used the SF-100 to project our image onto our substrate for varying amounts of exposure times (usually ranging between 1-2 seconds). The PPMs were developed in AZ-400 from 90 to 120 seconds.

Characterization. The physical, topographical characteristics of each PPM was determined using a differential interference contrast microscope, which allowed for the viewing of defects that could potentially disrupt the functionality of the PPM, as shown in Figure 3. To determine the functionality of each PPM, a microscopy system was used with a region where the PPM was placed and then imaged through a camera onto a computer.

Results and Conclusion:

Using a simple microscopy system, we demonstrated, successfully, the fabrication of PPMs. Two types of PPMs were implemented, which correlated to varying amounts of lobe rotation observed throughout the object's PSF.

These PPMs are now ready to be implemented into further microscopy experiments to progress towards more accessible 3D super-resolution.

Acknowledgements:

I would like to thank Dr. Rafael Piestun and my mentors Ginni Sharma and Sean Quirin for their incredible support and guidance. Funding and support provided by the NSF, the NNIN REU Program, and the Colorado Nanofabrication Laboratory also need to be appreciated and acknowledged. Additionally, DIC images and greyscale PPM bitmaps were provided courtesy of Sean Quirin and Ginni Sharma.

References:

- [1] Greengard, Y. Schechner, and R. Piestun, "Depth from diffracted rotation," *Opt. Lett.* 31, 181-183 (2006).
- [2] S. R. P. Pavani and R. Piestun, "High-efficiency rotating point spread functions," *Optics Express* 16, 3484-3489 (2008).
- [3] S. R. P. Pavani et al, "3D localization with nanometer accuracy using a detector-limited DH-PSF system," *APL* 95, 021103 (2009).

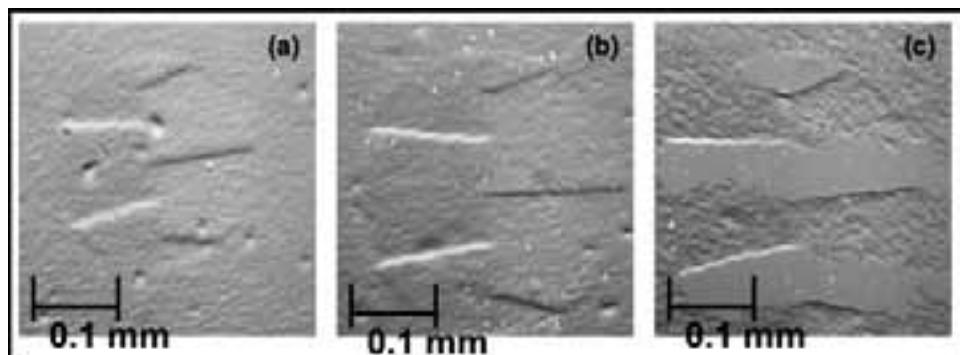


Figure 3: Images produced from DIC displaying varying qualities of fabricated PPMs. Image (a) depicts defect in the mask produced either by air or dust, rendering it useless. Image (b) depicts a PPM with little to no irregularities and should, thus, function properly. Image (c) depicts an underexposure as seen by the residual, non-sloping regions in the PPM.

Fabrication and Characterizations of Plasmonic Nanostructures for Organic Photovoltaics

Michael Hoerner

Engineering Physics, Rose Hulman Institute of Technology

NNIN REU Site: Colorado Nanofabrication Laboratory, University of Colorado, Boulder, CO

NNIN REU Principal Investigator(s): Won Park, Electrical Engineering, University of Colorado at Boulder

NNIN REU Mentor(s): Saumil Joshi, Electrical Engineering, University of Colorado at Boulder

Contact: hoernemj@rose-hulman.edu, won.park@colorado.edu, joshi.saumil@gmail.com

Abstract:

Metallic gratings with a periodicity in the subwavelength regime have been shown to produce a variety of effects. When combined with photovoltaics, these nanogrids can lead to an increase in absorption at wavelengths that are dependent upon the periodicity of the grating. Gold gratings of periodicity 500 nm and 350 nm were fabricated using electron beam lithography. Fabrication techniques for the nanogrids and the application of the photoactive layer are presented, as well as transmission and absorbance spectrums for organic photovoltaics with and without plasmonic enhancement.

Introduction:

Photovoltaics are semi-conducting materials that absorb photons to create electron hole pairs that are then collected as current. It is a clean power supply that, for all practical purposes, will never run out and there is more than enough of it to meet all of our energy needs. Despite this, photovoltaics make up a very small percent of our energy supply due to prohibitively high cost of production. Organic photovoltaics currently have low absorption efficiencies, low carrier diffusion lengths, degrade over time, and are expensive to fabricate [1]. However, many researchers believe that they have the potential to make photovoltaics cost effective for large scale power production in the near future. To compensate for the low carrier diffusion length, thin films are used. However, thin films demonstrate poor absorption.

To address this problem, we propose the use of metallic nanogrids in the subwavelength regime to enhance the absorption of thin film organic photovoltaics. These gratings interact plasmonically with incident light and couple it at the interface of the nanogrid and the photovoltaic interface, increasing the optical pathlength of the light while maintaining a thin film of the photovoltaic material [2,3].

Methods:

The substrates used were 25 mm \times 25 mm microscope slides. These slides were first cleaned using a 12 minute dip in piranha at 90°C. Electron beam lithography was then carried out using a JEOL 5710 SEM, a beam blanker, and the nano pattern generation software at the Colorado Nanofabrication Lab. The patterns were written into a polymer bilayer of 50 nm copolymer that was spun-on,

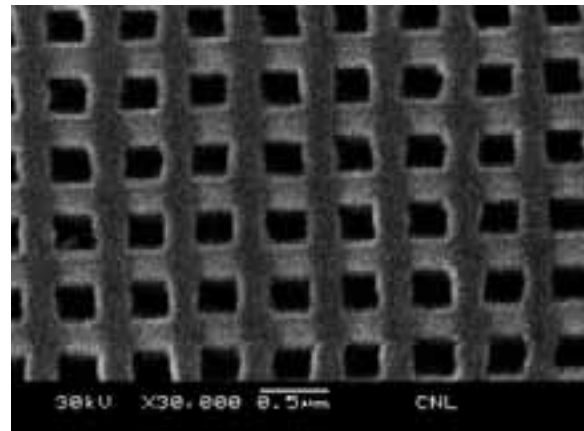


Figure 1: SEM image of the 500 nm periodicity grid.

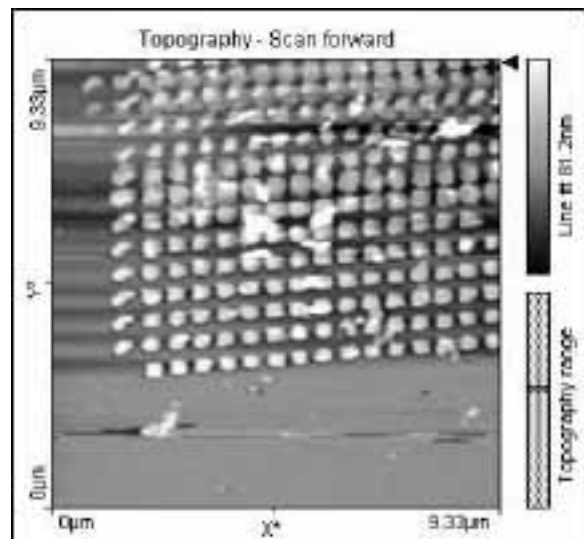


Figure 2: AFM of the 500 nm periodicity grid.

from a solution concentration of 4.5%, at 4000 RPM for 30 seconds, and 50 nm PMMA that was spun-on, from a solution concentration of 2%, for 4000 RPM for 30 seconds. After each deposition, the sample was baked at 170°C for 15 minutes. A beam current of 10 pA, an acceleration of 30 kV and an area dose of 75 μ C/cm² was used.

The patterns were then developed using a 1:3 MIBK:IPA solution for one minute, followed by a five second spray rinse in IPA, and were then blown dry. A metallic trilayer of 5 nm aluminum, 5 nm chromium, and 30 nm of gold was then deposited using a three boat thermal evaporator. Liftoff was then performed with PG remover at 60°C with ultrasonic vibration in five minute intervals until the pattern was observed to be clean.

Figure 1 shows a scanning electron microscope (SEM) image and Figure 2 shows an atomic force microscope (AFM) image of the 500 nm periodicity grid. The CuLCPC₁₂ was suspended in a solution of toluene at a concentration of 10 ± 1 mg/ml and spun on to the 350 nm grating at 2500 RPM with five seconds of acceleration and 30 seconds spin time. The PCDTBT was suspended in dichlorobenzene at a concentration of 7.0 ± 0.2 mg/ml and spun on to the 500 nm grating at 3000 RPM with five seconds of acceleration and 30 seconds spin time.

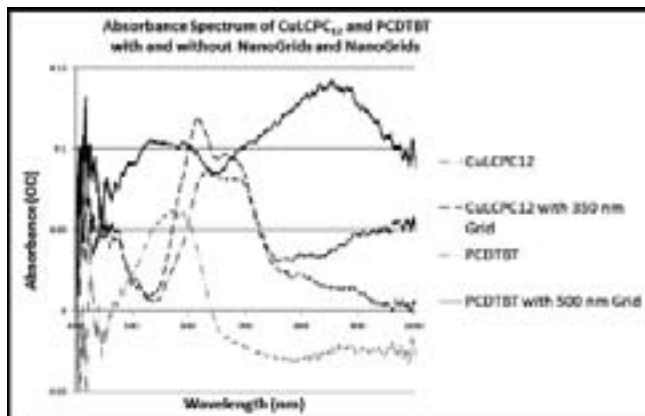


Figure 3: A graph showing the absorbance of the photovoltaics with and without nanogrids.

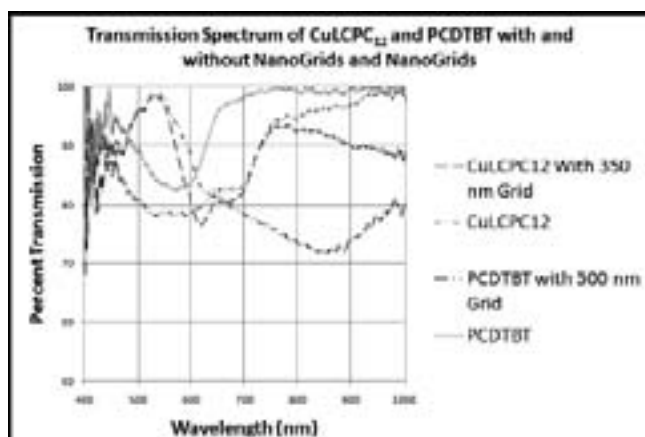


Figure 4: A graph showing the transmission of the photovoltaics with and without nanogrids.

Results and Conclusions:

The optical transmission of the nanogrids was measured using an optical spectrometer. As can be seen in Figures 3 and 4, the spectra with and without the grids for each respective photovoltaic have approximately the same shape with a shift up to a point. The shift is due to the inherent absorption of gold on the glass. However, when the spectra start to diverge, plasmonic effects are being seen.

As can be seen in Figure 3, an increase of ~ 0.12 OD was observed for PCDTBT at an optical wavelength of 860 nm and of 0.033 OD for CuLCPC₁₂ at an optical wavelength of 610 nm. These numbers take into account the absorption of the gold by subtracting the average distance between the curves in plasmonically inactive regions from the maximum difference between the curves in the active region.

Similarly, in Figure 4, a decrease of 21% transmission was observed for PCDTBT and 77% transmission for CuLCPC₁₂. These increases in the absorbance characteristics of these organic photovoltaics show great promise as a way to increase organic photovoltaic efficiency.

Future Work:

The next stage in this research is to fabricate a working photovoltaic chip with nanogrid enhancement and one without, and to perform comparative electrical measurements on the two samples. This would provide definitive evidence as to the exact effectiveness of the nanogrid enhancement for photovoltaic efficiency.

Acknowledgements:

I would like to thank the National Science Foundation and the National Nanotechnology Infrastructure Network Research Experience for Undergraduates (NNIN REU) Program for their funding and support this summer, the Colorado Nanofabrication Laboratory and staff for their crucial assistance in lab use, Saumil Joshi for mentoring me, and my P.I., Dr. Won Park, for his assistance and guidance this summer.

References:

- [1] Park, S.; Roy, A.; Beaupre, S.; Cho, S.; Coates, N.; Moon, J.; Moses, D.; Leclerc, M.; Lee, K.; Heeger, A.; "Bulk heterojunction solar cells with internal quantum efficiency approaching 100%", *Nature Photonics*, Vol. 3, April 2009.
- [2] Coe, J.; Heer, J.; Teeters-Kennedy, S.; Tian, H.; Rodriguez, K.; "Extraordinary Transmission of Metal Films with Arrays of Sub Wavelength Holes", *Annu. Rev. Phys. Chem.* 2008.
- [3] Atwater, H.; Polman, A.; "Plasmonics for improved photovoltaic devices", *Nature Materials*, Vol. 9, March 2010.

Close-Packed Monolayer of Silica Nanoparticles for use as Etch Mask in LED Active Region

Christina Jones

Engineering Physics, University of Colorado at Boulder

NNIN REU Site: Lurie Nanofabrication Facility, University of Michigan, Ann Arbor, MI

NNIN REU Principal Investigator(s): Pei-Cheng Ku, Electrical Engr. and Computer Science, University of Michigan, Ann Arbor

NNIN REU Mentor(s): Michael Kuo, Electrical Engineering and Computer Science, University of Michigan, Ann Arbor

Contact: christina.jones@colorado.edu, peicheng@umich.edu, michael.kuo@gmail.com

Abstract:

Uniform, nanostructured semipolar (NSSP) patterning of the active region of gallium nitride (GaN) light-emitting diodes (LEDs) improves several properties of the LEDs, including the efficiency, compared to planar active regions. We report the progress of a close-packed monolayer of silica nanoparticles for use as an etch mask, which was an essential part of creating this uniform pattern.

Introduction:

GaN LEDs show promise as efficient, solid-state lighting sources. However, improved efficiency and less dependence of output wavelength on injection current is necessary for GaN LEDs to compete with conventional lighting options [1]. Patterning the active region of the LEDs with an irregular NSSP texture reduces the polarization charges that contribute to these problems [2-3]. The incorporation of this texture has shown to improve the internal quantum efficiency by 30% compared to planar active regions, and significantly reduce the output wavelength's dependence on injection current [4]. By creating a more uniform NSSP pattern and using a less damaging surface treatment to create the pattern, the LED turn-on voltage can be lowered, resistance reduced, and internal quantum efficiency further improved. Essential to the regular patterning of the active region is an etch mask that results in periodic, nano-scale dips in the GaN (Figure 1). We report the progress of a close-packed monolayer of nanoparticles (NPs) on GaN implemented by spin-coating for use as this etch mask.

Materials and Methods:

The nanoparticles we used to form the close-packed monolayer were silicon dioxide nanoparticles with 100 nm diameters in a 5 wt.% aqueous solution. The method we used was spin-coating the nanoparticles in solution onto the substrates, which were glass and n-type GaN grown using metal-organic chemical vapor deposition on *c*-plane sapphire. We used glass in addition to n-type GaN substrates to check whether the spin recipe needed to be adjusted or the quality of the GaN surface was impeding the formation

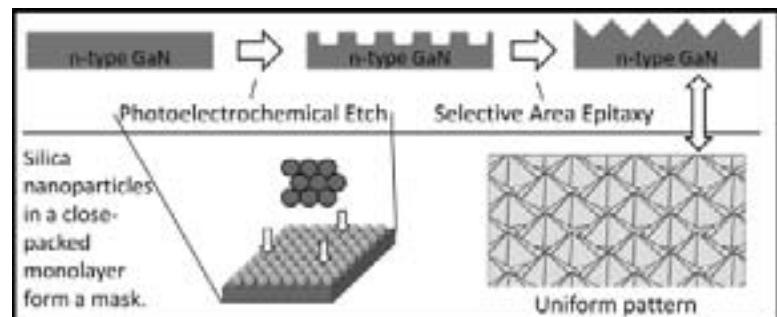


Figure 1: The proposed process for creating uniform NSSP.

of a close-packed monolayer. Prior to spin-coating, the NP solution was shaken for approximately 20 seconds to help ensure even dispersion of nanoparticles in the solution.

Results:

The primary parameters we adjusted in order to obtain a close-packed monolayer of nanoparticles were nanoparticle solution concentration and spin speed. Increasing the concentration of the solution resulted in a thicker nanoparticle layer, and increasing the spin speed resulted in less coverage of the substrate surface. This was characterized by optical and scanning electron microscopy (SEM).

Mostly close-packed monolayers were first obtained reproducibly on glass substrates using a spin recipe of 10 sec at 500 rpm followed by 240 sec at 1000 rpm. The monolayer was not completely close-packed; rather, it contained regions of close-packed nanoparticles with some dislocations and breaks between regions (Figure 2). Regions with more uniform nanoparticle size and shape resulted in

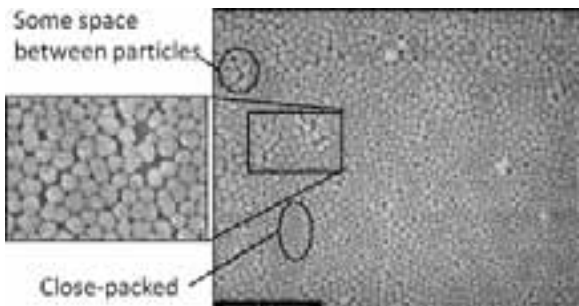


Figure 2: Mostly close-packed monolayer on glass. Spaces, close-packed regions, and irregularity of nanoparticles are highlighted.

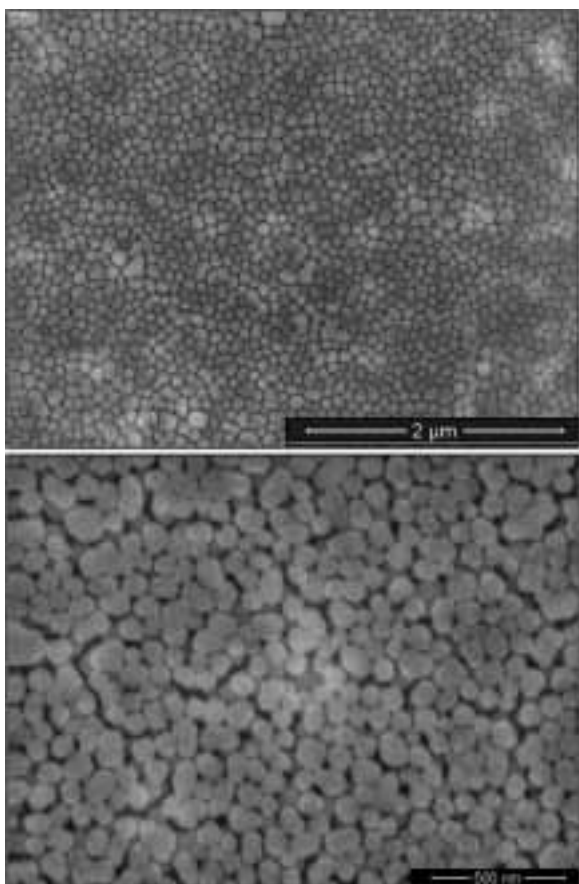


Figure 3: Monolayer and double layer, respectively, on GaN.

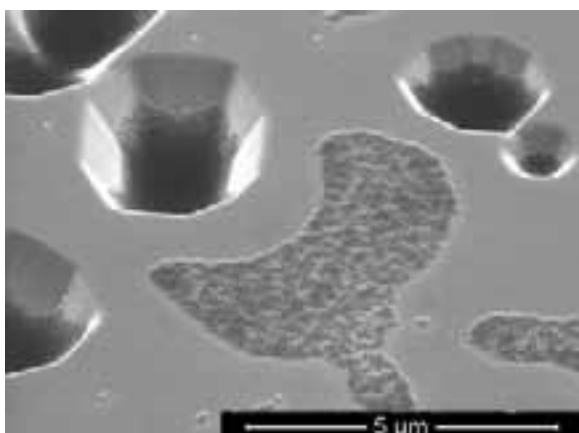


Figure 4: Sample illustrating the effect of many GaN defects on forming a monolayer.

much nicer close-packing. This indicates that the quality of the close-packed monolayer is currently limited by the non-uniformity in size and shape of the nanoparticles.

We then used this recipe on GaN and obtained a mostly close-packed monolayer on part of the GaN substrate as well; however, the coverage and thickness of the NP layer was less uniform.

On a different GaN substrate, we obtained a double layer of nanoparticles mostly uniformly over the substrate (Figure 3). Previous samples had shown that large numbers of defects in the substrate significantly affected the formation of a monolayer and that many of the nanoparticles fell into the defects (Figure 4). The irreproducibility of a close-packed monolayer on GaN so far indicates that the defects could still be affecting the formation of the monolayer, even on samples with few defects such as the monolayer and double layer on GaN discussed above.

Conclusions and Future Work:

We were able to obtain reproducible, mostly close-packed monolayers of silica nanoparticles on glass substrates. However, we were not able to do the same reproducibly on GaN substrates, likely because of the defects in the GaN. We plan to first try further optimizing the spin recipe on low-defect GaN substrates. If that does not result in reproducible layers, we plan to fill the GaN defects before spin-coating, or spin-coat close-packed monolayers onto glass and transfer the monolayers to GaN substrates.

Additionally, we observed that the non-uniformity of the NPs is limiting the close-packing of the nanoparticle monolayer. This can be addressed by obtaining NPs more uniform in size and shape.

Acknowledgments:

I would like to thank Professor Pei-Cheng Ku and Michael Kuo for their guidance with this research project. I would also like to thank the coordinators of the REU program at the University of Michigan, the staff in the Lurie Nanofabrication Facility and the Electron Microbeam Analysis Laboratory, the National Nanotechnology Infrastructure Network Research Experience for Undergraduates (NNIN REU) Program for this opportunity, and the National Science Foundation for funding this project.

References:

- [1] J.M. Phillips, et al., "Research challenges to ultra-efficient inorganic solid-state lighting," *Laser Photon. Rev.* 1, 307–333 (2007).
- [2] M. H. Kim, et al., "Origin of efficiency droop in GaN-based light-emitting diodes," *Appl. Phys. Lett.* 91, 183507 (2007).
- [3] S. H. Park, "Crystal orientation effects on electronic properties of wurtzite InGaN-GaN quantum wells," *J. Appl. Phys.* 91, 9904–9908 (2002).
- [4] T. Jung, et al., "Novel Epitaxial Nanostructures for the Improvement of InGaN LEDs Efficiency," *IEEE J. Sel. Top. Quantum Electron.* 15, 1073-1079 (2009).

Molecular Specific Biosensing Based on Engineered Quasi-3D Plasmonic Nanostructures

Roger Jordan

Biomedical Engineering, Texas A&M University

NNIN REU Site: Center for Nanotechnology, University of Washington, Seattle, WA

NNIN REU Principal Investigator(s): Qiuming Yu, Department of Chemical Engineering, University of Washington

NNIN REU Mentor(s): Jiajie Xu, Department of Chemical Engineering, University of Washington

Contact: jord1125@neo.tamu.edu, qyu@u.washington.edu, jiajiexu@u.washington.edu

Abstract and Introduction:

Raman scattering is inelastic light scattering, wherein the incoming photon collides with a molecule and transfers part of its energy to the vibrational energy of that molecule. The emitted photon leaves the molecule with less energy than when it entered the molecule. Due to the fact that Raman scattering is related to the vibrational energy of a molecule, a spectrum of this data is capable of demonstrating unique spectral fingerprints for the molecular vibrations of anything from a single molecule to unicellular organisms [1]. Raman scattering typically demonstrates a very low probability, in which 1 in 10^{12} photons exhibits this phenomenon [2].

Surface-Enhanced Raman Scattering (SERS) will be employed to greatly enhance the number of photons that will be inelastically scattered by placing the molecule under investigation at the surface of the nanostructure of noble metals (e.g., gold (Au), silver (Ag), or copper (Cu)).

In this study, two substrates, indium tin oxide (ITO)-coated glass and silicon (Si), were compared in order to determine which substrate yielded the greatest Raman signal enhancement. The goal was to aid in the optimization of nanostructure parameters in order to achieve an enhanced Raman signal. Also, we were looking to detect a single bacterium on our quasi-3D nanostructures in order to characterize and identify species of bacteria.

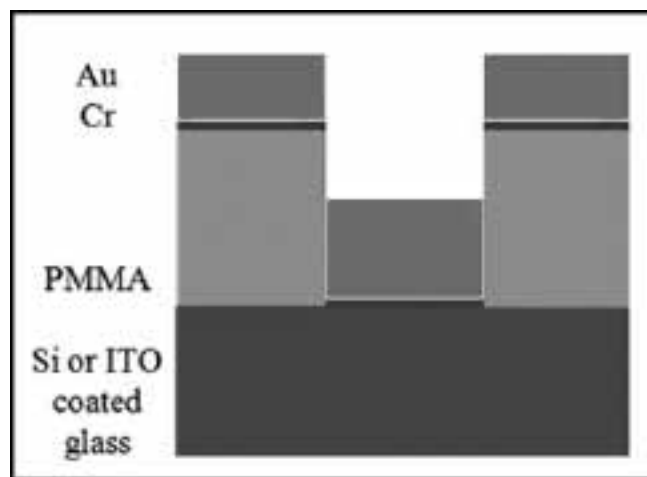


Figure 1: Schematic for Quasi 3-D nanostructures [3].

Experiment Methodology:

These quasi-3D nanostructures were created by employing electron beam lithography (EBL) on two different substrates, ITO-coated glass and Si, using two different nanopattern arrays, circular nanoholes and rectangular nanoholes.

First, a poly(methyl methacrylate) (PMMA) photoresist was spin-coated onto the two substrates until it reached a thickness of 300 nm. Next, the patterns were exposed to an electron beam with a current of 95.6 pA and a dose of 0.36 nC/cm², developed in 1:3 methyl isobutyl ketone/isopropanol (MIBK/IPA) PMMA developer for 70 seconds, rinsed with IPA, blown dry with N₂, then hard-baked at 95°C for 30 minutes.

Finally, a 2 nm layer of chromium adhesion was evaporated to the surface of the nanostructures, followed by a 50 nm layer of Au film. Figure 1 illustrates a schematic for the quasi-3D gold nanostructures. 4-mercaptopyridine (4-MP) was used as a probe molecule in order to determine the enhancement factor for quasi-3D nanostructures. A self-assembled monolayer of 4-MP was formed on the surface of the nanostructures by first cleaning the substrate in UV ozone for 20 minutes and then immersing the substrate into a 3 mM 4-MP solution for three hours. The resultant substrate was then washed with deionized water and dried using N₂ [3].

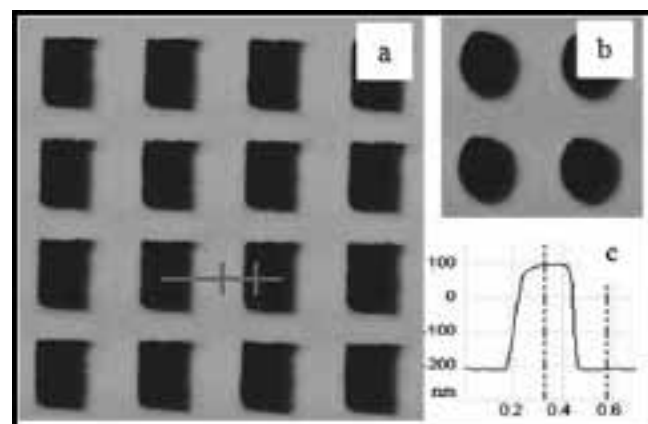


Figure 2: AFM images for rectangular (left) and circular (right) nanopatterns.

In the bacteria study, bacteria were placed on the surface of the nanostructures by preparing a solution of bacteria of a species and forming a solution of 10^6 CFU/mL and dropping this solution onto the substrate. The bacterial solution was allowed to dry on the surface then the Raman spectrum was taken.

In both cases, the 4-MP and bacteria, a Raman spectrometer and a 50x objective were used to illuminate the sample with a 785 nm excitation laser and to collect the scattered light. Once the Raman spectra for the bacteria and 4-MP were attained, scanning electron microscope (SEM) and atomic force microscope (AFM) images were taken in order to ensure that the correct patterns with the correct dimensions had been attained via EBL. Figure 2 shows an AFM image of the circular and rectangular quasi-3D nanostructures and a depth profile for the nanostructures.

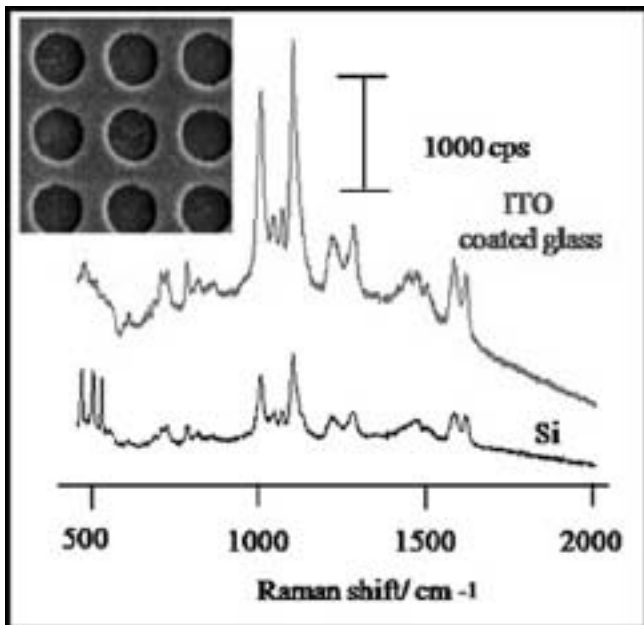


Figure 3: Raman spectra comparison for ITO-coated glass and Si.

Results and Conclusion:

Figure 3 illustrates a raw Raman spectral comparison of 4-MP on ITO-coated glass and Si. Based on this, it is clearly shown that the ITO-coated glass demonstrates about a two to three times higher Raman enhancement than the silicon substrate. It has been determined that this is due to the differences in optical properties between the two substrates. ITO coated glass demonstrates backside reflection, in which the light is reflected at different stages within the glass, thus “trapping” the light for a longer amount of time and increasing the level of localized surface plasmon resonances (LSPR) and increasing the amount of Raman signal. This is compared to the Si substrate, which was optically reflective and did not exhibit this extra electric field enhancement.

A Raman spectrum focused on a single *Escherichia coli* (*E. coli*) bacterium on both the Au circular nanopattern and flat Au surface is shown in Figure 4. The top spectrum is the Raman spectra focused on a single bacterium on the nanopattern surface.

It is clearly shown that the nanopatterns induce the SERS effect and make capable molecular characterization of the bacteria’s surface and the detection of a single bacterium. The bottom, flat Raman spectra is taken on a flat Au surface focused on a single bacterium and does not exhibit a significant enough Raman intensity in order to detect, nor identify the *E. coli* bacterium.

Future Work:

In the future, we plan on employing this molecular specific Raman technology in order to identify between different cancer cells and make comparisons of cancer cells versus normal tissue cells in order to aid in cancer diagnostics.

Acknowledgements:

I would like to thank my principal investigator, Dr. Qiuming Yu, my mentor, Jiajie Xu, and collaborator, Matthew Idso, at the University of Washington. The National Nanotechnology Infrastructure Network Research Experience for Undergraduates (NNIN REU) Program funded by the National Science Foundation is also greatly acknowledged for their support in this research.

References:

- [1] M. Kerker, “SERS by molecules adsorbed at spherical particles,” *Applied Optics* 19, 3373-3388 (1980).
- [2] K. Kneipp, “Single molecule detection using SERS,” *Physical Review Letters* 78, 1667-1670 (1997).
- [3] Q. Yu, “Inverted size-dependence of surface-enhanced Raman scattering on gold nanohole and nanodisk arrays,” *Nano Letters* 8, 1923-1928 (2008).

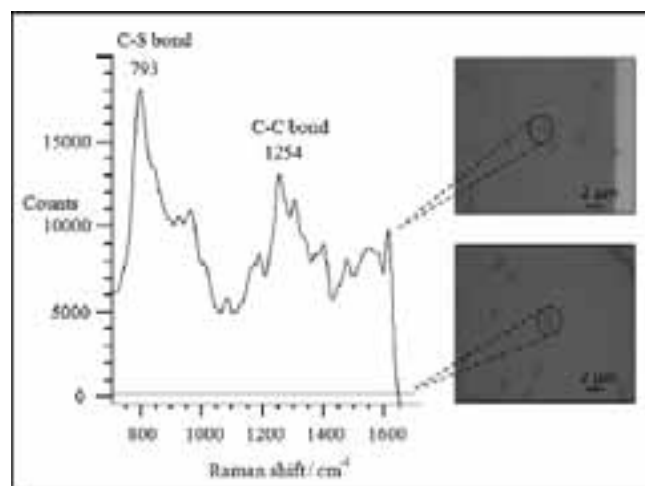


Figure 4: Raman spectra comparison for bacterium on nanopatterns (top) and on a flat, gold surface (bottom).

Lifetime of Charge Carriers in Single Silicon Nanowire

Jhim Handrex Meza

Electrical Engineering, University of California, Los Angeles, CA

NNIN REU Site: Center for Nanoscale Systems, Harvard University, Cambridge, MA

NNIN REU Principal Investigator(s): Prof. Kenneth B. Crozier; School of Engineering and Applied Sciences, Harvard University

NNIN REU Mentor(s): Dr. Yaping Dan, School of Engineering and Applied Sciences, Harvard University

Contact: handrex@ucla.edu, kcrozier@seas.harvard.edu, yapingd@seas.harvard.edu

Abstract:

The lifetime of charge carriers is one of the key parameters that determine the performance of semiconducting optoelectronic devices. However, due to their small size, the lifetime in silicon nanowire (SiNW) devices may be very different from their conventional bulky counterparts. We therefore investigated this difference during the REU program. We measured the charge carrier lifetime of a single SiNW indirectly using SPCM and found the electron lifetime to be a few orders of magnitude smaller than that in a Si bulky device.

Introduction:

In the past several decades, complementary metal oxide semiconductor (CMOS) technology has created many sophisticated devices and systems such as computers, cell phones, cameras and many other electronics. CMOS has changed almost every aspect of our life. These extraordinary technological advances are realized by constantly scaling down the size of CMOS transistors and integrating more and more devices on chip. However, when the size reaches into nanometer scale, CMOS technology encountered tremendous challenges, and nanotechnology may be able to provide solutions to those challenges.

Research in nanotechnology in the past decade has focused mainly on novel devices and concepts. In fact, the performances of nanodevices are equally important. Any performance of a device has a collective balance of physics behind it. Nanodevices have introduced their low dimensionality as a factor that may break this balance. In certain cases, this balance breakdown is favorable for improving the performance. For example, nano chemical gas sensors generally have higher sensitivity than their bulky counterparts because nanosensors have more surface areas that can interact with analytes. In many other cases, this may not be true. The lifetime of charge carriers in nanooptoelectronic devices fall into this latter category.

Methods:

In this summer REU program, we first used the standard photolithographic processes to electrically contact an SiNW, and then employed scanning photocurrent microscopy (SPCM) to measure the lifetime indirectly.

The p-type SiNWs (mostly 70 nm diameter) used in the experiments were synthesized at 460°C using Au NPs as

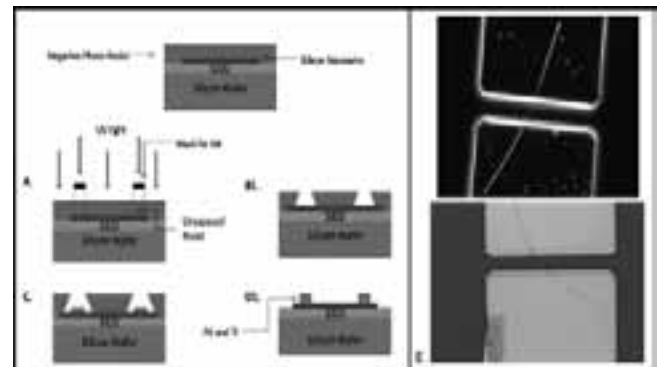


Figure 1: Nanofabrication process. A. During exposure, B1. After develop, electrodes in contact with nanowire ends, C. Coating with Ti and Pd, D1. After lift-off. E. SEMs of nanowire contacted with metals at both ends.

catalysts by the VLS method. The SiNWs were made into a suspension after sonication and purification by a centrifuge. The wires were randomly spread from the suspension onto a Si/SiO₂ substrate with prefabricated alignment markers. The position of the NWs were located under the optical mask aligner using those markers.

In Figure 1, we used a negative resist NR9 and liftoff process to make 180 nm thick palladium electrodes (using 2 nm thick titanium as the adhesion layer) that contacted single wires. The fabricated NW devices, with a Schottky barrier at each end, were electrically responding to light. SPCM uses a nanosized laser (through a near-field scanning optical microscopy, or NSOM, tip) to scan over the NW and excite the charge carriers, as shown in Figure 2.

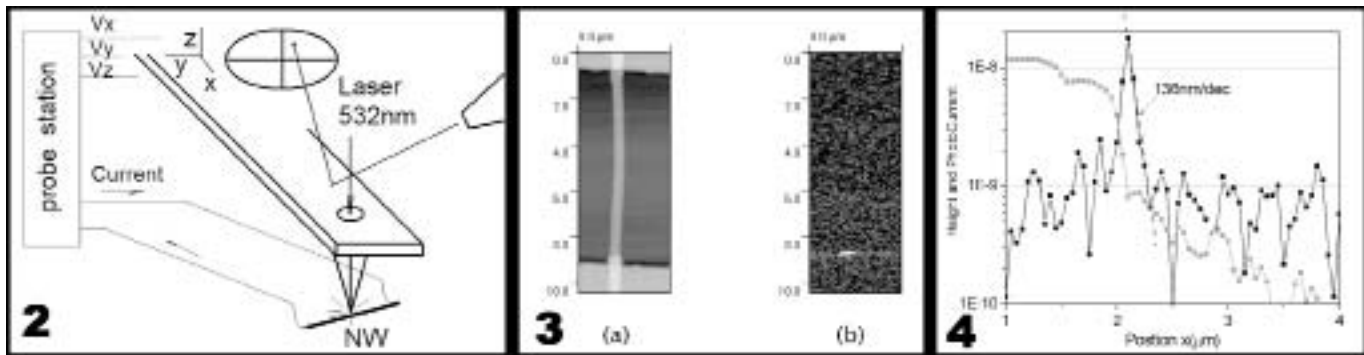


Figure 2: Schematic of SPCM.

Figure 3: (a) AFM image of nanowire with a diameter ~ 53 nm, and (b) the corresponding scanning photocurrent map where a brighter color represents a larger photocurrent.

Figure 4: Photocurrent in logarithm scale versus the position of the laser beam.

We applied a few volts as an electrical bias on the NW device. Due to the Schottky barriers, the bias mainly dropped over the barriers and only a very small fraction was on the NW bulk. In this case, the bulk NW was almost free of electric fields. Therefore, the locally excited charge carriers diffusively decayed from the laser location to the anode electrode and were eventually collected as photocurrent.

The position of the laser and the photocurrent, that were recorded simultaneously, followed the equation, $I_{ph} \sim \exp(-x/L_n)$, where I_{ph} is the photocurrent, x the distance and L_n the diffusion length. From this position-photocurrent relation, we could extract the diffusion length of charge carriers L which was related to their lifetime τ as $L = \sqrt{D\tau}$ where D is the diffusion coefficient.

Results:

The atomic force microscopic (AFM) image and a photocurrent map obtained from SPCM are shown in Figure 3. The photocurrent line profile along the NW can be obtained by drawing a line near the Schottky barrier at the bottom electrode where there was a photocurrent peak (Figure 3b). To ensure the photocurrent line profile was directly on top of the NW, a second line could be drawn in the AFM image (Figure 3a). Both lines were starting from the bottom.

We plotted these two lines in Figure 4 with the light grey for the AFM profile and the black for the photocurrent profile. The light grey line tells us that the photocurrent peak was right near the electrode. The Schottky barrier was buried under the metal electrode, which was not transparent and therefore blocked the laser. Therefore, no photocurrent was observed, as the NSOM tip was on the electrode initially. The laser excitation on the NW increased rapidly while the NSOM tip was moving up. For this reason, we observed a steep elevation in photocurrent. When the tip was further moving away from the electrode, the photocurrent quickly decayed because of the recombination of excited charge carriers when diffusing toward the electrode. This decay

slope was closely related to the diffusion of charge carriers. According to the equation aforementioned, we were able to extract the diffusion length if the photocurrent was plotted in a logarithm scale.

In Figure 4, the right decay slope is 136 nm per decade, which corresponds to a diffusion length ~ 55 nm. The lifetime of the charge carriers in this SiNW was calculated to be ~ 100 ps, which is three to four orders of magnitude smaller than that in silicon bulk. From the AFM image in Figure 3a, the NW diameter is approximately 70 nm. The diffusion is roughly equal to the size of the NW diameter. Larger sized NWs have longer diffusion lengths, which is true for many other NW devices, as we observed.

Conclusions:

We find the electron diffusion lengths in silicon nanowires are very short compared to those in bulk silicon and are closely related to the NW diameters. Considering that the smaller NWs have a higher density of surface recombination sites, the short diffusion lengths of charge carriers in NWs likely originate from the surface recombination [1]. This hypothesis is still under investigation.

Acknowledgements:

I would like to thank my mentor Dr. Yaping Dan for the support and time he dedicated to me, my PI Prof. Kenneth B. Crozier and his group, Dr. Kathryn Hollar, Prof. John Free, Harvard CNS staff, and Ms. Melanie-Claire Mallison for their assistance. I also acknowledge the National Nanotechnology Infrastructure Network Research Experience for Undergraduates Program and the National Science Foundation for their financial support.

References:

- [1] J. E. Allen, E. R. Hemesath, D. E. Perea, J. L. Lensch-Falk, Z. Y. Li, F. Yin, M. H. Gass, P. Wang, A. L. Bleloch, R. E. Palmer, L. J. Lauhon. "High-resolution detection of Au catalyst atoms in Si nanowires". *Nature Nanotechnology*. Vol 3, 168-173 (2008).

Quantum Well Intermixing on a Hybrid Silicon or Silicon Dioxide Bonded AlGaAs/GaAs/InGaAs Platform

Mohsin Pasha

Electrical Engineering, University of Texas at Austin

NNIN REU Site: Nanotech, University of California, Santa Barbara, CA

NNIN REU Principal Investigator(s): Dr. John Bowers, Electrical Engineering, University of California Santa Barbara

NNIN REU Mentor(s): Jock Bovington (2005 NNIN REU at UW), Physics and E.E., University of California, Santa Barbara

Contact: mip@mail.utexas.edu, bowers@ece.ucsb.edu, jock@ece.ucsb.edu

Abstract:

Quantum well intermixing (QWI) allows one to controllably alter the bandgap in a quantum well heterostructure for use in photonic integrated circuits. QWI has been successfully implemented on various platforms to create higher bandwidth photodetectors, modulators, and tunable lasers. The success of QWI can be measured by the shift in wavelength of a sample's photoluminescence (PL). The focus of this project was to develop a successful QWI process for a hybrid silicon or silicon oxide (Si, SiO_2)-bonded gallium arsenide/indium gallium arsenide (GaAs/InGaAs) laser platform. This low loss Si or $\text{SiO}_x(\text{N}_y)$ waveguide enables the world's longest integrated semiconductor lasers to displace currently used fiber lasers and solid state lasers in terrain mapping LIDAR systems. The first part of this project was to develop a way to measure the sample's PL. The second part of this project was to induce the greatest wavelength shift through impurity free vacancy diffusion (IFVD).

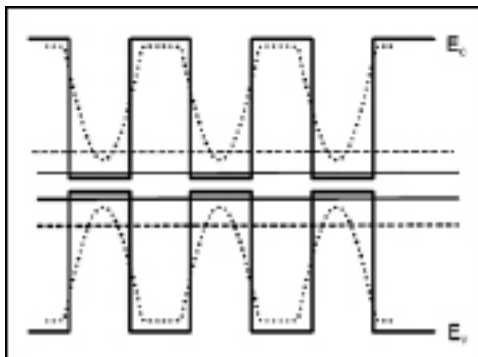


Figure 1: Energy band diagram of quantum wells before and after QWI.

Introduction:

In bulk semiconductor material, electrons and holes have a continuum of available states; however, at the nanoscale of quantum wells, these states become discretized in one dimension. This is a fundamental aspect of a quantum well laser. In this material system, QWI works by creating vacancies in the barriers and the wells. The vacancies then allow for indium from the InGaAs quantum wells to diffuse into the barriers, in exchange, gallium from the GaAs barriers diffuses into the wells. The subsequent disruption in band structure causes a change in wavelength of the sample's PL. The solid lines in Figure 1 indicate the bands of the wells before the intermixing process, and the dotted lines represent the wells after the intermixing process. The solid and dashed lines correspond to the respective discrete states that the carriers can occupy.

QWI can be implemented through three different mechanisms: impurity induced disordering (IID), impurity free vacancy disordering (IFVD), and ion implant enhanced interdiffusion (IIEI). Only the latter two were employed in this study.

IFVD was implemented by depositing a layer of SiO_2 on top of the sample using plasma-enhanced chemical vapor deposition (PECVD). The vacancies in porous SiO_2 then diffused downwards upon a rapid thermal anneal (RTA). IIEI worked by bombarding the sample with an ion, which then physically disrupted the structure, also creating vacancies.

Experimental Procedure:

First in the IIEI experiment, a sample was implanted with P^+ . To prevent outward diffusion the sample was capped with Si_xN_y . It then underwent a RTA for 30 seconds at 900°C .

In the IFVD experiment, another sample had SiO_2 deposited via PECVD. It was then capped with Si_xN_y to prevent any bonding with the carrier wafer and any outdiffusion of material during the RTA. This sample underwent a RTA process at 850°C for 3 minutes.

Figure 2 shows a diagram of the PL setup. A pump laser diode (780 nm) operating at 1.5 mW was already properly aligned. The laser diode was collimated and then focused onto our samples. The sample's PL was focused onto a multimode fiber which was fed into an Ando AQ6315 Optical Spectrum Analyzer controlled via Labview.

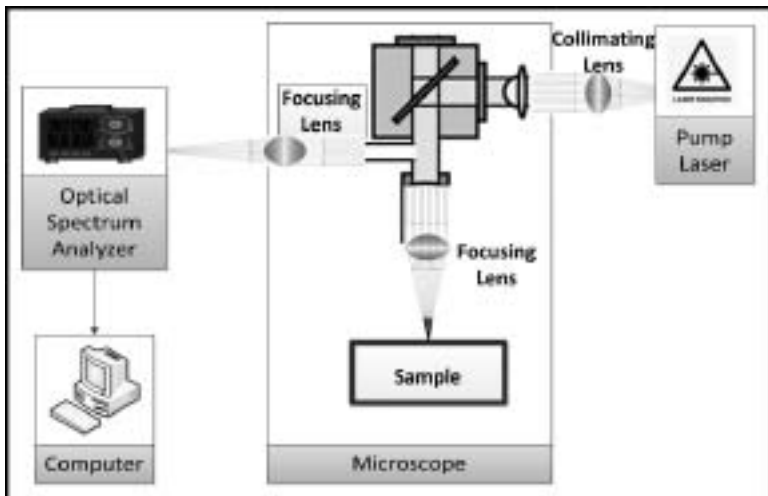


Figure 2: Diagram of PL setup.

Two other lasers, 658 nm at 60 mW and 780 nm at 100 mW, were also added to the system. They are in the process of being optimally aligned.

Results:

The sample that underwent IIEI was visibly damaged by the RTA process—opaque crystalline growths covered the phosphorous implanted regions at the surface of the SiN. Areas masked by the clips securing the sample while implanted were unaffected. Thus, no PL measurements were taken of this sample. Figure 3 shows a cross-sectional SEM of the sample with noticeable cracking and damage at the surface. Figure 4 shows the PL of the unmodified sample and the PL of the IFVD induced sample.

Conclusions:

EDAX was performed on the damaged P⁺ implanted sample to see the chemical composition of the distinct regions. The damage is believed to be due to an out diffusion of aluminum. It was found that this procedure of IIEI was not a feasible method for our material system [1].

The plots in Figure 4 show peaks around 870 nm. This corresponds to the bandgap of a GaAs layer closer to the surface of our device. It is believed that this top layer absorbed all the light and gave off this signal. An etch was performed to remove this layer and it was found that an H₂O: H₂SO₄: H₂O₂, 1:5:1, wet etch for at least 120 seconds would etch through 100 nm of GaAs. As seen in Figure 4, the GaAs peak is markedly diminished compared to the unmodified sample. However, no peak was observed at 1030 nm.

Future Work:

Two higher powered lasers are currently being added into the setup. It is believed that sufficient light from the current 1.5 mW pump lasers is not reaching the sample. Additionally, a larger core (1 mm) multimode fiber could potentially capture a larger signal than the current 65 μ m core.

After testing whether depositing SiO₂ induces any wavelength shift, selectively intermixing certain regions will be attempted. It has been proven in a similar material system that SiNx suppresses any wavelength shift [2].

Acknowledgements:

I would like to thank the NSF, the NNIN REU Program, UC Santa Barbara, my P.I. Dr. John Bowers, my mentor Jock Bovington, John Parker, Members of the Bowers Group, the Blumenthal Group, and the Coldren Group, the staff at the Nanofab, the other NNIN REU interns, and a special thanks to Angela Berenstein.

References:

- [1] Lofgreen, Daniel D., "Investigation of Selective Quantum Well Intermixing in Vertical Cavity Lasers", Electrical and Computer Engineering Department UC Santa Barbara, 73-98, (2004).
- [2] Wang, Chad S., "Short-Cavity DBR Lasers Integrated with High-Speed Electroabsorption Modulators using Quantum Well Intermixing", Electrical and Computer Engineering Department UCSB, 38-61, (2007).

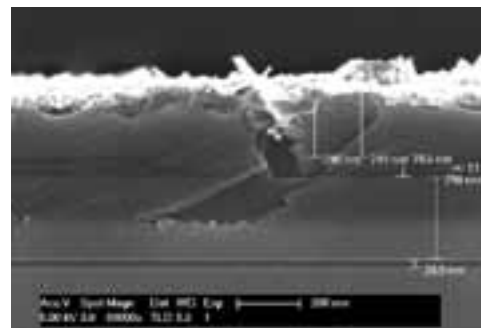


Figure 3: SEM of sample.

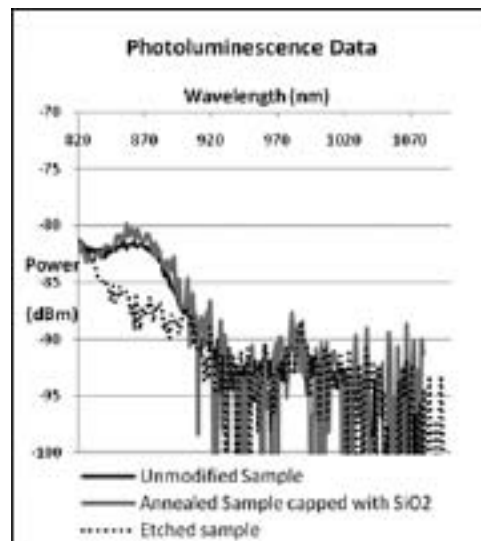


Figure 4: PL data of samples.

Unipolar Resistive Switching in 100 nm² Pt-NiO-Ni-Pt Cells

Matthew T. Hershberger
Physics, Bethel College, Kansas

NNIN iREU Site: Institut Für Bio- Und Nanosysteme (IBN), Forschungszentrum, Jülich, Germany

NNIN iREU Principal Investigator(s): Rainer Bruchhaus, Institut für Festkörperforschung (IFF), Forschungszentrum Jülich;

Professor Rainer Waser, Institut für Festkörperforschung (IFF), Forschungszentrum Jülich
and Electrical Engineering and Information Technology, RWTH Aachen

NNIN iREU Mentor(s): Robert Weng, Institut für Festkörperforschung (IFF), Forschungszentrum Jülich

Contact: matthew.hershberger@yahoo.com, r.bruchhaus@fz-juelich.de, r.weng@fz-juelich.de

NNIN iREU Program

Abstract:

We investigated the effects of a nickel adhesion layer in the resistive switching of nickel oxide (NiO) using platinum electrodes. Resistive switching has applications in making resistive random access memory (RRAM) devices. The nickel adhesion layers tested were five nanometers and ten nanometers thick. We concluded that varying the thickness of the nickel adhesion layer may affect the voltage required for forming.

Introduction:

In the ever continuing quest for Moore's Law and its accomplices, scalability is largely desirable. The dominant form of nonvolatile memory is silicon (Si)-based flash memory, but the low endurance, low write speed, and physical limits in scaling are significant disadvantages [1]. One future candidate to succeed flash memory is RRAM. In this form of memory the 0 and 1 states are represented by different resistive states [2].

There are several types of RRAM including electrochemical metallization, thermochemical memory, and phase change memory, but the exact physical models for these systems is unknown [1]. Each type of RRAM has a mechanism that allows it to be set from a high resistance state (HRS) to a low resistance state (LRS) and reset from the LRS to the HRS. This is achieved by applying a large enough voltage or current to trigger a physical or chemical change resulting in a change in resistance. The resistance state of the cell can be read by applying a small voltage which does not change the cell [2].

The first set operation of a cell is known as forming due to a distinctly higher voltage and current needed. The I-V curves for a form and a reset are shown in Figure 1. The numbers one through four are the set and five through seven are the reset. Note that the current compliance for the forming process is a resistor due to the forming process being faster than the current compliance of the equipment.

The different types of RRAM also may be categorized as bi-polar or uni-polar. In bi-polar switching the set and reset voltages have opposite signs. Uni-polar switching is completed with voltages of the same sign [1]. NiO belongs to the category of uni-polar switching materials. NiO is of particular interest because industry has experience working with Ni and its compounds.

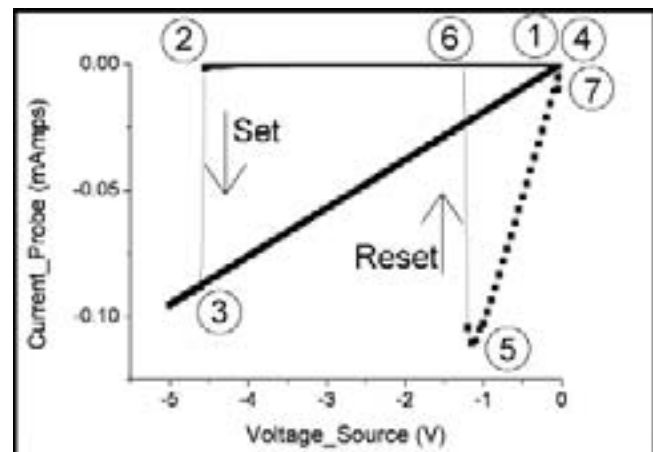


Figure 1: I-V curve of set and reset.

Procedure:

The four inch Si wafer was baked in the oxidation chamber until the silicon dioxide was 400 nm thick. Next, 5 nm of titanium was sputtered for an adhesion layer, and then 30 nm platinum (Pt) was sputtered for the bottom electrode. NanoNex NX2010 imprint resist was spun on at 3000 rpm. A UV imprint stamp was used to form the bottom electrode structures. The imprint resist was etched using a reactive ion beam etch (RIBE) with carbon tetrafluoride until the stamp formation was opened. The Pt was then etched using argon RIBE, leaving behind the bottom pads and electrodes. The imprint resist was removed using oxygen plasma ashing. At this point the wafer was diced into chips using a dicing saw.

Each chip had 25 nm NiO deposited by argon sputtering. A tri-layer electron beam resist of two layers of AllResist

AR-P 617 and one layer of AR-P 679 was used to form a large undercut for the 100 nm structures. Ni was evaporated as an adhesion layer for the 50 nm upper Pt electrode. The final step used MicroChemicals AZ 5214E photoresist and an argon RIBE to remove the NiO from the bottom pads.

We made several chips with varying thicknesses of the Ni adhesion layer. The chip RW9901 had 5 nm of Ni, and the chip RW9902 had 10 nm of Ni. The chip RW9901 had no Ni adhesion layer, and the top electrodes were destroyed during liftoff as were all other chips with no Ni adhesion layer.

Figure 2 shows a scanning electron microscope (SEM) image of a completed cell. The left pad is the bottom pad and the right pad is the top pad. The vertical line going across the bottom pad is the edge of the NiO. The actual cell is at the intersection of the two needles in the middle of the SEM image and is approximately 100 nm by 100 nm. Electrical characterization and switching were done on a Keithley 2611 System Sourcemeter.

Results and Conclusions:

We investigated the effects of the thickness of a nickel adhesion layer in the resistive switching of nickel oxide using platinum electrodes. Since the exact mechanism of resistive switching in NiO is unknown, there was concern that adding a layer of Ni could affect the resistive switching process.

Figure 3 shows the LRS for the chips RW9901 and RW9902 were similar in distribution and shape with a Student's T-Test P-value (STTPV) of 0.09. Figure 4 shows a scatterplot of the voltage and current at the point immediately before forming. Note that the voltage and current for each cell was nearly normal (histograms not shown). Comparing the current of the two chips resulted in an STTPV of 0.32. Comparing the voltage resulted in an STTPV of 0.0008.

We concluded that there may be a difference in the voltage required for forming as a result of the different nickel adhesion layer thicknesses, but more thicknesses would need to be examined.

Acknowledgements:

I would like to thank Professor Rainer Waser, Rainer Bruchhaus, Robert Weng, Marcel Gerst, Tobias Reuter, and the IFF-6 group. All SEM pictures were taken on the IFF Hitachi SEM. Funding was provided by the Forschungszentrum Jülich, the NNIN iREU Program, and the National Science Foundation.

References:

- [1] R. Waser, R. Dittmann, G. Staikov, K. Szot, *Adv. Mater.* 2009, 21, 2632-2663.
- [2] C. Kügeler, R. Weng, H. Schroeder, R. Symanczyk, P. Majewski, K.-D. Ufert, R. Waser, M. Kund, *Thin Solid Films* 2010, 518, 2258-2260.



Figure 2: SEM image of single cell.

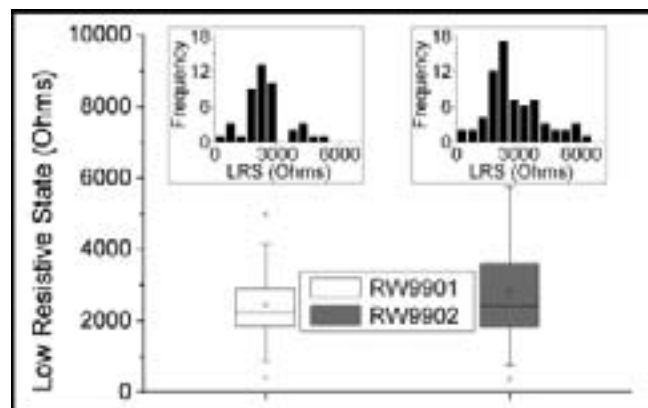


Figure 3: Boxplots of low resistive state by chip with histograms.

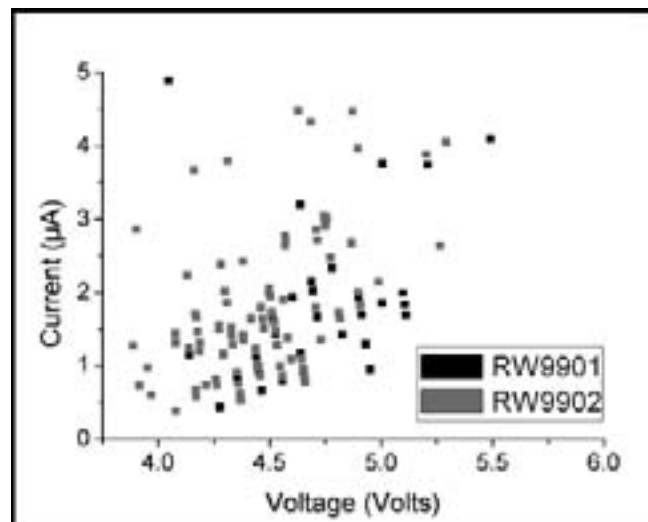


Figure 4: Scatterplot of voltage and current at forming.

Tunneling Electron Microscopy Investigation Strategy for InAs Nanowires

Jacob Alexander Sadie
Electrical Engineering, University of California-Berkeley

NNIN iREU Site: Institut Für Bio- Und Nanosysteme (IBN), Forschungszentrum, Jülich, Germany

NNIN iREU Principal Investigator(s): Hilde Hardtdegen, Institute of Bio and Nanotechnology, Forschungszentrum Jülich

NNIN iREU Mentor(s): Kamil Sladek, Institute of Bio and Nanotechnology, Forschungszentrum Jülich

Contact: jake.sadie@gmail.com, h.hardtdegen@fz-juelich.de, k.sladek@fz-juelich.de

NNIN iREU Program

Abstract:

We report on methods used for characterization of crystal structure in indium arsenide (InAs) nanowires grown by selective area metal organic vapor phase epitaxy (SA-MOVPE) on gallium arsenide (GaAs) substrates. Using selected area electron diffraction (SAED) and fast Fourier transforms (FFTs) of high-resolution transmission electron microscopy (HRTEM) images, we established appropriate means for nanowire (NW) characterization. We applied these new methods to a series of increasingly silicon-doped InAs wires in order to observe the effects of doping on structure. In addition, we discuss a novel method for HRTEM sample preparation.

	Factor 50	Factor 100	Factor 250	Factor 500
2 port p ($10^4 \Omega m$)	35	16	7.6	1.8
4 port p ($10^4 \Omega m$)	16	15	4.4	Not Taken

Table 1: Doping effects on InAs NW resistivity with increasing doping factors.

Introduction:

SA-MOVPE of InAs wires on GaAs substrates yields highly uniform, conductive, and appropriately proportioned NWs for future nanoscale device applications [1]. Our work involved establishing methods for characterizing the crystal structure of our NWs via HRTEM and SAED. In addition to the physical and electrical properties, InAs NWs are receptive to Si doping during growth, and we have observed that increased doping tends to decrease resistivity (Table 1).

Our work continued by investigating the effect doping had on crystal structure in order to potentially establish a correlation between structure on a nanoscale and electrical properties of nanowires.

Growth:

We spun and baked a layer of HSQ onto a GaAs wafer. Next, we spun on an electron beam resist and patterned our wafer with arrays of 50 nm diameter holes at various pitches with electron-beam lithography. After developing the resist, we etched the patterned holes through the HSQ layer, re-exposing the GaAs substrate. Finally, we cleaned the HSQ surface and grew the array of InAs wires by MOVPE.

Nanocrystal Structure:

In III-V nanowires, we see an alternation between wurtzite and zinc-blende (ZB) stacking patterns, whereas bulk growth of III-V materials is typically ZB [2]. The understanding and correlation between crystal structure and electrical transport properties is weak, and to our knowledge, this work is the first attempt to establish a relationship between nanowire doping and crystal structure.

Wurtzite structures stack in a hexagonal close packing pattern, while ZnS crystals follow cubic close packing. The presence of both structures in the wires leads to stacking faults, visible as streaks in HRTEM and SAED. Each structure produces a unique diffraction pattern, and it is critical to understand that the orientation angle of the sample in the tunneling electron microscope (TEM) determines the zone axis, and therefore, the structure we see.

As the angle changes, the zone axis and corresponding diffraction pattern also shift. Convenient relationships exist between low-indexed zone axes of wurtzite and ZnS structure (Table 2) and these relationships are useful for identifying and anticipating crystal structure.

HRTEM Sample Preparation:

Previously, we removed our wires from the substrate via

	0 °	20 °	30 °	40 °	60 °
Wurtzite	[1 0 0]	[3 1 0]	[2 1 0]	[3 2 0]	[1 1 0]
Zinc-blende	[0 1 1]	[-1 3 2]	[-1 2 1]	[-2 3 1]	[-1 1 0]

Table 2: Wurtzite and zinc-blende zone axis relationships.

mechanical force, and placed them onto TEM grids. The result was often large mounds of wires and no selectivity. We began investigating focused ion beam (FIB) methods to create ultra-thin slices of wires. We coated our nanowire arrays with carbon and tungsten. These two materials are highly conductive, but have much different atomic weights, resulting in high contrast in TEM images. After coating, we sliced the samples with FIB in order to isolate and test a small strip of nanowires. This process included the substrate, which was beneficial for confirming the zone axis and orientation angle.

HRTEM and SAED Results:

FFTs of HRTEM images produce reciprocal space images that aid in identification of crystal structure when compared to diffraction pattern simulations for perfect crystal structures, while SAED images are direct diffraction patterns of the sample. FFT and SAED images focus on much different areas, approximately $0.001 \mu\text{m}^2$ and $0.031 \mu\text{m}^2$, respectively, in our samples. Therefore, FFT is useful for the analysis of structural transitions while SAED is useful for predominant structural characterization. Stacking faults become evident via streaking between FFT or SAED spots.

Our first investigation involved confirming the rotational effects on the diffraction patterns in our wires. We selected a wire with unknown crystal structure (stacking faults confirmed with HRTEM), rotated it 0° , 20° , 30° , and 40° from a reference angle, and we obtained an SAED image at each rotation. When comparing diffraction pattern simulations between wurtzite and ZnS structures, we expected that the 30° rotation of a sample with stacking faults would yield a perfect (no streaks) structure in SAED, and we confirmed this, as seen in Figure 1.

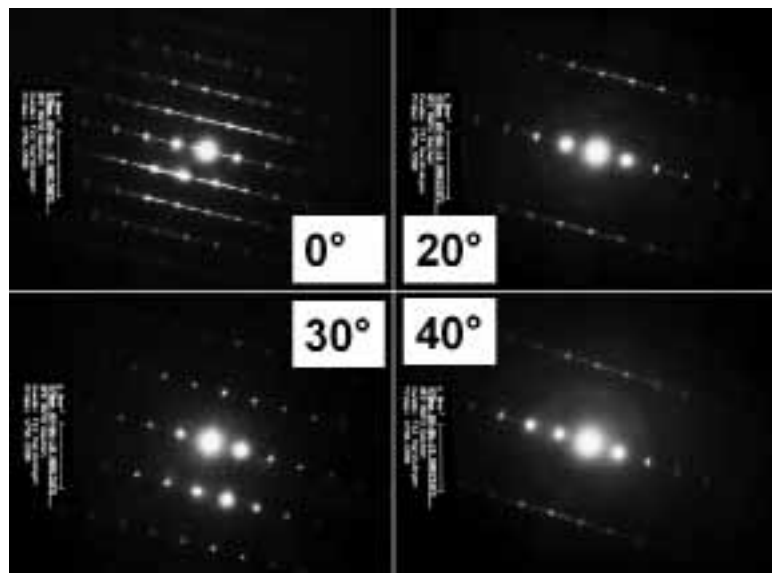


Figure 1: SAED images of rotated sample.
Stacking faults (streaks) not visible in 30° rotation.

We then performed a detailed analysis of the diffraction patterns in comparison to wurtzite and ZB simulated patterns. Using ratios representing the distances and angles between particular diffraction spots in the SAED images, we compared these to the ratios seen in the corresponding spots for both wurtzite and ZB simulations. This method allowed us to confidently characterize the predominant crystal structure for this sample was wurtzite.

We next began a new investigation into the effect of doping on crystal structure. Taking four samples of InAs nanowires grown on GaAs (111)B substrates doped at increasing factors, we obtained HRTEM and SAED images of each of the wires. Our first goal was to confirm the zone axes, and therefore the crystal diffraction patterns, we expected to see in the FFTs and SAED. Then, we compared the structures of the wires as doping increased. Our undoped wire showed predominant wurtzite growth, but as the doping factor increased, we began observing more ZB structure in the FFT images. Therefore, we observed doping affecting both electrical properties and structure.

Conclusions:

Our work confirmed the simulated diffraction patterns of both wurtzite and zinc-blende crystal structures via SAED and FFTs of HRTEM images. We established the importance of angle and zone axis when analyzing the samples in the TEM. Finally, we were able to use our characterization method to confidently identify a trend in structural variation due to doping. A continuation of this work may lead to important conclusions regarding doping, structure, and electrical properties of nanowires.

Acknowledgements:

I acknowledge Kamil Sladek, Hilde Hardtdegen, and Martina von der Ahe of Forschungszentrum Jülich, and Thomas Weirich from Aachen University for their many helpful discussions. Thanks to the National Science Foundation and the National Nanotechnology Infrastructure Network International Research Experience for Undergraduates (NNIN iREU) Program for funding.

References:

- [1] M. Akabori, K. Sladek, H. Hardtdegen, Th. Shäpers, and D. Grützmacher, *Jour. Crys. Growth* 311, 3813, 2009.
- [2] F. Glas, J.-C. Harmand, and G. Patriarche, *Phys. Rev. Letters* 99, 14601, 2007.

Domain Wall Track in a Praseodymium Strontium Manganite Oxide Nanobridge

Meng Shi

Physics, Case Western Reserve University

NNIN REU Site: Penn State Nanofabrication Laboratory, The Pennsylvania State University, State College, PA

NNIN REU Principal Investigator(s): Dr. Qi Li, Department of Physics, The Pennsylvania State University

NNIN REU Mentor(s): Peng Xu, Department of Physics, The Pennsylvania State University

Contact: mxs420@case.edu, qil1@psu.edu, pux1@psu.edu

Abstract and Introduction:

Research into spintronics has led to many discoveries that are unexpected and exotic. Some of these discoveries have already been implemented as electronic devices, most prominently as computer hard drives, read heads, and magnetic random access memories, yet there is still much more to be uncovered and understood [1,2]. The anomalous magnetoresistance of magnetic domain walls discovered in strained manganite films cannot yet be fully explained and it was our goal to discover the nature of this phenomenon [3].

This study looked into the fabrication and testing of constricted nanobridges made of manganite thin films that exhibit low-field magnetoresistance [4]. Two different methods of fabrication were implemented. The first method used electron beam lithography (EBL) and the second used focused ion beam (FIB) milling. The nanobridges were made in varying dimensions, with the goal of restricting the number of magnetic domains present so that its effects dominated the behavior of the devices.

Experimental Procedure:

Fabrication began with a lanthanum aluminum oxide (LAO) substrate with 50 nm of praseodymium strontium manganite oxide (PSMO) deposited using pulsed laser deposition [5]. We then evaporated 200 nm of gold (Au) and used standard photolithography techniques with a negative photoresist to prepare the sample for ion milling. The FIB removed the Au and manganite film where the photoresist was not protecting it. In later samples, the design was changed so that the fabrication of the bridge would not require a second, more difficult removal of the Au. In the revised design, the manganite oxide film underwent standard photolithography and FIB to leave a single long strip. Then, through use of the negative photoresist, Au lines were evaporated perpendicular to the film strip (Figure 1).

To make the nanobridge, two trenches were etched in line with each other, leaving a gap of ~ 100 nm in between the end of one trench and the beginning of the other. The gap would then bridge the two sides of the film/Au. In etching

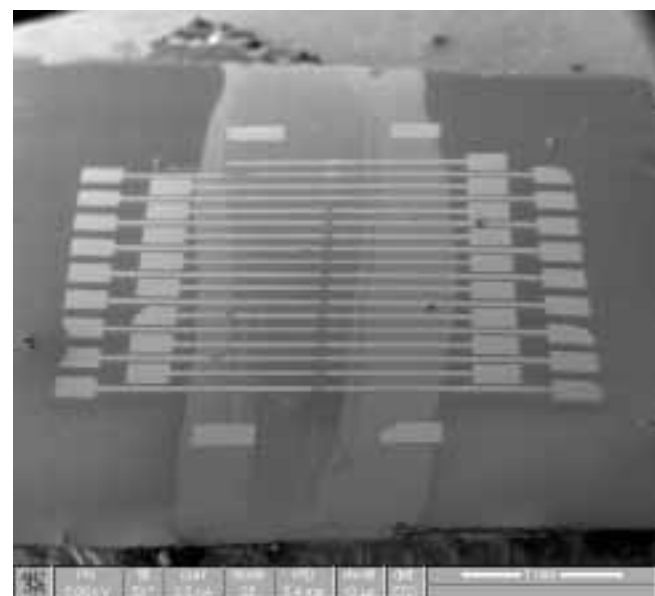


Figure 1: SEM image of revised pattern with gold leads across manganite film.

the trenches, two different methods were explored. In both cases the trenches were etched parallel to the Au leads and perpendicular to the film strip. The first technique used EBL in conjunction with reactive ion etching and the second used FIB. The beam used in the EBL had a minimum width of ~ 30 nm, while the FIB beam had a minimum of ~ 7 nm.

Results and Conclusions:

Fabrication using EBL and FIB each presented unique advantages and disadvantages. In EBL, sample viewing was made possible through the use of a scanning electron microscope (SEM). However, looking directly at the sample would damage the photoresist, and therefore we could only view the corners of the sample and use its dimensions to calculate the correct location for the bridges to be etched. In this method, it was important to make sure the measurements of the device dimensions were accurate so that the bridges were etched in between the Au leads and on the film.

Due to computer integration, it was easy to create multiple bridges on a single device. In contrast, while performing FIB, we could use the SEM to directly view the location where the nanobridge needed to be placed; however, there was a minimum magnification requirement that forced us to make multiple runs to create a single bridge. It was also necessary to make each bridge individually.

The most important factor in the fabrication process was how short the bridge length was, or how narrow the etched trenches could be made. Using the smallest beam width in EBL, the narrowest trench we made was ~ 100 nm. However, with the FIB, we were able to obtain a trench width of ~ 40 nm (Figure 2).

This one benefit alone made focused ion beam milling the preferred fabrication method. However, the FIB process was also superior to that of EBL because it was faster and less expensive.

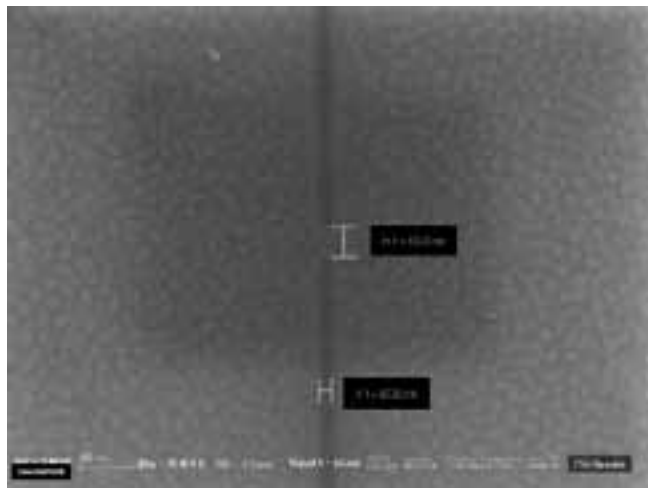


Figure 2: Field emitting SEM of nanobridge fabricated using focused ion beam milling.

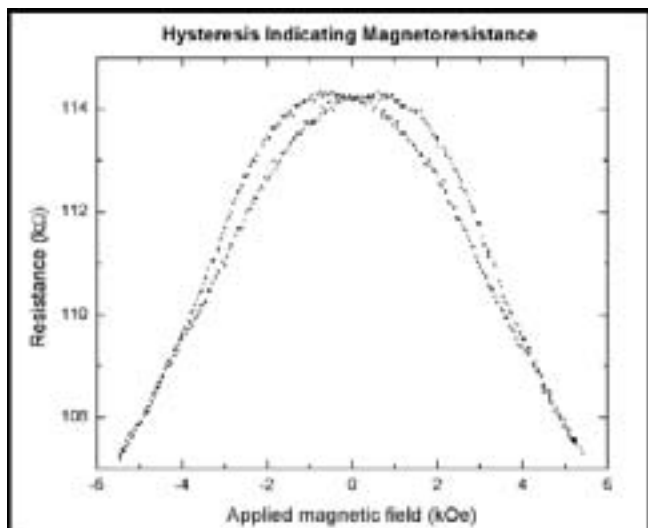


Figure 3: Evidence of magnetoresistance with noticeable hysteresis.

In testing a device made using the FIB, we were able to find signs of magnetoresistance (Figure 3). This was important because it meant the process was effective in limiting the number of magnetic domains present in the bridge, exposing the phenomena believed to create the low-field magnetoresistance to future measurements.

We concluded that the focused ion beam milling technique was better than the electron beam lithography process for our purposes of fabricating a nanobridge in manganite film. The combined benefits of shorter bridge length, faster fabrication, and lower cost made it the superior choice.

Future Work:

In the future, we will deposit a thinner layer of PSMO film of higher quality, narrowing the 50 nm thickness to ~ 12 nm. We hope to make the trench even narrower; having a thinner film will aid in this endeavor. In the new setup, a metal strip connecting the sides of the bridge to the gold leads should help prevent the measurement of resistance in the film outside the bridge.

And most importantly, in the future we will examine the nature of the anomalously large low-field magnetoresistance.

Acknowledgements:

I would like to acknowledge Professor Qi Li for hosting me this summer, as well as my mentor Peng Xu for his help throughout the summer, Greg Harkay for growing the film and the rest of the lab for their support. I would also like to thank the NNIN for the Research Experience for Undergraduate Program, the NSF for providing the funds for this research, and the Penn State MRI for providing the equipment, training, and personnel that helped realize these goals. Special thanks to Kathy Gehoski, Yan Tang, and Trevor Clark for their assistance. Also, thanks to Ronald D. Redwing and Leeanna R. Horner for coordinating the program at Penn State.

References:

- [1] Wolf, S. A., Awschalom, D. D., Buhrman, R.A., Daughton, J. M., von Molnar, S., Roukes, M.L., Chtchelkanova, A.Y., and Treger, D.M., "Spintronics: A Spin-Based Electronics Vision for the Future", *Science*, 294, 2001.
- [2] Das Sarma, S., Fabian, J., Hu, X., and Zutic, I., "Spin Electronics and Spin Computation, Solid State Community", 119, 2001.
- [3] Wang, H. S., Li, Q., Liu, K., Chien, C. L., "Low-field magnetoresistance anisotropy in ultrathin PSMO films grown on different substrates", *Applied Physics Letters*, 74, 1999.
- [4] Hu, Y., Li, Q., "Strain-Induced Magneto-Transport Properties of Manganite Thin Films", PhD Thesis Paper, Penn State University.
- [5] Chrisey, D. B., and Hubler G. K., "Pulsed Laser Deposition of Thin Films", Wiley-Interscience, New York, 1994.

Transport Properties of InAs Nanowires for Applications in Quantum Information Processing

Hamsa Sridhar

Physics and Mathematics, Harvard College

NNIN iREU Site: Institut Für Bio- Und Nanosysteme (IBN), Forschungszentrum, Jülich, Germany

NNIN iREU Principal Investigator(s): Prof. Thomas Schäpers, Institut für Bio- und Nanosysteme (IBN-1), Forschungszentrum

NNIN iREU Mentor(s): Yusuf Gunel, Institut für Bio- und Nanosysteme (IBN-1), Forschungszentrum Jülich

Contact: hsridhar@fas.harvard.edu, th.schaepers@fz-juelich.de, y.gunel@fz-juelich.de

NNIN iREU Program

Introduction:

Due to their high electron mobility, indium arsenide nanowires (InAs NWs) show promise for high-performance transistors and nanoelectronics. However, their transport properties are still not fully understood. The electron mobility of individual InAs NWs have been reported to be much lower than in bulk, suggesting strong electron scattering from the surface or from ionized impurities. Thus, protecting the surface may enhance transport properties.

In this work, NW transistors were fabricated using $\langle 110 \rangle$ InAs NWs. Room temperature measurements of top / back gate control and IV characteristics were performed and analyzed. Furthermore, the formation of quantum dots in InAs was investigated at low temperature.

Fabrication:

Undoped InAs NWs grown through metal organic vapor phase epitaxy (MOVPE) in the $\langle 110 \rangle$ crystal direction were dispersed on 25 fields of a degenerately n-doped silicon (Si) substrate, with a 100 nm layer of silicon nitride (SiN) above to act as a back gate. Scanning electron microscope (SEM) images of each field were taken and imported into AutoCAD to design ohmic contacts for selected NWs. Four single-strand isolated NWs were selected in each field—long, thin NWs were preferred. The chosen NWs had an average length of 2.3 μm and an average diameter of 140 nm. Where possible, four ohmic contacts were designed for each NW: the outer contacts were used as current source and drain, while the inner contacts were used to measure the voltage drop, avoiding effects of contact resistance.

Next, EBL and metal evaporation were performed to write the ohmic contacts. A 40 second Ar⁺ ion etch was used to remove any native oxide that had formed on the NWs.

Next, a 50 nm layer of high- κ dielectric lanthanum aluminate (LaLuO₃) was spun onto the chip. A wet etch was performed to remove the dielectric above the contact pads, allowing direct ohmic contact with the NWs. Then, top gates were designed on AutoCAD for selected devices. Again, electron beam lithography and metallization were performed to write the top gates. After processing, the top gates were typically measured to be 170 nm wide and 110 nm apart. Finally, the chip was diced into 25 fields. Each chip was mounted onto a chip carrier and wire-bonded for low-temperature measurements in the cryostat.

A second set of NWs was prepared with the same processing, using thinner NWs (typical diameter of 40 nm). However, due to time constraints, only ohmic contacts were written for these devices.

Measurements and Analysis:

After writing ohmic contacts, the four-probe and two-probe resistances of the NWs were measured at room temperature. The contact resistances were found to be negligible in comparison to the resistance of the NWs. Next, the back gate control was measured in order to calculate the threshold voltages and transconductances of each NW. The length and diameter of each wire was verified using SEM pictures.

The back gate capacitance is seen in Equation 1, where L_{SD} is the wire length between the ohmic contacts, t_{ox} is the thickness of the substrate oxide (back gate), and d_{NW} is the diameter of the NW. The three-dimensional and two-dimensional electron concentrations are shown in Equation 2 and 3, respectively, where V_{TH} is the threshold voltage. Finally, the field effect mobilities were calculated using Equation 4, where g_m is the transconductance and V_{SD} is the source-drain voltage for which this value was measured.

$$C_{BG} = \frac{2\pi\epsilon_0\epsilon L_{SD}}{\ln\left(\left(2t_{ox}+d_{NW}+2\sqrt{t_{ox}^2+t_{ox}d_{NW}}\right)/d_{NW}\right)}$$

Equation 1

$$n_{3D} = \frac{C_{BG}V_{TH}}{eL_{SD}\pi(d_{NW}/2)^2}$$

Equation 2

$$n_{2D} = \frac{n_{3D}d_{NW}}{4}$$

Equation 3

$$\mu_{FE} = \frac{g_m L_{SD}^2}{C_{BG}V_{SD}}$$

Equation 4

After the dielectric was deposited and the top gates were written, these values were measured again. Analogous formulae were used for calculating the top gate capacitance and resulting parameters.

The two-probe resistance of the NWs averaged $1.3\text{ M}\Omega$ before the deposition of the dielectric, but was reduced to an average of $0.29\text{ M}\Omega$ afterwards (see Figure 2). Consequently, the threshold voltages were also found to be lower, resulting in increased electron concentration and increased field effect mobility in the wires (see Figure 3). This suggests that the presence of the dielectric enhances strong surface transport states and that the transport in the NWs resembles that of a two-dimensional electron gas (2-DEG). Moreover, no correlation was found between wire geometry, typically parameterized by length divided by cross-sectional area, and wire resistance. This suggests that the wire's complex crystal structure, which alternates randomly between wurtzite and zincblende, plays a stronger role in determining the resistance of the NWs than the geometry itself.

Next, the device with the best top gate control was selected for low-temperature measurements. The hysteresis of the top gates was verified to be low, and the two most symmetric and adjacent top gates were chosen for quantum dot measurements at approximately 2 Kelvin.

Applying a gate voltage on adjacent top gates formed a double energy barrier, between which quantum confinement of electrons was realized. By fixing the gate bias on one top gate and sweeping the other, the energy barrier was dynamically modified. Current through the wire (electrons escaping the quantum dot) was then measured as Coulomb peaks (see Figure 4). These measurements prove the successful formation of a quantum dot in InAs NWs.

Conclusions:

The transport properties of InAs NWs were investigated at both room and low temperatures. The deposition of high- κ dielectric was found to induce strong surface states, enhancing electron mobility. Furthermore, a quantum dot was successfully formed in InAs.

Future Study:

There was no correlation found between wire geometry and wire resistance, suggesting the need to further study the crystal structure of these wires using TEM analysis. Additionally, measurements on the second prepared sample will yield more information on the quantum confinement regime (diameter $< 80\text{ nm}$).

Acknowledgments:

I would like to thank NSF, NNIN iREU Program, and Forschungszentrum, Jülich, for funding and providing facilities for conducting this research. Furthermore, I would like to thank Prof. Thomas Schäpers and Yusuf Gunel for including me in their research and guiding me through this work.

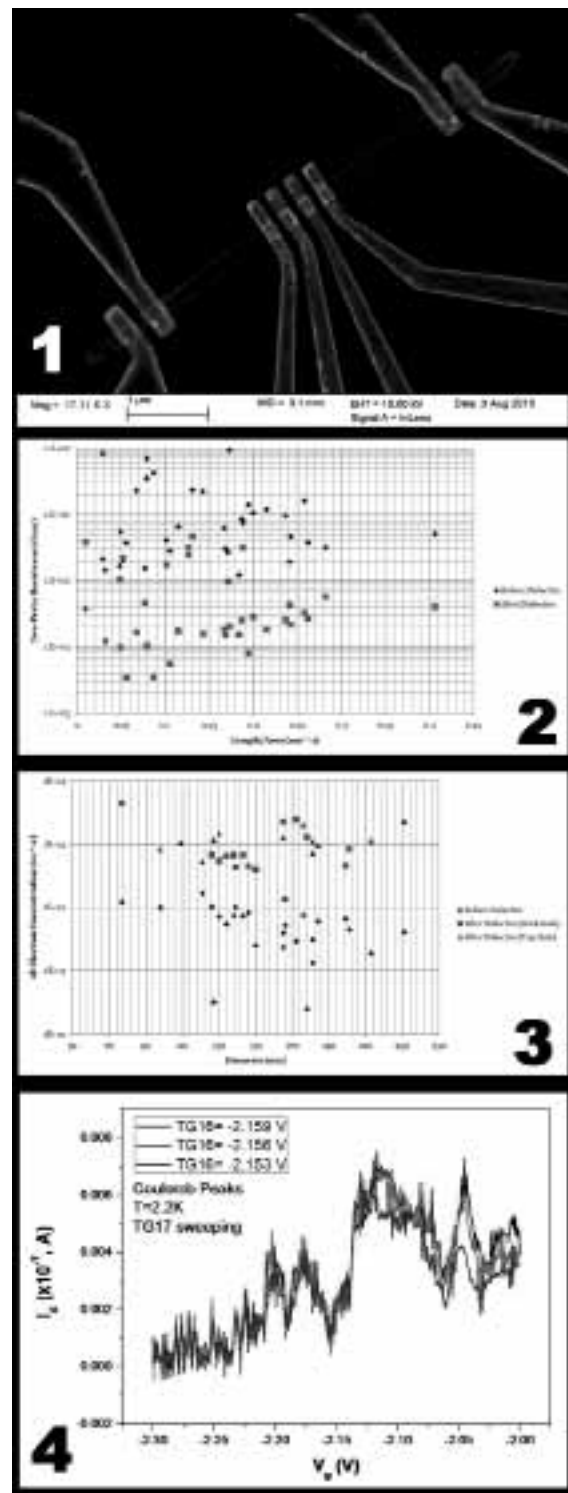


Figure 1, top: SEM of a typical NW transistor is shown with four ohmic contacts and four top gates.

Figure 2, upper middle: The 2-probe resistances of the NWs before (◆) and after (■) the deposition of the dielectric are compared.

Figure 3, lower middle: The 2D electron concentration in the NWs is calculated before dep. of the dielectric using the back gates (◆), and after dep. using both the back gates (■) and the top gates (▲).

Figure 4, bottom: One top gate voltage is held fixed while the other is swept. Coulomb peaks (nonzero current) can be observed at specific values of gate bias.

Characterization of Mercury and Copper Capped DMBP Monolayers

Narahi J. Alvarez

Chemical Engineering Department, University of Puerto Rico-Mayaguez Campus

NNIN REU Site: Howard Nanoscale Science and Engineering Facility, Howard University, Washington, DC

NNIN REU Principal Investigator(s): Dr. James Mitchell, Chemical Engineering, Howard University

NNIN REU Mentor(s): Dr. Tina Brower-Thomas, Chemical Engineering, Howard University

Contact: narahi.alvarez@gmail.com, jwinfieldm@yahoo.com, tina.browerthomas@howard.edu

Abstract and Introduction:

One bottom-up nanotechnology approach is self-assembly. Molecular self-assembly is a process by which atoms, molecules or groups of molecules arrange themselves spontaneously into regular patterns without outside interventions. Phenyl thiols are aromatic compounds that easily react with gold (Au), and have an electron flow through the π -system.

We formed a monolayer of 4,4'-dimercaptobiphenyl dithiol (DMBP) on an Au <111> substrate via self-assembly. We characterized the monolayer by ellipsometry and utilizing two surface probe microscopy (SPM) techniques including atomic force microscopy (AFM) and scanning tunneling microscopy (STM).

The DMBP monolayers were further reacted with solutions of either copper (Cu^{+2}) or mercury (Hg^{+2}) via an oxidation-reduction reaction resulting in either DMBP- Cu^{+1} or DMBP- Hg^{+1} to form a metal-capped monolayer. We examined the capped monolayers with SPM, and we also prepared a nanograft of DMBP in decanethiol in preparation for STM experiments. The expectation was that electrons in DMBP would flow through the π -systems of phenyl groups, the d orbitals of the terminating sulfur, and finally through the d orbitals of either Cu or Hg.

Objectives:

Our goals included; characterizing the monolayer surface using ellipsometry and SPM, determine if the redox behavior of Cu- and Hg- capped DMBP will affect the resistance of the monolayer using a probe station experiment of patterned substrates, and STM measurements of the n-decanethiol nanografted monolayer.

Experimental Procedure:

All glassware was cleaned with piranha solution. The Au substrates were cleaned by hydrogen flame annealing. This method also provided large grain terraces of Au. We heated the quartz and then swept back and forth on the Au substrate at a frequency of 1 Hz for 30 to 60 seconds, while keeping the flame tip at a 30° angle with respect to the Au surface.

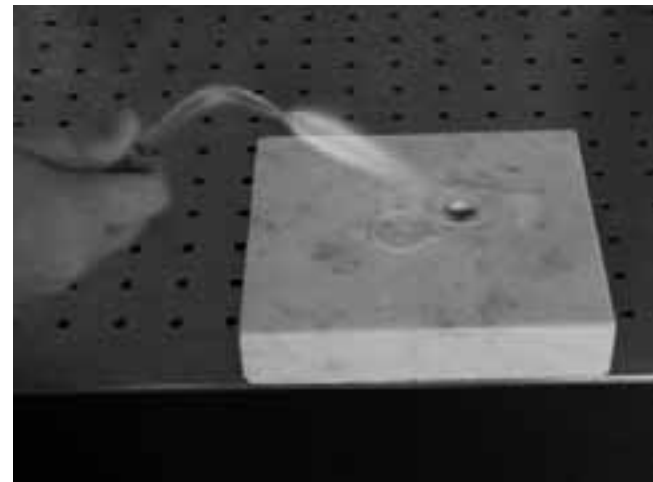


Figure 1: Hydrogen flame annealing.

With this procedure, we observed the desired small flame spot and dim orange colour on the Au substrate. In Figure 1, we see that this method assisted in cleaning the Au substrate. After flame annealing, the optical constants of the Au <111> were obtained by ellipsometry. A monolayer of DMBP was prepared via self-assembly by submerging a clean Au <111> substrate in a 1 μm solution

of DMBP under nitrogen (Figure 2). After forming a monolayer of DMBP, a two hour reaction, we obtained the optical constants associated with the monolayer.

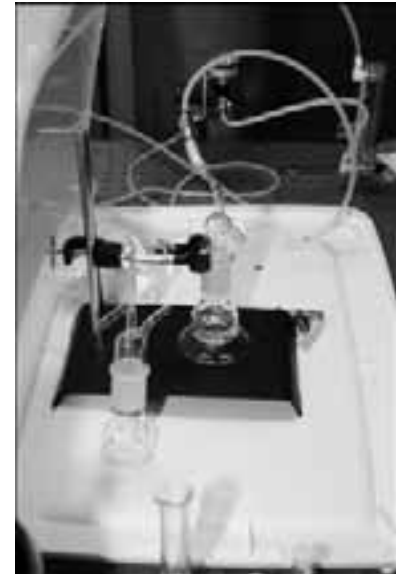


Figure 2: Monolayer apparatus.

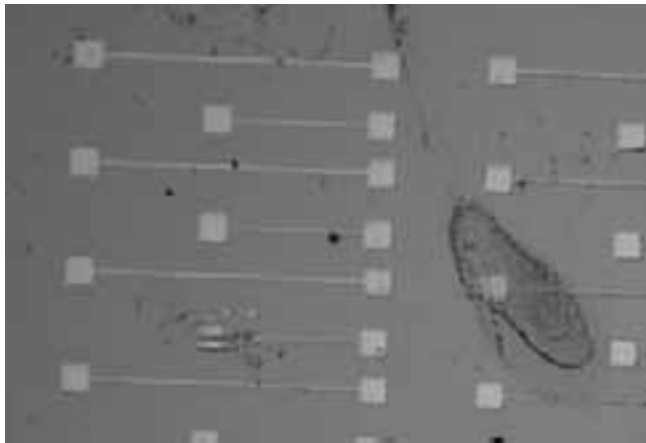


Figure 3: Photoresist pattern created by photolithography.

Given the optical constants and published refractive index, we were able to use a computational model to obtain the thickness of the monolayer. This procedure was repeated for three different areas on each substrate, and we reported the average thickness. Also, we created a photoresist pattern (Figure 3) by photolithography for the probe station experiment.

A nanografting technique was used to prepare samples for STM measurements. To nanograft, we zoomed into a $2\text{ }\mu\text{m} \times 2\text{ }\mu\text{m}$ area, which was relatively flat with a very small force. Then, we increased the force on the AFM probe and swept three times. Finally, we returned to low force, zoomed out and imaged the shaved area. If a hole was created by nanografting, it was back-filled with the molecule to be investigated, because the small area of molecule was an ideal to measure the resistance behavior.

Results:

The average thickness of the monolayer samples was 0.9 nm. We compared our results with the 1.06 nm thickness obtained by ChemDraw 3D. The average thickness of the monolayer measured by ellipsometry was consistent with the thickness of DMBP that was associated a 19° tilt with the surface normal, thus accounting for the difference in height between the model height of DMBP and the height measured by ellipsometry. Further the measurement was consistent with previous data of DMBP monolayer.

AFM and STM confirmed the surface order and provided a visual picture of local features. We compared the length of grain terraces of Au $<111>$ with and without flame annealing. Figure 4 shows that Au $<111>$ with flame annealing produces larger grain terraces. Also, the image of Au $<111>$ with flame annealing shows contamination. This contamination could be caused by not cleaning the quartz properly or by the condensation produced by the hydrogen flame. Later monolayers were prepared on fresh Au $<111>$ samples which were stored under nitrogen. Unfortunately, the STM was not working properly, and for this reason we could not complete the part of nanografting.

Future Work:

Run the probe station experiment and STM measurements of n-decanethiol nanografted monolayers to determine if there is a difference in resistance between Cu⁺¹ and Hg⁺¹ capped DMBP monolayer.

Conclusion:

We prepared DMBP and DMBP Cu- and Hg- capped monolayers on Au $<111>$ substrates. The average thickness of the monolayer measured by ellipsometry was consistent with the thickness of DMBP monolayer associated with a 19° tilt angle with respect to the surface normal, as reported in previous experiments.

Also, we characterized Au $<111>$, flame annealed Au $<111>$, and monolayers of DMBP, and Cu and Hg capped DMBP surfaces using contact mode AFM, contact mode AFM in liquid, and STM. By these methods we observed that flame annealing produces larger grain terraces of gold. We also discovered contamination from flame annealing. We used contact mode AFM for nanografting DMBP in a decanethiol matrix.

Acknowledgements:

I would like to thank my mentor, Dr. Tina Brower-Thomas, for guiding me through this research, my PI, Dr. James Mitchell, and all the Howard Nanoscale Science and Engineering Facility staff. Also, the Nanotechnology Infrastructure Network Research for Undergraduates Program, and the National Science Foundation for funding.

References:

- [1] Brower TL, Garno JC, Ulman A, Gang-yu L, Yan C, Golzhauser A, Grunze M; Self-assembled multilayers of 4,4'-dimercaptobiphenyl formed by Cu(II)-Catalyzed Oxidation.
- [2] Reed MA, Tour JM; Computer with molecules, (2000) Sci Am June:68.
- [3] Tour JA, Jones II L, Pearson DL, Lamba JS, Burgin TP, Whitesides GM, Allara DL, Parikh AN, Atre SV; Self-assembled monolayers and multilayers of conjugated thiols, •• Dithiols, and Thioacetyl-containing adsorbates.

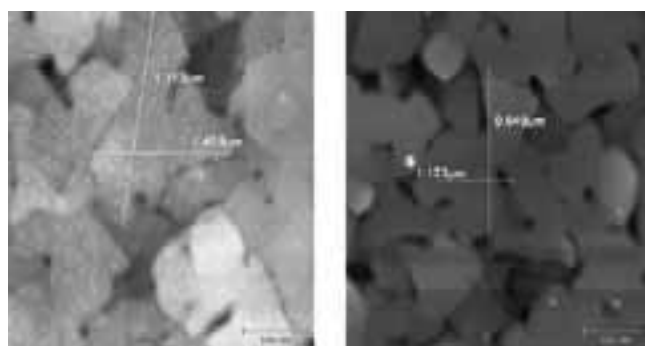


Figure 4: Hydrogen flame annealed Au $<111>$ and non flame annealed Au $<111>$.

Process Development for Writing Sub-100 nm Linewidths using a Scanning Electron Microscope

Hilton H. Augustine, III
Electrical Engineering, Harvard University

NNIN REU Site: Howard Nanoscale Science and Engineering Facility (HNF), Howard University, Washington, DC

NNIN REU Principal Investigator(s): Dr. Gary L. Harris, Electrical Engineering, Howard University

NNIN REU Mentor(s): Mr. James A. Griffin, HNF Lab Manager, Howard University

Contact: hilton.h.augustine@college.harvard.edu, gharris@msrce.howard.edu, jagriffin@howard.edu

Abstract:

Lithography is a process whereby a polymer resist is selectively exposed to some form of radiant energy such as UV light or, in our case, a concentrated beam of electrons, in order to create or transfer patterns. Although photolithography has a higher throughput, electron-beam lithography (EBL) can most reliably produce linewidths under 30 nm. To circumvent the restrictive costs associated with dedicated EBL systems, an existing JEOL 6360-LV scanning electron microscope (SEM) was paired with a RAITH ELPHY lithography system. The goal was to explore the boundaries of this machine and determine the minimum linewidths that could be written with this setup. A diluted solution of 950,000 MW polymethylmethacrylate (PMMA), when spun at 3000 rpm, created a 56 nm thick resist layer on a silicon wafer. An acceleration voltage of 30 kV and a working distance of 10 mm were kept constant while the beam spot size was varied between 10 and 50 (equivalent to a beam current range of 0.19 pA to 500 pA) and the dosage was varied from 90 μ As/cm to 9000 μ As/cm. A minimum linewidth of 100 nm was obtained, and after evaporating a 10 nm layer of chrome onto the sample and performing liftoff, metalized lines were measured to be 120 nm, with the discrepancy being due to chrome buildup along the non-vertical resist sidewalls and non-uniform liftoff.

Introduction:

Electron beam lithography (EBL) is an important technique in microelectronic fabrication because an electron beam's resolving power is not limited by the wavelengths of light. For this reason, EBL is essential in creating nanometer-scale features such as the gates in transistors. EBL, however, is a time-consuming serial process, and EBL systems are extremely expensive. The system utilized for this project was a stand-alone JEOL JSM-6360LV SEM attached to a Scanservice 890 beam blanker and a RAITH ELPHY

Quantum nanolithography system. The cost of this system is significantly lower than that of a dedicated e-beam writing system and puts it at cost parity with UV systems, which makes this an attractive solution for university labs.

The objective of this work was to characterize this system and determine the minimum linewidth possible using its setup.

Experimental Procedure:

The first step was e-beam resist characterization. The initial resist was a MicroChem 950 polymethylmethacrylate (PMMA) solution with 8% solids in anisole. The resist was diluted to create 4% and 2% solutions and characterized for thickness versus spin speed (Figure 1). The 2% solution yielded 56 nm at 3000 rpm and was the standard resist for the project. Silicon wafers were cut into 1 cm^2 pieces using a diamond-tip cutting blade. Samples were then washed using soap and water, followed by methanol and acetone rinses to clear the surface of debris. PMMA resist was spun on and baked on a hot plate at 180°C for 60 seconds.

After baking, a sample was inserted into the SEM and brought into high focus, then the beam current was set and the sample was exposed with patterns generated by the RAITH ELPHY Quantum software. Testing was system-

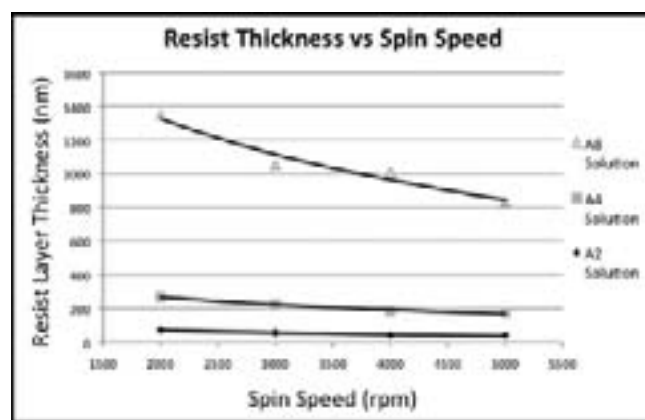


Figure 1: Plot of resist thickness vs. spin speed for A8, A4, and A2 PMMA solutions.

atically performed over a wide range of parameters: SEM spot size (10-50), SEM aperture (20-30 μm), beam current (0.2-500 pA) and line dose (90-9000 pAs/cm). The acceleration voltage was kept constant at 30kV.

After exposure, the samples were developed in a 1:3 methyl isobutyl ketone (MIBK) to isopropyl alcohol (IPA) solution for 90 seconds. The linewidths were measured using atomic force microscopy (AFM), after which, a 10 nm layer of chromium was evaporated onto the sample. After liftoff with *N*-methylpyrrolidone (NMP), linewidths were measured using SEM.

Results and Conclusions:

Given that acceleration voltage was kept constant, the experiment confirmed that the most important parameter affecting line resolution was dosage, or quantifiable amount of energy received during exposure. The best results were achieved with an acceleration voltage of 30 kV, a spot size of 20, a beam current of 0.5 pA, and a dosage of 1800 pAs/cm. A minimum linewidth of approximately 100 nm in PMMA was observed by AFM, however after metallization and liftoff, SEM imaging revealed linewidths of just over 120 nm (Figure 2). This discrepancy is a result of non-vertical sidewalls (Figure 3). The chromium evaporated into the V-shaped trench formed a contiguous layer, which tore unevenly during lift-off, resulting in larger, jagged lines (Figure 4).

The second issue resulted from the fact that linewidths measured at the top of the trench were larger than at the bottom. Since AFM and SEM techniques image from the top down, the resulting measurements were greater than the actual lines' widths.

In the future, to improve liftoff and create smaller metalized lines, a bi-layer resist technique could be used with an overhanging layer of PMMA on top of a co-polymer resist.

Acknowledgments:

Dr. Gary L. Harris, Principal Investigator; Mr. James A. Griffin, Mentor; Ms. Adaku Ochia, Graduate Student; National Science Foundation; National Nanotechnology Infrastructure Network Research Experience for Undergraduates (NNIN REU) Program; Howard Nanoscale Science and Engineering Facility (HNF) Staff.

References:

- [1] E. Chen, J. Deng, Y. Lu, S. Shepard, J. Tsakirgis, L. Xie, "E-Beam Lithography with 10nm-linewidth on," Marcus Lab, Harvard University, April 2005. [Slideshow]. Available: http://marcuslab.harvard.edu/how_to/raith_10nm_lines.pdf. [Accessed: Jul 1 2010].

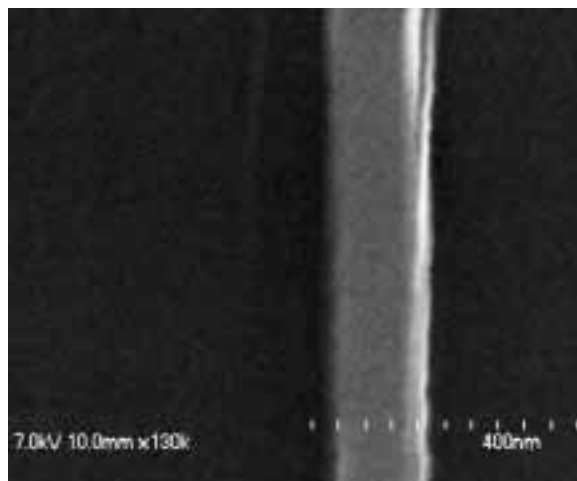


Figure 2: SEM image of an approximately 130 nm wide metalized structure.

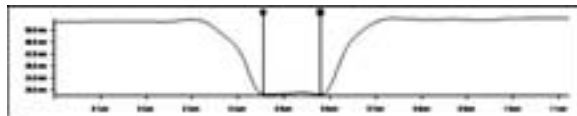


Figure 3: A X-Z line plot of an AFM-imaged cross-section of a 125 nm wide line fully exposed in resist. Note the sloped plot line.

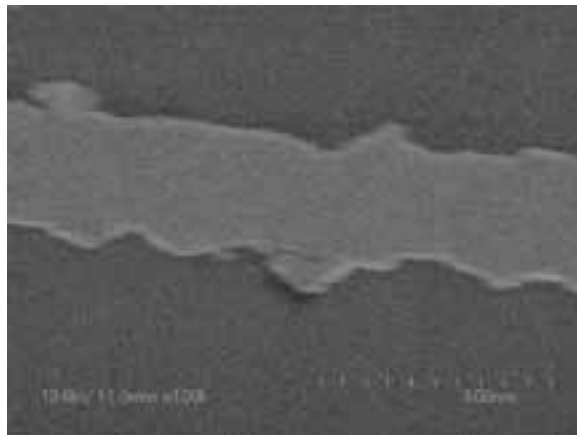


Figure 4: SEM image of a line left jagged by unclean liftoff.

The Role of Polyvinylpyrrolidone in the Toxicity Evaluation of Silver Nanocubes

Mark Brunson

Mechanical Engineering, San Francisco State University

NNIN REU Site: Nano Research Facility, Washington University in St. Louis, St. Louis, MO

NNIN REU Principal Investigator(s): Dr. Dong Qin, Nano Research Facility, Washington University in St. Louis

NNIN REU Mentor(s): Dr. Yujie Xiong, Nano Research Facility, Washington University in St. Louis

Contact: brunson@mail.sfsu.edu, dqin@seas.wustl.edu, xiongy@seas.wustl.edu

Introduction:

Nanotechnology is rapidly progressing from research and development to commercialization. Nanomaterials, the building blocks of nanotechnology, often exhibit unusual physicochemical properties when the dimensions of materials shrink down to nanoscale. However, the small size of materials often allows them to enter tissues, cells, organelles, and functional biomolecular structures. As a result, it is imperative to investigate the associated risks of these nanomaterials and formulate new regulations for handling them.

Silver nanoparticles have demonstrated their potential in applications including antibacterial agents, electronics interconnects, and surface plasmon resonance (SPR) and surface-enhanced Raman spectroscopy (SERS) sensors. The correlation of the toxicity of silver nanoparticles with their sizes and shapes was investigated in collaboration with researchers in the medical community. In a typical synthesis approach, capping agents, such as polyvinylpyrrolidone (PVP), are used to promote $<100>$ facets during the growth from a single-crystal seed into a nanocrystal with defined shape and size [1].

To perform reliable toxicity measurements of silver nanoparticles, it is important to understand the role that PVP plays in the course of evaluation. The goal of this project is to understand the effects of the PVP coating on the toxicity evaluation of silver nanocubes.

Experimental Procedure:

Silver nanocubes were synthesized using a solution-phase process in ethylene glycol (EG), which served as both a solvent and a reducing agent, following the protocol published by Xia and co-workers [2]. In a typical synthesis, silver trifluoroacetate (AgCF_3COO) and PVP were used as a silver precursor and a capping agent, respectively. The size of the nanocubes could be maneuvered as the reaction proceeded. All the samples were collected by centrifugation, washed in acetone to remove the remaining precursor and EG, and washed 1-5 times in deionized (DI) water to remove excess PVP. The morphology of samples was examined

using a transmission electron microscope (TEM, FEI G2 Spirit Twin) at 120 kV.

Washing cycles effectively controlled the amount of PVP physically adsorbed on the nanocubes. Each cycle consisted of ten minutes of centrifugation at 13,000 RPM, removal of supernatant fluid, and addition of 1 mL of DI water. Toxicological tests were performed with the nanocubes after one wash cycle and five wash cycles. The concentration of nanoparticles was measured with a Perkin Elmer Elan DRC II inductively coupled plasma mass spectrometry (ICP-MS) after dissolution with a mixture of HCl and HNO₃ (3:1).

To perform toxicity evaluation of the nanocubes, a 40-hour assay was performed using *Saccharomyces cerevisiae*, a strain of yeast often used as a model eukaryote with similar biological responses as human cells. The suspensions of nanocubes at different concentrations were placed into a 96-well microplate along with the yeast and synthetic culture media. Controls without any nanocubes and without any yeast were measured as references.

While the nanocubes were kept at 30°C, the optical density at 620 nm (OD620) through each well was measured every three minutes for 40 hours to monitor inhibition to yeast growth.

Results and Conclusions:

The edge lengths of the nanocubes used in this experiment were approximately 25 nm and 60 nm, which were obtained at the reaction time of 15 and 90 minutes, respectively. Figure 1 shows a typical TEM image of the 60 nm nanocubes.

The growth curves of yeast cells with 25 nm nanocubes (Figure 2) show that the growth inhibition becomes more severe with increasing wash cycles, indicating that the nanocubes become more toxic. This trend was expected since PVP is nontoxic as shown by the control experiments. Thus, it can shield the yeast cells from the effects of the silver nanoparticles. As the PVP coating was washed away, the cells were further exposed to the silver surface, causing higher toxicity.

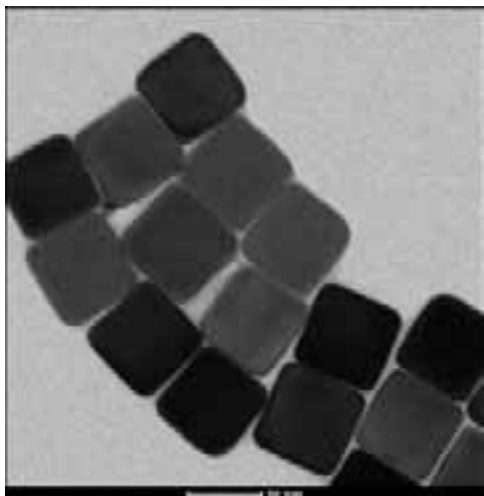


Figure 1: TEM image of 60 nm cubes with a reaction time of 90 minutes.

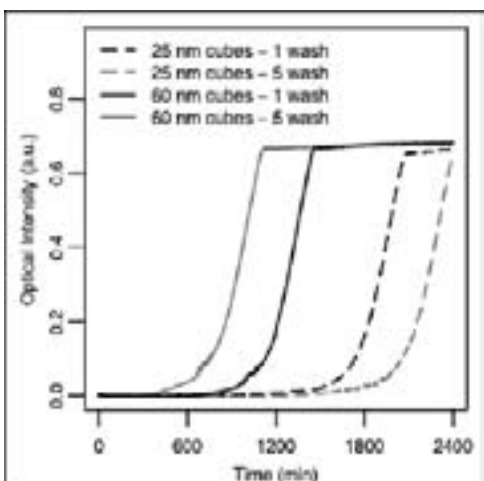


Figure 2: Growth curves of yeast cells in the presence of 25 nm and 60 nm nanocubes after 1-wash and 5-wash cycles.

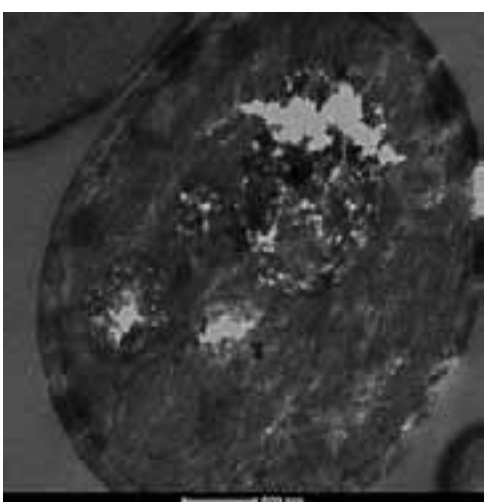


Figure 3: TEM image of yeast cells after 60 nm silver nanocube uptake.

However, the results of 60 nm cubes (Figure 2) showed the opposite effect. Increased wash cycles promoted lower toxicity, which clearly indicated that there might be a distinct difference in the surface coating of small and large nanocubes during the reaction. More investigation is necessary.

In order to determine the amount of nanoparticle uptake by cells, ICP-MS was used to measure the concentration of silver before and after the assay. The results show that over 95% nanoparticles were taken up by cells, regardless of the size of the nanocubes. The nanoparticle uptake was visualized by TEM after a fixation and sectioning process. Figure 3 shows a typical TEM image of yeast cells with 60 nm silver nanocubes taken up. The aggregation state of nanocubes was also investigated with dynamic light scattering (DLS). There was no significant aggregation before and after the assay, confirming that the measured toxicity resulted from silver nanocubes rather than aggregates.

Future Work:

As an extension of current work, the difference in surface chemistry between the 25 nm and 60 nm cubes will be examined in an effort to expand on the difference observed from toxicity measurements. As a fundamental study, the endocytotic effects should be further examined by TEM to explain the interaction between the yeast cells and the taken up nanocubes.

Acknowledgments:

We thank Aaron Huang for nanocube synthesis, and Adam Coster, Juyoung Huh, and Prof. Justin Fay for performing toxicological tests. This project was supported by the National Nanotechnology Infrastructure Network Research Experience for Undergraduates (NNIN REU) Program, and supervised by Drs. Dong Qin and Yujie Xiong. This work was performed at the Nano Research Facility (NRF), a member of NNIN, supported by the National Science Foundation under NSF award ECS-0335765. NRF is part of the School of Engineering and Applied Science at Washington University in St. Louis.

References:

- [1] Xia, Y., et al.; "Shape-Controlled Synthesis of Metal Nanocrystals: Simple Chemistry Meets Complex Physics?"; *Angew. Chem. Int. Ed.*, Vol. 48, 60-103 (2009).
- [2] Xia, Y., et al.; "Facile Synthesis of Ag Nanocubes of 30 to 70 nm in Edge Length with CF_3COOAg as a Precursor"; *Chem. Euro. J.*, Vol. 16, 10234-10239 (2010).

Characterization of Ruthenium Electrodes for Implantable Neurostimulation Applications

Christine Burdett

Chemical Engineering, North Carolina State University

NNIN iREU Site: Interuniversity Microelectronics Center (IMEC), Leuven, Belgium

NNIN iREU Principal Investigator(s): Dr. Hercules Neves, Heterogeneous Integrated Microsystems Group, IMEC, Leuven, Belgium

NNIN iREU Mentor(s): Dr. Aleksandar Radisic, Electrodeposition, CMP and Thinning Group, IMEC, Leuven, Belgium

Contact: cmburdett@gmail.com, herc@imec.be, alex.radisic@imec.be

NNIN iREU Program

Introduction:

Microelectrodes for use in neural recording and functional electrical stimulation (FES) have gained increasing interest over the last few years. These electrodes achieve stimulation by way of reversible charge injection which depolarizes specific cell membranes; this is obtained through capacitive or faradaic reactions [1]. Traditionally, platinum (Pt) or iridium oxide (IrO_2) electrodes have been used, due to exceptional biocompatibility and corrosion resistance. It is also known that charge can be stored or injected by way of valence changes in an electrode coating; oxidation and reduction (redox) reactions between different oxide states increase the ability of the electrode to quickly inject charge [1]. Namely, electrodes with multiple oxidation states have a higher injected charge rate.

Another metal that demonstrates promise as a stimulation electrode is ruthenium (Ru), which we have focused on in this study. Ruthenium has as many as seven oxidation states, though Ru^{2+} , Ru^{3+} and Ru^{4+} are the most common. With these three oxidation states, there is the potential for more charge delivery than with other electrode materials [2]. Additionally, Ru shares the biocompatibility and corrosion resistance associated with platinum-group metals [3]. In our study, we characterized Ru electrodes, focusing on generating low impedance values and high charge delivery capacity. Characterization was accomplished with cyclic voltammetry and electrochemical impedance spectroscopy.

Experimental Procedure:

Ru electrode films were electrochemically deposited onto gold wafers using varying current densities. In addition to electrochemically deposited (ED) films, samples made by atomic layer deposition (ALD) were also studied. We performed electrochemical tests on the samples in a suspended, clip-on cell; all tests used a three electrode system, with a $\text{Ag}|\text{AgCl}$ reference electrode, a Pt mesh and wire counter electrode, and the working electrode. Due to the cell set up, a piece of copper (Cu) foil over the Ru served as the working electrode; the foil was shielded by Teflon® tape to prevent unwanted Cu influence in the impedance or cyclic

voltammetry (CV) scans. A micropipette tip was placed in the cell to act as a Luggin capillary; the Pt mesh and wire combination were wrapped around the micropipette tip, and the reference electrode positioned in the top of the tip, to ensure identical electrode placement for every experiment.

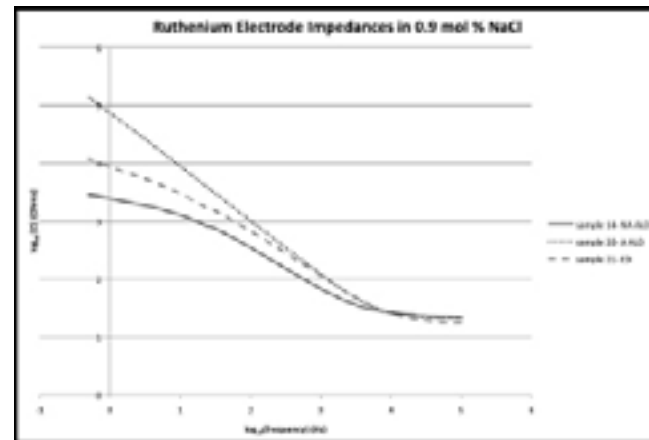


Figure 1: Impedance of ALD and ED samples in 0.9 mol% NaCl.

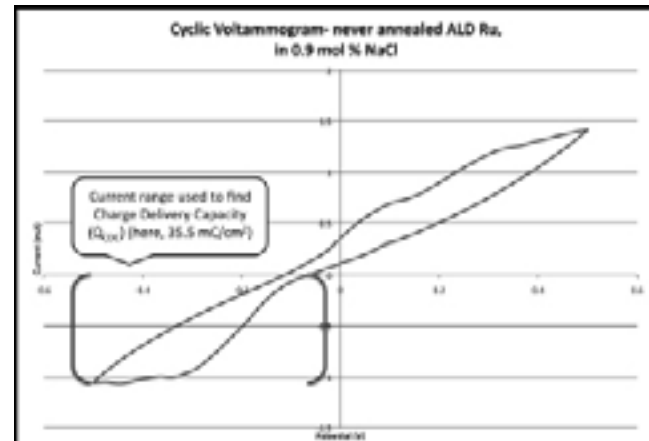


Figure 2: Never annealed ALD Ru data in 0.9 mol% NaCl.

Measurements were first conducted in 10% sulfuric acid by volume, due to concern that chlorine could etch the Ru samples. Further experiments were carried out in 0.9 mol% NaCl. All measurements were taken with a potentiostat (CompactStat, Ivium Technologies). Impedance data was gathered from 0.5 Hz to 100 kHz with 10 mV alternating current sinusoidal amplitude applied from the open circuit potential; cyclic voltammetry was run with 50 mV/s sweep rate and 10 mV step size through varying potential windows.

Results and Discussion:

Through analysis of our CV and impedance spectroscopy data, we have found that Ru fulfills the basic parameters needed for stimulation electrodes.

Interestingly, the ALD Ru samples that were never annealed demonstrate the best electrochemical properties, with the lowest overall impedance and a charge delivery capacity (CDC) of 35.5 mC/cm² for a potential window of -0.5 to +0.5 V (see Figures 1 and 2). Following these, the ED samples also performed relatively well, with CDCs of 13.4 mC/cm² for potentials of -0.25 to +0.3 V; the lowest charge delivery was found in ALD samples that had recently been annealed, which had CDCs of only 530 μ C/cm² for potentials of -0.25 to +0.25 V. We believe this is partially due to the removal of the oxide layer that takes place during annealing; while the oxide had time to re-form, a less developed oxide could mean less available oxidation states for reversible redox reactions, which are essential for good charge delivery capacity.

We encountered difficulties with Ru adhesion during testing in sulfuric acid: upon removal of the Ru sample from the cell, frequently it was found that part of the Ru had been removed. It is believed that this was occurring from water electrolysis effects at low potentials, and also the development of a soluble oxide at positive potentials which caused film damage. The importance of choosing an appropriate voltage window for CV scans is evident, as the amount of etching was significantly lowered by reducing the potential window during cyclic voltammetry scans. Additionally, we learned that choosing an appropriate current range during cyclic voltammetry scanning is important for obtaining smooth curves.

Conclusion and Future Work:

While the results are promising, the amount of data collected is inconclusive to explicitly declare Ru to be a superior metal for functional electrical stimulation, though it is certainly suitable for use in stimulation applications. It is recommended that the study be focused on fabricating Ru films of different thicknesses and varying surface roughness and porosity to determine the best fabrication parameters for FES usage. It would be beneficial to test the affects of electrochemical loading on the charge delivery capacity and impedance of Ru immediately after loading; also important is the testing of Ru in phosphate-buffered saline solutions, for more accurate comparison to current FES electrodes.

Acknowledgments:

I would like to thank Dr. Hercules Neves, Dr. Alex Radisic, and Filip Vanlerberghe for their help and guidance this summer. Special thanks to Dr. Lynn Rathbun for making this experience possible, and to Drs. Julie Nucci and Jim Overhiser for helping us get settled in Leuven. Thanks also to the National Nanotechnology Infrastructure Network International Research Experience for Undergraduates (NNIN iREU) Program, the National Science Foundation, and the Interuniversity Microelectronics Center (IMEC) in Belgium for research support and funding.

References:

- [1] Cogan, S.; "Neural Stimulation and Recording Electrodes"; *Ann. Rev. Biomed. Eng.*, 10, 275-309 (2008).
- [2] Slavcheva, E.; Vitushinsky, R.; Mokwa, W.; Schnakenberg, U.; "Sputtered Iridium Oxide Films as Charge Injection Material for Functional Electrostimulation"; *Journal Electrochemical Society*, 151, E226-E237 (2004).
- [3] Fröhlich, R.; Rzany, A.; Riedmüller, J.; Bolz, A.; Schaldach, M.; "Electroactive coating of stimulating electrodes"; *Journal Mat. Sci.: Materials in Medicine*, 7, 393-397 (1996).

Characterization of Iron Oxide Integration within Phospholipid Encapsulated Colloids

Jack Chen

Biomedical Engineering, Duke University

NNIN REU Site: Nano Research Facility, Washington University in St. Louis, St. Louis, MO

NNIN REU Principal Investigator(s): Dr. Gregory Lanza, Cardiology, Washington University in Saint Louis

NNIN REU Mentor(s): Dr. Angana Senpan, Cardiology, Washington University in Saint Louis

Contact: jack.chen@duke.edu, greg@cvu.wustl.edu, asenpan@cmrl.wustl.edu

Abstract and Introduction:

Contrast agents for magnetic resonance imaging (MRI) enhance the visibility of targeted tissues and cells. Many current T_1 -weighted (T_1w) contrast agents (bright) are gadolinium-based; however, gadolinium has been associated with nephrogenic systemic fibrosis, a severe connective tissue disease, among patients with impaired kidney function. Iron oxides are common non-gadolinium nanoparticles used for dark MRI imaging (T_2^* -weighted). They provide bold negative contrast due to their strong magnetic field interference, but their prolonged duration in the blood stream precludes imaging for 24 to 48 hours post-injection, until the circulating metal oxide concentration has decreased sufficiently.

Colloidal iron oxide nanoparticles (CION) also utilize iron oxide crystals, but uniquely produce bright T_1w contrast and allow imaging within an hour. The novelty arises from the chemical coupling of the magnetite particles within the inner aspect of a monolipid layer, which distributes the metal predominantly around the perimeter. By avoiding the clustering of iron within the core of the particle and using magnetite, a weaker form of iron oxide, T_2^* effects are reduced. While chemical cross-linking of the iron oxide particles with the lipid membrane after the formation of the particle has been effective, a new chemical formulation to achieve a self-assembly product is preferable. This project examined the utility of transmission electron microscopy (TEM) to characterize the spontaneous distribution of lipid-modified iron oxides into the hydrophobic surfactant of CION for development of a new chemical synthesis.

To further evaluate the model suggested by the CION particle chemistry, a particle in which the metal was oriented to the periphery and excluded from the center by an acrylamide hydrogel core was synthesized. The goal was to determine if the T_1/T_2^* ratio of these particles was improved.

Experimental Procedure:

A modification of our previously published formulation for synthesizing the CION particles was followed (Figure

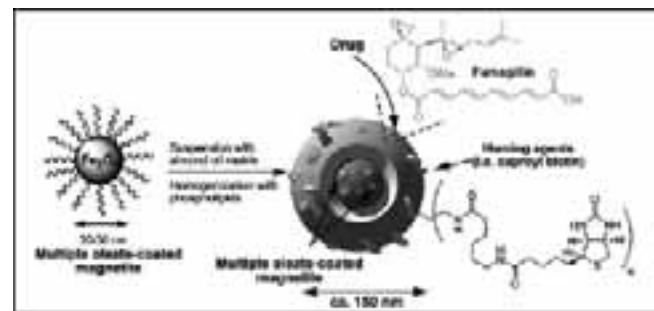


Figure 1: Schema of production of CION particles.

1) [1]. Cholesterol and undecenoyl chloride were heated to reflux in pyridine and the product was recrystallized from ethanol. The modified cholesterol was then cross-linked to oleate-coated magnetite to covalently anchor the iron oxide particles to the membrane.

CION samples were prepared for transmission electron microscopy (TEM) as follows: particles were fixed with 2.5% glutaraldehyde in phosphate buffered saline for 30 minutes, and centrifuged into a pellet. After post-fixing with 1% osmium tetroxide, 2% tannic acid, and 4% uranyl acetate, the particles were embedded in EMBED-812, sectioned, and imaged with TEM at 120 kV.

To prepare the hydrogel emulsion, a 5:1 molar ratio of lecithin:cholesterol was dissolved in chloroform, which was evaporated to make a thin lipid film. This film was hydrated by a mixture of 4.5% acrylamide, 0.5% *N,N*-methylenebis(acrylamide), and 0.0012% Irgacure 2959 (a photoinitiator) in HEPES buffered saline [2]. The mixture was sonicated and hand-extruded through a syringe using successive filters of 1 and 0.2 μ m pore size to reduce aggregates. Ascorbic acid was used to prevent peripheral cross-linking of the particles. The mixture was placed in a UV cross-linker for five minutes, and the experiment was repeated several times with manganese oleate incorporated into the lipid film to 30% and 50% by weight.

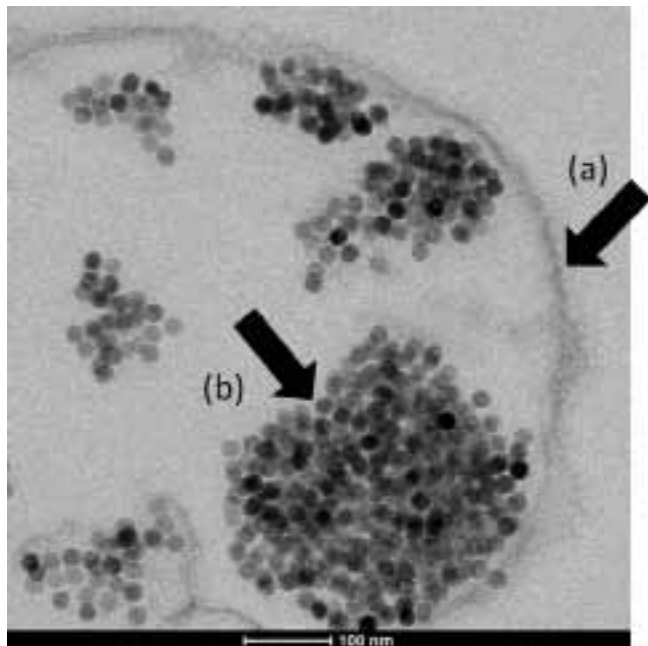


Figure 2: TEM of CION particles. (a) Lipid membrane ruptured during centrifugation. (b) Aggregation of iron oxide particles.

Results and Conclusions:

Size Determination. The hydrodynamic diameter and zeta potential of the CION particles were measured using dynamic light scattering and found to be 141.0 ± 0.3 nm and -27.32 ± 0.64 mV, respectively.

Transmission Electron Microscopy. TEM was used to examine the distribution of iron oxides within the membrane. Fixation of CION proved to be complex, as the images obtained show a ruptured lipid layer with evidence of aggregation (Figure 2). Review of the process suggested that the centrifugation step likely contributed to the particle breakdown. Work on a revised TEM processing scheme is continuing.

Magnetic Resonance Characterization. The MR relaxivity of successive dilutions was measured (Figure 3). The T_1 relaxivity of CION was found to be $0.1482 ([\text{Fe}] \text{mM} \cdot \text{s})^{-1}$, a very poor relaxivity. This result suggests that the anchoring

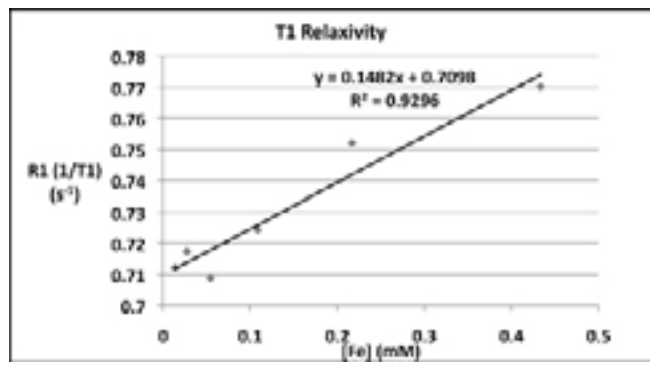


Figure 3: Graph of T_1 relaxivity versus iron concentration.

of iron oxides to the periphery of the membrane was too weak, allowing the metal to aggregate in the core within the strong magnetic field of the MRI.

Hydrogel. The size of the hydrogel particles was determined using dynamic light scattering. The hydrodynamic diameter of the particles without manganese oleate was found to be 442.0 ± 5.7 nm, and the diameter with manganese oleate incorporated to 30% was found to be 443.9 ± 12.4 nm, indicating that incorporating the manganese oleate was successful. Loading the manganese oleate at 50% was unsuccessful, leading to aggregation. Multiple populations were evident in the data (Figure 4), which indicates that the syringe extrusion process was not adequate, perhaps causing the large particle sizes.

Future Work:

Research will continue to improve the CION chemical coupling to achieve the proper morphology in a self-assembly synthesis without added post-crosslinking reagents.

Additionally, work on the hydrogels to study the physics of the metal distribution in nanoemulsions will continue.

Acknowledgments:

I would like to thank Drs. Angana Senpan, Gregory Lanza, and Dipanjan Pan, the C-TRAIN group, and the faculty and staff at the Nano Research Facility at Washington University in Saint Louis, especially Kristy Wendt and Dr. Dong Qin. Funding was provided by the National Nanotechnology Infrastructure Network Research Experience for Undergraduates (NNIN REU) Program and the National Science Foundation.

References:

- [1] Senpan, A.; Caruthers, S. D.; Rhee, I.; Mauro, N. A.; Pan, D.; Hu, G.; Scott, M. J.; Fuhrhop, R. W.; Gaffney, P. J.; Wickline, S. A.; Lanza, G. M. Conquering the Dark Side: Colloidal Iron Oxide Nanoparticles. *ACS Nano*. 2009, 3, 3917-3926.
- [2] Schillemans, J. P.; Flesch, F. M.; Hennink, W. E.; van Nostrum, C. F. Synthesis of Bilayer-Coated Nanogels by Selective Cross-Linking of Monomers inside Liposomes. *Macromolecules* 2006, 39, 5885-5890.

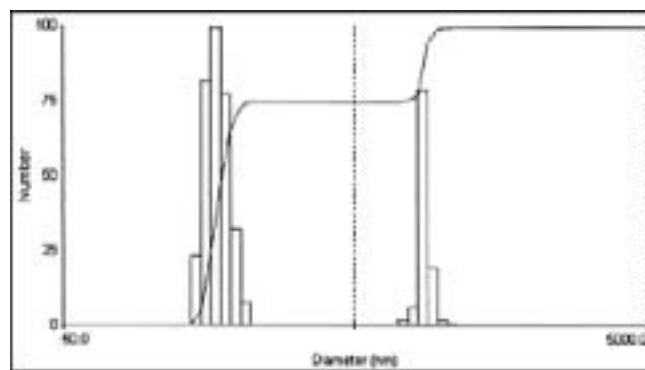


Figure 4: Distribution of particle sizes measured by dynamic light scattering.

Material Characterization of Advanced III-V Semiconductors for Nanophotonic Integration

Brian T. Chung

Engineering Physics, University of Michigan – Ann Arbor

NNIN REU Site: Nanotech, University of California, Santa Barbara, CA

NNIN REU Principal Investigator(s): Professor Larry A. Coldren, Electrical and Computer Engineering, UC Santa Barbara

NNIN REU Mentor(s): Robert S. Guzzon, Erik J. Norberg, and John S. Parker, Electrical and Computer Engineering, UCSB

Contact: btchung@umich.edu, coldren@ece.ucsb.edu, guzzon@ece.ucsb.edu, norberg@ece.ucsb.edu, jparker@umail.ucsb.edu

Abstract:

New applications for integrated nanophotonic components and circuits typically found in telecommunication and internet data transfer will utilize tunable microwave filters for the pre-filtering and channelizing of information in the radio frequency (RF) domain. Such applications will require the use of high optical saturation power quantum well designs in order to reduce detrimental nonlinear phenomena. The goal of this project was to experimentally characterize novel quantum well designs and extract material parameters to guide future design work. By fabricating and testing broad area laser structures, the material loss and gain parameters were extracted. We fabricated broad area laser structures using a standard wet-etch process defining surface ridge waveguides. The P-metal pattern was first defined using contact lithography and then deposited by electron beam evaporation followed by metal liftoff. Material characterization was performed using a pulse setup and cleave-back approach to determine light-current-voltage characteristics and differential efficiencies. Net internal optical loss and characteristic gain values were then calculated. Internal optical loss values as low as 4.175 cm^{-1} and characteristic modal gain values as low as 15.152 cm^{-1} were recorded.



Figure 1: (a) Schematic of CTL epitaxial design, (b) SEM of fabricated 100 nm CTL design active region.

Introduction:

The active confinement factor Γ of a device is defined as the overlapping integral between the optical mode and the active quantum well (QW) region. The optical saturation power of an amplifier is inversely proportional to Γ , thus decreasing Γ becomes the strategy for increasing saturation power. By placing QWs outside the waveguide where the optical intensity is smaller, Γ is reduced. A confinement tuning layer (CTL) of passive material may also be introduced between the QWs and waveguide of a structure. This further decreases Γ since the QWs are moved to the evanescent tail of the optical mode [1].

In this experiment, we have characterized the gain and loss parameters of two novel material designs employing five

QWs and CTLs of 100 and 250 nm thicknesses. Figure 1 depicts (a) a schematic of a sample epitaxial design utilizing a CTL, and (b) a scanning electron microscopy (SEM) image of the active region of the 100 nm CTL design.

Procedure:

Growth and Fabrication. The novel material designs investigated in this work were designed at the University of California, Santa Barbara, (UCSB) and the actual growths and regrowths were prepared by Land Mark Optoelectronics Corporation, using the metal organic vapor phase epitaxy technique. The finished dies were fabricated into 50 μm width broad area lasers at Nanotech at UCSB via a

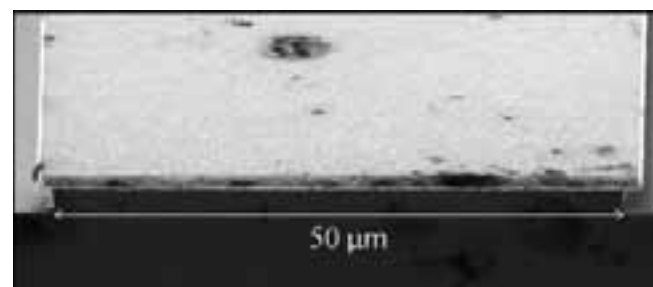


Figure 2: SEM image of 100 nm CTL design laser cross section.

single contact lithography process and a standard wet-etch for ridge definition. Ohmic contacts were established on the top and backside using electron beam metal deposition followed by metal liftoff. Figure 2 shows the cross section of a fully fabricated broad area laser.

Characterization Setup. To characterize the designs, we implemented the cleave-back method to extract the following loss and gain parameters: the internal quantum efficiency η_i , net internal optical loss $\langle\alpha_i\rangle$, transparent current density J_{tr} , and characteristic modal gain $\langle g_o \rangle$ [2]. In the measurement, we cleaved the ends of the lasers along crystal planes to ensure ideal mirrors.

Probes were attached to the contacts to facilitate the injection of a pulse current, and the light output power was measured using a photodiode. From the LIV curve obtained after a voltage sweep, we were able to determine the threshold current density J_{th} and the differential efficiency η_d of the device. We repeated this process and obtained values for lasers of differing lengths.

Plotting lengths versus the inverses of the recorded differential efficiencies yielded values for η_i and $\langle\alpha_i\rangle$. From these parameters, we calculated the threshold modal gains of the samples and plotted these versus J_{th} values. Similarly, these plots yielded values for J_{tr} and $\langle g_o \rangle$.

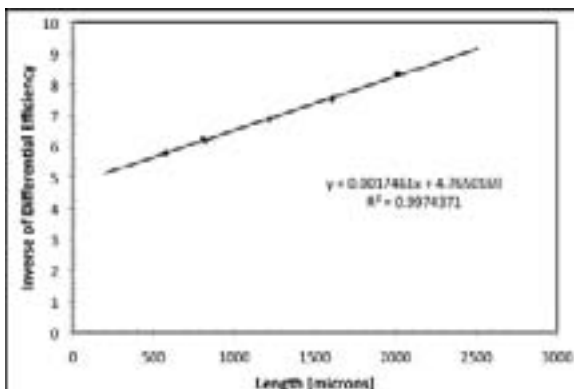


Figure 3: Internal loss of 250 nm CTL design.

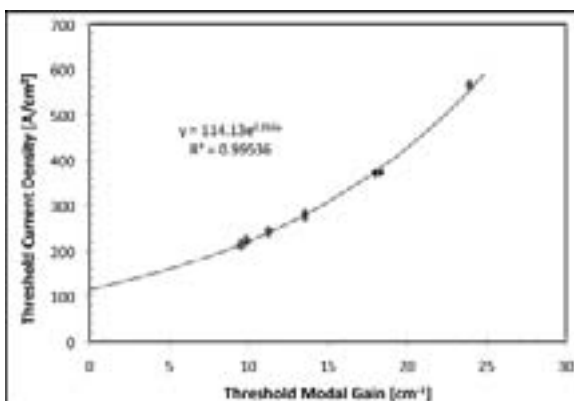


Figure 4: Characteristic gain of 250 nm CTL design.

Results:

Figures 3 and 4 delineate interpolations of the internal loss and gain data for the 250 nm CTL design. Similar plots for the 100 nm CTL design (not shown) were constructed. From these plots, we calculated η_i values of 0.262 for 100 nm and 0.21 for 250 nm; $\langle\alpha_i\rangle$ values of 5.882 cm^{-1} for 100 nm and 4.175 cm^{-1} for 250 nm; $\langle g_o \rangle$ values of 31.681 cm^{-1} for 100 nm and 15.152 cm^{-1} for 250 nm; and finally J_{th} values of 105.916 A/cm^2 for 100 nm and 114.13 A/cm^2 for 250 nm.

Results were largely consistent with anticipated values, however injection efficiencies were noticeably lower than anticipated. Possible explanations for this deficiency include the possibility of a leakage current through the device or an inconsistent material doping profile.

Conclusions and Future Work:

We have successfully demonstrated low loss and gain characteristics from far-offset QW and CTL designs. The 250 nm CTL design exhibited a low modal gain value of about one half that of the 100 nm design, making it preferential for applications that require a high saturation power.

Further characterization of the 250 nm CTL design will include fabricating and pulse testing ridge lasers and experimentally verifying the material's improved saturation power. Following these performance verifications, the design has the potential to be incorporated into a fully functional microwave photonic filter.

Acknowledgements:

Special thanks to Prof. Larry A. Coldren, mentors Robert Guzzon, Erik Norberg, and John Parker, and coordinator Angela Berenstein for their excellent support in this project, and to UCSB, DARPA under the PhASER program, the NNIN REU Program, and the NSF for funding and support.

References:

- [1] J. Raring, E. Skogen, M. Masanovic, S. DenBaars, and L. Coldren, "Demonstration of high saturation power/high gain SOAs using quantum well intermixing and MOCVD regrowth," IET Electronics Letts. vol.41, pp. 1345-1346, Nov. 2005.
- [2] L. Coldren and S. Corzine, Diode Lasers and Photonic Integrated Circuits, Wiley Series in Microwave and Optical Engineering, pp. 52-53, 1995.

Fabrication of Locally-Gated Bilayer Graphene Field Effect Transistors

Corey E. Clapp

Department of Chemistry, Amherst College, Amherst, MA

NNIN REU Site: Penn State Nanofabrication Laboratory, The Pennsylvania State University, State College, PA

NNIN REU Principal Investigator(s): Jun Zhu, Department of Physics, The Pennsylvania State University

NNIN REU Mentor(s): Ke Zou and Bei Wang, Department of Physics, The Pennsylvania State University

Contact: cclapp11@amherst.edu, jzhu@phys.psu.edu, kxz132@psu.edu

Abstract:

We fabricated local backgate stacks for bilayer graphene field effect transistors. Local gates were patterned onto 290 nm silicon oxide/silicon (SiO_2/Si) wafers using optical lithography. We etched the SiO_2 layer partially by reactive ion etching (RIE), and deposited metal gate electrodes, followed by a hafnium dioxide (HfO_2) dielectric layer. Since graphene conforms to the morphology of the substrate, a smooth HfO_2 surface was critical to obtaining smooth graphene flakes. HfO_2 follows the morphology of the metal and the SiO_2 underneath. We explored different etching recipes to achieve a smooth SiO_2 surface. Chlorine gas (Cl_2) etched SiO_2 exhibits a root mean square (rms) surface roughness of 5.1 Å. Bilayer graphene exfoliated onto HfO_2 in the completed gate stacks displays a rms roughness of 5.8 Å.

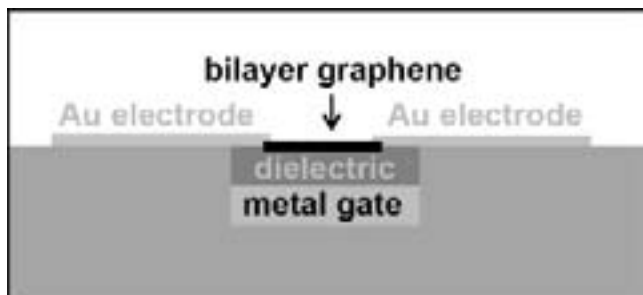


Figure 1: Gate stack diagram.

Introduction:

Bilayer graphene, composed of two carbon monolayers in Bernal stacking, displays the unique property of having a bandgap that is tunable by electric fields. The development of local gating would enable local control of the charge carrier density and band gap in bilayer graphene as shown in Figure 1.

Experimental Procedures:

We patterned the design for the backgate stacks with optical lithography onto 290 nm SiO_2/Si wafers. 60 nm deep wells were then etched using RIE. Early trials were run with carbon tetrafluoride (CF_4) and later trials with chlorine gas (Cl_2). We varied the parameters in the etching recipe to achieve a smooth SiO_2 surface. The resulting SiO_2 surfaces and etch depths were characterized with atomic force microscopy (AFM). We then constructed the gate stacks by depositing 5 nm titanium (Ti) / 25 nm gold (Au) using electron-beam evaporation, and subsequently 30 nm of HfO_2

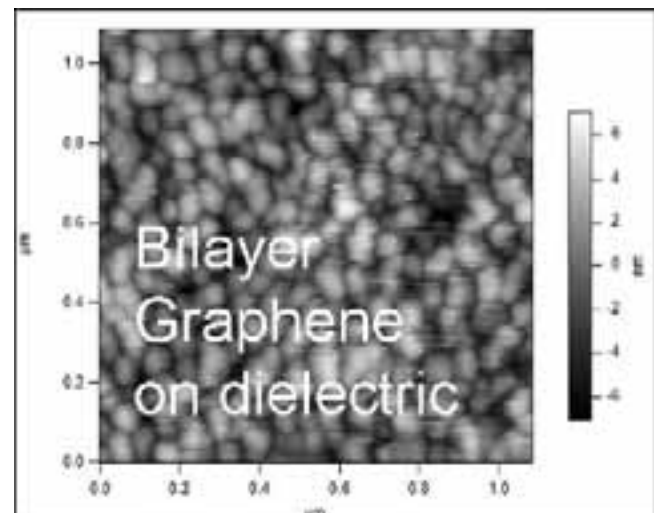


Figure 2: AFM image of bilayer graphene exfoliated on HfO_2 deposited on Au/SiO_2 stack. The SiO_2 was etched by CF_4 RIE. The rms surface roughness = 2.26 nm.

using atomic layer deposition. A lift-off procedure using acetone and sonication left only the completed gate stacks. Bilayer graphene was exfoliated onto the HfO_2 surface by tape, identified by optical microscope, and characterized by AFM.

Results and Discussions:

The bilayer graphene sheet exfoliated onto gate stacks fabricated with CF_4 RIE showed a surface rms roughness of 2.26 nm as shown in Figure 2. This roughness matched the

surface roughness of the HfO_2 dielectric (rms of 2.20 nm), indicating that the bilayer graphene followed the morphology of the dielectric. The roughness of the dielectric was also similar to the roughness of the Au (rms of 2.31 nm) and the SiO_2 (rms of 2.08 nm) beneath it. This showed that it is crucial to produce smoothly etched SiO_2 to obtain smooth bilayer graphene. The roughness of the SiO_2 was insensitive to the parameters used in the recipes including temperature, gas flow and pressure.

In contrast, we were able to produce a much smoother SiO_2 surface with a rms roughness of 5.1 Å using a Cl_2 etch. This resulted in a bilayer graphene roughness of 5.8 Å as shown in Figure 3.

The Cl_2 etch showed time-dependent etch rates which were much slower than the CF_4 etch. In several different trials, the etch rate dropped considerably within the first five minutes before leveling off to a constant 1.7 nm/min (see Figure 4).

Care should be taken when using Cl_2 etch since long etches may cause heating issues with the photoresist.

Conclusions:

To conclude, we studied the etching of SiO_2 by CF_4 and Cl_2 . A smooth surface of SiO_2 (rms \sim 5 Å) is achieved by Cl_2 etch. We successfully deposited metal gates and HfO_2 dielectric layers, and performed lift-off to create local back gates. Bilayer graphene exfoliated onto these local gates showed a rms roughness of 6 Å, similar to that of the etched SiO_2 .

Acknowledgements:

Special thanks to my mentor Ke Zou, Bei Wang, Xia Hong, my advisor Dr. Jun Zhu, and the MRI staff. Thanks also to the National Science Foundation, and the National Nanotechnology Infrastructure Network Research Experience for Undergraduates (NNIN REU) Program for funding.

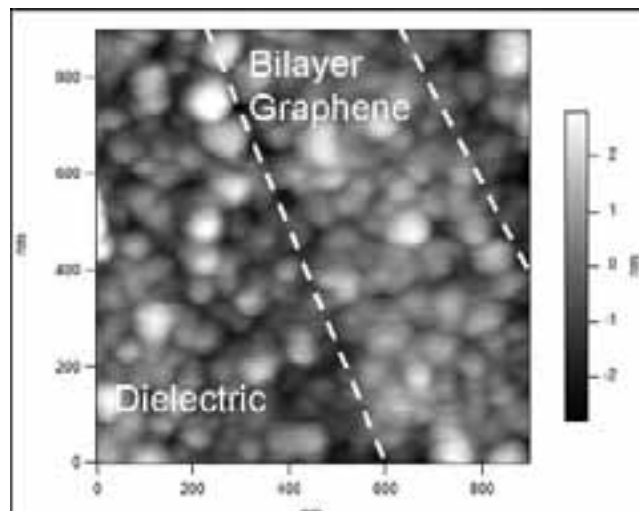


Figure 3: AFM image of bilayer graphene exfoliated on HfO_2 deposited on Au/SiO_2 stack. The SiO_2 is etched by Cl_2 RIE. The rms surface roughness = 5.8 Å.

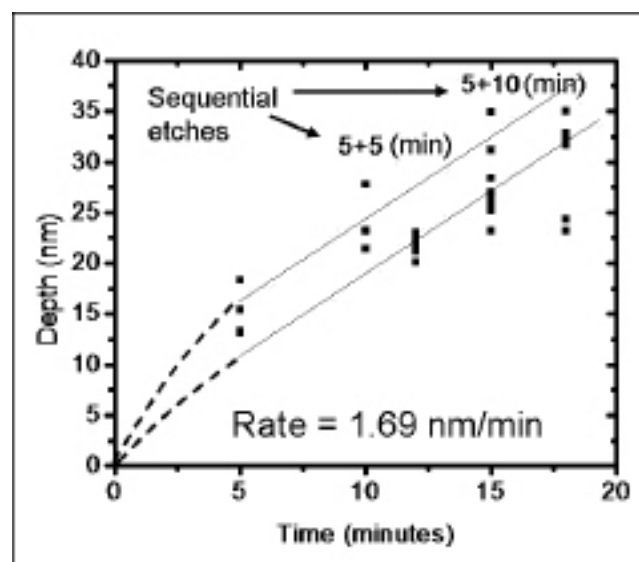


Figure 4: Cl_2 etch rates.

Graphene Growth on Palladium (111)

Scott Isaacson

Chemical Engineering, University of Minnesota

NNIN iREU Site: National Institute for Materials Science (NIMS), Tsukuba, Ibaraki, Japan

NNIN iREU Principal Investigator(s): Dr. Daisuke Fujita, Advanced Nano Characterization Center, NIMS

NNIN iREU Mentor(s): Dr. Jian-Hua Gao and Dr. Nobuyuki Ishida,

Advanced Nano Characterization Center, National Institute for Materials Science

Contact: isaac145@umn.edu, fujita.daisuke@nims.go.jp, gao.jian-hua@nims.go.jp, ishida.nobuyuki@nims.go.jp

NNIN iREU Program

Abstract:

Growth of graphene films on a palladium (111) (Pd(111)) surface has been achieved by surface segregation of carbon. The resulting films were characterized by Auger electron spectroscopy (AES), atomic force microscopy (AFM), and scanning tunneling microscopy (STM). A growth procedure was found that results in the formation of large-scale ($> 1 \text{ mm}^2$), single layer graphene on the Pd(111) surface. Graphene islands were found to follow the Stranski-Krastanov growth mode. In most cases, graphene islands imaged with a scanning tunneling microscope (STM) exhibit a Moiré pattern with a periodicity of $2.3 \pm 0.1 \text{ nm}$, consistent with the $[2\bar{1}\bar{1}0]$ direction in graphene being aligned with the $[1\bar{1}0]$ direction of the Pd(111) surface.

Introduction:

Graphene, a two-dimensional crystalline sheet of sp^2 -bonded carbon atoms arranged in a honeycomb lattice, has garnered the interest of many researchers in recent years due to its remarkable structure and electronic properties [1]. These unique properties have sparked interest in the practical applications of graphene, from its use in electric batteries to graphene-based electronics [1]. For many of these applications, the fabrication of large-area, high-quality, single-layer graphene films is essential to their success.

Several methods of fabrication that aim to satisfy these requirements exist, each with advantages and disadvantages. The results reported below are based on a graphene fabrication method that operates by the segregation and precipitation of carbon from the bulk of a metal to the metal surface [2]. The objective of the work presented here was to determine a growth procedure capable of producing large-scale, single layer graphene on a Pd(111) surface.

The precipitation of carbon on carbon-doped metal surfaces has been studied by Hamilton and Blakely [3]. Figure 1 shows their qualitative findings of carbon coverage versus the temperature to which the metal sample was heated. This figure shows that there is an intermediate temperature range in which single-layer graphene is formed on the metal surface.

Experimental Procedures:

Graphene films were grown by a surface segregation and precipitation process on a carbon-

doped Pd(111) surface. The Pd sample was 2 mm thick and had a 10×3 mm area available for graphene growth. The substrate was doped to 0.5 at % carbon by a solid-state diffusion method in which the metal surface was covered in high-purity graphite powder and annealed at 800°C for 200 hours under ultra-high vacuum (UHV) conditions.

To produce a graphene layer on the Pd(111) surface, the carbon-doped metal sample was heated by electron back-bombardment under UHV conditions. The temperature and duration of the heating was varied depending on the desired growth conditions. The sample temperature was monitored with an optical pyrometer. After characterization, the Pd(111) surface was cleaned by argon ion sputtering, followed by heating to 900°C to dissolve all remaining surface carbon into the bulk. The cleaned sample was then ready to undergo another growth procedure.

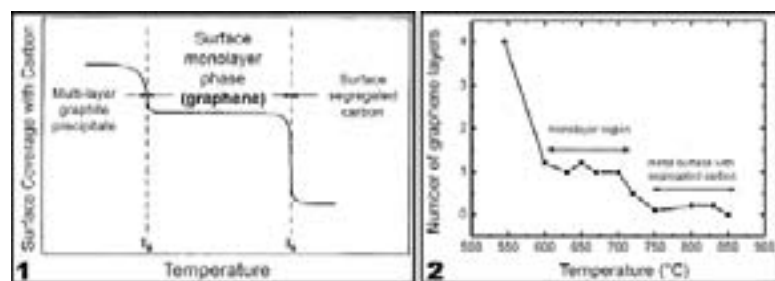


Figure 1, left: Qualitative dependence of carbon coverage on growth temperature as determined by Hamilton and Blakely [3].

Figure 2, right: Dependence of carbon coverage on growth temperature.

Resulting graphene films were characterized with a scanning Auger microscope (ULVAC-PHI model SAM650) and a STM at room temperature in UHV conditions. Films were also examined with an AFM (SPA300 AFM) at ambient conditions.

Results and Conclusions:

Using AES, the growth of graphene on the Pd(111) surface was characterized over a range of growth temperatures. Figure 2 illustrates the dependence of the thickness of the graphene film on the growth temperature. This result clearly resembles the results of Hamilton and Blakely [3] from Figure 1.

In addition to this characterization, a growth procedure was found that resulted in large-area, single layer graphene films. This procedure involved heating the sample to 720°C for 10 minutes. Also, before growth, the sample was heated to 900°C to dissolve surface carbon. Unlike the typical growth procedure, argon ion sputtering was not used to clean the surface before growth. The resulting graphene film was determined to be a single layer by AES and covered almost the entire Pd(111) surface.

For growth temperatures at and below 600°C, the formation of three-dimensional, multi-layer graphene islands was observed. These islands formed on top of a single graphene layer, providing evidence that this mechanism of graphene growth follows the Stranski-Krastanov growth mode.

STM images of graphene islands revealed a clear superstructure with six-fold symmetry and a periodicity of 2.3 ± 0.1 nm (see Figure 3). This superstructure has been interpreted as a Moiré pattern resulting from the superposition of the graphene lattice on the palladium surface [4], and the value of the pattern's periodicity indicates that the [2110] direction in graphene is parallel to the [110] direction of the Pd(111) surface [4]. This orientation implies that the growth of graphene on the Pd(111) surface is nearly epitaxial.

All graphene islands examined with STM and AFM were located adjacent to or spanning a step edge of the palladium surface (see Figure 4), suggesting that graphene islands preferentially nucleate at step edges.

Acknowledgements:

This work was sponsored by the National Nanotechnology Infrastructure Network's International Research Experience for Undergraduates (NNIN REU) Program, the National Science Foundation, and the National Institute for Materials Science. The author would like to thank Dr. Daisuke Fujita, Dr. Jian-Hua Gao, Dr. Nobuyuki Ishida, Dr. Tamaki Iwasaki, and Dr. Keisuke Sagisaka for their guidance and support.

References:

- [1] Geim, A. K.; Novoselov K. S. *Nature Materials*. 6, 183 (2007).
- [2] Fujita, D; Yoshihara K. *J. Vac. Sci. Technol. A*. 12, 2134 (1994).
- [3] Hamilton, J. C.; Blakely J. M. *Surface Science*. 91, 199 (1980).
- [4] Kwon, S.Y.; Ciobanu, C.V.; Petrova, V.; Shenoy, V.B.; Bareño, J.; Gambin, V.; Petrov, V.; Kodambaka, S. *Nano Letters*. 9, 3985 (2009).

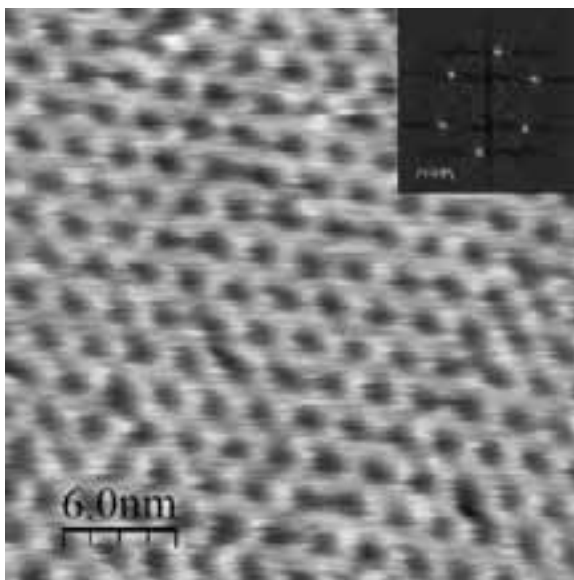


Figure 3: An STM image of a graphene island formed from heating the sample to 700°C for 10 minutes (Inset: Fourier transform of the image).

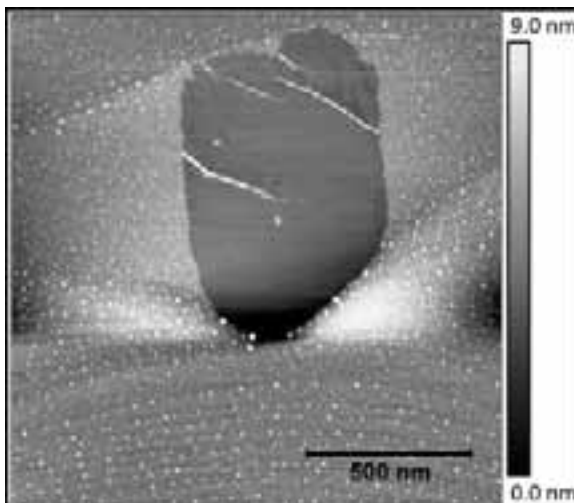


Figure 4: An AFM image of a small graphene island that is adjacent to a step in the Pd(111) surface. Carbon nanowires can be seen on the graphene surface.

DNA Electrophoresis in Microfabricated Post Arrays

Jason Lee

Chemical Engineering, University of Massachusetts-Amherst

NNIN REU Site: Nanofabrication Center, University of Minnesota-Twin Cities, Minneapolis, MN

NNIN REU Principal Investigator(s): Dr. Kevin Dorfman, Chem.Eng. and Materials Science, University of Minnesota-Twin Cities

NNIN REU Mentor(s): Dan Olson and Dr. Jia Ou, Chem.Eng. and Materials Science, University of Minnesota-Twin Cities

Contact: jasonl@student.umass.edu, dorfman@umn.edu, olso1887@umn.edu, ouxxx023@umn.edu

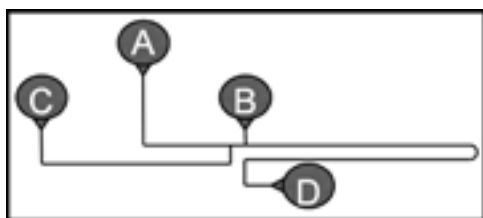


Figure 1: Schematic of dual channel sparse post array device.

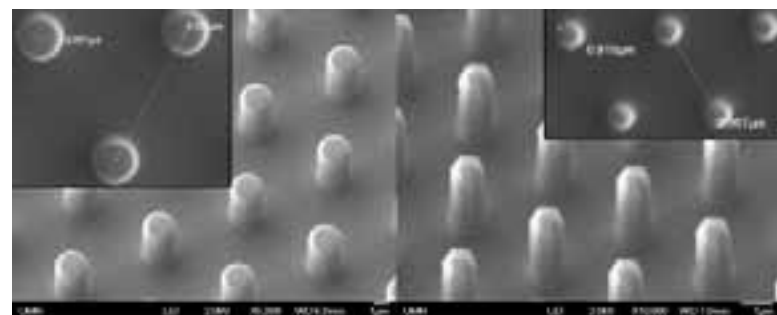


Figure 2: First post array (left) and second post array (right).

Abstract and Introduction:

Agarose and polyacrylamide gel electrophoresis enable researchers to study biological systems through numerous applications that require separating deoxyribonucleic acid (DNA) by size. However under many conditions, gels cannot resolve large DNA unless using pulsed field gel electrophoresis, which turns an hour process into a day. Hexagonal post arrays have been shown to be more efficient. Separation ability depends on post diameter and spacing [1]. The microfluidic device fabricated employs two arrays, the first with $2\text{ }\mu\text{m}$ posts at $6\text{ }\mu\text{m}$ spacing and the second with $1\text{ }\mu\text{m}$ posts at $3\text{ }\mu\text{m}$ spacing, to look for greater separation than either array alone. Rearrangement of the reservoirs (Figure 1, A-D) decreased DNA loading times during experiments. Post fences at reservoirs were added to block debris and improve device lifetime.

Device Fabrication:

A 1000\AA layer of silicon dioxide (SiO_2) was grown on cleaned silicon $<100>$ wafers using thermal oxidation. Oxide thickness was confirmed using a Nanospec spectrophotometer. The wafers were primed with hexamethyldisilazane before spinning Shipley 1805 photoresist at 3000 rpm for 60 seconds. Following a one minute, 105°C softbake, the resist was exposed for 4.5 seconds using chrome mask contact lithography. The pattern was inverted in an ammonia image reversal oven followed by 14 minutes of ultraviolet flood exposure. The mask was developed in a 7x dilution of developer 351 for about

25 seconds. A single drop of developer was placed on each fence for four extra minutes for full development. After passing inspection under an optical microscope, wafers were oxygen cleaned for 30 seconds in a reactive ion etcher followed by buffered oxide etching of the dioxide for roughly 150 seconds. The resist was removed with acetone, methanol, isopropyl alcohol, distilled water, and then 10 minutes of oxygen plasma cleaning. Using the silicon dioxide mask, the silicon was etched in the deep trench etcher down to about $4.5\mu\text{m}$ deep. A P16 profilometer confirmed channel depth and the dioxide was removed with buffered oxide etcher. After inspecting the quality of individual devices, the wafers were spun with Shipley 1818 resist to protect the posts during dicing and reservoir drilling. Devices were then thermally oxidized for 7 hours.

Devices were imaged by scanning electron microscope (SEM) (Figure 2) before being glued to drilled glass back-plates. Glass cover slips were spun with Norland Optical Adhesive 81 (NOA81) and then sandwiched between two flat silanized slabs of polydimethylsiloxane (PDMS). Ultraviolet light cured the adhesive except at the surface of the PDMS to provide a thin film for attaching the cover slip and sealing the channels. Reservoir connectors were glued onto the backplate. Distilled water followed by 5x Tris/Borate/EDTA (TBE) electrophoresis buffer with polyvinylpyrrolidone was pumped into the channel prior to usage.

DNA Electrophoresis:

Lambda DNA, purchased from New England Biolabs, was digested with *Xba*I restriction enzyme to yield a 15 kilobase and a 33 kilobase fragment. These fragments were mixed with uncut lambda DNA for final concentrations of 24 μ g/mL and 8 μ g/mL respectively. The DNA was dyed with YOYO-1 and pipetted into reservoir B (Figure 1). Other reservoirs were filled with 5x TBE with 10% dithiothreitol. DNA was pulled from reservoir B towards reservoir C into the shifted-T by setting electric fields. DNA in the shifted-T was injected by setting fields to push from A and pull towards D at 10 V/cm. Fluorescence intensity was measured over time using a photomultiplier tube on an oil immersion lens microscope with a motorized stage. Measurements were made at four locations: immediately before and after each array.

Results and Conclusions:

Two peaks in the intensity vs. time plot showed the first array resolves the three species into two groups (Figure 3). The addition of the second array improves separation, resolving all three species (Figure 4). However, peaks overlap greatly, reducing the measured resolution. The overlap is likely due to DNA dispersion. The U-turn is a likely source of additional dispersion because the DNA on the outer side of the turn must travel farther than the DNA on the inside of the turn, which results in a widening of the DNA band before entering the second array. More trials are necessary to pinpoint the cause of performance loss. In comparison to previous processes that used photoresist or chrome etch masks, this process proved more reliable and cost effective.

Other Processes:

A 2 μ m deep channel was made with regular reactive ion etching instead of deep trench etching to eliminate scalloping. From this wafer, a PDMS mold was cast and then silanized. The mold was placed on a cover slip spun with NOA81 and cured similarly to the above process. SEM images show cured NOA81 replicates the posts. This process makes devices for DNA separation studies to be even easier to produce. A new etch recipe is needed to eliminate the undesired sloped profiles.

Acknowledgements:

Thanks to Dr. Kevin Dorfman, Dr. Jia Ou, and Dan Olson, for giving me new insights and attitudes for becoming a greater engineer. Also to the NSF, the NNIN REU program, and the NFC staff at the University of Minnesota for making this amazing summer possible.

References:

[1] Kevin D. Dorfman, "DNA Electrophoresis in Microfabricated Devices," *Reviews of Modern Physics* (in press).

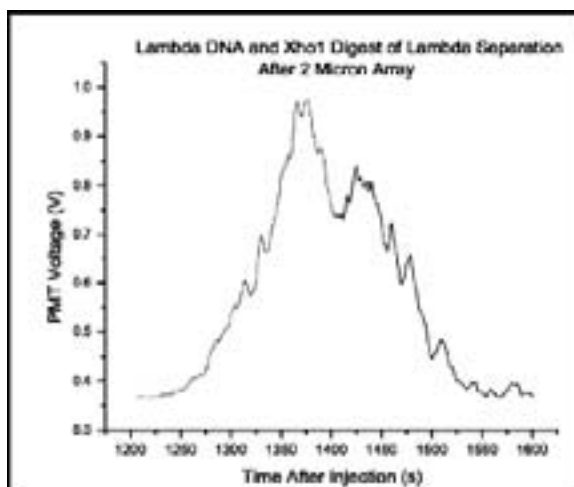


Figure 3: DNA fluorescence intensity over time after the first array.

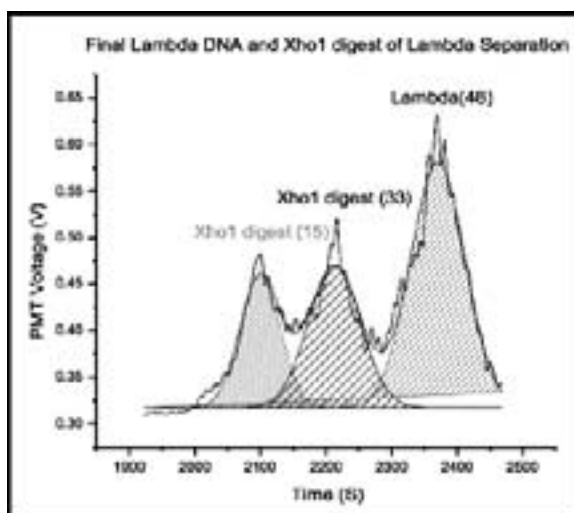


Figure 4: DNA fluorescence intensity over time after both arrays.

Process for Detaching Suspended Graphene Structures from Silicon Carbide

Charles Mackin
Electrical Engineering, University of Arizona

NNIN REU Site: Cornell NanoScale Science and Technology Facility, Cornell University, Ithaca, NY

NNIN REU Principal Investigator(s): Prof. Michael G. Spencer, Electrical and Computer Engineering, Cornell University

NNIN REU Mentor(s): Shriram Shivarajan, School of Electrical and Computer Engineering, Cornell University

Contact: mackin@email.arizona.edu, spencer@ece.cornell.edu, ss626@cornell.edu

Abstract:

Epitaxial graphene was grown on the silicon-terminated face of silicon carbide (SiC). A novel approach was developed to produce suspended graphene structures for transmission electron microscope (TEM) analysis. TEM analysis allows for structural and chemical characterization of graphene structures at the atomic level. TEM analysis, however, is constrained to ultra-thin materials because the microscope's electron beam must travel through the material before collection by the detector. Consequently, TEM analysis of suspended graphene structures requires detachment from the SiC substrate. This paper details the success of the fabrication process, which marks the first time graphene structures have been detached from the SiC substrate by means other than mechanical exfoliation.

Introduction:

Graphene consists of an atomically-thin planar sheet of sp^2 -bonded carbon atoms arranged in a hexagonal lattice. Graphite can be envisioned as a large number of graphene sheets stacked atop one another. Since graphene's isolation in 2004, it has become one of the most widely researched materials [1,2]. At room temperature, graphene claims the highest known carrier mobility, thermal conductivity, and in-plane strength [3-5]. These promising electrical, thermal, and structural properties may lead to applications in high speed and flexible electronic devices.

Of the existing graphene fabrication processes, epitaxial growth from SiC is particularly promising. The semiconducting character of SiC allows for seamless integration with existing Si-based electronics [6]. In addition, graphene growth from SiC is a well characterized and mature process potentially suitable for large-scale graphene production [1].

The aim of the research was two-fold: to experimentally verify the novel fabrication process' ability to detach sus-

pended graphene structures from the SiC substrate, and to analyze the suspended graphene chemically and structurally using transmission electron microscopy.

Experimental Procedure:

Figures 1 and 2 complement the following description.

Graphene was grown epitaxially on the Si face of chemically-mechanically polished n-type 4H SiC. Raman spectroscopy and atomic force microscopy were employed to verify the presence of quality graphene. The graphene was patterned using a reactive ion oxygen (RIE) etch. A sacrificial nickel (Ni) layer was deposited around the patterned graphene using a photolithographic lift off process. The entire sample was then blanketed with 2 nm of electron beam evaporated hafnium, 15 nm of atomic layer deposition hafnium oxide (HfO_2), and 500 nm of plasma-enhanced chemical vapor deposition low stress silicon nitride (Si_3N_4).

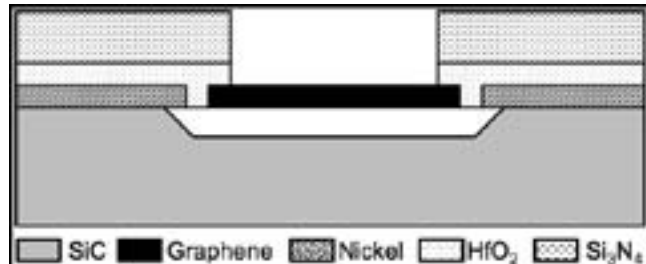


Figure 1: Cross-sectional view of all layers involved in the fabrication process.

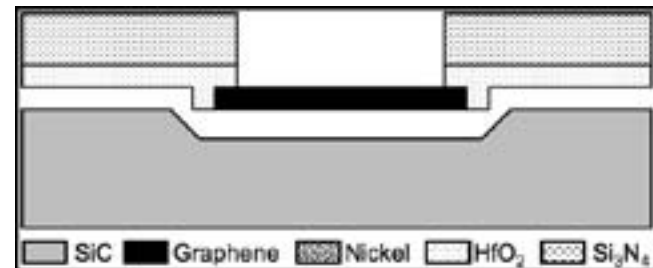


Figure 2: Cross-sectional view after dissolution of nickel layer. Notice the SiC substrate is entirely detached from the graphene and the graphene support structure.

SiN was chosen for its rigidity and would serve as the support structure after detachment of the graphene structures from the SiC substrate. HfO was employed to prevent the plasma-enhanced deposition of SiN from destroying the graphene structures. To enhance the uniformity of the HfO deposition, a seed layer of electron beam evaporated Hf was deposited and allowed to oxidize. This ensured a continuous protective coating of HfO over the graphene structures. The concept stemmed from literature reporting the use of seed layer aluminum for enhanced aluminum oxide growth [7].

The SiN atop the patterned graphene areas was partially etched away using a CF_4 RIE. Subsequent immersion in buffered oxide etch 6:1 removed the HfO layer. The graphene was then suspended by removing the underlying SiC via a newly developed photoelectrochemical (PEC) etch process [8]. Successful lift off required the SiC undercut to reach the Ni layer (see Figure 1). Finally, Ni etchant was employed to dissolve the sacrificial Ni layer. The graphene—now wholly supported by the low stress SiN—was lifted off the SiC substrate and transported to a TEM grid for analysis. Preliminary imaging was conducted using scanning electron microscopy (SEM).

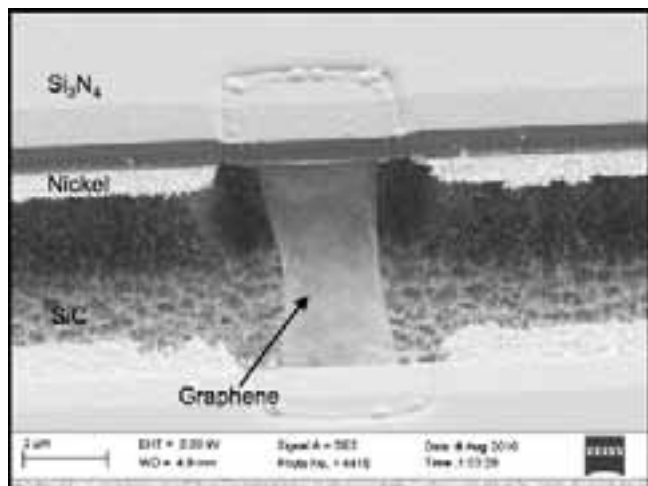


Figure 3: SEM of sample after PEC etch of SiC. [8]

Results and Discussion:

Figure 3 depicts a suspended graphene structure after a PEC etching of the SiC [8]. The transparency of the graphene structure suggests that it is a few monolayers. The SiN support structure is only attached to the SiC substrate via the sacrificial Ni layer. The PEC etch appears to have adequately undercut the SiC, so the nickel layer was dissolved.

Figure 4 depicts the SiN support structure lifted off the SiC substrate with the suspended graphene structure intact. Notice the wrinkles in the graphene, especially in the center and fringe areas. This undesirable effect is the result of a compromise in the fabrication process. A low stress SiN support structure was required to prevent the support structure from folding onto itself after detachment. This low stress constraint prevented the support structure from

providing the tensile stress necessary to hold the graphene taut.

The research demonstrated the ability of the fabrication process to detach suspended graphene structures from the SiC substrate. The graphene structures were successfully transported to a TEM grid for analysis. The research marks the first time graphene structures have been detached from the SiC substrate by means other than mechanical exfoliation.

Future Work:

Suspended graphene structures will be analyzed at the atomic level using TEM. TEM analysis will be employed to confirm the hexagonal lattice structure and carbon composition of the suspended graphene structures. TEM analysis will provide further information about the grain structure and overall quality of the silicon-face epitaxial growth process. Lastly, TEM analysis may provide new insights into silicon-face graphene growth.

Acknowledgements:

I thank my principal investigator, Prof. Michael Spencer, and mentor, Shriram Shivaraman, for their invaluable research guidance and patience. I also express my gratitude to the NSF for funding the NNIN REU Program through which this research was conducted.

References:

- [1] Castro Neto, A. et al., Physics World. Nov. (2006).
- [2] Katsnelson, M. Materials Today. 10, 20 (2007).
- [3] Tedesco, J.L. et al., Applied Phys. Lett. 96, 222103 (2010).
- [4] Balandin, A. et al., Nano Lett. 8, 902 (2008).
- [5] Lee, C. et al., Science 321, 385 (2008).
- [6] First, P.N. et al., MRS Bulletin 35, 296 (2010).
- [7] Kim, S. et al., Appl. Phys. Lett. 94, 062107 (2009).
- [8] Shivaraman, S. et al., Nano Lett. 9, 3100 (2009).

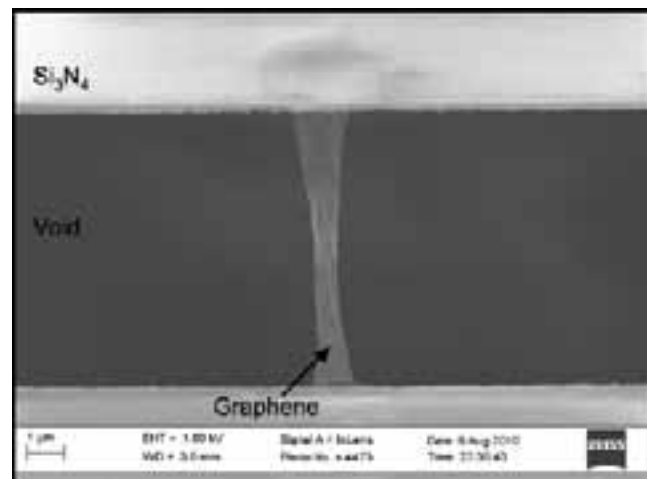


Figure 4: SEM of sample after dissolution of nickel layer and transport to transmission electron microscope grid.

Sub-20 Nanometer Electron Beam Induced Deposited Gold Plasmonic Nanostructures

Claire McLellan
Physics, Wake Forest University

NNIN iREU Site: National Institute for Materials Science (NIMS), Tsukuba, Ibaraki, Japan

NNIN iREU Principal Investigator(s): Dr. Kazutaka Mitsuishi, High Voltage Electron Microscopy, NIMS, Tsukuba, Japan

NNIN iREU Mentor(s): Dr. Ilya Sychugov, High Voltage Electron Microscopy, NIMS, Tsukuba Japan

Contact: mcleca8@wfu.edu, mitsuishi.kazutaka@nims.go.jp, sychugov.ilya@nims.go.jp

NNIN iREU Program

Introduction:

Photons provide a very fast medium with which to transfer information, but photonic devices' sizes are limited by the diffraction limit. The smallest photonic devices are in the order of 100 nanometers. In order to use photons in a smaller device, one can employ surface plasmons. Surface plasmons are resonant modes formed from oscillations of the conducting band in a metal when they interact with an electromagnetic wave. The modes propagate along the metal and semiconductor substrate with the same frequency as the incoming light but a shorter wavelength allowing for smaller devices [1].

We studied gold (Au) because, when deposited on silica, it has short wavelength surface plasmons when interacting with visible light according to Maxwell's equations (see Figure 1) [2, 3].

Our method for studying Au involved using electron microscopy. We used electron beam induced deposition (EBID) to create our structures. EBID provides a method that is reproducible and has high resolution. EBID is a direct write lithography method that uses a focused electron beam (e-beam) in an electron microscope. The beam breaks the bonds in a precursor molecules located in the vacuum chamber into volatile and nonvolatile components.

The nonvolatile component, in our case gold, will stick to the substrate, while the volatile component, carbon, remains in the chamber or the electron microscope. EBID devices have a large amount of carbon contamination. In order to develop structures, it is important to remove any contamination in the structures. We annealed the devices in the presence of oxygen to help remove contamination [4].

The purpose of this project was to create Au nanodots and improve their carbon to Au ratio using annealing.

Experimental Procedure:

Au nanodots were deposited by e-beam-induced deposition using a scanning electron microscope (SEM, JEOL JSM-6700-F). A silicon membrane substrate was milled to about 100 nm, using a dimpling machine and ion milling. A gold precursor powder, dimethylgold(trifluoro)acetylacetone [$\text{Me}_2\text{Au}(\text{tfac})$], at 65°C, was used as the Au source. The vacuum chamber was 4×10^{-4} Pa. and the beam current was 30 pA at 30 keV. A pattern with a line of dots was predetermined using the microscope's computer software. Nanodots were deposited for times between 4 seconds to 12 seconds in rows of 4 to 10 dots.

Deposited nanodots were analyzed by two microscopes. A transmission electron microscope (TEM, JEOL 2100) with energy dispersive x-ray spectroscopy (EDS) was used to determine if Au was present in the dots [5]. A scanning transmission electron microscope (STEM, JEOL JEM-2500SES) with electron energy loss spectroscopy (EELS) was used to image the sample and determine if carbon was present [5].

To remove carbon contamination from the Au dots we annealed the samples. The first set of dots was annealed at 400°C for 10 minutes. The second set of dots was annealed at 200°C for 10 minutes.

The dots were then reanalyzed using STEM.

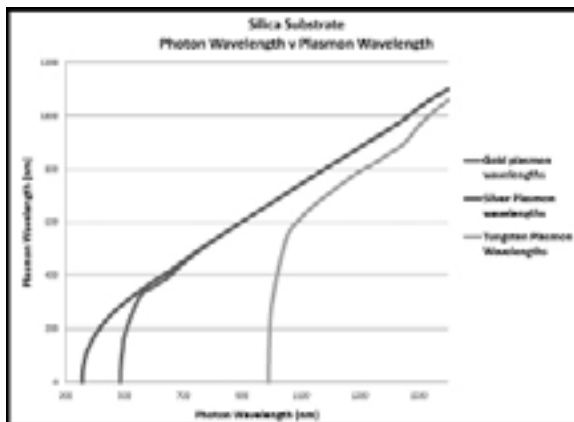


Figure 1: This graph is a simulation of using the solutions to Maxwell's equations. The plasmon wavelength becomes very small in the visible light range for Au, Ag, and tungsten.

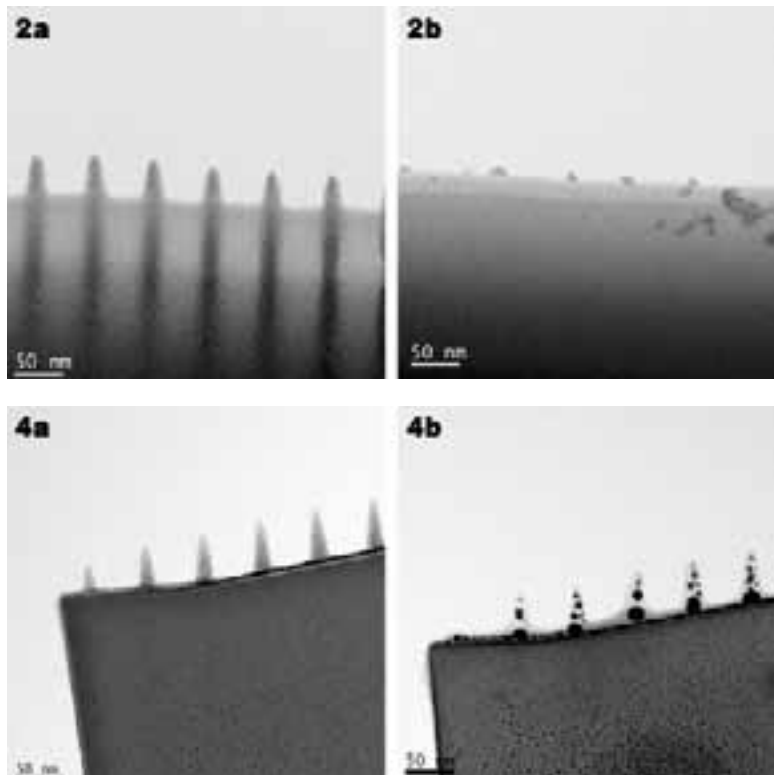


Figure 2, top: STEM bright field images of Au nanodots deposited for 8 seconds. [2a] was taken before annealing at 400°C and [2b] was taken after annealing. Gold is dark and carbon is light.

Figure 4, bottom: STEM bright field images of Au nanodots deposited for 8s. [4a] was taken before annealing at 200°C and [4b] was taken after annealing. One can see the how the gold agglomerated after annealing.

Results and Conclusions:

EDS and EELS confirmed that the dots were composed of gold with carbon contamination.

Annealing at 400°C for 10 minutes was too abrasive such that only $9.1\% \pm 5.4\%$ of the original dot remained (Figure 2). An interesting affect was that the gold crystallized during annealing (Figure 3).

Annealing at 200°C for 10 minutes caused the gold to crystallize as well as agglomerate (figure 4). The lower annealing temperature created dots that were closer to our goal of creating pure gold nanodots since the gold particles became larger.

Future Work:

We would like to adjust the temperature and time of annealing for optimal carbon removal. There are other methods for removing carbon including plasmon etching and incorporating gas assisted EBID.

Also, sample preheating has been shown to help the purity for tungsten and could be employed for gold [7].

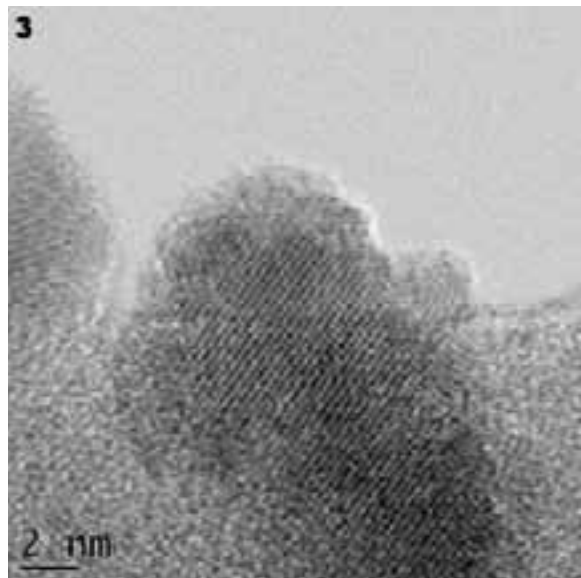


Figure 3: A high resolution image of an Au nanodot after annealing at 400°C. The Au crystal structure is visible.

Acknowledgements:

I would like to acknowledge the NNIN iREU Program and the NSF for funding this internship, and NIMS for providing the resources for my project. I would like to thank the principal investigator of this work, Dr. Kazutaka Mitsuishi, and my mentor, Ilya Sychugov, for their guidance in this project and scientific research.

References:

- [1] Atwater, H. "The promise of plasmonics" *Scientific American*. April, 56-63, (2007).
- [2] Murray, A. W. and Barnes W. L. "Plasmonic Materials" *Advanced Materials*, 19, 3771-3782, (2007).
- [3] Refractive Index database. [Refractiveindex.info](http://www.refractiveindex.info) (2010).
- [4] van Dorp, W and Hagan, C. "A critical review of focused electron beam induced deposition" *Sub-10 nm focused electron beam induced deposition*, 5-73 (2008).
- [5] Williams, D. and Carter, B. *Transmission Electron Microscopy*, 5- 11, 131-152, 573-585, 637-651. (1996).
- [6] Brydson, R. *Electron Energy Loss Spectroscopy*, 1-26 (2001).
- [7] Sychugov I., Nakayama Y., and Mitsuishi K. "Composition Control of E-beam Induced Nanodeposits by Surface Pretreatment and Beam Focusing" *J. Phys. Chem. C*. Volume 113. Page 21516-21519 (2009).

Fabrication of Graphene Structures Using an Atomic Force Microscope

Christopher O'Connell

Mechanical Engineering, University of Rhode Island

NNIN REU Site: Cornell NanoScale Science and Technology Facility, Cornell University, Ithaca, NY

NNIN REU Principal Investigator(s): Amit Lal, School of Electrical and Computer Engineering, Cornell University

NNIN REU Mentor(s): Bryan Hicks, School of Electrical and Computer Engineering, Cornell University

Contact: chrsr34@hotmail.com, amit.lal@cornell.edu, bryan.t.hicks@gmail.com

Abstract:

Graphene has been theoretically and experimentally shown to display exceptional thermal, electrical and mechanical properties, which could potentially revolutionize modern electromechanical devices. Despite the possibilities, the capabilities of this two dimensional (2-D) crystal have yet to be harnessed due to limitations on fabrication techniques and large-scale manufacturing processes. To address these limitations, we investigated an atomic force microscope (AFM) technique, known as anodic oxidation, to etch graphene. This technique achieved graphene patterning on a sub-100 nm scale at a fraction of the time and cost of other methods. Line-widths of the graphene etches were roughly 50 nm. Graphene Van Der Pauw structures and nanoribbon devices will be fabricated on top of 300 nm silicon nitride (SiN) membranes. Chrome/gold electrodes will be evaporated onto the nitride membranes and chemical vapor deposition (CVD)-grown graphene will be transferred on top of them. The graphene will then be patterned into specified dimensions for the Van Der Pauw structures and nanoribbon devices. They will then be electrically characterized and optimized.

Introduction:

Currently there are a limited number of ways to pattern graphene at the nanoscale. The most precise method thus far is electron-beam lithography (EBL) with its finest features in the 10 nm range. Despite the strengths of EBL, it is both extremely costly and time-consuming. A viable alternative is anodic oxidation via an atomic force microscope (AFM) [1]. Anodic oxidation occurs by applying a voltage between the tip and substrate in the presence of water. With graphene on the substrate surface accompanied by a water meniscus, an electrochemical reaction is induced as shown in Figure 1. This reaction causes the graphene to locally oxidize and results in two different scenarios: an etching away of the graphene at sample voltages above 6V and a buildup of reaction products at voltages below 6V. This AFM technique has been established with graphite [2], but has not yet been fully developed with graphene.

This technique is promising for a number of reasons. The sample requires no preparation before etching, unlike EBL, thus there would be no added impurities introduced, such as photoresist. The technique is also versatile; it can be controlled in real-time using programming software. Furthermore, it is cost-effective and efficient using almost the same amount of power and time required to operate the AFM by itself.

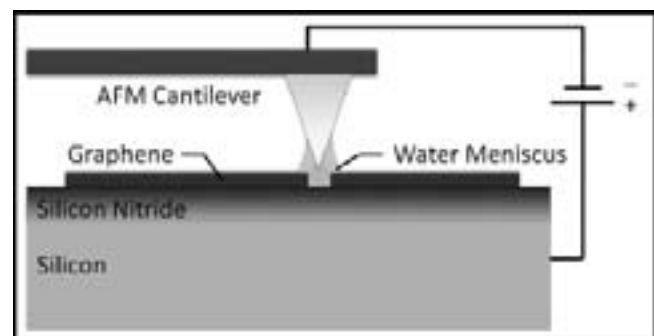


Figure 1: Schematic of anodic oxidation using an AFM.

Experimental Methods:

Graphene etching was first achieved on a sample of graphene on silicon dioxide (SiO_2). Humidity of the room was routinely checked to be above 30%. This was above the threshold for a water meniscus to form and facilitate the electrochemical reaction. The etch process consisted of imaging a specific area, writing a program for the etching parameters and subsequently imaging the same area. The anodic oxidation hardware and AFM tip translation was controlled using a C++ program. A bias of -7V was applied

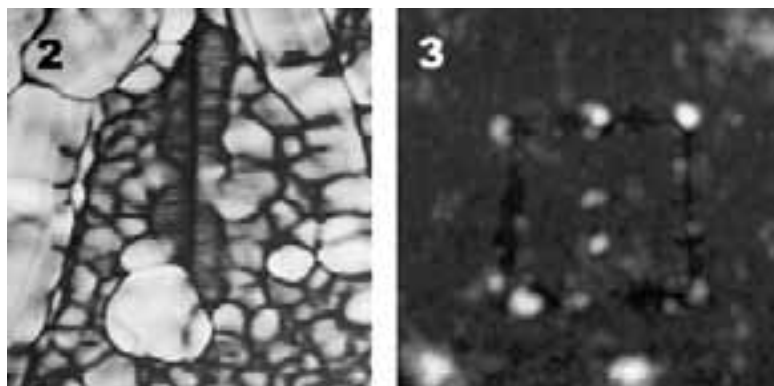


Figure 2, left: AFM image of an 800 nm line with depth of 2 nm.

Figure 3, right: AFM image of a 600 nm box etch with 3 nm depth.

between the tip and substrate for etching. The tip z-depth into the surface was set to -40 nm in order to ensure contact between the tip and surface.

An 800 nm line was successfully etched into multi-layer graphene with a depth of about 2 nm as shown in Figure 2. A box etch was also successfully etched into multi-layer graphene with a depth of 3 nm as seen in Figure 3. Note the accumulations along the etch lines. These are believed to be carbon-based products from the reaction. There was also a tip wear dependence to the etching such that as the tip radius became larger, the etch width also increased proportionally.

In order to fully display the capabilities of this graphene etching technique, Van Der Pauw structures and graphene nanoribbon devices were made on top of silicon nitride (Si_3N_4) membranes. Membranes were used for optical transparency and future piezoresistance measurements. The membranes were made by depositing 300 nm of Si_3N_4 on both sides of the Si wafer using low-pressure chemical vapor deposition. The backside nitride was then patterned using photolithography and subsequently plasma etched using CHF_3/O_2 . With the nitride layer acting as a mask, the Si was then etched using potassium hydroxide (KOH), thus creating the nitride membranes on the front side. Electrodes consisting of an 8 nm chrome adhesion layer followed by 40 nm of gold were then evaporated onto the membranes. Graphene was grown on top of a copper foil using CVD and then coated with a transfer layer of poly(methyl methacrylate) (PMMA) on top. The copper was then etched away in ferric chloride and the remaining graphene was transferred onto the electrodes and membranes (Figure 4).

Results and Conclusion:

While graphene was successfully etched on the SiO_2 substrate, the Si_3N_4 membranes were not so cooperative. The failure to etch was believed to be attributed to several factors.

First, because the membranes were suspended, the voltage between the tip and substrate was indirect, and would result in a non-localized electric field. This could be resolved by applying the voltage between an electrode and the tip, thus isolating the graphene. Another problem may have been the z-depth to which the tip was pushed into the surface. If it was pushed too far, the water meniscus may have been pushed aside, thus suppressing the reaction. There is also a chance that the parameters, such as the meniscus layer and mechanical control of the AFM, were not being controlled to the precision needed at the nanoscale. These parameters become critical factors for a controlled etch, yet may not be precise at such a small scale.

Acknowledgements:

Special thanks to Melanie-Claire Mallison, Amit Lal, Bryan Hicks, Lynn Rathbun, the CNF staff and all those who helped make this experience extraordinary. Also to the National Nanotechnology Infrastructure Network Research Experience for Undergraduates (NNIN REU) Program and National Science Foundation for funding.

References:

- [1] Weng L, Zhang L, Chen Y P, Rokhinson L P, Applied Physics Letters 93, 093107 (2008).
- [2] Yoshimizu N, Hicks B, Lal A and Pollock C R, Nanotechnology 21, 095306, (2010).

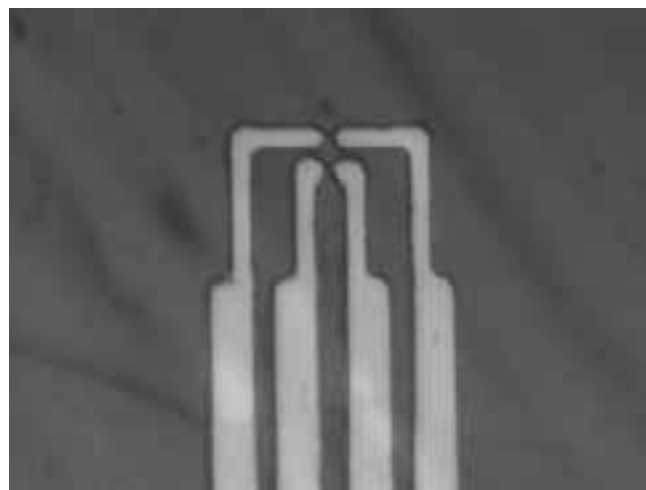


Figure 4: Graphene on top of electrodes and membrane.

Fabrication of Gold Nanoparticles Using E-beam Lithography: Effect of Development Conditions on Shape and Resolution

Fiona O'Connell

Materials Engineering, Loyola University Maryland

NNIN REU Site: Nanotechnology Research Center, Georgia Institute of Technology, Atlanta, GA

NNIN REU Principal Investigator(s): Dr. Mostafa El-Sayed, School of Chemistry and Biochemistry, Georgia Institute of Technology

NNIN REU Mentor(s): Rachel Near, School of Chemistry and Biochemistry, Georgia Institute of Technology

Contact: fmoconnell@loyola.edu, mostafa.el-sayed@chemistry.gatech.edu, rachelgivens@gatech.edu

Abstract and Introduction:

Due to the short wavelengths of electrons relative to those of the light photons used in optical lithography, electron beam lithography (EBL) is an extremely high-resolution lithographic process. Importantly, however, the overall resolution achieved is greatly affected by the development conditions used.

The purpose of the work described in this paper was to determine the optimal development conditions for the fabrication of rectangular gold (Au) nanoparticles via EBL.

Silicon (Si) wafer substrates were coated with a polymer resist (PMMA) prior to exposure to the electron beam used to write the desired pattern via EBL. Following exposure, the substrates were developed. The developers tested were solutions comprised of different mixtures of methyl isobutyl ketone (MIBK) and isopropyl alcohol (IPA), ranging from a MIBK:IPA ratio of 1:3 (v/v) to pure IPA. The 1:3 MIBK:IPA is a common developer that produces high-resolution samples with small feature sizes.

Pure IPA was chosen as a developer based on the results of Yasin [1], which yielded higher-resolution samples than those developed using 1:3 MIBK:IPA.

Experimental Procedure:

Hollow, rectangular, Au nanoparticle arrays were fabricated using a JEOL JBX-9300FS 100kV electron beam lithography (EBL) system. The substrates were pieces of Si wafers approximately $3 \times 3 \text{ cm}^2$. The array consisted of 42 windows, each measuring $300 \times 300 \mu\text{m}^2$. Each window contained an array of thousands of particle pairs with varying interparticle separations. The desired outcome was the production of homogeneous particles that measured $180 \times 240 \text{ nm}$ and contained hollow centers $60 \times 120 \text{ nm}$ in area. To prevent unwanted interactions between particle pairs, every particle pair was spaced $1 \mu\text{m}$ from the next. All particle and pattern parameters were specified while writing the files for the EBL system.

To prepare the Si substrates for exposure, they were rinsed with acetone, dried with N_2 , spin-coated with 80 nm

of poly(methyl methacrylate) (PMMA), and baked for two minutes at 180°F. The substrates were patterned using electron beam doses of 500-3500 $\mu\text{C}/\text{cm}^2$ at 2 nA.

Following exposure, the samples were developed to remove the exposed patterns. During the development process, the following ratios of solutions containing MIBK (methyl isobutyl ketone) and IPA (isopropyl alcohol) were tested to optimize resolution: 1:3 MIBK:IPA, 1:5 MIBK:IPA, 1:7 MIBK:IPA, and pure IPA.

All the samples, except for the pure IPA sample, were developed for 10 seconds in the above solutions followed by a rinse in IPA for 30 seconds. The pure IPA sample was developed for 40 seconds. A CVC electron beam evaporator was then used to deposit a 0.5 nm chromium (Cr) adhesion layer (0.1 Å/s) followed by a 22 nm layer of Au (0.5 Å/s). Finally, the remaining resist was removed by soaking the wafer in 1165 for approximately 4.5 hours. The samples were imaged using scanning electron microscopy (SEM).

Results and Conclusion:

The initial base dose used for fabrication was $3500 \mu\text{C}/\text{cm}^2$. It was apparent upon examination of the substrate, via SEM (LEO 11530 FE-SEM) at 8 kV accelerating voltage using a secondary detector, that the particles were overdosed causing the exposure of a wider pattern than specified. Particle dimensions became progressively more accurate as the base dose was modulated to $1000 \mu\text{C}/\text{cm}^2$ (see Figure 1).

Changes in particle resolution due to development conditions were determined using SEM images taken on the Zeiss Ultra 60 FE-SEM at 10 kV accelerating voltage using a secondary electron detector by Rachel Near (see Figure 2). Resolution was measured based on the linearity of the particles edges and the measure of perpendicularity of the vertices (corners).

The resolution trended as predicted, with the 1:3 MIBK:IPA sample having the highest resolution followed by the 1:5 MIBK:IPA sample, and the 1:7 MIBK:IPA sample producing the poorest-resolution samples.

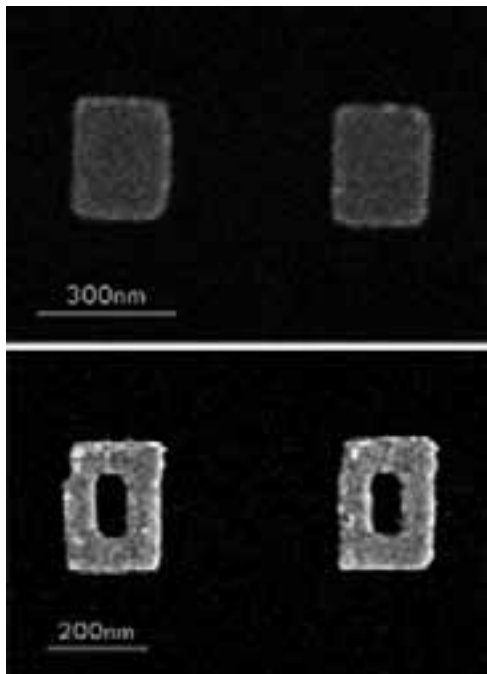


Figure 1: Comparison of overdosed particle with base dose of $3500 \mu\text{C}/\text{cm}^2$ (L) and accurately dosed particle with base dose of $1000 \mu\text{C}/\text{cm}^2$ (R).

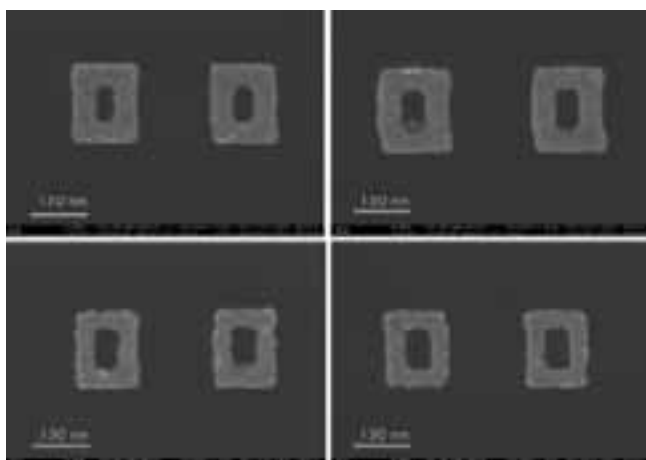


Figure 2: Results of varied developers on particle resolution. 1:3 MIBK:IPA top left, 1:5 MIBK:IPA top right, 1:7 MIBK:IPA bottom left, Pure IPA bottom right.

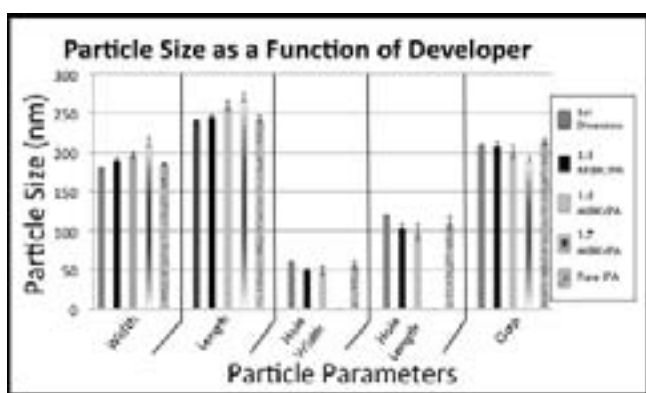


Figure 3: Graph of particle size accuracy.

Surprisingly, the pure IPA sample produced much better resolution than anticipated and actually had a resolution comparable to that obtained with the 1:3 MIBK:IPA sample.

To provide a quantitative measure of the particle size accuracy, the particle parameters were measured using images taken on the Leo SEM (see Figure 3). The pure IPA sample had measurements that were closest to the specified particle dimensions.

Based on the foregoing results, the 1:3 MIBK:IPA and pure IPA outperformed both 1:7 and 1:5 solutions of MIBK:IPA. While pure IPA produced particles with sharper edges, corners, and centers as well as more accurately sized particles, 1:3 MIBK:IPA had a higher ratio of particles that were actually hollow. IPA thus appears to be a viable option as a developer, producing very accurately sized particles of satisfactory resolution.

Future Work:

Further experimentation using IPA as a developer is necessary. Future research should also vary the development time to further optimize resolution. Nonetheless, the particle resolution is adequate for characterization of their optical properties as a function of size, shape, orientation, and interparticle spacing.

Acknowledgements:

I would like to thank the National Science Foundation (NSF), the NNIN REU Program, and the Georgia Institute of Technology for funding and providing facilities for conducting this research. Furthermore I would like to express my appreciation to Dr. El-Sayed, Rachel Near, and the Laser Dynamics Lab for including me in their research and guiding me through this work. Finally, the success of the program would not have been achievable without the combined efforts of Dr. Nancy Healy, Katie Hutchison, and Joyce Palmer.

References:

- [1] Shazia Yasin, D.G. Hasko, H. Ahmed. "Comparison of MIBK/IPA and water/IPA as PMMA developers for electron beam nanolithography," *Microelectronic Engineering*. Volumes 61-62, 745-753, 2002.

C₁₀- and C₁₂-BTBT Single Crystalline Organic Field Effect Transistor

Si Hui Athena Pan
Physics, Brandeis University

NNIN iREU Site: National Institute for Materials Science (NIMS), Tsukuba, Ibaraki, Japan

NNIN iREU Principal Investigator(s): Dr. Kazuhito Tsukagoshi, Materials Nanoarchitectonics, NIMS, Japan

NNIN iREU Mentor(s): Chuan Liu, Materials Nanoarchitectonics, National Institute for Materials Science, Japan

Contact: fromaspan@gmail.com, tsukagoshi.kazuhito@nims.go.jp, liu.chuan@nims.go.jp

NNIN iREU Program

Introduction:

An organic field-effect transistor (OFET) is the key component in realizing flexible organic electronics, and an OFET is cheaper and more energy-efficient for production than its inorganic counterpart [1]. In particular, single crystalline OFETs have been shown to exhibit higher carrier mobility than thin film OFETs made of polycrystalline or amorphous semiconductors [1].

Recently, materials based on a [1]benzothieno[3,2-*b*][1]benzothiophene (BTBT) core structure with 2,7-dialkyl derivatives (C_n-BTBT) have been found to be air-stable and solution-processible organic semiconductors [2]. C₈-BTBT has been demonstrated to form single crystals of hundreds of microns in length on polymer dielectric surface [3]. Single-crystal C₈-BTBT OFETs exhibit average mobility of 3 cm²V⁻¹s⁻¹, which is higher than conventional thin-film OFETs and comparable to some inorganic FETs [1, 3]. Until this work, none of the other C_n-BTBT materials have been explored for single-crystal OFETs applications.

Here we report the fabrication and characterization of C₁₀-BTBT and C₁₂-BTBT single crystal OFETs.

Experimental Technique:

To fabricate single-crystal OFETs, we followed the procedures previously reported by Liu, et al. [3], which involved spin-coating, solvent vapor annealing (SVA) and thermal evaporation of metal electrodes.

Results and Discussion:

Figure 1 compares the crystal size of C₈-BTBT, C₁₀-BTBT and C₁₂-BTBT. C₈-BTBT crystals are typically several 100 microns long. On the other hand, a large crystal on a C₁₀-BTBT sample could be longer than 50 μ m, but shorter than 100 μ m. Most C₁₂-BTBT crystals do not exceed 50 μ m.

We suspect this is due to the different solubility of the three functional materials in chloroform. For solubility in chloroform, we have the following relationship: C₈-BTBT > C₁₀-BTBT > C₁₂-BTBT.

Since C₈-BTBT is most soluble, more C₈-BTBT molecules become mobilized during SVA than C₁₀- and C₁₂-BTBT molecules. Therefore, C₈-BTBT molecules form the largest crystal.

Large crystals are more desirable for OFET fabrication. Treossi, et al. have demonstrated that lowering the temperature of the samples with respect to that of the solvent by 1~2°C will increase the amount of vapor absorbed on the sample surface, which in turn enhances the molecules' functional long-range mobility [4]. Hence, larger crystals can be obtained.

We conducted two temperature-enhanced solvent vapor annealing (TESVA) experiments using C₁₀-BTBT molecules only. First, we put a glass of cool water on top of the sample during SVA. Since there was no external cooling device to

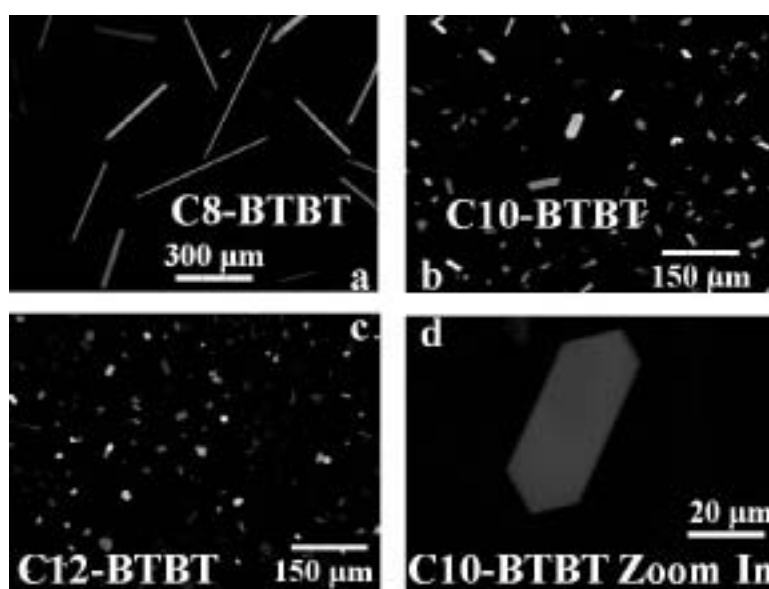


Figure 1: C₈- (reproduced from Liu, et al. [3]), C₁₀- and C₁₂- BTBT crystals.

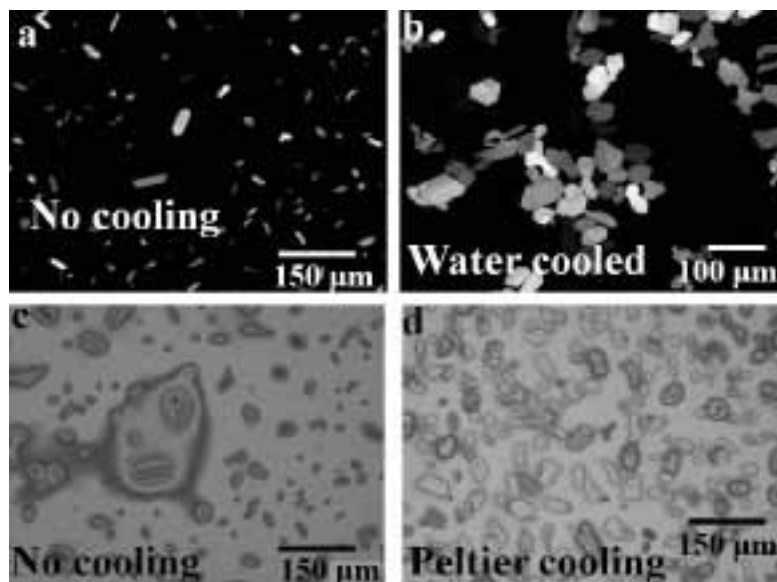


Figure 2: Comparison between cooled and non-cooled C_{10} -BTBT samples.

keep the water temperature constant, the cooling is only effective during the first hour.

Figure 2a and 2b compares a water-cooled sample with a non-cooled sample. The crystal size of a water-cooled sample is relatively larger and aggregation of these crystals is observed. We believe this result shows that cooling effect help the crystal growth.

In order to better control the cooling effect, we employed a Peltier cooler to set the sample temperature to be $1\text{--}2^{\circ}\text{C}$ lower than room temperature (T_{room}). However, since T_{room} fluctuates, the temperature difference between the sample and the solvent is often more than 2°C . As Treossi, et al. have explained, when the temperature difference between sample and solvent is too large, macroscopic droplets will form on the surface of the sample [4]. Hence, the functional materials will be completely dissolved and become amorphous once again.

Since it is difficult to control T_{room} , we carried out the Peltier cooling experiment discontinuously, stopping it every two hours to adjust the sample temperature. At the end, only one cooled sample was successfully made (Figure 2d).

Comparing Figure 2c and 2d, we observe little difference in crystal size between the two samples. However, since only one sample was successfully made and the experiment was carried out discontinuously, we cannot conclusively determine whether the cooling effect is promoting the crystal growth or not. More samples and better control of the solvent temperature is needed before we can obtain any conclusive results.

It is relatively difficult to fabricate OFETs with C_{10} -BTBT or C_{12} -BTBT since the channel between two electrodes is usually longer than the crystals. Nonetheless, after many trials, we successfully obtained four devices. The mobilities and threshold voltages of these OFETs are listed in Table 1. Notice devices a and b exhibit very different mobilities from devices c and d. The electrodes of devices a and b were evaporated together. Devices c and d were also fabricated together, but on a different day and with a different evaporator from devices a and b. It is very likely that the electrodes of devices a and b were not well made, leading to large contact resistance and lower mobilities. The mobilities of devices c and d are among the highest ones of single-crystalline OFETs.

At this point, we cannot compare the electronic properties of C_8 -BTBT and C_{10} -BTBT due to the limited sample size (i.e., four) obtained for C_{10} -BTBT. However, these results once again demonstrate that our fabrication method has high potential of producing inexpensive high performance single-crystal OFETs on polymer substrate.

Acknowledgements:

I would like to thank Dr. Chuan Liu, Dr. Kazuhito Tsukagoshi, and the rest of the pi-electronic group for their guidance and support, to the NNIN iREU program and NIMS of Japan for providing me with this opportunity and to the NSF for funding this project.

References:

- [1] T. Hasegawa and J. Takeya, *Sci. Technol. Adv. Mater.* 10, 024314 (2009).
- [2] H. Ebata, T. Izawa, E. Miyazaki, K. Takimiya, M. Ikeda, H. Kuwabara, T. Yui, *J. Am. Chem. Soc.* 129(51), 15732 (2007).
- [3] C. Liu, T. Minari, X. Lu, A. Kumatai, K. Takimiya, K. Tsukagoshi, *Adv. Mater.*, submitted.
- [4] E. Treossi, A. Liscio, X. Feng, V. Palermo, K. Müllen, P. Samori, *Small* 5(1), 112(2009).

OFET Device	Mobility (cm V ⁻¹ s ⁻¹)	Threshold Voltage (V)
a	0.03	-19.98
b	0.03	-19.64
c	6.00	-11.67
d	5.18	-15.28

Table 1: Characteristics of four C_{10} -BTBT single-crystal OFETs.

Transferring Chemical Vapor Deposition Grown Graphene

Phi Pham

Physics, University of Colorado Boulder

NNIN REU Site: Microelectronics Research Center, The University of Texas, Austin, TX

NNIN REU Principal Investigator(s): Rodney Ruoff, Mechanical Engineering, University of Texas at Austin

NNIN REU Mentor(s): Ji Won Suk, Mechanical Engineering, University of Texas at Austin

Contact: Phi.Pham@colorado.edu, R.Ruoff@mail.utexas.edu, jwsuk@mail.utexas.edu

Abstract:

Since the unique properties of graphene have made it a candidate to be integrated into a wealth of applications, an industrial process for creating graphene should be developed. Although the technique to produce graphene on copper foils using chemical vapor deposition (CVD) [1] has been discovered by the Ruoff Group, it is still needed to develop an efficient way to transfer graphene onto arbitrary substrates, while maintaining its electrical and mechanical properties over large length scales. Our research investigated methods to optimize graphene transfer using two different ‘carrier’ materials. First, we explored using poly(methyl methacrylate) (PMMA) as a carrier for the graphene and tried to optimize the quality of the transferred graphene. We also looked into the use of thermal release tape as a carrier and investigated the role that adhesion plays in transfer.

Experimental Process:

By flowing hydrogen and methane through a high temperature furnace, monolayer graphene can be formed on the surface of the copper foils. The methane is catalytically decomposed on the copper surface at the high temperature (typically around 1000°C), which leads to nucleation, island growth, and finally complete coverage with a poly-domain film of monolayer graphene (Professor Ruoff and colleagues use ‘domain’ rather than ‘grain,’ as a grain is typically considered to be three dimensional). Because a copper foil cannot be used as a substrate in the electrical testing of graphene, the graphene must be transferred to a different substrate for various applications.

Our transfer process started with etching one side of the copper using an iron nitrate solution [2]. After a short copper etch, we applied a solid carrier to help transfer the graphene; subsequently, the rest of the copper was etched away. The carrier with graphene was then transferred onto a substrate like silicon dioxide / silicon (SiO_2/Si). After removal of the carrier, only graphene was left on the substrate. This transfer procedure can be modified with the objective of getting the highest quality graphene after transfer.

The first portion of our research focused on using PMMA from Aldrich as a graphene carrier [3]. Our first experiment was to explore the method in which graphene contacted the substrate, in our case, SiO_2 . After the PMMA layer was dried, and the copper foil was fully etched, the graphene/PMMA stack was placed on top of a silicon wafer with graphene contacting the SiO_2 . The first method of creating contact was to apply an additional drop of liquid PMMA.

This method, invented by the Ruoff group, allowed the existing dried PMMA to dissolve, and the graphene to relax onto the substrate.

The next method to create contact of graphene to substrate was to heat the silicon wafer with the graphene/PMMA stack on top. We learned that heating the wafer allowed PMMA to become malleable, and our goal was to see if the graphene could thereby relax on the wafer surface.

We compared the results of each method using an optical microscope. Generally, transfers where the Si wafer substrate had been heated had fewer voids in the graphene film compared to transfers that used additional liquid PMMA. Decreasing the number of voids is important when configuring graphene in electrical and mechanical experiments.

In addition to exploring contact methods using PMMA, the removal of the PMMA was also investigated. The first method tried was to try to wash away the PMMA using acetone. Another method tried was to evaporate the PMMA using a furnace at 400°C with H_2 and N_2 gases. Comparing the results of each removal method with optical microscopy, it seems that evaporation removed PMMA to a greater extent than the acetone wash. Unfortunately, the evaporation process did create amorphous carbon, verified using Raman spectroscopy.

Thermal release tape (TRT) from Nitto Denko was also tested as a solid graphene carrier [4]. TRT was applied to graphene on copper foils and the TRT/graphene was trans-

ferred to a target substrate after dissolving copper. When the substrate was heated to a specific temperature, TRT released the graphene onto the target substrate.

We investigated three different types of TRT for graphene transfer. Figures 1-3 show optical microscope images of TRT transfers using TRT with increasing adhesion strengths. Our findings suggest that the strongest TRT used yielded the least amount of voids after transfer, but contained the most surface residue on graphene.

Results and Discussion:

In summary, after comparing methods for creating contact using PMMA, we found that the number of voids can be decreased by heating the substrate instead of using additional liquid PMMA. We found that evaporating PMMA, rather than using acetone to try to remove it by dissolution, can decrease the amount of residual PMMA left on the graphene surface. Our research also suggests that the strength of the adhesion of the TRT is apparently important in the transfer of graphene in terms of the number of voids per unit area in the graphene after transfer.

Future Work:

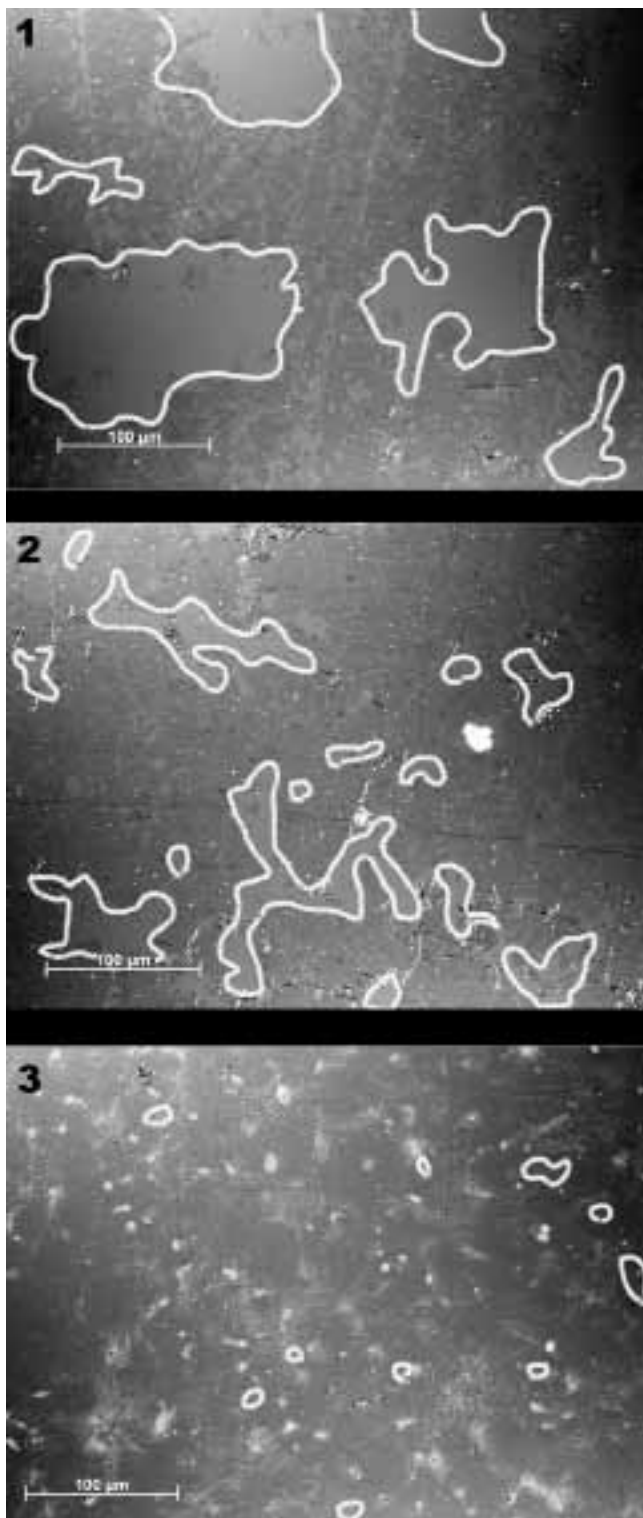
Our research efforts suggest directions for further work, and more measurements such as sheet resistance and transmittance should be conducted in order to further test which methods optimize transfer.

Acknowledgements:

I would like to thank Professor Ruoff, the Ruoff Group, and the University of Texas at Austin for hosting me, Weiwei Cai, and Richard Piner, Allison Cargile, the National Nanotechnology Infrastructure Network Research Experience for Undergraduates (NNIN REU) Program, and the National Science Foundation.

References:

- [1] Li, X, et al.: Large-Area Synthesis of High Quality and Uniform Graphene Films on Copper Foils, *Science*, 324, 1312-1314 (2009).
- [2] Yu, Q, et al.: Graphene Segregated on Ni Surfaces and Transferred to Insulators, *Applied Physics Letters*, 93, 113103 (2008).
- [3] Reina, A, et al.: Transferring and Identification of Single-and Few-layer Graphene on Arbitrary Substrates, *Physical Chemistry*, 112, 17741 (2008).
- [4] Anh, J, et al.: Roll-to-roll Production of 30-inch Graphene Films for Transparent Electrodes, *Nature Nanotechnology*, 10, 138 (2010).



Figures 1-3 show graphene transfers using thermal release tape. As adhesion strength increases, the amount of voids decreases.

High Spatial Resolution Kelvin Probe Force Microscopy with Shielded Probes

Kevin J. Satzinger

Physics and Mathematics, Truman State University

NNIN REU Site: Center for Nanoscale Systems, Harvard University, Cambridge, MA

NNIN REU Principal Investigator(s): Professor Robert M. Westervelt, Ph.D., Department of Physics and School of Engineering and Applied Sciences, Harvard University

NNIN REU Mentor(s): Keith A. Brown, School of Engineering and Applied Sciences, Harvard University

Contact: kjs8718@truman.edu, westervelt@seas.harvard.edu, kabrown@fas.harvard.edu

Abstract:

Kelvin probe force microscopy (KPFM) is a powerful technique to study electrical properties of materials on the nanoscale, but its spatial resolution is inherently limited by the long range of the electrostatic interaction. In this study, we mitigated these resolution limitations by electrically shielding the cantilever and the bulk of the tip. Shielded probes were created by coating conducting atomic force microscopy (AFM) probes with an insulating layer followed by a conducting layer. The tip of the probe was then exposed by focused ion beam (FIB) milling. The external metal layer formed a grounded electrical shield that extended to within two micrometers of the tip. The improvement in resolution due to shielding was analyzed using finite element electrostatic simulations.

Introduction:

KPFM was invented in 1991 at IBM by M. Nonnenmacher, M.P. O'Boyle, and H.K. Wickramasinghe as an extension of AFM that mapped sample work functions with spatial resolution of about 50 nm [1]. The Kelvin technique is non-contact and can operate in ambient conditions [2]. It has been used to study electronics, solar cells [3], biological cells [4], arrayed proteins, and deoxyribonucleic acid [2].

The basic principle of KPFM is illustrated in Figure 1. The tip of a conducting probe is brought into close proximity to the sample so that the tip and sample form a capacitor. The tip experiences a force proportional to the square of the tip-sample potential difference V_{ts} .

We electrically drove the tip at its mechanical resonance frequency while applying a DC Kelvin voltage, V_K , which we adjusted to null the oscillation and thus determine the

contact potential difference between the tip and sample. We used V_K to calculate the local sample work function Φ_s as described in Figure 1. The probe scans across an area of the sample to map the work function [1].

Several studies have sought to improve the resolution of KPFM, including operating under ultrahigh vacuum with simultaneous electrostatic and topographic data collection [5], optimization of tip and cantilever geometry through both simulations and experiments [6], and modifications to probes such as nanowire tipped probes [7].

We report on our efforts to improve the technique's spatial resolution by building electrostatically shielded probes. First, we present simulation data indicating the benefits of electrostatic shielding, and second, we present the actual fabrication of shielded probes.

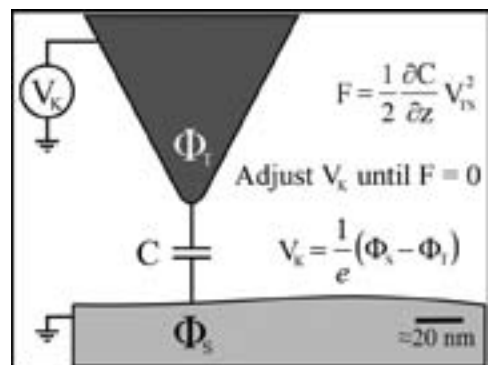


Figure 1: Schematic explanation of Kelvin probe force microscopy.

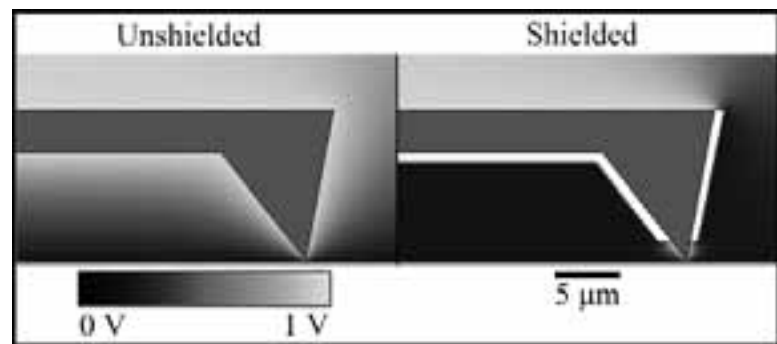


Figure 2: Two dimensional electrostatic simulations of the cross sections of unshielded and shielded probe-sample interactions.

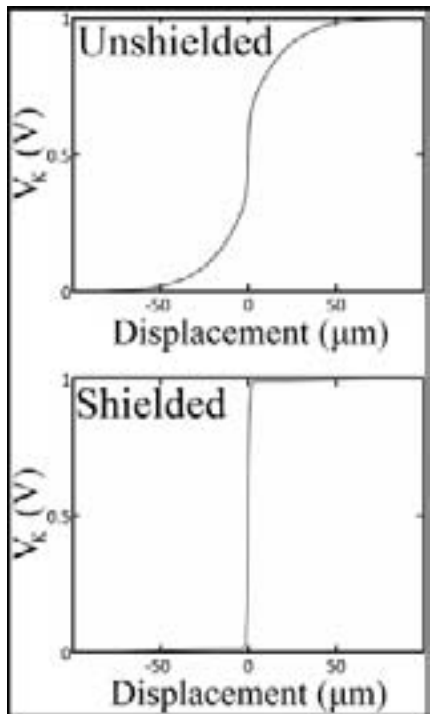


Figure 3: Results of three dimensional electrostatic simulations of probes traversing a 1 volt potential step.

Simulation of Shielded Probes:

We qualitatively demonstrated the benefits of shielding in Figure 2 with two dimensional (2D) electrostatic simulations. We simulated the local potential V while the probe was held at 1V and the sample was grounded. The left plot shows an unshielded probe, and the right plot shows a shielded probe with the same dimensions as those we fabricated. The potential profile of the unshielded probe exhibited a large gradient between all of the lower surfaces of the probe and the sample, indicating that the interaction area was not confined to the tip. The potential profile of the shielded probe showed that there was still interaction between the tip and sample, but it was limited to a much smaller region of the probe and sample, which will lead to improved resolution.

We quantified the resolution improvement afforded by shielding by 3D simulations of probes crossing a potential step from 0.0 volts to 1 volt. The results are plotted in Figure 3. Each probe measured a V_k that transitioned from 0.0 volts to 1 volt, but it took the unshielded probe substantially greater distances to resolve the change. The shielded probe exhibited remarkably superior performance.

Fabrication of Shielded Probes:

We started our fabrication process with commercially available conducting probes. We then coated them with approximately 1 mm of insulator using CVD. This enabled the probe and shield to be electrically disjoint. Next, we coated them with approximately 100 nm of metal, using thermal evaporation, forming the shield itself. Finally, we

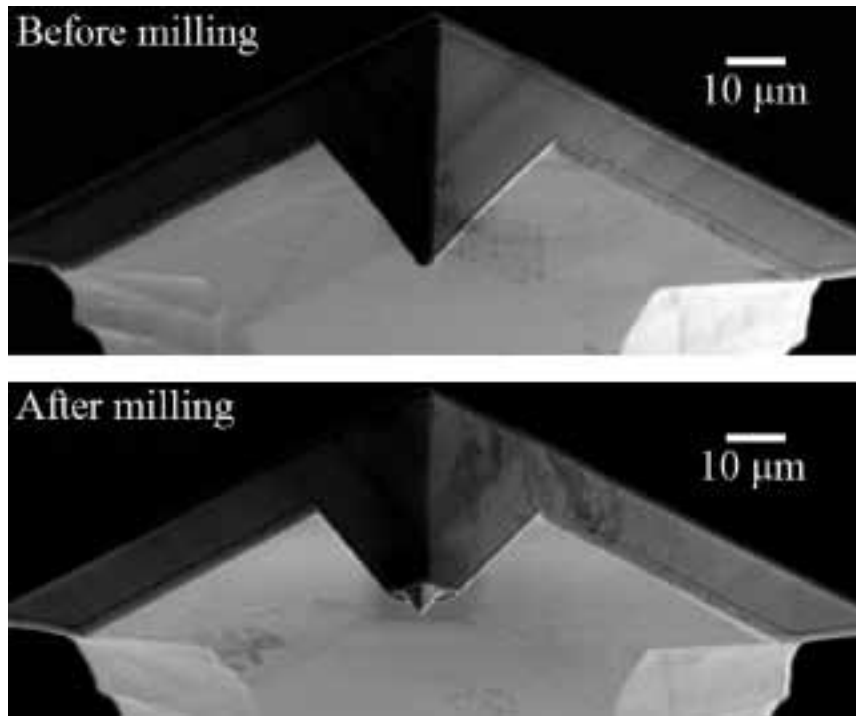


Figure 4: Scanning electron microscope images of probes before and after focused ion beam milling to expose the tip (front view).

exposed the lower 2 mm of the probe using FIB milling. Figure 4 shows shielded probes before and after milling to expose the tip.

Conclusion:

KPFM is a very useful technique in numerous fields because of its ability to measure the local work function with high spatial resolution. We present electrostatic shielding as a viable method of further improving the spatial resolution of Kelvin probe force microscopy.

Acknowledgements:

I thank Professor Robert M. Westervelt, Keith Brown, Dr. Kathryn Hollar, Professor John Free, Dr. Rafael Jaramillo, and Ruby Lee. This work was supported by the Harvard University Center for Nanoscale Systems, the NSF, and the NNIN REU Program.

References:

- [1] M. Nonnenmacher, et al., "KPFM," *Appl. Phys. Lett.* 58 2921 (1991).
- [2] A.K. Sinensky and A.M. Belcher, "Label-free and high-resolution protein/DNA nanoarray analysis using KPFM," *Nature Nanotech.* 2 653 (2007).
- [3] T. Martens, et al., "Morphology of MDMO-PPV PCBM bulk hetero-junction organic solar cells studied by AFM, KFM and TEM," *Proc. SPIE-Int. Soc. Opt. Eng.*, 4801, 40 (2003).
- [4] S. Yamashina and M. Shigeno, "Application of AFM to Ultrastructural and Histochemical Studies of Fixed and Embedded Cells," *J. Electron Microsc.* 44 462 (1995).
- [5] C. Sommerhalter, et al., "High-sensitivity quantitative KPFM by noncontact ultra-high-vacuum AFM," *Appl. Phys. Lett.* 75 286 (1999).
- [6] H. Jacobs, et al., "Resolution and contrast in KPFM," *J. A. Phys.* 84 1168 1998.
- [7] D.P. Burt et al., "Nanowire Probes for High Resolution Combined Scanning Electrochemical Microscopy – AFM," *Nano Lett.* 5 639 (2005).

Characterization of High Aspect Ratio Silver Micromachining for Radio Frequency Inductors

Natalie Swider

Material Science and Engineering, University of Illinois Champaign-Urbana

NNIN REU Site: Lurie Nanofabrication Facility, University of Michigan, Ann Arbor, MI

NNIN REU Principal Investigator(s): Professor Mina Rais-Zadeh, Department of Electrical Engineering and Computer Science, University of Michigan, Ann Arbor

NNIN REU Mentor(s): Yonghyun Shim, Department of Electrical Engineering and Computer Science, University of Michigan
Contact: natalieswider@gmail.com, minar@umich.edu, yhshim@umich.edu

Abstract:

This paper fully characterizes silver (Ag) electroplating and polishing processes for the implementation of low-loss integrated inductors. Silver was the chosen conductor material as it exhibits the highest electrical conductivity of all metals. Electroplating deposits a thick metal layer from a metal anode on a substrate by passing an electrical current between them. Depending on the type of electric current, the electroplating process can be classified into three categories: direct current (DC), pulse, and pulse-reverse (PR). PR electroplating offers the best surface profile and uniformity by decreasing the porosity of the electroplated regions. Therefore, in this study, we characterized silver PR electroplating and compared the results with DC electroplating. To reduce the surface roughness and further increase the uniformity, we utilized a silver polishing process and achieved a surface uniformity of better than $0.13 \mu\text{m}$. The same electroplating and polishing methods can be used with higher aspect ratio silicon molds enabling fast, smooth, and uniform deposition of silver.

Introduction:

Silicon technologies are becoming more desirable for wireless communication applications as they offer low-cost and high performance systems. In lumped radio frequency (RF) filters, high quality factor (Q) inductors and capacitors are needed for reduced insertion loss. Two loss mechanisms affect the inductor Q : the metal loss and the substrate loss [1]. The metal loss dominates at low frequencies while the substrate loss determines the Q at higher frequencies. To reduce the metal loss, several approaches have been taken including depositing thick layers of high conductivity metals and shaping the inductor geometry.

In this project, we electroplated thick Ag layers to decrease the metal loss. Furthermore, we used coplanar structures

with a distant ground to alleviate any uneven distribution of the current flow [1]. Since the current flows on the outer most surface of the conductor, the surface roughness plays an important role in determining the metal loss.

We optimized the deposition and polishing processes of inductors to obtain smooth surfaces and high Q values. We optimized the electroplating conditions using PR electroplating, which offered good uniformity and reduced surface roughness. We polished the silver layer to further smooth out the surface. When comparing DC with PR plus polishing samples, the inductor Q improved by 20% at low frequencies where the metal loss is dominant.

Experimental Methods:

The fabrication process started with sputtering the seed layer (100Å Ti/ 500Å Ag/100Å Ti) onto the passivated silicon wafer. Then negative resist NR-4 was spin-coated and patterned to form the electroplating mold.

Once a plasma process removed the top titanium (Ti) layer, the photoresist mold was ready for Ag electroplating. With an Ag anode positioned parallel to the silicon wafer cathode in a cyanide solution, an electrical current was induced into the system, and the Ag cations were redeposited onto the Ag seed layer.

The plating rate depended on the open areas on the photoresist. After over-electroplating 0.5-1 μm , we polished the

Feature Size	DC Height (μm)	PR Height (μm)
200 μm	7.52 ± 0.22	9.34 ± 0.31
20 μm	8.24 ± 0.19	9.58 ± 0.21
Overall Uniformity	8.00 ± 0.40	9.49 ± 0.27

Figure (Table) 1: Comparing DC and PR electroplating overall surface uniformity and deposition rate.

wafer to remove the excess Ag and obtain uniform thickness of Ag on the wafer. Finally, the Si substrate was selectively removed to reduce the substrate loss.

Results and Conclusions:

The forward and reverse current bias and duration were varied to find the optimum electroplating conditions. The optimal PR electroplating occurred with an effective current density of 5 mA/cm^2 . The respective forward and reverse current amplitude was 60 mA for 17 ms and 180 mA for 1 ms, with a pulse off time of 1 ms.

Table 1 compares the electroplating rate and uniformity using the optimum PR conditions with those of DC plating. The measurements recorded in Table 1 were from two extreme mask widths, 20 μm and 200 μm . Comparing the data in Table 1 and the surface profiles in Figure 2, we observe two distinct differences: 1) across a 4" wafer, the electroplated Ag thickness in the DC sample varied up to 1.24 μm , while the variance was only 0.35 μm on the PR sample; 2) PR plating deposited 16% faster than the DC electroplating wafer. Therefore, under the optimal conditions, the PR electroplating sample had an improved overall surface uniformity and a faster deposition rate than the DC plating sample.

To further improve the surface roughness and therefore the inductor Q , we polished both samples. The polishing process incorporated a 0.3 μm aluminum oxide slurry and a 8:1:1 volume ratio solution with distilled water, hydrogen peroxide (H_2O_2) and ammonium hydroxide, respectively. We achieved a 0.13 μm surface roughness for both samples (Figure 3). The surface roughness (0.13 μm) was lower than the size of aluminum oxide slurry (0.3 μm) as the additional solution aided the polishing process by wet removal of silver: the hydrogen peroxide oxidized the silver layer, and the ammonium hydroxide removed silver oxide.

When quantifying the Q , we tested four samples: DC electroplating, DC plus polishing, PR electroplating and PR plus polishing. At 200 MHz, there was a 20% Q improvement between the DC plating and PR electroplating plus polishing samples (Figure 4).

Scanning electron microscopy images of the inductors in Figure 4 illustrates the extreme porosity in DC plating and the varying surface grain size between the two samples: 1.24 μm in the DC sample and 0.13 μm in the PR plus polishing sample.

Acknowledgements:

I want to thank my professor Mina Rais-Zadeh and mentor Yonghyun Shim for their dedicated time and effort throughout my research experience. I also want to thank Lurie Nanofabrication Facility, the National Nanotechnology Infrastructure Network REU Program and National Science Foundation.

References:

- [1] Rais-Zadeh, Mina; "High-Q integrated inductors on trenched Si islands," Master thesis, Department of Electrical and Computer Engineering, Georgia Institute of Technology, Atlanta, GA, 2005.

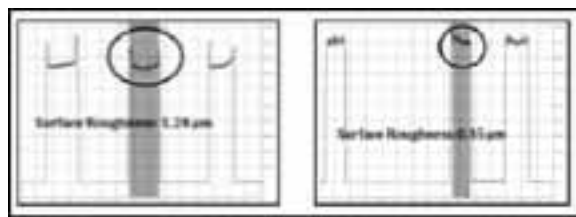


Figure 2: Showing the surface profiles of the PR and DC sample.

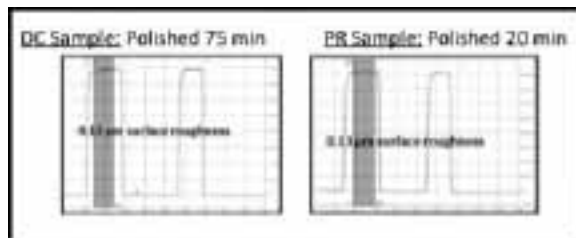


Figure 3: Achieving a 0.13 μm surface roughness using a 0.3 μm slurry, H_2O_2 , and ammonium hydroxide.

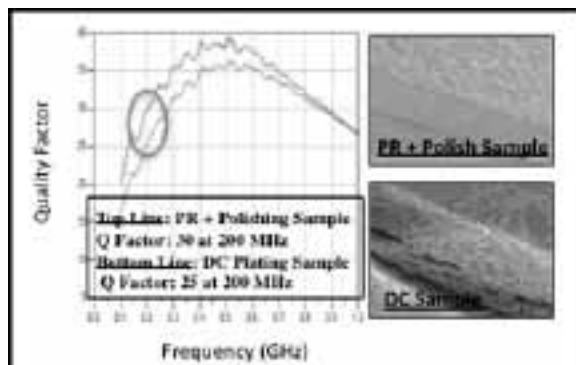


Figure 4: Q is improved by 20% in PR + Polish sample. This is due to improvement of surface roughness.

Template Stripping for High Throughput Fabrication of Nanohole Arrays

Benjamin Treml

Engineering Physics, University of Wisconsin-Madison

NNIN REU Site: Nanofabrication Center, University of Minnesota-Twin Cities, Minneapolis, MN

NNIN REU Principal Investigator(s): Sang-Hyun Oh, Electrical and Computer Engineering, University of Minnesota-Twin Cities

NNIN REU Mentor(s): Hyungsoon Im, Department of Electrical and Computer Engineering,

and Si Hoon Lee, Department of Biomedical Engineering, University of Minnesota-Twin Cities

Contact: btreml@wisc.edu, sang@umn.edu, imxxx019@umn.edu, leex3487@umn.edu

Abstract and Introduction:

Surface plasmons are electromagnetic waves created at a metal-insulator interface that can confine optical energy well below the diffraction limit. Surface plasmons can be excited by periodic nanohole arrays in an optically thick metal film, which leads to the extraordinary optical transmission effect through the nanoholes [1]. The locations of the transmission peaks are dependent on the local refractive index in the nearest 100-200 nm to the interface. This makes nanohole arrays useful for biosensing as a way to monitor molecular binding kinetics in a real-time label-free manner, as molecular binding onto the metal surface results in changes in refractive index [2].

Currently, most ordered nanohole arrays are fabricated on a small scale using focused ion beam (FIB) or electron-beam lithography (EBL). However, these serial fabrication techniques are slow, expensive and lead to sample-to-sample variation. Nanosphere lithography was used to make nanoholes in a large area, but the method cannot easily create nanohole arrays with arbitrary shape, size and periodicity [3]. There is a need for a high throughput method of fabricating nanohole arrays with reproducibility so that biosensing experiments can proceed with a lower substrate cost.

Template stripping is a method of transferring nanoscale structures to metal films by depositing metal on the surface of a mold and peeling it off using an adhesive backing layer [4].

The goal of this project was to determine whether template stripping could serve as a high throughput method to manufacture nanohole arrays.

Mold Fabrication:

A silicon wafer with 200 nm of thermally grown silicon dioxide (SiO_2) was spin-coated with polymethylmethacrylate (PMMA) resist at 3000 rpm for 30 seconds and baked at 180°C for 90 seconds. This substrate was exposed using EBL with an accelerating voltage of 20 kV and a 10 μm aperture to produce the desired pattern of nanohole arrays.

The patterned wafer was developed in a 1:3 mixture of methyl isobutyl ketone and isopropyl alcohol for 30-60 seconds.

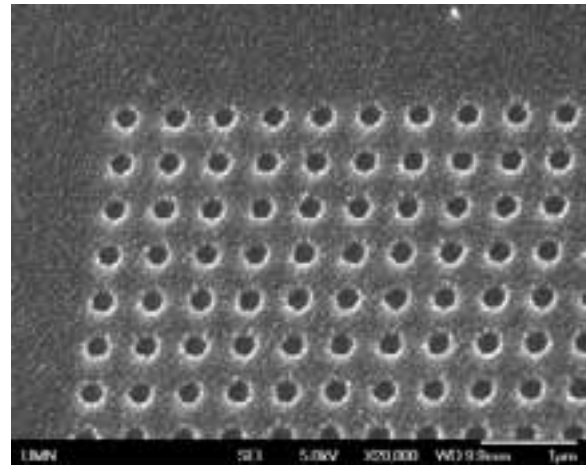


Figure 1: Nanohole pattern in a mold.

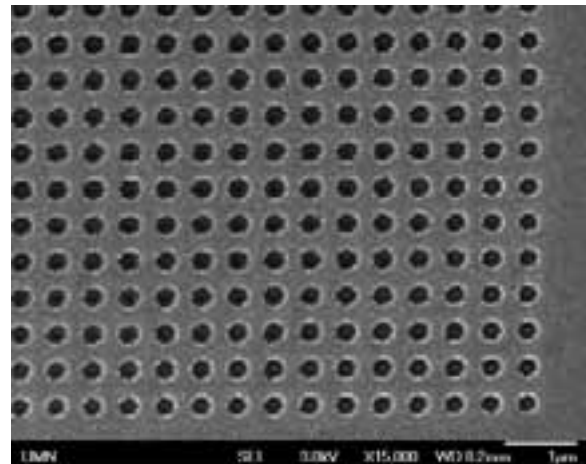


Figure 2: Nanohole array in silver film.

The mold was etched through reactive ion etching (RIE, STS etcher) to etch the thermal oxide. After cleaning in acetone and piranha (1:1 sulfuric acid:hydrogen peroxide) for 10 minutes each, the Si wafer was etched in a potassium hydroxide (KOH) solution at 30°C, which anisotropically etched the Si below the SiO_2 mask. The resulting mold has the desired nanohole array pattern in SiO_2 with under-etched pyramidal pits in Si. The pits prevented the formation of a suspended film of metal by creating discontinuous sidewalls in the mold.

Template Stripping:

After the mold had been fabricated, 100 nm of silver (Ag) was deposited on the mold using a Temescal EB evaporator. An optical epoxy was applied to a clean glass slide, and both the slide and epoxy were placed onto the Ag-coated mold. After curing the epoxy, the Ag film and slide could be easily separated from the mold. The mold could then be used again.

Spectral Measurements:

Optical transmission spectra were taken using an optical microscope and fiber optic spectrometer. The spectra were normalized with respect to a reference spectrum of incident light to produce the graphs shown. In order to examine the sensitivity of the nanoholes to changes in local refractive index, approximately 7 nm of SiO_2 was deposited using atomic layer deposition and the transmission spectra were again measured. This process occurred three times for a total SiO_2 thickness of 21 nm.

Results and Conclusions:

Figure 3 shows the optical transmission spectra of multiple nanohole arrays produced from the same mold through repeated template stripping. The spectra are consistent in shape and location of peak position. This shows that template stripping is capable of repeatedly producing samples with the same characteristics.

In Figure 4, spectra from the same nanohole array are plotted as the thickness of a thin layer of SiO_2 increases. The layer of SiO_2 increases the local refractive index near the interface, and so changes the position and intensity of the extraordinary optical transmission peaks. This result shows that the nanoholes are sensitive to refractive index changes and so can be used in refractive index sensing experiments [5].

Future Research:

Looking forward, the next steps are further work at optimizing the nanohole parameters, such as hole size and distance between holes, to produce spectra with transmission peaks at the desired wavelengths, and integration of template-stripped samples into experiments that are currently employing nanohole arrays fabricated by FIB lithography.

Acknowledgements:

I would like to thank Professor Sang-Hyun Oh and my mentors, Hyungsoon Im and Si Hoon Lee, for their help and advice, the Nanofabrication Center and its staff for the facilities and training that made this work possible, and the NNIN REU Program and NSF for providing me with this opportunity.

References:

- [1] Ebbesen, T.W. et al; "Extraordinary optical transmission through sub-wavelength hole arrays"; *Nature*, 391(6668), 667-669. (1998).
- [2] Im, H. et al; "Plasmonic nanoholes in a multichannel microarray format for parallel kinetic assays and differential sensing"; *Analytical chemistry*, 81(8), 2854-9 (2009).
- [3] Lee, S.H. et al; "Self-assembled plasmonic nanohole arrays"; *Langmuir*, 25(23), 13685-93 (2009).
- [4] Nagpal, P. et al; "Ultrasmooth patterned metals for plasmonics and metamaterials"; *Science*, 325(5940), 594-7 (2009).
- [5] Im, H. et al; "Atomic layer deposition of dielectric overlayers for enhancing the optical properties and chemical stability of plasmonic nanoholes"; *ACS nano*, 4(2), 947-54. (2010).

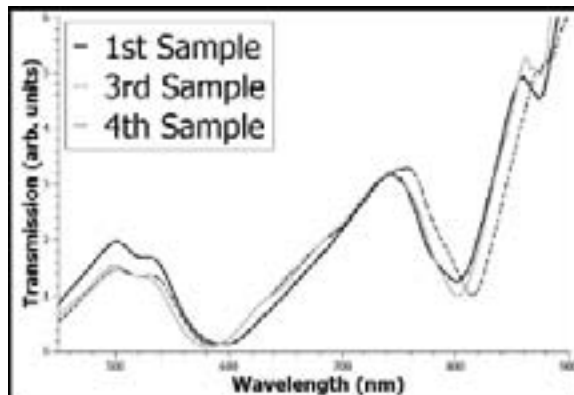


Figure 3: Transmission spectra from repeated template stripping.

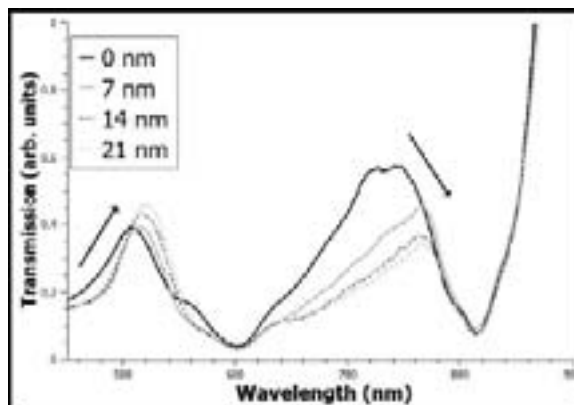


Figure 4: Transmission spectra of the same array as silicon dioxide thickness increases.

Sputtered TiW/W Emitter Contact Stack Design in Terahertz Bipolar Transistors

Jeremy Wachter

Physics and Electrical Engineering, Rose-Hulman Institute of Technology

NNIN REU Site: Nanotech, University of California, Santa Barbara, CA

NNIN REU Principal Investigator(s): Dr. Mark Rodwell, Electrical and Computer Engr., University of California, Santa Barbara

NNIN REU Mentor(s): Evan Lobisser, Electrical and Computer Engineering, University of California, Santa Barbara

Contact: wachtejm@rose-hulman.edu, rodwell@ece.ucsb.edu, lobisser@ece.ucsb.edu

Abstract:

The conditions under which the emitter contact metal of a mesa-type bipolar transistor is sputter-deposited influence the contact's stress and sheet resistance, which in turn affect the transistor's structural stability and bandwidth, respectively. Through aggressive scaling of emitter dimensions, emitter-base and base-collector junction capacitances are reduced and high radio frequency (RF) bandwidth can be realized [1]; however, this scaling results in a high aspect ratio emitter contact, which requires low stress for structural stability.

The purpose of this project was to develop a recipe for use in a sputtering tool that satisfied both the low stress and low resistance requirements for the contact. It has been found that the most significant factors in determining the characteristics of interest of the resultant sputtered film are the working pressure of the deposition chamber and the working temperature of the substrate. The desired resistance has been obtained via low working pressure and elevated working temperature, while preliminary experiments indicate the desired stress can be obtained via compensation between the titanium-tungsten (TiW) alloy and tungsten (W) layers of the emitter contact. By using tensile stress in the tungsten layer and compressive stress in the TiW alloy layer, fabrication of bipolar transistors with bandwidths in excess of one terahertz was possible.

Experimental Procedure:

The sputtering system used for depositions of W and TiW onto the substrate allows control over a multitude of variables. To achieve high deposition rates, the substrate was placed as close to the sputtering gun as possible and the substrate was rotated to provide uniform film deposition. Argon was used as the sputtering process gas.

The effects of varying working pressure, working temperature, and gas flow rate were investigated to determine their effects on the resultant stress and resistance of the sputtered film. The stress was determined by using an optical measurement system to find the curvature of the wafer before and after metal deposition. Sheet resistance was measured using a four-point probe measurement system. To calibrate the deposition rate to achieve the proper film thickness, cross-sectional images of the deposited films were taken using a scanning electron microscope (SEM); very small standard deviations in four-point resistance measurements were used as an indicator of uniform film thickness.

Properties of W films were characterized before those of the TiW alloy. This was because the alloy was 10% Ti, 90% W; therefore, its characteristics were highly similar to that of pure tungsten.

Results:

Working pressure was shown to affect the stress of the deposited tungsten film as shown in Figure 1, which followed predicted trends [2]. The resistance of the deposited film was above tolerance in the low stress region seen at higher pressures, while the zero stress transition point seen at lower pressures proved to be too unstable to yield repeatable results. Cross-sectional images taken with an SEM revealed that the low-stress, high-resistance region at higher pressures was caused by high stresses in the deposited film, breaking the film into columnar growth (see Figure 2). This columnar growth caused the film to appear low-stress while also giving it high resistance.

The working temperature was shown to affect the stress of the deposited tungsten film as shown in Figure 3. As temperature increased, the magnitude of the stress curve's slope decreased; this proved to be useful in controlling the fluctuations in stress caused by machine drift, yielding more stable points for later use.

Gas flow rate was shown to be instrumental in obtaining repeatable results, with a gas flow rate in the middle of the sputter tool's operational range proving more stable than rates situated at either extreme. This was an issue related to

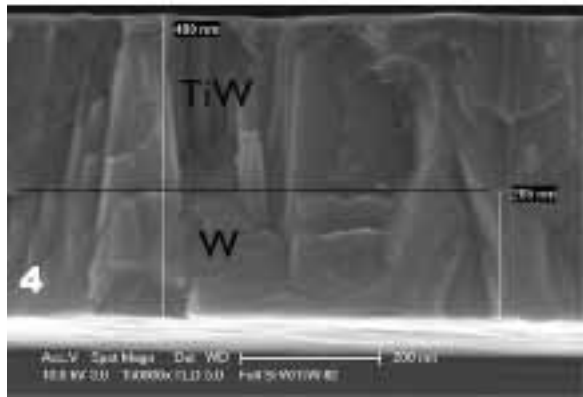
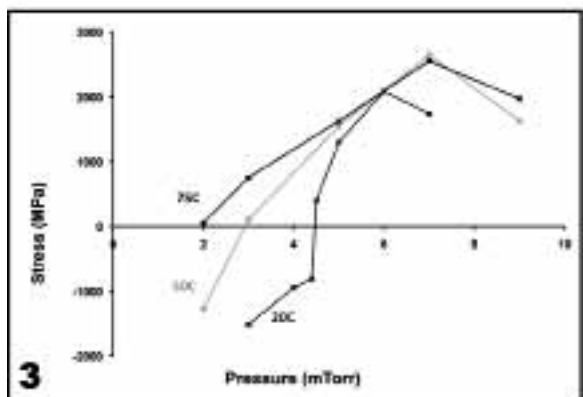
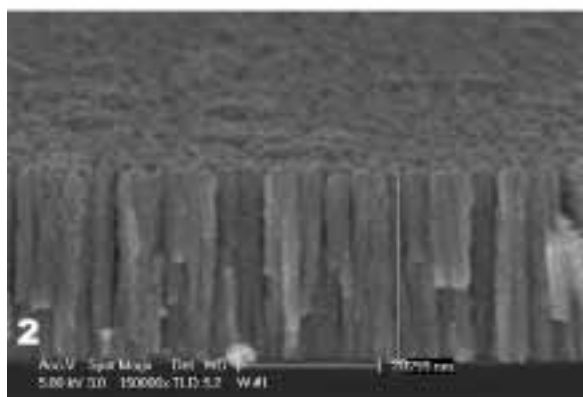
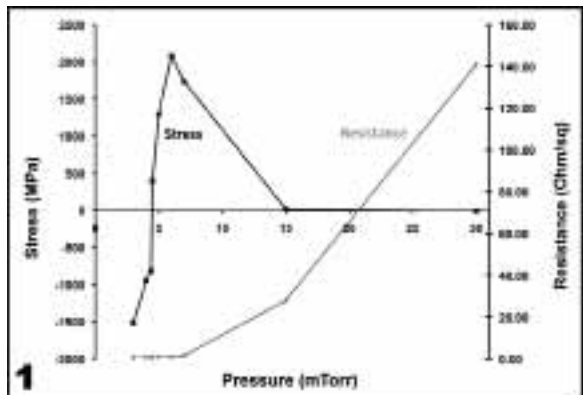


Figure 1: Tungsten stress and sheet resistance vs. pressure.

Figure 2: Columnar tungsten film growth.

Figure 3: Tungsten stress due to temperature.

Figure 4: Tungsten / titanium-tungsten film.

the mass flow controller unit; as such, the effects of gas flow rate on sputtered film stress and resistance were not fully characterized. Therefore, the ideal sputtering deposition conditions were found to be at lower pressures, elevated temperatures, and mid-range gas flow rate. Despite the higher level of control and repeatability afforded by these conditions, the compressive-tensile stress transition point still proved difficult to obtain consistently due to the differences in the microstructure of film growth between compressive and tensile films [3]. The solution to this problem was to deposit the W film such that it was slightly tensile, then deposit the TiW alloy film such that it was slightly compressive. The equal and opposite stresses canceled each other out, resulting in a low-stress film. An example of this technique can be seen in Figure 4, which shows a tungsten and TiW alloy film with low stress, low resistivity, and desired thickness.

Future Work:

Some work must still be done to ensure repeatability and reliability of the overall emitter contact fabrication process before it can be incorporated into the transistor fabrication process. Transistors made using this metal-contact process can operate at frequencies in the terahertz range, enabling high-data-rate wireless communications and highly-efficient digital-to-analog and analog-to-digital converters.

Acknowledgements:

I would like to thank the following: Dr. Mark Rodwell, for accepting me onto his research group; Evan Lobisser, for being an all-around excellent mentor; the other members of my research group, for being patient, helpful, and friendly; the cleanroom staff, for training, assistance, and recommendations; Angela Berenstein, for her coordinating skills and unbounded cheerfulness; and the National Nanotechnology Infrastructure Network Research Experience for Undergraduates (NNIN REU) Program and the National Science Foundation for funding this entire endeavor.

References:

- [1] Rodwell, M. et al.; "InP Bipolar ICs: Scaling Roadmaps, Frequency Limits, Manufacturable technologies"; Proceedings of the IEEE, Vol. 96, No. 2, pp. 271-286, Feb 2008.
- [2] Shen, Y. et al.; "Residual stress, microstructure, and structure of tungsten thin films deposited by magnetron sputtering"; Journal of Applied Physics, Vol. 87, No. 1, pp. 177-187, January 2000.
- [3] Thornton, J. and Hoffman, D.; "Stress-related effects in thin films"; Thin Solid Films, Vol. 171, pp. 5-31, 1989.

Public Service Posters for the Societal and Ethical Issues (SEI) of Nanotechnology

Chloe Lake
Communication and Psychology, University at Buffalo

NNIN REU Site: Cornell NanoScale Science and Technology Facility, Cornell University, Ithaca, NY
NNIN REU Principal Investigator(s): Professor Katherine McComas, Communication, Cornell University
NNIN REU Mentor(s): Norman Porticella, Communication, Cornell University
Contact: clake@buffalo.edu, kam19@cornell.edu, nap28@cornell.edu

Abstract:

Due to nanotechnology's current and potential impact on society, the National Nanotechnology Infrastructure Network (NNIN) recognizes the importance of promoting consideration and awareness of the societal and ethical implications of nanotechnology among its facilities' users. The goal of this project was to develop a series of posters encouraging NNIN laboratory users to consider societal and ethical issues (SEI) in their research, especially with regard to maximizing the benefits and reducing the potential societal risks of their work. Five thematically-integrated posters were finalized and placed in the fourteen NNIN sites across the country.

Introduction:

To effectively stimulate SEI consideration, poster messages were created employing the motives of nanotechnology researchers to conduct research, since there is evidence that such underlying motives influence individual attitudes and behaviors. A series of focus groups were conducted, with Cornell NanoScale Facility (CNF) users, to gain insight into these underlying motivations and to receive feedback throughout the development of the campaign posters.

Methods:

Focus groups were conducted using CNF users as participants. Users were asked to volunteer 30 minutes or more, during a 2.5 period of time, in order to provide feedback on various aspects of the project. Discussion participants were provided lunch, and could arrive or leave at any time during the time period. These focus groups allowed us to develop posters that were closely aligned with the interests of the intended audience.

Three different focus groups were used to:

- a) Identify the motivations of nanotechnology researchers to conduct research.
- b) Test and discuss possible poster messages developed from previous focus group feedback.
- c) Test, discuss, and refine initial mock-ups of posters developed from revised messages based on CNF user feedback.

Results:

Several key motivating factors were identified in Focus Group 1; the opportunity to work in an emerging field, the belief that field is growing, opportunities for career advancement, opportunities to work with diverse fields, enjoyment of the challenges encountered in one's work, and a desire to

increase one's personal expertise in nanotechnology. Some participants also identified the desire to facilitate discoveries and applications that would be beneficial to humanity as a motivating factor. Focus Group 1 also provided insight into the obstacles we faced. The posters needed to overcome low self-efficacy beliefs among CNF users with regard to the degree of control they could have over the application of their research or their ability to reduce societal risks. Another obstacle was participants' belief that risk management and risk prevention is the responsibility of non-scientists, and therefore not something scientists should think about. Furthermore, considering the potential risks of one's work was sometimes felt to be uncomfortable, threatening, or disruptive to research and personal goals. Lastly, the potential risks in nanotechnology are often uncertain or unknown, making them difficult to address.

Using these findings, fifteen messages were developed and evaluated in Focus Group 2. Any messages perceived to be from a non-scientist or "outsider" source were rejected by users. Such "outsider" messages were usually perceived to be alarmist or create unrealistic expectations for researchers. Messages that were well-received tended to emphasize giving equal consideration to both the benefits and potential risks of research. Including some degree of inspiration was also effective, as seen in messages incorporating personal and professional goals with pro-social goals associated with the desired societal impact of one's research.

Six messages were selected and revised to use for posters. With the help of a graphic designer, mock-ups of posters were developed around each message. A slogan intended to serve as a tagline for the campaign was also incorporated into all the posters. Three different slogans were tested.

In Focus Group 3, participants provided feedback on the posters and ranked the slogans in order best to worst.

Users liked posters using natural imagery, and considered it a welcome addition to the relatively stark environment of the clean room. Images that inspired an immediate and meaningful connection to the message were most effective. Posters conveying a mutually beneficial relationship between nanotechnology research and SEI consideration were well received, highlighting the importance of avoiding any images that would make the posters seem alarmist or ominous.

Five of the posters were selected for revision and finalization.

Conclusions:

CNF user reactions during focus groups can serve as a predictor of the poster campaign's success. During focus groups, messages and posters sparked in depth discussions about the societal impact and the ethical responsibilities of researchers.

Some participants reported that they thought more about the societal and ethical implications of their research after attending even one focus group. This suggests that posters will be effective in stimulating some degree of SEI consideration among researchers. It also suggests that users are often ready to think critically about these issues and questions, but prompting is necessary.

Future Directions:

Once the five posters were finalized, they were distributed to the fourteen NNIN sites. In addition, full posters or elements of the posters may be incorporated into the NNIN's website.

A method of evaluating the effect of the posters has yet to be determined, but this would provide a valuable insight into the effectiveness of the posters.

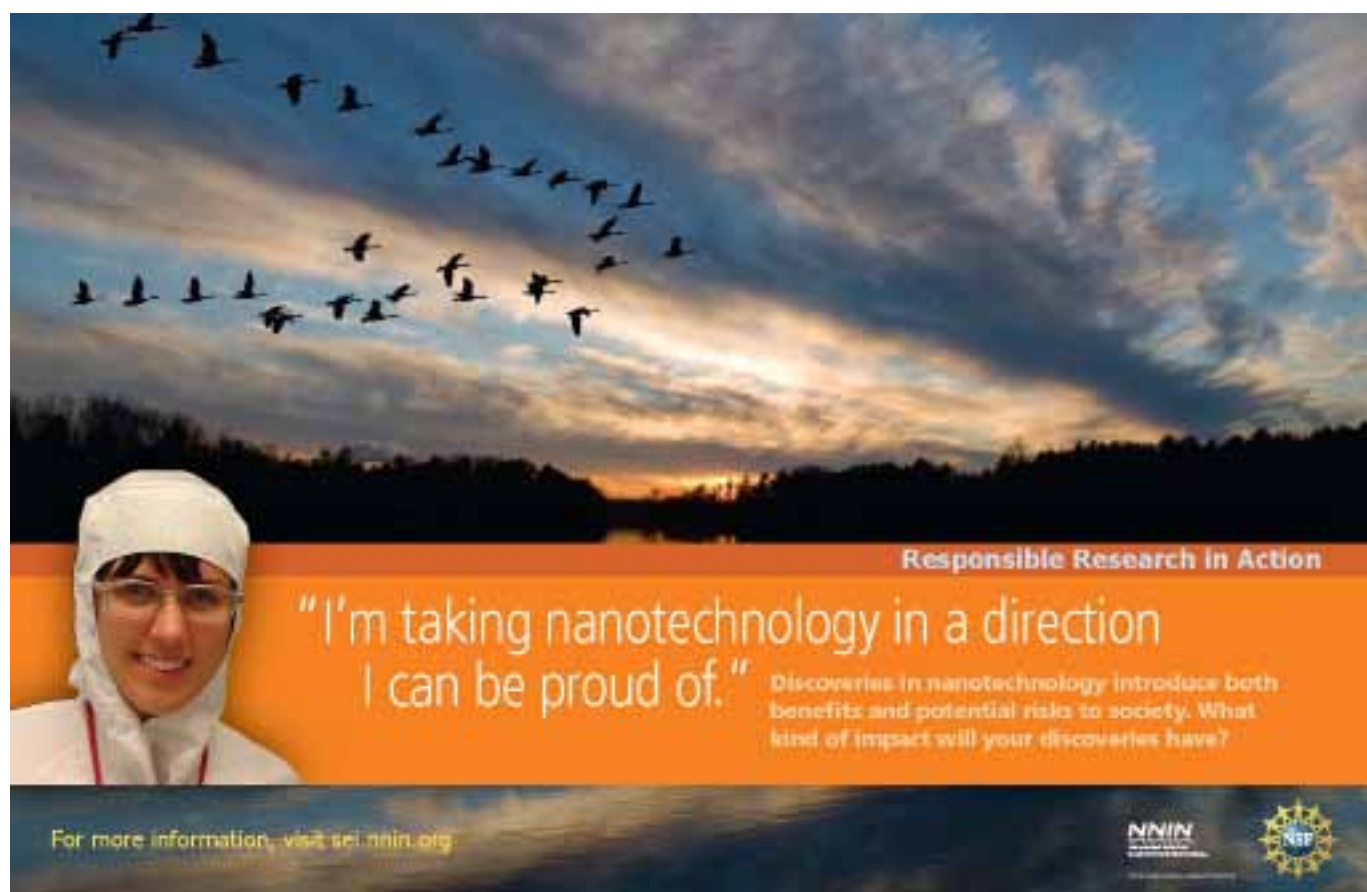
The five posters are shown below and on the next pages.

Acknowledgements:

Professor Katherine McComas and Norman Porticella of Cornell University, CNF REU Program Coordinators Rob Illic and Melanie-Claire Mallison, Graphic Designer Jennifer Infante, CNF staff and users, National Nanotechnology Infrastructure Network Research Experience for Undergraduates Program, National Science Foundation.

References:

- [1] Gustin, B. H. (1973). Charisma, recognition, and the motivation of scientists. *American Journal of Sociology*, 78(5), 1119-1134.
- [2] Jackson, D. N. (1987). Scientific and technological innovation: Its personological and motivational context. In D. N. Jackson, and J. P. Rushton (Eds.), *Scientific excellence: Origins and assessment* (pp. 149-149-164). Newbury Park: SAGE Publications, Inc.
- [3] Ladd, J., Lappe, M. D., McCormick, J. B., Boyce, A. M., and Cho, M. K. (2009). The "how" and "whys" of research: Life scientists' views of accountability. *Journal of Medical Ethics*, 35(12), 762-767.





Responsible Research in Action

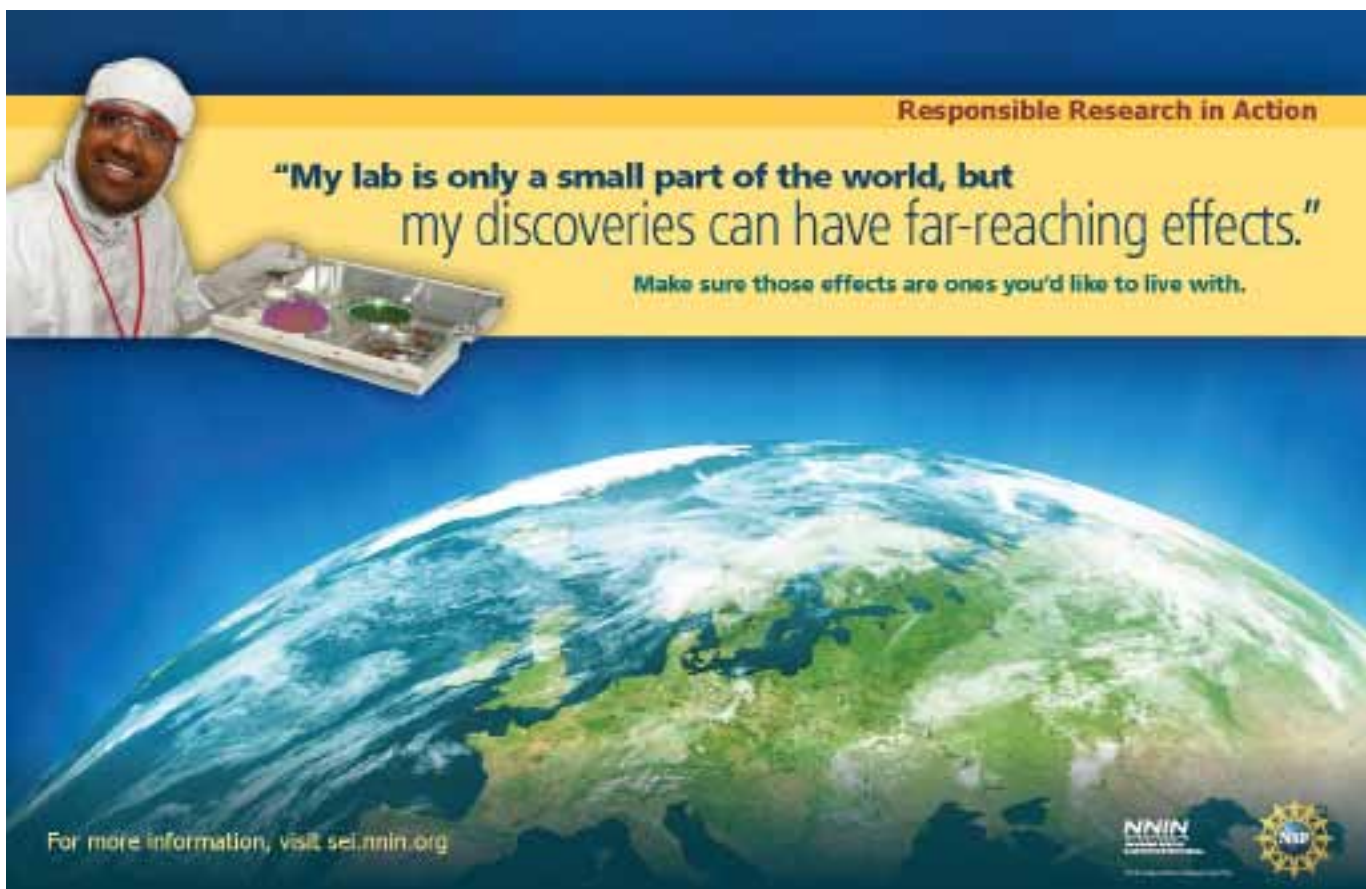
Make nanotechnology more than a buzzword:
Keep the world's attention by keeping the world's trust.

Nanotechnology holds exciting opportunities, but also potential risks. Ensure that opportunities keep growing by addressing potential risks from the start.

For more information, visit sei.nnin.org

NNIN
Nanotechnology
Innovation
Institution

Nanopart



Responsible Research in Action

"My lab is only a small part of the world, but my discoveries can have far-reaching effects."

Make sure those effects are ones you'd like to live with.

For more information, visit sei.nnin.org

NNIN
Nanotechnology
Innovation
Institution

Nanopart



Responsible Research in Action

**"I consider every aspect of my research,
including what happens with it outside of the lab."**

The work of a few can impact the lives of thousands.
Think about the impact you want your work to have.

For more information, visit sei.nnin.org

NNIN
National Nanotechnology Infrastructure Network

NSF



Responsible Research in Action

"The research I'm publishing on biosensors will help provide the world with clean, safe drinking water."

When I choose projects, I consider both the benefits and risks they might introduce to the world.

For more information, visit sei.nnin.org

NNIN
National Nanotechnology Infrastructure Network

NSF

INDEX

National Nanotechnology Infrastructure Network Program Sites

NNIN REU Sites:

Arizona State University, Tempe, AZ	xiv, 22, 26, 114, 116, 126
Cornell University, Ithaca, NY	xiv, 16, 42, 54, 62, 70, 86, 128, 182, 186, 202
Georgia Institute of Technology, Atlanta, GA	xv, 4, 52, 74, 98, 110, 188
Harvard University, Cambridge, MA	xv, 94, 134, 142, 152, 194
Howard University, Washington, DC	xvi, 80, 82, 138, 164, 166
The Pennsylvania State University, State College, PA	xvi, 90, 120, 124, 160, 176
Stanford University, Stanford, CA	xvii, 28, 50, 60, 72, 96
University of California, Santa Barbara, CA	xvii, 38, 46, 108, 154, 174, 200
University of Colorado, Boulder, CO	xviii, 118, 130, 136, 144, 146
University of Michigan, Ann Arbor, MI	xviii, 56, 64, 106, 122, 148, 196
University of Minnesota-Twin Cities, Minneapolis, MN	xix, 34, 66, 140, 180, 198
The University of Texas, Austin, TX	xix, 10, 58, 68, 84, 192
University of Washington, Seattle, WA	xx, 2, 8, 12, 30, 102, 150
Washington University in St. Louis, St. Louis, MO	xx, 18, 32, 48, 132, 168, 172

NNIN iREU Sites:

NNIN iREG Sites:

INDEX

NNIN Interns are in **Bold**

A

Achilefu, Samuel 48
Adams, Siatta **xvi, 82**
 Akhavan, Vahid 68
Alvarez, Narahi J. **xvi, 164**
Anger, Richard **xiv, 54**
Appel, Jennie **xiv, 114**
Augustine, III, Hilton H. **xvi, 166**
Ault, Jesse **xiv, 116**
 Aziz, Michael 134

B

Bakkila, Scott **xviii, 56**
 Bank, Seth R. 84
 Bao, Xinyu. 60
 Barton, Robert 128
 Bates, Clayton 138
Bennett, Kathleen **xx, 2**
Benton, Brian **xviii, 130**
Bersin, Lia **xix, 58**
Bolser, Diana **xx, 132**
Borysiak, Mark **40**
 Boukai, Akram 106
 Bovington, Jock 154
 Bowers, John 108, 154
 Brower-Thomas, Tina 164
 Brown, Keith A. 194
 Brown, Kenneth R. 110
 Bruchhaus, Rainer 156
Brunson, Mark **xx, 168**
 Bryan, Sarah 98
 Bunch, Scott 118
Burdett, Christine **170**
 Burgess, Ian 142

C

Campbell, Gavin P. **xix, 84**
Cantley, Lauren **xviii, 118**
Cardona, Edy **xv, 134**

Carroll, Sylvia **xiv, 86**
 Castner, David G. 12
 Chae, Junseok 114
 Chamberlain, Jeff. 8
Chase, Steven **xv, 4**
Chen, Jack **xx, 172**
 Chen, Jennifer I.L. 30
Chen, Kevin **xviii, 136**
 Chikyow, Toyohiro 104
 Choi, Seok-Youl 64, 78
 Choi, Sung-Wook. 32
Chow, Clara **xvii, 60**
Chung, Brian T. **xvii, 174**
Clapp, Corey E. **xvi, 176**
 Coldren, Larry A. 174
Connell, Zachary J. **xvi, 120**
Conner, Austin **xiv, 62**
Connolly, Sarah **xxi, 6**
Conwill, Arolyn **88**
 Copic, Davor 36
 Craighead, Harold 16
 Crook, Adam C. 84
 Crozier, Kenneth B. 152
Cummings, Lauren **xx, 8**

D

Dai, Hongjie 72
 Dan, Yaping 152
 Dauskardt, Reinhold 96
Davis, John **xiv, 42**
Dawley, Natalie M. **xvi, 90**
 De Volder, Michael 92
DesHarnais, Marie **xvi, 138**
DeWilde, Joseph **xix, 140**
 Diduck, Quentin 62
Djanal-Mann, D. Johann **xv, 142**
 Dodabalapur, Ananth. 58
 Dorfman, Kevin. 180
Downing, Fraser **xix, 10**
 Duarte, Davianne. 58
Dunn, Megan **xx, 12**

E

Eastman, Lester 62
 El Kallassi, Pascale 50
 El-Sayed, Mostafa 188
 Engstrom, James R. 42
 Erickson, David 54

F

Fabbri, Emiliana 100
 Fedorov, Andrei 74
Feig, Vivian **xxi, 14**
 Felbinger, Jonathan 62
Fiedler, Callie **xviii, 144**
 Forest, Craig 4
 Franck, John 46
 Frank, Michael 40
Fujii, Hiromasa **xxi, 44**
 Fujita, Daisuke 178
 Fung, Wayne 64, 78

G

Gao, Jian-Hua 178
 Ginger, David S. 30
 Goryll, Michael 126
 Green, Craig 74
 Griffin, James A. 166
 Gruev, Viktor 132
 Gunel, Yusuf 162
 Guzzon, Robert S. 174

H

Hale, Paul D. 136
 Hall Sedlak, Ruth 2
Hammack, Audrey **xvii, 46**
 Han, Song-I 46
 Hanagata, Nobutaka 6
 Haque, Aman 120
 Hardtdegen, Hilde 158
 Harris, Gary L. 80, 82, 166
 Harris, James S. 50
 Hart, Anastasios John 36, 122
 Hayamizu, Yuhei 102
 Haynes, Christy 34
Henderson, Zachary **xviii, 64**
Hershberger, Matthew T. **xxi, 156**

Hessel, Colin. 44
 Hicks, Bryan 186
Hoerner, Michael **xviii, 146**
Hoffman, Emily **xiv, 16**
Hogrebe, Nathaniel **xxi, 92**
 Hoshino, Kazunori 10
 Huang, Yu-Yen 10
 Hughes, Kevin. 42

I

Im, Hyungsoon 198
Isaacson, Scott **xxi, 178**
 Ishida, Nobuyuki 178

J

Jaramillo, Rafael 94
 Jiao, Liying 72
Jones, Christina **xviii, 148**
Jones, Kristen **xx, 18**
Jordan, Roger **xx, 150**
 Josephson, David 140
 Joshi, Punarvasu 126
 Joshi, Saumil 146

K

Kendrick, Chito E. 90
 Kim, Donghyuk 34
 Kim, Taek-Soo 96
Klemm, Angeline **xix, 66**
 Kohl, Paul A. 52
 Koide, Yasuo 88
 Koo, Hyo-Chol 52
 Korgel, Brian A. 44, 68
Kozak, Adam **xxi, 20**
 Krysak, Marie 86
 Kumar, Sandeep 120
 Ku, Pei-Cheng. 148
 Kuo, Michael 148
Kuruvilla, Sibu **xviii, 122**

L

Lake, Chloe **xiv, 202**
Lal, Amit 186
Lanza, Gregory 172
Le, Chantalle **xx, 48**
Lee, Chien-Chung 130
Lee, Jason **xix, 180**
Lee, Meredith M. 50
Lee, Ruby **xv, 94**
Lee, Si Hoon 198
Lepsa, Mihail 76
Li, Melissa 4
Li, Qi 160
Liu, Chuan 190
Liu, Xinghui 118
Liu, Yang 124
Lobisser, Evan 200
Lončar, Marko 142
Lowe, Christopher **xiv, 22**
Lu, Wei 64, 78
Lui, Gillian **xvii, 96**
Lyle, Andrew 66

M

MacGriff, Christopher 26
Mackin, Charles **xiv, 182**
Mahala, Benjamin D. **xv, 98**
Marks, Zefram 136
Markus, Isaac **xxi, 100**
Matthews, Kristopher 62
Mayer, Dirk 14
McComas, Katherine 202
McLellan, Claire **xxi, 184**
Meffert, Simone 24
Merrill, J. True 110
Merritt, Margaret 24
Meschewski, Ryan 38
Meza, Jhim Handrex **xv, 152**
Mirts, Evan **xiv, 26**
Mitchell, James 164
Mitsuishi, Kazutaka 184
Moore, Sean 54
Moran, Jeffrey 116
Morse, Kelsey **xvii, 28**
Murali, Raghunath 98

N

Near, Rachel 188
Nelson, Heidi **xx, 30**
Neves, Hercules 20, 92, 170
Nguyen, Nam 104
Njuguna, Raphael 132
Norberg, Erik J. 174

O

O'Connell, Christopher **xiv, 186**
O'Connell, Fiona **xv, 188**
Ober, Christopher K. 86
Oghedo, Nkemdilim **xx, 102**
Oh, Sang-Hyun 198
Ohashi, Naoki 112
Olson, Dan 180
Ou, Jia 180

P

Palmstrom, Axel 104
Palomino, Gabriel **xix, 68**
Pan, Si Hui Athena **190**
Park, Jiwoong 70
Park, Won 146
Parker, Jason 60
Parker, John S. 174
Parpia, Jeevak 128
Pasha, Mohsin **xvii, 154**
Pham, Phi **xix, 192**
Phare, Christopher **xiv, 70**
Phillips, Jamie 56
Piestun, Rafael 144
Pillers, Michelle **xvii, 72**
Pizzo, Amber **xv, 74**
Ponce de Leon, Philip **xvii, 50**
Porticella, Norman 202
Posner, Jonathan 116

Q

Qin, Dong 168
Quirin, Sean 144

R

Radisic, Aleksandar 170
 Rais-Zadeh, Mina 196
 Ramanathan, Shriram 94
 Ramos, James 22
 Ramu, Ashok 108
 Ratner, Daniel 8
 Recht, Daniel 134
 Redwing, Joan M. 90
 Rege, Kaushal 22
 Roberts, Megan J. 36
 Rodwell, Mark 200
Romanczuk, Christopher **xviii, 106**
 Rose, William 80
 Ruoff, Rodney 192
 Ryder, Matthew 12

S

Sadie, Jacob Alexander **158**
 Sanetra, Nils 14
 Sarikaya, Mehmet 102
Satzinger, Kevin J. **xvi, 194**
 Schäpers, Thomas 162
 Schibli, Thomas 130
 Senpan, Angana 172
 Sharma, Ginni 144
Shi, Meng **xvi, 160**
 Shim, Yonghyun 196
 Shivaraman, Shriram 182
 Sladek, Kamil.. 158
Smalley, Joseph S.T. **xvii, 108**
 Spencer, Michael G. 182
Sridhar, Hamsa **xxi, 162**
 Stein, Andreas 140
 Suk, Ji Won 192
Sukhdeo, Devanand **xxi, 76**
Swider, Natalie **xviii, 196**
 Sychugov, Ilya 184

T

Takeuchi, Masayuki 40
Tsukamoto, Takashiro **xxi**
 Tang, Rui 48
 Tang, Yinjie 18
 Tayson-Frederick, Mallory **xviii**
 Tao, Nongjian.. 26
 Tawfick, Sameh H. 122

Taylor, Crawford 82
 Traversa, Enrico 100
 Traxler, Beth 2
Treml, Benjamin **xix, 198**
 Tsen, Adam Wei 70
 Tsukagoshi, Kazuhito. 190
 Tsuya, Daiju 88
 Tuteja, Anish 106
Twigg, Stephen **xvi, 124**

U

Uchinoumi, Takeshi **xxi, 78**

V

Valentine, Megan T.. 38
 Van Zegbroeck, Bart 136
 Vanherberge, Filip 20
 Varshney, Madhukar.. 16

W

Wachter, Jeremy **xvii, 200**
Wallace, Margeaux **xv, 110**
 Wang, Bei 176
Wang, Jennifer **xx, 32**
 Wang, Jian-Ping 66
 Wang, Shan X. 28
 Wang, Weiming.. 56
Wang, Yingxia **xix, 34**
Wardwell, Clare. **xiv, 126**
 Waser, Rainer.. 156
 Watanabe, Eiichiro.. 88
Watanabe, Masaki **xxi, 36**
Watson, Erin **xvii, 38**
 Wei, Xianhe 106
 Weng, Robert 156
 Westervelt, Robert M. 194
 Williams, Dylan F. 136
 Williams, Jesse 112
 Wilson, Robert 28
Wingfield, Amber C. **xvi, 80**
 Wong, H.-S. Philip 60
 Wooten, A. Lake 32
Worley, Barrett.. **xv, 52**
 Wu, Bing.. 18
Wu, Diana **xiv, 128**

x

Xia, Younan	32
Xiong, Yujie	168
Xu, Jiajie	150
Xu, Peng	160
Xu, Wencheng	114

Y

z

Zhang, Chichang	138
Zhang, John X.J.	10
Zhang, Mingliang	28
Zhang, Qiming	124
Zhang, Yu	32
Zhu, Jun	176
Zhuang, Fei	6
Zhuo, Denys	112
Zou, Ke	176

